



2016 | Faculty of Sciences

DOCTORAL DISSERTATION

Theoretical study of the reaction mechanisms and kinetics of the oxidation processes of naphthalene and thiophene initiated by hydroxyl radicals

Doctoral dissertation submitted to obtain the degree of
Doctor of Science: Chemistry, to be defended by

Abolfazl Shiroudi

Promoter: Prof. Dr Michael S. Deleuze





2016 | Faculty of Sciences

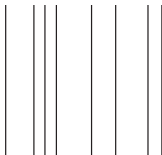
DOCTORAL DISSERTATION

Theoretical study of the reaction mechanisms and kinetics of the oxidation processes of naphthalene and thiophene initiated by hydroxyl radicals

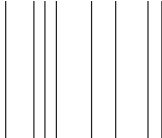
Doctoral dissertation submitted to obtain the degree of
Doctor of Science: Chemistry, to be defended by

Abolfazl Shiroudi

Promoter: Prof. Dr Michael S. Deleuze



D/2016/2451/14



Jury Members

Prof. Dr. Michael S. Deleuze (Promoter)
Hasselt University, Belgium

Prof. Dr. Karin Coninx (Chairman)
Hasselt University, Belgium

Prof. Dr. Marie-Françoise Reyniers
Ghent University, Belgium

Prof. Dr. Frank De Proft
Vrije Universiteit Brussel (VUB), Belgium

Prof. Dr. Tom Leysens
Université Catholique de Louvain, Belgium

Prof. Dr. Frédéric Bohr
Université de Reims-Champagne-Ardenne, France

Prof. Dr. Sébastien Canneaux
Lille 1 University-Science and Technology, France

Prof. Dr. Jean-Pierre François
Hasselt University, Belgium

Dr. Vincent Liégeois
University of Namur, Belgium

25th February 2016
Hasselt University, Belgium

Acknowledgments

This work would not have been possible without the encouragement and support of a number of people who were directly and indirectly involved in the completion of my PhD degree. This is the only way to express my sincere gratitude towards them.

First and foremost, I would like to express my deepest thanks to my supervisor Prof. Michael S. Deleuze for his great dedication to all his PhD students and for offering me the opportunity to start and to complete within three years only a PhD thesis on a highly exciting scientific topic, namely reaction mechanisms and chemical kinetics, and for making the whole project possible. His support and guidance have been invaluable over the last three years. I have been very fortunate to have him as my adviser, because he strongly elevated my knowledge in the fields of physical chemistry and chemical physics, more specifically quantum mechanics and statistical thermodynamics, chemical kinetics, as well as quantum and computational chemistry overall.

I would also like to thank my co-advisor: Prof. Sébastien Canneaux, from the Université de Lille1 in France, who introduced me to the field of chemical kinetics and whose help over the last three years with the KiSThELP package has been invaluable.

There are a number of people without whom completing this work would not have been possible. I would like to thank Prof. Jean-Pierre François, Dr. Filippo Morini, Dr. Reza Shojaei, Dr. Geert Jan Bex, Jon Collins, Meg Collins, and Iman Zamanzad-Ghavidel for their help.

I need to thank all of my family for their love and support. Especially my daughter Kimiya, beloved parents, Asieh and Yadollah, mother-in-law, and my sisters and brother.

And finally, to my wife, Fatemeh, Thank You. You have helped me through every step of this process. You have been my motivational force to get this done. I wish to dedicate this PhD thesis to you.

Thank you all!
Abolfazl Shiroudi
25th February 2016
Diepenbeek

Table of Contents

Chapter 1: Focus and content of the dissertation

1.1. Napthalene.....	1
1.2. Thiophene.....	7
1.3. References.....	9

Chapter 2: Theoretical methods

2.1. Introduction.....	17
2.2. Electronic Structure Theories.....	18
2.2.1. Hartree-Fock Theory.....	20
2.2.1.1. Restricted Closed-shell Hartree-Fock Theory.....	24
2.2.1.2. Restricted and Unrestricted Open-shell Hartree-Fock Theories.....	25
2.2.2. Møller-Plesset Perturbation Theory.....	27
2.2.3. Coupled Cluster Theory.....	31
2.2.4. Density Functional Theory Methods.....	32
2.2.4.1. The B3LYP Functional.....	37
2.2.4.2. The ω B97XD Exchange-correction Functional.....	38
2.2.4.3. The M05-2x Exchange-correlation Functional.....	40
2.2.4.4. The M06-2x Exchange-correlation Functional.....	41
2.2.5. Basis Sets.....	42
2.2.5.1. Minimal Basis Sets.....	43
2.2.5.2. Split Valence Basis Sets.....	44
2.2.5.3. Double Zeta Basis Sets.....	44
2.2.5.4. Polarized Basis Sets.....	45
2.2.5.5. Diffuse Functions.....	45
2.2.6. Location of Transition States.....	46
2.2.7. Composite Methods.....	47
2.2.8. The Nucleus Independent Chemical Shift Parameters.....	50
2.2.9. Bond Order Analysis.....	50
2.2.10. Natural Bond Orbital Analysis.....	51
2.3. Elements of Quantum and Statistical Thermodynamics.....	55
2.3.1. Quantum Mechanical Description of Nuclear Motions.....	55
2.3.1.1. Translations.....	56
2.3.1.2. Rotations.....	57
2.3.1.3. Vibrations.....	62
2.3.2. Elements of Statistical Thermodynamics.....	69
2.3.2.1. Partition Functions.....	69

2.3.2.2. Elements of Statistical Thermodynamics	72
2.3.2.3. Practical Calculation of Thermodynamical Quantities.....	74
2.3.2.3.1. Contribution from the Translational Motions	75
2.3.2.3.2. Contribution from the Electronic Motions	76
2.3.2.3.3. Contribution from the Rotational Motions	76
2.3.2.3.4. Contribution from the Vibrational Motions	76
2.4. Thermochemical Kinetics.....	77
2.4.1. Early Theories of Unimolecular Reactions	78
2.4.1.1. Lindemann's Theory	79
2.4.1.2. Hinshelwood's Theory	83
2.4.1.3. Slater's Theory	86
2.4.1.4. Rice-Ramsperger-Kassel Theory	87
2.4.1.5. Rice-Ramsperger-Kassel-Marcus Theory	90
2.4.2. Transition State Theory	102
2.4.3. Variational Transition State Theory	107
2.5. Tunneling Effects	110
2.6. Softwares	111
2.7. References	112

Chapter 3: Theoretical study of the oxidation mechanisms of naphthalene initiated by hydroxyl radicals: The H abstraction pathway

3.1. Introduction	123
3.2. Theory and Computational Details.....	126
3.3. Results and Discussion	129
3.3.1. Structural Characteristics of Stationary Points.....	129
3.3.2. Bond Order Analysis	134
3.3.3. Energetic and Thermodynamic Parameters.....	135
3.3.4. Kinetic Parameters	137
3.4. Conclusions	140
3.5. References	141

Chapter 4: Theoretical study of the oxidation mechanisms of naphthalene initiated by hydroxyl radicals: The OH addition pathway

4.1. Introduction	145
4.2. Theory and Computational Details.....	150
4.3. Results and Discussion	153
4.3.1. Geometry Optimizations	153
4.3.2. Energetic and Thermodynamic Parameters.....	155
4.3.3. Kinetic Parameters	160
4.3.4. Bond Order Analysis	168

4.3.5. Natural Bond Orbital Analysis	169
4.4. Conclusions	170
4.5. References	172

Chapter 5: Theoretical study of the oxidation mechanisms of naphthalene initiated by hydroxyl radicals: The O₂ addition pathway

5.1. Introduction	177
5.2. Computational Details	180
5.3. Results and Discussion	183
5.3.1. Energetic and Thermodynamic Parameters	183
5.3.2. Structural Characteristics of Stationary Points	188
5.3.3. Natural Bond Orbital Analysis	193
5.3.4. Kinetic Parameters	194
5.4. Conclusions	201
5.5. References	202

Chapter 6: Theoretical study of the oxidation mechanisms of naphthalene initiated by hydroxyl radicals: The isomerization processes of naphthalene peroxy radicals

6.1. Introduction	207
6.2. Computational Details	211
6.3. Results and Discussion	212
6.3.1. Energetic and Thermodynamic Parameters	212
6.3.2. Structural Characteristics of Stationary Points	217
6.3.3. Kinetic Parameters	220
6.4. Conclusions	224
6.5. References	225

Chapter 7: Theoretical study of the oxidation mechanisms of thiophene initiated by hydroxyl radicals

7.1. Introduction	229
7.2. Theory and Computational Details	233
7.3. Result and Discussion	236
7.3.1. Structural Analysis	236
7.3.2. Thermodynamical Analysis	240
7.3.3. Natural Bond Orbital Analysis	244
7.3.4. Kinetic Analysis	245
7.4. Conclusions	254
7.5. References	255

Chapter 8: Conclusions	261
-------------------------------------	-----

List of publications	267
List of attended conferences, poster presentations and invited lectures.....	269
Appendices	
Appendix I.....	273
Appendix II.....	275
Appendix III	283
Appendix IV	293
Appendix V	301
Samenvatting.....	313

Chapter 1

Focus and content of the dissertation

1.1. Naphthalene

The purpose of the present section is to motivate the selection of molecules and chemical reactions that are the subject of this PhD thesis. Polycyclic aromatic hydrocarbons (PAHs) refer to a class of compounds consisting of only carbon and hydrogen atoms. These compounds are key molecules in chemistry, physics, life, and material sciences. Over the past 25 years, evidence has been mounting to support the suggestions that PAHs account for a substantial fraction (10%) of all the interstellar carbon and are the carriers of interstellar IR absorption and emission bands in a wide variety of sources, including planetary and stellar nebula, the diffuse interstellar medium, as well as starburst galaxies [1–3]. Polycyclic aromatic hydrocarbons (PAHs), both neutral and charged, are ubiquitous in space [4]. They are expected to form in the C-rich ejecta of asymptotic giant branch stars – stars at the end of their life – as molecular intermediaries or byproducts of the soot formation process. The presence of PAHs in interstellar ices has been recently demonstrated by astronomical detection of their C–H stretching and out-of-plane bending modes in absorption in the spectra of stars embedded within dense nebular clouds [5]. High-molecular-weight PAHs have been recovered through hydrolysis of the carbonaceous matter contained in a giant meteorite (100 kg) that fell in Australia in 1969 [6]. These compounds and their derivatives may have, therefore, been involved in the prebiotic chemical evolution that led to the emergence of life on Earth, in the form of prokaryotic cells, some 3.5×10^9 years ago [7]. Studies of PAHs are therefore highly topical nowadays in view of the new and highly exciting field of exo-planetary research. Such studies are timely as they will result into producing data relevant to the interpretation of measurements by research facilities such as The Atacama Large Millimeter/submillimeter Array

(ALMA) and the James Webb Space Telescope (JWST), which will be launched in 2018. Closer to our daily and terrestrial concerns, PAHs represent a major environmental issue (see refs 1,8–11 and references therein) because of their varied mutagenic and carcinogenic activities [12] combined with their ubiquity as combustion products of virtually all organic substances, from the burning of fuel [13] or coal to forest fires [14]. These compounds are also known as precursors of flame produced soots [15] and fullerenes [16,17]. Last, but not least, large PAHs are very promising molecules for the manufacture of electronic devices (e.g., field effect transistors, solar cells, electroluminescent diodes) based on intrinsically well-ordered organic thin films [18] with high charge-carrier mobility [19,20].

Polycyclic aromatic hydrocarbons (PAHs) and their derivatives, such as nitrated, oxygenated, and hydroxylated PAHs are released into the atmosphere during incomplete combustion processes and account for ~20% of nonmethane hydrocarbons (NMHCs) in urban air [21]. Most of these compounds are formed by thermal decomposition (pyrolysis) and subsequent recombination of organic molecules. PAHs enter the environment through various routes and are usually found as mixtures containing two or more of these compounds, e.g., soot [22]. Since PAHs are present in gasoline as well as diesel fuels [23–26], they are also emitted as air pollutants from volatilization during fuel usage and from vehicle exhaust [23–27]. Alkylated-PAH species present in vehicle emissions are known to be largely due to unburned fuels [23,27,28]. PAHs are also manufactured, and these pure PAHs usually exist as colorless, white or pale yellow solids.

PAHs affect organisms through various toxic actions. The toxicity of PAHs is ascribed to interferences with enzyme systems associated with cellular membranes [29]. PAHs are known to be carcinogenic and mutagenic [30,31], and are potent immunosuppressants [32]. Their effects have been documented with respect to immune system development, humoral immunity, and host resistance. Therefore, PAHs have attracted much attention in recent years because of their inherent toxicity [33–37].

PAHs containing up to six fused aromatic rings are often referred to as “small” PAHs and those containing more than six aromatic rings are called “large” PAHs. In the atmosphere, PAHs containing two and three rings are found predominantly in the gas-phase, while PAHs containing six or more rings principally adsorb onto particles. PAHs with four or five rings are found in both phases [38–40]. Much research on PAHs has mainly focused on the 16 unsubstituted (parent) PAHs (Figure 1.1) due to their larger availability [33]. These compounds have therefore been designated as priority pollutants by the American (US) Environmental Protection Agency (USEPA). It is however recognized that many more PAHs are

present in environmental samples [41,42], some of which have equal or greater toxicity than the 16 parent PAHs [43].

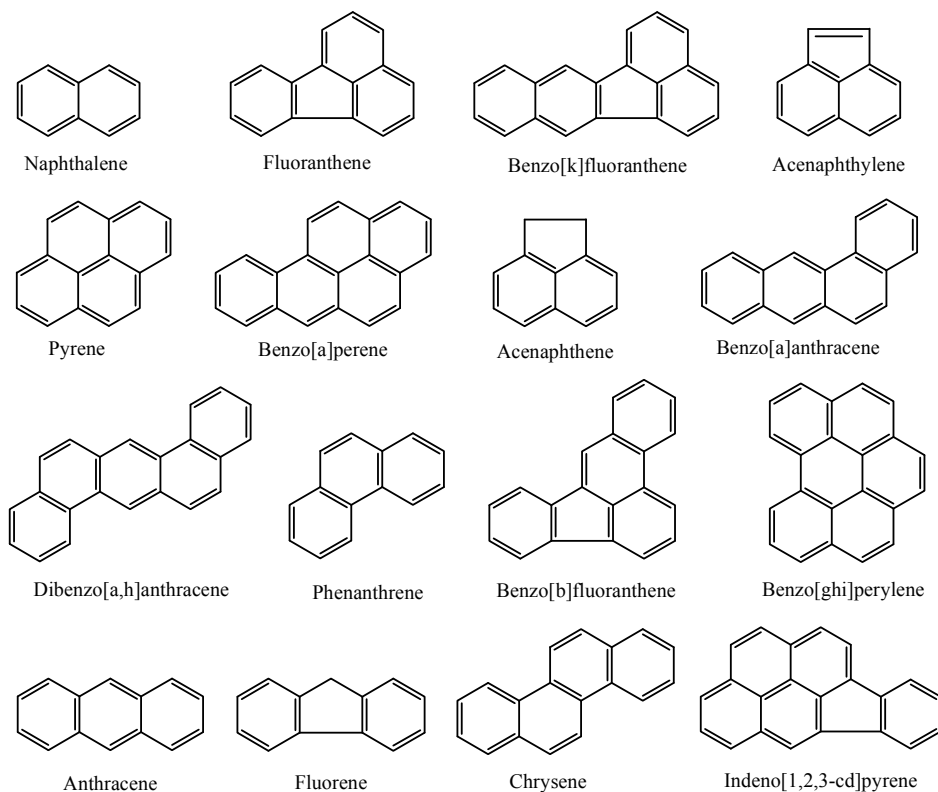


Figure 1.1. Chemical structures of the 16 PAHs polycyclic aromatic hydrocarbons [42]

In the gas-phase, PAHs can be chemically transformed via reaction with tropospheric gases such as hydroxyl radicals (OH^\bullet), ozone (O_3), and nitrate radicals (NO_3^\bullet) [38,44] (Figure 1.2). These reactions are known to produce a range of products [38,44–47] which have adverse effects on human health [33], as well as secondary organic aerosols (SOAs) [32,48]. Despite their importance in polluted environments, our knowledge and understanding of the mechanisms for the atmospheric degradation of PAHs is far from complete [38,44]. In the troposphere, the major atmospheric loss process for semi-volatile PAHs is expected to be by gas-phase reaction with OH radicals [49,50]. Photooxidation of PAHs produces more hydrophilic oxygenated compounds with higher molecular weights and

even lower vapor pressures, contributing significantly to SOA formation. Nitrated-PAHs, which generally exhibit higher mutagenicity and carcinogenicity than the parent PAHs, are also generated from atmospheric reactions of PAHs released into the gas-phase with radical species such as OH• and NO₃• radicals, as well as nitrogen oxides [33,45,51,52]. Among all known oxidants, it is now well established that hydroxyl radicals play a leading role in both combustion and atmospheric chemistry [53–62]. Accurate determination of the kinetics of hydroxyl radical reactions and the elucidation of their mechanisms and products have been the focus of a large number of experimental investigations.

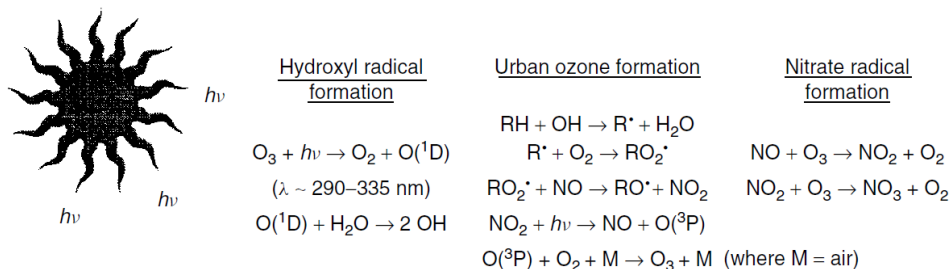


Figure 1.2. Photochemical formation of reactive radicals and ozone

Naphthalene is the smallest PAH. This is also the most volatile and abundant PAH in urban areas. This compound is reactive at ambient temperature and pressure [63,64]. Reactions of naphthalene in the atmosphere often yield degradation products which may be more carcinogenic and more mutagenic than the other PAHs. Unsurprisingly therefore, the atmospheric reactions of naphthalene have been subject of considerable attention [65]. It is indeed of utmost importance to understand the degradation mechanisms of naphthalene in the presence of oxidant species [66–70]. Naphthalene and its alkyl derivatives occur naturally in coal tar and petroleum residues, as well as crude oil and natural gas and enter the atmosphere by evaporation during storage, transport, and refining processes [71]. An important source of these compounds in urban areas is vehicle exhaust, especially from diesel-fueled vehicles [71–76]. In urban areas, naphthalene and alkylnaphthalene concentrations that are significantly higher than those of particle-associated PAHs have been observed [63,64,77].

In the atmosphere, naphthalene and its methyl and ethyl derivatives are the most abundant aromatic hydrocarbons among all known PAHs [38,78,79]. These alkylnaphthalenes are sufficiently volatile to be present essentially entirely in the gas-phase in the lower troposphere [80–82]. The oxidation of naphthalene in the

atmosphere is initiated by OH• and NO₃• radicals. In the atmosphere, naphthalene and alkylnaphthalenes react with OH• radicals during daylight hours and with NO₃• radicals during the evening and nighttime hours [38,82–84]. Table 1.1 gives rate constants for the reactions of OH• and NO₃• radicals at room temperature with these PAHs.

Table 1.1. Room temperature rate constants k (cm³ molecule⁻¹ s⁻¹) for the reaction of OH• and NO₃• radicals with naphthalene and alkylnaphthalenes [44,85].

PAH	Reaction with OH•	Reaction with NO ₃ •
	$k \times 10^{12}$	$k \times 10^{28} [\text{NO}_2]$
Naphthalene	23.9	3.65
1-Methylnaphthalene	40.9	7.15
2-Methylnaphthalene	48.6	10.2
1-Ethylnaphthalene	36.4	9.82
2-Ethylnaphthalene	40.2	7.99
1,2-Dimethylnaphthalene	59.6	64.0
1,3-Dimethylnaphthalene	74.9	21.3
1,4-Dimethylnaphthalene	57.9	13.0
1,5-Dimethylnaphthalene	60.1	14.1
1,6-Dimethylnaphthalene	63.4	16.5
1,7-Dimethylnaphthalene	67.9	13.5
1,8-Dimethylnaphthalene	62.7	212
2,3-Dimethylnaphthalene	61.5	15.2
2,6-Dimethylnaphthalene	66.5	21.2
2,7-Dimethylnaphthalene	68.7	21.0

Table 1.2 gives the calculated tropospheric lifetimes due to reaction with OH• and NO₃• radicals using a 12-hr average daytime OH• radical concentration of 2×10^6 molecule cm⁻³ [86,87], and a 12-hr average nighttime NO₃• radical concentration of 5×10^8 molecule cm⁻³ [66]. Note that the calculated lifetimes are inversely proportional to the assumed OH• or NO₃• radical concentrations. It is worth noticing that the major sources of OH• radicals in the troposphere are photolytic and hence the OH• radical concentrations depend on a number of factors including time of day, the season and latitude, and the cloud cover. NO₃• radical concentrations are highly spatially and temporally variable with the measured maximum nighttime concentrations varying from $< 5 \times 10^7$ molecule cm⁻³ up to 1×10^{10} molecule cm⁻³ [88]. The reported lifetimes in Table 1.2 indicate that the

OH• radical reactions are the dominant atmospheric loss processes for naphthalene and its alkyl derivatives.

Table 1.2. Ranges of tropospheric lifetimes for naphthalene and alkylnaphthalenes calculated for their reactions with OH• and NO₃• radicals [44].

Aromatic	Lifetime due to reaction with	
	OH• radical ^a	NO ₃ • radical ^b
Naphthalene	5.8 hr	52 day ^c
Methylnaphthalene	2.9–3.4 hr	18–26 day ^c
Dimethylnaphthalene	1.9–2.4 hr	0.9–14 day ^c

^a Calculated using a 12-hr daytime average OH• radical concentration of 2×10^6 molecule cm^{-3} [86,87].

^b Calculated using a 12-hr nighttime average NO₃• radical concentration of 5×10^8 molecule cm^{-3} [85].

^c Reaction rate also depends on the NO₂ concentration. Lifetimes have been calculated using an average NO₂ concentration of 2.46×10^{12} molecule cm^{-3} (100 ppbv mixing ratio), which would represent a heavily polluted airmass.

Rate constant measurements suggest that the reactions of OH radicals with naphthalene are of importance to both photochemical air pollution and hydrocarbon flame chemistry [89]. The reaction with singlet oxygen is competitive only under UV (< 290 nm) radiation [90]. Reaction mechanisms for the OH-initiated oxidation of naphthalene have been suggested in experimental studies by identifying and analyzing a small fraction of reaction products. However, only a fraction of gas-phase products and 53–68 % of the SOA mass have been characterized chemically even in the most recent experimental study, by Kautzman *et al.*, due to technical difficulties [91]. A long list of stable closed-shell intermediates and products have been identified in simulating smog chambers and ambient particulate matters [21,45,91–96]. However, the detailed mechanism in forming these compounds remains highly ambiguous because of the existence of multiple possible reaction steps and pathways. Experimentally, the main difficulty in deducing the reaction mechanism is that no radical intermediate has been detected directly in the gas-phase reaction of naphthalene, although the UV/Vis absorption of naphthalene-OH adducts was observed following the photolysis of naphthalene in the solution phase [97]. Reaction pathways similar to those suggested for the oxidation of benzene [98–106] have been retained to interpret the formation of products such as glyoxal, dicarbonyl, naphthoquinone, 2-formylcinnamaldehyde with, however, not much verification.

Theoretical studies are needed for understanding the oxidation mechanism by examining the energetics of radical intermediates and the kinetics of key elementary reaction steps [100,107]. Little effort has been made so far to interpret the production of the various observed compounds. In this thesis, we present a theoretical investigation on the reaction of hydroxyl radicals with naphthalene and the ensuing reactions, focusing on some key reaction steps, such as hydrogen abstraction from naphthalene (**Chapter 3**), OH[•] addition to naphthalene (**Chapter 4**), O₂ addition to naphthalene-OH adducts (**Chapter 5**), and isomerization of the resulting peroxy radicals (**Chapter 6**). Prior to these studies, a detailed survey of all employed theoretical methods is given in **Chapter 2**.

1.2. Thiophene

A variety of natural processes contribute to sulfur emission directly into the atmosphere, such as volcanic eruptions, bacterial processes, decaying organisms, and through the evaporation of water from the oceans (Figure 1.3). When sulfur dioxide enters the atmosphere, it reacts with oxygen to produce sulfur trioxide gas, or with other chemicals to produce sulfur salts. Sulfur dioxide can also react with water to produce sulfuric acid. All these compounds will eventually settle back onto the earth, or react with rain and fall back to earth as acid deposition. These pollutants will then be absorbed by plants, and the sulfur cycle will start over again (Figure 1.3). In recent years, studies of the atmospheric sulfur cycle have become important as a result of the increase of sulfur emissions due to human activities [108]. Increasing emissions of sulfur compounds into the atmosphere due to fossil fuel refining and combustion produce acid rains [109]. If overall man-made emissions increase, they may reach or exceed natural ones in the next few years [110,111].

The limitation of the sulfur content in diesel fuels has become more stringent all around the world. Much emphasis has been put on the use of clean diesel fuels by most countries [112–114]. Sulfur compounds present in liquid fuels may possibly be changed into SO_x in fuel engines which pollutes the air and causes acid rain. The combustion efficiency of fuels may be reduced by sulfur compounds, which destroy the active catalyst, and promote further the emissions of pollutants. Hence, reducing the content in sulfur as much as possible in order to produce clean sulfur fuels is a substantial task but essential requirement [115].

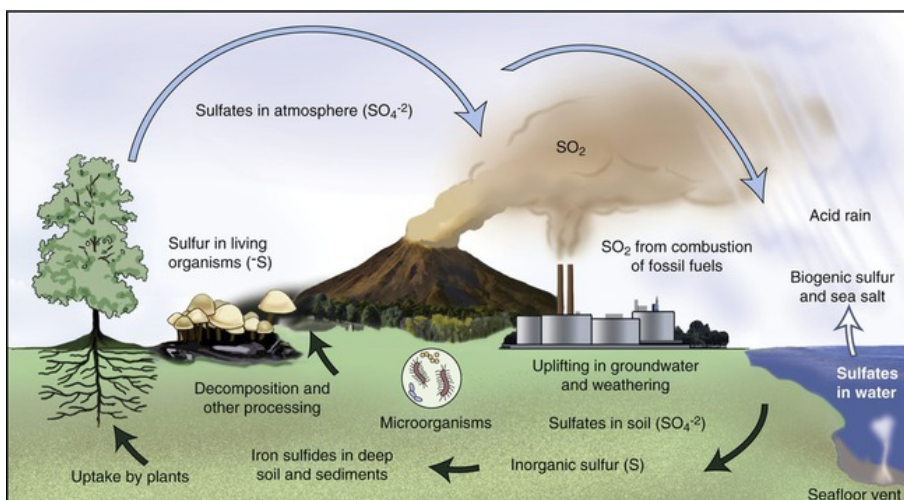


Figure 1.3. The sulfur cycle

Polycyclic aromatic sulfur heterocycles (PASHs) share the carcinogenic and/or mutagenic properties of their parent PAHs [116–119]. It is well-known that subtle changes in the skeleton or alkylation pattern of aromatic compounds can have an extreme influence on their carcinogenic potential. This observation has led to a demand for improved identification and quantitation of such compounds in fuels and in the environment.

PASHs occur as widespread as and, as a matter of fact, nearly always together with the PAHs which they resemble in many respects. Thus, they are present in most petroleum and coal products, combustion products, sediments, air particulates, organisms inhabiting polluted water, etc. [120–122]. There is a considerable interest in the removal of sulfur from fossil fuels in order to decrease sulfur dioxide emissions. The presence of sulfur compounds in fuels is undesirable also from the viewpoint of catalyst poisoning during refining and, consequently, desulfurization processes are a very active research area. Many experiments suggest that aromatics are the most difficult compounds to desulfurize [123].

Among the reduced sulfur compounds released into the atmosphere from both natural and industrial sources, natural emissions of COS , H_2S and CH_3SCH_3 dominate, but other species like thiophene, tetrahydrothiophene and diethylsulfide have also to be considered [124]. Kinetic and mechanistic data for the reactions of sulfur compounds such as thiophene with important oxidant species like OH^\bullet , O_3 , and NO_3^\bullet are required in order to evaluate their atmospheric residence times as well as the ultimate fates of these compounds [53,125–135]. Since during day-time the major gas-phase chemical loss processes in the atmosphere are via reactions

with O₃ and OH• radicals, kinetic and mechanistic data for these reactions are especially needed in order to develop physico-chemical models of atmospheric pollution [133–135].

An important step in the oxidation of sulfur compounds after release into the atmosphere from both natural and anthropogenic sources involves reactions with OH• radicals [33,136], which play a key role in determining the oxidation power of the atmosphere [137]. Determining the rate constant for these reactions will contribute to a better understanding of sulfur cycle in the atmosphere [108]. Moreover, studies of the mechanisms of these reactions can give some information on the further oxidation steps which lead to SO₂ and sulfates. Thiophene may become of increasing importance both in combustion and in atmospheric chemistry as a result of the development of new energy technologies related to conversion or combustion of coal, shale oil and petroleum [138,139]. Specially, the kinetics of the oxidation reaction of thiophene by OH radicals has to be quantified in order to estimate the lifetime of this compound in the atmosphere. The reaction mechanism and kinetics of OH• addition processes onto thiophene will be the subject of **Chapter 7**.

1.3. References

- [1] A. Leger, L. D'hendecourt, N. Boccara, *Polycyclic Aromatic Hydrocarbons and Astrophysics*; Reidel: Dordrecht: Netherlands, 1987.
- [2] (a) M.K. Crawford, A.G.G.M. Tielens, L.J. Allamandola, *Astrophys. J.*, **1985**, 293, L45; (b) L.J. Allamandola, S.A. Sanford, B. Wopencka, *Science*, **1987**, 237, 56; (c) L.J. Allamandola, A.G.G.M. Tielens, J.R. Barker, *Astrophys. J. Suppl. Ser.*, **1989**, 71, 733; (d) J.L. Puget, A. Leger, *Annu. Rev. Astron. Astrophys.*, **1989**, 27, 161; (e) L.J. Allamandola, *Top. Curr. Chem.*, **1990**, 1; (f) F. Salama, L.J. Allamandola, *Astrophys. J.*, **1992**, 395, 301; (g) D.K. Bohme, *Chem. Rev.*, **1992**, 92, 1487; (h) F. Salama, L.J. Allamandola, *J. Chem. Soc., Faraday Trans.*, **1993**, 89, 2277; (i) J. DeFrees, M.D. Miller, D. Talbi, F. Pauzat, Y. Ellinger, *Astrophys. J.*, **1993**, 408, 503; (j) S.J. Clemett, C.R. Maechling, R.N. Zare, P.D. Swan, R.M. Walker, *Science*, **1993**, 262, 721; (k) F. Salama, C. Joblin, L.J. Allamandola, *J. Chem. Phys.*, **1994**, 101, 10252; (l) S.R. Langhoff, *J. Phys. Chem.*, **1996**, 100, 2819; (m) L.J. Allamandola, D.M. Hudgins, S.A. Sanford, *Astrophys. J.*, **1999**, 511, L115; (n) W.W. Duley, S.S. Seahra, *Astrophys. J.*, **1999**, 522, L129; (o) D.M. Hudgins, C.W. Bauschlicher, L.J. Allamandola, J.C. Fetzer, *J. Phys. Chem. A*, **2000**, 104, 3655.

- [3] J. Szczepanski, M. Vala, *Astrophys. J.*, **1993**, 414, 646; (b) J. Szczepanski, M. Vala, *Nature*, **1993**, 363, 699; (c) D.M. Hudgins, S.A. Sandford, L.J. Allamandola, *J. Phys. Chem.*, **1994**, 98, 4243; (d) D.M. Hudgins, L.J. Allamandola, *J. Phys. Chem.*, **1995**, 99, 8978.
- [4] A.G.G.M. Tielens, *The Physics and Chemistry of the Interstellar Medium*; Cambridge University Press: Cambridge, UK, 2005.
- [5] (a) K. Sellgren, T.Y. Brooke, R.G. Smith, T.R. Geballe, *Astrophys. J.*, **1995**, 449, L69; (b) T.Y. Brooke, K. Sellgren, T.R. Geballe, *Astrophys. J.*, **1999**, 517, 883. (c) J.D. Bregman, T.L. Hayward, G.C. Sloan, *Astrophys. J.*, **2000**, 544, L75; (d) J.E. Chiar, A.G.G.M. Tielens, D.C.B. Whittet,; W.A. Schutte, A.C.A. Boogert, D. Lutz, E.F. van Dishoeck, M.P. Bernstein, *Astrophys. J.*, **2000**, 537, 749.
- [6] M.A. Sephton, G.D. Love, J.S. Watson, A.B. Verchovsky, I.P. Wright, C.E. Snape, I. Gilmour, *Geochim. Cosmochim. Acta*, **2004**, 68, 1385.
- [7] M.P. Bernstein, J.P. Dworkin, S.A. Sanford, L.J. Allamandola, *Adv. Space Res.*, **2002**, 1510, 30.
- [8] H. Hopf, *Classics in Hydrocarbon Chemistry*; Wiley-VCH: Weinheim: Germany, 2000.
- [9] R.I. Frundental, P.W. Jones, *Polynuclear Aromatic Hydrocarbons*; Raven: New York, 1976.
- [10] R.A. Hites, W.J. Simonsick Jr., *Calculated Properties of Polycyclic Aromatic Hydrocarbons*; Elsevier: New York, 1987.
- [11] R.M. Harrison, *Understanding our Environment: An Introduction to Environmental Chemistry and Pollution*; 2nd Ed., Royal Society of Chemistry: Cambridge, U.K., 1992.
- [12] H. Busch, *The Molecular Biology of Cancer*; Academic: New York, 1974.
- [13] J. Ahrens, A. Keller, R. Kovacs, K.-H. Homann, *Ber. Bunsen-Ges. Phys. Chem.*, **1998**, 102, 1823 and references therein.
- [14] M. Fang, M. Zheng, F. Wang, K.L. To, A.B. Jaafar, S.L. Tong, *Atmos. Environ.*, **1999**, 33, 783.
- [15] S.H. Bauer, P.M. Jeffers, *Energy Fuels*, **1988**, 2, 446.
- [16] H.W. Kroto, J.E. Fischer, D.E. Cox, *The Fullerenes*; Pergamon: Oxford, U.K., 1993.
- [17] (a) H.W. Kroto, A.W. Alaf, S.P. Balm, *Chem. Rev.*, **1991**, 91, 1213; (b) R.F. Curl, *Nature*, **1993**, 363, 14.
- [18] S. Verlaak, S. Steudel, P. Heremans, D. Janssen, M.S. Deleuze, *Phys. Rev. B*, **2003**, 68, 195409.
- [19] (a) T. Minakata, H. Imai, M. Ozaki, *J. Appl. Phys.*, **1992**, 72, 4178; (b) A.R. Brown, A. Pomp, C.M. Hart, D.M. de Leeuw, *Science*, **1995**, 270, 972; (c) A.

- Dodabalapur, J. Laquidano, H.E. Katz, Z. Bao, *Appl. Phys. Lett.*, **1996**, *69*, 4227. (d) C.D. Dimitrakopoulos, S. Purishotoman, J. Kymissis, A. Callegari, J.M. Shaw, *Science*, **1999**, *283*, 822. (e) S. Verlaak, V. Arkhipov, P. Heremans, *Appl. Phys. Lett.*, **2003**, *82*, 745.
- [20] R. Farchioni, G. Grosso, *Organic Electronic Materials: Conjugated Polymers and Low Molecular Weight Solids*; Springer: New York, 2001.
- [21] N. Nishino, R. Atkinson, J. Arey, *Environ. Sci. Technol.*, **2008**, *42*, 9203.
- [22] A.L. Robinson, N.M. Donahue, M.K. Shrivastava, E.A. Weitkamp, A.M. Sage, A.P. Grieshop, T.E. Lane, J.R. Pierce, S.N. Pandis, *Science*, **2007**, *315*, 1259.
- [23] P.T. Williams, M.K. Abbass, G.E. Andrews, K.D. Bartle, *Combust. Flame.*, **1989**, *75*, 1.
- [24] S.K. Hoekman, *Environ. Sci. Technol.*, **1992**, *26*, 1206.
- [25] L.C. Marr, T.W. Kirchstetter, R.A. Harley, A.H. Miguel, S.V. Hering, S.K. Hammond, *Environ. Sci. Technol.*, **1999**, *33*, 3091.
- [26] B. Zielinska, J. Sagebiel, J.D. McDonald, K. Whitney, D.R. Lawson, *J. Air & Waste Manage. Assoc.*, **2004**, *54*, 1138.
- [27] M.P. Fraser, G.R. Cass, B.R.T. Simoneit, *Environ. Sci. Technol.*, **1998**, *32*, 2051.
- [28] P.J. Tancell, M.M. Rhead, R.D. Pemberton, J. Braven, *Environ. Sci. Technol.*, **1995**, *29*, 2871.
- [29] J.H. Kroll, A.W.H. Chan, N.L. Ng, R.C. Flagan, J.H. Seinfeld, *Environ. Sci. Technol.*, **2007**, *41*, 3545.
- [30] D. Schuetzle, *Environ. Health Perspect.*, **1983**, *47*, 65.
- [31] I.T. Salmeen, A.M. Pero, R. Zator, D. Schuetzle, T.L. Riley, *Environ. Sci. Technol.*, **1984**, *18*, 375.
- [32] K.M. Shakya, R.J. Griffin, *Environ. Sci. Technol.*, **2010**, *44*, 8134.
- [33] R. Atkinson, J. Arey, *Environ. Health Perspect.*, **1994**, *102*, 117.
- [34] M.P. Hannigan, G.R. Cass, *Environ. Sci. Technol.*, **1998**, *32*, 3502.
- [35] R.A. Hites, *Acc. Chem. Res.*, **1990**, *23*, 196.
- [36] H. Tokiwa, Y. Ohnishi, *CRC Crit. Rev. Toxicol.*, **1986**, *17*, 23.
- [37] P.D. Josephy, B. Mannervik, P.O. de Montellano, *Molecular Toxicology*; Oxford University Press: Oxford, UK, 1997.
- [38] J.G. Calvert, R. Atkinson, K.H. Becker, R.M. Kamens, J.H. Seinfeld, T.J. Wallington, G. Yarwood, *The Mechanisms of Atmospheric Oxidation of Aromatic Hydrocarbons*; Oxford University Press: Oxford, 2002.
- [39] B.J. Finlayson-Pitts, J.N. Pitts, *Chemistry of the Upper and Lower Atmosphere*; Academic Press: San Diego, 2000.
- [40] K. Ravindra, R. Sokhi, R.V. Grieken, *Atmos. Environ.*, **2008**, *42*, 2895.

- [41] J.C. Means, *J. AOAC Int.*, **1998**, *81*, 657.
- [42] S.M. Bamforth, I. Singleton, *J. Chem. Technol. Biot.*, **2005**, *80*, 723.
- [43] F.I. Onuska, *Analysis of Polycyclic Aromatic Hydrocarbons in Environmental Samples*, In: B.K. Afghan, A.S.Y. Chau (Eds.), *Analysis of Trace Organics in the Aquatic Environment*, CRC Press: Florida, pp. 205–241, 1989.
- [44] R. Atkinson, J. Arey, *Polycycl. Aromat. Comp.*, **2007**, *27*, 15.
- [45] J. Sasaki, S.M. Aschmann, E.S.C. Kwok, R. Atkinson, J. Arey, *Environ. Sci. Technol.*, **1997**, *31*, 3173.
- [46] F. Reisen, J. Arey, *Environ. Sci. Technol.*, **2002**, *36*, 4302.
- [47] J. Lee, D.A. Lane, *Atmos. Environ.*, **2010**, *44*, 2469.
- [48] A.W.H. Chan, K.E. Kautzmanm, P.S. Chhabra, J.D. Surratt, M.N. Chan, J.D. Crouse, A. Kürten, P.O. Wennberg, R.C. Flagan, J.H. Seinfeld, *Atmos. Chem. Phys.*, **2009**, *9*, 3049.
- [49] R. Atkinson, *J. Phys. Chem. Ref. Data, Monograph*, **1994**, *2*, 1.
- [50] R. Atkinson, *Atmos. Environ.*, **2000**, *34*, 2063.
- [51] B. Zielinska, J. Arey, R. Atkinson, T. Ramdahl, A.M. Winer, *Atmos. Environ.*, **1989**, *23*, 223.
- [52] P. Ciccioli, A. Cecinato, E. Brancaleoni, M. Frattoni, P. Zacchei, A.H. Miguel, P.D.C. Vasconcellos, *J. Geophys. Res.*, **1996**, *101*, 19567.
- [53] R. Atkinson, K.R. Darnall, A.C. Lloyd, A.M. Winer, J.N. Pitts, Jr., *Adv. Photochem.*, **1979**, *11*, 375.
- [54] J.A. Logan, M.J. Prather, S.C. Wofsy, M.B. McElroy, *J. Geophys. Res.*, **1981**, *86*, 7210.
- [55] R. Atkinson, A.C. Lloyd, *J. Phys. Chem. Ref. Data*, **1984**, *13*, 315.
- [56] R. Atkinson, D.C. Bull, P. Shuff, *Combust. Flame.*, **1980**, *39*, 287.
- [57] C.K. Westbrook, *Combust. Flame.*, **1982**, *46*, 191.
- [58] C.K. Westbrook, *Combust. Sci. Technol.*, **1982**, *29*, 67.
- [59] P.W. Fairchild, G.P. Smith, D.R. Crosley, *19th International Symposium on Combustion*, The Combustion Institute, pp. 107–115, 1982.
- [60] C.K. Westbrook, F.L. Dryer, K.P. Schug, *19th International Symposium on Combustion*, The Combustion Institute, pp. 153–166, 1982.
- [61] J.A. Miller, R.E. Mitchell, M.D. Smooke, R.J. Kee, *19th International Symposium on Combustion*, The Combustion Institute, pp. 181–196, 1982.
- [62] J. Warnatz, H. Bockhorn, A. Möser, H.W. Wenz, *19th International Symposium on Combustion*, The Combustion Institute, pp. 197–209, 1982.
- [63] J. Arey, B. Zielinska, R. Atkinson, A.M. Winer, *Atmos. Environ.*, **1987**, *21*, 1437.

- [64] J. Arey, R. Atkinson, B. Zielinska, P.A. McElroy, *Environ. Sci. Technol.*, **1989**, 23, 321.
- [65] J.L. Durant, A.L. Lafleur, E.F. Plummer, K. Taghizadeh, W.F. Busby Jr., W.G. Thilly, *Environ. Sci. Technol.*, **1998**, 32, 1894.
- [66] R. Atkinson, *J. Phys. Chem. Ref. Data*, **1991**, 20, 459.
- [67] W.W. Brubaker, R.A. Hiter Jr., *J. Phys. Chem. A*, **1998**, 102, 915.
- [68] J. Arey, B. Zielinska, R. Atkinson, S.M. Aschmann, *Int. J. Chem. Kinet.*, **1989**, 21, 775.
- [69] R. Atkinson, E.C. Tuazon, J. Arey, *Int. J. Chem. Kinet.*, **1990**, 22, 1071.
- [70] R. Atkinson, E.C. Tuazon, I. Bridier, J. Arey, *Int. J. Chem. Kinet.*, **1994**, 26, 605.
- [71] X. Qu, Q. Zhang, W. Wang, *Chem. Phys. Lett.*, **2006**, 432, 40.
- [72] P.T. Williams, K.D. Bartle, G.E. Andrews, *Fuel*, **1986**, 65, 1150.
- [73] P.F. Nelson, *Fuel*, **1989**, 68, 283.
- [74] J. Bundt, W. Herbel, H. Steinhart, S. Franke, W. Francke, *J. High Resolut. Chromatogr.*, **1991**, 14, 91.
- [75] B. Zielinska, J.C. Sagebiel, G. Harshfield, A.W. Gertler, W.R. Pierson, *Atmos. Environ.*, **1996**, 30, 2269.
- [76] T.J. Truex, J.M. Norbeck, M.R. Smith, J. Arey, N. Kado, B. Okamoto, *Evaluation of Factors That Affect Diesel Exhaust Toxicity*, Contract No. 94-312, Final Report to California Air Resources Board, 1998.
- [77] R. Atkinson, J. Arey, A.M. Winer, B. Zielinska, *A Survey of Ambient Concentrations of Selected Polycyclic Aromatic Hydrocarbons (PAHs) at Various Locations in California*, Contract No. A5-185-32, Final Report to California Air Resources Board, 1988.
- [78] F. Reisen, S. Wheeler, J. Arey, *Atmos. Environ.*, **2003**, 37, 3653.
- [79] F. Reisen, J. Arey, *Environ. Sci. Technol.*, **2005**, 39, 64.
- [80] T.F. Bidleman, *Environ. Sci. Technol.*, **1988**, 22, 361.
- [81] F. Wania, D. Mackay, *Environ. Sci. Technol.*, **1996**, 30, A390.
- [82] J. Arey, R. Atkinson, *Photochemical Reactions of PAHs in the Atmosphere*. In: P.E.T. Douben (Ed.) *PAHs: An Ecotoxicological Perspective*, Wiley: West Sussex Ltd., pp.47–63, 2003.
- [83] R. Atkinson, J. Arey, *Chem. Rev.*, **2003**, 103, 4605.
- [84] J. Arey, *Atmospheric Reactions of PAHs Including Formation of Nitroarenes*. In: O. Hutzinger, A.H. Neilson (Ed.) *The Handbook of Environmental Chemistry*, Vol. 3, Springer-Verlag: Berlin, pp. 347–385, 1998.
- [85] P.T. Phouongphouang, J. Arey, *Environ. Sci. Technol.*, **2002**, 36, 1947.
- [86] M. Krol, J. Lelieveld, *J. Geophys. Res.*, **2003**, 108, 4125.

- [87] R.G. Prinn, J. Huang, R.F. Weiss, D.M. Cunnold, P.J. Fraser, P.G. Simmonds, A. McCulloch, C. Harth, P. Salameh, S. O'Doherty, R.H.J. Wang, L. Porter, B.R. Miller, *Science*, **2001**, 292, 1882.
- [88] R. Atkinson, A.M. Winer, J.N. Pitts Jr., *Atmos. Environ.*, **1986**, 20, 331.
- [89] T.E. Graedel, *Chemical Compounds in the Atmosphere*; Academic Press: New York, 1978.
- [90] D.A. Lane, S.S. Fielder, S.J. Townsend, *Polycyclic Aromat. Compd.*, **1999**, 14/15, 129.
- [91] K.E. Kautzman, J.D. Surratt, M.N. Chan, A.W.H. Chan, S.P. Hersey, P.S. Chhabra, N.F. Dalleska, P.O. Wennberg, R.C. Flagan, J.H. Seinfeld, *J. Phys. Chem. A*, **2010**, 114, 913.
- [92] L. Wang, R. Atkinson, J. Arey, *Environ. Sci. Technol.*, **2010**, 44, 2981.
- [93] D.A. Lane, J. Lee, *Polycyclic Aromat. Compd.*, **2010**, 30, 309.
- [94] N. Nishino, J. Arey, R. Atkinson, *Environ. Sci. Technol.*, **2009**, 43, 8554.
- [95] L. Wang, R. Atkinson, J. Arey, *Environ. Sci. Technol.*, **2007**, 41, 2803.
- [96] N. Nishino, J. Arey, R. Atkinson, *Environ. Sci. Technol.*, **2009**, 43, 1349.
- [97] B. Ouyang, H. Fang, W. Dong, H. Hou, *J. Photochem. Photobiol., A*, **2006**, 181, 348.
- [98] J.G. Calvert, R. Atkinson, K.H. Becker, R.M. Kamens, J.H. Seinfeld, T.J. Wallington, G. Yarwood, *The Mechanisms of Atmospheric Oxidation of the Aromatic Hydrocarbons*; Oxford University Press: Oxford, 2002.
- [99] D.R. Glowacki, L. Wang, M.J. Pilling, *J. Phys. Chem. A*, **2009**, 113, 5385.
- [100] J.M. Andino, A. Vivier-Bunge, *Adv. Quantum Chem.*, **2008**, 55, 297.
- [101] B. Bohn, C. Zetzsch, *Phys. Chem. Chem. Phys.*, **1999**, 1, 5097.
- [102] G. Ghigo, G. Tonachini, *J. Am. Chem. Soc.*, **1998**, 120, 6753.
- [103] G. Ghigo, G. Tonachini, *J. Am. Chem. Soc.*, **1999**, 121, 8366.
- [104] D. Johnson, S. Raoult, M.-T. Rayez, J.-C. Rayez, R. Lesclaux, *Phys. Chem. Chem. Phys.*, **2002**, 4, 4678.
- [105] B. Klotz, R. Volkamer, M.D. Hurlet, M.P.S. Andersen, O.J. Nielsen, I. Barnes, T. Imamura, K. Wirtz, K.-H. Becker, U. Platt, T.J. Wallington, N. Washida, *Phys. Chem. Chem. Phys.*, **2002**, 4, 4399.
- [106] S. Raoult, M.-T. Rayez, R. Lesclaux, *Phys. Chem. Chem. Phys.*, **2004**, 6, 2245.
- [107] J. Zhao, R. Zhang, *Adv. Quantum Chem.*, **2008**, 55, 177.
- [108] H. MacLeod, J.L. Jourdain, G. Poulet, G. Le Bars, *Atmos. Environ.*, **1984**, 18, 2621.
- [109] D. Martin, J.L. Jourdain, G. Le Bras, *Int. J. Chem. Kinet.*, **1985**, 17, 1247.
- [110] D. Möller, *Atmos. Environ.*, **1984**, 18, 19.
- [111] C.F. Cullis, M.M. Hirschler, *Atmos. Environ.*, **1980**, 14, 1263.

- [112] United States Environmental Protection Agency (U.S. EPA). Diesel Fuel; U.S. EPA: Washington, D.C., 2011; <http://www.epa.gov/otaq/fuels/diesel-fuels/index.htm>.
- [113] European Standards Organization (CEN). European Union Fuel Regulations; CEN: Brussels, Belgium, 2010; <http://www.dieselnet.com/standards/eu-fuel.php>.
- [114] C.S. Song, *Catal. Today.*, **2003**, 86, 211.
- [115] G. Yu, J. Zhao, D. Song, C. Asumana, X. Zhang, X. Chen, *Ind. Eng. Chem. Res.*, **2011a**, 50, 11690.
- [116] J.T. Andersson, B. Schmid, *J. Chromatogr. A*, **1995**, 693, 325.
- [117] T. MacFall, G.M. Booth, M.L. Lee, Y. Tominaga, R. Pratap, M. Tedjamulia, R.N. Castle, *Mutat. Res.*, **1984**, 135, 97.
- [118] S.G. Mössner, S.A. Wise, *Anal. Chem.*, **1999**, 71, 58.
- [119] J. Jacob, *Sulfur Analogues of Polycyclic Aromatic Hydrocarbons (Thiaarenes)*; Cambridge University Press: Cambridge, 1990.
- [120] W. Brack, A. Schirmer, *Environ. Sci. Technol.*, **2003**, 37, 3062.
- [121] U. Thuß, P. Popp, C. Ehrlich, W.-D. Kalkoff, *J. High. Res. Chromatog.*, **2000**, 23, 457.
- [122] N.E. Moustafa, J.T. Andersson, *Fuel. Process. Technol.*, **2011**, 92, 547.
- [123] J.T. Andersson, *Int. J. Environ. Anal. Chem.*, **1992**, 48, 1.
- [124] G. Mouvier, P. Carlier, *Physico Chemical Behavior of Atmospheric Pollutants*; 3rd European Symposium, Varese, Italy, 10–12 April, 1984.
- [125] R. Atkinson, R.A. Perry, J.N. Pitts Jr., *J. Chem. Phys.*, **1979**, 66, 1578.
- [126] R. Atkinson, R.A. Perry, J.N. Pitts Jr., *Chem. Phys. Lett.*, **1978**, 54, 14.
- [127] M.J. Kurylo, *Chem. Phys. Lett.*, **1978**, 58, 233.
- [128] R.A. Cox, D. Sheppard, *Nature*, **1980**, 284, 330.
- [129] P.H. Wine, N.M. Kreutter, C.A. Gump, A.R. Ravishankara, *J. Phys. Chem.*, **1981**, 85, 2660.
- [130] J.H. Lee, I.N. Tang, *J. Chem. Phys.*, **1983**, 78, 6646.
- [131] H. MacLeod, G. Poulet, G. Le Bras, *J. Chim. Phys.*, **1983**, 80, 287.
- [132] R. Atkinson, J.N. Pitts Jr, S.M. Aschmann, *J. Phys. Chem.*, **1984**, 88, 1584.
- [133] B.J. Finlayson-Pitts, J.N. Pitts Jr., *Adv. Environ. Sci. Technol.*, **1977**, 7, 75.
- [134] D.G. Hendry, R.A. Kenley, *Atmospheric Reaction Products of Organic Compounds*; EPA-560/12-79-001, June, 1979.
- [135] J.T. Herron, R.E. Huie, J.A. Hodgeson, *Chemical Kinetic Data Needs for Modeling the Lower Troposphere*; NBS Spec, Publ. 557, August, 1979.
- [136] N.J. Bunce, L. Liu, J. Zhu, D.A. Lane, *Environ. Sci. Technol.*, **1997**, 31, 2252.

- [137] X. Qu, Q. Zhang, W. Wang, *Chem. Phys. Lett.*, **2006**, 429, 77.
- [138] J.E. Sickles, W.C. Eaton, L.A. Ripperton, R.S. Wright, *Literature Survey of Emissions Associated with Emerging Energy Technologies*; EPA report 600/7-77-104, 1977.
- [139] D. Lucas, N.J. Brown, *Combustion Flame*, **1983**, 49, 283.

Chapter 2

Theoretical methods

2.1. Introduction

In this section a short review is given of all theoretical techniques which have been used in the present thesis. This section starts with an overview of electronic structure theory including Hartree-Fock theory and traditional treatments of electron correlation, such as Møller-Plesset perturbation theory [1] and Coupled Cluster theory [2,3]. Attention will be focused on Density Functional Theory (DFT) [4] with emphasis on the employed exchange correlation functionals such as the B3LYP (Becke-3-parameters–Lee–Yang–Parr) functional [5,6], the dispersion-corrected ω B97XD functional [7] as well as the UM05-2x [8] and UM06-2x functionals [8,9]. For the sake of quantitative insights into the studied reaction mechanisms, comparison will be made with benchmark computational results obtained at the high-level composite CBS-QB3 level [10–18], in order to determine which exchange-correlation functional gives the most accurate energy barriers and reaction energies. Statistical thermodynamics (RRHO approximation) is also briefly summarized. The main objective of this chapter is not so much to give highly rigorous mathematical derivations of all the employed theories and computational methods, but rather to discuss their main features, strengths and weaknesses. Specific attention is nevertheless given to a formally complete derivation of the employed theories of chemical kinetics (standard and variational transition state theory, RRKM theory), which is an altogether entirely new research topic at Hasselt University. Researchers that are already familiar with these theories may skip this chapter and focus directly on chapters 3 to 7. These latter chapters describe extensive applications of the above theories and methods, which have been the subject of publications in international and peer reviewed scientific journals.

2.2. Electronic Structure Theories

Quantum mechanical methods have been developed to describe at the electronic level molecular properties and various aspects of the molecular structure of matter. The central equation in quantum mechanics from which all molecular properties can be derived is the time-independent Schrödinger equation [19–23]:

$$\hat{H}\Psi = E\Psi \quad (2.1)$$

where \hat{H} is the Hamiltonian operator accounting for all energy contributions of the system, Ψ represents the total wave function depending on the Cartesian coordinates of these particles, and E denotes the total energy of the system. The Hamiltonian operator \hat{H} contains both kinetic and potential energy contributions, as follows:

$$\hat{H} = \hat{T} + \hat{V} \quad (2.2)$$

with

$$\hat{T} = -\frac{1}{2} \sum_i^{\text{electrons}} \nabla_A^2 - \frac{1}{2} \sum_A^{\text{nuclei}} \frac{1}{M_A} \nabla_i^2 \quad (2.3)$$

and

$$\hat{V} = \sum_i \sum_A \frac{Z_A}{r_{iA}} + \sum_{i>j} \frac{1}{r_{ij}} + \sum_{A<B} \frac{Z_A Z_B}{R_{AB}} \quad (2.4)$$

where ∇_i^2 and ∇_A^2 represent the Laplacian operators for the electron i and nucleus A , respectively. $r_{iA} = |\mathbf{r}_i - \mathbf{R}_A|$ is the distance between electron i and nucleus A which contains Z_A protons, and $r_{ij} = |\mathbf{r}_i - \mathbf{r}_j|$ is the distances between electron i and electron j , while Z_A and Z_B denote the nuclear charges of atoms A and B . $\mathbf{R}_{AB} = \mathbf{R}_A - \mathbf{R}_B$ is the corresponding interdistance. The two terms in eq. (2.3) represent the kinetic energy operators for N electrons and M nuclei. In eq. (2.4) the first term represents the Coulomb attraction force between electrons and nuclei, and the last two terms are the nuclear-nuclear repulsion and electron-electron repulsion terms, respectively. In the above equation, atomic units are used.

The Schrödinger equation can only be solved analytically for very small and specific systems (e.g. H, He⁺, Li⁺², H₂⁺, ...). In general, several approximations have to be considered in order to numerically solve eq. (2.1) for more complex systems. The first one is the Born-Oppenheimer approximation [24], which arises from the assumption that nuclei are much heavier than electrons, and move therefore much more slowly than electrons. Therefore, the Schrödinger equation [eq. (2.1)] can be separated into two independent equations which describe (*i*)

electronic motions in the field of fixed nuclei, and (ii) the motions of the nuclei in the average field of the electrons.

In the framework of the Born-Oppenheimer approximation, on the time scale of electronic motions, the Hamiltonian terms corresponding to the *nuclear kinetic energy* and *nuclear repulsion energy* (*nuclei-nuclei repulsions*) terms can be considered as constants. Since any constant added to an operator does not have any effect on the eigenfunctions of this operator, these two terms can be neglected. The remaining terms define the so-called electronic Hamiltonian, as follows:

$$\hat{H}_{el} = -\frac{1}{2} \sum_{i=1}^N \nabla_i^2 - \sum_{i=1}^N \sum_{A=1}^M \frac{Z_A}{r_{iA}} + \sum_{i=1}^N \sum_{j>i}^N \frac{1}{r_{iA}} \quad (2.5)$$

with

$$v(\mathbf{r}_i) = - \sum_{i=1}^N \sum_{A=1}^M \frac{Z_A}{r_{iA}} \quad (2.6)$$

where $v(\mathbf{r}_i)$ is an external potential generated by the charges Z_A of the M fixed nuclei acting on electron i . The solution of the Schrödinger equation involving the electronic Hamiltonian,

$$\hat{H}_{elec} \Psi_{elec} = E_{elec} \Psi_{elec} \quad (2.7)$$

is the electronic wave function:

$$\Psi_{elec} = \Psi_{elec} \{(\mathbf{r}_i); (\mathbf{R}_A)\} \quad (2.8)$$

which depends explicitly on the electron coordinates \mathbf{r}_i , and parametrically on the nuclear coordinates \mathbf{R}_A . Thus, the electronic energy E_{elec} depends parametrically on the nuclear coordinates, which means that it needs to be calculated for each atomic configuration [19]. In order to obtain the total energy for a system of fixed nuclei, one has also to account for the repulsions between nuclei:

$$E_{tot} = E_{elec} + \sum_{A=1}^M \sum_{B>A}^M \frac{Z_A Z_B}{R_{AB}} \quad (2.9)$$

Upon solving eq. (2.7) and obtaining the total energy from eq. (2.9), it is then possible to investigate internal nuclear motions, considering that $E_{tot}(\{\mathbf{R}_A\})$ provides the relevant potential energy function:

$$\hat{H}_{nucl} \Psi_{nucl} = E \Psi_{nucl} \quad (2.10)$$

with

$$\hat{H}_{nucl} = -\frac{1}{2} \sum_{A=1}^M \frac{1}{M_A} \nabla^2 + E_{tot}(\{\mathbf{R}_A\}) \quad (2.11)$$

Solving the nuclear Schrödinger equation $\hat{H}_{nuc} \Psi_{nuc} = E \Psi_{nuc}$ enables us therefore to study the rotational, and vibrational motions of the molecule, and to calculate the Born-Oppenheimer approximation to the total energy E , which for a molecule with a fixed center of mass includes electronic, vibrational, and rotational contributions. The total wave function in this approximation is given by

$$\Psi(\{\mathbf{r}_i\}; \{\mathbf{R}_A\}) = \Psi_{elec}(\{\mathbf{r}_i\}; \{\mathbf{R}_A\}) \Psi_{nuc}(\{\mathbf{R}_A\}) \quad (2.12)$$

The electronic Hamiltonian of a molecule containing N electrons depends on the $3N$ Cartesian coordinates of the electrons, but does not completely define the states of electrons. In order to specify these states completely, one has to account for an additional property of the electron, namely, its spin. For this purpose, we introduce for each electron two orthonormal spin functions $\alpha(\omega)$ and $\beta(\omega)$, associated with *spin-up* and *spin-down*, respectively. In a non-relativistic context, an electron is described by the three spatial coordinates \mathbf{r} and one spin coordinate ω . These four coordinates are denoted collectively by $\mathbf{x} = \{\mathbf{r}, \omega\}$. The wave function of an electron, which describes both its spatial distribution and its spin, is referred to as a *spin orbital* $\chi_i(\mathbf{x}_i)$, which is obtained as a product of a space function $\psi(\mathbf{r}_i)$ and a spin function $\sigma(\omega)$:

$$\chi_i(\mathbf{x}_i) = \psi(\mathbf{r}_i) \sigma(\omega) \quad (2.13)$$

The electronic wave function obtained upon solving the electronic Schrödinger equation [eq. (2.7)] must satisfy an independent postulate of quantum mechanics, the so-called *Pauli's exclusion principle* or *antisymmetry principle*. Specifically, a many electron wave function has to be antisymmetric with respect to the interchange of the spin-space coordinates of any two electrons:

$$\Psi_{elec}(\mathbf{x}_1, \mathbf{x}_2, \dots, \mathbf{x}_i, \dots, \mathbf{x}_j, \dots, \mathbf{x}_N) = -\Psi_{elec}(\mathbf{x}_1, \mathbf{x}_2, \dots, \mathbf{x}_j, \dots, \mathbf{x}_i, \dots, \mathbf{x}_N) \quad (2.14)$$

The *antisymmetry principle* ensures the indistinguishability of electrons upon any interchange of their spin-space coordinates, and prevents that two electrons with the same spin occupy the same orbital.

2.2.1. Hartree-Fock Theory

The main purpose of the Hartree-Fock (HF) theory is to reduce the complicated many electron problem to one in which electron-electron repulsions are treated in an average way. Each electron therefore experiences only the average Coulomb repulsion of all other electrons. This reduces the computationally untreatable N -body problem to a solvable effective one-electron problem. Hartree-Fock theory is a variational quantum mechanical method [25–27], which defines the variational

wave function of the electronic ground state (Ψ_0) in the form of a single Slater determinant. The Hartree-Fock equations [28,29] enable us to find a set of spin orbitals such that this determinant, formed from the occupied spin orbitals, is the best possible approximation to the electronic ground state of the system. This means that it is necessary to find the set of spin orbitals which minimizes the electronic energy of the system under the constraint that all spin orbitals remain orthonormal. Indeed, orbitals have to remain orthonormal while the electronic wave function varies, because they are eigenfunctions of a Hermitian operator. Correspondingly, the associated eigenvalues, namely the canonical orbital energies, remain real.

The Pauli principle requires the electronic wave function to be antisymmetric with respect to the interchange of the coordinates of any two electrons [27]. In a first approximation, the electronic wave function Ψ_{elec} is therefore written as a Slater determinant of spin-orbitals, as follows:

$$\Psi_{el,approx} = \frac{1}{\sqrt{N!}} \begin{vmatrix} \chi_1(1) & \chi_2(1) & \dots & \chi_N(1) \\ \chi_1(2) & \chi_2(2) & \dots & \chi_N(2) \\ \cdot & \cdot & \dots & \cdot \\ \cdot & \cdot & \dots & \cdot \\ \cdot & \cdot & \dots & \cdot \\ \chi_1(N) & \chi_2(N) & \dots & \chi_N(N) \end{vmatrix} \quad (2.15)$$

where N is the number of electrons, and $\chi_1(1)$ denotes spin orbital **1** containing electron **1**. A spin-orbital is one-electron spatial wave function (an atomic orbital for atoms or a molecular orbital for molecule) multiplied by a spin function, and the Slater determinantal wave function is only approximate because of the assumption that each electron can be assigned to a spin-orbital. The only way to find the approximate solutions $\Psi_{el,approx}$ to the Schrödinger equation ($\hat{H}\Psi_{el,approx} = E\Psi_{el,approx}$) is by means of the variational principle, which asserts that any well-behaved trial wave function satisfying the boundary conditions of the system of interest gives an upper bound (W) to the exact ground state energy (E_0):

$$W = \frac{\langle \Psi_{el,approx} | \hat{H}_{el} | \Psi_{el,approx} \rangle}{\langle \Psi_{el,approx} | \Psi_{el,approx} \rangle} \geq E_0 \quad (2.16)$$

where $\Psi_{el,approx}$ represents any arbitrary electronic function, which depends on the same coordinates as the exact solution of the Schrödinger equation, and \hat{H}_{elec} denotes the Hamiltonian of the N -electron system under consideration. The above

equality is valid only when $\Psi_{el,approx} = \Psi_0$, where Ψ_0 is the exact solution of the Schrödinger equation for the electronic ground state [27].

The Hartree-Fock method uses the Slater determinantal wave function of eq. (2.15) as the trial wave function in order to minimize the value of W using Lagrange multipliers [30]. This result in a set of N coupled one-electron pseudo-eigenvalue equations known as the Hartree-Fock equations. In canonical form, these equations take the form:

$$\hat{f}(1)\chi_i(1) = \varepsilon_i \chi_i(1) \quad (2.17)$$

In this equation ε_i is the energy corresponding to the spin orbital χ_i , and $\hat{f}(1)$ is an effective one-electron operator for electron 1, the so-called Fock operator, which is given by:

$$\hat{f}(1) = \hat{h}(1) + v^{HF}(1) \quad (2.18)$$

The first term $\hat{h}(1)$ in eq. (2.18) is the one-electron operator defined as:

$$\hat{h}(1) = -\frac{1}{2}\nabla_1^2 - \sum_{A=1}^Z \frac{Z_A}{r_{1A}} \quad (2.19)$$

where the first accounts for the kinetic energy and the second term for the nuclear-electronic attraction. The second term in eq. (2.18) is the Hartree-Fock potential.

$$v^{HF}(1) = \sum_j [\hat{J}_j(1) - \hat{K}_j(1)] \quad (2.20)$$

where the summation \sum_j runs over all occupied spin orbitals of the system under consideration. $\hat{J}_j(1)$ is a local operator, describing the physical effect of (classical) electrostatic forces, which is referred to as the Coulomb operator.

$$\hat{J}_j(1) = \int \chi_j^*(2) \frac{1}{r_{12}} \chi_j(2) d\mathbf{x}_2 \quad (2.21)$$

whereas $\hat{K}_j(1)$ represents a non-local operator, referred to as the exchange operator. This operator arises as a non-classical, i.e. quantum consequence of the antisymmetry principle, and is defined via its action on the spin orbital $\chi_i(1)$, according to:

$$\hat{K}_j(1)\chi_i(1) = \left[\int \chi_j^*(2) \frac{1}{r_{12}} \chi_i(2) d\mathbf{x}_2 \right] \chi_j(1) \quad (2.22)$$

The Fock operator depends on the orbitals it is operating on, therefore solving the integro-differential equation (2.17) must be done self-consistently: an initial guess of the orbitals is used to construct the Fock operator that is used to compute improved orbitals, which are used in turn to construct an improved Fock operator; the process is continued until no further significant change in the energy (or orbitals) is observed. In practice, the molecular orbitals are expanded as linear combinations of atomic orbitals, which are often composed of Gaussian-type basis functions [27]. This allows the problem to be solved using the methods of matrix algebra [31].

Each individual molecular orbital (MO) ψ_j can be expressed as a linear combination of a finite set of K one-electron functions known as basis functions, $\phi_1, \phi_2, \dots, \phi_K$. When atomic orbitals of the constituting atoms are used as basis functions, this approximation is referred to as the linear combination of atomic orbitals (LCAO) theory:

$$\psi_j = \sum_{\mu=1}^K c_{\mu j} \phi_{\mu} \quad (2.23)$$

where the MO expression coefficients $c_{\mu j}$ are adjusted to minimize the expectation value of the total energy E . The final value of E will be as close to the exact energy as is possible within the limitations of Hartree-Fock theory, namely the limitations of a single determinant wave function and of the selected basis set. The variational conditions lead to a set of algebraic equation for the LCAO coefficients $c_{\mu j}$, which were derived independently for closed shell wave functions by Roothaan [31] and Hall [32]. The Roothaan-Hall equations are defined by

$$\sum_{\nu=1}^K (F_{\mu\nu} - \varepsilon_i S_{\mu\nu}) c_{\nu} = 0 \quad ; \quad \mu=1,2,\dots,K \quad (2.24)$$

where ε_i is the one-electron energy of molecular orbital ψ_i , $S_{\mu\nu}$ denotes the elements of an $K \times K$ matrix termed the overlap matrix, and $F_{\mu\nu}$ are the elements of another $K \times K$ matrix, the Fock matrix. This matrix itself depends on the molecular orbitals which are derived from their own effective potential, hence the above equation must be solved iteratively using the so-called self-consistent field (SCF) approach.

The Hartree-Fock wave function is the best wave function that can be written as a single Slater determinant if a complete basis set is used. However, it has some deficiencies [27]. Analysis shows that the method treats each electron as feeling repulsion from a smeared-out cloud of the other electrons, rather than taking into account the instantaneous interactions based on their actual locations (electronic

motions are correlated in reality). The difference between the Hartree-Fock energy and the exact electronic energy is thus termed the correlation energy.

In many cases, the Hartree-Fock approximation breaks down and fails to reproduce experiment. It can be corrected by explicitly accounting for electron correlation by means of density functional theory (DFT), many-body perturbation theory (MBPT) [33], configuration interaction theory (CI) [34,35], and further many-body quantum mechanical approaches.

2.2.1.1. Restricted Closed-shell Hartree-Fock Theory

At this stage, one has to specify in details the form of the spin orbitals to be used prior to calculating the Hartree-Fock wave function. Two types of spin-orbitals are considering in quantum mechanical calculations: spin-up (α) and spin-down (β) orbitals.

The restricted Hartree-Fock (RHF) formalism is devised for obtaining the Hartree-Fock solution for *closed-shell systems* with an even number of electrons (N), which are paired in such a way that $n=N/2$ spatial functions $\psi_i(\mathbf{r}_i)$ (molecular orbitals) are doubly occupied. Since the spatial function is the same for spin-up (α) and spin-down (β) orbitals associated to the same energy level, the calculation of molecular orbitals is equivalent to the problem of solving an integro-differential equation of the forms:

$$\hat{f}(\mathbf{r}_1)\psi_i(\mathbf{r}_1) = \varepsilon_i \psi_i(\mathbf{r}_1) \quad (2.25)$$

with $\hat{f}(\mathbf{r}_1)$ the closed-shell Fock operator

$$\hat{f}(\mathbf{r}_1) = \int d\omega_1 \alpha^*(\omega_1) \hat{f}(\mathbf{x}_1) \alpha(\omega_1) \quad (2.26)$$

Upon integrating the HF potential [eq. (2.20)] over spin one finds that

$$\hat{f}(\mathbf{r}_1) = \hat{h}(1) + \sum_a^{N/2} 2J_a(1) - K_a(1) \quad (2.27)$$

where the summation over a runs over doubly occupied orbitals, and where the closed-shell coulomb and exchange operators are defined by

$$J_a(1) = \int d\mathbf{r}_2 \psi_a^*(2) r_{12}^{-1} \psi_a(2) \quad (2.28)$$

$$K_a(1)\psi_i(1) = \left[\int d\mathbf{r}_2 \psi_a^*(2) r_{12}^{-1} \psi_i(2) \right] \psi_a(1) \quad (2.29)$$

These equations are quite analogous to those obtained for spin orbitals, except for the factor 2 occurring with the Coulomb operator, versus the factor (-1) for the exchange operator. The main reason for this difference in counting factors is that,

whereas any pair of electrons is subject to Coulomb repulsion forces, there exist no exchange interactions between electrons having opposite spin.

In order to solve eq. (2.25), Roothaan [31] introduced a set of known basis spatial functions and converted the HF equation into a set of simple algebraic equations that may be solved using standard matrix diagonalization techniques. In this purpose, one has to introduce a set of K known basis function $\{\phi_\mu(\mathbf{r})|\mu=1,2,\dots,K\}$, and expand the unknown molecular orbitals $\psi_i(\mathbf{r})$ in the linear expansion is defined by

$$\psi_i = \sum_{\mu=1}^K C_{\mu i} \phi_\mu, \quad i = 1, 2, \dots, K \quad (2.30)$$

In order to avoid truncation errors in the expansion, one should use a complete basis set $\{\phi_\mu\}$, corresponding formally to an infinite number of basis functions. In fact, finite basis sets of K basis functions have to be used. As the basis set approaches completeness ($K \rightarrow \infty$), molecular orbitals converge to the exact eigenfunctions of the Fock operator. In practice, once a finite set of basis functions is chosen, one has to determine the set of expansion coefficients $C_{\mu i}$ in order to obtain the Hartree-Fock molecular orbitals.

By substituting eq. (2.30) into eq. (2.25), one obtains a matrix equation that is usually referred to as the Hartree-Fock-Roothaan matrix equation:

$$\mathbf{FC} = \mathbf{SC}\boldsymbol{\varepsilon} \quad (2.31)$$

where \mathbf{C} is a $K \times K$ square matrix containing the expansion coefficient $C_{\mu i}$, $\boldsymbol{\varepsilon}$ denotes a diagonal matrix containing the orbital energies ε_i , and \mathbf{F} and \mathbf{S} represents the Fock and overlap matrices, respectively.

$$F_{\mu\nu} = \int \phi_\mu^*(\mathbf{r}_1) \hat{f}(\mathbf{r}_1) \phi_\nu(\mathbf{r}_1) d\mathbf{r}_1, \quad \mu, \nu = 1, 2, \dots, K \quad (2.32)$$

$$S_{\mu\nu} = \int \phi_\mu^*(\mathbf{r}_1) \phi_\nu(\mathbf{r}_1) d\mathbf{r}_1, \quad \mu, \nu = 1, 2, \dots, K \quad (2.33)$$

The basis functions used in molecular calculations are not orthogonal to each other ($\mathbf{S} \neq \mathbf{1}$), and have therefore to be orthogonalized so that eq. (2.31) can be solved by means of standard diagonalization techniques. Orthogonalization procedures are described in details in the book by Szabo and Ostund [19].

2.2.1.2. Restricted and Unrestricted Open-shell Hartree-Fock Theories

For *open-shell systems* (that is, those having one or more unpaired electrons), two approaches are possible: *Restricted-open-shell Hartree-Fock* (ROHF) and *Unrestricted Hartree-Fock* (UHF) theories.

In the restricted-open-shell Hartree-Fock (ROHF) formalism [36], a single set of molecular orbitals is used, which are either doubly or singly occupied, according to the multiplicity of the species. For instance, for a radical (doublet) species, the determinant would be formed from $(n+1)/2$ orbitals, and one of these would be singly occupied (see Figure 2.1). This ensures that there is exactly one unpaired spin in the system, and the species is therefore a pure doublet.

In unrestricted Hartree-Fock (UHF), the α and β spin orbitals are defined and optimized separately [20]. Therefore there would be $(n+1)/2$ occupied α spin orbitals, and $(n-1)/2$ occupied β spin orbitals. In this approach, two different sets of molecular orbitals are defined by

$$\psi_i^\alpha = \sum_{\mu=1}^K c_{\mu i}^\alpha \phi_\mu \quad , \quad \psi_i^\beta = \sum_{\mu=1}^K c_{\mu i}^\beta \phi_\mu \quad ; \quad i=1,2,\dots,K \quad (2.34)$$

Upon using the LCAO expression for molecular orbitals, the following matrix equations are obtained

$$\mathbf{F}^\alpha \mathbf{C}^\alpha = \mathbf{S} \mathbf{C}^\alpha \boldsymbol{\varepsilon}^\alpha \quad (2.35)$$

$$\mathbf{F}^\beta \mathbf{C}^\beta = \mathbf{S} \mathbf{C}^\beta \boldsymbol{\varepsilon}^\beta \quad (2.36)$$

These equations that represent a generalization of the Hartree–Fock–Roothaan equation to open-shell systems are called the Pople–Nesbet equations [36]. An explicit expression for the Fock matrix elements in eqs. (2.35–2.36) shows that the \mathbf{F}^α and \mathbf{F}^β matrices depend both on the \mathbf{C}^α and \mathbf{C}^β expansion coefficients [19].

The advantages of the UHF method are that it is capable of providing a qualitatively correct description of bond dissociations, and converges more easily to a numerically stable solution than the ROHF method [23]. Because it accounts for spin polarization effects, the UHF method can also provide a better qualitative treatment of hyperfine coupling constants [37]. However, the principal disadvantage of UHF is that the independent optimization of the α and β spin orbitals can result in nominally equivalent α and β orbitals having slightly different eigenvalues. In other words, a doublet species (UHF) could have effectively more than one unpaired electron (ROHF) in the system (see Figure 2.1). This physically unrealistic phenomenon is known as *spin contamination*, and can be for instance a particularly serious problem for the transition structures in the propagation steps of free-radical polymerizations [38].

An UHF calculation on a system with an extra α electron often leads to a wave function which is a mixture of a double and a quartet, and incorporating higher spin states, rather than a pure doublet (ROHF). Spin contamination is identified by examining the expectation value of the spin operator $\langle \hat{S}^2 \rangle$, which is defined as

$\langle \hat{S}^2 \rangle_{exact} - \langle \hat{S}^2 \rangle_{observed}$. The exact eigenvalues of $\langle \hat{S}^2 \rangle$ are $S(S+1)$ in atomic unit, where S can take the values 0 (singlet), 1/2 (doublet), 1 (triplet), 3/2 (quartet), and so forth. For a UHF wave function to be a reliable approximation it has been proposed that the deviation in $\langle \hat{S}^2 \rangle$ must be less than 10% [1]. There is however no clear relationship between the accuracy of the total calculated energy and the deviation of $\langle \hat{S}^2 \rangle$ from its exact value, which makes the whole problem extremely difficult to discuss. Spin contamination is therefore nothing more than a qualitative criterion to judge the reliability of a single-determinantal calculation.

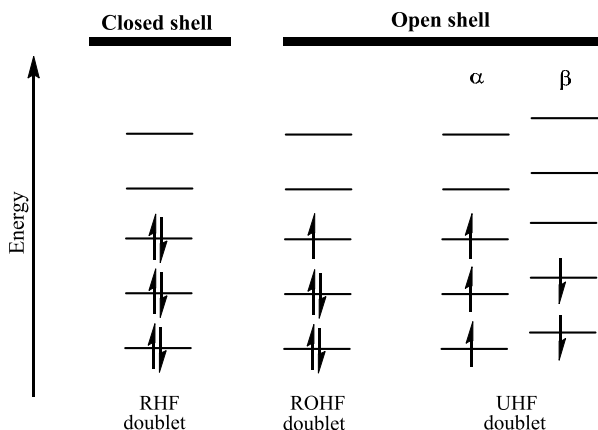


Figure 2.1. Electron configuration diagrams highlighting the differences between RHF, ROHF, and UHF.

2.2.2. Møller-Plesset Perturbation Theory

Many body perturbation theory (MBPT) is a systematic procedure for obtaining the correlation energy, which is not variational, but which is size consistent at each level of the expansion. The general frame of perturbation theory was devised by Rayleigh and Schrödinger and hence it is referred to as Rayleigh-Schrödinger perturbation theory (RSPT). RSPT employing the Hartree-Fock Hamiltonian as a zeroth-order Hamiltonian of an N -electron system is more specifically referred to as Møller-Plesset perturbation theory (MPPT) [1].

MPPT is one of the most widely used methods for taking into account the effect of electron correlation. Its use is most common because it is relatively inexpensive as compared to the other available electron correlation methods. The starting point is the assumption that the problem of finding eigenfunctions of the Hamiltonian may be divided into two parts; a zeroth-order or unperturbed part \hat{H}_0 (the HF Hamiltonian) and a perturbation \hat{V} reintroducing the effect of electron correlation.

$$\hat{H}|\Phi_i\rangle = (\hat{H}_0 + \hat{V})|\Phi_i\rangle = \varepsilon_i |\Phi_i\rangle \quad (2.37)$$

whereas eq. (2.37) cannot be solved exactly, it is assumed that the eigenfunctions ($|\Psi_i^{(0)}\rangle$) and eigenvalues ($E_i^{(0)}$) of \hat{H}_0 are known:

$$\hat{H}_0 |\Psi_i^{(0)}\rangle = E_i^{(0)} |\Psi_i^{(0)}\rangle \quad (2.38)$$

If the perturbation is small, we expect $|\Phi_i\rangle$ and ε_i to be reasonably close to $|\Psi_i^{(0)}\rangle$ and $E_i^{(0)}$, respectively. We wish to devise a procedure by which we can systematically improve the eigenfunctions and eigenvalues of \hat{H}_0 so that they become closer and closer to the eigenvalues and eigenfunctions of the exact Hamiltonian \hat{H} . This is done by introducing an ordering parameter λ , which will later be set equal to unity.

$$\hat{H} = \hat{H}_0 + \lambda \hat{V} \quad (2.39)$$

We now expand both the energy eigenvalues and eigenfunctions in powers of the perturbation.

$$\varepsilon_i = E_i^{(0)} + \lambda E_i^{(1)} + \lambda^2 E_i^{(2)} + \dots \quad (2.40)$$

$$|\Phi_i\rangle = |\Psi_i^{(0)}\rangle + \lambda |\Psi_i^{(1)}\rangle + \lambda^2 |\Psi_i^{(2)}\rangle + \dots \quad (2.41)$$

where the superscripts (0), (1), (2), ... are the zeroth, first, and second, ... order terms. For example, we call $E_i^{(n)}$ the n th-order energy. Let us take the wave functions of \hat{H}_0 to be normalized and then choose the normalization of $|\Phi_i\rangle$ such that $\langle \Psi_i^{(0)} | \Phi_i \rangle = 1$. Upon multiplying eq. (2.41) by $\langle \Psi_i^{(0)} |$ we have

$$\langle \Psi_i^{(0)} | \Phi_i \rangle = \langle \Psi_i^{(0)} | \Psi_i^{(0)} \rangle + \lambda \langle \Psi_i^{(0)} | \Psi_i^{(1)} \rangle + \lambda^2 \langle \Psi_i^{(0)} | \Psi_i^{(2)} \rangle + \dots = 1 \quad (2.42)$$

This equation holds for all values of λ . Therefore, the coefficients of λ on both sides must be equal and

$$\langle \Psi_i^{(0)} | \Psi_i^{(n)} \rangle = 0 \quad ; \quad n = 1, 2, 3, \dots \quad (2.43)$$

The Schrödinger equation then becomes

$$(\hat{H}_0 + \lambda \hat{V})(\Psi_i^{(0)} + \lambda \Psi_i^{(1)} + \lambda^2 \Psi_i^{(2)} \dots) = (E_i^{(0)} + \lambda E_i^{(1)} + \lambda^2 E_i^{(2)} \dots)(\Psi_i^{(0)} + \lambda \Psi_i^{(1)} + \lambda^2 \Psi_i^{(2)} \dots) \quad (2.44)$$

for each power n of λ we find

$$n = 0: \quad \hat{H}_0 |\Psi_i^{(0)}\rangle = E_i^{(0)} |\Psi_i^{(0)}\rangle \quad (2.45)$$

$$n=1: \quad \hat{V}|\Psi_i^{(0)}\rangle + \hat{H}_0|\Psi_i^{(1)}\rangle = E_i^{(1)}|\Psi_i^{(0)}\rangle + E_i^{(0)}|\Psi_i^{(1)}\rangle \quad (2.46)$$

$$n=2: \quad \hat{H}_0|\Psi_i^{(2)}\rangle + \hat{V}|\Psi_i^{(1)}\rangle = E_i^{(0)}|\Psi_i^{(2)}\rangle + E_i^{(1)}|\Psi_i^{(1)}\rangle + E_i^{(2)}|\Psi_i^{(0)}\rangle \quad (2.47)$$

and so on.

Multiplying each of these equations by $\langle\Psi_i^{(0)}|$ and using the orthogonality relation [eq. (2.43)], we obtain the following expressions for the n th-order energies

$$E_i^{(0)} = \langle\Psi_i^{(0)}|\hat{H}_0|\Psi_i^{(0)}\rangle \quad (2.48)$$

$$E_i^{(1)} = \langle\Psi_i^{(0)}|\hat{V}|\Psi_i^{(0)}\rangle \quad (2.49)$$

$$E_i^{(2)} = \langle\Psi_i^{(0)}|\hat{V}|\Psi_i^{(1)}\rangle \quad (2.50)$$

and so on until infinite order in the correlation potential.

Upon expanding the exact wave function Φ_i under the constraint of intermediate normalization $\langle\Psi_i^{(0)}|\Phi_i\rangle = 0$, which implies that at all orders $\langle\Psi_i^{(0)}|\Psi_i^{(n)}\rangle = 0$, the higher energies are obtained in terms of zeroth-order energies $E_i^{(0)}$ and zeroth-order wave function $\Psi_i^{(0)}$; for example, the second-order energy $E_i^{(2)}$ is obtained as follows:

$$E_i^{(2)} = \sum_{n \neq i} \frac{\langle\Psi_i^{(0)}|\hat{V}|\Psi_n^{(0)}\rangle \langle\Psi_n^{(0)}|\hat{V}|\Psi_i^{(0)}\rangle}{E_i^{(0)} - E_n^{(0)}} = \sum_{n \neq i} \frac{\left| \langle\Psi_i^{(0)}|\hat{V}|\Psi_n^{(0)}\rangle \right|^2}{E_i^{(0)} - E_n^{(0)}} \quad (2.51)$$

For the third-order energy $E_i^{(3)}$, we have:

$$E_i^{(3)} = \sum_{n, m \neq i} \frac{\langle\Psi_i^{(0)}|\hat{V}|\Psi_n^{(0)}\rangle \langle\Psi_n^{(0)}|\hat{V}|\Psi_m^{(0)}\rangle \langle\Psi_m^{(0)}|\hat{V}|\Psi_i^{(0)}\rangle}{(E_i^{(0)} - E_n^{(0)})(E_i^{(0)} - E_m^{(0)})} - E_i^{(1)} \sum_{n \neq i} \frac{\left| \langle\Psi_i^{(0)}|\hat{V}|\Psi_n^{(0)}\rangle \right|^2}{(E_i^{(0)} - E_n^{(0)})^2} \quad (2.52)$$

Within the frame of MPPT, the Hartree-Fock Hamiltonian ($\hat{H}_0 = \sum_i [\hat{h}(i) + \hat{v}^{HF}(i)]$)

is employed as a zeroth-order Hamiltonian, and the corresponding perturbation operator reads:

$$\hat{V} = \sum_{i < j} r_{ij}^{-1} - \hat{V}^{HF} = \sum_{i < j} r_{ij}^{-1} - \sum_i \hat{v}^{HF}(i) \quad (2.53)$$

Since the Hartree-Fock energy corresponds to the sum of the zeroth-order ($\sum_{ij} \varepsilon_i$)

and first-order perturbation energies ($-\frac{1}{2} \sum_{ij} \langle ij || ij \rangle$), the first contribution to the

correlation energy arises at second-order of Møller-Plesset theory (MP2). Because of the rules by Slater, and Brillouin's theorem, which forbids couplings of singly excited states with the electronic ground state, the only terms that contribute to eq. (2.51) are the doubly excited determinants $|\Psi_{ij}^{rs}\rangle$. It follows therefore that:

$$E_o^{(2)} = \frac{1}{4} \sum_{ijrs} \frac{|\langle ij || rs \rangle|^2}{\varepsilon_i + \varepsilon_j - \varepsilon_r - \varepsilon_s} \quad (2.54)$$

By means of a similar procedure, one obtains the following expression for the third-order perturbation energy (MP3):

$$\begin{aligned} E_o^{(3)} = & \frac{1}{8} \sum_{ijklrs} \frac{\langle ij || rs \rangle \langle kl || ij \rangle \langle rs || kl \rangle}{(\varepsilon_i + \varepsilon_j - \varepsilon_r - \varepsilon_s)(\varepsilon_k + \varepsilon_l - \varepsilon_r - \varepsilon_s)} \\ & + \frac{1}{8} \sum_{ijrstu} \frac{\langle ij || rs \rangle \langle rs || tu \rangle \langle tu || ij \rangle}{(\varepsilon_i + \varepsilon_j - \varepsilon_r - \varepsilon_s)(\varepsilon_i + \varepsilon_j - \varepsilon_t - \varepsilon_u)} \\ & + \sum_{ijkrst} \frac{\langle ij || rs \rangle \langle ks || tj \rangle \langle rt || ik \rangle}{(\varepsilon_i + \varepsilon_j - \varepsilon_r - \varepsilon_s)(\varepsilon_i + \varepsilon_k - \varepsilon_r - \varepsilon_l)} \end{aligned} \quad (2.55)$$

In the above equations, the i, j, k and l indices correspond to occupied spin orbitals, whereas the r, s, t and u indices refer to unoccupied (virtual) spin orbitals. $\langle ij || kl \rangle$ are anti-symmetrized bielectron integrals, which are defined as follows:

$$\langle ij || kl \rangle = \iint d\mathbf{x}_1 d\mathbf{x}_2 \chi_i^*(\mathbf{x}_1) \chi_j^*(\mathbf{x}_2) \left(\frac{1 - P_{12}}{r_{12}} \right) \chi_k(\mathbf{x}_1) \chi_l(\mathbf{x}_2) \quad (2.56)$$

where P_{12} is a permutation operator over the spin-space coordinates of electrons 1 and 2.

Fourth and higher order expressions for the energies [39–41] can also be written down. The computational cost of MP2, MP3, MP4 calculations scales like N^5 , N^6 and N^7 , respectively, where N is the number of basis functions. MP4 requires single (S), double (D), triple (T) and quadruple (Q) excitations. This is the reason why there are two implementations of the MP4 approach: the MP4(SDQ) approach [40], which neglects the triple contribution, and the MP4(SDTQ) approach, which is the complete one.

2.2.3. Coupled Cluster Theory

Coupled Cluster (CC) theory is widely used these days because of its very high accuracy. This approach [2,3] is based on the *exponential Ansatz* of Coester and Kümmel [42,43]. The exact wave function is obtained by applying an excitation operator \hat{T} on a reference wave function (usually the HF wave function, Ψ_{HF}):

$$\Psi_{CC} = e^{\hat{T}} \Psi_{HF} = \left(1 + \hat{T} + \frac{1}{2!} \hat{T}^2 + \frac{1}{3!} \hat{T}^3 + \dots \right) \Psi_{HF} \quad (2.57)$$

The excitation operator generates n -fold excitations from a reference state. It is defined as:

$$\hat{T} = \hat{T}_1 + \hat{T}_2 + \hat{T}_3 + \dots \hat{T}_n \quad (2.58)$$

where the sum of all operators of a particular class forms a single \hat{T}_n operator.

In the CCD expansion, the excitation operator only includes double excitations, i.e. $\hat{T} = \hat{T}_2$. Accordingly, the CCD wave function is given by

$$\begin{aligned} \Psi_{CCD} &= e^{\hat{T}_2} \Psi_{HF} = \left(1 + \hat{T}_2 + \frac{1}{2!} \hat{T}_2^2 + \frac{1}{3!} \hat{T}_2^3 + \dots \right) \Psi_{HF} \\ &= \Psi_{HF} + \sum_{i \setminus j} \sum_{a \setminus b} t_{ij}^{ab} \Psi_{ij}^{ab} + \sum_{i \setminus j \setminus k \setminus l} \sum_{a \setminus b \setminus t \setminus u} t_{ij}^{ab} t_{kl}^{tu} \Psi_{ijkl}^{abtu} + \dots \end{aligned} \quad (2.59)$$

with the operator \hat{T}_2 generating excitations from pairs of occupied states to pairs of virtual states. The usual convention is adopted here: the i, j, k, l, \dots are occupied Hartree-Fock spin orbitals and r, s, t, u, \dots are the unoccupied ones. The unknown expansion coefficients t_{ij}^{ab} are referred to as cluster amplitudes. The crucial point is to optimize these coefficients. The CC equations are obtained by inserting Ψ_{CC} [eq. (2.57)] into the electronic Schrödinger equation projected by the reference function Ψ_{HF} and single, double and higher-order excitations.

$$\hat{H} e^{\hat{T}} \Psi_{HF} = E e^{\hat{T}} \Psi_{HF} \quad (2.60)$$

When the operator $\hat{W} = \hat{H} - E_{HF}$ (E_{HF} is the HF energy) is introduced, the following equations are obtained for the CCD method:

$$\left\langle \Psi_{HF} \left| \hat{W} \right| \hat{T}_2 \Psi_{HF} \right\rangle = \Delta E \quad (2.61)$$

$$\left\langle \Psi_{ij}^{ab} \left| \hat{W} \right| \left(1 + \hat{T}_2 + \frac{1}{2} \hat{T}_2^2 \right) \Psi_{HF} \right\rangle = \Delta E t_{ij}^{ab} \quad ; \quad \forall ij, ab \quad (2.62)$$

where ΔE is the correlation energy and the t_{ij}^{ab} coefficients are the cluster amplitudes.

Similarly, in the coupled cluster singles and doubles (CCSD) method, single and double excitations are considered, i.e. $\hat{T}=\hat{T}_1+\hat{T}_2$ is used. The CCSD(T) method [19,44,45] includes also single, double and perturbative triple excitations ($\hat{T}=\hat{T}_1+\hat{T}_2+\hat{T}_3$).

The key limitation of the CC methods is the rapid increase of their computational cost with system size. Formally, CCSD scales as the sixth power of the number of basis functions included in the expansion; hence, the practical value of such an approach is limited to rather small molecular systems. For the CCSDT method the computational demand is even higher due to the *expensive* triple excitations. Therefore the CCSD(T) method is often used. The CCSD(T) method attempts to estimate the effects of the inclusion of the \hat{T}_3 operator in the exponential excitation operator through perturbation theory. It has proved to be extremely successful in providing chemically accurate predictions. In the present thesis, single point CCSD(T) calculations have been performed in order to obtain benchmark activation energies for chemical reactions.

2.2.4. Density Functional Theory Methods

The easier way to solve the problem of electronic correlation is by means of Density Functional Theory (DFT). DFT is less expensive than any other correlation methods, and it is much more precise in many situations. It is the only way to include electron-correlation in calculations on large systems. Since DFT calculations include the effects of electron correlation, they can give the benefits of some more expensive *ab initio* methods at a much lower cost.

Density functional theory-based methods ultimately derive from quantum mechanics research from the 1920's, especially from the Thomas-Fermi-Dirac model, and from Slater's fundamental work in quantum chemistry in the 1950's. The DFT approach is based upon a strategy of modelling electron correlation via general functionals of the electron density [46].

DFT is based upon the idea that the energy of an electronic system can be expressed in terms of its density. The one-electron density $\rho(\mathbf{r})$ for a N -electron system is obtained by carrying out the integration of the square of the wave function ($|\Psi|^2$) over the space and spin coordinates of all electrons, except one:

$$\rho(\mathbf{r}_1) = N \int \dots \int |\Psi(\mathbf{x}_1, \mathbf{x}_2, \dots, \mathbf{x}_N)|^2 d\omega_1 d\mathbf{x}_2 \dots d\mathbf{x}_N \quad (2.63)$$

where the coordinates \mathbf{x}_i for the i^{th} electron comprise both space and spin coordinates, i.e. \mathbf{r}_i and ω_i , respectively. $\rho(\mathbf{r})$ is a non-negative function of the three

variable x, y, z , which represents the electron density of the electron could carrying N electron, such that the integration of $\rho(\mathbf{r})$ over space gives the total number of electrons:

$$\int \rho(\mathbf{r}) d\mathbf{r} = N \quad (2.64)$$

Two fundamental theorems in DFT have been introduced by Hohenberg and Kohn [46,47]: The first theorem of Hohenberg and Kohn states that “The external potential $v(\mathbf{r})$ is determined within an additive constant by the electron density $\rho(\mathbf{r})$.” Therefore $\rho(\mathbf{r})$ also determines the ground state wave function Ψ and all other electronic properties of the system. Indeed, suppose one has the electronic density of an unknown system. The number of electrons in the system is obtained by integrating the electronic density over space. By looking at values of the function $\rho(\mathbf{r})$ at each point in space in order to find the locations of the cusps, one is able to indicate the positions of the nuclei. By examining how fast the electron density drops at the position of a nucleus, the charge of the nucleus can be determined (Kato’s theorem) [48]. So far, one has thus enough information to write down the Hamiltonian and the corresponding Schrödinger equation, which determines the wave function of the system. Hence, the electron density $\rho(\mathbf{r})$ contains the same precise information about the system just as does the wave function Ψ .

The energy of the system can be expressed as a functional of the electron density ρ , as follows:

$$E[\rho] = V_{ne}[\rho] + T[\rho] + V_{ee}[\rho] \quad (2.65)$$

where $V_{ne}[\rho]$ is the nucleus-electron energy functional, $T[\rho]$ is the kinetic energy functional, and $V_{ee}[\rho]$ is given by:

$$V_{ne}[\rho] = \int \rho(\mathbf{r}) v(\mathbf{r}) d\mathbf{r} \quad (2.66)$$

with $v(\mathbf{r})$ the external potential defined by eq. (2.6). The electron-electron interaction energy $V_{ee}[\rho]$ has two terms: the classical Coulomb repulsion term $J[\rho]$ and a term with a non-classical origin. The classical Coulomb repulsion term $J[\rho]$ is expressed as follows:

$$J[\rho] = \frac{1}{2} \iint \frac{1}{r_{12}} \rho(\mathbf{r}_1) \rho(\mathbf{r}_2) d\mathbf{r}_1 d\mathbf{r}_2 \quad (2.67)$$

The exact form of the non-classical contribution to $V_{ee}[\rho]$ is unknown and represents the main challenge of DFT.

The second theorem by Hohenberg and Kohn [46] is an analogue of the variation principle, which states that: “For a given number of electrons and an external potential $v(\mathbf{r})$, there exists a functional of ρ denoted by $E_v^{HK}[\rho]$, for which the following variation principle is satisfied.

$$E_v^{HK}[\rho] \geq E_v^{HK}[\rho_0] = E_0 \quad (2.68)$$

where ρ_0 stands for the ideal electronic density distribution for the ground state.”

The Hohenberg-Kohn functional $E_v^{HK}[\rho]$ attains the minimum $E_v^{HK}[\rho_0] = E_0$ for the ideal (exact) density distribution, ρ_0 . The ultimate goal of DFT is to find mathematically suitable forms of the Hohenberg-Kohn energy functional. A most basic problem is that there exists no exact formula for this functional. The best which can be achieved is to devise good enough approximations to the exact energy functional.

Kohn and Sham invented an approach to the kinetic energy functional, known as the Kohn-Sham method. This method first considers a system with non-interacting electrons. In a first approximation, the total electron density $\rho_s(\mathbf{r})$ of a non-interacting N -electron system can be considered as the sum of N one-electron orbital densities which are constructed from one-electron wave functions $\chi_i(\mathbf{r})$ as follows:

$$\rho_s(\mathbf{r}) = \sum_i^N \sum_{\sigma} |\chi_i(\mathbf{r}, \sigma)|^2 \quad (2.69)$$

The orbitals $\chi_i(\mathbf{r})$ are eigenfunctions of the one-electron Hamiltonian operator, \hat{h}_s , with the corresponding orbital energies.

$$\hat{h}_s(\mathbf{r})\chi_i(\mathbf{r}) = \varepsilon_i(\mathbf{r})\chi_i(\mathbf{r}) \quad (2.70)$$

The corresponding Hamiltonian operator is then

$$\hat{H}_s = \sum_i^N \hat{h}_s = \sum_i^N \left[-\frac{1}{2} \nabla_i^2 + v_s(\mathbf{r}) \right] \quad (2.71)$$

when the external potential is given by

$$v_s(\mathbf{r}) = - \sum_A \frac{Z_A}{|\mathbf{r} - \mathbf{R}_A|} \quad (2.72)$$

These equations can be solved iteratively in order to find the appropriate density. When considering a determinantal wave function for a system with N non-interacting electrons,

$$\Psi_s = \frac{1}{\sqrt{N!}} \begin{vmatrix} \chi_1(\mathbf{1}) & \chi_2(\mathbf{1}) & \dots & \chi_N(\mathbf{1}) \\ \chi_1(\mathbf{2}) & \chi_2(\mathbf{2}) & \dots & \chi_N(\mathbf{2}) \\ \dots & \dots & \dots & \dots \\ \chi_1(\mathbf{N}) & \chi_2(\mathbf{N}) & \dots & \chi_N(\mathbf{N}) \end{vmatrix} \quad (2.73)$$

the kinetic energy and the electron density are given by:

$$T_s[\rho_s] = \sum_i^N \langle \chi_i | -\frac{1}{2} \nabla_i^2 | \chi_i \rangle \quad (2.74)$$

The total energy of the non-interacting system is (notice that there are no electron-electron repulsion terms)

$$E_s[\rho_s] = T_s[\rho_s] + \int v_s(\mathbf{r}) \rho_s(\mathbf{r}) d\mathbf{r} \quad (2.75)$$

The basic idea of the Kohn-Sham procedure is to map the electron density derived from a model non-interacting system $\rho_s(\mathbf{r})$ onto the exact density of the interacting system $\rho(\mathbf{r})$, by substituting an effective potential to the external potential $v_s(\mathbf{r})$. For systems with interacting electrons the total energy can be expressed as:

$$\begin{aligned} E[\rho] &= \int v(\mathbf{r}) \rho(\mathbf{r}) d\mathbf{r} + T[\rho] + U_{elec-elec}[\rho] \\ &= \int v(\mathbf{r}) \rho(\mathbf{r}) d\mathbf{r} + T_s[\rho] + (T[\rho] - T_s[\rho]) + J[\rho] + (U_{elec-elec}[\rho] - J[\rho]) \\ &= \int v(\mathbf{r}) \rho(\mathbf{r}) d\mathbf{r} + T_s[\rho] + J[\rho] + E_{xc}[\rho] \end{aligned} \quad (2.76)$$

$E_{xc}[\rho]$ is called the exchange-correlation energy functional which captures all many-body interactions. It contains the difference between $T[\rho]$ and $T_s[\rho]$ and the non-classical part of $U_{elec-elec}[\rho]$.

$$E_{xc}[\rho] = (T[\rho] - T_s[\rho]) + (U_{elec-elec}[\rho] - J[\rho]) \quad (2.77)$$

The effective potential is defined by

$$v_{eff}(\mathbf{r}) = v(\mathbf{r}) + \frac{\delta J[\rho]}{\delta \rho(\mathbf{r})} + \frac{\delta E_{xc}[\rho]}{\delta \rho(\mathbf{r})} \quad (2.78)$$

with $v_{xc}(\mathbf{r}) = \frac{\delta E_{xc}[\rho]}{\delta \rho(\mathbf{r})}$ the exchange-correlation potential.

A system with interacting electrons can be regarded as a system of non-interacting electrons moving in an external potential $v_s(\mathbf{r}) = v_{eff}(\mathbf{r})$. The density $\rho(\mathbf{r})$ can then be obtained by solving the following set of N one-electron equations:

$$h^{KS}(\mathbf{r})\chi_i(\mathbf{r}, \omega) = \varepsilon_i \chi_i(\mathbf{r}, \omega) \quad (2.79)$$

$$\left[-\frac{1}{2}\nabla^2 + v_{eff}(\mathbf{r})\right]\chi_i(\mathbf{r}, \omega) = \varepsilon_i \chi_i(\mathbf{r}, \omega) \quad (2.80)$$

with $\chi_i(\mathbf{r}, \omega)$ the Kohn-Sham spin-orbitals and h^{KS} the Kohn-Sham one-electron Hamiltonian operator [46], and with

$$\rho(\mathbf{r}) = \sum_i^N \sum_{\omega} |\chi_i(\mathbf{r}, \omega)|^2 \quad (2.81)$$

Since $v_{eff}(\mathbf{r})$ depends on $\rho(\mathbf{r})$ through $E_{xc}[\rho]$, the problem has to be solved self-consistently starting from an initial guess for $\rho(\mathbf{r})$. $v_{eff}(\mathbf{r})$ is constructed through eq. (2.72) and a new $\rho(\mathbf{r})$ is found from eq. (2.80) and eq. (2.81). The self-consistent field (SCF) procedure proceeds further until convergence in the energy and electron density is reached.

The ultimate goal of DFT is to find mathematically suitable forms of the Hohenberg-Kohn energy functional $E_{xc}[\rho(\mathbf{r})]$. A most basic problem is that there exists no exact formula for this functional. The best which can be achieved is to devise good enough approximations to the exact energy functional. In practice, $E_{xc}[\rho(\mathbf{r})]$ is divided into two separate parts:

$$E_{xc}[\rho] = E_x[\rho] + E_c[\rho] \quad (2.82)$$

$E_x[\rho]$ takes into account the exchange energy arising from the antisymmetry of the wave function (Fermi correlation) and $E_c[\rho]$ accounts for the correlation of the motions of electrons of different spin (dynamic correlation). In general, $E_{xc}[\rho(\mathbf{r})]$ is approximated as an integral involving only the spin densities and possibly their gradients.

$$E_{xc}[\rho] = \int f[\rho_{\alpha}(\mathbf{r}), \rho_{\beta}(\mathbf{r}), \nabla\rho_{\alpha}(\mathbf{r}), \nabla\rho_{\beta}(\mathbf{r})] d\mathbf{r} \quad (2.83)$$

ρ_{α} represents the α spin electron density and ρ_{β} the β spin electron density.

Various approaches exist to calculate the exchange and correlation energy terms in DFT methods. These approaches differ in using either only the electron density ρ (local methods) or the electron density as well as its gradients $\nabla\rho$ (gradient corrected methods). The only local exchange functional available in *Gaussian* is the Slater functional [49]. Combination with the local VWN (Vosko–Wilk–Nusair) correlation functional gives the local density approximation (LDA) [50–52]. In LDA, the exchange-correlation energy functional is given as:

$$E_{xc}[\rho] = \int \rho(\mathbf{r})\varepsilon_{xc}(\rho) d\mathbf{r} \quad (2.84)$$

where $\varepsilon_{xc}(\mathbf{r})$ is the exchange and correlation energy per particle of a uniform electron gas of density $\rho(\mathbf{r})$.

In the last few years, methods based on DFT have gained steadily in popularity. The best DFT methods achieve significantly greater accuracy than HF theory at only a modest computational cost [47]. They do so including some of the effects of electron correlation much less expensively than traditional perturbation methods. A variety of functionals have been defined, generally distinguished by the way that they treat the exchange and correlation components:

- (i) Local exchange and correlation functionals involve only the values of the electron spin densities. Slater and X_a are well-known local exchange functionals and the local spin density treatment of WVN is a widely used local correlation functional.
- (ii) Gradient-corrected functionals involve both the values of the electron-spin densities and their gradients. A popular gradient-corrected correlational functional is the one proposed by Becke in 1988 [53]; a widely-used gradient-corrected correlational functional is the LYP functional of Lee, Yang and Parr [6]. The combination of the two forms gives the B-LYP method (available via the BLYP keyword in the Gaussian package of programs). Perdew has also proposed some important gradient-corrected functionals, known as Perdew 86 and Perdew–Wang 91 [54].

There are several hybrid functionals, which define the exchange functional as a linear combination of Hartree-Fock, local, and gradient-corrected correlation functionals. Hybrid approximations to the exchange-correlation functional are very popular, because the results obtained with these approximations are usually found to be in very good agreement with experiment. In this thesis, we have used the B3LYP (Becke-3-parameters-Lee–Yang–Parr) functional [5,6], the dispersion-corrected ω B97XD functional [7] as well as the UM05-2x [8] and UM06-2x [8,9] functionals, which are briefly reviewed in the sequel.

2.2.4.1. The B3LYP Functional

One of the most common density functionals is the combination of Becke’s three-parameter exchange functional with the correlation functional of Lee, Yang and Parr, giving the Becke-3-parameters-Lee–Yang–Parr (B3LYP) functional [5,6,54–58]. The B3LYP functional is comprised of the Becke’s 1988 exchange functional [53], the Lee–Yang–Parr (LYP) correlation functional [6], the Vosko–Wilk–Nusair (VWN) correlation functional [51] and the difference

between the Hartree-Fock and local spin-density approximation (LSDA) exchange energy. The relevant coefficients for these contributions are given by [48,51,55]:

$$E_{xc}^{B3LYP} = E_{xc}^{LSDA} + 0.20(E_x^{HF} - E_x^{LSDA}) + 0.72 E_x^{B88} + 0.81 E_c^{LYP} - 0.19 E_c^{VWN} \quad (2.85)$$

Although the B3LYP functional is widely used in computational chemistry, it has some serious shortcomings [8]: (i) it is inadequate for compounds containing transition metals; (ii) it systematically underestimates reaction barrier heights; (iii) it is inaccurate for interactions dominated by medium range correlation energy, such as van der Waals forces or aromatic-aromatic π -stacking interactions.

The B3LYP functional which is a hybrid GGA (generalized gradient approximation) functional is largely responsible for the success of density functional theory. However, it does have unsatisfactory performance issues, as follows:

- (1) Barrier heights: B3LYP was found [59] to underestimate barrier heights by an average of 4.4 kcal mol⁻¹. This underestimation is usually ascribed to the self-interaction error (unphysical interaction of an electron with itself) in local DFT.
- (2) Noncovalent interactions: B3LYP is unable to describe van der Waals complexes bound by dispersion interactions. This inability of B3LYP (and most other popular functionals) to accurately describe medium-range exchange correlation energy limits their applicability for biological systems and soft materials where medium-range dispersion-like interactions play a vital role. Moreover, some recent studies have shown that the inaccuracy of the medium-range exchange correlation energies leads to large systematic errors in the prediction of heats of formation of organic molecules [60–67], and incorrect trends in the bond energies of organometallic catalytic systems [68,69].
- (3) Transition metal chemistry: B3LYP and many other hybrid functionals have been found to give unreliable results for transition metal chemistry [70–73], where better performance is often obtained with local functionals that are poor for main-group organic chemistry. For instance, popular functionals containing Hartree-Fock exchange often overestimate the spin polarization of systems containing transition metals.

2.2.4.2. The ω B97XD Exchange-Correction Functional

The ω B97X-D parametrized functional includes 100% long-range exact exchange, a small fraction (about 22%) of short-range exact exchange, a modified B97 exchange density functional for short-range interaction, the B97 correlation density functional [74], and empirical dispersion corrections. When the constraint

of $\omega=0$ is applied, ω B97X-D reduces to the existing B97 functional form with the same empirical dispersion corrections. The constrained form ($\omega=0$), when reoptimized on the same training set of data, provides poorer fits, indicating that the single extra degree of freedom corresponding to long-range exchange is physically important. The ω B97X-D functional provides significant improvement only for non-covalent interactions [7].

Recent theoretical studies have shown that fully optimized long-range corrected functionals (such as ω B97 and ω B97X) can yield better results for covalent systems than traditional hybrids or long-range corrected functionals that are not fully reoptimized. It seems therefore natural to explore whether further improvements are possible by incorporating empirical atom-atom dispersion corrections [7].

Density functional theory with functionals that include empirical dispersion corrections (DFT-D) is generally somewhat superior in overall performance. A most successful functional is the ω B97X-D one, which is used for applications where non-covalent interactions are expected to be significant. The ω B97X-D functional is free of long-range self-interaction, but still suffers from some self-interaction at short-range. We also note that long-range correlation effects are solely treated by the empirical dispersion corrections in the ω B97X-D functional, and therefore the Kohn-Sham orbitals themselves are not directly influenced by dispersion effects [7].

Following the general form of the density functional theory with empirical dispersion corrections (DFT-D) scheme [75–88] (which have shown generally satisfactory performance on a large set of non-covalent system [80,85]), the total energy is given by:

$$E_{\text{DFT-D}} = E_{\text{KS-DFT}} + E_{\text{disp}} \quad (2.86)$$

The energy is then computed as the sum of a KS-DFT part, using the ω B97X functional [89], and an empirical atomic-pairwise dispersion correction. We opted for using an unscaled dispersion correction, given by

$$E_{\text{disp}} = - \sum_{i=1}^{N_{\text{at}}-1} \sum_{j=i+1}^{N_{\text{at}}} \frac{C_6^{ij}}{R_{ij}^6} f_{\text{damp}}(R_{ij}) \quad (2.87)$$

where N_{at} is the number of atoms in the system, C_6^{ij} is the dispersion coefficient for atom pair ij , and R_{ij} is an interatomic distance.

2.2.4.3. The M05-2x Exchange-Correlation Functional

Minnesota functionals (Myz) are a set of approximated exchange-correlation energy functionals in density functional theory which have been developed by the research group of Professor Truhlar at the University of Minnesota. These functionals are based on meta-generalized gradient approximation (meta-GGA), since they all include terms that depend on the kinetic energy density, and are all based on flexible functional forms parametrized on high-quality benchmark databases. These functionals are nowadays widely used in quantum chemistry and solid state physics. These functionals are available in a large number of popular quantum chemistry computer programs [90–93]. The first family of Minnesota functionals (Minnesota 05), is represented by the M05 [94] and M05-2x [95] global hybrid functionals, with 26% and 52% HF exchange, respectively.

The M05 functional was parametrized including both metallic and nonmetallic elements, whereas M05-2x is a highly nonlocal functional with double the amount of nonlocal exchange (2x) that is parametrized only for nonmetals. The M05-2x functional has the best performance for thermochemical kinetics, noncovalent interactions (especially weak interaction, hydrogen bonding, $\pi\cdots\pi$ stacking, and interactions energies of nucleobases), as well as alkyl bond dissociation energies. It provides also the best composite results for energetics, excluding metals.

In a recent review [96], Scuseria and Staroverov summarized the six strategies that have been widely employed for designing density functionals: (1) local spin density approximation (LSDA), (2) density-gradient expansion, (3) constraint satisfaction, (4) modeling the exchange-correlation hole, (5) empirical fits, and (6) mixing Hartree-Fock and approximate DFT exchange. The M05-2x functional was constructed using strategies (3), (5), and (6). It is designed only for main-group chemistry, in particular for calculations of the barrier heights and noncovalent interactions. As a side effect, this functional turns out to be excellent for non-charge-transfer states in electronic spectroscopy.

By taking account of all the problems which have been mentioned previously for the B3LYP functional (section 2.2.4.1), the M05 functional [94,95] (“Minnesota 2005”) was developed, and it gives good performance for transition metal chemistry [97] as well as main-group thermochemistry, barrier heights, and noncovalent interactions. With the same functional form as M05, Truhlar’s research group also developed the M05-2x functional that focuses on problems about barrier heights and noncovalent interactions, and performs even better than M05 or other previously developed functionals for main group kinetics, thermochemistry, and noncovalent interactions [60,98–102].

2.2.4.4. The M06-2x Exchange-Correlation Functional

In 2006, Truhlar research group at the University of Minnesota developed a new suite of functionals called the M06 suite, which essentially supersedes Minnesota 05 functionals. The rest of this account is focused on the most recently developed functionals, namely the M06 suite, which corresponds to functionals designed with improved functional forms (M06 and M06-2x) and increased accuracy, especially for kinetic data. The Minnesota 06 family represents a general improvement over the Minnesota 05 family and is composed by the [60]:

- M06 functional: Global hybrid functional with 27% Hartree-Fock exchange. For main group thermochemistry and noncovalent interactions, transition metal thermochemistry and organometallics. It is usually the most versatile of the M06 functionals, and because of this large applicability it can be slightly worse than M06-2x for specific properties that require high percentage of Hartree-Fock exchange, such as thermochemistry and kinetics.
- M06-2x functional: Global hybrid functional with 54% HF exchange. It is the top performer within the 06 functionals for main group thermochemistry, kinetics and noncovalent interactions, however it cannot be used for cases where multireference effect are high or might be involved, such as in transition metal thermochemistry and organometallic chemistry.

The hybrid meta-GGA exchange-correlation functional M06-2x is a highly nonlocal functional, which doubles the amount of nonlocal exchange (2x), and is parametrized only for nonmetals. M06-2x is the best functional for main-group thermochemistry, kinetics, noncovalent interactions, and electronic excitation energies to valence and Rydberg states [103,104].

The local parts of the M06 and M06-2x functionals depend on three variables: the spin density (ρ_σ), the reduced spin density gradient x_σ , and the spin kinetic energy density τ_σ

$$x_\sigma = \frac{|\nabla \rho_\sigma|}{\rho_\sigma^{\frac{4}{3}}} ; \sigma = \alpha, \beta \quad (2.88)$$

$$\tau_\sigma = \frac{1}{2} \sum_i^{occup} |\nabla \Psi_{i\sigma}|^2 \quad (2.89)$$

The M06 functional includes terms based on the van Voorhis and Scuseria's τ -dependent gradient-corrected correlation (VSXC) functional [105,106], and these terms involve a working variable z_σ and two working functions γ and h :

$$z_\sigma = \frac{2\tau_\sigma}{\rho_\sigma^{\frac{5}{3}}} - C_F ; C_F = \frac{3}{5} (6\pi^2)^{\frac{2}{3}} \quad (2.90)$$

$$\gamma(x_\sigma, z_\sigma) = 1 + \alpha(x_\sigma^2 + z_\sigma) \quad (2.91)$$

$$h(x_\sigma, z_\sigma) = \left(\frac{d_0}{\gamma(x_\sigma, z_\sigma)} + \frac{d_1 x_\sigma^2 + d_2 z_\sigma}{\gamma_\sigma^2(x_\sigma, z_\sigma)} + \frac{d_3 x_\sigma^4 + d_4 x_\sigma^2 z_\sigma + d_5 z_\sigma^2}{\gamma_\sigma^3(x_\sigma, z_\sigma)} \right) \quad (2.92)$$

where σ is the component along an arbitrary space fixed axis of electron spin angular momentum.

The M06 functional form is a linear combination of the functional forms of the M05 [94,95] and VSXC exchange functionals. In particular the M06 exchange functional is given by

$$E_X^{M06} = \sum_\sigma \int dr [F_{X\sigma}^{\text{PBE}}(\rho_\sigma, \nabla\rho_\sigma) f(w_\sigma) + \epsilon_{X\sigma}^{\text{LSDA}} h_X(x_\sigma, z_\sigma)] \quad (2.93)$$

where $f(w_\sigma)$ is the spin kinetic-energy-density enhancement factor.

The functional form of the exchange functional in M06-2x is the special case in which $h_X(x_\sigma, z_\sigma) = 0$; in this special case, the M06 functional form for exchange reduces to the M05 functional form for exchange.

$$E_X^{M06-2x} = \sum_\sigma \int dr [F_{X\sigma}^{\text{PBE}}(\rho_\sigma, \nabla\rho_\sigma) f(w_\sigma)] \quad (2.94)$$

2.2.5. Basis Sets

There are many different *ab initio* methods that can be used to find approximate solutions to the Schrödinger equation, and the one to use for a specific problem is usually chosen by comparing the performance against known experimental data. One of the most crucial approximations which is inherent to essentially all *ab initio* methods is the introduction of a basis set [107].

A basis set is the mathematical set of atomic orbitals within a molecular system, which is used to expand molecular orbitals (LCAO approximation). Basis sets assign a group of basis functions to each atom within a molecule. Larger basis sets result in larger computational demands but more accurate molecular orbitals by imposing fewer restrictions on the locations of the electrons in space. In a correct quantum mechanical depiction, electrons have indeed a finite probability of existing anywhere in space [46]. There are two types of basis functions most commonly used for calculating electronic structure, as follows:

(i) Slater-type orbitals (STOs) [108], which are the closest form to the exact expressions of atomic orbitals in atomic calculations, but which are not appropriate for numerical computations of multi-centered integrals because of the lack of exact analytical expressions, making the numerical evaluation of such integrals

extremely difficult and costly in computer time. Thus, their practical use in quantum-mechanical calculations is limited. Their general definition is given by:

$$\phi_{\zeta,n,l,m}(r,\theta,\varphi) = N Y_{l,m}(\theta,\varphi) r^{n-1} e^{-\zeta r} \quad (2.95)$$

with N being a normalization factor and $Y_{l,m}$ being the spherical harmonics. A main advantage of Slater type orbitals is the correct exponential decay of the radial factor at large distances.

(ii) Gaussian-type orbitals (GTOs) [107,109] are used in most quantum mechanics programs as basis functions, despite severe shortcomings in correctly describing electron densities in the “cusp” regions around nuclei. Also, GTO’s decay too fast at large distances. Their main advantage is that there exist analytical expressions for evaluating multi-centered bielectron integrals over GTOs, which enables easy evaluations of such integrals. Therefore, GTOs are largely preferred over STOs, and are generally used in computational calculations.

$$\phi_{\zeta,n,l,m}(r,\theta,\varphi) = N Y_{l,m}(\theta,\varphi) r^{n-1} e^{-\alpha r^2} \quad (2.96)$$

where N is the normalization constant, and α represents the exponent coefficient. The main advantage of GTOs is that they enable easy calculations of bielectron integrals, because products of Gaussian functions are themselves Gaussians.

The absence of the r^{n-1} pre-exponential factor restricts single Gaussian primitives to approximating only $1s$, $2p$, $3d$, $4f$... orbitals. This factor was removed for practical reasons, namely, for fast integral calculations. However, suitable combinations of Gaussians are able to approximate the correct nodal properties of atomic orbitals.

2.2.5.1. Minimal Basis Sets

The smallest possible basis set is the minimal basis set, which contains the minimal number of basis functions required for each element in the periodic table, as follows:

Element	Minimal basis set
Hydrogen, Helium	a single s -function
First row elements	2 s -functions ($1s$ and $2s$) and a set of p -functions ($2p_x, 2p_y, 2p_z$) Li and Be formally only require 2 s -functions but a set of p -functions is also added
Second row elements	3 s -functions ($1s, 2s, 3s$) and 2 sets of p -functions ($2p$ and $3p$)

Minimal basis sets use fixed-size atomic-type orbitals. The STO-3G basis set is a minimal basis set which uses three Gaussian primitives per basis function, as

is accounted for by the “3G” suffix in its name. “STO” stands for “Slater-type orbitals”, and the STO-3G basis set approximates Slater orbitals with Gaussian functions.

2.2.5.2. Split Valence Basis Sets

The first way to improve a minimal basis set is to increase the number of basis functions per atom. Split valence basis sets have two or more sets of basis functions for each valence orbital [110]. For example, with the 3-21G and 6-31G basis sets, hydrogen and carbon atoms have the following sets of basis functions, as follows:

H : $1s, 1s'$

C : $1s, 2s, 2s', 2p_x, 2p'_x, 2p_y, 2p'_y, 2p_z, 2p'_z$

where the primed and unprimed orbitals differ in size.

The number of basis functions for the 3-21G and 6-31G basis sets are the same, but the 6-31G basis set has more GTOs than the 3-21G basis set. Therefore, a 6-31G basis set describes molecular properties better than a 3-21G basis set [109].

2.2.5.3. Double Zeta Basis Sets

The next improvement in the basis set is by doubling all basis functions, producing a Double Zeta (DZ) type basis set [107,109]. Doubling the number of basis functions allows a much better description of electron distribution in the chemical bonding which occurs between valence orbitals. For instance, doubling the $1s$ functions in carbon allows for a better description of the $1s$ -electrons. However, the $1s$ orbital is independent of the chemical environment. The DZ basis sets, such as the Dunning-Huzinaga basis set (D95), form all molecular orbitals from linear combinations of two sizes of functions for each atomic orbital. A variation of DZ type basis only doubles the number of valence orbitals, producing split valence basis sets. In actual calculations, a doubling of the core orbitals would rarely be considered, and the term DZ basis is also used for split valence basis sets or sometimes VDZ, for valence double zeta [109]. The minimal DZ basis set functions needed for each element in the periodic table are specified as follows:

Element	Minimal basis set
Hydrogen and helium	2 s -function ($1s$ and $1s'$)
First row elements	4 s -functions ($1s, 1s', 2s, 2s'$) and 2 sets of p -functions ($2p, 2p'$)
Second row elements	6 s -functions and 4 sets of p -functions

The next steps in improving the basis set are as follows [109]:

- Triple Zeta (TZ), which contains *three* times as many functions as the minimum basis set. e.g., **6** *s*-functions and **3** sets of *p*-functions for the first row elements in the periodic table, etc.
- Quadruple Zeta (QZ), which contains *four* times as many functions as the minimum basis set. e.g., **8** *s*-functions and **4** sets of *p*-functions for the first row elements in the periodic table, etc.
- Quintuple Zeta (5Z), which contains *five* times as many functions as the minimum basis set. e.g., **10** *s*-functions and **5** sets of *p*-functions for the first row elements in the periodic table, etc.

2.2.5.4. Polarized Basis Sets

Split valence basis sets allow orbitals to change size, but not to change shape. Polarized basis sets remove this limitation by adding orbitals with angular momentum beyond what is required for the ground state to the description of each atom. For instance, polarized basis sets add *d*-functions to carbon atoms and *f*-functions to transition metals, and some of them add *p*-functions to hydrogen atoms. An example of a polarized basis set is 6-31G(d) [6-31G*], which adds six *d*-functions to the 6-31G basis set on each non-hydrogen atom. The 6-31G(d,p) [6-31G**] basis set is another popular polarized basis set, which adds three *p*-functions to hydrogen atoms in addition to the *d*-functions on first row atoms.

- Double Zeta plus Polarization (DZP): one set of polarizing functions added to the first row atoms very often neglecting the *p* polarizing functions on hydrogen and helium atoms.
- Double Zeta plus Double Polarization (DZ2P): two sets of polarizing functions with different exponents.
- Triple Zeta plus Double Polarization (TZ2P): TZ basis with two sets of polarizing functions

For correlated methods the higher angular momentum, polarization functions are especially important. Widely used polarized basis sets are the correlation consistent polarized valence basis sets (cc-pVXZ set with $X=D, T, Q, 5 \dots$) which have been developed by Dunning and co-workers [111]. The smallest basis set in this series is the correlation consistent polarized valence double-zeta basis set (cc-pVDZ).

2.2.5.5. Diffuse Functions

Basis sets can be ultimately improved by adding diffuse functions that are large-size versions of *s*- and *p*-type functions [107,109]. They allow orbitals to

occupy a larger region of space. Basis sets with diffuse functions are important for systems such as molecules with lone pairs, anions and other systems with significant negative charge, electronically excited systems, systems with low ionization potentials, etc. The 6-31+G(d) basis set is obtained by adding four diffuse functions (s , p_x , p_y , p_z) on first row atoms to the 6-31G(d) basis set. Its double plus version, 6-31++G(d), adds diffuse functions to the hydrogen atoms as well. Diffuse functions on hydrogen atoms seldom make a significant difference in accuracy [46].

The addition of diffuse functions on all atoms to the cc-pVXZ basis sets is denoted by the “aug” prefix. One diffuse function of each function type in use for a given atom is added [112,113] for functions on hydrogen atoms, and one set of s , p , d , and f diffuse functions on heavy atoms (B through Ne and Al through Ar).

Energies computed using the cc-pVXZ and aug-cc-pVXZ basis sets of improving quality ($X=D$, T , Q , 5 , ...) converge smoothly at the Hartree-Fock level [114] and at correlated levels [115], enabling extrapolations to the limit of an asymptotically complete basis set ($X=\infty$).

2.2.6. Location of Transition States

Reactants, products, and transition states correspond all to stationary points on the potential energy surface, meaning that at these points the derivative of the energy with respect to the reaction coordinate is zero. Minima (reactants, products) are points where the second energy derivative is positive, whereas first-order saddle points (transition states) are characterized by *one* negative second energy derivative with respect to the reaction coordinate.

Gaussian uses the Synchronous Transit-Guided Quasi-Newton (STQN) method, developed by Schlegel and coworkers, for locating transition structures [116]. A linear synchronous transit or quadratic synchronous transit (QST) approach is used to get closer to the quadratic region around the transition state and then uses a quasi-Newton or eigenvector following algorithm to complete the optimization. This method is requested with the QST2 and/or QST3 options to the Opt keyword. QST2 requires two molecule specifications as input, namely the reactant and the product, while QST3 requires three molecule specifications: the reactant, the product, and an initial structure for the transition state.

In the QST2-guided search, the method of linear synchronous transit (LST) locates an initial transition state along the path connecting the reactant and the product. For each of the first few steps of a QST2-guided search, the optimizer is restricted to search along the circular curve connecting the reactant, an initial guess for the transition state, and product structures. This restriction prevents the

optimizer from being led far astray by the inaccuracies of the guessed Hessian, and prevents it from exploring transition states that do not correspond to the reaction of interest. During these steps, the optimizer approaches the maximum-energy structure (total energy gradient is zero) along the reactant-to-product curve, and also greatly improves the Hessian. Once it has obtained the improved Hessian and transition state guess, the optimizer removes the strict requirement that the search must be along the circular curve between the structures. For all subsequent steps in the search, the optimizer follows the Hessian eigenvector that is most similar to the tangent of the circular curve.

In a QST3-guided search an approximate transition state is provided. For the search to work best, the reactant and product structures should not be too radically different from the transition state. For instance, to find the transition state in a bond breaking reaction, it is preferable to provide a product structure in which the breaking bond is fairly long and weak rather than a true minimum-energy structure in which the bond has completely dissociated.

Hammond's postulate states that the structure of a transition state resembles that of the species nearest to it in free energy [117]. This can be quantified in terms of the position of the transition structure along the reaction coordinate, n_T , as defined by Agmon [118]

$$n_T = \frac{1}{2 - (\Delta G / \Delta G^\ddagger)} \quad (2.97)$$

The magnitude of n_T indicates the degree of similarity between the transition structure and the product. According to this equation, the position of the transition state along the reaction coordinate is determined solely by the Gibbs free energy of reaction, ΔG (a thermodynamic quantity), and the Gibbs free activation energy, ΔG^\ddagger (a kinetic quantity).

2.2.7. Composite Methods

Quantum chemistry composite methods [119] are computational methods that aim to reach high accuracy by combining the results of several calculations. They combine methods with a high level of theory for treating electron correlation, and a small basis set with methods that employ lower levels of theory and larger basis sets. They are commonly used to calculate thermodynamic quantities such as enthalpies of formation, atomization energies, ionization energies and electron affinities. Composite methods aim at chemical accuracy, which is usually defined as within 1 kcal mol⁻¹ of the experimental value. Specifically the first systematic model chemistry of this type with broad applicability was called Gaussian-1 (G1),

it has been introduced by John Pople. This was quickly replaced by the Gaussian-2 (G2) approach which has been used extensively. The Gaussian-3 (G3) approach was introduced later.

The CBS-QB3 composite method belongs to the family of the complete basis set methods of Petersson and co-workers [15], which were developed with the idea that a major source of error in quantum mechanical calculations arises from truncation of the basis set. In comparison, the Gaussian-n methods perform their approximation using additive corrections.

The complete basis set (CBS) models extrapolate to the CBS limit by using N^{-1} asymptotic convergence of MP2 pair energies calculated from pair natural orbital expansions. CBS models involve low-level (SCF and ZPE) calculations on large basis sets, mid-sized basis sets for second-order correlation corrections, and small basis sets for high-level correlation corrections. They include an extrapolation of energies up to the CCSD(T) level (Coupled Cluster Theory along with Single, Double and perturbative Triple electronic excitations [44,45,120]) in the limit of a complete basis set in order to correct Møller-Plesset second-order (MP2) energies [19]. In addition, this approach includes empirical corrections for spin contamination.

The CBS-QB3 method involves five steps, starting with a geometry optimization at the B3LYP level of theory [5,6], followed by a calculation of vibrational frequencies and thermodynamic state functions [121] obtained from canonical partition functions that were computed for an ideal gas, using Boltzmann statistical thermodynamics along with the rigid rotor-harmonic oscillator approximation (RRHO) [6,122]. Specifically, the CBS-QB3 method involves the following steps [14]:

- B3LYP/6-311G(2d,d,p) geometry optimization.
- B3LYP/6-311G(2d,d,p) frequency calculation with a 0.99 scale factor for the ZPE.
- CCSD(T)/6-31+G* energy calculation.
- MP4(SDQ)/6-31+G(d(f),p) energy calculation.
- UMP2/6-311+G(3d2f,2df,2p) energy calculation and CBS extrapolation.

When applied to conjugated systems, the B3LYP approach is known to deliver geometrical parameters (bond lengths and bond angles) of quality comparable to CCSD(T) results [123]. B3LYP geometries are therefore widely employed in other benchmark composite quantum mechanical approaches, such as the *W1* approach [124]. A weakness of the B3LYP approach is that it neglects dispersion forces, which may have some influence on torsional characteristics.

The CBS-QB3 method amounts to an extrapolation of energies to the level of Coupled Cluster Theory including single, double and perturbative triple excitations [CCSD(T)], in conjunction with a complete basis set. The N^{-1} asymptotic convergence of MP2 pair energies calculated from pair natural orbital expansions is used to extrapolate energies to the CBS limit [10–13]. This approach is known to yield a mean absolute deviation of 1.1 kcal mol⁻¹ on the G2/97 test set [13] for reaction energies. A more recent work indicates a maximum error of 2.8 kcal mol⁻¹ for the G2 test set of reaction energies, as well as average and mean absolute errors of 0.2 and 0.98 kcal mol⁻¹ [125]. It seems justified therefore to employ the CBS-QB3 method as a benchmark quantum chemical approach, in order to calibrate the accuracy of DFT methods employing necessarily approximate exchange-correlation functionals. This is only in case of an extreme spin contamination of the underlying UHF wave functions in which more accurate but also much more costly methods, such as the G2 or G4 approaches, should be used [126]. However, spin-contamination for doublet radicals is known to be very small in symmetry-broken UHF-based CCSD calculations, even when the UHF spin contamination is very large. For instance, the NO₂ radical, the value of $\langle S^2 \rangle$ is 1.18 and 0.76, respectively, for UHF and UHF-based CCSD wave functions [127].

Finally, the total energy is calculated from the following [14]:

$$E_{\text{CBS-QB3}} = E_{\text{MP2}} + \Delta E_{\text{MP4}} + \Delta E_{\text{CCSD(T)}} + \Delta E_{\text{ZPE}} + \Delta E_{\text{CBS}} + \Delta E_{\text{empirical}} + \Delta E_{\text{spin-orbit}} \quad (2.98)$$

where ΔE_{CBS} is the term correcting the basis set truncation error in the second-order energies, and the energy terms ΔE_{MP4} , $\Delta E_{\text{CCSD(T)}}$, $\Delta E_{\text{empirical}}$, and $\Delta E_{\text{spin-orbit}}$ are calculated (in atomic units) according to the following equations:

$$\Delta E_{\text{MP4}} = E_{\text{MP4(SDQ)/6-31+G(d(f),p)}} - E_{\text{MP2/6-31+G(d(f),p)}} \quad (2.99)$$

$$\Delta E_{\text{CCSD(T)}} = E_{\text{CCSD(T)/6-31+G*}} - E_{\text{MP4(SDQ)/6-31+G*}} \quad (2.100)$$

$$\Delta E_{\text{empirical}} = -0.00579 \sum_{i=1}^{n_{\beta}} \left(\sum_{\mu=1}^{N_{\text{virt}+1}} C_{\mu ii} \right)^2 |S_{ii}^2| \quad (2.101)$$

$$\Delta E_{\text{spin-orbit}} = -0.00954 \left[\langle S^2 \rangle - S_z(S_z - 1) \right] \quad (2.102)$$

The slow convergence of basis set expansions makes it very difficult to reduce the errors in calculated *ab initio* energies to chemical accuracy (~ 1 kcal mol⁻¹) by direct calculation. However, if the errors are systematic and we know their pattern, empirical corrections (ΔE_{emp}) can be used to improve the accuracy of the calculated

results [16]. In eq. (2.101), $|S|_{ii}$ is the absolute overlap integral between the most similar α and β orbitals [12], as follows:

$$|S|_{ii} = \int |\phi_i^\alpha \phi_i^\beta| d\tau \quad (2.103)$$

and the interference factor $(\sum_i C_{\mu_i})^2$ is the square of the trace of the first order wave function. As a bond is stretched, the interatomic absolute overlaps decay smoothly to zero at infinite separation, giving a size consistent generalization of the “number of pairs” correction [128–130]. The above interference factor includes thus the effects of near energy degeneracies.

2.2.8. The Nucleus Independent Chemical Shift Parameters

Nucleus independent chemical shift (NICS) parameters are local measures of aromaticity in benzenoid and related systems. These parameters are obtained by applying the gauge-independent atomic orbital (GIAO) method to estimate diamagnetic ring current intensity [131].

NICS indices are defined as the negative values of the absolute magnetic shielding in centers of benzenoid rings or above or below the molecular plane [132]. Rings with large negative NICS values are considered aromatic. The more negative the NICS values, the more aromatic the rings are. Non-aromatic species have NICS values close to zero and positive NICS values are indicative of antiaromaticity. NICS is usually computed at ring centers [NICS(0)] determined by the non-weighted mean of the heavy atoms coordinates. NICS indices can also be calculated at certain distance above or below the center of the ring taken into analysis. The NICS(0) values calculated at the center of the ring are the most influenced by σ -bonds, whereas the NICS(1) values calculated at the 1 Å above the plane are more affected by the π -electron system [133]. Therefore, the NICS values obtained at 1 Å above the molecular plane [NICS(1)] are considered to better reflect the π -electron effects than NICS(0) values [134].

2.2.9. Bond Order Analysis

A more balanced measure of the extent of bond formation or bond breaking along the reaction pathway is provided by the concept of bond order calculations [135–137]. This theoretical technique has been used to investigate the molecular mechanism of chemical reactions [135]. To investigate the nature of the reaction pathway, Wiberg bond indices [138] were computed using the natural bond orbital

(NBO) analysis program [139] as implemented in Gaussian 09 [140]. Wiberg bond indices between atoms x and y are defined as follows:

$$B_{xy} = \sum_{\gamma} \sum_{\delta} P_{\gamma\delta}^2 \quad (2.104)$$

where $P_{\gamma\delta}$ are elements of the density matrix, with the subscript γ and δ referring to atomic orbitals centered at atoms x and y , respectively. These indices can be used to estimate bond orders from population analysis. Bond breaking and bond making processes involved in the reaction mechanism can be monitored by means of the synchronicity (S_y) concept proposed by Moyano *et al.* [141], which is defined by the expression:

$$S_y = 1 - \frac{\left(\sum_{i=1}^n \frac{|\delta B_i - \delta B_{av}|}{\delta B_{av}} \right)}{2n - 2} \quad (2.105)$$

where n is the number of bonds directly involved in the reaction and the relative variation of the bond index (δB_i) for a bond i at the transition state is given as a percentage by eq. (2.106),

$$\delta B_i = \frac{B_i^{TS} - B_i^R}{B_i^P - B_i^R} \quad (2.106)$$

where the superscripts R, TS, and P, represent reactant, transition state and product, respectively. The evolution in bond change is evaluated as $\%EV = \delta B_i \times 100$. The average value in the change of bond orders is calculated by

$$\delta B_{av} = \frac{1}{n} \sum_{i=1}^n \delta B_i \quad (2.107)$$

In this analysis, the B_i values indicate bond order and δB_i is the change in bond order as the reaction progresses from reactant (B_i^R) to the transition state TS (B_i^{TS}) and to products (B_i^P). The percent evolution $\%EV$ is used to show the relative advance of the different reaction coordinates considered. The synchronicity parameter S_y varies between 0 and 1, with a value of $S_y=0$ for asynchronous processes and $S_y=1$ for a concerted synchronic.

2.2.10. Natural Bond Orbital Analysis

Natural bond orbitals (NBOs) are used in computational chemistry to calculate the distribution of electron density in atoms and in bonds between atoms. The NBOs are one of a sequence of natural localized orbital sets that include “natural atomic orbitals” (NAOs), “natural hybrid orbitals” (NHOs), “natural bonding

orbitals” (NBOs) and “natural semi-localized molecular orbitals” (NLMOs). These natural localized sets are intermediate between basis atomic orbitals (AOs) and canonical molecular orbitals (MOs) [142–144]:

AOs \rightarrow NAOs \rightarrow NHOs \rightarrow NBOs \rightarrow NLMOs \rightarrow MOs

We recall that natural orbitals are the eigenfunctions of the one-electron density matrix, and that the associated eigenvalues, known as the occupation numbers, represent a measure of the contribution that the different natural orbitals make to the density matrix. Natural bond orbitals (NBOs) have the maximum-occupancy (natural) character in localized 1-center and 2-center regions of the molecule. NBOs include the highest possible percentage of the electron density, ideally close to 2.000. Such orbitals provide the most accurate possible “natural Lewis structure” depiction of the wave function ψ , because all orbital details (polarization coefficients, atomic hybrid compositions, ... etc.) are mathematically chosen to include the *highest possible* percentage of the electron density. This percentage (denoted % ρ_L) gives an intrinsic measure of the accuracy of the natural Lewis structure picture, and is often found to be $> 99\%$ for common organic molecules, which gives a dramatic testimony to the reliability of the simple Lewis’s concepts [142,145,146].

All these natural localized sets are complete and orthonormal, and thus able to *exactly* describe any property of the wave function ψ . Compared to standard AOs, e.g., the NAOs give a much more condensed description of ψ , with only a small number of orbitals (i.e., corresponding to the formal “minimal basis”) having appreciable occupancy. Thus, a “minimal” description in terms of core and valence-shell NAOs is often found adequate for chemical purposes, providing a compact representation of ψ that is intimately related to standard valence concepts. The mutual orthogonality [142] of natural localized orbitals may seem to be a conceptual liability, inasmuch as the concept of “orbital overlap” seems to be lost. However, each orthogonal NAO (or NHO, NBO, etc.) can be uniquely associated with a corresponding “pre-orthogonal” PNAO (or PNHO, PNBO, etc.) which remains orthogonal to PNAOs on the same atom but has non-vanishing overlap integrals with those on other atoms. In accordance with the Mulliken approximation [147–149], the corresponding Hamiltonian interaction elements are found to be closely proportional to these overlap integrals. That is, if \hat{F} denotes the effective orbital Hamiltonian (Fock or Kohn-Sham operator), the interaction strength $\langle h_A | \hat{F} | h_B \rangle$ of bonding NHOs h_A, h_B can be approximated in terms of overlapping PNHOs \tilde{h}_A, \tilde{h}_B as

$$\langle h_A | \hat{F} | h_B \rangle \cong k \langle \tilde{h}_A | \tilde{h}_B \rangle \quad (2.108)$$

where k is a proportionality constant which is close to unity. Thus, PNHO overlap diagrams remain highly effective for teaching students the “principle of maximum overlap,” but without encouraging the frequent misconception that geometrical orbital overlaps (rather than the matrix elements of the Hamiltonian energy operator) are somehow at the origin of chemical bonding.

In accordance with the simple bond orbital picture [150], each bonding NBO σ_{AB} (the donor) can be written in terms of two directed valence hybrids h_A , h_B [natural hybrid orbitals (NHOs)] on atoms **A** and **B**, with corresponding polarization coefficients c_A , c_B , as follows:

$$\sigma_{AB} = c_A h_A + c_B h_B \quad (2.109)$$

so that the bonds can vary smoothly from the covalent ($c_A = c_B$) to the ionic ($c_A \gg c_B$) limits. The natural hybrids in turn are composed from a set of effective valence-shell atomic orbitals [natural atomic orbitals (NAOs)], optimized for the chosen wave function [137,151]. A distinguishing feature of such natural localized functions is the simultaneous requirement of *orthonormality* and *maximum occupancy*, leading to compact expressions for atomic and bond properties. *Ab initio* wave functions transformed to NBO form are found to be in good agreement with Lewis structure concepts and with the basic Pauling–Slater–Coulson picture [152] of bond hybridization and polarization. The filled NBOs σ_{AB} of the “natural Lewis structure” are therefore well adapted to describing covalency effects in molecules.

Each valence bonding NBO σ [eq. (2.109)] must be paired with a corresponding valence antibonding NBO σ^* (the acceptor) to complete the span of the valence space [153]:

$$\sigma_{AB}^* = c_B h_A + c_A h_B \quad (2.110)$$

which arise from the same set of atomic valence-shell hybrids that unite to form the bond functions σ_{AB} , [eq. (2.109)]. The antibonding orbitals represent unused valence-shell capacity, spanning portions of the atomic valence space that are formally unsaturated by covalent bond formation. Small occupancies of these antibonding orbitals correspond, in Hartree-Fock theory, to irreducible departures from the idealized Lewis picture and thus to small noncovalent corrections to the picture of localized covalent bonds [136].

The energy associated with the antibonding orbitals can be numerically assessed by *deleting* these orbitals from the basis set and recalculating the total energy to determine the associated variational energy lowering. In this way one obtains a

decomposition of the total energy E into components associated with covalent ($E_{\sigma\sigma}=E_{\text{Lewis}}$) and noncovalent ($E_{\sigma\sigma^*}=E_{\text{non-Lewis}}$) contributions, as follows:

$$E = E_{\sigma\sigma} + E_{\sigma\sigma^*} \quad (2.111)$$

NBO decompositions of this form have been supplied for a large number of closed-shell and open shell molecular species [154]. In the NBO decomposition [eq. (2.111)], the noncovalent contributions $E_{\sigma\sigma^*}$, are typically much less than 1% of the contribution of $E_{\sigma\sigma}$, reflecting the dominance of the Lewis-type component of the bonding.

The interactions due to electron delocalization are generally analyzed by selecting a number of bonding and antibonding NBOs, namely, those relevant to the analysis of donor and acceptor properties. As a result, the NBO program searches for an optimal natural Lewis structure, which has the maximum occupancy of its occupied NBOs, and in general agrees with the pattern of bonds and lone pairs of the standard structural Lewis formula. Delocalization of electron density among the filled Lewis-type NBOs (bonding or lone pair) and the empty (antibonding and Rydberg) non-Lewis NBOs leads to transfer of occupancy from the localized NBOs of the idealized Lewis structure into the empty non-Lewis orbitals, and thus, a departure from an idealized Lewis structure description. This transfer is referred to as a “delocalization” correction to the zeroth-order natural Lewis structure through a stabilizing donor-acceptor interaction. The energies of these interactions can be estimated by second-order perturbation theory [143]. The energetic stabilization due to such $\sigma \rightarrow \sigma^*$ donor-acceptor interactions can be estimated according to the following equation [144]:

$$E_2 = \Delta E_{\sigma\sigma^*}^{(2)} = -2 \frac{\langle \sigma^* | \hat{F} | \sigma \rangle^2}{\varepsilon_{\sigma^*} - \varepsilon_{\sigma}} \quad (2.112)$$

where \hat{F} is the effective orbital Hamiltonian (Fock or Kohn-Sham operator) and $\varepsilon_{\sigma} = \langle \sigma | \hat{F} | \sigma \rangle$, and $\varepsilon_{\sigma^*} = \langle \sigma^* | \hat{F} | \sigma^* \rangle$ are the respective orbital energies of donor and acceptor NBOs, respectively. Consideration of valence antibonding orbitals [eq.(2.110)] therefore leads to far-reaching extension of elementary Lewis structure concepts to encompass leading delocalization corrections in simple NBO perturbative estimates such as eq. (2.112) [142].

As is illustrated with Figure 2.2, the corrections to the Lewis-type picture are usually so small as to be well approximated by simple second-order perturbative. This figure depicts the interaction of a filled orbital σ of the formal Lewis structure with one of the unfilled antibonding orbitals σ^* to give the second-order energy lowering, $\Delta E_{\sigma\sigma^*}^{(2)}$ [136].

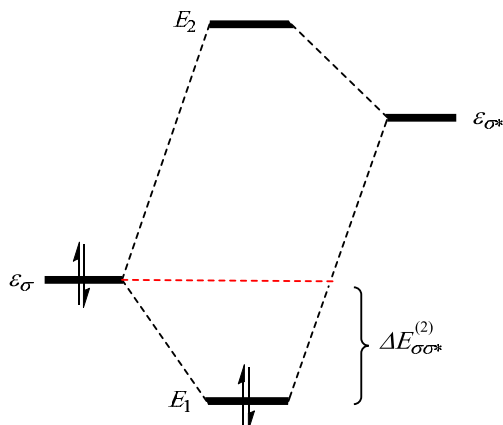


Figure 2.2. Perturbative donor-acceptor interaction, involving a filled orbital σ and an unfilled orbital σ^* .

As a result of each $\sigma_i \rightarrow \sigma_j^*$ perturbation, the starting NBO acquires a weak antibonding “tail” in the final (doubly occupied) NLMO Ω_i . More generally, each semi-localized NLMO Ω_i can be expressed as a linear combination of the parent Lewis-type NBO σ_i (with coefficient $c_{ii} \cong 1$) and residual weak contributions ($c_{ji} \cong 0$) from non-Lewis NBO σ_j^* as follows:

$$\Omega_i = c_{ii}\sigma_i + \sum_j^{NL} c_{ji}\sigma_j^* \quad (2.113)$$

which reflects the irreducible physical effect of $\sigma_i \rightarrow \sigma_j^*$ delocalizations. Despite the compact, recognizable forms of NLMOs and their close connection to chemical structure concepts, it is important to recognize that a Slater determinant of doubly occupied NLMOs is *equivalent* to the usual MO wave function. Hence, the simplicity of NBO-based expansions such as eq. (2.113) is achieved with *no* loss of accuracy in the description of ψ [142].

2.3. Elements of Quantum and Statistical Thermodynamics

2.3.1. Quantum Mechanical Description of Nuclear Motions

In the next sections we will present an overview of the approximations and models used to describe the nuclear motions (translation, vibrations and rotations) in polyatomic molecules on quantum mechanical grounds. In section 2.3.2 the quantum mechanical energy levels of molecules, related to the nuclear motions, will then be connected to macroscopically measurable thermodynamic state functions, such as the entropy (S), the enthalpy (H), and the Gibbs free energy (G).

2.3.1.1. Translations

The motions of any mechanical system can always be decomposed into independent motions, namely a translational part on the one hand and an internal part on the other hand, which relates to vibrational and rotational motions. Correspondingly, the Hamiltonian and the energy can be decomposed as the sum of independent terms:

$$\hat{H} = \hat{H}_{trans} + \hat{H}_{rot,vib} \quad (2.114)$$

$$E = \varepsilon_{trans} + \varepsilon_{rot,vib} \quad (2.115)$$

The translational motion is that described by the motion of a freely translating point of mass $M = \sum_i^N m_i$ situated at the center of mass (center of mass motion) of the system. By definition, the coordinates $(\bar{x}, \bar{y}, \bar{z})$ of the center of mass are given by:

$$\bar{x} = \frac{\sum_i^N m_i x_i}{\sum_i^N m_i}, \bar{y} = \frac{\sum_i^N m_i y_i}{\sum_i^N m_i}, \text{ and } \bar{z} = \frac{\sum_i^N m_i z_i}{\sum_i^N m_i} \quad (2.116)$$

Thus, the location of the center of mass can be calculated if the mass m_i and location (x_i, y_i, z_i) of each atom in the molecule is known.

The translational energies of a molecule can be calculated by modelling the molecule as a structureless particle of mass M moving freely in a three-dimensional cubic box with a volume equal to a^3 [155,156]. The quantum energy levels associated with the translational motions of this particle are then given by:

$$\varepsilon_{trans} = \frac{h^2}{8Ma^2} (n_x^2 + n_y^2 + n_z^2) \quad (2.117)$$

where $n_x, n_y, n_z = 1, 2, 3, \dots, \infty$ represent translational quantum numbers. M is the mass of the molecule and h is Planck's constant ($h = 6.62618 \times 10^{-34}$ J.s). The location of each of the N atoms in a polyatomic molecule is defined in terms of three coordinates; hence, $3N$ coordinates are required to completely describe the molecule. Of these $3N$ coordinates, three coordinates are required to specify the location in space of the center of mass $(\bar{x}, \bar{y}, \bar{z})$ of the molecule (translational degrees of freedom).

2.3.1.2. Rotations

The internal motions of the nuclei consist of rotational motions about the center of mass and of vibrational motions of the nuclei. In the rigid-rotor approximation, the rotational and vibrational motions are decoupled i.e. it is assumed that rotation occurs for a fixed value of interatomic distances. This allows rewriting the Hamiltonian related to the internal motions, as follows:

$$\hat{H}_{rot,vib} = \hat{H}_{rot} + \hat{H}_{vib} \quad (2.118)$$

The eigenstates can then be quantified according to the rotational and vibrational energy of the system:

$$\varepsilon_{rot,vib} = \varepsilon_{rot} + \varepsilon_{vib} \quad (2.119)$$

The classical kinetic energy of a *rigid rotor* E_{rot} is given by

$$E_{rot} = \frac{1}{2} I \omega^2 \quad (2.120)$$

where $\omega = 2\pi\nu$ is the angular velocity and I corresponds to the moment of inertia. For a diatomic molecule containing two atoms of mass equal to m_1 and m_2 :

$$I = \mu R_0^2 \quad (2.121)$$

where μ is the reduced mass ($\mu = \frac{m_1 m_2}{m_1 + m_2}$) and R_0 is the bond length. With the *rigid*

rotor approximation, it is assumed that molecular rotations and vibrations are uncoupled, i.e. one neglects for instance bond elongations as the molecule rotates.

The classical angular momentum is

$$L = I\omega \quad (2.122)$$

The rotational energy can thereby be rewritten as

$$E_{rot} = \frac{L^2}{2I} \quad (2.123)$$

The rotational Hamiltonian operator is thus the kinetic energy operator

$$\hat{H} = -\frac{\hbar^2}{8\pi^2 I} \nabla^2 = \frac{\hat{L}^2}{2I} \quad (2.124)$$

where

$$\hat{L}^2 = -\frac{\hbar^2}{4\pi^2} \left[\frac{1}{\sin\theta} \frac{\partial}{\partial\theta} \left(\sin\theta \frac{\partial}{\partial\theta} \right) + \frac{1}{\sin^2\theta} \frac{\partial^2}{\partial\varphi^2} \right] \quad (2.125)$$

The eigenvalues of \hat{H} defining quantized rotational energies are

$$\varepsilon_{rot} = \frac{\hbar^2}{8\pi^2 I} J(J+1) \quad ; \quad J = 0, 1, 2, \dots \quad (2.126)$$

Angular momenta are also quantized, with the eigenvalues of the square (\hat{L}^2) and projection on a privileged axis (\hat{L}_z) of the angular momentum operator having eigenvalues equal to $J(J+1)\hbar^2$ and $m\hbar$, with $\hbar=h/2\pi$ ($\hbar =1$ in atomic units) and $m= -J, -J+1, -J+2, \dots, 0, \dots, J-2, J-1, J$. Whereas vibrational normal modes are most usually non degenerate (except for molecules exhibiting non abelian symmetry point groups), it follows that each rotational energy level J has an energy degeneracy (multiplicity) equal to $2J+1$.

For a *linear* molecule, *two angular coordinates* are required to specify its orientation in space (Figure 2.3, the molecule has only two axes where rotations can take place into physical distinguishable positions, the third is along the molecular axis), whereas for a *non-linear* molecule *three coordinates* are needed (the molecule as a whole can rotate around the X, Y and Z directions).

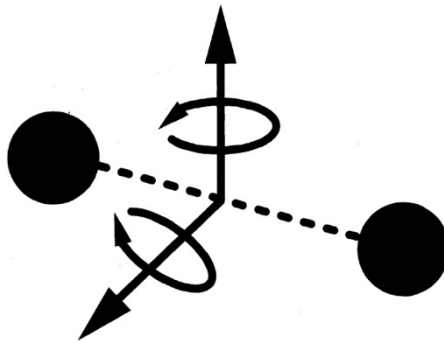


Figure 2.3. Rotational axes of a linear molecule.

For a polyatomic molecule, $I = \sum_i^N m_i R_i^2$ where m_i is the atomic mass and R_i the distance of the i^{th} atom from the molecular center of mass. The moments of inertia of a rigid body characterize the rotational properties of the body. The moments of inertia about any set of Cartesian axes (with origin at the center of mass) are:

$$I_{xx} = \sum_{i=1}^n m_i \left[(y_i - \bar{y})^2 + (z_i - \bar{z})^2 \right] \quad (2.127)$$

$$I_{yy} = \sum_{i=1}^n m_j \left[(x_i - \bar{x})^2 + (z_i - \bar{z})^2 \right] \quad (2.128)$$

$$I_{zz} = \sum_{i=1}^n m_i \left[(x_i - \bar{x})^2 + (y_i - \bar{y})^2 \right] \quad (2.129)$$

In addition there are also products of inertia such as:

$$I_{xy} = \sum_{i=1}^n m_i (x_i - \bar{x})(y_i - \bar{y}) \quad (2.130)$$

Classically, the rotation of a rigid body is described by the vector of angular velocity $\vec{\omega}$ such that the velocity \vec{v}_i of i^{th} particle (atomic nucleus) is given by:

$$\vec{v}_i = \vec{\omega} \times \vec{R}_i \quad (2.131)$$

The angular momentum \vec{L} of the rigid body is then given by

$$\vec{L} = \sum_{i=1}^N \vec{R}_i \times (m_i \vec{v}_i) = \sum_{i=1}^N m_i \vec{R}_i \times (\vec{\omega} \times \vec{R}_i) = \mathbf{I} \vec{\omega} \quad (2.132)$$

where \mathbf{I} is the matrix (or more correctly tensor $\mathbf{I} = \vec{\vec{I}}$) of the moment of inertia:

$$\mathbf{I} = \begin{bmatrix} \sum_i m_i (Y_i^2 + Z_i^2) & -\sum_i m_i X_i Y_i & -\sum_i m_i X_i Z_i \\ -\sum_i m_i Y_i X_i & \sum_i m_i (X_i^2 + Z_i^2) & -\sum_i m_i Y_i Z_i \\ -\sum_i m_i Z_i X_i & -\sum_i m_i Z_i Y_i & \sum_i m_i (X_i^2 + Y_i^2) \end{bmatrix} \quad (2.133)$$

The matrix \mathbf{I} is symmetric, e.g., $I_{xy} = I_{yx}$. In the coordinate system fixed to the rotating molecule, the matrix \mathbf{I} does not depend on time. As each symmetric matrix the matrix \mathbf{I} can be diagonalized. The angular momentum \vec{L} can be written in matrix notation as follows

$$\begin{pmatrix} L_x \\ L_y \\ L_z \end{pmatrix} = \begin{bmatrix} I_{xx} & I_{xy} & I_{xz} \\ I_{yx} & I_{yy} & I_{yz} \\ I_{zx} & I_{zy} & I_{zz} \end{bmatrix} \begin{pmatrix} \omega_x \\ \omega_y \\ \omega_z \end{pmatrix} \quad (2.134)$$

with ω_x , ω_y and ω_z the angular velocity related to the angular rotations about the X , Y , and Z axes, respectively.

There always exists a particular set of Cartesian axes X , Y , Z called the principal axes such that all the products of inertia (I_{xy}, \dots) vanish. The moments of inertia about these axes are called the principal moments of inertia I_{xx} , I_{yy} , I_{zz} (also referred to as I_A , I_B , I_C) and can be obtained through diagonalization of the inertia tensor \mathbf{I} .

$$\begin{pmatrix} L_A \\ L_B \\ L_C \end{pmatrix} = \begin{pmatrix} I_A & 0 & 0 \\ 0 & I_B & 0 \\ 0 & 0 & I_C \end{pmatrix} \begin{pmatrix} \omega_A \\ \omega_B \\ \omega_C \end{pmatrix} \quad (2.135)$$

The normalized eigenvectors \vec{A} , \vec{B} , and \vec{C} , corresponding to the eigenvalues I_A , I_B , and I_C determines the orientation of the so-called principal rotational axes of the molecule. If the molecule has a rotational symmetry then \vec{A} , \vec{B} , and \vec{C} coincide with the symmetry rotational axes of the molecule. The principal moments of inertia are given by the formulas:

$$I_A = \sum_i m_i (B_i^2 + C_i^2); I_B = \sum_i m_i (A_i^2 + C_i^2); I_C = \sum_i m_i (A_i^2 + B_i^2) \quad (2.136)$$

where A_i , B_i and C_i are the coordinates of the i^{th} nucleus in the coordinate frame determined by the principal axes \vec{A} , \vec{B} , and \vec{C} , for instance $B_i^2 + C_i^2$ is the distance of the i^{th} nucleus from the \vec{A} axis.

In the coordinate frame \vec{A} , \vec{B} , and \vec{C} , the matrix \mathbf{I} is diagonal so the angular momentum vector $\vec{L} = \mathbf{I} \vec{\omega}$ has the following coordinates in this frame:

$$\vec{L}_A = I_A \vec{\omega}_A; \vec{L}_B = I_B \vec{\omega}_B; \vec{L}_C = I_C \vec{\omega}_C \quad (2.137)$$

One can easily show that the kinetic energy of rotations is given by

$$E_{rot} = \frac{1}{2} \sum_{i=1}^N m_i \vec{v}_i \cdot \vec{v}_i = \frac{1}{2} \sum_{i=1}^N m_i \vec{v}_i \cdot (\vec{\omega} \times \vec{R}_i) = \frac{1}{2} \sum_{i=1}^N m_i \vec{\omega} \cdot (\vec{R}_i \times \vec{v}_i) = \frac{1}{2} \vec{\omega} \cdot \vec{L} \quad (2.138)$$

In the frame of principal axes, $\vec{\omega} \cdot \vec{L} = \omega_A L_A + \omega_B L_B + \omega_C L_C$, hence classically the energy of rotation is given by

$$E_{rot} = \frac{1}{2} I_A \omega_A^2 + \frac{1}{2} I_B \omega_B^2 + \frac{1}{2} I_C \omega_C^2 \quad (2.139)$$

or

$$E_{rot} = \frac{1}{2I_A} L_A^2 + \frac{1}{2I_B} L_B^2 + \frac{1}{2I_C} L_C^2 \quad (2.140)$$

The corresponding quantum mechanical Hamiltonian reads:

$$\hat{H}_{rot} = \frac{1}{2I_A} \hat{L}_A^2 + \frac{1}{2I_B} \hat{L}_B^2 + \frac{1}{2I_C} \hat{L}_C^2 \quad (2.141)$$

where $\hat{L}_A^2, \hat{L}_B^2, \hat{L}_C^2$ denote the angular momentum operators around the main rotational axes. Eigenvalues and eigenfunctions of \hat{H}_{rot} depend therefore on the values of the principal moments of inertia.

For polyatomic molecules, separate principal moments of inertia are considered as the molecule rotates around the principal axes depending on the shape of the molecule. The analysis of the rotation of polyatomic molecules of arbitrary complexity proceeds by choosing a coordinate system of three perpendicular axes

about which the moment of inertia can be determined. We distinguish four kinds of “rotational tops” as follows:

(i) Oblate symmetric tops ($I_A = I_B < I_C$): The two smaller moments of inertia are equal; this corresponds to a flattened inertia ellipsoid. e.g., C_6H_6 or $CHCl_3$. In this case, we have:

$$\hat{H}_{rot} = \frac{1}{2I_A} \hat{L}_A^2 + \frac{1}{2I_B} \hat{L}_B^2 + \frac{1}{2I_C} \hat{L}_C^2 = \frac{1}{2I_A} \hat{L}_A^2 + \frac{1}{2I_A} \hat{L}_B^2 + \frac{1}{2I_A} \hat{L}_C^2 + \frac{1}{2I_C} \hat{L}_C^2 - \frac{1}{2I_A} \hat{L}_C^2$$

hence

$$\hat{H}_{rot} = \frac{1}{2I_A} \hat{L}^2 + \left(\frac{1}{2I_C} - \frac{1}{2I_A} \right) \hat{L}_C^2 \quad (2.142)$$

Since the eigenvalues of \hat{L}^2 and \hat{L}_C are given by $J^2 = J(J+1)\hbar^2$ and $J_z = K\hbar$, where $-J \leq K \leq J$, therefore the eigenvalues of \hat{H}_{rot} must be given by (in atomic units)

$$E_{JK} = \frac{1}{2I_A} J(J+1) + \left(\frac{1}{2I_C} - \frac{1}{2I_A} \right) K^2 \quad (2.143)$$

(ii) Prolate symmetric tops ($I_A < I_B = I_C$): The two larger moments of inertia are equal. This corresponds to a rotational ellipsoid which is elongated along the symmetry axis. e.g., NH_3 or CH_3Cl . In this case, we obtain a similar formula. Only the smallest and largest moments of inertia I_A and I_C are interchanged:

$$E_{JK} = \frac{1}{2I_C} J(J+1) + K^2 \left(\frac{1}{2I_A} - \frac{1}{2I_C} \right) \quad (2.144)$$

For symmetric tops the degeneracy of the level E_{JK} is $2(2J+1)$. Most specifically, the degeneracy is 2 with respect to K , and $(2J+1)$ with respect to M .

(iii) Spherical tops ($I_A = I_B = I_C$): All three moments of inertia are the same, as for instance in CH_4 . In this case:

$$E_J = \frac{1}{2I_A} J(J+1) \quad (2.145)$$

The degeneracy in this case is $(2J+1)^2$.

(iv) Asymmetric tops ($I_A \neq I_B \neq I_C$): The three moments of inertia values may be different, such as for H_2O , C_2H_4 , or C_8H_{10} . The energy levels of the asymmetric top cannot be represented by an explicit formula analogous to that for the spherical or symmetric top. The energy levels of an asymmetric top can be compared with

two limiting cases, one in which $I_B=I_C$ (prolate symmetric top) and the other in which $I_B=I_A$ (oblate symmetric top) (Figure 2.4). By letting I_B decrease gradually from $I_B=I_C$ to $I_B=I_A$ we can expect a continuous change of the energy levels. In a rough approximation the energy levels of the asymmetric top are obtained simply by connecting (by smooth curves) the levels of a given J . For a more detailed description the book “Infrared and Raman spectra of polyatomic molecules” by Herzberg should be consulted [155]. For each value of J there are $(2J+1)$ different energy levels. There is no quantum number having a physical meaning that distinguishes the $(2J+1)$ different levels with equal J . Therefore they are distinguished by adding a subscript τ to J such that τ takes the values $\tau=-J, (-J+1), \dots J$.

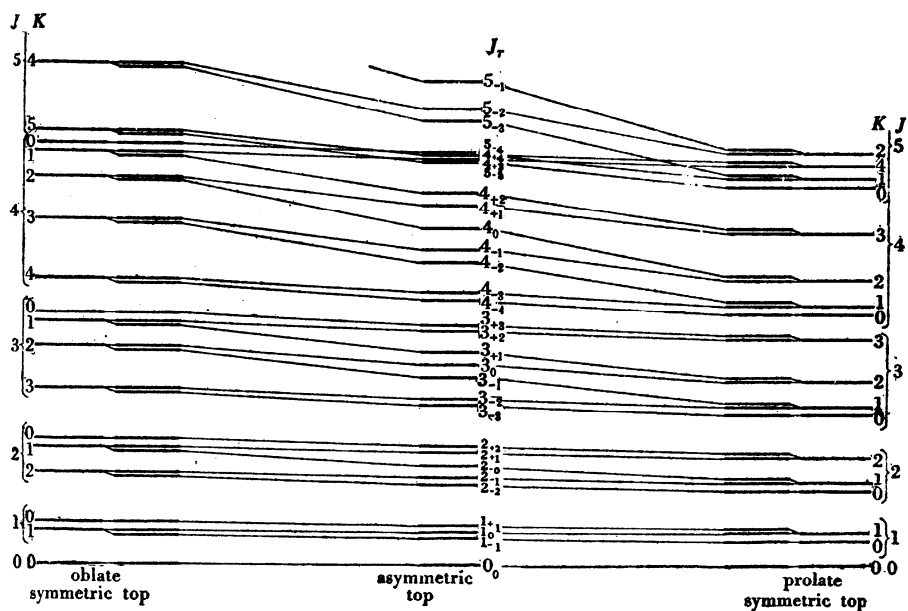


Figure 2.4. Energy levels of the asymmetric top; correlation to those of symmetric tops.

2.3.1.3. Vibrations

The remaining $3N-5$ (for linear molecules) or $3N-6$ (for non-linear molecules) internal coordinates (vibrational degrees of freedom) determine the potential in which the nuclei vibrate. In the harmonic approximation, the anharmonic terms of the potential are dropped, couplings between vibrational normal modes are neglected, and a vibration is described as a harmonic oscillator. Such oscillator is defined by the potential energy being proportional to the square of the displacement distance (x) from the equilibrium position.

$$V(x) = \frac{1}{2} k x^2 = \frac{1}{2} (m \omega^2) x^2 \quad (2.146)$$

where ω is the angular frequency ($\omega = \sqrt{k/\mu}$), k represents the force constant, and μ denotes the reduced mass. Solution of the Schrödinger equation with this form of potential leads to a sequence of evenly spaced energy levels that are characterized by a unique quantum number n (see Figure 2.5)

$$\varepsilon_{vib} = \left(n + \frac{1}{2}\right) \hbar \omega \quad \text{with } n=1,2,3,\dots \quad (2.147)$$

Eq. (2.147) shows that in the lowest vibrational state, $n=0$, vibrations contribute in a non-vanishing way to the energy. This so-called “zero-point vibration energy” of the vibrational ground state ($n=0$) implies that molecules are not completely at rest, even at absolute zero temperature.

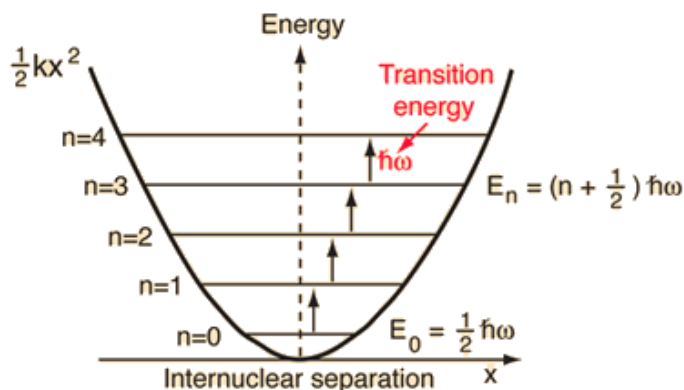


Figure 2.5. Potential energy form of a harmonic oscillator.

The ground state energy for the quantum harmonic oscillator can be shown to be the minimum energy allowed by the uncertainty principle by Heisenberg

$$\Delta x \Delta p \geq \frac{\hbar}{2} \quad (2.148)$$

Indeed, the energy of the quantum harmonic oscillator must be at least

$$E = \frac{(\Delta p)^2}{2m} + \frac{1}{2} m \omega^2 (\Delta x)^2 \quad (2.149)$$

where Δx and Δp describe the uncertainty on the position and on the momentum respectively.

Taking the lower limit allowed by the uncertainty principle,

$$\Delta x \Delta p = \frac{\hbar}{2} \quad (2.150)$$

the energy expressed in terms of the position uncertainty can be written as follows

$$E = \frac{\hbar^2}{8m(\Delta x)^2} + \frac{1}{2}m\omega^2(\Delta x)^2 \quad (2.151)$$

Minimizing this energy by taking the derivative with respect to the position energy and setting it equal to zero gives

$$-\frac{\hbar^2}{4m(\Delta x)^3} + m\omega^2\Delta x = 0 \quad (2.152)$$

Solving for the position uncertainty gives

$$\Delta x = \sqrt{\frac{\hbar}{2m\omega}} \quad (2.153)$$

Substitution of eq. (2.153) into eq. (2.151) gives the allowed minimum value of energy:

$$E_0 = \frac{1}{2}\hbar\omega \quad (2.154)$$

Polyatomic molecules can be considered in a first approximation as a set of uncoupled harmonic oscillators. The collective motions of the atoms in a molecule can thus be decomposed into a set of independent harmonic oscillators by introducing suitable normal modes of vibration and normal coordinates (q_j). When using these coordinates, cross terms in the potential of polyatomic molecules are eliminated and the Hamiltonian can be written as a sum of independent harmonic oscillators:

$$\hat{H} = -\sum_{j=1}^{\infty} \frac{\hbar^2}{2\mu} \frac{\partial^2}{\partial q_j^2} + \sum_{j=1}^{\infty} \frac{1}{2}k_j q_j^2 \quad (2.155)$$

The motion of an N -atomic non-linear molecule possessing $3N-6$ vibrational normal modes ($3N-5$ in the case of linear molecule) can be defined by $3N$ atomic Cartesian displacement coordinates Δx_α , Δy_α and Δz_α , where α is an atomic index. In describing vibrational motions, it is necessary to express the vibrational kinetic and potential energies into a basis set of coordinates that are independent of the translation and rotation of the molecule in space. This is achieved by imposing on the $3N$ Cartesian displacement coordinates conditions that eliminate the coupling between the three types of molecular motions. In explicit form, these conditions as defined by Eckart [157] and Sayvetz [158] as follows:

$$\begin{aligned}
\sum_{\alpha} m_{\alpha} \Delta x_{\alpha} &= 0 \\
\sum_{\alpha} m_{\alpha} \Delta y_{\alpha} &= 0 \\
\sum_{\alpha} m_{\alpha} \Delta z_{\alpha} &= 0 \\
\sum_{\alpha} m_{\alpha} (y_{\alpha}^0 \Delta z_{\alpha} - z_{\alpha}^0 \Delta y_{\alpha}) &= 0 \\
\sum_{\alpha} m_{\alpha} (z_{\alpha}^0 \Delta x_{\alpha} - x_{\alpha}^0 \Delta z_{\alpha}) &= 0 \\
\sum_{\alpha} m_{\alpha} (x_{\alpha}^0 \Delta y_{\alpha} - y_{\alpha}^0 \Delta x_{\alpha}) &= 0
\end{aligned} \tag{2.156}$$

In expression (2.156), m_{α} are atomic masses, and $x_{\alpha}^0, y_{\alpha}^0$ and z_{α}^0 are the equilibrium coordinates of the α^{th} nucleus. As defined above, the Eckart-Sayvetz conditions neglect the vibrational-rotational interactions accounting for a part of the kinetic energy of the molecule, which is called the Coriolis energy. It has been shown that, most generally, compared to the vibrational kinetic energy, the Coriolis interaction terms are small and may be neglected.

The Eckart-Sayvetz conditions imply that, if during the vibration a small translation of the center of masses is invoked, the origin of the Cartesian reference system is displaced so that no linear momentum is produced. The second Sayvetz condition, expressed in the last three equations of (2.156), imposes the constraint that, during vibrational displacements, no angular momentum is produced. Eq. (2.156) implies that the reference Cartesian system translates and rotates with the molecule in such a way that the displacement coordinates Δx_{α} , Δy_{α} and Δz_{α} reflect pure vibrational distortions. It is evident that through eq. (2.156) certain mass-dependency is imposed on the atomic Cartesian displacement coordinates [159].

For vibrational analysis, it is most convenient to treat the vibrational motion in terms of mass-weighted Cartesian coordinates, as follows:

$$q_{\alpha x} = \sqrt{m_{\alpha}} \Delta x_{\alpha} \quad ; \quad q_{\alpha y} = \sqrt{m_{\alpha}} \Delta y_{\alpha} \quad ; \quad q_{\alpha z} = \sqrt{m_{\alpha}} \Delta z_{\alpha} \tag{2.157}$$

The Eckart-Sayvetz conditions can easily be expressed in terms of the coordinates $q_{\alpha g}$ ($g=x, y, z$). Summarizing, the vibrational motion of an N -atomic molecule with $3N-6$ vibrational degree of freedom can be described by $3N$ nuclear Cartesian displacement coordinates forming a column matrix \mathbf{X} . Six degrees of freedom are related to the translational and rotational motions of the molecule, defining the external coordinates (three translations and three rotations) [159].

A stationary state of a polyatomic molecule is described in quantum mechanics by a wave function ψ and by an energy value E , which represent an eigenfunction and eigenvalue, respectively, of the complete molecular Hamiltonian H .

$$H\psi = E\psi \quad (2.158)$$

where H contains terms depending upon the electronic, nuclear and spin coordinates. In order to treat the vibrational problem, it is first necessary to separate the various contributions to H to the maximum extent, so that eq. (2.158) can be divided into separate equations, one for each problem.

Classically, the nuclear motions can be separated to a fairly good approximation. This is also true in quantum mechanics [160]. Therefore, if an axis system is introduced which rotates with the molecule and satisfies the second Sayvetz condition, the wave function ψ_n can be written as the product of a *rotational* wave function ψ_r and a *vibrational* wave function ψ_v .

$$\psi_n = \psi_v \psi_r \quad (2.159)$$

and the nuclear Hamiltonian H_n can be decomposed further into

$$H_n = H_v + H_r \quad (2.160)$$

where H_r is the rotational Hamiltonian (including the interaction of the angular moments of rotation and vibration) and H_v is the vibrational Hamiltonian, which satisfies the equation

$$H_v \psi_v = E_v \psi_v \quad (2.161)$$

The rotational Hamiltonian H_r and the rotational wave function ψ_r are discussed in detail in the book by Allen and Cross [161].

The vibrational Hamiltonian H_v and the vibrational wave functions ψ_v are written in terms of a coordinate system rotating with the molecule and satisfying the Sayvetz conditions. Among the possible sets of coordinates that one can choose, normal coordinates are by far the most convenient ones since to each normal coordinate is associated one single mode of vibration of the molecule.

The quantum-mechanical vibrational Hamiltonian operator H_v for a molecule is easily obtained by using the postulates of quantum mechanics from the classical Hamiltonian function in terms of the normal coordinates Q_i and the associated momenta P_i

$$P_i = (\partial Q_i / \partial t) = \dot{Q}_i \quad (2.162)$$

$$H = T + V = \frac{1}{2} \sum_{i=1}^{3N-6} (P_i^2 + \lambda_i Q_i^2) \quad (2.163)$$

$$H_v = -\frac{\hbar^2}{2} \sum_{i=1}^{3N-6} \left(\frac{\partial^2}{\partial Q_i^2} - \frac{\lambda_i}{\hbar^2} Q_i^2 \right) \quad (2.164)$$

where $\hbar = h/2\pi$. Since the normal coordinates constitute a set of $3N-6$ independent variable, the wave function ψ_v of eq. (2.161) can be written as the product of $3N-6$ independent functions $\psi_{v_i}(Q_i)$, each a function of one single normal coordinate Q_i

$$\psi_v(Q_1, Q_2, Q_3, \dots, Q_{3N-6}) = \psi_{v_1}(Q_1) \psi_{v_2}(Q_2) \dots \psi_{v_{3N-6}}(Q_{3N-6}) \quad (2.165)$$

The vibrational energy E_v becomes thus the sum of $3N-6$ independent contributions

$$E_v = E_1 + E_2 + E_3 + \dots + E_{3N-6} \quad (2.166)$$

By application of the Hamiltonian operator eq. (2.164) to the wave function eq. (2.165), we obtain $3N-6$ independent equations in one variable, of the form

$$-\frac{\hbar^2}{2} \frac{\partial^2 \psi_{v_i}}{\partial Q_i^2} + \frac{\lambda_i}{2} Q_i^2 \psi_{v_i} = E_{v_i} \psi_{v_i} \quad (2.167)$$

which is the well-known Schrödinger equation for a one-dimensional harmonic oscillator. The solution of equation (2.161) can thus be expressed as the product of $3N-6$ harmonic oscillator wave functions and the total vibrational energy as the sum of the energies of these $3N-6$ oscillators.

The solution of equation (2.167) was obtained by Schrödinger himself in terms of a dimensionless variable q_i related to Q_i by the expression

$$q_i = \gamma_i^{1/2} Q_i \quad (2.168)$$

where

$$\gamma_i = 2\pi c \nu_i / \hbar = \lambda_i^2 / \hbar \quad (2.169)$$

With this dimensionless normal coordinate, equation (2.167) becomes

$$\frac{d^2 \psi_{v_i}}{dq_i^2} + \left(\frac{2E}{\hbar \lambda_i^{1/2}} - q_i^2 \right) \psi_{v_i} = 0 \quad (2.170)$$

and can be solved exactly. The eigenvalues are given by

$$E_{v_i} = \left(\nu_i + \frac{1}{2} \right) h c \nu_i \quad (2.171)$$

where c represents the velocity of light, ν_i is the classical frequency of vibration (in units of cm^{-1}), associated with the vibrational normal coordinate q_i , and ν_i denotes a quantum number which can take any integral positive value including zero.

According to eq. (2.171), the vibrational energy of a polyatomic molecule is given by

$$E_v = \sum_{i=1}^{3N-6} \left(\nu_i + \frac{1}{2} \right) h c \nu_i \quad (2.172)$$

The lowest vibrational level of the molecule is called the *ground level* and corresponds to a vibrational situation in which all normal coordinates have zero quantum number. The energy of the ground level is not zero but has from eq. (2.172) the value

$$E_0 = \frac{1}{2} h c \sum_i \nu_i \quad (2.173)$$

which can be relatively high for a polyatomic molecule. This quantity takes the name of *zero-point* energy and is of great importance in many physical situations [162]:

- If all quantum numbers have value zero except one, which is equal to unity, the corresponding energy levels take the name of *fundamental level*. From eq. (2.172) we see that the number of fundamental levels is equal to $3N-6$ and each corresponds to the excitation of a single normal mode. If the molecule possesses two-fold degenerate normal coordinates Q_1 and Q_k ($\nu_1 = \nu_k$), the energy levels for $\nu_1=1, \nu_k=0$ and $\nu_1=0, \nu_k=1$ are two-fold degenerate. If there are three-fold degenerate normal coordinates, Q_1, Q_k and Q_m , the levels corresponding to ν_1 or ν_k or $\nu_m=1$ (all other $\nu_i=0$) are triply degenerate [$(\nu_1=1, \nu_k=\nu_m=0)$, $(\nu_k=1, \nu_1=\nu_m=0)$, and $(\nu_m=1, \nu_1=\nu_k=0)$].
- If all quantum numbers have value zero except one, which has value greater than one (≥ 1), the corresponding energy levels take the name of *overtone* levels. In this case, if the quantum number ν_k takes the value 2 ($\nu_k=2$), we speak of the first overtone level, if it takes the value 3 ($\nu_k=3$), we speak of the second overtone level of the ν_k vibration, and so on.
- If two or more quantum numbers are different from zero, the resulting levels are called *combination* levels. The number of combination levels becomes very large as the energy increases, and above a given limit they build almost a continuum of energies. Usually these levels with many excited quantum numbers are of little relevance in vibrational spectroscopy, but are essential in chemical kinetics (section 2.4.1.5)

Since the frequencies are measured in units of cm^{-1} , it is convenient to measure the vibrational energies in the same units, by dividing eq. (2.172) by hc .

Transition between two energy levels are governed by the Bohr's rule

$$\nu_{\nu',\nu''} = \frac{E_{\nu'} - E_{\nu''}}{hc} \quad (2.174)$$

where $E_{\nu'}$ is the energy of the upper level and $E_{\nu''}$ the energy of the lower level. Among these levels, by far the most important in absorption spectra are the transitions between the ground ($\nu_k=0$) and the fundamental levels, i.e. between the ground level and the levels corresponding to the excitation of a single quantum number ($\nu_k=1$). From equations (2.172) and (2.174), we see that the frequencies associated with these transitions are simply the classical normal frequencies. The name "fundamental" is thus used for the level $\nu_k=1$. Transitions from $\nu_k=0$ to higher levels $\nu_k=2,3,\dots$ are called overtones, whereas transitions from the ground level to combination levels are called combinations [162].

In the harmonic approximation the fundamental and the overtone levels of a given mode ν_k are, according to eq. (2.174), equally spaced. The transition from the ground to the fundamental level $\nu_k=1$ thus has exactly the same frequency as the transition from the overtone level $\nu_k=m$ to the level $\nu_k=m+1$. Such transitions between two excited levels of the same mode are called hot transitions since the lower excited level must be thermally populated in order that a sufficient number of molecules experience the transition. Transition can also occur between two excited levels corresponding to two different quantum numbers ν_k and ν_l . The frequency associated with this transition state is called the *difference* frequency since, from eq. (2.174), it is just the difference between the frequencies ν_k and ν_l of the transitions between the ground and the two excited levels [162].

2.3.2. Elements of Statistical Thermodynamics

The essence of statistical mechanics is to connect the quantum mechanical energy levels of molecules to macroscopically measured thermodynamic quantities. In this section, important macroscopic observables such as the entropy S , the enthalpy H , and the Gibbs free energy G are expanded in terms of the partition function derived from molecular properties.

2.3.2.1. Partition Functions

First let us consider the canonical partition function Q for a system of N distinguishable particles at thermal equilibrium, in which the Hamiltonian can be written as a sum of individual terms. The individual energy states are represented by $\{\mathcal{E}_j^a\}$, where the superscript denotes the particle (they are distinguishable), and

the subscript denotes the state. Q is defined as the mean number of quantum energy levels which are thermally accessible at a given temperature.

$$\begin{aligned}
 Q(N, V, T) &= \sum_j e^{-\frac{E_j}{k_B T}} = \sum_{i, j, k, \dots} e^{-\frac{(\varepsilon_i^a + \varepsilon_j^b + \varepsilon_k^c + \dots)}{k_B T}} \\
 &= \sum_i e^{-\frac{\varepsilon_i^a}{k_B T}} \sum_j e^{-\frac{\varepsilon_j^b}{k_B T}} \sum_k e^{-\frac{\varepsilon_k^c}{k_B T}} \dots = q_a q_b q_c \dots
 \end{aligned}
 \tag{2.175}$$

where E_j describes the energy of the j^{th} level, k_B is Boltzmann's constant ($1.3806 \times 10^{-23} \text{ J mol}^{-1} \text{ K}^{-1}$), and q_x is the partition function of the x^{th} molecule, which is defined as:

$$q_x(V, T) = \sum_i \exp(-\varepsilon_i^x / k_B T)
 \tag{2.176}$$

Equation (2.175) shows that if we can write the N -particle Hamiltonian as a sum of independent terms, and if all particles are distinguishable and independent (ideal gas), the original N -body problem [the partition function of the entire system $Q(N, V, T)$] can be reduced to a one-body problem [individual molecular partition functions $q(V, T)$]. Indeed, if the energy states of all the particles are the same, $q_x(V, T) = q(V, T)$, and eq. (2.175) for N distinguishable particles becomes

$$Q(N, V, T) = [q(V, T)]^N
 \tag{2.177}$$

The partition function for a single molecule can be written as the product of partition functions for the translational, vibrational, rotational, electronic, and nuclear degrees of freedom which can be calculated separately, as discussed in the sequel.

$$q_{\text{molecule}} = q_{\text{trans}} \cdot q_{\text{vib}} \cdot q_{\text{rot}} \cdot q_{\text{elec}} \cdot q_{\text{nucl}}
 \tag{2.178}$$

Each of the above partition functions can be defined as an average number of thermally accessible translational, vibrational, rotational, electronic and nuclear excited states, since they correspond to weighted summations of all available energy states (weighted according to their availability or probability of occupation at temperature T). It may also be viewed as the normalization factor for the Boltzmann probability distribution:

$$P(\varepsilon_i) = q^{-1} e^{-\varepsilon_i / k_B T}
 \tag{2.179}$$

where q is the partition function for a single particle; the corresponding quantity Q for a collection of N *non-interacting* particles (ideal gas) reads:

$$\begin{aligned}
Q &= q^N \quad (\text{different [i.e. distinguishable] non-interacting particles}) \\
Q &= \frac{q^N}{N!} \quad (\text{identical [indistinguishable] non-interacting particles})
\end{aligned} \tag{2.180}$$

If the particles are *interacting* (liquid or solid state), the partition function Q must be calculated by summing over all energy states E_i for the whole system. Note that Q describes the whole system consisting of N interacting particles, and the energy states E_i are therefore for all the particles.

$$Q = \sum_i^{\infty} \exp(-E_i/k_B T) \tag{2.181}$$

The **electronic partition function** is defined as

$$q_{elec} = \sum_i g_i \exp(-\varepsilon_{elec}/k_B T) = g_0 \exp(-\varepsilon_0/k_B T) + g_1 \exp(-\varepsilon_1/k_B T) + \dots \tag{2.182}$$

where g_i and ε_i describe the degeneracy and the electronic energy of the i^{th} electronic level, respectively. Mostly, an arbitrary zero of energy is fixed such that $\varepsilon_i=0$. The higher electronic energies are then determined relative to the ground state. When the first electronic excitation is much greater than $k_B T$, the first and higher excited states are inaccessible at the considered temperature. In such a case, the electronic partition function simply becomes $q_{elec}=g_0$.

By assuming the molecule as a particle of mass M moving freely in a three-dimensional cubic box with volume a^3 , the translational energies are then given by:

$$\varepsilon_{trans} = \frac{h^2}{8Ma^2} (n_x^2 + n_y^2 + n_z^2) \tag{2.183}$$

Subsequently, the translational partition function will be:

$$q_{trans} = \sum_{n_x, n_y, n_z=1} e^{-\beta \varepsilon_{trans}} = \sum_{n_x=1} e^{-\frac{\beta n_x^2 h^2}{8Ma^2}} \sum_{n_y=1} e^{-\frac{\beta n_y^2 h^2}{8Ma^2}} \sum_{n_z=1} e^{-\frac{\beta n_z^2 h^2}{8Ma^2}} = \left(\sum_{n=1} e^{-\frac{\beta n^2 h^2}{8Ma^2}} \right)^3 \tag{2.184}$$

with $\beta=1/k_B T$.

The successive terms in these summations differ so little from each other that it can be considered that such terms vary continuously. Thus, the summation can be replaced by an integral:

$$q_{trans} = \left(\int_0^{\infty} e^{-\frac{\beta n^2 h^2}{8Ma^2}} dn \right)^3 = \left(\frac{2\pi M k_B T}{h^2} \right)^{\frac{3}{2}} V \tag{2.185}$$

The **rotational partition function** is given by

$$\text{Spherical top: } q_{rot} = \frac{\pi^{\frac{1}{2}}}{\sigma} \left(\frac{8\pi^2 I k_B T}{h^2} \right)^{\frac{3}{2}} \quad (2.186)$$

$$\text{Symmetric top: } q_{rot} = \frac{\pi^{\frac{1}{2}}}{\sigma} \left(\frac{8\pi^2 I_A k_B T}{h^2} \right) \left(\frac{8\pi^2 I_C k_B T}{h^2} \right)^{\frac{1}{2}} \quad (2.187)$$

$$\text{Asymmetric top: } q_{rot} = \frac{\pi^{\frac{1}{2}}}{\sigma} \left(\frac{8\pi^2 I_A k_B T}{h^2} \right)^{\frac{1}{2}} \left(\frac{8\pi^2 I_B k_B T}{h^2} \right)^{\frac{1}{2}} \left(\frac{8\pi^2 I_C k_B T}{h^2} \right)^{\frac{1}{2}} \quad (2.188)$$

It should be noticed that for the symmetric top $I_A=I_B$, for the spherical top $I_A=I_B=I_C=I$, and for an asymmetric top molecule no closed expression can be derived for q_{rot} on the quantum mechanical level [155,157,163]. σ is the symmetry number, giving the number of rotations which leave the molecule invariant. This number avoids overcounting indistinguishable configurations.

Finally, the **vibrational partition function** for a polyatomic molecule reads:

$$q_{vib} = \prod_{j=1}^{\alpha} \left(\frac{e^{-hv_j/2k_B T}}{1 - e^{-hv_j/k_B T}} \right) \quad (2.189)$$

where the summation over j runs over the $\alpha=3N-6$ vibrational normal modes of a *non-linear* molecules or over the $3N-5$ vibrational normal modes of a *linear* molecule. Nuclear degrees of freedom (isotopic effects and nuclear spins) have not been taken into account in this study and the nuclear partition function, q_{nucl} , is simply set equal to 1 [164,165]. Thus, for non-linear polyatomic molecules, the total partition function is given by

$$q_{tot} = \left(\frac{2\pi M k_B T}{h^2} \right)^{\frac{3}{2}} V \frac{\pi^{\frac{1}{2}}}{\sigma} \left(\frac{8\pi^2 I_A k_B T}{h^2} \right)^{\frac{1}{2}} \left(\frac{8\pi^2 I_B k_B T}{h^2} \right)^{\frac{1}{2}} \left(\frac{8\pi^2 I_C k_B T}{h^2} \right)^{\frac{1}{2}} \prod_{j=1}^{\alpha} \left(\frac{e^{-hv_j/2k_B T}}{1 - e^{-hv_j/k_B T}} \right) g_o \quad (2.190)$$

2.3.2.2. Elements of Statistical Thermodynamics

After determination of the canonical partition function Q , one can easily calculate thermodynamic state functions and heat capacities, which all relate to canonical partition functions [155,156].

$$Q = \sum_j e^{-E_j/k_B T} \quad (2.191)$$

By differentiating Q with respect to the temperature at a constant volume, the following equation is obtained:

$$\left(\frac{\partial Q}{\partial T}\right)_V = \frac{1}{k_B T^2} = \sum_i E_i e^{-E_i/k_B T} \quad (2.192)$$

Since $e^{-E_i/k_B T} = P_i/Q$, where P_i is the fraction of the system with energy E_i , and since $U = \sum_i P_i E_i$, it follows immediately that the internal energy U relates to the partition function Q via:

$$U = \frac{k_B T^2}{Q} \left(\frac{\partial Q}{\partial T}\right)_V = k_B T^2 \left(\frac{\partial \ln Q}{\partial T}\right)_V \quad (2.193)$$

A similar derivation along with Boltzmann's mathematical definition of the entropy S yields the following expression:

$$S = -k_B \sum_i P_i \ln P_i = k_B T \left(\frac{\partial \ln Q}{\partial T}\right)_V + k_B \ln Q \quad (2.194)$$

The Helmholtz function ($F=U-TS$) is easily obtained from a combination of eqs. (2.193) and (2.194):

$$F = -k_B T \ln Q \quad (2.195)$$

At constant temperature, the pressure is given by

$$P = -\left(\frac{\partial F}{\partial V}\right)_T \quad (2.196)$$

$$P = k_B T \left(\frac{\partial \ln Q}{\partial V}\right)_T \quad (2.197)$$

From the definition of the enthalpy ($H=U+PV$) and the Gibbs free energy ($G=H-TS$), we have:

$$H = k_B T^2 \left(\frac{\partial \ln Q}{\partial T}\right)_V + k_B T V \left(\frac{\partial \ln Q}{\partial V}\right)_T \quad (2.198)$$

and

$$G = -k_B T \left[\ln Q - V \left(\frac{\partial \ln Q}{\partial V}\right)_T \right] \quad (2.199)$$

2.3.2.3. Practical Calculation of Thermodynamical Quantities

In order to derive practical expressions for the computations of molar thermodynamic state functions from individual molecular partition functions (q), we substitute eq. (2.180) in eq. (2.194):

$$S = k_B T \left(\frac{q^N}{N!} \right) + k_B T \left(\frac{\partial \ln(q^N/N!)}{\partial T} \right)_V \quad (2.200)$$

In practice, the partition functions of macroscopic systems are too large to use eq. (2.200). To solve this difficulty, Stirling's approximation is used:

$$\ln(N!) \approx N \ln(N) - N \quad (2.201)$$

Therefore, it follows that

$$S = N_A k_B + N_A k_B \ln \left(\frac{q(V, T)}{N} \right) + N_A k_B T \left(\frac{\partial \ln q}{\partial T} \right)_V \quad (2.202)$$

Mostly molar values are used, so that partition functions can be divided by $n = N/N_A$. Upon using the relationship $N_A k_B = R$, with N_A and k_B are Avogadro's and Boltzmann's constants, respectively, one gets eq. (2.203), which gives the relation between the partition function and the entropy.

$$S = R + R \ln(q(V, T)) + RT \left(\frac{\partial \ln q}{\partial T} \right)_V \quad (2.203)$$

We can also move the first term into the natural logarithm as e .

$$S = R \ln(q(V, T) e) + RT \left(\frac{\partial \ln q}{\partial T} \right)_V \quad (2.204)$$

$$S = R \left(\ln(q_{trans} q_{elec} q_{rot} q_{vib} e) + T \left(\frac{\partial \ln(q_{trans} q_{elec} q_{rot} q_{vib})}{\partial T} \right)_V \right) \quad (2.205)$$

The internal energy U can also be obtained from the partition function via:

$$U = RT^2 \left(\frac{\partial \ln(q_{trans} q_{elec} q_{rot} q_{vib})}{\partial T} \right)_V \quad (2.206)$$

The contributions to the entropy and the internal energy resulting from the translational, the electronic, the rotational and the vibrational motions are individually calculated. The starting point of the calculations is the partition function for each individual contribution.

2.3.2.3.1. Contribution from the Translational Motions

The translational partition function is given by eq. (2.185).

$$q_{trans} = \left(\frac{2\pi M k_B T}{h^2} \right)^{\frac{3}{2}} V \quad (2.207)$$

where M is the total molecular mass, and V denotes the volume of one mole of ideal gas [$V = Nk_B T/P$]. The volume depends on the number of particles. We have replaced a^3 with the volume V that the N molecules occupy at the temperature of interest. The partition function of eq. (2.207) is unitless. It is an extrinsic quantity, increasing with the volume of molecules considered. It is also useful to define a translational partition function per unit volume, namely $\bar{q}_{trans} = q_{trans}/V$,

$$\bar{q}_{trans} = \left(\frac{2\pi M k_B T}{h^2} \right)^{\frac{3}{2}} \quad (2.208)$$

which has units scaling like m^{-3} .

The partial derivative of q_{trans} with respect to T is:

$$\left(\frac{\partial \ln q_{trans}}{\partial T} \right)_V = \frac{3}{2T} \quad (2.209)$$

which can be used to calculate both the energy S_{trans} and the internal energy U_{trans} . For an ideal gas ($PV = Nk_B T$), the translation partition function then becomes

$$q_{trans} = \left(\frac{2\pi M k_B T}{h^2} \right)^{\frac{3}{2}} \frac{Nk_B T}{P} \quad (2.210)$$

The translational partition function is used to calculate the translational entropy via:

$$S_{trans} = R \left(\ln(q_{trans} e) + T \left(\frac{3}{2T} \right) \right) = R \left(\ln q_{trans} + 1 + \frac{3}{2} \right) \quad (2.211)$$

and the contribution to the internal energy due to translation is:

$$U_{trans} = RT^2 \left(\frac{\partial \ln q_{trans}}{\partial T} \right)_V = RT^2 \left(\frac{3}{2T} \right) = \frac{3}{2} RT \quad (2.212)$$

2.3.2.3.2. Contribution from the Electronic Motions

The electronic partition function involves a sum over electronic quantum states (i.e. the lowest electronic state and all electronic excited states). The first electronic excitation energy is most usually much greater than $k_B T$ at standard temperature. Further, the energy of the ground state is set equal to zero. These assumptions simplify the electronic partition function to $q_{elec} = g_0$, which is simply the electronic spin multiplicity of the molecule. The entropy due to electronic motions is very simply therefore:

$$S_{elec} = R \left(\ln q_{elec} + T \left(\frac{\partial \ln q_{elec}}{\partial T} \right)_V \right) = R \ln q_{elec} \quad (2.213)$$

The internal energy due to the electronic motions is zero ($U_{elec} = 0$) since there are no temperature dependent terms in the partition function.

2.3.2.3.3. Contribution from the Rotational Motions

For the study of molecular rotations, we restrict ourselves to the general case of non-linear polyatomic molecules (asymmetric tops). For such molecules, the rotational partition function is given by

$$S_{rot} = R \left(\ln q_{rot} + T \left(\frac{\partial \ln q_{rot}}{\partial T} \right)_V \right) = R \left(\ln q_{rot} + \frac{3}{2} \right) \quad (2.214)$$

$$U_{rot} = RT^2 \left(\frac{\partial \ln q_{rot}}{\partial T} \right)_V = \frac{3}{2} RT \quad (2.215)$$

2.3.2.3.4. Contribution from the Vibrational Motions

The contribution from vibrational motions is composed of the contributions from each harmonic vibrational normal mode. Therefore, the vibrational partition function, [eq. (2.189)] can be rewritten as:

$$q_{vib} = \prod_{j=1}^{\alpha} \left(\frac{e^{-\Theta_{v,j}/2T}}{1 - e^{-\Theta_{v,j}/T}} \right) \quad (2.216)$$

where $\Theta_{v,j} = h \nu_j / k_B$ is the characteristic vibrational temperature of each vibrational mode. Only the modes corresponding to positive second-order energy derivatives and thus, with real frequencies need to be considered in the above summation.

Indeed, modes relating to negative energy derivatives and having thus imaginary vibrational frequencies cannot contribute to thermodynamic partition functions, because they relate to energetically unstable and transient configurations.

The entropy contribution from the vibrational partition function is:

$$S_{vib} = R \left(\ln q_{vib} + T \left(\frac{\partial \ln q_{vib}}{\partial T} \right)_V \right) = R \sum_j \left(\left(\frac{\Theta_{v,j}/T}{e^{\Theta_{v,j}/T} - 1} \right) - \ln(1 - e^{-\Theta_{v,j}/T}) \right) \quad (2.217)$$

The contribution to the internal energy from molecular vibrations is:

$$U_{vib} = RT^2 \left(\frac{\partial \ln q_{vib}}{\partial T} \right)_V = R \sum_j \Theta_{v,j} \left(\frac{1}{2} + \left(\frac{1}{e^{\Theta_{v,j}/T} - 1} \right) \right) \quad (2.218)$$

2.4. Thermochemical Kinetics

Reaction kinetic models with detailed mechanisms based on fundamental thermochemical and kinetic principles have been developed by researchers aiming at the optimization and investigation of the properties of systems subject to many complex chemical reactions. These include among others combustion, flame inhibition, ignition in applied science, atmospheric smog formation and transport, or stratospheric ozone depletion. Research in chemical kinetics has applications in atmospheric and materials sciences, and is of relevance in particular for the incineration of municipal and hazardous wastes, chemical vapor deposition, semiconductor etching and many further chemical processes.

Computational fluid dynamics, gas phase combustion processes, modeling and simulation of ignition processes, or atmospheric chemistry are just a few of the areas that need accurate kinetic rate constants for chemical reactions. Predicting rate constants is as matter of fact a major goal of computational chemistry. Calculations of rate constants require both the accuracy of the dynamical theory and high efficiency in obtaining quantitative information on potential energy surfaces. Typically, at room temperature, errors of the order of 1 kcal mol⁻¹ on energy barriers result in errors by about one order of magnitude in kinetic rate constants. Despite all advances made so far in quantum mechanics and statistical thermodynamics, thermochemical kinetics therefore still remains an extremely challenging research field.

Ab initio and density functional theory calculations enable accurate estimations of the thermochemical properties of reactants, intermediate radicals and products, as well as activation energies, which is often impossible to achieve through experiment.

A chemical reaction of the form $A+B\rightarrow C+D$ can be characterized by a kinetic rate constant (k) through the equalities:

$$\frac{d[C]}{dt} = \frac{d[D]}{dt} = -\frac{d[A]}{dt} = -\frac{d[B]}{dt} = k[A]^n [B]^m \quad (2.219)$$

If k is known, the concentration of the various species can be calculated at any given time from the initial concentration. The rate constant is a function of the quantum states of A, B, C and D, i.e. of all the electronic, translational, rotational and vibrational quantum numbers of these molecular species at the microscopic level. The macroscopic (*canonical*) rate constant $k(T)$ is an average of all microscopic (*microcanonical*) rate constants $k(E)$, weighted by the probability of finding a molecule with a given set of quantum numbers corresponding to the molecular energy E . For systems in equilibrium the probability of finding a molecule in a particular state depends on its energy E , as determined by the Boltzmann distribution, and the macroscopic rate constant thereby becomes a function of the temperature [30].

2.4.1. Early Theories of Unimolecular Reactions

At the beginning of the 20th century, many gas phase reactions were known to be first-order processes and were assumed to be unimolecular reactions (i.e. reactions of the form $A\rightarrow P$). Many reactions which were studied since then have been found not to be unimolecular processes according to the modern definition, but to involve free radical chains. Despite their limitations, the early studies of these reactions were important in the development of unimolecular reaction theory. They focused attention upon the central problem of how the reacting molecule acquires the activation energy which is needed for the reaction to take place [109]. It was difficult to see how first-order processes could result if molecules were energized by bimolecular collisions, which were expected to be second-order processes. It was assumed (quite erroneously) that even at those very low pressures where molecular collisions were rare, unimolecular reactions would continue to occur with the same first-order rate constant and therefore molecular collisions would appear to be unimportant.

The disadvantages of earlier theories were overcome by the theory of Lindemann. The importance of molecular collisions in the energization process was finally established when it was found that the first-order rate constant for unimolecular reactions is not a true constant but does decline at low pressure. The decline or falloff in the first-order rate constant with pressure has since become recognized as an important experimental criterion of unimolecular reactions.

A consequence of this decline in the rate constant is that at low pressures, the initial rate constant becomes proportional to the total pressure and concentration of the reactant. The reaction is then second-order overall, although for reasons which will be apparent later the time-development of a given reaction mixture remains first-order. As still lower pressures it is possible that wall effects may become important in energization processes and there is some evidence that the rate constant then becomes a true first-order constant again.

2.4.1.1. Lindemann's Theory

The first basic theory of unimolecular reactions was developed by Lindemann [166] in 1922, who proposed that reacting molecules in a thermal system are energized by collisions [167]. He proposed that molecules become energized by bimolecular collisions, with a time lag between the moment of collisional energy transfer and the moment the molecule decomposes. Energized molecules could then undergo deactivating collisions before decomposition occurred. Steinfeld *et al.* [168] showed that "A major achievement of Lindemann's theory is its ability to explain the experimental finding that the reaction rate constant changes from first to second order in going from the high- to the low-pressure limits." The main concepts of the Lindemann theory may be stated briefly as follows:

(a) By collisions, a certain fraction of the molecules becomes energized, i.e. gain energy more than a critical quantity E_0 , which is required for the reaction to occur. The rate constant of the energization process depends thus on the rate constant of bimolecular collisions. This process can be written as follows



where A^* represents an energized molecule that is sufficiently excited to react with no further input of energy, and M is a product molecule, an added "inert" gas molecule, or a second molecule of reactant. In the simple Lindemann theory, k_1 is taken to be energy-independent and is calculated from the simple collision theory equation.

(b) Energized molecules are de-energized by collision, which is the reverse of process eq. (2.220), as follows:



The rate constant k_{-1} is again taken to be energy-independent, and is equated with some collision number Z_1 (see eq. 2.239 further for a precise and quantitative definition), by assuming that every collision of A^* leads to de-energization.

(c) There is a time lag between the energization and unimolecular dissociation or isomerization of the energized molecule. The excited reactant A^* then undergoes unimolecular dissociation process to form the products, which occurs with a rate constant k_2 independent of the energy content of A^*



By applying a steady state approximation for the production of energized molecules A^* , the overall rate constant of product formation can be expressed as [167]:

$$\frac{d[A^*]}{dt} = k_1[A][M] - k_{-1}[A^*][M] - k_2[A^*] \quad (2.223)$$

Assuming a steady state regime, $\frac{d[A^*]}{dt} = 0$, one obtains:

$$k_1[A][M] = k_{-1}[A^*][M] + k_2[A^*] \quad (2.224)$$

Rearranging this expression yields the concentration in A^* :

$$[A^*] = \frac{k_1[A][M]}{k_{-1}[M] + k_2} \quad (2.225)$$

The overall rate constant of the reaction is then given through

$$\nu = k_2[A^*] = \frac{k_1 k_2 [A][M]}{k_{-1}[M] + k_2} = k_{\text{uni}}[A] \quad (2.226)$$

Therefore, the Lindemann's expression for the overall unimolecular rate constant is thus:

$$k_{\text{uni}} = \frac{k_1 k_2 [M]}{k_{-1}[M] + k_2} \quad (2.227)$$

which shows that the rate constant is not really a constant at all but depends on the total pressure, or equivalently on $[M]$ (and on the temperature).

The interesting feature of this law is that the unimolecular rate constant, k_{uni} , changes from second-order (in A and M) in the low-pressure limit where $k_{-1}[M] \ll k_2$, to first-order in $[A]$ in the high-pressure limit [167]. Application of the steady state hypothesis to the concentration of A^* allows the unimolecular rate constant in the high- and low pressures limits to be determined as follows:

In the high-pressure limit ($[M] \rightarrow \infty$), there are many collisions, and collisional de-excitation of A^* is therefore much more likely to occur than unimolecular reaction of A^* to form products (i.e. $k_{-1}[M] \gg k_2$). In this limit, we can neglect the k_2 contribution to the denominator of eq. (2.226), and the rate constant of the reaction simplifies therefore into

$$k_{\infty} = k_{\text{uni}} = \frac{k_1 k_2}{k_{-1}} \quad (2.228)$$

$$\nu = k_2[A^*] = k_{\text{uni}}[A] = \frac{k_1 k_2}{k_{-1}}[A] \quad (2.229)$$

This mechanism explains the observed first-order kinetics at intermediate pressures, when the unimolecular step is rate determining. The rate constant of energization and de-energization are relatively fast steps which can be treated as a fast pre-equilibrium. Thus, in the high-pressure limit, the rate determining step (unimolecular step) is the one transforming A^* into products.

In the low-pressure limit ($[M] \rightarrow 0$), there are few collisions, and A^* will generally undergo unimolecular reaction before it undergoes collisional de-excitation (i.e. $k_2 \gg k_{-1}[M]$). In this limit, we can neglect the $k_{-1}[M]$ term in the denominator of eq. (2.226), and the rate constant for product formation is then given by

$$k_o = k_{\text{uni}} = k_1[M] \quad (2.230)$$

$$\nu = k_2[A^*] = k_{\text{uni}}[A] = k_1[A][M] \quad (2.231)$$

Therefore, the low pressure limiting form for the bimolecular rate constant is proportional to pressure (i.e., to the diluent gas concentration). In other words, at low pressures, the kinetics takes thus the form of a second-order rate constant. This is because formation of the excited species A^* shows a bimolecular kinetics, which is rate determining at such pressures.

At low pressures, Lindemann's theory predicts a change in the order of the initial rate of reaction on concentrations. This is showed in a decline in the pseudo first-order rate constant k_{uni} with concentration, where k_{uni} is defined as in eq. (2.232).

$$\nu = \frac{-d[A]}{dt} = k_{\text{uni}}[A] \Rightarrow k_{\text{uni}} = \frac{1}{[A]} \left(\frac{-d[A]}{dt} \right) = \frac{k_1[M]}{1 + k_{-1}[M]/k_2} \quad (2.232)$$

The extent of this 'fall-off' is conveniently measured in terms of the ratio $k_{\text{uni}}/k_{\infty}$, given by

$$\frac{k_{\text{uni}}}{k_{\infty}} = \frac{1}{1 + k_2/k_{-1}[M]} \quad (2.233)$$

This ratio can be used to find the total pressure, or equivalently the total concentration of molecules $[M]$, at which k_{uni} drops to half its high-pressure limit (i.e., $k_{\text{uni}}=k_{\infty}/2$). We define this concentration as $[M]_{1/2}$, and from eq. (2.227) and defining k_{∞} in eq. (2.228), we obtain

$$[M]_{\frac{1}{2}} = \frac{k_2}{k_{-1}} = \frac{k_{\infty}}{k_1} \quad (2.234)$$

By replacing $[M]$ with the total pressure, we find that the fall-off pressure $p_{1/2}$ corresponds to:

$$p_{\frac{1}{2}} = \frac{k_2}{k_{-1}} = \frac{k_{\infty}}{k_1} \quad (2.235)$$

Although the “fall-off” of k_{uni} against pressure is not always amenable over the whole range of pressures, it is sometime useful to quote the transition pressure for a specific reaction at a particular temperature.

It is easily seen from eq. (2.233) that the predicted effect of adding inert gas below the high pressure limit of a unimolecular reaction (i.e. in the fall-off region) is to increase the rate constant back to its high pressure value. The effect is comparable to increasing the pressure of the reactant, although added gases are often less efficient than the reactant itself in the energization process.

Thus, Lindemann’s theory and eq. (2.234) can be used to predict the fall-off concentration $[M]_{1/2}$. Unfortunately, in many tests against experiment, the predicted fall-off concentration was found to be as much as 10 orders of magnitude greater than the measured one (the experimental fall-off concentration is determined by measuring k_{uni} as a function of pressure to find the concentration at which $k_{\text{uni}}=k_{\infty}/2$). We can see in eq. (2.234) that since k_{∞} is a measured quantity, the excitation rate constant k_1 , which is predicted by the theory, must be grossly too small (i.e., by up to 10 orders of magnitude). This is the first of the breakdowns of the Lindemann’s theory that led to further improvement of the model, as will be discussed shortly [169].

The expression for k_{uni} in eq. (2.227) and eq. (2.228) can be combined to give:

$$\frac{1}{k_{\text{uni}}} = \frac{1}{k_{\infty}} + \frac{1}{k_1[M]} \quad (2.236)$$

Thus, Lindemann’s theory predicts that a plot of $1/k_{\text{uni}}$ versus $1/[M]$ should yield a straight line.

One conclusion which can be drawn from Lindemann's theory is that k_∞ is a true constant, which is independent of pressure. Adding inert gases is expected therefore to have no effect on a unimolecular reaction in its first-order region, since in this case the equilibrium proportion of energized molecules is already achieved. However, it is possible that a small change in k_∞ can occur at very high pressures, due to a non-vanishing volume of activation ΔV^\ddagger . From eqs. (2.233 and 2.235), the general first-order rate constant can be written as eq. (2.237), in which $[M]$ is replaced by the total pressure p .

$$k_{\text{uni}} = \frac{k_\infty}{1 + k_\infty/k_1 p} \quad (2.237)$$

According to Lindemann's theory, the rate constant k_1 is calculated from collision theory, using the expression:

$$k_1 = Z_1 \exp(-E_0/k_B T) \quad (2.238)$$

with Z_1 , the collision number, which is usually expressed in $\text{Torr}^{-1}\text{s}^{-1}$ (which is consistent with giving $[M]$ in Torr and k_2 in s^{-1}).

$$Z_1 = (\sigma_d^2 N_A / R) (8\pi N_A k_B / \mu)^{1/2} (1/T)^{1/2} \quad (2.239)$$

In the above equation, the following parameters are used:

σ_d : collision diameter (in cm)

μ : reduced molar mass (in g mol^{-1})

T : temperature (in K)

N_A : Avogadro constant ($6.02 \times 10^{23} \text{ mol}^{-1}$)

R : gas constant ($8.314 \text{ J mol}^{-1} \text{ K}^{-1}$)

k_B : Boltzmann constant ($1.3805 \times 10^{-23} \text{ J K}^{-1}$)

Lindemann's theory predicts thus the correct behavior of unimolecular kinetic rate constant in the high- and low-pressure limits. However, quantitative comparisons between this theory and experiment showed several severe problems [169].

2.4.1.2. Hinshelwood's Theory

A main failure of Lindemann's mechanism relates to the fact that first-order rate constants are maintained down to much lower concentrations than appear to be permitted by the theory, a failure which Hinshelwood [170] successfully overcame. This failure of Lindemann's theory has been illustrated by the calculation of the transition pressure $p_{1/2}$, which is often much too high to agree with experiment. Besides, it could be shown that the rate constant of energization given by

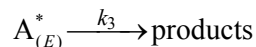
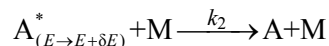
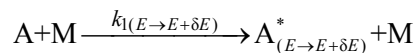
eq. (2.238) is too low to account for the observed global rate constant. Both deficiencies are remedied by an increase in the rate constant k_1 .

More specifically, Hinshelwood developed a suggestion by Lindemann that k_1 could be increased by assuming that the required energy could be drawn in part from the internal degrees of freedom (mainly vibrational) of the reactant molecules. The chance that a molecule possesses an energy E larger than or equal to the critical energy E_0 ($E \geq E_0$) clearly increases with the number of available degrees of freedom. Hinshelwood showed that the probability this energy gets distributed in s classical degrees of freedom $[\exp(-E_0/k_B T)(E_0/k_B T)^{s-1}]/(s-1)!$ is much higher than that used in Lindemann's theory $[\exp(-E_0/k_B T)]$. The rate constant k_1 in the modified Hinshelwood-Lindemann theory is therefore given by eq. (2.240), which even for moderate values of s leads to much larger values of k_1 than does [eq. (2.238)]:

$$k_1 = Z_1 \frac{1}{(s-1)!} \exp(-E_0/k_B T) (E_0/k_B T)^{s-1} \quad (2.240)$$

Since k_1 increases with s classical degrees of freedom in the Lindemann-Hinshelwood theory, it is clear that k_2 ($k_2 = k_{\infty} k_{-1}/k_1$) must correspondingly decrease. Therefore, the lifetime of the energized molecule $t \approx 1/k_2$ increases when the molecule can store energy among a greater number of degrees of freedom. Therefore, k_2 is expected to depend on the energy of the excited species A^* .

According to the Hinshelwood-Lindemann mechanism, k_1 becomes a function of the energy. Attention is first concentrated upon the rate constant $k_{1(E \rightarrow E + \delta E)}$ for energization into an infinitesimally small energy range comprised between E and $E + \delta E$. The rate constant k_2 for de-energization is still assumed to be independent of the energy [107]:



As in Lindemann's theory, the high pressure limit corresponds to a situation in which the energized molecules are present at their equilibrium proportion for any specified infinitesimal energy interval, as follows:

$$f_{(E \leq E \leq E + \delta E)} = (E/k_B T)^{s-1} \exp(-E/k_B T) \frac{1}{(s-1)!} (\delta E/k_B T) \quad (2.241)$$

The equilibrium proportion of molecules that are energized in the infinitesimal energy range comprised between E and $E+\delta E$ is given by $\delta k_{1(E \rightarrow E+\delta E)}/k_2$, and if this latter quantity is equated to the right-hand side of eq. (2.241), an equation for $\delta k_1/k_2$ is obtained. By integrating between the limits $E=E_0$ and $E=\infty$, where E_0 is the critical energy which is required to initiate the unimolecular reaction, one gets the following ratios:

$$\frac{k_1}{k_2} = \int_{E=E_0}^{\infty} \frac{dk_1}{k_2} = \int_{E=E_0}^{\infty} \frac{1}{(s-1)!} (E/k_B T)^{s-1} \exp(-E/k_B T) d(E/k_B T) \quad (2.242)$$

Upon equating $E/k_B T$ to X and integrating by parts over dX , one finds:

$$\frac{k_1}{k_2} = \left(\frac{1}{(s-1)!} (E_0/k_B T)^{s-1} + \frac{1}{(s-2)!} (E_0/k_B T)^{s-2} + \dots \right) \exp(-E_0/k_B T) \quad (2.243)$$

Since usually $E_0 \gg (s-1)k_B T$, the second term in eq. (2.243) is negligible, compared with the first term. If the second term is neglected, then the ratio k_1/k_2 is given by

$$\frac{k_1}{k_2} = \frac{1}{(s-1)!} (E_0/k_B T)^{s-1} \exp(-E_0/k_B T) \quad (2.244)$$

When $k_2 \approx Z_1$, one obtains Hinshelwood's expression for k_1 , which has been given previously [eq. (2.240)]. According to the Hinshelwood-Lindemann theory, the high pressure rate constant is given by

$$k_{\infty} = \frac{k_1 k_3}{k_2} = \frac{k_3}{(s-1)!} (E_0/k_B T)^{s-1} \exp(-E_0/k_B T) \quad (2.245)$$

Thus, eq. (2.240) for k_1 and eq. (2.245) for k_{∞} are the basic Hinshelwood-Lindemann equations for the rate constants at low and high pressures. According to the Hinshelwood-Lindemann theory, the rate constant k_3 is independent of the energy of the energized molecule but does depend on the molecular characteristics because it is a function of the number of available vibrational modes, s .

The first of the shortcomings of the Lindemann theory underestimating the excitation rate constant k_1 was addressed by Hinshelwood [170]. The Hinshelwood's model corrects one of the major deficiencies in the Lindemann's theory of unimolecular reactions. The larger kinetic rate constant which is obtained from eq. (2.240) brings the predicted fall-off concentration $[M]_{1/2}$ of eq. (2.234) into much better agreement with experiment. However, because of the many simplifying assumptions which were invoked in the model by Hinshelwood, there are still several shortcomings.

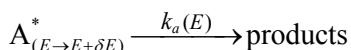
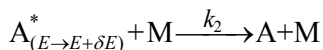
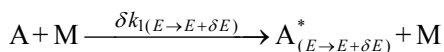
The principal weakness in this model is the assumption that the molecule contains s harmonic vibrational modes with identical frequency. In addition, the

number of modes s in the theory is not strictly associated with the number of vibrational degrees of freedom of the molecule. In fact, s is usually taken as a free parameter in the model that is adjusted to obtain the best agreement with experiment. Typically, the optimal value of s is about half of the actual number of vibrational frequencies in the molecule. Another deficiency of the model by Hinshelwood is that it cannot account for the downward curvature in the plot of $1/k_{\text{uni}}$ versus $1/[M]$ which was mentioned at the end of the previous section [169].

2.4.1.3. Slater's Theory

Slater pictured in 1939 the energized molecule A^* as an assembly of excited harmonic oscillators [171]. Within this theoretical frame, vibrational relaxation between normal modes is forbidden, and the unimolecular reaction occurs only when a reaction progress variable, the so-called "reaction coordinate", reaches a critical value by superposition of the various harmonic mode displacements [172].

In further developments of kinetic theories for unimolecular reactions, both the rate constants k_1 and k_2 are made energy-dependent. The rate constant k_1 is decomposed, as in Hinshelwood-Lindemann theory, into energy-dependent contributions $\delta k_{1(E \rightarrow E+\delta E)}$ for energization in infinitesimally small energy intervals ranging from E to $E+\delta E$. The rate constant k_3 is also replaced by an energy-dependent rate constant $k_a(E)$. Slater's theory makes use of earlier ideas for the overall mechanism of unimolecular reactions in order to represent the rate constant at any pressure. Therefore, when incorporating Slater's idea for molecular energizations, the Hinshelwood-Lindemann mechanism takes the form



The steady state approximation is applied to the concentration of $A_{(E \rightarrow E+\delta E)}^*$, which leads to the following expression for the contribution to the unimolecular rate constant k_{uni} for energized molecules in the considered infinitesimal energy range,

$$\delta k_{\text{uni}(E \rightarrow E+\delta E)} = \frac{k_a(E)(\delta k_1/k_2)_{(E \rightarrow E+\delta E)}}{1 + k_a(E)/k_2[M]} \quad (2.246)$$

As usual, the total (canonical) rate constant k_{uni} is then obtained by integration, as follows:

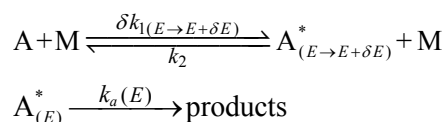
$$k_{uni} = \int_{E=E_0}^{\infty} \frac{k_a(E) \delta k_{1(E \rightarrow E+\delta E)} / k_2}{1 + k_a(E) / k_2 [M]} \quad (2.247)$$

In order to enable accurate predictions of the fall-off behavior of a unimolecular reaction, it is essential to take into account the energy-dependence of the rate constant $k_a(E)$ for the conversion of energized molecules into activated complexes where products result from decomposition of the energized complex.

Steinfeld *et al.* [168] noted that two quite different approaches may be taken to determine $k_a(E)$: (i) consider the explicit nature of the intramolecular motion of highly energized molecules in Slater's theory, (ii) invoke statistical assumptions, such as RRK (Rice–Ramsperger–Kassel) theory and its extension, RRKM (Rice–Ramsperger–Kassel–Marcus) theory. Most modern theories of unimolecular reactions (Slater, RRK and RRKM theories) are based on the fundamental Lindemann's mechanism involving collision energy transfer of the reactant molecules, and more specifically on Hinshelwood's development.

2.4.1.4. Rice–Ramsperger–Kassel Theory

The Rice-Ramsperger-Kassel (RRK) theory was developed simultaneously by Rice and Ramsperger [173,174] and by Kassel [175,176]. This theory uses the basic Hinshelwood-Lindemann mechanism of collision energy transfer and de-energization, but considers more realistically that the rate constant for conversion of an energized molecule to products is proportional to a specific probability (which increases with E). In this theory, the following reaction mechanism is considered:



Both Kassel on the one hand and Rice and Ramsperger on the other hand, considered that for the reaction to occur a critical energy E_0 must become concentrated in one particular part of the molecule. The total energy E of a molecule under consideration is assumed to be rapidly redistributed around the molecule, so that for any energized molecule with E greater than E_0 , there is a finite statistical probability that the required critical energy E_0 will be found in the relevant part of the energized molecule, e.g. in one oscillator (Kassel's theory) or in one squared term (Rice-Ramsperger theory).

The RRK theory assumes that the rate constant for conversion of energized molecules into products is proportional to this probability (which increases with the

total energy E), and therefore derives expressions for the energy dependence of k_a . The differences between the two models are twofold:

- (i) Rice and Ramsperger used classical statistical mechanics throughout, while Kassel used both a classical treatment and developed latter a quantum model, which is much more realistic and accurate.
- (ii) Different assumptions were made about the part of the molecule into which the critical energy E_0 has to be concentrated. Kassel's model seems slightly more realistic by assuming that the energy has to be concentrated into one oscillator only.

Kassel's widely used classical theory is based on a calculation of the probability that a system of s classical oscillators with total energy E should have energy $\geq E_0$ in one chosen oscillator. The derivation of this theory is clearly documented elsewhere [175] and the result is given by the following equation:

$$\text{Probability } (E \geq E_0 \text{ in one oscillator}) = A \left(\frac{E - E_0}{E} \right)^{s-1} \quad (2.248)$$

This probability equation can be converted into the rate constant $k_a(E)$ for the conversion of energized molecules to products. This gives the classical RRK rate constant expression, as follows [177]:

$$k_a(E) = A \left(\frac{E - E_0}{E} \right)^{s-1} = A \left(1 - \frac{E_0}{E} \right)^{s-1} \quad (2.249)$$

where A is no more than a proportionality constant which it acquires significance when eq. (2.249) is inserted into eq. (2.250), using Hinshelwood's expression for δk_1 . The high pressure limit is then given by eq. (2.251) which on substitution of $x = (E - E_0) / kT$ and use of the defining integral for $\Gamma(s) = (s-1)!$ gives eq. (2.252). Thus, the theory predicts strict adherence to the Arrhenius equation, and the constant A can be identified with the high pressure A factor for the reaction.

$$k_{\text{uni}} = \int_{E=E_0}^{\infty} \frac{k_a(E) dk_{1(E \rightarrow E + \delta E)} / k_2}{1 + k_a(E) / k_2 [M]} \quad (2.250)$$

$$k_{\infty} = \int_{E=E_0}^{\infty} A \left(1 - \frac{E_0}{E} \right)^{s-1} \left(\frac{(E/k_B T)^{s-1} \exp(-E/k_B T)}{(s-1)!} \right) d \left(\frac{E}{k_B T} \right) \quad (2.251)$$

$$k_{\infty} = A \exp(-E_0 / k_B T) \quad (2.252)$$

The quantum version of Kassel's theory (QRRK) is in principle very similar to the classical theory outlined above. It is based on the calculation of the probability that a system of s quantum oscillators possess an energy E larger

than or equal to the critical energy E_o , whereas the classical version considered s classical oscillators for distributing the energy. QRRK theory assumes that there are s identical harmonic oscillators in the molecule, all having the same frequency ν ; hence energy $h\nu$, and so the critical energy E_o is expressed as a critical number of quanta being equal to $m=E_o/h\nu$. The energy E of the energized molecule is then expressed as a total of n energy quanta when $n=E/h\nu$. The number of ways to distribute n energy quanta among s oscillators is equal to $(n+s-1)!/n!(s-1)!$, which corresponds to the degeneracy of a state with n quanta of s equally-spaced oscillators. The number of ways that the n quanta can be placed in the molecule, such that at least m quanta are in the critical oscillator, is then equal to $(n-m+s-1)!/(n-m)!(s-1)!$.

The expression corresponding to eq. (2.248) is now the probability of the molecule to be in a dissociative state such that if s oscillators contain at least n quanta (where $n=E/h\nu$), one chosen oscillator will contain at least m quanta. Due to the fast redistribution of the energy, there is a certain probability that the critical quantum m is populated, which can be defined purely stochastically. The ratio between distributing n quanta among s oscillators with at least m quanta in the critical oscillator, and the same distribution without the restriction read as [109,168]

$$Probability = \frac{n!(n-m+s-1)!}{(n-m)!(n+s-1)!} \quad (2.253)$$

where n represents the total number of vibrational quanta, m denotes the number of quanta in the critical coordinate, and s is the number of identical oscillators. Thus, the corresponding expression for k_a is given by

$$k_a(nh\nu) = A \frac{n!(n-m+s-1)!}{(n-m)!(n+s-1)!} \quad (2.254)$$

where A is a constant.

The expression used for $k_1(E)$ is a similar development of Hinshelwood's expression, namely eq. (2.255) [175,176]. It refers to energization into a specific quantum state rather than into an energy ranging from E to $E+\delta E$, as follows:

$$k_1(E) = k_1(nh\nu) = k_2 \alpha^n (1-\alpha)^s \frac{(n+s-1)!}{n!(s-1)!} \quad (2.255)$$

where $\alpha = \exp(-h\nu/k_B T)$.

The overall rate constant is obtained by summation over all energy levels, which gives the following expression for the rate constant in the high-pressure limit:

$$k_{\infty} = \sum_{n=m}^{\infty} \frac{k_1(nh\nu)k_a(nh\nu)}{k_2} = A \exp(-E_o/k_B T) \quad (2.256)$$

and expression which can be shown to result once more in the correct Arrhenius form eq. (2.252). The interpretation of the constant A is thus the same as in the classical treatment.

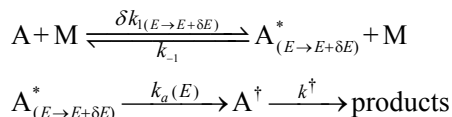
It is worth noting that both in the classical and quantum forms of Kassel's theory, the same value of s has been used for defining k_1 and k_a . Besides, in the quantum theory, the same oscillator frequency ν was assumed for both the energized molecule and the activated complex. The first of these assumptions seems to be perfectly valid in the light of subsequent work with more sophisticated theories, but the second consideration shows the extreme simplicity of the model used by Kassel, which was abandoned in later theories. The statistical approach of the RRK theories to the calculation of $k_a(E)$ is correct, but improvements of the model for the frequencies were needed. These developments later formed the basis of the RRKM theory.

Indeed, the RRK expression is incapable of giving a correct rate constant even within an order of magnitude [177] due to several reasons: (i) It assumes a collection of classical oscillators with $(n-m) \gg s$ which is inappropriate for most chemical systems; (ii) The RRK theory neglects the zero point energy. Other quantum theories such as RRKM were developed through the years and eliminated the problems associated with the RRK expression by treating the vibrational and rotational degrees of freedom in detail on quantum grounds.

2.4.1.5. Rice–Ramsperger–Kassel–Marcus Theory

As explained previously, the main statistical concepts for understanding unimolecular dissociation reactions from activated species were developed initially by Rice and Ramsperger [173,178] and Kassel [175]. As RRK theory, RRKM is a microcanonical transition state theory from which *canonical* (temperature-dependent) kinetic rate constants are obtained through a Boltzmann averaging of *microcanonical* (energy-dependent) rate constants. The assumed mechanism is the same as the one invoked in RRK theory, i.e. a collision activation process, followed by intramolecular vibrational and rotational relaxations leading to the transition state, and then to products. As in RRK theory and TST, it is assumed that energized molecules pass through the transition state only once (an approximation which may not always be exact, hence RRKM rate constants necessarily represent upper bounds to the exact kinetic rate constants). RRKM theory relies upon a proper quantum treatment of vibrations and rotations, most usually at the

level of the standard rigid-rotor-harmonic-oscillator (RRHO) approximation (thus without any assumption about the frequencies of normal modes), and upon an exact counting of all possible states (i.e. without any approximation regarding thermodynamic partition functions). The reaction scheme used in this theory is as follows:



where k_1 is evaluated as a function of the energy by a quantum statistical mechanical treatment (instead of a classical treatment), and where E represents the total energy which is distributed in the active degrees of freedom of a given energized molecule A^* . The energy E is now a variable quantity, which is assumed to result from vibrational and rotational energy contributions, denoted by E_v and E_r , respectively, as follows:

$$E = E_{vr} = E_v + E_r \quad (2.257)$$

The reactant molecules A are energized and de-energized by collisions with inert molecules M to and from the infinitesimal energy range comprised between E and $E + \delta E$. The kinetic rate constants for these processes are set equal to δk_1 and k_{-1} , respectively. The energized molecules A^* are converted to activated complexes A^\ddagger with a rate constant $k_a(E)$. The activated complexes subsequently dissociate with a rate constant k^\ddagger leading to the reaction product P . It is assumed that the decay rate constant k^\ddagger for the activated complex A^\ddagger is much faster than $k_a(E)$. A careful distinction has to be made between the energized molecule A^* and the activated complex A^\ddagger , as follows:

- The energized molecule A^* is defined as a molecule A that is described loosely as having enough energy to react. The energy distribution will not usually be such that the reaction occurs immediately. However, there will be many quantum states of the energized molecule A^* in the considered infinitesimal energy range and only a few of these states can enable conversion to products. In addition, the energized molecule A^* will not react rapidly. Thus, it has a final lifetime to de-energization or decomposition, which depends on the values of $k_{-1}[\text{M}]$ and $k_a(E)$.
- The activated complex A^\ddagger is mainly a species which is obviously defined as being intermediate between the reactants and the products. It is characterized by having a configuration related to the top of an energy barrier between the reactants and products. The energy profile along the reaction coordinate involves a potential energy barrier E_0 between the reactants and products. This is the

required critical energy which must be overcome for the reaction to occur. The activated complex A^\ddagger is a molecule that lies in an arbitrarily small range at the top of the energy barrier. Thus, it is unstable to movement in either direction along the reaction coordinate and has no measurable lifetime.

Assuming the processes of activation and de-activation to be essentially single-step processes (the so-called **strong collision assumption**), the quantity $\delta k_1/k_{-1}$ may be equated to the equilibrium Boltzmann distribution of molecules in the considered infinitesimally small energy range,

$$\frac{\delta k_{1(E \rightarrow E+\delta E)}}{k_{-1}} = \frac{N(E) \exp(-E/k_B T)}{Q_A} \delta E \quad (2.258)$$

where $N(E)$ is the number of quantum states at an energy E in the reactant molecule **A**. More specifically, $N(E)$ represents the number of vibrational and rotational configurations with an energy comprised between E and $E+\delta E$. In the above expression Q_A is the molecular partition function for all the active modes of the reactant **A**. Since relatively large amounts of energy are generally transferred in molecular collisions of highly excited polyatomic molecules (5 kcal mol⁻¹ or more), and since the average excitation energies in thermal reactions are typically 5–15 kcal mol⁻¹ above the critical energy E_o , the strong collision assumption is reasonably good for most thermal reactions [179].

A key concept in the derivation of RRKM theory is that of **phase space**, which is used to enforce energy randomization. Any choice of generalized coordinates q_i for positions in the configuration space defines generalized conjugated momenta p_i , which together define coordinates in phase space ($i=1,2,3,\dots,n$) for a system possessing n (translational, rotational and vibrational) degrees of freedom ($n=3N$ for a molecule containing N atoms). In statistical mechanics, when considering systems with continuous energies, the concept of phase space provides a classical analog to the quantum concept of partition function (sum over states), which is referred to as a **phase integral**. Instead of summing the Boltzmann factor ($e^{-E/k_B T}$) over discretely spaced energy states (defined by appropriate integer quantum numbers for each degree of freedom), one integrates suitably weighted energies over continuous phase space. Once the phase integral is known, it can be straightforwardly related to the partition function. Multiplication by a normalization constant representing the number of quantum energy states per unit phase space is required however, in order to ensure that the quantum partition functions coincide with their classical limits when $T \rightarrow \infty$. This normalization constant is simply the inverse of Planck's constant ($h=6.6256 \times 10^{-34}$ J.s) raised to a power equal to the

number of degrees of freedom n for the system [180]. For instance, for a particle moving in one dimension ($n=1$), we have:

$$q = \frac{1}{h} \iint e^{-E(x, p_x)/k_B T} dx dp_x \quad (2.259)$$

which implies that any such particle occupies an elementary space element $d\tau = dx dp_x = h$ in phase space. Similarly, for a particle moving in three dimensions ($n=3$), we have:

$$q = \frac{1}{h^3} \iiint e^{-E(\vec{r}, \vec{p})/k_B T} dx dy dz dp_x dp_y dp_z \quad (2.260)$$

which amounts to stating that any quantum particle occupies a generalized elementary volume ($d\tau = dp_x dp_y dp_z dx dy dz$) equal to h^3 in phase space.

An essential assumption of RRKM theory is the *equilibrium hypothesis*, which states that the steady state concentration of activated complexes \mathbf{A}^\ddagger is equal to the equilibrium concentration which would be present if no reaction was occurring. Another central assumption is a division of modes into active (rapidly equilibrating) and non-active (adiabatic) vibrational and rotational degrees of freedom, with energy redistribution between active modes being fast enough that a statistically random distribution of the excitation energy results on a time scale much faster than that for the reaction (*ergodic hypothesis*, also referred to as the *energy randomization hypothesis*). The physical idea behind the ergodicity assumption is that all parts of phase space are accessible on the time scale of the reaction, under the constraints of conservation of the total energy (E) and of the total angular momentum (\vec{L}). This randomization implies that all initial distributions of internal modes with energy E become rapidly equivalent. In other words, if the energy E exceeds the critical energy E_0 for the reaction to occur, then eventually that energy will end up in being localized in the breakable bond, no matter how the excited molecule was initially prepared.

The two above assumptions of RRKM theory are quite different in nature. The energy randomization hypothesis is directed toward single isolated molecules and permits calculations of the microscopic rate constant k_a as a function of the energy in the molecule. It assumes that the intramolecular dynamics is ergodic on the time scale of the reaction rates process, so that statistical considerations alone can predict the reaction rates and product energy distributions. On the other hand, the strong collision assumption is related to the special case of thermal energization and de-energization of molecules by molecular collisions. It leads to a Boltzmann distribution of energized molecules above the critical energy and predicts an Arrhenius dependence of the global rate constant on temperature at high pressures.

Due to the redistribution of energy between active modes, the location of the molecules in phase space changes in the course of time. According to the ergodic assumption, the degrees of freedom of a highly excited, isolated molecule or collision complex are so strongly coupled that, no matter how localized in phase space an ensemble of such complexes is prepared, the ensemble will evolve to fill the entire phase space available to it *uniformly* (consistent with the conservation of the total energy E , and of the total angular momentum \vec{L}) on a time scale much smaller than the characteristic time for an elementary reaction step. Each step thus takes place exclusively from a microcanonical/fixed- \vec{L} ensemble (which is most commonly approximated simply by a microcanonical ensemble). This is illustrated schematically in Figure 2.6. The isolated pockets of complexes on the left of the figure might correspond to depositing energy in a particular bond or normal mode of the molecule, or they might correspond to isolating the complexes near a transition-state dividing surface through which they were formed. The subsequent trajectories of the complexes are considered to be chaotic with the ensemble rapidly becoming uniform in the accessible phase space of a given energy well [181]. Therefore, by virtue of the ergodicity assumption, instead of one molecule passing through all configurations, one may equivalently consider a very large ensemble of molecules N with a fixed total energy E (and a fixed total angular momentum \vec{L}), where each of them has a different configuration.

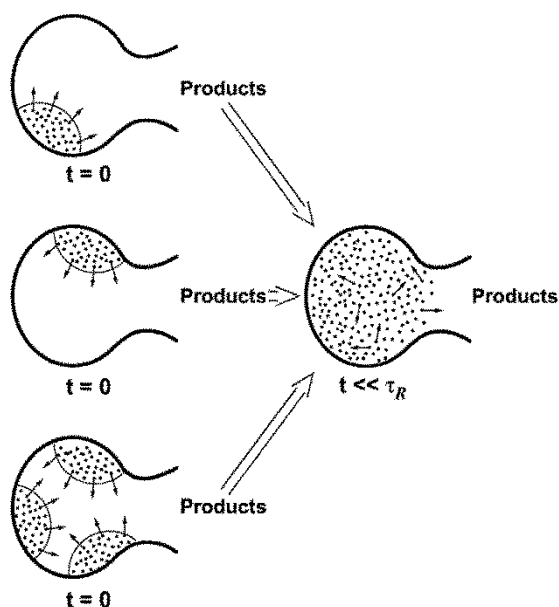


Figure 2.6. Schematic diagram illustrating RRKM dynamics in phase space. The time τ_R is the characteristic time for reaction to occur [181].

If the energy E is greater than the critical energy E_0 , the molecule has a chance to reach a part of the hypersurface which is associated with the critical surface at or around the transition state, which is defined as a subvolume of phase space where the reaction is considered to take place. Two special coordinates, one spatial variable p^\ddagger and its conjugate momentum variable q^\ddagger , are retained for describing the nuclear motions involved in the bond breaking and/or reforming processes occurring at the level of the transition state. These reaction coordinates p^\ddagger and q^\ddagger define a trajectory in phase space along which the reaction takes place (see Figure 2.7). If the system possess n degrees of freedom, the critical surface dividing the reactants and products regions in phase space is therefore defined as a $2n-2$ dimensional hypersurface, which is located in such a way that a trajectory in phase space, once having pass through it, will proceed on to reaction products without re-crossing it. For reactions involving sharp energy barriers, the critical hypersurface is unambiguously located at the saddle point. In contrast, for barrierless reactions, or for reactions involving shallow energy barriers, the location of the critical (hyper) surface depends very much upon Gibbs free energies (see further).

Therefore, in line with the ergodic assumption, instead of one molecule passing through all configurations, imagines a large ensemble of molecules N with fixed energy E , where each of them has a different configuration. The subvolume of the phase space which defines the critical region is related to a fraction of molecules dN in this volume. This part is compared to the total, available phase space volume at a fixed energy E and hence, to the density of states ρ of the reactant molecule, as follows:

$$\frac{dN}{dt} = \frac{\text{fraction of molecules in critical region}}{\text{total number of molecules}} \propto \frac{d\rho^\ddagger}{\rho} \quad (2.261)$$

where $d\rho$ denotes the density of states in the critical region (densities of states correspond to numbers of states per energy units).

The ergodic assumption that the total phase space is populated statistically means that the population density over the whole phase space is uniform. This is an enormous simplification. Rather than having to compute many molecular dynamical trajectories in full details, this permits the ratio of the number $[dN(q^\ddagger, p^\ddagger)/N]$ of molecules in the critical region (i.e. with reaction coordinates ranging from p^\ddagger to $p^\ddagger+dp^\ddagger$ and from q^\ddagger to $q^\ddagger+dq^\ddagger$) to the total number of molecules N to be expressed as the ratio of phase space which is accessible at the critical hypersurface to the total accessible phase space [167]:

$$\frac{dN(q^\ddagger, p^\ddagger)}{dt} = \frac{dq^\ddagger dp^\ddagger \int_{H=E-E_0-\varepsilon_i} dq_2 \dots dq_n dp_2 \dots dp_n}{\int_{H=E} dq_1 \dots dq_n dp_1 \dots dp_n} = \frac{dq^\ddagger dp^\ddagger h^{n-1} \rho^\ddagger(E-E_0-\varepsilon_i)}{h^n \rho(E)} \quad (2.262)$$

where h is the Planck's constant. In the above equation, ρ and ρ^\ddagger represent the densities of states of the reactant and at the saddle point, and ε_i is the translational energy associated with the momentum p^\ddagger in the reaction coordinate:

$$\varepsilon_i = \frac{p^{\ddagger 2}}{2\mu^\ddagger} \quad (2.263)$$

where μ^\ddagger is the reduced mass of the two moving molecular fragments (A and B)

$$\mu^\ddagger = \frac{m_A m_M}{m_A + m_M} \quad (2.264)$$

At the saddle point, the activation energy E_0 and the translational energy ε_i must be subtracted [eq. (2.262)] from the total energy E because these energies are not available for the remaining $n-1$ coordinates q_i^\ddagger in configuration space as well as for the remaining $n-1$ conjugate momenta p_i^\ddagger (Figure 2.8).

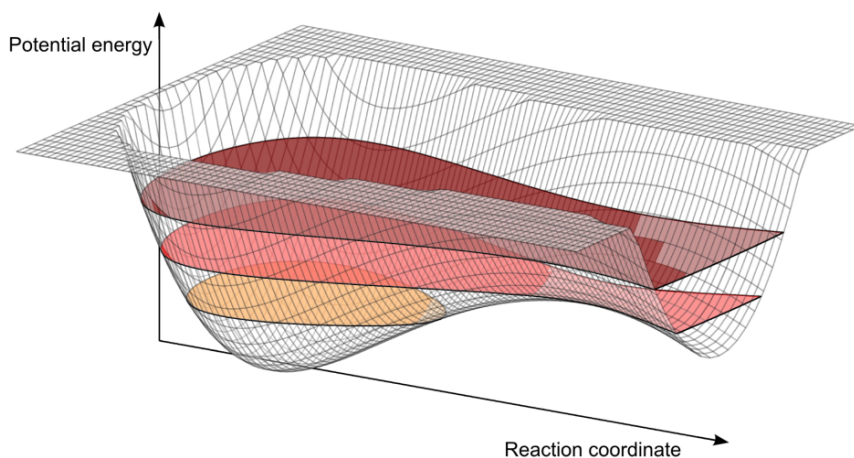


Figure 2.7. Potential energy surface with a saddle point and the phase space for three different total internal energies. At the lowest energy the reaction cannot be induced, at higher energies the density of states at the saddle point determines the reaction rate when compared to the total phase space surface at this energy [182].

The decay rate of the N molecules determining the reaction flux is then by definition given by the time derivative of their number.

$$\frac{dN(q^\ddagger, p^\ddagger)}{dt} = N dk(E, \varepsilon_t) \quad (2.265)$$

Because of the assumption that the reaction coordinate is perpendicular to (and thus separable from all) other coordinates, the time derivative of eq. (2.262) only involves the $dp^\ddagger dq^\ddagger$ term. The $dp^\ddagger dq^\ddagger/dt$ factor can be rearranged by noting that $dq^\ddagger/dt = p^\ddagger/\mu^\ddagger$. Therefore:

$$\frac{dp^\ddagger dq^\ddagger}{dt} = \frac{p^\ddagger dp^\ddagger}{\mu^\ddagger} \quad (2.266)$$

Since:

$$d\varepsilon_t = \frac{p^\ddagger dp^\ddagger}{\mu^\ddagger} \quad (2.267)$$

one can use the relationship:

$$\frac{dp^\ddagger dq^\ddagger}{dt} = d\varepsilon_t \quad (2.268)$$

and find therefore:

$$\frac{dN(q^\ddagger, p^\ddagger)}{N} = N \frac{d\varepsilon_t \rho^\ddagger(E - E_o - \varepsilon_t)}{h\rho(E)} = N dk(E, \varepsilon_t) \quad (2.269)$$

The above rate constant is expressed in terms of the total energy, E , and of the translational energy of the colliding fragments (A and M) at the transition state, ε_t . As shown in Figure 2.8, there are many ways for the reaction to pass through the transition state region, and these ways differ in how the available energy, $E - E_o$, is partitioned between the internal energy of the transition state and the translational energy of the fragments. However, for calculating the total reaction rate, an integration over all possible translational energies ε_t from zero to $E - E_o$ in the transition state is required. This yields the microcanonical RRKM reaction rate constant:

$$k(E) = \frac{\int_0^{E-E_o} \rho^\ddagger(E - E_o - \varepsilon_t) d\varepsilon_t}{h\rho(E)} = \frac{N^\ddagger(E)}{h\rho(E)} \quad (2.270)$$

where $N^\ddagger(E)$ is the sum of states in the critical phase space area along the reaction coordinate. This sum of states is obtained by summing all possible ways of partitioning the energy at the transition state. It depends on the activation (or critical) energy E_o and determines the microcanonical rate constant $k(E)$ for a molecule with a given internal energy E [183]. For a more complete and highly rigorous derivation of RRKM theory for microcanonical rate constants at fixed

total energy (E) and total angular momentum (\bar{L}), see also the text book by Gilbert and Smith [184].

In the above equation, $N^\ddagger(E)$ corresponds more specifically to the sum of all ro-vibrational quantum states that are present at energies above the activation energy E_0 , in an energy interval ranging from E_0 to E (see Figure 2.8). More qualitatively, the sum of states at the transition state $N^\ddagger(E)$ can be regarded as the number of ways the reacting molecule can cross the dividing surface to products (i.e. the probability that the reaction will proceed to products), whereas the density of states of the reactant $\rho(E)$ reflects the probability that the energy in the molecule will get distributed (lost) among all active modes, regardless of the probability it will get transferred into the mode which effectively brings the reaction to the transition state [167,185,186], and then to products. Very logically therefore, $k(E)$ increases proportionally to the sum of states at the transition state [$N^\ddagger(E)$] whereas it decreases inversely to the density of states for the reactant [$\rho(E)$].

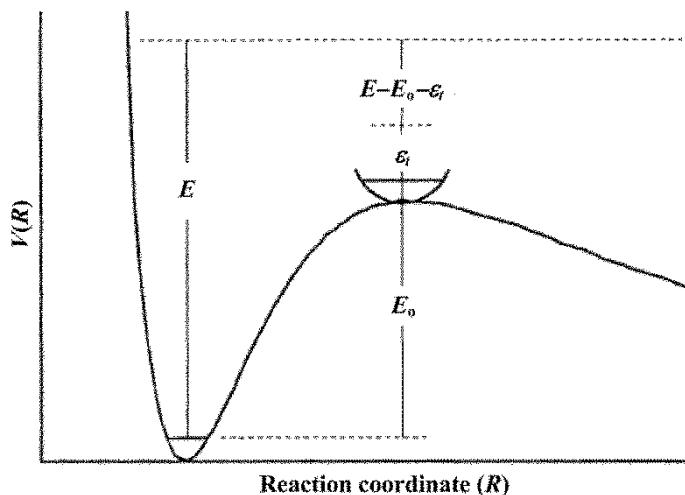


Figure 2.8. The reaction coordinate and the partitioning of the energy in the transition state ($E-E_0$) between the translational energy, ϵ_t , and the vibrational energy of the modes normal to the reaction coordinate [167].

In practice, vibrational densities of states can be very rapidly and efficiently computed using for instance the Beyer-Swineheart direct count algorithm [183], and convolved with rotational densities of states, for which there exist detailed analytical formula. For a detailed review of these equations and techniques, see also the text book by Gilbert and Smith [184].

When accounting for the reaction pathway degeneracy σ , i.e. a statistical factor which measures the possibility of the reaction to proceed through different pathways which are equivalent by symmetry, the RRKM microcanonical rate constants $k(E)$ are given by the standard expression [109]:

$$k(E) = \frac{\sigma N^\ddagger(E)}{h\rho(E)} \quad (2.271)$$

Canonical RRKM rate constants $k(T)$ are then ultimately determined by state integration and Boltzmann averaging:

$$k(T) = \int_{E_0}^{\infty} f(E, T) k(E) dE \quad (2.272)$$

along with:

$$f(E, T) = \frac{1}{Q(T)} \rho(E) \exp(-\beta E) \quad (2.273)$$

where $\beta=1/k_B T$ and $Q(T)$ is the reactant partition function:

$$Q(T) = \int_0^{\infty} \rho(E) \exp(-\beta E) dE \quad (2.274)$$

More specifically, upon expanding the above equation, one gets [109,187,188]:

$$k(T) = \frac{\sigma Q_1^\ddagger}{h Q_1 Q_2} \int_{E=E_0}^{\infty} \frac{\left\{ \sum P(E_{vr}^\ddagger) \right\} \exp(-E/k_B T) dE}{1 + k_a(E)/k_2[M]} \quad (2.275)$$

where Q_2 is the partition function for the active degrees of freedom of the reactant molecule **A**, and Q_1^\ddagger and Q_1 are the partition functions for the activated complex **A**[‡] and the reactant molecule **A**, respectively. In the above integration over dE , $\sum P(E_{vr}^\ddagger)$ is the sum of the numbers of vibrational-rotational quantum states of the activated complex at all the quantized energy levels of energy less than or equal to E . $k_a(E)$ is comparably determined by ro-vibrational sum of states for the activated state **A**[‡]:

$$k_a(E) = \frac{\sigma Q_1^\ddagger}{h Q_1 N(E)} \sum_{E_{vr}^\ddagger}^E P(E_{vr}^\ddagger) \quad (2.276)$$

(i) High-Pressure Limit

The rate constant in the high pressure limit can be obtained from eq. (2.275) by setting $[M] \rightarrow \infty$, a limit at which $k(T)$ becomes the pressure-independent first-order rate constant k_∞ , which is given by the well-known expression:

$$k_\infty = \sigma \frac{k_B T}{h} \frac{Q^\ddagger}{Q} \exp(-E_0/k_B T) \quad (2.277)$$

In the above equation, Q and Q^\ddagger represent the complete vibrational-rotational partition functions for the reactant and the activated complex ($Q = Q_1 Q_2$ and $Q^\ddagger = Q_1^\ddagger Q_2^\ddagger$), respectively. Except for the omission of a transmission coefficient, this result is identical with the result obtained from transition state theory (TST) [also referred to as absolute rate theory (ART)] for unimolecular reactions. This was to be expected in view of the similarity of the treatments involved. TST [189–192] calculates the rate constant on the assumption that the activated complex A^\ddagger is in thermal equilibrium with the reactant molecule A . Generally, RRKM theory admits equilibrium between A^\ddagger and A^* . However, in the high pressure limit, A^* and A are also in equilibrium so that the model becomes the same as that considered in Transition State Theory. Quite naturally therefore, results obtained with the two models fully coincide.

(ii) Low-Pressure Limit

In the limit of very low pressures, the first-order rate constant obtained from eq. (2.275) becomes proportional to the pressure. In this limit, the rate constant becomes a second-order bimolecular rate constant:

$$\begin{aligned} k_{\text{bim}} &= \lim_{[M] \rightarrow 0} \left(\frac{k_{\text{uni}}}{[M]} \right) = \frac{k_2}{Q_2} \exp(-E_0/k_B T) \int_{E=E_0}^{\infty} N^*(E) \exp(-E/k_B T) dE \\ &= \frac{k_2}{Q_2} \int_{E=E_0}^{\infty} N^*(E) \exp(-E/k_B T) dE = \frac{k_2 Q_2^*}{Q_2} \end{aligned} \quad (2.278)$$

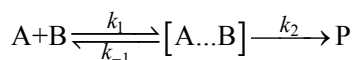
where $N^*(E)$ is the number of energized molecules (i.e. specifically those A molecules which have energy E larger than E_0), whereas Q_2^* is the corresponding partition function which is obtained using the ground state of the reactant molecule A for defining the zero of energy. Equation (2.278) can be rewritten in terms of the partition function $Q_2^{*'}$ for the ground state of energized molecules. These partition functions are simply related by the equation $Q_2^{*'} = Q_2^* \exp(-E_0/k_B T)$. It follows immediately therefore that:

$$k_{bim} = \frac{Q_2^*}{Q_2} k_2 \exp(-E_o/k_B T) \quad (2.279)$$

In this equation, note that the factor $k_2 \exp(-E_o/k_B T)$ corresponds to the expression which was obtained by Lindeman for k_1 [see eq. (2.238)]. The ratio Q_2^*/Q_2 is therefore the quantum-statistical equivalent of the term $(E_o/k_B T)^{s-1}/(s-1)!$ which was derived in Hinshelwood's theory for k_1 [see eq. (2.240)]. The density of quantum states increases rapidly with the energy, and Q_2^* is therefore larger than Q_2 .

(iii) Unimolecular versus Bimolecular Reaction Rate Constants

RRKM theory is strictly applicable to unimolecular reactions only. Nevertheless, it can also be used to calculate kinetic rate constants for bimolecular reactions through the interplay of chemical equilibrium constants that can be easily derived from statistical thermodynamics. Indeed, it can be generally assumed that bimolecular reactions involve a two-step mechanism of the form:



where $A\dots B$ is a stable intermediate complex resulting from a fast pre-equilibrium reaction step. According to this mechanism, k_1 and k_{-1} are the forward and reverse kinetic rate constants for this first reversible step. k_2 is the kinetic rate constant which characterized the second unimolecular reaction step, which is considered to be irreversible, and can be obtained using RRKM theory. A steady-state analysis yields therefore the global bimolecular kinetic rate constant:

$$k = \frac{k_1 k_2}{k_{-1} + k_2} \quad (2.280)$$

For bimolecular reactions, the energy barrier for k_{-1} is in general comparable to that for k_2 , in terms of enthalpy. However, the entropy change is much larger in the reverse reaction (k_{-1}) than in the unimolecular reaction leading to products (k_2). Indeed, the activation entropy ΔS_2^\ddagger is small and negative because the transition state structure which is involved in the second unimolecular reaction step is tighter than the intermediate complex, while the reaction entropy ΔS_{-1} is large and positive because six vibrational degrees of freedom are converted into three translational plus three rotational degrees of freedom. This leads to k_{-1} values that are much larger than k_2 . Since k_2 can be neglected compared with k_{-1} , the global bimolecular kinetic rate coefficient can be rewritten [193] as:

$$k = \frac{k_1 k_2}{k_{-1}} = \left(\frac{k_1}{k_{-1}} \right) k_2 = K_{1,C} k_2 \quad (2.281)$$

In the above equation, $K_{1,C}$ is the equilibrium constant for the first reversible step connecting the isolated reactants to the reactant complex, which can be easily obtained from elementary thermodynamics (mass action law by Guldberg–Waag). Indeed, upon applying basic statistical thermodynamic principles, the equilibrium constant (k_1/k_{-1}) of the fast pre-equilibrium between the reactants (**R**: A, B) and the reactant complex (**RC**: A···B) may be obtained as [194]:

$$K_1^C = \frac{[\text{RC}]}{[\text{A}][\text{B}]} = \frac{1}{RT} K_{1,P} \quad (2.282)$$

together with:

$$K_{1,P} = \frac{k_1}{k_{-1}} = \exp(-\Delta G_1/RT) \quad (2.283)$$

where $\Delta G_1 = G_{\text{RC}} - (G_{\text{A}} + G_{\text{B}})$.

2.4.2. Transition State Theory

Transition state theory (TST) [190,195–198] is one of the earliest attempts to calculate from first principles kinetic rate constants for chemical reactions in both the gas phase [199] and in solution [200]. It was initially developed by Evans and Polayni [201,202], and Eyring [203]. Derivation of this theory has been reviewed by Laidler and King [204] as well as by Truhlar *et al.* [205]. TST is most widely used by experimentalists to interpret rate constant data, as it requires no calculations of the dynamics of the reacting system. The popularity of TST is largely due to its simplicity and usefulness for correlating trends in reaction rate constants in terms of easily interpretable quantities. The approximation made in this theory enables one to calculate the rate constant only in terms of the statistical properties of the system, specifically the thermodynamical characteristics of the activated complex. Moreover, the properties of the activated complex (i.e. the transition state) can often be estimated *a priori*, and thus the theory can be used predictively, both qualitatively and quantitatively [184].

Transition state theory is based on the assumption that a reaction coordinate (RC) proceeds from one energy minimum (reactant) to another (product) through an activated complex (transition state). TST is valid only in the high-pressure limit [201] (see Figure 2.9). In this limit, there are many collisions available to equilibrate the populations of reactants and the activated complex species which

has the correct limiting high-pressure behavior. TST cannot account for the complex pressure dependence of rate constant for unimolecular and bimolecular reactions [169].

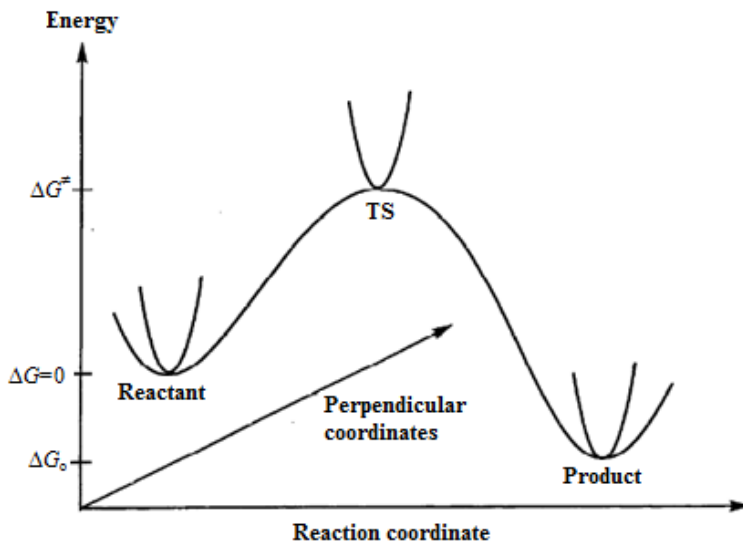


Figure 2.9. The potential energy surface along the reaction coordinate

The position of the dividing surface along the reaction coordinate is allowed to vary with different energies and angular momenta in order to determine the minimum microcanonical flux. The transition state region is a vital step in the reaction path, of which the lower energy contours are the most important. This is because such a surface is less likely to intersect non-reactive trajectories than a surface that is not parallel to the potential contours. Therefore, the reaction coordinate should run essentially parallel to the lower energy potential contours in the intermediate region between the reactant and product regions of the potential energy surface. In general, the minimum energy path satisfies this criterion better than all other possible pathways, and is selected therefore to calculate the reaction coordinate pathway from the reactant to the product [184].

Derivation of transition state theory assumes that, in order for chemical species **A** and **B** to react to form products **D** and **E**, a barrier height to reaction must be overcome. The system passes over the energetic barrier corresponding to a short lived activated complex C^\ddagger .



TST says nothing about the mechanism of excitation to form the activated complex C^\ddagger or the de-excitation processes of the activated complex C^\ddagger back to the

reactant species. This theory simply considers that an equilibrium exists between the activated complex C^\ddagger and the reactants. For simplicity, it is assumed that no reverse reactions occur between the products **D** and **E** to form the reactants **A** and **B** that would also go through the transition state C^\ddagger . Another assumption of TST is that the activated complex C^\ddagger can be treated as a separate chemical species. Thus, standard statistical mechanics expressions can be used to characterize this complex thermodynamically [169].

The activated complex is assumed to decompose rapidly about a vibrational period in a critical bond, which corresponds to the reaction coordinate, and its frequency is taken to be ν_{RC} . Furthermore, it is assumed that this is a very weakly bound vibrational mode, corresponding to a very low frequency.

If the activated complex C^\ddagger and reactants are in equilibrium, the ratio of their concentrations is defined as the equilibrium constant (in concentration units) as

$$K_c = \frac{[C^\ddagger]}{[A][B]} \quad (2.284)$$

By rearranging $K_{c,i} = K_{p,i} (P/RT)^{\nu^\ddagger}$, the concentration equilibrium constant, K_c^\ddagger can be related to the pressure equilibrium constant, K_p^\ddagger as follows [158]

$$K_c^\ddagger = \left(\frac{P}{RT} \right)^{\nu^\ddagger} K_p^\ddagger \quad (2.285)$$

where ν^\ddagger is the net change in the number of gas phase species in passing from the reactants to the activated complex: for instance, $\nu^\ddagger = 0$ for a unimolecular reaction, or $\nu^\ddagger = -1$ for a bimolecular reaction. The pressure equilibrium constant can be written in terms of the partition functions of each species, as follows:

$$K_p^\ddagger = \frac{(Q^\ddagger/N_A)}{(Q_A/N_A)(Q_B/N_A)} \exp(-E_o/RT) \quad (2.286)$$

where Q^\ddagger represents the partition function for the activated complex C^\ddagger , Q_A and Q_B are the partition functions for the reactants **A** and **B**, respectively, and N_A is the Avogadro's number. E_o is now the molar activation energy (in $J \text{ mol}^{-1}$, with $R = 8.314 \text{ J mol}^{-1} \text{ K}^{-1}$). Therefore

$$K_c^\ddagger = \left(\frac{P}{RT} \right)^{\nu^\ddagger} \frac{(Q^\ddagger/N_A)}{(Q_A/N_A)(Q_B/N_A)} \exp(-E_o/RT) \quad (2.287)$$

From eq. (2.284) and eq. (2.287), the concentration in the activated complex is readily obtained

$$[C^\ddagger] = K_c^\ddagger [A][B] = \left(\frac{P}{RT}\right)^{\nu^\ddagger} \frac{(Q^\ddagger/N_A)}{(Q_A/N_A)(Q_B/N_A)} \exp\left(-\frac{E_o}{RT}\right) [A][B] \quad (2.288)$$

The rate constant at which the products are formed is assumed to equal the activated complex concentration times at which C^\ddagger decomposes, which we define as ν_{RC} . This frequency straightforwardly relates to the imaginary frequency characterizing the associated saddle point.

$$\begin{aligned} \frac{d[D]}{dt} &= \frac{d[E]}{dt} = \nu_{RC} [C^\ddagger] \\ &= \nu_{RC} \left(\frac{P}{RT}\right)^{\nu^\ddagger} \frac{(Q^\ddagger/N_A)}{(Q_A/N_A)(Q_B/N_A)} \exp(-E_o/RT) [A][B] \\ &= k(T) [A][B] \end{aligned} \quad (2.289)$$

Therefore, the kinetic rate constant k is given by

$$k(T) = \nu_{RC} \left(\frac{P}{RT}\right)^{\nu^\ddagger} \frac{(Q^\ddagger/N_A)}{(Q_A/N_A)(Q_B/N_A)} \exp(-E_o/RT) \quad (2.290)$$

We now consider the partition function for the activated complex in more detail. Upon factorizing, the contributions of the reaction coordinate from the partition function for the activated complex C^\ddagger , we find

$$Q^\ddagger = \left(\frac{1}{1 - e^{-h\nu_{RC}/k_B T}}\right)^{-1} Q^\ddagger(\neq) \quad (2.291)$$

where $Q^\ddagger(\neq)$ is the partition function for all degrees of freedom of the activated complex, except for the reaction coordinate. Since $k_B T \gg h\nu_{RC}$, upon expanding the exponential function as a Taylor series, it is easy to show that

$$\lim_{\nu_{RC} \rightarrow 0} \left(\frac{1}{1 - e^{-h\nu_{RC}/k_B T}}\right) \approx \frac{1}{1 - (1 - h\nu_{RC}/k_B T)} = \frac{k_B T}{h\nu_{RC}} \quad (2.292)$$

By substituting eq. (2.292) into eq. (2.290), we find:

$$k(T) = \frac{k_B T}{h} \left(\frac{P}{RT}\right)^{\nu^\ddagger} \frac{(Q^\ddagger/N_A)}{(Q_A/N_A)(Q_B/N_A)} \exp(-E_o/RT) \quad (2.293)$$

Further simplification gives the well-known expression for bimolecular kinetic rate constants ($\nu^\ddagger = -1$) in conventional transition state theory:

$$k(T) = \frac{k_B T}{h} \frac{\bar{Q}^\ddagger}{\bar{Q}_A \bar{Q}_B} V_m(T) \exp(-E_o/RT) N_A \quad (2.294)$$

where R is the ideal gas constant, k_B and h are the Boltzmann's and Planck's constants, respectively, \bar{Q} 's denote the partition functions per unit volume, and $V_m(T)$ represent the molar volume of an ideal gas at the considered pressure and temperature. For a unimolecular reaction of the form $\mathbf{A} \rightarrow \mathbf{B}$ ($\nu^\ddagger = 0$), the TST rate constant simplifies into

$$k_{\text{uni}} = \frac{k_B T}{h} \frac{\bar{Q}^\ddagger}{\bar{Q}_A} \exp(-E_o/RT) \quad (2.295)$$

Within the TST assumption, a reaction proceeds from reactants to products through a transition state and the calculated rate constant will only be expected to be accurate in the high-pressure limit [201]. Comparing eq. (2.295) with the usual Arrhenius expression, we can write the TST expression for the high pressure Arrhenius pre-exponential constant as follows:

$$A_\infty = \frac{k_B T}{h} \frac{\bar{Q}^\ddagger}{\bar{Q}_A} \quad (2.296)$$

Thus, transition state theory provides a relatively straightforward way of estimating A_∞ if it is unavailable from experiment.

Summarizing and in slightly more elaborate forms of TST, the kinetics of bimolecular and unimolecular reactions can thus be determined using the following equations [200,206,207]:

$$k_{\text{TST}} = \kappa(T) \frac{\sigma k_B T}{h} V_m(T) \frac{Q_{\text{TS}}(T)}{Q_A(T) \cdot Q_B(T)} \exp(-E_o/RT) \quad (\text{in cm}^3 \text{ molecule}^{-1} \text{ s}^{-1}) \quad (2.297)$$

$$k_{\text{TST}} = \kappa(T) \frac{\sigma k_B T}{h} \frac{Q_{\text{TS}}(T)}{Q_A(T)} \exp(-E_o/RT) \quad (\text{in s}^{-1}) \quad (2.298)$$

In above equations, σ denotes the reaction symmetry number (reaction path degeneracy), Q_{TS} is the partition function for all degrees of freedom of the transition state except the reaction coordinate, Q_A and Q_B represents the total partition functions per unit volume for the reactants, and E_o is the classical barrier height (including zero-point vibrational energy contributions). Since the computed energy differences account for zero-point vibrational energies, vibrational partition functions are computed using the vibrational ground state as energy reference. TST gives an estimate of the upper-limit for rate constants as a function of the temperature, and is known to give reliable estimations of rate constants [208,209] in the high pressure limit [184], especially for cases with significant barrier heights [210].

To allow for “re-crossings”, where a molecule passes over the transition state but returns back to the reactant side, a correction factor $\kappa(T)$ is introduced. This factor also accounts for the quantum mechanical phenomenon of tunneling, i.e. molecules that have insufficient energy to pass over the transition state may tunnel through the barrier and appear on the product side. The tunneling factor $\kappa(T)$ is usually close to 1, and rarely falls outside the range 0.5–2. At low temperatures, the tunneling contribution dominates, leading to $\kappa(T) > 1$, while the re-crossing effect is the most important one at high temperatures, given $\kappa(T) < 1$ [30]. Models for computing tunneling corrections are presented in section 2.5.

2.4.3. Variational Transition State Theory

Transition state theory (TST) is exact if and only if no trajectories cross the transition state dividing (hyper) surface more than once. When this assumption fails, TST overestimates the exact rate constant. One should therefore pick the transition state dividing (hyper) surface to minimize the reaction flux through it [211–214].

Variational transition state theory (VTST) [215] is a refinement of TST. It always provides an equal or a better estimate of the rate constant than TST. With VTST the position of the transition state is varied until the maximum value of the Gibbs free activation energy (ΔG^\ddagger) is found for reactions in the gas phase and at gas surface interfaces [216–218]. When using VTST, the position of the transition state (dividing hyper surface) between reactant and product regions is therefore variationally optimized to minimize the reaction rate constant [177,215,218], which is consistent with the idea that RRKM rate constants (and thus TST rate constants in the high pressure limit) are upper bounds to the exact kinetic rate constants. The variational TST procedure minimizes thus the re-crossing effects at the dividing critical surface, and gives therefore much more accurate results for rate constants. The VTST approach is therefore most commonly regarded as a benchmark approach for determining rate constants in the high pressure limit.

The variational TST approach provides thus an upper limit to the exact rate constant for a given potential energy surface. Consequently, the best dividing surface between the reactants and products corresponds to the smallest kinetic rate constant. This corresponds to a local minimum in the sum of states (N_{\min}^\ddagger) at the transition state, which is often referred to as an entropic bottleneck [177,219,220]. In other words, the transition state dividing surface is optimized in order to find the dynamical bottleneck where the kinetic rate constant is a minimum, which is

equivalent to maximizing the free activation energy with respect to the parameters σ that define the transition state dividing surface [221].

VTST is the method of choice for reactions involving loose transition states corresponding to shallow energy barriers, for which it is difficult to unambiguously define a dividing surface between reactant and product regions. A central aspect of the VTST approximation involves an assumed separation between the conserved modes, which correspond to vibrations of the separated molecules, and the remaining modes, referred to as the transitional modes. The transitional modes gradually transform their character throughout the transition state region as the rotations of the separated reactants couple together to form bending and torsional vibrations, and overall rotations in the adduct [222]. The VTST expression for the rate constant is of the form [221]:

$$k^{\text{GT}}(T, \sigma) = \frac{k_{\text{B}}T}{h} K^{\circ} \exp \left[-\frac{\Delta G^{\text{GT}}(T, \sigma)}{k_{\text{B}}T} \right] \quad (2.299)$$

where σ represents a collection of parameters defining the dividing surface between the reactants and products, K° defines the standard state, which we choose as $1 \text{ cm}^3 \text{ molecule}^{-1}$, and $\Delta G^{\text{GT}}(T, \sigma)$ is the generalized transition state free activation energy, which is given by:

$$\Delta G^{\text{GT}}(T, \sigma) = V_{\text{MEP}}(\sigma) - k_{\text{B}}T \ln \left(\frac{Q^{\text{GT}}(T, \sigma)}{K^{\circ} \Phi^{\text{R}}(T)} \right) \quad (2.300)$$

In the above equation, $V_{\text{MEP}}(\sigma)$ is the potential along the reaction coordinate, $Q^{\text{GT}}(T, \sigma)$ is the generalized transition state partition function, and $\Phi^{\text{R}}(T)$ is the reactant partition function per unit volume.

With VTST, the accuracy of the potential energy surface is often the major factor limiting the precision of the calculated rate constants. Applications of VTST have been reviewed by Truhlar and Garrett [215] as well as by Truhlar and Gordon [223]. For further applications of VTST including multidimensional tunneling corrections, see also works by Garrett *et al.* [224], as well as by Garrett and Truhlar [225] or McRae *et al.* [226].

For reactions that imply a substantial activation energy barrier, the transition state is well defined. The reaction barrier can be located by searching for the saddle point along the reaction coordinate between reactants and products. Nevertheless, if no obvious barrier height exists along the reaction coordinate, both activation energy and activation entropy play an important role in defining the transition state. For instance, the potential energy curve, $V(R)$, for a simple bond cleavage reaction does not present a maximum between the reactants and products [177] (see Figure 2.10). Therefore, the location of the transition state is not properly defined and the

calculation of the activation entropy ΔS^\ddagger is difficult. In this case, the transition state is referred to as a "generalized" transition state that does not necessarily pass through a saddle point [218]. This generalized transition surface is defined as being perpendicular to the minimum energy path and crossing it at a certain bond distance R^\ddagger . The position of the transition state is identified by maximizing the Gibbs free energy.

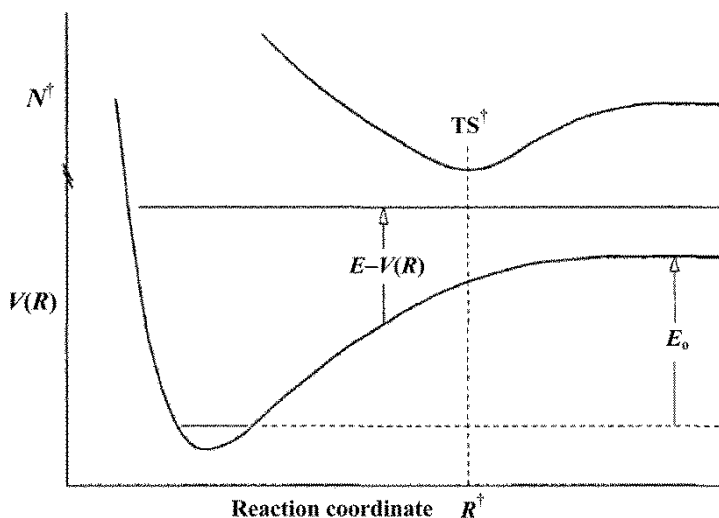


Figure 2.10. (below) Potential energy surface of an ion leading to a dissociation. (above) The variation of the sum of states N^\ddagger as a function of the reaction coordinate R for a reaction with no saddle point [177].

The location of the transition state will shift as the molecular internal energy increases, as is to be expected from the theory [177,227]. As the dissociating bond gets elongated, two factors come into play: (i) the increase in the potential energy $V(R)$; (ii) the decrease in the vibrational frequencies of the transitional modes, which convert into product rotations and translations. As the reaction proceeds, the increase in potential energy $V(R)$ leads to a reduction in the available energy $[E - V(R)]$ and, thus, in the sum of states, while the decrease in vibrational frequencies for the transitional modes (which are evolving into product rotations and translations) leads to an increase in the sum of states. These two opposing trends result in a minimum in the sum of states at some critical bond distance R^\ddagger [177,227] where the transition state is located. At low internal energies, the first factor (the available energy) dominates and the transition state occur at large R values. As the internal energy increases, the two factors become important and transition state switching is expected [227].

2.5. Tunneling Effects

Tunneling of a light atom (usually hydrogen) through a reaction barrier can be investigated by several one-dimensional methods, including the methods of Wigner [228] and Eckart [229], which have been used in the present work. These methods are based on the assumption that the reaction and tunneling path coincide leading to simple algebraic expressions for the transmission coefficient, which thereby makes these tunneling methods computationally very attractive. The Wigner method is the most basic approximation to account for tunneling of a particle through a reaction barrier [228]. Assuming a parabolic potential for nuclear motions near the transition state, the transmission coefficient $\kappa(T)$ can be obtained from perturbation theory:

$$\kappa(T) = 1 + \frac{1}{24} \left(\frac{h \operatorname{Im}(v^\ddagger)}{k_B T} \right)^2 \quad (2.301)$$

where v^\ddagger represents the unique imaginary frequency characterizing the saddle-point connecting reactants to products. Note that the above equation is valid provided $k_B T \gg h \operatorname{Im}(v^\ddagger)$.

With the Eckart method [229], a model potential is fitted to the energies of three stationary points, i.e., the zero-point-corrected energies of the reactants ($s=-\infty$), the saddle point ($s=s_0$), and the products ($s=+\infty$):

$$V(s) = \frac{ae^{\alpha(s-s_0)}}{1 + e^{\alpha(s-s_0)}} + \frac{be^{\alpha(s-s_0)}}{(1 + e^{\alpha(s-s_0)})^2} + c \quad (2.302)$$

where s is the reaction coordinate and a , b , c , α , and s_0 are parameters that can be calculated from the classical potential energies at the reactants, saddle point, and products and from the imaginary frequency, according the following equations:

$$\alpha = -\frac{2\pi\mu c \operatorname{Im}(v^\ddagger)}{2V^\ddagger(V^\ddagger - a)} \quad (2.303)$$

$$a = V_{(s=+\infty)} - V_{(s=-\infty)} \quad (2.304)$$

$$b = (2V^\ddagger - a) + 2\sqrt{V^\ddagger(V^\ddagger - a)} \quad (2.305)$$

$$c = \mathcal{E}^{ZPE}(-\infty) \quad (2.306)$$

$$s_0 = -\frac{1}{\alpha} \ln \left(\frac{a+b}{b-a} \right) \quad (2.307)$$

In eq. (2.306), $\mathcal{E}^{ZPE}(s)$ is the zero point energy as function of the reaction coordinate s . Hence c equals the zero point energy of the reactants.

The Schrödinger equation accounting for tunneling can be solved exactly for the Eckart model reaction barrier [eq. (2.302)], allowing the construction of an analytical expression for the transmission probability. The final result is:

$$p(E) = 1 - \left(\frac{\cosh[2\pi(\alpha - \beta)] + \cosh(2\pi\delta)}{\cosh[2\pi(\alpha + \beta)] + \cosh(2\pi\delta)} \right) \quad (2.308)$$

where

$$\alpha = \frac{1}{2\sqrt{C}}\sqrt{E} \quad ; \quad \beta = \frac{1}{2\sqrt{C}}\sqrt{E - A} \quad ; \quad \delta = \frac{1}{2\sqrt{C}}\sqrt{B - C} \quad (2.309)$$

along with the following parameters, which depend only upon the zero-point corrected energy barriers in the reverse and forward directions, namely $\Delta H_r^{\ddagger,0}$ and $\Delta H_f^{\ddagger,0}$, respectively:

$$A = \Delta H_f^{\ddagger,0K} - \Delta H_r^{\ddagger,0K} \quad (2.310)$$

$$B = \left(\sqrt{\Delta H_f^{\ddagger,0K}} - \sqrt{\Delta H_r^{\ddagger,0K}} \right)^2 \quad (2.311)$$

$$C = \left(h \operatorname{Im}(v^\ddagger) \right)^2 \left(\frac{B^3}{A^2 - B^2} \right)^2 \quad (2.312)$$

Finally, in TST or VTST, the Eckart tunneling correction $\chi(T)$ is obtained by numerically integrating the transmission probabilities $p(E)$ over a Boltzmann distribution of energies:

$$\chi(T) = \frac{\exp(\Delta H_f^{\ddagger,0K}/k_B T)}{k_B T} \int_0^\infty p(E) e^{-\frac{E}{k_B T}} dE \quad (2.313)$$

2.6. Softwares

Nowadays, theoretical chemistry is often used to estimate thermodynamic state functions and properties such as the enthalpy, the entropy, heat capacities, free energies, etc., through calculations of partition functions. Hence, equilibrium constants can be derived upon calculating free energy differences between minima of the potential energy surface. Analogously, prediction of chemical reaction rate constants requires electronic quantum-mechanical calculations to evaluate activation barriers. As has been shown in the preceding sections, the use of statistical mechanics is required for relating the microscopic properties of individual atoms and molecules to the macroscopic limit, and for determining kinetic rate constants from quantum results.

The Kinetic and Statistical Thermodynamical Package (**KiSThelP**) [230] has been developed with the aim to facilitate the treatment of quantum results to estimate molecular and reaction properties. It has been designed to perform statistical mechanics calculations from *ab initio* quantum chemistry data, without the need for an analytical potential energy function. It should be noted that the standard state of pure gaseous species (ideal gas at $P^0=1$ bar) is used in chemical equilibrium and TST kinetic properties computations, but the molecular properties calculated with KiSThelP can also be estimated at any pressure. At all stages of the present work, all calculations of unimolecular and bimolecular kinetic rate constants were performed using the KiSThelP package. KiSThelP enables the theoretical prediction of canonical and microcanonical rate constants for gas phase chemical reactions. The methods used are conventional TST or VTST, as well as RRKM theory. One-dimensional (1D) quantum mechanical tunneling treatments through Wigner correction [228] or an unsymmetrical Eckart potential energy barrier [229] can also be involved. Both gas phase unimolecular and bimolecular elementary reactions with a barrier height are considered. KiSThelP uses a 15-point Gauss-Laguerre integration for numerically integrating energy-dependent tunneling transmission coefficients over a Boltzmann distribution of energies. In KiSThelP package, Laplace-transform method based on the inversion of the partition functions is employed for the calculation of the sum of states $N^\ddagger(E)$ and density of states $\rho(E)$.

The **Gaussian** package can perform a variety of semi-empirical and *ab initio* calculations. In our work, Gaussian 09 [140] has been used to explore reaction mechanisms, and perform all reported electronic structure and thermochemical calculations. In all reported DFT calculations, a standard prune integration grid has been retained, which consists of grid, having 75 radial shells and 302 angular points per shell, resulting in about 7000 points per atom [140].

The **GaussView** [231] is standard and efficient graphical interface, which is widely used to visualize the results of calculations performed with Gaussian and many other quantum chemical packages.

2.7. References

- [1] C. Møller, M.S. Plesset, *Phys. Rev.*, **1934**, *46*, 618.
- [2] G.D. Purvis, R.J. Bartlett, *J. Chem. Phys.*, **1982**, *76*, 1910.
- [3] S.A. Kucharski, R.J. Bartlett, *J. Chem. Phys.*, **1992**, *97*, 4282.
- [4] R.G. Parr, W. Yang, *Density Functional Theory of Atoms and Molecules*; Oxford University Press: Oxford, 1989.
- [5] A.D. Becke, *J. Chem. Phys.*, **1993**, *98*, 5648.

- [6] C. Lee, W. Yang, R.G. Parr, *Phys. Rev. B*, **1988**, *37*, 785.
- [7] J.D. Chai, M. Head-Gordon, *Phys. Chem. Chem. Phys.*, **2008**, *10*, 6615.
- [8] Y. Zhao, D.G. Truhlar, *Acc. Chem. Res.*, **2008**, *41*, 157.
- [9] Y. Zhao, D.G. Truhlar, *Theor. Chem. Acc.*, **2008**, *120*, 215.
- [10] J.A. Montgomery, M.J. Frisch, J.W. Ochterski, G.A. Petersson, *J. Chem. Phys.*, **1999**, *110*, 2822.
- [11] M.R. Nyden, G.A. Petersson, *J. Chem. Phys.*, **1981**, *75*, 1843.
- [12] G.A. Petersson, M.A. Al-Laham, *J. Chem. Phys.*, **1991**, *94*, 6081.
- [13] J.A. Montgomery, J.M. Frisch, J.W. Ochterski, G.A. Petersson, *J. Chem. Phys.*, **2000**, *112*, 6532.
- [14] R. Casanovas, J. Frau, J. Ortega-Castro, A. Salvà, J. Donoso, F. Muñoz, *Int. J. Quantum. Chem.*, **2010**, *110*, 323.
- [15] G.A. Petersson, A.K. Yee, A. Bennett, *J. Chem. Phys.*, **1983**, *83*, 5105.
- [16] J.W. Ochterski, G.A. Petersson, J.A. Montgomery, *J. Chem. Phys.*, **1996**, *104*, 2598.
- [17] G.A. Petersson, A. Bennett, T.G. Tensfeld, M.A. Al-Laham, W. Shirley, J. Matzaris, *J. Chem. Phys.*, **1988**, *89*, 2193.
- [18] J.A. Montgomery, J.W. Ochterski, G.A. Petersson, *J. Chem. Phys.*, **1994**, *101*, 5900.
- [19] A.S. Szabo, N.S. Ostlund, *Modern Quantum Chemistry: Introduction to Advanced Electronic Structure Theory*; McGraw-Hill: New York, 1989.
- [20] W.J. Hehre, L. Radom, P.v.R. Scheyler, J.A. Pople, *Ab initio Molecular Orbital Theory*; Wiley: New York, 1986.
- [21] R. McWeeny, *Methods of Molecular Quantum Mechanics*; 2nd Edition, Academic Press: London, 1989.
- [22] J. Almlöf, *Notes on Hartree-Fock Theory and Related Topics*; In: "Lecture Notes in Quantum Chemistry II", Springer-Verlag: Berlin, 1994.
- [23] F. Jensen, *Introduction to Computational Chemistry*; Wiley: New York, 1999.
- [24] M. Born, J.R. Oppenheimer, *Ann. Physik.*, **1927**, *84*, 457.
- [25] E. Schrödinger, *Ann. Physik.*, **1926**, *79*, 361.
- [26] E.C. Kemble, *Fundamental Principles of Quantum Mechanics*; McGraw-Hill: New York, 1965.
- [27] I.N. Levine, *Quantum Chemistry*; Prentice-Hall, Upper Saddle River: New Jersey, 2000.
- [28] (a) D.R. Hartree, *Proc. Cambridge. Phil. Soc.*, **1928a**, *24*, 89; (b) D.R. Hartree, *Proc. Cambridge. Phil. Soc.*, **1928b**, *24*, 111; (c) D.R. Hartree, *Proc. Cambridge. Phil. Soc.*, **1928c**, *24*, 426.
- [29] V. Fock, *Z. Phys.*, **1930**, *61*, 126.

- [30] F. Jensen, *Introduction to Computational Chemistry*; 2nd Edition, Wiley: New Jersey, 2007.
- [31] C.C.J. Roothaan, *Rev. Mod. Phys.*, **1951**, 23, 69.
- [32] C.C. Hall, *Proc. Roy. Soc. (London)*, **1951**, A205, 541.
- [33] R.J. Bartlett, *Ann. Rev. Phys. Chem.*, **1981**, 32, 359.
- [34] R. Krishnan, H.B. Schlegel, J.A. Pople, *J. Chem. Phys.*, **1980**, 72, 4654.
- [35] K. Raghavachari, J.A. Pople, *Int. J. Quant. Chem.*, **1981**, 20, 167.
- [36] J.A. Pople, R.K. Nesbet, *J. Chem. Phys.*, **1954**, 22, 571.
- [37] D.M. Chipman, *Theor. Chim. Acta*, **1992**, 82, 93.
- [38] M.L. Coote, *Computational Quantum Chemistry for Free-radical Polymerization*; In *Encyclopedia of Polymer Science and Technology*, 3rd Edition, Wiley: New York, 2004.
- [39] J.A. Pople, J.S. Binkley, R. Seeger, *Int. J. Quant. Chem.*, **1976**, 10, 1.
- [40] R. Krishnan, J.A. Pople, *Int. J. Quant. Chem.*, **1978**, 14, 91.
- [41] R. Krishnan, J.S. Binkley, R. Seeger, J.A. Pople, *J. Chem. Phys.*, **1980**, 72, 650.
- [42] F. Coester, *Nucl. Phys.*, **1958**, 17, 477.
- [43] F. Coester, H. Kümmel, *Nucl. Phys.*, **1975**, 9, 105.
- [44] R.J. Bartlett, J.D. Watts, S.A. Kucharski, J. Noga, *Chem. Phys. Lett.*, **1990**, 165, 513.
- [45] J.F. Stanton, *Chem. Phys. Lett.*, **1997**, 281, 130.
- [46] P. Hohenberg, W. Kohn, *Phys. Rev.*, **1964**, 136, B864.
- [47] W. Kohn, L.J. Sham, *Phys. Rev.*, **1965**, 140, A1133.
- [48] T. Kato, *Commun. Pure Appl. Math.*, **1957**, 10, 151.
- [49] J.C. Slater, *Phys. Rev.*, **1951**, 81, 385.
- [50] T.H. Dunning, Jr. *J. Phys. Chem. A*, **2000**, 104, 9062.
- [51] S.H. Vosko, L. Wilk, M. Nusair, *Can. J. Phys.*, **1980**, 58, 1200.
- [52] T.H. Dunning, Jr., K.A. Peterson, D.E. Woon, *Basis Sets: Correlation Consistent Sets*; In "Encyclopedia of Computational Chemistry", Wiley: New York, 1998.
- [53] A.D. Becke, *J. Chem. Phys.*, **1988**, 88, 1053.
- [54] (a) J.P. Perdew, *Phys. Rev B*, **1986**, 33, 8822; (b) J.P. Perdew, *Physica B*, **1991**, 172, 1; (c) J.P. Perdew, J.A. Chevary, S.H. Vosko, K.A. Jackson, M.R. Pederson, D.J. Singh, C. Fiolhais, *Phys. Rev. B*, **1992**, 46, 6671.
- [55] (a) P.J. Stephens, F.J. Devlin, C.F. Chabalowski, M.J. Frisch, *J. Phys. Chem.*, **1994**, 98, 11623; (b) A.D. Becke, *Phys. Rev. A*, **1988**, 38, 3098.
- [56] J. Harris, R.O. Jones, *J. Phys. F*, **1974**, 4, 1170.
- [57] O. Gunnarsson, B.I. Lundqvist, *Phys. Rev. B*, **1976**, 13, 4274.
- [58] J. Harris, *Phys. Rev. A*, **1984**, 29, 1648.

- [59] Y. Zhao, N.González-García, D.G. Truhlar, *J. Phys. Chem. A*, **2005**, *109*, 2012.
- [60] Y. Zhao, D.G. Truhlar, *Org. Lett.*, **2006**, *8*, 5753.
- [61] C.E. Check, T.M. Gilbert, *J. Org. Chem.*, **2005**, *70*, 9828.
- [62] S. Grimme, *Angew. Chem., Int. Ed.*, **2006**, *45*, 4460.
- [63] M.D. Wodrich, C. Corminboeuf, P.v.R. Schleyer, *Org. Lett.*, **2006**, *8*, 3631.
- [64] P.R. Schreiner, A.A. Fokin, R.A. Pascal, Jr., A. de Meijere, *Org. Lett.*, **2006**, *8*, 3635.
- [65] E.I. Izgorodina, M.L. Coote, L. Radom, *J. Phys. Chem. A*, **2005**, *109*, 7558.
- [66] H.L. Woodcock, H.F. Schaefer, P.R. Schreiner, *J. Phys. Chem. A*, **2002**, *106*, 11923.
- [67] M.D. Wodrich, C. Corminboeuf, P.R. Schreiner, A.A. Fokin, P.v.R. Schleyer, *Org. Lett.*, **2007**, *9*, 1851.
- [68] A.C. Tsepis, A.G. Orpen, J.N. Harvey, *Dalton Trans.*, **2005**, 2849.
- [69] Y. Zhao, D.G. Truhlar, *Org. Lett.*, **2007**, *9*, 1967.
- [70] M. Reiher, O. Salomon, B.A. Hess, *Theor. Chem. Acc.*, **2001**, *107*, 48.
- [71] N. Schultz, Y. Zhao, D.G. Truhlar, *J. Phys. Chem. A*, **2005**, *109*, 4388.
- [72] N. Schultz, Y. Zhao, D.G. Truhlar, *J. Phys. Chem. A*, **2005**, *109*, 11127.
- [73] J.N. Harvey, *Annu. Rep. Prog. Chem. Sect. C*, **2006**, *102*, 203.
- [74] A.D. Becke, *J. Chem. Phys.*, **1997**, *107*, 8554.
- [75] X. Wu, M.C. Vargas, S. Nayak, V. Lotrich, G. Scoles, *J. Chem. Phys.*, **2001**, *115*, 8748.
- [76] Q. Wu, W. Yang, *J. Chem. Phys.*, **2002**, *116*, 515.
- [77] U. Zimmerli, M. Parrinello, P. Koumoutsakos, *J. Chem. Phys.*, **2004**, *120*, 2693.
- [78] S. Grimme, *J. Comput. Chem.*, **2004**, *25*, 1463.
- [79] S. Grimme, *J. Comput. Chem.*, **2006**, *27*, 1787.
- [80] J. Antony, S. Grimme, *Phys. Chem. Chem. Phys.*, **2006**, *8*, 5287.
- [81] P. Jurečka, J. Černý, P. Hobza, D.R. Salahub, *J. Comput. Chem.*, **2006**, *28*, 555.
- [82] A. Goursot, T. Mineva, R. Kevorkyants, D. Talbi, *J. Chem. Theory Comput.*, **2007**, *3*, 755.
- [83] S. Grimme, J. Antony, T. Schwabe, C. Mück-Lichtenfeld, *Org. Biomol. Chem.*, **2007**, *5*, 741.
- [84] J. Černý, P. Jurečka, P. Hobza, H. Valdés, *J. Phys. Chem. A*, **2007**, *111*, 1146.
- [85] C. Morgado, M.A. Vincent, I.H. Hillier, X. Shan, *Phys. Chem. Chem. Phys.*, **2007**, *9*, 448.
- [86] T. Schwabe, S. Grimme, *Phys. Chem. Chem. Phys.*, **2007**, *9*, 3397.

- [87] M. Kabeláč, H. Valdés, E.C. Sherer, C.J. Cramer, P. Hobza, *Phys. Chem. Chem. Phys.*, **2007**, *9*, 5000.
- [88] J. Černý, P. Hobza, *Phys. Chem. Chem. Phys.*, **2007**, *9*, 5291.
- [89] J.-D. Chai, M. Head-Gordon, *J. Chem. Phys.*, **2008**, *128*, 84106.
- [90] A.J. Cohen, P. Mori-Sánchez, W. Yang, *Chem. Rev.*, **2012**, *112*, 289.
- [91] E.G. Hohenstein, S.T. Chill, C.D. Sherrill, *J. Chem. Theor. Comput.*, **2008**, *4*, 1996.
- [92] K.E. Riley, M. Pitoňák, P. Jurečka, P. Hobza, *Chem. Rev.*, **2010**, *110*, 5023.
- [93] L. Ferrighi, Y. Pan, H. Grönbeck, B. Hammer, *J. Phys. Chem.*, **2012**, *116*, 7374.
- [94] Y. Zhao, N.E. Schultz, D.G. Truhlar, *J. Chem. Phys.*, **2005**, *123*, 161103.
- [95] Y. Zhao, N.E. Schultz, D.G. Truhlar, *J. Chem. Theor. Comput.*, **2006**, *2*, 364.
- [96] G.E. Scuseria, V.N. Staroverov, *Progress in the Development of Exchange-correlation Functionals*; In: "Theory and Application of Computational Chemistry: The First 40 years" C.E. Dykstra, G. Frenking, K.S. Kim, G.E. Scuseria (Eds.), Elsevier: Amsterdam, 2005.
- [97] Y. Zhao, D.G. Truhlar, *J. Chem. Phys.*, **2006**, *124*, 224105.
- [98] Y. Zhao, D.G. Truhlar, *J. Phys. Chem. A*, **2006**, *110*, 10478.
- [99] Y. Zhao, D.G. Truhlar, *J. Phys. Chem. A*, **2006**, *110*, 5121.
- [100] Y. Zhao, D.G. Truhlar, *J. Chem. Theory Comput.*, **2006**, *2*, 1009.
- [101] Y. Zhao, D.G. Truhlar, *J. Org. Chem.*, **2006**, *72*, 295.
- [102] Y. Zhao, D.G. Truhlar, *J. Chem. Theory Comput.*, **2007**, *3*, 289.
- [103] Y. Zhao, D.G. Truhlar, *Theor. Chem. Acc.*, **2008**, *120*, 215.
- [104] Y. Zhao, N.E. Schultz, D.G. Truhlar, *J. Chem. Phys.*, **2005**, *123*, 161103.
- [105] T. Van Voorhis, G.E. Scuseria, *J. Chem. Phys.*, **1998**, *109*, 400.
- [106] T.V. Voorhis, G.E. Scuseria, *Mol. Phys.*, **1997**, *92*, 601.
- [107] J. Perrin, *Ann. Phys.*, **1919**, *11*, 1.
- [108] R.E. Weston, G.W. Flynn, *Ann. Rev. Phys. Chem.*, **1992**, *43*, 559.
- [109] P.J. Robinson, K.A. Holbrook, *Unimolecular Reactions*; Wiley: New York, 1972.
- [110] P.J. Stephens, F.J. Devlin, J.R. Cheeseman, *VCD Spectroscopy for Organic Chemists*; CRC Press: New York, 2012.
- [111] T.H. Dunning, Jr., *J. Chem. Phys.*, **1989**, *90*, 1007, and references therein.
- [112] R.A. Kendall, T.H. Dunning, Jr., R.J. Harrison, *J. Chem. Phys.*, **1992**, *96*, 6796.
- [113] D.E. Woon, T.H. Dunning, Jr., *J. Chem. Phys.*, **1993**, *98*, 1358.
- [114] (a) D. Feller, *J. Chem. Phys.*, **1992**, *96*, 6104; (b) D. Feller, *J. Chem. Phys.*, **1993**, *98*, 7059.

- [115] C. Schwartz, *Estimating Convergence Rates of Variational Calculations*; Academic Press: New York, 1963.
- [116] C. Peng, P.Y. Ayala, H.B. Schlegel, M.J. Frisch, *J. Comp. Chem.*, **1996**, *17*, 49.
- [117] G.S. Hammond, *J. Am. Chem. Soc.*, **1953**, *77*, 334.
- [118] N. Agmon, R.D. Levine, *Chem. Phys. Lett.*, **1977**, *52*, 197.
- [119] W.S. Ohlinger, P.E. Klunzinger, B.J. Deppmeier, W.J. Hehre, *J. Phys. Chem. A*, **2009**, *113*, 2165.
- [120] K. Raghavachari, G.W. Trucks, J.A. Pople, M. Head-Gordon, *Chem. Phys. Lett.*, **1989**, *157*, 479.
- [121] J.A. Sousa, P.P. Silva, A.E.H. Machado, M.H.M. Reis, L.L. Romanielo, C.E. Hori, *Braz. J. Chem. Eng.*, **2013**, *30*, 83.
- [122] D.A. McQuarrie, *Statistical Mechanics*; Harper and Row: New York, 1976.
- [123] J.M.L. Martin, J. El-Yazal, J.-P. François, *Mol. Phys.*, **1995**, *86*, 1437.
- [124] J.M.L. Martin, G. De Oliveira, *J. Chem. Phys.*, **1999**, *111*, 1843.
- [125] D.H. Ess, *Quantum Mechanical Theory of Reactivity and Selectivity in Organic and Organometallic Reactions*; Ph.D. Dissertation; University of California, Los Angeles, 2007.
- [126] A.G. Vandeputte, M.K. Sabbe, M.F. Reyniers, V.V. Speybroeck, M. Waroquier, G.B. Marin, *J. Phys. Chem. A*, **2007**, *111*, 11771.
- [127] J.F. Stanton, *J. Chem. Phys.*, **1994**, *101*, 371.
- [128] L.A. Curtiss, K. Raghavachari, G.W. Trucks, J.A. Pople, *J. Chem. Phys.*, **1991**, *94*, 7221.
- [129] J.A. Pople, M. Head-Gordon, D.J. Fox, K. Raghavachari, L.A. Curtiss, *J. Chem. Phys.*, **1989**, *90*, 5622.
- [130] L.A. Curtiss, C. Jones, G.W. Trucks, K. Raghavachari, J.A. Pople, *J. Chem. Phys.*, **1990**, *93*, 2537.
- [131] P. Cysewski, *J. Mol. Struct. (THEOCHEM)*, **2005**, *714*, 29.
- [132] P.v.R. Schleyer, C. Maerker, A. Dransfeld, H. Jiao, N.J.R. Van Eikema Hommes, *J. Am. Chem. Soc.*, **1996**, *118*, 6317.
- [133] S. Nigam, C. Majumder, S.K. Kulshreshtha, *J. Chem. Sci.*, **2006**, *118*, 575.
- [134] P.v.R. Schleyer, M. Manoharan, Z.X. Wang, B. Kiran, H.J. Jiao, R. Puchta, N. Hommes, *Org. Lett.*, **2001**, *3*, 2465.
- [135] G. Lendvay, *J. Phys. Chem.*, **1989**, *93*, 4422.
- [136] A.E. Reed, L.A. Curtiss, F. Weinhold, *Chem. Rev.*, **1988**, *88*, 899.
- [137] A.E. Reed, R.B. Weinstock, F.J. Weinhold, *J. Chem. Phys.*, **1985**, *83*, 735.
- [138] K.B. Wiberg, *Tetrahedron*, **1968**, *24*, 1083.
- [139] A.E. Reed, J.E. Carpenter, F. Weinhold, NBO version 3.1.

- [140] M.J. Frisch, G.W. Trucks, H.B. Schlegel, G.E. Scuseria, M.A. Robb, J.R. Cheeseman, G. Scalmani, V. Barone, B. Mennucci, G.A. Petersson, H. Nakatsuji, M. Caricato, X. Li, H.P. Hratchian, A.F. Izmaylov, J. Bloino, G. Zheng, J. L. Sonnenberg, M. Hada, M. Ehara, K. Toyota, R. Fukuda, J. Hasegawa, M. Ishida, T. Nakajima, Y. Honda, O. Kitao, H. Nakai, T. Vreven, J. Montgomery, J.A.J. E. Peralta, F. Ogliaro, M. Bearpark, J.J. Heyd, E. Brothers, K.N. Kudin, V.N. Staroverov, R. Kobayashi, J. Normand, K. Raghavachari, A. Rendell, J.C. Burant, S.S. Iyengar, J. Tomasi, M. Cossi, N. Rega, J.M. Millam, M. Klene, J.E. Knox, J.B. Cross, V. Bakken, C. Adamo, J. Jaramillo, R. Gomperts, R.E. Stratmann, O. Yazyev, A.J. Austin, R. Cammi, C. Pomelli, J.W. Ochterski, R.L. Martin, K. Morokuma, V.G. Zakrzewski, G.A. Voth, P. Salvador, J.J. Dannenberg, S. Dapprich, A.D. Daniels, Ö. Farkas, J.B. Foresman, J.V. Ortiz, J. Cioslowski, D.J. Fox, Gaussian 09 Revision A.1; Gaussian: Wallingford, 2009.
- [141] A. Moyano, M.A. Periclas, E. Valenti, *J. Org. Chem.*, **1989**, 54, 573.
- [142] F. Weinhold, C.R. Landis, *Chem. Educ. Res. Pract. Eur.*, **2001**, 2, 91.
- [143] J.K. Badenhop, F. Weinhold, *Int. J. Quantum. Chem.*, **1999**, 72, 269.
- [144] J.E. Carpenter, F. Weinhold, *J. Mol. Struct. (Theochem)*, **1988**, 169, 41.
- [145] G.N. Lewis, *J. Am. Chem. Soc.*, **1916**, 38, 762.
- [146] G.N. Lewis, *Valence and the Structure of Atoms and Molecules*; The Chemical Catalog Co.: New York, 1923.
- [147] R.S. Mulliken, *J. Chem. Phys.*, **1944**, 46, 497.
- [148] J. Hinze, H.H. Jaffe, *J. Am. Chem. Soc.*, **1962**, 84, 540.
- [149] R. Hoffmann, *J. Chem. Phys.*, **1963**, 39, 1397.
- [150] R.S. Mulliken, *J. Chem. Phys.*, **1935**, 3, 573.
- [151] A.E. Reed, F. Weinhold, *J. Chem. Phys.*, **1983**, 78, 4066.
- [152] (a) L. Pauling, *J. Am. Chem. Soc.*, **1931**, 53, 1367; (b) J.C. Slater, *Phys. Rev.*, **1931**, 37, 481; (c) C.A. Coulson, *Valence*, 2nd ed.; Oxford University Press: London, 1952.
- [153] (a) M.J.S. Dewar, R. Pettit, *J. Chem. Soc.*, **1954**, 1625; (b) F. Weinhold, T.K. Brunck, *J. Am. Chem. Soc.*, **1976**, 98, 3745; (c) T.K. Brunck, F. Weinhold, *J. Am. Chem. Soc.*, **1976**, 98, 4392; (d) T.K. Brunck, F. Weinhold, University of Wisconsin Theoretical Chemistry Institute Report, WIS-TCI-560, 1985.
- [154] (a) J.E. Carpenter, F. Weinhold, University of Wisconsin Theoretical Chemistry Institute Report, WIS-TCI-689, 1985; (b) J.T. Blair, J.C. Weisshaar, J.E. Carpenter, F. Weinhold, *J. Chem. Phys.*, **1987**, 87, 392; (c) J.T. Blair, J.C. Weisshaar, F. Weinhold, *J. Chem. Phys.*, **1988**, 88, 1467.

- [155] G. Herzberg, *Infrared and Raman Spectra of Polyatomic Molecules*; Van Nostrand Reinhold Compagny: New York, 1945.
- [156] D.A. McQuarrie, J.D. Simon, *Physical Chemistry, A Molecular Approach*; University Science Books: Sausalito, California, 1997.
- [157] C. Eckart, *Phys. Rev.*, **1935**, 47, 552.
- [158] A. Sayvetz, *J.Chem. Phys.*, **1939**, 6, 383.
- [159] B.S. Galabov, T. Dudev, *Vibrational Intensities*; Elsevier Science: Amsterdam, 1996.
- [160] H. Eyring, J. Walter, G.E. Kimball, *Quantum Chemistry*; Wiley: New York, 1944.
- [161] H.C. Allen, P.C. Cross, *Molecular Vib-Rotors*, Wiley: New York, 1963.
- [162] S. Califano, *Vibrational States*, Wiley: London, 1976.
- [163] J.M.L. Martin, J.-P. François,; R. Gijbels, *J. Chem. Phys.*, **1991**, 95, 8374.
- [164] S.I. Konyaev, *Mat. Zametki.*, **1979**, 25, 629.
- [165] P.M.W. Gill, B.G. Johnson, J.A. Pople, *Chem. Phys. Lett.*, **1993**, 209, 506.
- [166] F.A. Lindemann, *Trans. Faraday Soc.*, **1922**, 17, 598.
- [167] T. Baer, W.L. Hase, *Unimolecular Reaction Dynamics: Theory and Experiments*; Oxford University Press: New York, 1996.
- [168] J.I. Steinfeld, J.S. Francisco, W.L. Hase, *Chemical Kinetics and Dynamics*; Prentice Hall: Englewood Cliffs, New Jersey, 1989.
- [169] R.J. Kee, M.E. Coltrin, P. Glarborg, *Chemically Reacting Flow: Theory and Practice*; Wiley: Hoboken, New Jersey, 2003.
- [170] C.N. Hinshelwood, *Proc. Roy. Soc. (A).*, **1927**, 113, 230.
- [171] N.B. Slater, *Proc. Cambridge. Phil. Soc.*, **1939**, 56, 35.
- [172] W.L. Hase, *Dynamics of Molecular Collisions, Part. B*; Plenum Press: New York, 1976.
- [173] O.K. Rice, H.C. Ramsperger, *J. Amer. Chem. Soc.*, **1927**, 49, 1617.
- [174] R.C. Tolman, *Statistical Mechanics with Applications to Physics and Chemistry*; Chemical Catalog Co.: New York, 1927.
- [175] (a) L.S. Kassel, *J. Phys. Chem.*, **1928**, 32, 225; (b) L.S. Kassel, *J. Phys. Chem.*, **1928**, 32, 1065.
- [176] L.S. Kassel, *Kinetics of Homogenous Gas Reactions*; Chemical Catalog Co.: New York, 1932.
- [177] T. Baer, W.L. Hase, *Unimolecular Reactions Dynamics-Theory and Experiments*; Oxford University Press: New York, 1996.
- [178] O.K. Rice, H.C. Ramsperger, *J. Amer. Chem. Soc.*, **1928**, 50, 617.
- [179] C.D. Cantrell, *Multiple-Photon Excitation and Dissociation of Polyatomic Molecules*; Springer Topics. Curr. Phys., vol. 35, Springer: Berlin, 1986.

- [180] T.L. Hill, *An Introduction to Statistical Thermodynamics*; Dover Publications: New York, 1986.
- [181] A.Fernández-Ramos, J.A. Miller, S.J. Klippenstein, D.G. Truhlar, *Chem. Rev.*, **2006**, *106*, 4518.
- [182] S. Menk, *Vibrational Auto-Detachment of the Sulfur Hexafluoride Anion in a Low-background Cryogenic Ion Beam Trap*; Ph.D. Dissertation; University of Heidelberg, Germany, 2013.
- [183] T. Beyer, D.F. Swineheart, *Comm. Assoc. Comput. Machines*, **1973**, *16*, 379.
- [184] R.G. Gilbert, S.C. Smith, *Theory of Unimolecular and Recombination Reactions*; Blackwell Scientific: Oxford, 1990.
- [185] T. Baer, P.M. Mayer, *J. Am. Soc. Mass Spectrom.*, **1977**, *3*, 103.
- [186] T. Baer, J.A. Booze, K.M. Weitzel, *Vacuum Ultraviolet Photoionization and Photodissociation of Molecules and Clusters*; World Scientific: Singapore, 1991.
- [187] W. Forst, *Theory of Unimolecular Reactions*; Academic Press: New York, 1973.
- [188] D.M. Hirst, *A Computational Approach to Chemistry*; Blackwell Scientific Publications, 1990.
- [189] K.J. Laidler, *Theories of Chemical Reaction Rates*; McGraw-Hill: London, 1969.
- [190] S. Glasstone, K.J. Laidler, H. Eyring, *The Theory of Rate Processes*; McGraw-Hill: New York, 1941.
- [191] R.H. Fowler, E.A. Guggenheim, *Statistical Thermodynamics*; Cambridge University Press: Cambridge, 1939.
- [192] K.J. Laidler, J.C. Polanyi, *Progr. React. Kinetics.*, **1965**, *3*, 1.
- [193] D.L. Singleton, R.J. Cvetanovic, *J. Am. Chem. Soc.*, **1976**, *98*, 6812.
- [194] A. Galano, J.R. Alvarez-Idaboy, Chapter 12, pp. 245-274. In “Advances in Quantum Chemistry”, vol. 55. M.E. Goodsie, M.S. Johnson (Eds.), Elsevier Pub: Amsterdam, 2008.
- [195] D.L. Bunker, *Theory of Elementary Gas Reaction Rates*; Pergamon Press: New York, 1966.
- [196] K.J. Laidler, *Chemical Kinetics*; Harper & Row: New York, 1987.
- [197] H.S. Johnston, *Gas Phase Reaction Rate Theory*; Ronald: New York, 1966.
- [198] P. Pechukas, *Dynamics of Molecular Collisions, Part B*; Plenum: New York, 1976.
- [199] S.W. Benson, *Thermochemical Kinetics*; Wiley: New York, 1976.
- [200] J.W. Moore, R.G. Pearson, *Kinetics and Mechanism-The Study of Homogeneous Chemical Reactions*; 3rd Edition, Wiley: New York, 1981.
- [201] M.G. Evans, M. Polanyi. *Trans. Faraday Soc.*, **1935**, *31*, 875.

- [202] M.G. Evans, M. Polanyi. *Trans. Faraday Soc.*, **1937**, 33, 448.
- [203] H. Eyring. *J. Chem. Phys.*, **1935**, 3, 107.
- [204] K.J. Laidler, M.C. King, *J. Phys. Chem.*, **1983**, 87, 2657.
- [205] D.G. Truhlar, W.L. Hase, J.T. Hynes, *J. Phys. Chem.*, **1983**, 87, 2664.
- [206] R. Chang, *Physical Chemistry for the Biosciences*; University Science Books: Sausalito, California, 2005.
- [207] H.H. Carstensen, A.M. Dean, O. Deutschmann, *Proc. Combust. Inst.*, **2007**, 31, 149.
- [208] D.H. Varma, P. Raghunath, M.C. Lin, *J. Phys. Chem. A*, **2010**, 114, 3642.
- [209] S.Y. Wu, P. Raghunath, J.S. Wu, M.C. Lin, *J. Phys. Chem. A*, **2010**, 114, 633.
- [210] H.B. Rao, X.Y. Zeng, H. He, Z.R. Li, *J. Phys. Chem. A*, **2011**, 115, 1602.
- [211] D.H. Lu, T.N. Truong, V.S. Melissas, G.C. Lynch, Y.P. Liu, B.C. Garrett, R. Steckler, A.D. Isaacson, S.N. Rai, G.C. Hancock, J.C. Lauderdale, T. Joseph, D.G. Truhlar, *Comput. Phys. Commun.*, **1992**, 71, 235.
- [212] D.M. Bishop, K.J. Laidler, *Trans. Faraday Soc.*, **1970**, 66, 1685.
- [213] J.C. Keck, *J. Chem. Phys.*, **1960**, 32, 1035.
- [214] J.C. Keck, *Adv. Chem. Phys.*, **1967**, 13, 85.
- [215] D.G. Truhlar, B.C. Garrett, *Ann. Rev. Phys. Chem.*, **1984**, 35, 159.
- [216] D.G. Truhlar, A.D. Isaacson, B.C. Garrett, *Theory of Chemical Reaction Dynamics*; CRC Press: Boca Raton, Florida, 1985.
- [217] A.D. Isaacson, D.G. Truhlar, S.N. Rai, R. Steckler, G.C. Hancock, B.C. Garrett, M.J. Redmon, *Comput. Phys. Commun.*, **1987**, 47, 91.
- [218] D.G. Truhlar, B.C. Garrett, *Accts. Chem. Res.*, **1980**, 13, 440.
- [219] W.J. Chesnavich, M.T. Bowers, *Statistical Methods in Reaction Dynamics*; In: "Gas Phase Ion Chemistry", Academic Press: New York, 1979.
- [220] C. Lifshitz, *Adv. Mass Spectrom.*, **1978**, 7A, 3.
- [221] Y.A. Borisov, E.E. Arcia, S.L. Mielke, B.C. Garrett, T.H. Dunning Jr., *J. Phys. Chem. A*, **2001**, 105, 7724.
- [222] C.A. Taatjes, S.J. Klippenstein, *J. Phys. Chem. A*, **2001**, 105, 8567.
- [223] D.G. Truhlar, M.S. Gordon, *Science*, **1990**, 249, 491.
- [224] B.C. Garrett, D.G. Truhlar, G.C. Schatz, *J. Am. Chem. Soc.*, **1986**, 108, 2876.
- [225] B.C. Garrett, D.G. Truhlar, *J. Phys. Chem.*, **1991**, 95, 10374.
- [226] R.P. McRae, G.K. Schenter, B.C. Garrett, G.R. Haynes, G.A. Voth, G.C. Schatz, *J. Chem. Phys.*, **1992**, 97, 7392.
- [227] C. Lifshitz, F. Louage, V. Aviyente, *J. Phys. Chem.*, **1991**, 95, 9298.
- [228] (a) E. Wigner, *J. Chem. Phys.*, **1937**, 5, 720; (b) E. Wigner, *Z. Phys. Chem. B*, **1932**, 19, 203.

- [229] C. Eckart, *Phys. Rev.*, **1930**, 35, 1303.
- [230] S. Canneaux, F. Bohr, E. Henon, *J. Comput. Chem.*, **2014**, 35, 82.
- [231] I.I.R. Dennington, T. Keith, J. Millam, K. Eppinnett, W.L. Hovell, R. Gilliland, *GaussView*, Version 3.09; Semichem, Inc.: Shawnee Mission, KS, 2003.

Chapter 3

Theoretical study of the oxidation mechanisms of naphthalene initiated by hydroxyl radicals: The H abstraction pathway

3.1. Introduction

Polycyclic aromatic hydrocarbons (PAHs) are ubiquitous environmental pollutants. Many PAHs are potentially genotoxic, mutagenic, or carcinogenic [1,2]. They are emitted into the atmosphere during incomplete combustion and account for ~20% of nonmethane hydrocarbons (NMHCs) in urban air [3]. Chemical sinks for gas-phase PAHs include direct photolysis and reactions with reactive tropospheric gases such as ozone, nitrate radicals and hydroxyl radicals are the major reactants responsible for the homogeneous degradation of organics emitted into the atmosphere [4,5]. Among the different oxidants, reaction with hydroxyl radical is usually the most important reaction [6,7]. It plays a key role in determining the oxidation power of the atmosphere [8]. Naphthalene is the most volatile and abundant PAH in the urban atmosphere and is reactive at ambient temperature and pressure [9,10]. The reactions of OH radicals with naphthalene are of importance to both photochemical air pollution and hydrocarbon flame chemistry [11].

Lorenz and Zellner [12,13] have experimentally studied the reaction of OH radicals with naphthalene at temperatures lower than 410 K and at temperatures ranging from 636 to 873 K, by means of laser flash photolysis using laser-induced fluorescence [13–15]. At $T \leq 410$ K and $T \geq 600$ K, a least-squares analysis of

the temperature dependence of the measured rate constants yields the following Arrhenius expressions [13]:

$$k_{(T \leq 410\text{K})} = \left(1.05_{-0.54}^{+1.11}\right) \times 10^{-12} e^{(902 \pm 240)/T} \text{ cm}^3 \text{ molecule}^{-1} \text{ s}^{-1}$$

$$k_{(T \geq 600\text{K})} = \left(1.12_{-0.73}^{+2.12}\right) \times 10^{-17} T^2 e^{-(969 \pm 752)/T} \text{ cm}^3 \text{ molecule}^{-1} \text{ s}^{-1}$$

where the indicated errors correspond to two least-squares standard deviations. The first regression implies a negative activation energy, which can be interpreted as corresponding to the addition of OH radicals and its equilibration [13,16–18]. In contrast, the second regression implies a positive activation energy, which has been ascribed to hydrogen abstraction [14]. The only theoretical study so far of the thermochemistry for the latter reaction is the one by Qu *et al.*[8], at the BB1K/6-311+G(3df,2p) level of theory. At this level, it was found that the energy barriers for the removal of hydrogen atoms bonded to the C₁ and C₂ atoms (see Figure 3.1) by hydroxyl radicals amount to 4.79 and 4.89 kcal mol⁻¹, respectively. Great care is required in using these data, because reaction barriers are known in general to be strongly dependent on the employed exchange-correlation functional [19]. Also, to the best of our knowledge, the corresponding rate constants have never been theoretically analyzed. Therefore, besides providing energy barriers and reaction energies at a high many-body quantum mechanical level of theory (CBS-QB3), a main purpose of our work is to supply good kinetic equations, kinetic rate constants and branching ratios for the purpose of fully unraveling the original experiments, by Lorenz and Zellner [12,13] or Atkinson [14], on hydrogen abstraction from naphthalene by hydroxyl radicals at high temperatures ($T \geq 600$ K).

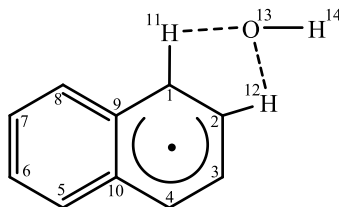


Figure 3.1. Retained atom labeling for characterizing the structures of intermediate and transition states (see Tables 3.1 and 3.2 for numerical details).

The aim of the present study is therefore to provide comprehensive and quantitative theoretical insights into the two reaction pathways **1** and **2** that are

depicted in Figure 3.2. In this purpose, we shall first use density functional theory (DFT) along with various exchange-correlation functionals, and compare the obtained reaction energies and energy barriers with the results of benchmark theoretical calculations employing the high-level composite CBS-QB3 *ab initio* approach [20–28]. With the CBS-QB3 approach, an extrapolation scheme is used to evaluate energies at the CCSD(T) level [29–31] in the limit of a complete basis set (CBS). Kinetic parameters for the reaction pathways depicted in Figure 3.2 are correspondingly calculated by means of transition state theory (TST) [32–39].

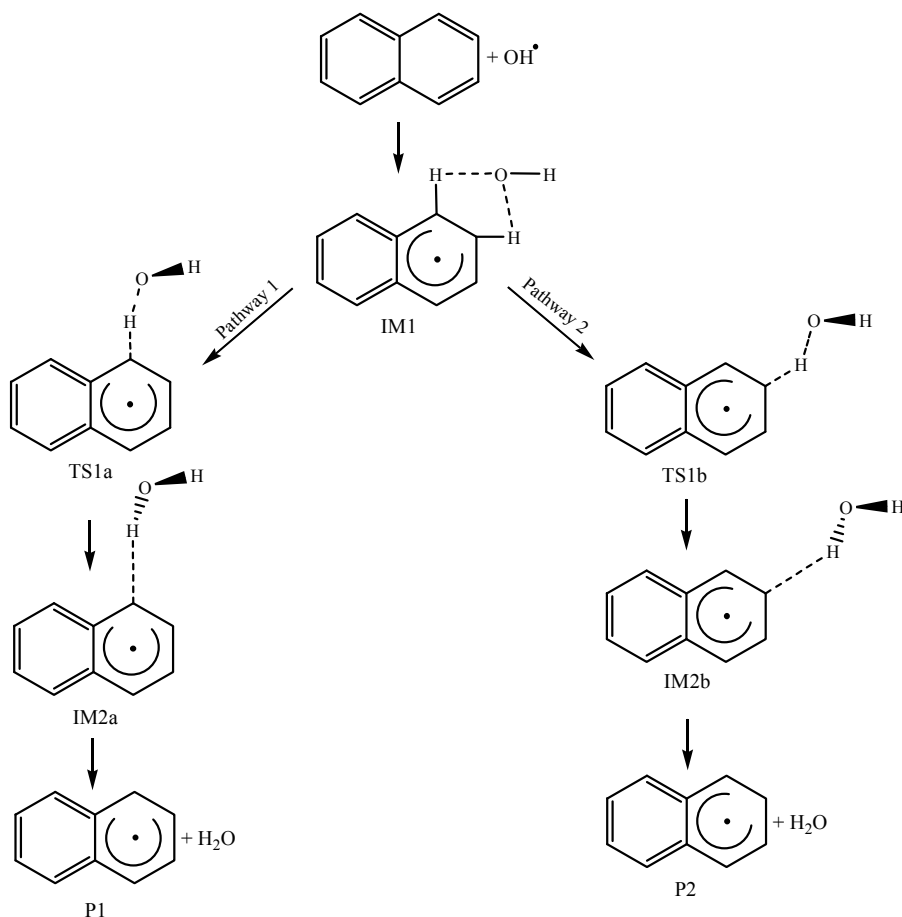


Figure 3.2. Reaction pathways for H-abstraction at the C₁ and C₂ positions in naphthalene by hydroxyl radicals, yielding water and 1-naphthyl (P1) or 2-naphthyl (P2) radicals.

3.2. Theory and Computational Details

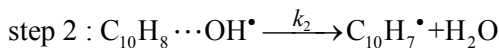
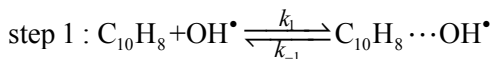
All calculations that are discussed in the present work have been performed using the Gaussian 09 package of programs [40] at the Flemish Supercomputer Center. Molecular structures were visualized with GaussView [41]. The molecular structures and harmonic vibrational frequencies of all stationary points involved in the reaction pathways **1** and **2** depicted in Figure 3.1 were calculated using density functional theory along with a variety of exchange-correlation functionals, namely, B3LYP [42,43], ω B97XD [44], UM05-2x [45] and UM06-2x [45,46] functionals, in conjunction with the aug-cc-PVTZ basis set [47].

The energies of reactants, intermediates, transition states and products were re-evaluated using the so-called complete basis set CBS-QB3 model chemistry originally developed by Peterson and co-workers [20–28].

In order to determine which exchange-correlation functional is the most appropriate one for thermochemical and kinetic studies. Indeed, a weakness of the B3LYP functional is that it neglects dispersion forces, which may have some influence on torsional characteristics. However, since hydrogen abstraction from naphthalene merely yields changes in bond lengths and bond angles without any noticeable change in torsion angles, this deficiency should not have particularly strong effect on the computed internal reaction energies (or enthalpies) and internal energy barriers (or enthalpies).

Intrinsic reaction coordinate (IRC) calculations [48] were carried out at the B3LYP/6-31G(d,p) level using the second-order Gonzalez-Schlegel integration method [49,50], in order to verify whether the located transition state structures connect the expected energy minima. Energy barriers obtained on DFT grounds were systematically corrected for basis set superposition errors (BSSEs) [51], according to the counterpoise method proposed by Boys and Bernardi [52]. In this a *posteriori* correction method, the energy calculations for the individual monomers are performed using the whole supermolecular basis sets instead of the monomer basis sets. No symmetry constraints were imposed during the geometry optimizations. The keyword *nosymm* was used in order to guarantee this matter.

In our study, the removal of hydrogen atoms from naphthalene by OH radicals is analyzed according to the scheme advocated by Singleton and Cvetanovic [53]. With this scheme, it is assumed that this reaction occurs according to a two-step mechanism [54], involving first a fast pre-equilibrium between the reactants ($C_{10}H_8$ and OH radicals) and a pre-reactive complex (IM1), followed by the abstraction of a hydrogen atom leading to a post-reactive complex (IM2) and, then to the products:



In the above scheme, k_1 and k_{-1} denote the rate constants of the forward and backward reactions associated with the first step, whereas k_2 is the rate constant corresponding to the second step. A steady-state analysis of the overall reaction pathway leads to the following expression for the associated rate constant [53,55]:

$$k_{\text{overall}} = \frac{k_1 k_2}{k_{-1} + k_2} \quad (3.1)$$

Even though the energy barrier for k_{-1} has about the same height as that for k_2 , the entropy change for the reverse reaction (IM1→R) is much larger than that for the formation of the products (IM1→P). Thus, k_{-1} is expected to be considerably larger than k_2 [53]. Therefore, the overall rate constant can be rewritten as:

$$k_{\text{overall}} = K_c k_2 \quad (3.2)$$

With $K_c = k_1/k_{-1}$ the equilibrium constant for fast pre-equilibrium between the reactants and the pre-reactive complex (step 1):

$$K_c = \frac{[\text{C}_{10}\text{H}_8 \cdots \text{OH}^\bullet]}{[\text{C}_{10}\text{H}_8][\text{OH}^\bullet]} \quad (3.3)$$

By applying basic statistical thermodynamic principles (see in particular eq. 26.3–20 in ref.[56]) this equilibrium constant can be obtained (see Table S1 of the Appendix I) according to

$$K_c = \frac{Q_{\text{IM1}}}{Q_{\text{naph}} \cdot Q_{\text{OH}}} \times \frac{V_m(T)}{N_{\text{Av}}} \times \exp\left(-\frac{[E_{\text{IM1}} - E_{\text{naph}} - E_{\text{OH}}]}{RT}\right) \quad (3.4)$$

with N_{Av} the Avogadro number, R the ideal gas constant, and $V_m(T) = RT/P$ the molar volume of an ideal gas. The kinetic rate constant characterizing the unimolecular dissociation reaction of the pre-reactive complex is obtained in the high pressure limit by means of transition state theory [32–39,57]:

$$k_2 = \kappa(T) \times \frac{\sigma k_B T}{h} \times \frac{Q_{\text{TS1}}}{Q_{\text{IM1}}} \times \exp\left[-\frac{(E_{\text{TS1}} - E_{\text{IM1}})}{RT}\right] \quad (3.5)$$

where k_B and h are the Boltzmann's and Planck's constants, respectively. In the above equations, Q_{naph} , Q_{OH} , Q_{IM1} and Q_{TS1} represent the total molecular partition functions for the isolated reactants (naphthalene and OH radical), of the pre-reactive molecular complex (IM1), and of the transition state (TS1) associated with the unimolecular dissociation reaction (step 2), respectively. E_{naph} , E_{OH} , E_{IM1} , and E_{TS1} are the corresponding energies, including B3LYP/6-311G(2d,d,p) estimates for zero-point vibrational contributions. In eq. (3.5), $\kappa(T)$ and σ denote the tunneling factor [58] and reaction symmetry number characterizing step 2 [59]:

$$\kappa(T) = 1 + \frac{1}{24} \left(\frac{h\nu_i}{k_B T} \right)^2 \quad (3.6)$$

where ν_i is the imaginary vibrational frequency characterizing the transition state. Therefore, upon combining eqs. (3.3–3.5), we find

$$k_{\text{overall}} = \kappa(T) \times \frac{\sigma k_B T}{h} \times \frac{Q_{\text{TS1}}}{Q_{\text{naph}} Q_{\text{OH}}} \times \frac{V_m(T)}{N_{\text{Av}}} \times \exp\left(-\frac{\Delta E_o}{RT}\right) \quad (3.7)$$

with ΔE_o the net vibrationally adiabatic barrier for the overall reactions scheme [60]:

$$\Delta E_o = E_{\text{TS1}} - E_{\text{naph}} - E_{\text{OH}} \quad (3.8)$$

Thus, the vibrationally adiabatic barrier at high pressures can be calculated as the difference between the energies of the transition states and reactants, without having to consider the pre-reactive complex. In the present work, rate constants and branching ratios for each reaction pathways were evaluated in the high pressure limit, according to eqs. (3.2–3.8), and using B3LYP/6-311G(2d,d,p) molecular partition functions that were computed using the vibrational ground state as energy reference, along with the CBS-QB3 estimates for activation energies. We note that TST gives an estimate of the upper limit of kinetic rate constants as a function of the temperature, and is known to give reliable estimations of rate constants [61,62] in the high pressure limit [63], especially for cases with significant barrier heights [64]. In this limit, since partition functions are proportional to the molar volume (see e.g. ref. [56]), k_{overall} [eq. (3.7)] only depends on the temperature.

Our kinetic analysis is essentially the same as that by Uc *et al.* [55], for hydrogen abstraction from benzene and toluene by hydroxyl radicals and shows that the pre-reactive complex (IM1) has no *direct* influence on the overall kinetics. However, since there is a possibility of quantum mechanical tunneling through the $\text{IM1} \rightarrow \text{TS1}_x \rightarrow \text{IM2}_x$ ($x = \text{a, b}$) energy barriers, the existence of the reactant complex

implies that the actual barrier is higher and that there are additional energy levels from where tunneling may occur; thus, the tunneling factor increases. Therefore, the pre-reactive complex IM1 does have some indirect influence on the kinetics of these pathways, through the interplay of the tunneling factor $\kappa(T)$. Accordingly, one can ignore reactant complexes in addition channels, but they are essential for quantitative calculations of hydrogen abstraction rate constants.

3.3. Results and Discussion

3.3.1. Structural Characteristics of Stationary Points

The optimized molecular structures of the intermediate complexes (IM1 and IM2), transition states (TS1 and TS2), and products (P1 and P2) in the reactions between naphthalene and OH radicals along pathways **1–2** are presented in Tables 3.1 and 3.2, according to the atom labels given in Figure 1. In analogy to the oxidation mechanism of benzene initiated by OH radicals [19], a pre-reactive molecular complex (IM1) has been identified (Figure 3.2) in the reactions of naphthalene with OH radicals. According to Alvarez-Idaboy *et al.* [65], such a pre-reactive complex is a common feature to reactions in between radical species and unsaturated molecules, which finds its origin into long-range coulomb interactions between the reactant molecules [66]. According to our best CBS-QB3 data, this intermediate complex is located at about $2.5 \text{ kcal mol}^{-1}$ below the total energy of the reactants, and is characterized by $\text{H}_{11}\text{--O}_{13}$ and $\text{H}_{12}\text{--O}_{13}$ bond lengths equal to 2.479 and 2.779 Å, respectively (Figure 1). Proceeding further along reaction pathways **1** or **2**, the abstraction process of H_{11} or H_{12} via the transition states TS1a and TS1b require activation energies of ~ 2.2 and $\sim 2.4 \text{ kcal mol}^{-1}$ relative to the reactant energies (Figure 3.3). Two post-reactive molecular complexes IM2a and IM2b are identified further on the product side of the reaction barriers, which corresponds to the dissociation of IM1 into a water molecule and a 1- or 2-naphthyl radical species. These post-reactive molecular complexes are stabilized by a hydrogen bonding between the oxygen atom in the OH radicals and a hydrogen atom bonded to an aromatic ring. They are located at ~ 1.1 to $\sim 1.5 \text{ kcal mol}^{-1}$ below the products. With reaction energies around -6.0 to $-6.4 \text{ kcal mol}^{-1}$, the removal of a hydrogen atom from naphthalene by a hydroxyl radical appears to be a rather strongly exothermic process.

Inspection of the B3LYP/6-311G(2d,d,p) geometries obtained for the transition states TS1a (TS1b) along pathway **1** (**2**) shows that the breaking of the $\text{C}_1\text{--H}_{11}$ ($\text{C}_2\text{--H}_{12}$) bond and the formation of the $\text{O}_{13}\text{--H}_{11}$ ($\text{O}_{13}\text{--H}_{12}$) bond is a concerted

process. During the reaction, the carbon backbone remains almost planar, which justifies using the B3LYP approach at the start of the CBS-QB3 computations and for evaluating vibrational frequencies.

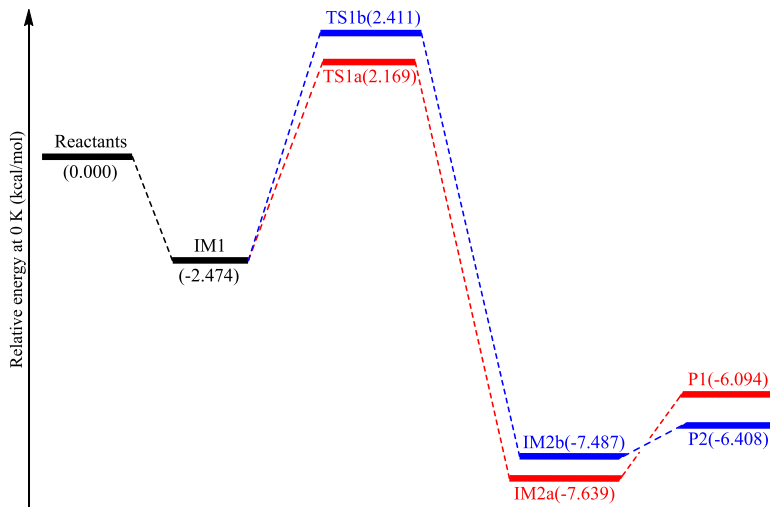


Figure 3.3. Potential energy diagram for the reaction pathways **1–2** obtained using the CBS-QB3 method.

At the level of the transition states TS1a and TS1b, the breaking C–H bond is elongated by $\sim 15.5\%$ (~ 0.17 Å in absolute value), compared to the equilibrium structure computed for naphthalene. In contrast, the forming O–H bond has, quite naturally, a larger length than in the isolated H₂O molecule. Compared with the latter, the elongation of the O–H bond in the transition states TS1a and TS1b is on the order of $\sim 29\%$ (~ 0.28 Å in absolute value).

At the starting B3LYP/6-311G(2d,d,p) level of theory used to optimize the geometries of reactants, transition states and adducts, the spin contamination [$\langle S^2 \rangle_{\text{obs}} - 0.75$] never exceeds 0.036 and can thus, for all practical purposes, be regarded as negligible.

Upon exploring further the B3LYP/6-311G(2d,d,p) potential energy surface describing the interaction between the incoming hydroxyl radical and hydrogen atoms at the C₁ and C₂ positions in naphthalene, we found another pre-reactive complex with the OH radical on top of the ring (see Table 3.3 and Figure 3.4). By analogy with the study by Uc *et al.* [55], the identified pre-reactive complexes

can be referred to as *ipso*- and *ortho*- adducts (Figure 3.4). At the ω B97XD/aug-cc-pVTZ and CBS-QB3 levels, the *ipso* and *ortho* intermediates have almost equal energies, with the *ipso* intermediate being more stable by 0.2 kcal mol⁻¹ only. These two pre-reactive complexes are connected by a very flat potential, so there is little chemical significance to this tiny energy difference except at very low temperatures. Besides, the *ipso*-complex does not readily connect to the transition states TS1a and TS1b leading to the post-reactive complexes (IM2a, and IM2b), and subsequently to the products (1- or 2-naphthyl radicals and water). The *ipso*-intermediate can only reversibly convert to the *ortho* one, or back to the reactants. Even at low temperatures, its influence on the kinetics of hydrogen removal from naphthalene by a hydroxyl radical must be therefore extremely limited. Therefore, in the sequel of the discussion, unless specified, the *ipso* intermediate will be ignored, and the *ortho* intermediate will simply be referred to as the IM1 intermediate.

The fact that the relative elongation of the C–H bond is smaller than that inferred for the forming O–H bond indicates that the transition states TS1a and TS1b are structurally closer to the reactants than to the products. This is in line with Hammond’s principle [67], and the observation that the removal of a hydrogen atom from naphthalene by a hydroxyl radical is an exothermic process.

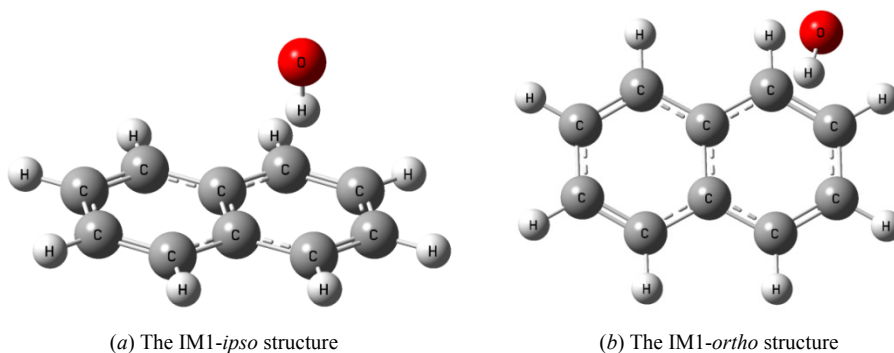


Figure 3.4. Identified equilibrium structures for the pre-reactive intermediate IM1 (*ipso*- and *ortho*-), the loose complex between naphthalene and the OH radical.

Table 3.1. Structural parameters for the reactant, intermediate, transition state and product on the chemical reaction pathway **1** for the oxidation of naphthalene by OH[•] into 1-naphthyl radical.

Parameter	B3LYP/aug-cc-pVTZ				ω B97XD/aug-cc-pVTZ				UM05-2x/aug-cc-pVTZ				UM06-2x/aug-cc-pVTZ				B3LYP/6-311G(2d,d,p)							
	R	IM1	TS1a	P1	R	IM1	TS1a	P1	R	IM1	TS1a	P1	R	IM1	TS1a	P1	R	IM1	TS1a	P1				
$r(C_1-C_2)$	1.370	1.384	1.361	1.351	1.365	1.371	1.356	1.346	1.365	1.368	1.357	1.346	1.366	1.367	1.358	1.349	1.374	1.384	1.364	1.354	(1.365)	(1.357)	(1.348)	
																	[1.381]							
$r(C_1-C_9)$	1.417	1.422	1.407	1.396	1.415	1.419	1.407	1.397	1.413	1.415	1.406	1.396	1.415	1.417	1.408	1.398	1.420	1.424	1.410	1.400	(1.412)	(1.403)	(1.394)	
																	[1.422]							
$r(C_2-C_3)$	1.412	1.408	1.417	1.422	1.410	1.411	1.414	1.420	1.410	1.412	1.414	1.420	1.412	1.414	1.417	1.421	1.415	1.414	1.420	1.425	(1.408)	(1.412)	(1.417)	
																	[1.412]							
$r(C_9-C_{10})$	1.428	1.426	1.433	1.437	1.418	1.416	1.420	1.425	1.416	1.415	1.418	1.396	1.419	1.418	1.421	1.424	1.431	1.430	1.435	1.440	(1.417)	(1.420)	(1.424)	
																	[1.420]							
$r(C_1-H_{11})$	1.083	1.079	1.243	-	1.083	1.081	1.226	-	1.080	1.079	1.198	-	1.083	1.082	1.208	-	1.085	1.081	1.253	-	(1.081)	(1.243)		
																	[1.092]							
$r(H_{11}-O_{13})$	-	2.417	1.261	0.962	-	2.656	1.271	0.957	-	2.892	1.309	0.958	-	3.293	1.295	0.959	-	2.479	1.244	0.962		(1.233)		
$\angle(C_1-H_{11}-O_{13})$	-	74.7	169.8	-	-	71.8	167.3	-	-	67.9	162.3	-	-	59.9	164.9	-	-	75.2	165.1	-		(166.2)		

- Bond lengths are in angstroms (Å) and torsion angles are in degrees (°).
- The values in parentheses are obtained at the B3LYP/6-31+G(d,p) level [8].
- The values in bracket are the theoretical data [68,69].

Table 3.2. Structural parameters for the reactant, intermediate, transition state, and product on the chemical reaction pathway **2** for the oxidation of naphthalene by OH[•] into 2-naphthyl radical.

Parameter	B3LYP/aug-cc-pVTZ				ω B97XD/aug-cc-pVTZ				UM05-2x/aug-cc-pVTZ				UM06-2x/aug-cc-pVTZ				B3LYP/6-311G(2d,d,p)			
	R	IM1	TS1b	P2	R	IM1	TS1b	P2	R	IM1	TS1b	P2	R	IM1	TS1b	P2	R	IM1	TS1b	P2
r (C ₁ -C ₂)	1.370	1.384	1.360	1.350	1.365	1.371	1.355	1.346	1.365	1.368	1.357	1.346	1.366	1.367	1.358	1.348	1.374	1.384	1.364	1.354
																	(1.365)		(1.356)	(1.348)
																	[1.381]			
r (C ₁ -C ₉)	1.417	1.422	1.421	1.427	1.415	1.419	1.421	1.424	1.413	1.415	1.417	1.423	1.415	1.417	1.419	1.424	1.420	1.424	1.424	1.429
																	(1.412)		(1.415)	(1.421)
																	[1.422]			
r (C ₂ -C ₃)	1.412	1.408	1.402	1.391	1.410	1.411	1.401	1.391	1.410	1.412	1.403	1.392	1.412	1.414	1.404	1.394	1.415	1.414	1.405	1.395
																	(1.408)		(1.399)	(1.390)
																	[1.412]			
r (C ₃ -C ₄)	1.370	1.372	1.373	1.377	1.365	1.364	1.367	1.370	1.365	1.364	1.366	1.370	1.366	1.367	1.368	1.371	1.374	1.374	1.376	1.380
r (C ₂ -H ₁₂)	1.082	1.080	1.241	-	1.081	1.080	1.225	-	1.078	1.078	1.197	-	1.081	1.081	1.206	-	1.085	1.082	1.254	-
																	(1.080)		(1.242)	
																	[1.092]			
r (H ₁₂ -O ₁₃)	-	2.861	1.261	0.962	-	2.876	1.269	0.957	-	2.974	1.307	0.958	-	3.326	1.292	0.959	-	2.779	1.235	0.962
																			(1.230)	
\angle (C ₂ -H ₁₂ -O ₁₃)	-	69.0	170.2	-	-	68.6	167.5	-	-	66.6	163.0	-	-	59.4	165.6	-	-	71.2	165.3	-
																			(167)	

- Bond lengths are in angstroms (Å) and torsion angles are in degrees (°).
- The values in parentheses are obtained at the B3LYP/6-31+G(d,p) level [8].
- The values in bracket are the theoretical data [68,69].

Table 3.3. Structural characteristics of the IM1-*ipso*-intermediat

Parameter	Method	Method/aug-cc-pVTZ			B3LYP/6-311G(2d,d,p)
	B3LYP	ω B97XD	UM05-2x	UM06-2x	
r (C ₁ -C ₂)	1.372	1.366	1.367	1.368	1.375
r (C ₁ -C ₉)	1.417	1.415	1.414	1.416	1.420
r (C ₂ -C ₃)	1.413	1.412	1.412	1.413	1.417
r (C ₃ -C ₄)	1.372	1.366	1.367	1.366	1.375
r (C ₉ -C ₁₀)	1.428	1.417	1.415	1.418	1.432
r (C ₁ -H ₁₁)	1.083	1.083	1.080	1.082	1.085
r (C ₂ -H ₁₂)	1.082	1.081	1.078	1.079	1.084
r (H ₁₁ -O ₁₃)	4.350	4.124	4.032	4.029	4.362
r (H ₁₂ -O ₁₃)	3.855	3.970	3.902	3.907	3.540
\angle (C ₁ -H ₁₁ -O ₁₃)	54.04	53.39	52.53	53.17	55.47
\angle (C ₂ -H ₁₂ -O ₁₃)	63.40	56.34	54.99	55.06	71.25

- Bond lengths are in angstroms (Å) and torsion angles are in degrees (°).

3.3.2. Bond Order Analysis

Several bonds are breaking whereas other chemical bonds get formed during the H abstraction process. Bond indices were calculated for those bonds that were substantially altered by OH addition, namely, the C₁-C₂, C₂-C₃, C₃-C₄, C₄-C₁₀, C₁-C₉, C₉-C₁₀, C₁-H₁₁, C₂-H₁₂, H₁₁-O₁₃, H₁₂-O₁₃ and O₁₃-H₁₄ bonds (Figure 3.1); all other bonds remain practically unaltered during the reaction.

Table 3.4. Bond order analysis of the structures involved in the chemical reaction pathways **1** and **2** [B3LYP/6-311G(2d,d,p) results].

Reaction	Bond	C ₁ -C ₂	C ₂ -C ₃	C ₃ -C ₄	C ₄ -C ₁₀	C ₉ -C ₁₀	C ₁ -C ₉	C ₁ -H ₁₁	H ₁₁ -O ₁₃	O ₁₃ -H ₁₄	C ₂ -H ₁₂	H ₁₂ -O ₁₃	δB_{av}	S_p
	(1)	B_i (R)	1.554	1.308	1.554	1.271	1.233	1.271	0.926	0.000	0.858			0.528
B_i (TS)		1.564	1.286	1.559	1.272	1.216	1.274	0.520	0.349	0.818				
B_i (P)		1.588	1.273	1.564	1.272	1.208	1.292	0.000	0.813	0.813				
%EV		29.73	63.90	50.54	71.43	67.48	16.91	43.88	42.93	88.71				
(2)	B_i (R)	1.554	1.308	1.554	1.271	1.233	1.271			0.858	0.927	0.000	0.483	0.816
	B_i (TS)	1.562	1.313	1.538	1.272	1.235	1.252			0.819	0.516	0.356		
	B_i (P)	1.584	1.335	1.528	1.274	1.236	1.240			0.813	0.000	0.813		
	%EV	25.09	19.33	60.99	38.24	55.56	61.42			86.46	44.31	43.74		

Wiberg bond indexes (B_i), %evolution through the reaction coordinate (%EV), average bond index variation (δB_{av}) and Synchronicity parameter (S_p) are shown.

The calculated Wiberg indices B_i for the reactants, transition states, and products enable us (Table 3.4) to examine the progress of the reactions **1** and **2**, and to discuss the position of the transition states between reactants and products. For both reactions, according to the relative changes in bond order, the most strongly affected chemical bond is the O₁₃–H₁₄ single bond. The chemical reaction pathways **1** and **2** are characterized by a synchronicity value around ~0.81, which reveals a chemical process that is concerted, but not fully synchronic.

Hammond's postulate [67] states that the structure of a transition state resembles that of the species nearest to it in free energy. This can be quantified in terms of a parameter L , defined as the ratio between the elongation of the C–H bond and the elongation of the H–O bond:

$$L = \frac{\delta r(\text{C-H})}{\delta r(\text{H-O})} \quad (3.9)$$

Values of L larger than 1 indicate that the transition state lies closer to the products, whereas values of L smaller than 1 indicate on the contrary that the transition state lies closer to the reactants [70]. The values obtained for the parameter L for pathways **1** and **2** amount to 0.60 and 0.62, respectively, which confirms that the transition states are structurally closer to the reactants than to the products. The two reaction pathways being characterized by early transition states are expected to be exoergic.

3.3.3. Energetic and Thermodynamic Parameters

A schematic potential energy diagram of the reaction pathways **1** and **2** is given in Figure 3.3. CBS-QB3 estimates at room temperature for Gibbs free reaction energies (ΔG_r) and energy barriers (ΔG^\ddagger) are listed in Tables 3.5 and 3.6. In line with the structural characteristics of the transition states discussed previously, both reaction pathways **1** and **2** are exothermic ($\Delta H_r < 0$) and exoergic ($\Delta G_r < 0$) processes. Upon comparing the Gibbs free reaction energies for pathways **1** and **2**, it can be noticed that pathway **1** involving H-abstraction at the C₁-position in naphthalene is significantly less exergonic than pathway **2** (H-abstraction at the C₂-position). Under thermodynamic control, i.e., at chemical equilibrium, the formation of 2-naphthyl should therefore predominate.

Results obtained from this study confirm for all employed exchange-correlation functionals the importance of BSSE-CP corrections, even when using a basis set as large as the aug-cc-pVTZ one. BSSE values for TS1a and TS1b are in the 0.193–0.311 and 0.177–0.283 kcal mol⁻¹ ranges, respectively. At the CBS-QB3 level, since the basis set is complete, BSSEs are assumed to identically cancel.

Table 3.5. Internal energies, enthalpies and Gibb's free energies (in kcal mol⁻¹) of intermediate states relative to the reactants along the chemical pathways 1–2 for the oxidation of naphthalene into 1- and 2-naphthyl radicals.

Species	Method	B3LYP/aug-cc-pVTZ			ω B97XD/aug-cc-pVTZ			UM05-2x/aug-cc-pVTZ			UM06-2x/aug-cc-pVTZ			CBS-QB3			literature ΔH°_{298K} (kcal/mol)
		ΔE_{0K}	ΔH°_{298K}	ΔG°_{298K}	ΔE_{0K}	ΔH°_{298K}	ΔG°_{298K}	ΔE_{0K}	ΔH°_{298K}	ΔG°_{298K}	ΔE_{0K}	ΔH°_{298K}	ΔG°_{298K}	ΔE_{0K}	ΔH°_{298K}	ΔG°_{298K}	
Naphthalene + OH*		0.000	0.000	0.000	0.000	0.000	0.000	0.000	0.000	0.000	0.000	0.000	0.000	0.000	0.000	0.000	
IM1- <i>ipso</i> [C ₁₀ H ₈ ...OH]*		-1.423	-1.148	3.195	-3.141	-2.937	2.188	-3.511	-3.824	2.854	-3.945	-4.612	3.017	-2.668	-2.359	1.438	
IM1- <i>ortho</i> [C ₁₀ H ₈ ...OH]*		-3.003	-3.112	3.377	-2.942	-2.998	3.211	-3.285	-3.348	2.701	-3.716	-4.214	3.224	-2.474	-2.566	3.668	
IM1- <i>ortho</i> ^a		-2.867	-2.968	3.489	-2.745	-3.047	3.449	-3.026	-3.603	3.148	-3.495	-3.992	3.451	-2.474	-2.566	3.668	
B SSE energy-IM1- <i>ortho</i>		0.153			0.226			0.237			0.229			0.000			
IM2a [C ₁₀ H ₈ ...H ₂ O]*		-6.274	-5.760	-1.545	-7.130	-6.679	-2.213	-7.201	-6.868	-1.591	-8.421	-7.951	-3.104	-7.639	-7.204	-2.201	
IM2b [C ₁₀ H ₈ ...H ₂ O]*		-6.303	-5.732	-2.007	-6.709	-6.216	-2.283	-7.129	-6.665	-2.262	-8.262	-7.861	-2.966	-7.487	-6.930	-2.622	
P1 (1-naphthyl+H ₂ O)		-5.283	-4.989	-6.950	-4.636	-4.353	-6.293	-4.937	-4.639	-6.603	-6.184	-5.900	-7.842	-6.094	-5.804	-7.765	-4.02 [8]
P2 (2-naphthyl+H ₂ O)		-5.356	-5.063	-7.003	-5.036	-4.758	-6.669	-5.333	-5.033	-6.982	-6.431	-6.159	-8.063	-6.408	-6.114	-8.062	-4.30 [8]

^a BSSE-corrected relative energies

- Values obtained at the BB1K/6-31+G(d,p) level[8].

Table 3.6. Internal energies, enthalpies and Gibb's free energies (in kcal mol⁻¹) of transition states relative to the reactants along the chemical pathways 1–2 for the oxidation of naphthalene into 1- and 2-naphthyl radicals.

Species	Method	B3LYP/aug-cc-pVTZ			ω B97XD/aug-cc-pVTZ			UM05-2x/aug-cc-pVTZ			UM06-2x/aug-cc-pVTZ			CBS-QB3			literature ΔE_{0K}^\ddagger (kcal/mol)
		ΔE_{0K}^\ddagger	$\Delta H^\circ_{298K}^\ddagger$	$\Delta G^\circ_{298K}^\ddagger$	ΔE_{0K}^\ddagger	$\Delta H^\circ_{298K}^\ddagger$	$\Delta G^\circ_{298K}^\ddagger$	ΔE_{0K}^\ddagger	$\Delta H^\circ_{298K}^\ddagger$	$\Delta G^\circ_{298K}^\ddagger$	ΔE_{0K}^\ddagger	$\Delta H^\circ_{298K}^\ddagger$	$\Delta G^\circ_{298K}^\ddagger$	ΔE_{0K}^\ddagger	$\Delta H^\circ_{298K}^\ddagger$	$\Delta G^\circ_{298K}^\ddagger$	
Naphthalene + OH*		0.000	0.000	0.000	0.000	0.000	0.000	0.000	0.000	0.000	0.000	0.000	0.000	0.000	0.000		
TS1a		0.338	-0.148	7.487	1.419	0.876	8.599	3.419	2.830	10.705	3.075	2.527	10.264	2.169	1.601	9.506	4.79 [8]
TS1a ^a		0.534	0.0339	7.716	1.526	1.111	8.283	3.532	3.065	10.561	3.226	2.762	10.203	2.169	1.601	9.506	
B SSE energy-TS1a		0.193			0.292			0.311			0.298			0.000			
TS1b		0.430	-0.030	7.489	1.826	1.322	8.867	3.638	3.132	10.683	3.441	2.974	10.379	2.411	1.939	9.431	4.89 [8]
TS1b ^a		0.439	-0.472	8.058	2.031	1.564	8.973	3.672	2.798	10.964	3.752	3.251	10.767	2.411	1.939	9.431	
B SSE energy-TS1b		0.177			0.263			0.283			0.261			0.000			

^a BSSE-corrected relative energies

- Values obtained at the BB1K/6-311+G(3df,2p) level[8].

As is readily apparent from Table S2 of the Appendix I, spin contamination of the UHF electronic wave functions used at the start of all CBS-QB3 computations never exceeds 0.11 in the present study and can thus, for all practical purposes, be regarded as marginal. The obtained CBS-QB3 results may therefore safely be regarded as benchmark results. Besides, it is worth noticing that, at all employed levels of density functional theory, the spin contamination [$\langle S^2 \rangle_{\text{obs}} - 0.75$] never exceeds 0.045 and can thus also, for all practical purposes, be regarded as insignificant.

Comparison of the CBS-QB3 results with data obtained using various exchange-correlation functionals (Tables 3.5 and 3.6) shows that the standard and widely used B3LYP functional performs rather poorly in calculating reaction and activation energies. A much better agreement with the benchmark CBS-QB3 results is obtained with the ω B97XD, UM05-2x and UM06-2x functionals. Nevertheless, differences in reaction and activation energies of the order of 1.0 kcal mol⁻¹ or more are still noticed when comparing the ω B97XD, UM05-2x and UM06-2x results with the CBS-QB3 estimates. This along with the extreme variability of the DFT results with respect to the employed exchange-correlation functional shows that DFT still remains unsuited for highly quantitative studies of kinetic rate constants.

3.3.4. Kinetic Parameters

Total and individual rate constants and the relative contribution from each pathway to the total rate constant at temperatures ranging from 636 to 873 K are listed and compared with available experimental values [12–15] in Figure 3.5 and Table 3.7. As previously expected, k_{-1} is considerably (10^3 times) larger than k_2 , on both pathways **1** and **2**. We have assumed that the total rate constant (k) for the hydrogen abstraction process can be calculated as the sum of the individual rate constants for the two reaction pathways that are depicted in Figure 3.2: $k_{\text{total}} = k_{\text{overall}}(\mathbf{1}) + k_{\text{overall}}(\mathbf{2})$.

In line with energy barriers that do not differ by more than 0.24 kcal mol⁻¹ (see Figure 3.3), pathways **1** and **2** exhibit global kinetic rate constants of equal magnitude. Our calculated total rate constants appear to be in excellent agreement with the available experimental data [12–15], an observation which validates the two-step reaction scheme proposed by Singleton and Cvetanovic [53]. These rate constants only differ by one order of magnitude for the experimental ones. At the reported temperatures, this means that the errors on the corresponding Gibb's free activation energies are between ~2.9 and 4.0 kcal mol⁻¹. These errors are quite acceptable, considering that the main contribution to these Gibb's free

reaction energies and activation energies are essentially entropic in origin (see Tables S3 and S4 of the Appendix I). More elaborate treatments of statistical thermodynamical partition functions, taking dispersion forces, anharmonic effects, and hindered rotations into account, are presumably needed for improving further the agreement between theory and experiment.

Table 3.7. Overall rate constants (in $\text{cm}^3 \text{molecule}^{-1} \text{s}^{-1}$) and branching ratios (%) for the reported reaction channels at temperatures ranging from 636 to 873 K by means of TST theory ($P = 1 \text{ bar}$).

T (K)	Rate constant						Branching ratio		$k_{\text{exp}} \times 10^{12}$ [12–15]
	IM1→R $k_{-1} (\text{s}^{-1})$	IM1→P1 $k_{2a} (\text{s}^{-1})$	IM1→P2 $k_{2b} (\text{s}^{-1})$	R→P1 $k_{\text{tot}}(1)$	R→P2 $k_{\text{tot}}(2)$	k_{tot} [$k(1)+k(2)$]	R(1)	R(2)	
636	2.42×10^{14}	4.48×10^{11}	8.67×10^{11}	3.51×10^{-12}	6.78×10^{-12}	1.03×10^{-11}	34.05	65.95	(1.1±0.1)
665	2.23×10^{14}	4.67×10^{11}	9.09×10^{11}	3.78×10^{-12}	7.36×10^{-12}	1.11×10^{-11}	33.93	66.07	(1.1±0.2)
727	1.92×10^{14}	5.09×10^{11}	9.97×10^{11}	4.46×10^{-12}	8.74×10^{-12}	1.32×10^{-11}	33.79	66.21	(1.4±0.2)
873	1.51×10^{14}	6.05×10^{11}	1.21×10^{12}	6.47×10^{-12}	1.29×10^{-11}	1.94×10^{-11}	33.40	66.60	(3.0±0.5)

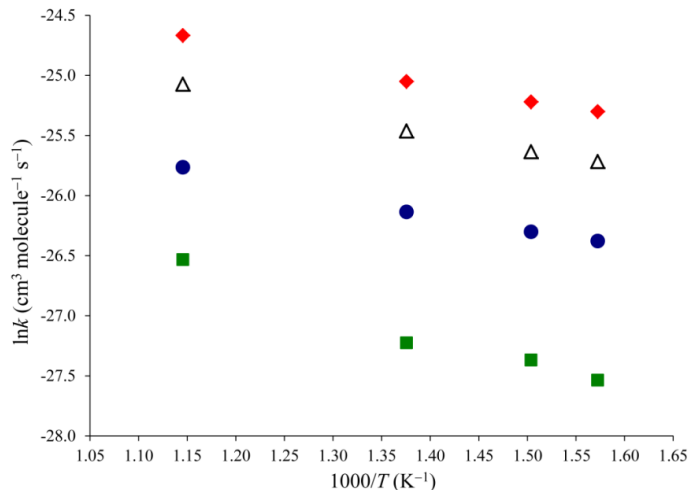


Figure 3.5. Arrhenius plot of our computed bimolecular rate constants versus experimental data. Legend: (●) theoretical rate constant for pathway 1; (△) theoretical rate constant for pathway 2; (◆) theoretical total rate constant for pathways 1 and 2; (■) experimental data [12–15].

The associated Wigner factors approach unity (Table 3.8), which shows that tunneling effects have only a limited influence on the computed rate constants. Our calculated rate constants for pathways 1 and 2 vary from 3.51×10^{-12} to 6.47×10^{-12} and from 6.78×10^{-12} to $1.29 \times 10^{-11} \text{ cm}^3 \text{molecule}^{-1} \text{s}^{-1}$, respectively. The fact that the rate constants for these two pathways are almost equal indicate that there is no

significant selectivity for the removal of a hydrogen atom from the C₁ or C₂ positions in naphthalene by a hydroxyl radical. It can be seen from Table 3.7 that the rate constants increase gradually with increasing temperatures (Figure 3.6). Fitting these data through a least-square procedure within the selected temperature range to a three-parameter Arrhenius-like equation [$k(T)=A.T^n.\exp(-E_a/RT)$] gives the following regressions (in cm³ molecule⁻¹ s⁻¹):

$$\text{Pathway 1: } k_1(T)=5.33\times 10^{-13}T^{0.503}\exp(-867.1/T) \quad (3.10)$$

$$\text{Pathway 2: } k_2(T)=2.49\times 10^{-15}T^{1.319}\exp(-389.7/T) \quad (3.11)$$

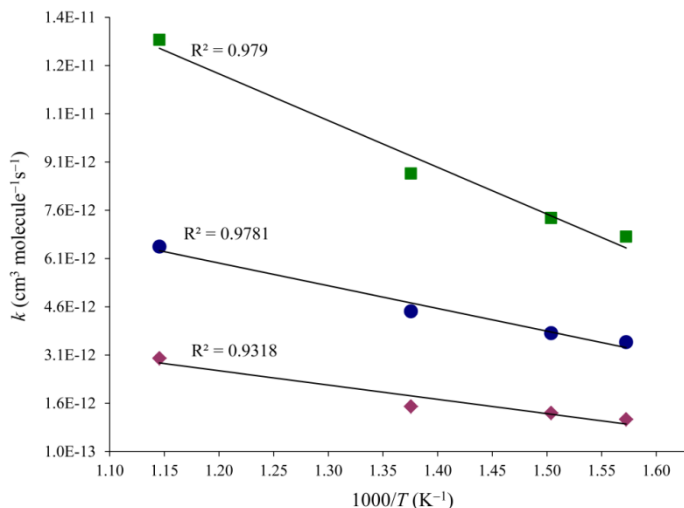


Figure 3.6. Plot of our computed bimolecular rate constants versus experimental data. Legend: (●) theoretical rate constant for pathway 1; (■) theoretical rate constant for pathway 2; (◆) experimental data [12–15].

Branching ratios for the reaction pathways **1** and **2** are reported in Table 3.7. These ratios were computed as the selected temperatures, as follows:

$$R(1)=\frac{k_{R\rightarrow P1}}{k_{R\rightarrow P1}+k_{R\rightarrow P2}} \quad (3.12)$$

$$R(2)=\frac{k_{R\rightarrow P2}}{k_{R\rightarrow P1}+k_{R\rightarrow P2}} \quad (3.13)$$

When taking tunneling corrections into account (Table 3.8), abstraction of the H-bonded to the C₁- and C₂-atoms accounts for 34.05–33.4 % and 65.95–66.6 % of the overall adduct products, respectively. These branching ratios for pathways **1** and **2** only slightly vary with the temperature (Figure 3.7), which demonstrates that

under the considered experimental conditions the removal of hydrogen atoms in naphthalene by a hydroxyl radical is essentially a nonselective process. Only a slight preference for the removal of a hydrogen atom from the C₂ position can be reported. Some caution is required, however, because of the limitations inherent to our calculations.

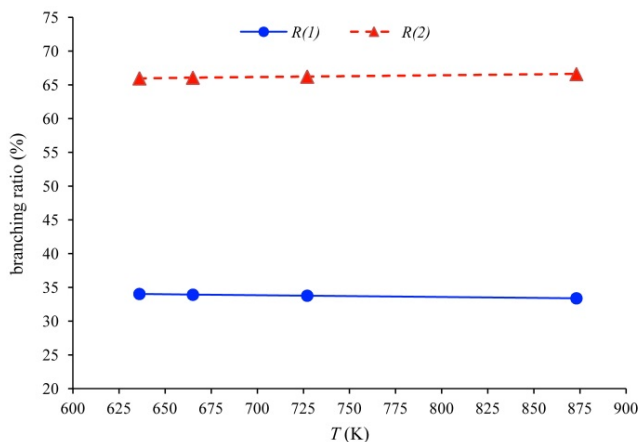


Figure 3.7. Evaluation of branching ratios in function of the temperature for pathways 1–2.

Calculations of branching ratios within accuracy of a few percent would indeed require more sophisticated treatments for calculating partition functions and energy differences, taking in particular, anharmonic and dispersion force hindered rotations into account.

Table 3.8. Wigner tunneling factor for the reaction of naphthalene with OH radicals at temperatures ranging from 636 to 873 K.

Pathway	Temperature	636	665	727	873
	(1)		1.3380	1.3091	1.2587
(2)		1.3474	1.3178	1.2659	1.1844

3.4. Conclusions

Reaction mechanisms for the initial stages of naphthalene oxidation at high temperatures ($T \geq 600$ K) have been studied theoretically using Density Functional Theory in conjunction with various exchange-correlation functionals (B3LYP, ω B97XD, UM05-2x, and UM06-2x) and the aug-cc-pVTZ basis set. These stages correspond to the removal of hydrogen atoms by hydroxyl radicals and the formation thereby of 1- and 2-naphthyl radicals. The supplied reaction energies

and activation barriers incorporate zero-point vibrational energy differences and counterpoise corrections for basis set superposition errors. Comparison has been made with the results of benchmark calculations employing the composite CBS-QB3 approach. This comparison indicates that the most reliable exchange-correlation functionals for kinetic calculations are the UM05-2x and UM06-2x ones. Bimolecular kinetic rate constants were correspondingly estimated by means of transition state theory, on the grounds of partition functions calculated using the rigid rotor-harmonic oscillator approximation. The all-in-all rather excellent agreement with the available experimental kinetic rate constants confirms that the two-step reaction scheme proposed by Singleton and Cvetanovic [53] is valid. Since the main contributions to Gibb's free reaction and activation energies were found to be entropic in origin, more elaborate treatments of statistical thermodynamical partition functions, taking dispersion forces, anharmonic effects, and hindered rotations [71] into account, should certainly be considered for improving further the agreement between theory and experiment.

Analysis of the computed structures, bond orders, and free energy profiles demonstrate that the reaction steps involved in the removal of hydrogen atoms by OH radicals satisfy Hammond's principle: indeed, whatever the site of the reaction in naphthalene, the transition states for the first exergonic bimolecular reaction steps are structurally closer to the pre-reactive molecular complexes. The energy profiles for removal of hydrogen atoms at the C₁ and C₂ positions are very similar, with differences in activation energies and reaction energies that do not exceed ~0.3 kcal mol⁻¹. Therefore, these reaction processes do not appear to exhibit a particularly pronounced site-selectivity: only a slight preference for a reaction at site C₁ and formation thereby of 1-naphthyl can be reported from the computed branching ratios.

3.5. References

- [1] H. Tokiwa, Y. Ohnishi, H.S. Rosenkranz, *CRC Crit. Rev. Toxicol.*, **1986**, *17*, 23.
- [2] P.D. Josephy, B. Mannervik, P.O. De Montellano, *Molecular Toxicology*; Oxford University Press: Oxford, 1997.
- [3] N. Nishino, R. Atkinson, J. Arey, *Environ. Sci. Technol.*, **2008**, *42*, 9203.
- [4] D.G. Hendry, R.A. Kenley, Atmospheric Reaction Products of Organic Compounds. U.S. Environmental Protection Agency, EPA-560112-79-001, 1979.
- [5] R. Atkinson, K.R. Darnall, A.C. Lloyd, A.M. Winer, J.N. Pitts, *Adv. Photochem.*, **1979**, *11*, 375.

- [6] N.J. Bunce, L. Liu, J. Zhu, *Environ. Sci. Technol.*, **1997**, *31*, 2252.
- [7] R. Atkinson, J. Arey, *Environ. Health Perspect.*, **1994**, *102*, 117.
- [8] X. Qu, Q. Zhang, W. Wang, *Chem. Phys. Lett.*, **2006**, *429*, 77.
- [9] J. Arey, B. Zielinska, R. Atkinson, A.M. Winer, *Atmos. Environ.*, **1967**, *21*, 1437.
- [10] J. Arey, R. Atkinson, B. Zielinska, P.A. McElroy, *Environ. Sci. Technol.*, **1989**, *23*, 321.
- [11] T.E. Graedel, *Chemical Compounds in the Atmosphere*; Academic Press: New York, 1978.
- [12] K. Lorenz, R. Zellner, *Ber. Bunsen-Ges. Phys. Chem.*, **1983**, *87*, 629.
- [13] K. Lorenz, R. Zellner, *8th International Symposium on Gas Kinetics*; University of Nottingham, Nottingham, UK, 15–20 July, 1984.
- [14] R. Atkinson, *J. Phys. Chem. Ref. Data, Monograph*, **1989**, *1*, 1.
- [15] L.C. Sander, S.A. Wise, In *NIST Chemistry WebBook*; NIST Standard Reference Database 69; National Institute of Standards and Technology; <http://kinetics.nist.gov/>.
- [16] R.A. Perry, R. Atkinson, J.N. Pitts Jr., *J. Phys. Chem.*, **1977**, *81*, 296.
- [17] R. Atkinson, S.M. Aschmann, J.N. Pitts, *Environ. Sci. Technol.*, **1984**, *18*, 110.
- [18] R. Atkinson, S.M. Aschmann, *Int. J. Chem. Kinet.*, **1986**, *18*, 569.
- [19] D.S. Hollman, A.C. Simmonett, H.F. Schaefer, *Phys. Chem. Chem. Phys.*, **2011**, *13*, 2214.
- [20] J.A. Montgomery, J.W. Ochterski, G.A. Petersson, *J. Chem. Phys.*, **1994**, *101*, 5900.
- [21] J.A. Montgomery, M.J. Frisch, J.W. Ochterski, G.A. Petersson, *J. Chem. Phys.*, **1999**, *110*, 2822.
- [22] J.W. Ochterski, G.A. Petersson, J.A. Montgomery, *J. Chem. Phys.*, **1996**, *104*, 2598.
- [23] M.R. Nyden, G.A. Petersson, *J. Chem. Phys.*, **1981**, *75*, 1843.
- [24] G.A. Petersson, A. Bennett, T.G. Tensfeld, M.A. Al-Laham, W. Shirley, J. Matzaris, *J. Chem. Phys.*, **1988**, *89*, 2193.
- [25] G.A. Petersson, M.A. Al-Laham, *J. Chem. Phys.*, **1991**, *94*, 6081.
- [26] G.A. Petersson, A.K. Yee, A. Bennett, *J. Chem. Phys.*, **1983**, *83*, 5105.
- [27] J.A. Montgomery, J.M. Frisch, J.W. Ochterski, G.A. Petersson, *J. Chem. Phys.*, **2000**, *112*, 6532.
- [28] R. Casanovas, J. Frau, J. Ortega-castro, A. Salva, J. Donoso, F. Munoz, *Int. J. Quantum. Chem.*, **2010**, *110*, 323.
- [29] R.J. Bartlett, J.D. Watts, S.A. Kucharski, J. Noga, *Chem. Phys. Lett.* **1990**, *165*, 513.

- [30] J.F. Stanton, *Chem. Phys. Lett.*, **1997**, *281*, 130.
- [31] A. Szabo, N.S. Ostlund, *Modern Quantum Chemistry: Introduction to Advanced Electronic Structure Theory*; McGraw-Hill: New York, 1989.
- [32] H. Eyring, *J. Chem. Phys.* **1935**, *3*, 107.
- [33] H.S. Johnston, *Gas Phase Reaction Rate Theory*; The Roland Press Co: New York, 1966.
- [34] K.J. Laidler, *Theories of Chemical Reaction Rates*; McGraw-Hill: New York, 1969.
- [35] R.E. Weston, H.A. Schwartz, *Chemical Kinetics*; Prentice-Hall: New York, 1972.
- [36] D. Rapp, *Statistical Mechanics*; Holt, Rinehart, and Winston: New York, 1972.
- [37] E.E. Nikitin, *Theory of Elementary Atomic and Molecular Processes in Gases*; Clarendon Press: Oxford, 1974.
- [38] I.W.M. Smith, *Kinetics and Dynamics of Elementary Gas Reactions*; Butterworths: London, 1980.
- [39] J.I. Steinfeld, J.S. Francisco, W.L. Hase, *Chemical Kinetics and Dynamics*; Prentice-Hall: Englewood Cliffs, New Jersey, 1989.
- [40] M.J. Frisch, G.W. Trucks, H.B. Schlegel, G.E. Scuseria, M.A. Robb, J.R. Cheeseman, G. Scalmani, V. Barone, B. Mennucci, G.A. Petersson, *et al.* *Gaussian 09*, Revision B.01; Gaussian: Wallingford, CT, 2009.
- [41] I.I.R. Dennington, T. Keith, J. Millam, K. Eppinnett, W.L. Hovell, R. Gilliland, *GaussView*, Version 3.09; Semichem, Inc.: Shawnee Mission, KS, 2003.
- [42] A.D. Becke, *J. Chem. Phys.*, **1993**, *98*, 5648.
- [43] C. Lee, W. Yang, R.G. Parr, *Phys. Rev B*, **1988**, *37*, 785.
- [44] J.D. Chai, M. Head-Gordon, *Phys. Chem. Chem. Phys.*, **2008**, *10*, 6615.
- [45] Y. Zhao, D.G. Truhlar, *Acc. Chem. Res.*, **2008**, *41*, 157.
- [46] Y. Zhao, D.G. Truhlar, *Theor. Chem. Acc.*, **2008**, *120*, 215.
- [47] T.H. Dunning, *J. Chem. Phys.*, **1989**, *90*, 1007.
- [48] C. Gonzalez, H.B. Schlegel, *J. Chem. Phys.*, **1989**, *90*, 2154.
- [49] J.W. McIver Jr., *Acc. Chem. Res.*, **1974**, *7*, 72.
- [50] F. Fukui, *J. Phys. Chem.*, **1970**, *74*, 4161.
- [51] K.B. Wiberg, *J. Org. Chem.*, **1997**, *62*, 5720.
- [52] S.F. Boys, F. Bernardi, *Mol. Phys.*, **1970**, *19*, 553.
- [53] D.L. Singleton, R.J. Cvetanovic, *J. Am. Chem. Soc.*, **1976**, *98*, 6812.
- [54] J.R. Alvarez-Idaboy, N.M. Diez, A. Vivier-Bunge, *J. Am. Chem. Soc.*, **2000**, *122*, 3715.

- [55] V.H. Uc, J.R. Alvarez-Idaboy, A. Galano, A. Vivier-Bunge, *J. Phys. Chem. A*, **2008**, *112*, 7608.
- [56] R.G. Mortimer, *Physical Chemistry*; 3rd ed., Elsevier Academic Press: Burlington, 2008.
- [57] R.G. Gilbert, S.C. Smith, *Theory of Unimolecular and Recombination Reactions*; Blackwell Scientific: Oxford, 1990.
- [58] E.P. Wigner, *Z. Phys. Chem.*, **1932**, *B19*, 203.
- [59] S. Canneaux, F. Bohr, E. Henon, *J. Comput. Chem.*, **2013**, *35*, 82.
- [60] C. Hammaecher, S. Canneaux, F. Louis, L. Cantrel, *J. Phys. Chem. A*, **2011**, *115*, 6664.
- [61] D.H. Varma, P. Raghunath, M.C. Lin, *J. Phys. Chem. A*, **2010**, *114*, 3642.
- [62] S.Y. Wu, P. Raghunath, J.S. Wu, M.C. Lin, *J. Phys. Chem. A*, **2010**, *114*, 633.
- [63] K. Raghavachari, G.W. Trucks, J.A. Pople, M. Head-Gordon, *Chem. Phys. Lett.*, **1989**, *157*, 479.
- [64] H.B. Rao, X.Y. Zeng, H. He, Z.R. Li, *J. Phys. Chem. A*, **2011**, *115*, 1602.
- [65] J.R. Alvarez-Idaboy, N. Mora-Diez, R.J. Boyd, A. Viver-Bunge, *J. Am. Chem. Soc.*, **2001**, *123*, 2018.
- [66] C.W. Zhou, A.M. Mebel, X.Y. Li, *J. Phys. Chem. A*, **2009**, *113*, 10667.
- [67] G.S. Hammond, *J. Am. Chem. Soc.*, **1953**, *77*, 334.
- [68] S.N. Ketkar, M. Fink, *J. Mol. Struct. (THEOCHEM)*, **1981**, *77*, 139.
- [69] Z. Zhang, L. Lin, L. Wang, *Phys. Chem. Chem. Phys.*, **2012**, *14*, 2645.
- [70] M.T. Rayez, J.C. Rayez, J.P. Sawerysyn, *J. Phys. Chem.*, **1994**, *98*, 11342.
- [71] S. Canneaux, R. Vandeputte, C. Hammaecher, F. Louis, M. Ribaucour, *J. Phys. Chem. A*, **2012**, *116*, 592.

Chapter 4

Theoretical study of the oxidation mechanisms of naphthalene initiated by hydroxyl radicals: The OH addition pathway

4.1. Introduction

Polycyclic aromatic hydrocarbons (PAHs) are ubiquitous environmental pollutants. Many PAHs are potentially genotoxic, mutagenic, or carcinogenic [1,2]. They are emitted into the atmosphere during incomplete combustion of a variety of sources such as fossil fuels and biomass [3–5]. PAHs are chemically reactive to tropospheric gases such as ozone, nitrate radicals, and hydroxyl radicals. The most important sink reactions of organic compounds in the troposphere are the reactions with OH radicals [6,7], which play a key role in determining the oxidation power of the atmosphere [8]. Under ambient conditions, the oxidation of aromatic rings by OH radicals in the gas phase yields hydroxycyclohexadienyl-type radicals, which can back decompose to the reactants or react with NO_2 or O_2 to yield further strongly mutagenic derivatives [9–14]. Naphthalene is the most abundant PAH in polluted urban areas and is reactive in ambient atmospheres [15,16]. Reactions of naphthalene in the atmosphere often yield degradation products that may be more carcinogenic than the parent PAH [17]. Therefore, it is of utmost importance to understand the degradation mechanisms of naphthalene in the presence of oxidant species.

Lorenz and Zellner [14,18] as well as Atkinson and co-workers [19–21] have experimentally studied the gas phase reaction between hydroxyl radicals and naphthalene at temperatures lower than 410 K and at temperatures ranging from 636 to 873 K, by means of laser flash photolysis using laser-induced fluorescence,

at pressures between 6 and 128 mbar, under inert (He) conditions [9,14]. An Arrhenius plot of all the kinetic rate constants that were measured or experimentally inferred so far under such conditions [22] is depicted in Figure 4.1.

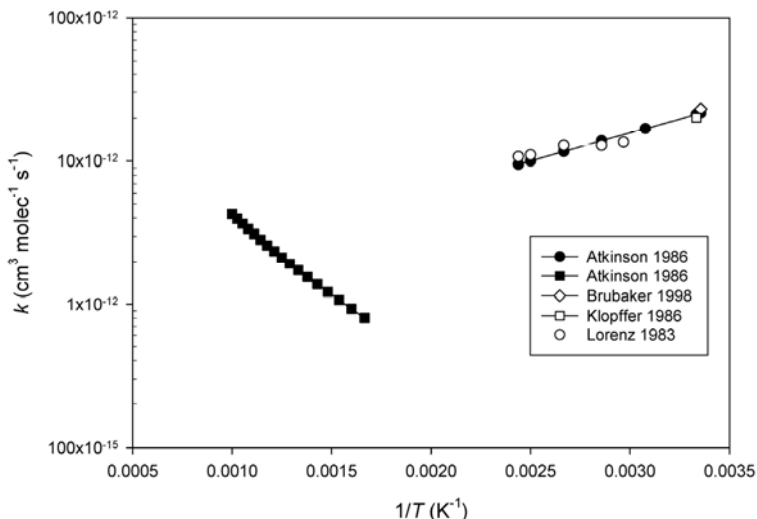
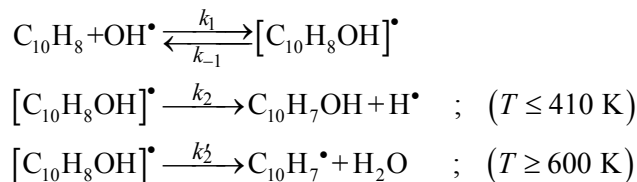


Figure 4.1. Arrhenius plot of the rate constants for the reaction of OH radicals with naphthalene: Legend: (●) Atkinson *et al.* [19]; (■) Atkinson *et al.* [21]; (◇) Brubaker and Hites [23]; (□) Klöpffer *et al.* [24]; (○) Lorenz and Zellner [14].

As is quite apparent from this Figure, different energy barriers prevail at temperatures lower than 410 K and at temperatures larger than 636 K. To explain such features, two different pathways have been suggested [8] for the reaction between naphthalene and OH radicals in the gas phase.

At low temperatures (at $T \leq 410$ K), an OH-addition process, involving first an attack of OH radicals on naphthalene at the C₁ and C₂ positions (Figure 4.2), followed by H elimination, is assumed to prevail, whereas at high temperatures (at $T \geq 600$ K), the mechanism which is believed to dominate is an OH-addition process, via attack of OH radicals on the hydrogen atoms linked to the C₁ and C₂ atoms, followed by water elimination. These low and high temperature pathways are commonly referred to as the hydroxyl radical addition and hydrogen abstraction pathways, respectively.



As is immediately apparent from Figure 4.1, the rate constant of the reaction between OH radicals and naphthalene at $T \leq 410$ K exhibits [14,19–21] a negative temperature dependence, which is equivalent to an Arrhenius activation energy of $-1.27 \text{ kcal mol}^{-1}$ [18,19] or $-1.8 \text{ kcal mol}^{-1}$ [25]. A least-square fit of experimental rate constants yields accordingly the following Arrhenius expression [25]:

$$k_{(T \leq 410 \text{ K})} = (1.335 \pm 0.825) \times 10^{-12} e^{(902 \pm 240)/T} \text{ cm}^3 \text{ molecule}^{-1} \text{ s}^{-1}$$

The above Arrhenius rate constant decreases with increasing temperature at pressures between 6 and 128 mbar (He). The corresponding values vary from $(18.6 \pm 1.0) \times 10^{-12}$ to $(10.5 \pm 4.0) \times 10^{-12} \text{ cm}^3 \text{ molecule}^{-1} \text{ s}^{-1}$ over the temperature range 300–407 K.

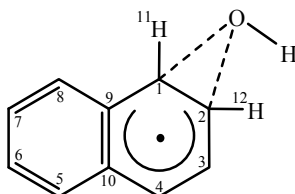
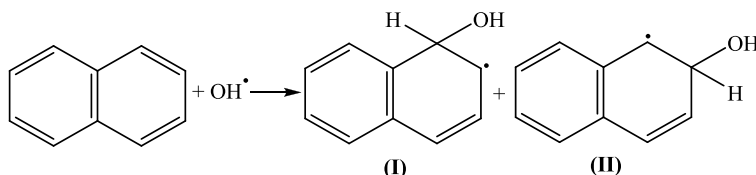


Figure 4.2. Retained atom labeling for characterizing the structures of intermediate and transition states during the oxidation of naphthalene by OH radicals (see Tables 4.1 and 4.2 for numerical details).

Under atmospheric conditions, attack of OH radicals on naphthalene is initiated by addition at the C₁ and C₂ positions (Figure 4.3) to give the adducts (I) and (II) (scheme 4.1) [14,19,20]. In line with the assumption of a first reversible addition step, the negative or slightly positive activation energies of these reactions indicates that a major reaction channel of these adducts is loss of OH radicals to regenerate reactants [6]. Upon investigating the regioselectivity of the OH-addition reactions on naphthalene under inert (He) atmosphere, Bernstein and co-workers experimentally observed that the production of 1-hydroxynaphthalene (or 1-naphthol) was favored by a ratio 2:1 over 2-hydroxynaphthalene (or 2-naphthol), according to a personal communication to Ricca and Bauschlicher [26].



Scheme 4.1

The interactions between naphthalene and hydroxyl radical at total pressures between 6 and 128 mbar (He) were found to be essentially pressure independent [14]. This is only at pressures smaller than 10 mbar that a slight decrease of the rate constants measured at 379 K has been observed [14]. Rate constants at 525 K show no pressure effects but are lower in absolute magnitude by almost an order of magnitude. This behavior was interpreted [14] as to arise from an addition reaction at lower temperatures and from its reversibility at higher temperatures.

These addition reactions have been the subject of a few theoretical studies, comprising the investigations at the B3LYP/6-31G* level of theory by Ricca and Bauschlicher [26] and at the BB1K/6-311+G(3df,2p)//BB1K/6-31+G(d,p) level of theory by Qu *et al.* [8]. More recently, Zhang *et al.* [27], found that the initial OH-addition reactions upon naphthalene at the C₁ and C₂ positions (Figure 4.3) are characterized by negative energy barriers of -3.42 and -2.22 kcal mol⁻¹, respectively, at the B3LYP/6-311+G(2df,p) level of theory, whereas positive energy barriers of 0.41 and 1.65 kcal mol⁻¹ were correspondingly obtained at the BB1K/6-311++G(2df,2p) level of theory.

The main purpose of our work is to reinvestigate the OH addition pathway through a detailed analysis of the kinetic rate constants obtained in the experimental study by Lorenz and Zellner [14] of the reaction of naphthalene by hydroxyl radicals under inert conditions, i.e., using He as diluent gas, and thus, in the absence of O₂. For this purpose, we will study the two reaction pathways **1** and **2** that are depicted in Figure 4.3 by means of density functional theory (DFT), along with various exchange-correlation functionals. These pathways are initiated by OH-addition on naphthalene at the C₁ and C₂-positions (Figure 4.2), which leads to 1-naphthol and 2-naphthol, respectively.

The addition of the hydroxyl radical to naphthalene starts with the formation of a pre-reactive molecular complex, IM1 (Figure 4.3). The reaction proceeds in two steps, involving first a fast and reversible reaction between the OH radical and naphthalene to form an energized adduct [C₁₀H₈OH][•] (IM2), followed by an irreversible step, corresponding to the unimolecular dissociation of this adduct into 1- or 2-naphthol and one H-atom (H[•]). We note here that the likelihood of the hydroxyl radical addition pathway under inert conditions has been discussed in the past by Hollman *et al.* in the frame of a theoretical study of the oxidation mechanisms of benzene by hydroxyl radicals [28]. Benzene, however, is much less reactive than naphthalene, and conclusions drawn from calculations on the former compound are not necessarily transposable to the latter one. Indeed, as *n*-acene length increases, their reactivity generally increases [29]. Such progressions in *n*-acene properties appear to coincide with the sequential loss of benzenoid

character (aromaticity) predicted by early molecular orbital treatments and Clar's qualitative sextet concept [30].

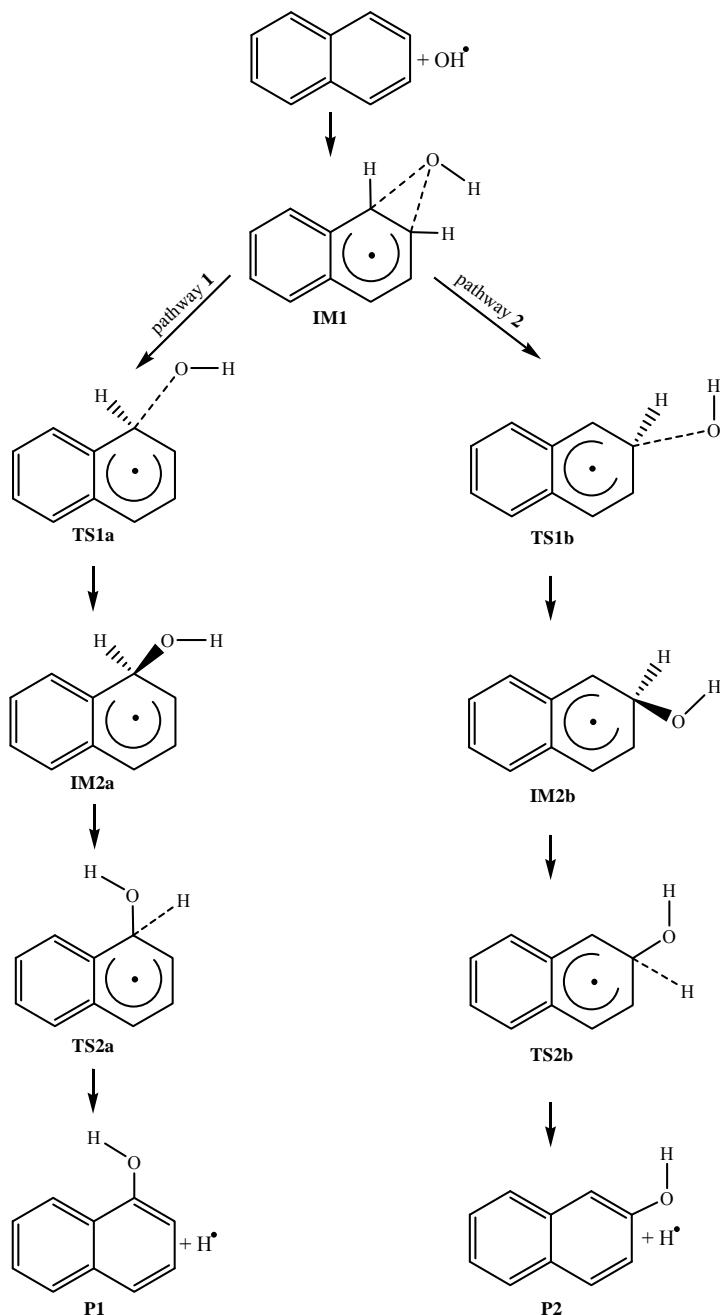


Figure 4.3. Reaction pathways for the oxidation of naphthalene by OH radicals into 1-naphthol (P1) and 2-naphthol (P2).

For the sake of quantitative insights into these reaction mechanisms, comparison will be made with benchmark theoretical calculations employing the high-level composite CBS-QB3 *ab initio* approach [31–39], to determine which exchange-correlation functional gives the most accurate energy barriers and reaction energies. We note that DFT methods alone were found to be insufficient for quantitatively investigating the potential energy surface associated with the OH-addition reactions upon benzene [28]. With the CBS-QB3 approach, an extrapolation scheme is used to evaluate SCF and correlation energies in the limit of a complete basis set (CBS). The obtained results are analyzed in terms of nucleus independent chemical shift (NICS) indices of aromaticity [40–44], bond orders, natural bond orbital (NBO) occupancies [45,46], and donor-acceptor interaction energies.

4.2. Theory and Computational Details

All calculations that are discussed in the present work have been performed using the Gaussian 09 package of programs [47] at the Flemish Supercomputer Center. Molecular structures were visualized with GaussView [48]. The most accurate of these calculations were conducted at the CBS-QB3 level of theory [31–39].

DFT calculations, comprising geometry optimizations and frequency calculations, were performed using a variety of exchange-correlation functionals, such as B3LYP [49,50], ω B97XD [51], UM05-2x [52] and UM06-2x [52] functionals in conjunction with the aug-cc-pVTZ basis set [53]. Thermodynamic state functions were correspondingly computed from canonical partition functions for an ideal gas, using Boltzmann statistical thermodynamics along with the rigid rotor harmonic oscillator approximation (RRHO), and neglecting thereby hindered rotations of the OH group in the intermediates and transition states [54,55]. We note that, upon considering the results of a systematic study of the thermochemical properties of ten target species involved in the oxidation of *o*-xylene, it is reasonable to assume that internal rotations need only to be accounted for at temperatures larger than 400 K [56].

The intrinsic reaction coordinate (IRC) path [57] was traced at the B3LYP/6-31G(d,p) level of theory to check the energy profiles connecting each transition structure to the two associated minima of the proposed mechanism by using the second-order Gonzalez-Schlegel integration method [57,58]. Energy barriers obtained on DFT grounds were systematically corrected for basis set superposition errors (BSSEs) [59], according to the counterpoise method proposed by Boys and

Bernardi [60]. In this *a posteriori* correction method, the energy calculations for the individual monomers are performed using the whole supermolecular basis sets instead of the monomer basis sets. No symmetry constraints were imposed during the geometry optimizations [61,62]. The keyword *nosymm* was used in order to guarantee this matter.

The rate constants and the branching ratios for each reaction channels were evaluated using transition state theory (TST) at a pressure of 1 bar, and at temperatures ranging from 300 to 407 K, using the CBS-QB3 estimates for activation energies, and B3LYP/6-311G(2d,d,p) partition functions. In atmospheric chemistry, the kinetics of bimolecular and unimolecular reactions can be determined using conventional transition state theory. The rate constants for these reactions are therefore given by [63–75]

$$k_{\text{TST}} = \kappa(T) \frac{\sigma k_{\text{B}} T}{h} V_{\text{m}}(T) \frac{Q_{\text{TS}}^{\dagger}(T)}{Q_{\text{A}}(T) Q_{\text{B}}(T)} \exp(-E_{\text{a}}/RT) \quad (4.1)$$

$$k_{\text{TST}} = \kappa(T) \frac{\sigma k_{\text{B}} T}{h} \frac{Q_{\text{TS}}^{\dagger}(T)}{Q_{\text{A}}(T)} \exp(-E_{\text{a}}/RT) \quad (4.2)$$

along with $\kappa(T)$ a relevant tunneling correction factor. Because the moving entity at the transition state involves a relatively heavy oxygen atom, this factor has been assumed to be equal to 1 for the first bimolecular OH-addition step. On the other hand, in view of a strongly asymmetric energy barrier, and because the moving entity corresponds to a hydrogen atom, an Eckart tunneling correction factor [66] has been considered for evaluating the rate constant of the unimolecular dissociation step (step 2) on TST grounds, using the CBS-QB3 energy profiles (these factors range from 1.5 to 2.4, see Table S1 of the Appendix II for details).

Equation 4.1 applies to the first bimolecular reaction step ($\text{R} \rightarrow \text{IM2a}$ or IM2b), whereas eq. (4.2) applies to all other reaction steps that are depicted in Figure 4.3. Note that eq 1 derives from a steady state analysis involving a reversible reaction, followed by an irreversible step ($\text{R} \rightleftharpoons \text{IM1} \rightarrow \text{IM2x}$, with $x = \text{a, b}$), upon considering that $k_{\text{IM1} \rightarrow \text{IM2a}}$ or $k_{\text{IM1} \rightarrow \text{IM2b}}$ are much (at least 10^4 times) smaller than $k_{\text{IM1} \rightarrow \text{R}}$ – an assumption in line with detailed theoretical estimates of unimolecular reaction rate constants (see further discussion).

In the above equations, σ denotes the reaction symmetry number, Q_{TS}^{\dagger} is the total partition function of the transition state, Q_{A} and Q_{B} represent the total partition functions of the reactants, E_{a} is the classical barrier height (including zero-point vibrational energy contributions), R is the ideal gas constant, k_{B} and h are the Boltzmann's and Planck's constants, respectively, and $V_{\text{m}}(T) = RT/P$ is the molar

volume of an ideal gas at the considered temperatures. Because the computed energy differences account for zero-point vibrational energies, vibrational partition functions were computed using the vibrational ground state as energy reference. TST gives an estimate of the upper limit for rate constants as a function of the temperature, and is known to give reliable estimations of rate constants [67,68] in the high pressure limit [69], especially for cases with significant barrier heights [70].

Furthermore, in the present study, statistical RRKM theory [71–73] has been considered to evaluate pressure effects on a microcanonical basis, both in the falloff regime and towards the high pressure limit, using the implementation of this approach in the KiSThelP package [74]. As shall be seen, ambient pressure may not necessarily be sufficient to warrant that the TST approximation is necessarily valid. Again, in these RRKM calculations, a scaling factor of 0.99 was imposed on the frequencies calculated at the B3LYP/6-311G(2d,d,p) level of theory. Collisional stabilization rate constants were computed using Lennard–Jones (LJ) collision rate theory [75]. The strong collision approximation is used, assuming therefore that every collision deactivates with $\omega = \beta_c \cdot Z_{LJ} \cdot [M]$ being the effective collision frequency, where β_c is the collisional efficiency, Z_{LJ} is the Lennard–Jones collision frequency and $[M]$ is the total gas concentration. The retained value for β_c is 0.2. The collision frequencies (Z_{LJ}) were calculated using the LJ parameters: ε/k_B , which depends on the energy depth (ε) of the LJ potential, and σ , which represents a dimensional scale of the molecular radius [74]. The LJ potential parameters for helium as diluent gas [76] amount to $\sigma = 2.28 \text{ \AA}$ and $\varepsilon/k_B = 10.2 \text{ K}$. For naphthalene and the naphthol radicals, the following parameters have been retained: $\sigma = 6.45 \text{ \AA}$, $\varepsilon/k_B = 554.4 \text{ K}$; [77] and $\sigma = 6.57 \text{ \AA}$, $\varepsilon/k_B = 612.7 \text{ K}$ [77], respectively.

Assuming again a steady state regime, the rate constants k for the bimolecular reactions leading to the energized adducts ($R \rightarrow IM2x$, $x = a, b$) were calculated according to the scheme advocated by Singleton and Cvetanovic [78] for pre-reactive complexes. We assume therefore that these bimolecular reactions occur according to a mechanism involving first a fast pre-equilibrium (K_c) between the reactants and the pre-reactive van der Waals complex (IM1), followed by an irreversible step corresponding to the formation of a covalent bond between the hydroxyl radical and naphthalene, which leads to the post-reactive complexes IM2a or IM2b. Upon using this scheme, the rate constants for the bimolecular reactions (step 1) yielding IM2a or IM2b can be obtained by means of

$$k_{R \rightarrow IM2x} = \frac{k_{IM1 \rightarrow R} \times K_c \times k_{IM1 \rightarrow IM2x}}{k_{IM1 \rightarrow R} + k_{IM1 \rightarrow IM2x}} \quad (4.3)$$

where $k_{IM1 \rightarrow R}$ and $k_{IM1 \rightarrow IM2x}$ represent reverse and forward unimolecular reaction rate constants (in s^{-1}).

4.3. Results and Discussion

4.3.1. Geometry Optimizations

The optimized molecular structures of the intermediate complexes (IM1 and IM2), transition states (TS1 and TS2), and products (P1 and P2) in the reactions between naphthalene and OH radicals along pathways **1–2** are presented in Tables 4.1 and 4.2, according to the atom labels given in Figure 4.2. In line with changes in chemical bond orders, examination of Tables 4.1 and 4.2 and comparison of the structures for the intermediates IM1 and IM2a (IM2b) show that addition of an hydroxyl radical at position C₁ (C₂) results into a significant lengthening of the chemical bonds C₁–C₂ and C₁–C₉ (C₁–C₃). For both chemical pathways (**1** and **2**), it appears that the corresponding transition state (TS1a or TS1b) is structurally much closer to the pre-reactive intermediate (IM1) than the produced energized adducts (IM2a or IM2b). The C₂–O forming bond is slightly shorter by ~0.05 to ~0.15 Å, in the TS1b transition structure on pathway **2** than in the TS1a transition structure on pathway **1** (Figure 4.3).

In the next step, from the energized adducts (IM2a and IM2b) to the naphthol products (P1 and P2), the elimination of the hydrogen atom allows IM2a and IM2b to return to an aromatic system. Therefore, also in line with changes in chemical bond orders, the departure of one hydrogen atom (H₁₁ or H₁₂) results into a significant shortening of the chemical bonds C₁–C₂ and C₁–C₉ (C₁–C₃). In this case, the corresponding transition states are structurally much closer to the products.

Prior to ending this discussion of geometric parameters, it is worth noticing that, at the starting B3LYP/6-311G(2d,d,p) level of theory used to optimize the geometries of reactants, transition states and adducts, the spin contamination [$\langle S^2 \rangle_{obs} - 0.75$] never exceeds 0.034 (Table S2 of the Appendix II) and can thus, for all practical purposes, be regarded as negligible.

Table 4.1. Main structural parameters for all stationary points which are involved in the chemical reaction pathway 1 (see Figure 4.3) for the oxidation of naphthalene by OH[•] into 1-naphthol. (see Figure 4.2 for atom labeling)

Parameter	B3LYP/aug-cc-pVTZ					ω B97XD/aug-cc-pVTZ					UM05-2x/aug-cc-pVTZ					UM06-2x/aug-cc-pVTZ					B3LYP/6-311G(2d,d,p)				
	IM1	TS1a	IM2a	TS2a	P1	IM1	TS1a	IM2a	TS2a	P1	IM1	TS1a	IM2a	TS2a	P1	IM1	TS1a	IM2a	TS2a	P1	IM1	TS1a	IM2a	TS2a	P1
$r(C_1-C_2)$	1.384	1.391	1.495	1.395	1.373	1.371	1.385	1.494	1.390	1.368	1.368	1.385	1.491	1.387	1.366	1.367	1.388	1.494	1.391	1.368	1.384	1.395	1.500	1.400	1.377
$r(C_1-C_9)$	1.422	1.428	1.517	1.439	1.425	1.419	1.428	1.514	1.437	1.424	1.415	1.427	1.509	1.433	1.421	1.417	1.430	1.513	1.439	1.424	1.424	1.433	1.516	1.443	1.429
$r(C_2-C_3)$	1.408	1.404	1.367	1.400	1.406	1.411	1.403	1.363	1.400	1.405	1.412	1.403	1.363	1.400	1.405	1.414	1.405	1.363	1.401	1.407	1.414	1.407	1.369	1.403	1.409
$r(C_9-C_{10})$	1.426	1.424	1.415	1.424	1.430	1.416	1.414	1.407	1.414	1.420	1.415	1.411	1.404	1.412	1.418	1.418	1.414	1.408	1.414	1.421	1.430	1.428	1.418	1.427	1.433
$r(C_1-H_{11})$	1.079	1.078	1.096	1.832	-	1.081	1.079	1.095	1.823	-	1.079	1.076	1.092	1.814	-	1.082	1.080	1.096	1.749	-	1.081	1.080	1.105	1.830	-
$r(C_1-O)$	2.372	2.190	1.448	1.369	1.366	2.535	2.154	1.431	1.359	1.357	2.679	2.112	1.436	1.364	1.362	2.907	2.091	1.429	1.364	1.359	2.439	2.156	1.445	1.368	1.366
$\angle H_{11}-C_1-O$	79.3	81.3	102.2	97.9	-	84.4	83.6	103.0	98.8	-	90.2	84.7	103.1	98.6	-	101.3	84.8	103.0	99.1	-	79.4	82.4	107.6	98.1	-

Bond lengths are given in angstroms (Å), and bond angles are given in degrees (°).

Table 4.2. Main structural parameters for all stationary points which are involved in the chemical reaction pathway 2 (see Figure 4.3) for the oxidation of naphthalene by OH[•] into 2-naphthol. (see Figure 4.2 for atom labeling)

Parameter	B3LYP/aug-cc-pVTZ					ω B97XD/aug-cc-pVTZ					UM05-2x/aug-cc-pVTZ					UM06-2x/aug-cc-pVTZ					B3LYP/6-311G(2d,d,p)				
	IM1	TS1b	IM2b	TS2b	P2	IM1	TS1b	IM2b	TS2b	P2	IM1	TS1b	IM2b	TS2b	P2	IM1	TS1b	IM2b	TS2b	P2	IM1	TS1b	IM2b	TS2b	P2
$r(C_1-C_2)$	1.384	1.396	1.492	1.395	1.372	1.371	1.388	1.491	1.390	1.366	1.368	1.387	1.488	1.387	1.365	1.367	1.389	1.491	1.390	1.367	1.384	1.399	1.496	1.399	1.376
$r(C_1-C_9)$	1.422	1.411	1.393	1.410	1.416	1.419	1.412	1.392	1.410	1.415	1.415	1.410	1.392	1.407	1.413	1.417	1.412	1.396	1.409	1.415	1.424	1.415	1.397	1.413	1.419
$r(C_2-C_3)$	1.408	1.430	1.495	1.432	1.413	1.411	1.428	1.494	1.431	1.412	1.412	1.427	1.493	1.429	1.411	1.414	1.430	1.496	1.434	1.414	1.414	1.433	1.499	1.436	1.417
$r(C_9-C_{10})$	1.372	1.360	1.338	1.359	1.367	1.364	1.355	1.332	1.353	1.361	1.364	1.355	1.331	1.353	1.361	1.367	1.356	1.333	1.354	1.362	1.374	1.364	1.341	1.362	1.369
$r(C_1-H_{11})$	1.080	1.078	1.102	1.774	-	1.080	1.078	1.102	1.767	-	1.078	1.075	1.097	1.754	-	1.081	1.078	1.102	1.702	-	1.082	1.080	1.106	1.772	-
$r(C_1-O)$	2.672	2.070	1.454	1.372	1.368	2.678	2.065	1.435	1.362	1.359	2.732	2.057	1.442	1.367	1.364	2.932	2.043	1.434	1.367	1.361	2.637	2.056	1.450	1.370	1.366
$\angle H_{11}-C_1-O$	88.8	83.7	106.9	97.3	-	89.3	85.2	107.7	98.2	-	92.2	85.6	107.4	97.7	-	102.2	85.7	107.6	97.8	-	85.9	84.8	107.5	97.7	-

Bond lengths are given in angstroms (Å), and bond angles are given in degrees (°).

4.3.2. Energetic and Thermodynamic Parameters

The reader is referred to Tables 4.3 and 4.4, for the total internal energies (comprising BSSE and ZPVE corrections) at 0 K and enthalpies and Gibb's free energies at 298 K of all identified transition states and intermediates along pathways **1** and **2** relative to the reactants. In line with experimental Arrhenius activation energies of -1.27 kcal mol⁻¹ [18] or -1.8 kcal mol⁻¹[25], all our calculations locate the transition state TS1a on pathway **1** at 0.6 – 3.9 kcal mol⁻¹ below the reactants. Our best (CBS-QB3) estimated value for the corresponding activation energy amounts to -1.5 kcal mol⁻¹. On the other hand, at this level, the transition state TS1b on pathway **2** is located at 1 kcal mol⁻¹ above the reactants. According to Ricca and Bauschlicher [26], this difference in activation energies for the bimolecular reactions R→IM2a and R→IM2b explains that the production of 1-naphthol is kinetically favored over 2-naphthol. However, the subsequent unimolecular dissociation reaction steps IM2a→P1 and IM2b→P2 are characterized by much higher activation energies (Figures 4.4 and 4.5). In the high pressure limit, and in the absence of O₂ (as was the case in the original experiment by Lorenz and Zellner [14]), these unimolecular reaction steps may also strongly influence the overall reaction dynamics – an observation which justifies the forthcoming discussion of TST and RRKM kinetic rate constants.

As can be seen in Tables 4.3 and 4.4, the newly supplied CBS-QB3 data differ sensitively from those reported by Ricca and Bauschlicher [26] or by Zhang *et al.* [27]. Among all supplied data, energy values obtained with the UM05-2x functional appear in average to be in closest agreement with the benchmark CBS-QB3 results. From the data supplied in Table 4.4, we characterize in detail (Table 4.5) the energy barriers associated with the conversion of the pre-reactive intermediate IM1 into the energized adduct IM2 and with the conversion of the latter into the naphthol products (see also Figures 4.4 and 4.5). The CBS-QB3 results show that the first energy barriers (IM1→TS1) encountered along the chemical reaction pathways **1** and **2** amount to 0.9 and 3.5 kcal mol⁻¹, respectively. TS1a and TS1b are characterized by NICS indices equal to -15.43 and -13.56 , respectively. Evidently, the more pronounced aromatic nature of TS1a explains its higher stability, compared with that of TS1b. Also, the lower energy of IM2a compared with that for IM2b reflects the more strongly pronounced aromatic nature of the former energized adduct: indeed, IM2a and IM2b are characterized by NICS indices equal to -3.94 and -1.28 , respectively.

Table 4.3. Internal energies, standard enthalpies and Gibb's free energies (in kcal mol⁻¹) of transition states relative to the reactants along the chemical pathways 1–2 (see Figure 4.3) for the oxidation of naphthalene into 1- and 2-naphthol ($P=1$ atm) at different levels of theory.

Species	Method	B3LYP/aug-cc-pVTZ			ω B97XD/aug-cc-pVTZ			UM05-2x/aug-cc-pVTZ			UM06-2x/aug-cc-pVTZ			CBS-QB3			literature ΔE_{0K}^\ddagger (kcal mol ⁻¹)
		ΔE_{0K}^\ddagger	ΔH_{298K}^\ddagger	ΔG_{298K}^\ddagger	ΔE_{0K}^\ddagger	ΔH_{298K}^\ddagger	ΔG_{298K}^\ddagger	ΔE_{0K}^\ddagger	ΔH_{298K}^\ddagger	ΔG_{298K}^\ddagger	ΔE_{0K}^\ddagger	ΔH_{298K}^\ddagger	ΔG_{298K}^\ddagger	ΔE_{0K}^\ddagger	ΔH_{298K}^\ddagger	ΔG_{298K}^\ddagger	
Naphthalene + OH*		0.0	0.0	0.0	0.0	0.0	0.0	0.0	0.0	0.0	0.0	0.0	0.0	0.0	0.0	0.0	
TS1a		-3.0	-3.6	4.4	-2.3	-3.0	5.1	-1.3	-2.0	6.2	-1.2	-0.9	7.4	-1.5	-2.2	5.9	-3.4 ^b ; -3.6 ^c ; 0.4 ^d ; 0.1 ^e
TS1b		-1.8	-2.5	5.8	-0.8	-1.6	6.8	0.1	-0.7	7.7	1.2	0.4	8.8	1.0	0.3	8.6	-2.2 ^b ; -2.6 ^c ; 1.7 ^d ; 1.3 ^e
TS1a ^d		-2.8	-3.5	4.6	-2.1	-2.8	5.4	-0.9	-1.7	6.7	-0.9	-0.6	7.6	-1.5	-2.2	5.9	
BSSE energy-TS1a		0.2			0.2			0.3			0.3			0.0			
TS1b ^d		-1.6	-2.3	5.9	-0.6	-1.4	7.0	0.2	-0.6	7.8	1.4	0.7	8.9	1.0	0.3	8.6	
BSSE energy-TS1b		0.2			0.3			0.1			0.3			0.0			
TS2a		10.1	9.2	18.5	8.9	7.9	17.2	7.6	6.6	15.9	5.8	4.8	14.1	6.5	5.5	14.8	
TS2b		10.9	9.9	19.1	10.0	9.0	18.3	9.0	8.1	17.3	7.4	6.4	15.7	9.8	8.9	18.1	
TS2a ^d		10.2	9.2	18.5	9.0	8.0	17.3	7.7	6.7	16.0	7.7	6.7	15.9	6.5	5.5	14.8	
BSSE energy-TS2a		0.1			0.1			0.1			0.1			0.0			
TS2b ^d		10.9	9.9	19.2	10.1	9.1	18.4	9.1	8.2	17.4	7.6	6.6	15.8	9.8	8.9	18.1	
BSSE energy-TS2b		0.1			0.1			0.1			0.1			0.0			

a: BSSE-corrected relative energies; b: Ref.[27a]; B3LYP/6-311+G(2df,p) level of theory; c: Ref. [26]; B3LYP/6-31G(d) level of theory; d: Ref.[27b]; BB1K/6-311++G(2df,2p) level of theory; e: ref.[8]; BB1K/6-31+G(d,p) level of theory.

Table 4.4. Internal energies, standard enthalpies and Gibb's free energies (in kcal mol⁻¹) of pre-reactive (IM1) and post-reactive (IM2) intermediate states relative to the reactants along the chemical pathways 1–2 (see Figure 4.3) for the oxidation of naphthalene into 1- and 2-naphthol ($P=1$ atm) at different levels of theory.

Species	Method	B3LYP/aug-cc-pVTZ			ω B97XD/aug-cc-pVTZ			UM05-2x/aug-cc-pVTZ			UM06-2x/aug-cc-pVTZ			CBS-QB3			literature ΔE_{0K}^\ddagger (kcal mol ⁻¹)
		ΔE_{0K}^\ddagger	ΔH_{298K}^\ddagger	ΔG_{298K}^\ddagger	ΔE_{0K}^\ddagger	ΔH_{298K}^\ddagger	ΔG_{298K}^\ddagger	ΔE_{0K}^\ddagger	ΔH_{298K}^\ddagger	ΔG_{298K}^\ddagger	ΔE_{0K}^\ddagger	ΔH_{298K}^\ddagger	ΔG_{298K}^\ddagger	ΔE_{0K}^\ddagger	ΔH_{298K}^\ddagger	ΔG_{298K}^\ddagger	
Naphthalene + OH*		0.0	0.0	0.0	0.0	0.0	0.0	0.0	0.0	0.0	0.0	0.0	0.0	0.0	0.0	0.0	
IM1 [C ₁₀ H ₈ ...OH]*		-3.0	-3.1	3.4	-2.9	-3.0	3.2	-3.3	-3.4	2.7	-3.7	-4.2	3.2	-2.5	-2.6	3.7	-1.9 ^b
IM1 ^d		-2.9	-3.0	3.5	-2.5	-3.1	4.5	-3.1	-3.2	2.9	-3.6	-4.1	3.4	-2.5	-2.6	3.7	
BSSE energy- IM1		0.2			0.2			0.2			0.2			0.0			
IM2a [C ₁₀ H ₈ OH]*		-20.2	-21.1	-12.3	-25.0	-26.0	-17.1	-25.9	-26.8	-18.1	-24.7	-25.7	-16.8	-22.9	-23.8	-15.3	-19.3 ^b
IM2b [C ₁₀ H ₈ OH]*		-14.1	-14.9	-6.3	-18.1	-18.9	-10.2	-18.5	-19.4	-10.7	-17.6	-18.5	-9.8	-18.4	-19.2	-10.6	-14.4 ^b
P1 (1-naphthol+H*)		5.8	6.1	7.9	1.9	2.1	3.9	0.3	0.2	2.7	-0.4	-0.1	1.4	0.6	1.0	2.5	
P2 (2-naphthol+H*)		4.4	4.5	6.6	0.5	0.7	2.8	-0.6	-0.5	1.6	-1.3	-1.2	0.9	-0.3	-0.1	2.0	

a: BSSE-corrected relative energies; b: Ref.[8]; values obtained at the BB1K/6-31+G(d,p) level of theory.

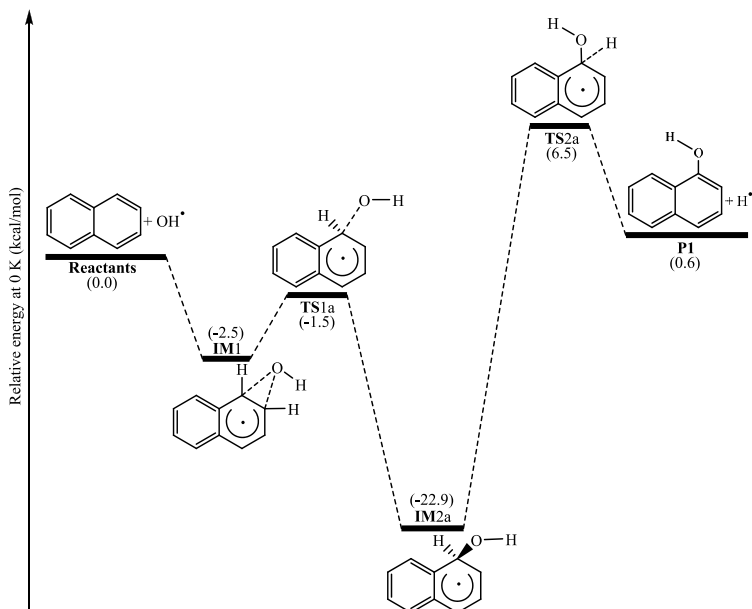


Figure 4.4. CBS-QB3 energy profile for the reaction pathway 1 characterizing the oxidation of naphthalene by OH radicals into 1-naphthol.

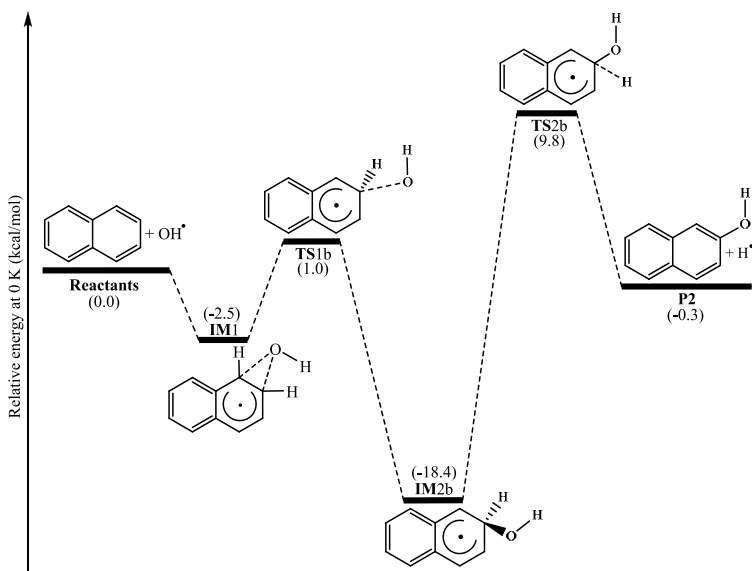


Figure 4.5. CBS-QB3 energy profile for the reaction pathway 2 characterizing the oxidation of naphthalene by OH radicals into 2-naphthol.

In Table 4.5, we provide reaction energies, enthalpies, entropies and Gibb's free energies for the conversion of naphthalene and OH radical (the reactants, R) into 1- and 2-naphthol plus one hydrogen atom (the products, P). Pathway **1** (R→P1) is an endothermic process ($\Delta H=1$ kcal mol⁻¹), whereas pathway **2** (R→P2) is slightly exothermic ($\Delta H=-0.1$ kcal mol⁻¹). Both pathways are found to be endergonic processes ($\Delta G > 0$) at ambient temperature and pressure. On both pathways (Figures 4.4 and 4.5), the global energy minima correspond to the energized adducts, IM2a and IM2b. At the benchmark CBS-QB3 level of theory, these are found to lie at 22.9 and 18.4 kcal mol⁻¹, respectively, below the reactants (Table 4.4). These stabilization energies are rather close to the BB1K/6-31+G(d,p) values (21.19 and 16.34 kcal mol⁻¹) supplied in the last theoretical study by Qu *et al.* [8]. The highest energies on both pathways correspond to the second transition states (TS2) describing the unimolecular dissociation of the energized adduct into 1- or 2-naphthol and one H-atom.

Table 4.5. Energy variations along the chemical reaction pathways **1–2** (see Figure 4.3) for the oxidation of naphthalene by OH[•] into 1-naphthol and 2-naphthol (results obtained at the benchmark CBS-QB3 level, at $T=298.15$ K and $P=1$ atm).

Reaction	step 1		step 2	
	R→IM2a	R→IM2b	IM2a→P1	IM2b→P2
ΔE^\ddagger (kcal mol ⁻¹)	-1.5	1.0	29.4	28.2
ΔH^\ddagger (kcal mol ⁻¹)	-2.2	0.3	29.3	28.0
ΔG^\ddagger (kcal mol ⁻¹)	5.9	8.6	30.1	28.6
ΔE (kcal mol ⁻¹)	-22.9	-18.3	23.6	18.1
ΔH° (kcal mol ⁻¹)	-23.8	-19.2	24.7	19.1
ΔG° (kcal mol ⁻¹)	-15.3	-10.8	17.8	12.5

Our calculations show that, for the hydrogen elimination from the C₁ and C₂-positions, the corresponding transition states (TS2a and TS2b) lie 6.5 and 9.8 kcal mol⁻¹, respectively, above the reactants (Figures 4.4 and 4.5). The barrier heights for the IM2a→P1 and IM2b→P2 decomposition reactions amount to 29.4 and 28.2 kcal mol⁻¹, respectively (Table 4.3).

As was to be expected, DFT calculations in conjunction with the B3LYP functional underestimate the reaction barriers, due to the self-interaction error. We also note that, in line with observations made in recent works [79,80], excluding the BSSE from UM05-2x and UM06-2x energy barriers would slightly improve the agreement with the benchmark and BSSE-free CBS-QB3 results, presumably because of a fortuitous cancellation of further errors (basis set convergence error

versus the approximate treatment of electron correlation and neglect of spin-orbit interactions). This observation seems to confirm the superiority of the latter two functionals for chemical kinetics. Nevertheless, some care is needed, because the UM05-2x and UM06-2x functionals do not incorporate corrections for dispersion forces, such as the ω B97XD functional. The computed BSSE corrections are around 0.2 kcal mol⁻¹ whereas the differences between the B3LYP and UM06-2x energy barriers are around 3 kcal mol⁻¹, so the exchange-correlation functional appears to be far more important than the BSSE corrections, when a basis set as large as aug-cc-pVTZ is used. More specifically, BSSE values for TS1a and TS1b range from 0.2 to 0.3 and 0.1 to 0.3 kcal mol⁻¹, respectively. Similarly, BSSE values for TS2a and TS2b are both equal to 0.1 kcal mol⁻¹. At the CBS-QB3 level of theory, because the basis set is complete, BSSEs are assumed to identically cancel.

On the basis of our benchmark CBS-QB3 estimates, Agmon's analysis [81] in line with the Leffler–Hammond's postulate [82] yield n_T values that are equal to 0.1 and 0.21 for the IM1→IM2a and IM1→IM2b reaction steps, respectively. For the IM2a→P1 and IM2b→P2 reaction steps, n_T is found to be equal to 0.71 and 0.64, respectively. In line with the energy profiles and structural observations made in the preceding section, this sequence implies that the TS1a and TS1b transition structures are more similar to the pre-reactive complex, whereas the TS2a and TS2b transition structures are more similar to the products.

Prior to ending this discussion of reaction energies and energy barriers, it is worth noticing that, at all employed levels of density functional theory, the spin contamination [$\langle S^2 \rangle_{\text{obs}} - 0.75$] never exceeds 0.051 (Table S2 of the Appendix II) and can thus, for all practical purposes, be regarded as relatively marginal. Some more care is needed for the CBS-QB3 results, because the successive MP2, MP3, MP4SDQ, and CCSD(T) calculations are based on strongly spin-contaminated symmetry-broken unrestricted Hartree-Fock (UHF) wave functions: at this level, the reported $\langle S^2 \rangle$ values are far above 0.75. It is, however, well-known that, in symmetry-breaking situations, the extent of spin contamination decreases with improving treatments of electron correlation [83], as is precisely the case with CBS-QB3 calculations. Besides, spin contamination for doublet radicals is known to be very small in symmetry-broken UHF-based CCSD calculations, even when the UHF spin contamination is very large [84]. A CBS-QB3 treatment is therefore expected to progressively compensate the artificial energy lowering [85,86] due to the symmetry breaking of the starting spin-contaminated UHF wave functions (see also refs. [87–90]), by including correlation corrections of improving quality. We

note indeed that, in spite of gigantic spin contamination problems [88,90], it has been possible to recover on extrapolated CCSD(T)/CBS theoretical grounds the ionization energies, electron attachment energies and singlet–triplet excitation energies of notoriously difficult compounds like *n*-acenes (*n*=1–6) within or very close to chemical accuracy (1 kcal mol⁻¹; i.e., 43 meV, see refs. 87, 91 and 92). Whereas the spin contamination observed for the IM1, TS1a, TS1b, and TS2a structures at the UHF level of theory is smaller than the spin contamination observed at the same level for the NO₂ radical, the situation seems more problematic with the energized adducts, IM2a and IM2b, and for the transition state (TS2b) associated with the unimolecular dissociation step in the pathway leading to 2-naphthol, which at the HF level yields $\langle S^2 \rangle$ values around 1.55, 1.66, and 1.87 respectively. An essential remark therefore for the forthcoming discussion of kinetic parameters is that, in view of the observed relative spin-contaminations at the HF level (Table S2 of the Appendix II), the CBS-QB3 energy barrier (TS2b) characterizing the irreversible unimolecular dissociation reaction step in the pathway leading to 2-naphthol may be underestimated by 1–2 kcal mol⁻¹, which may in turn result in an overestimation of the corresponding rate constant (IM2b→P2) by a factor 10–100. On the other hand, because the IM2b energized adduct is also afflicted by a rather severe spin contamination of the HF electronic wave function (Table S2 of the Appendix II), this intermediate species is also most likely subject to a comparable energy underestimation, in which case some error compensation is to be expected for the energy difference between the IM2b and TS2b structures.

4.3.3. Kinetic Parameters

TST and RRKM estimates for individual rate constants are listed in Tables 4.6 and 4.7 at a pressure of 1 bar, and at temperatures ranging from 300 to 407 K. In these tables, theoretical rate constants can also be compared with available experimental data [9,14,18]. Further RRKM data computed at lower and higher pressures are provided for the same temperatures in Tables S3a–S3e of the Appendix II. It is important to note that, on the experimental side [9,14,18], rate constants were obtained [14] using excimer laser photolysis to generate OH• radicals from HNO₃ as photolytic precursor. Since the reaction between OH• and its photolytic precursor contributes to the overall first order decay in the presence of the reactant (naphthalene), its concentration can be monitored continuously at the entrance of the reaction cell using UV absorption at 194 nm. The experimentally determined rate constants must correspond therefore to the first

hydroxyl radical addition step (i.e., the bimolecular reactions $R \rightarrow IM2a$ + $R \rightarrow IM2b$). The reader is referred to Figure 4.6 for a graphical display of the RRKM estimates for the individual rate constants for these two bimolecular reaction steps at the experimental pressure of 128 mbar [14] and the experimentally available values [9,14,18]. In line with experiment, whatever the pressure (Tables S3a–S3e of the Appendix II), the TST and RRKM data for the first bimolecular reaction step ($R \rightarrow IM2a$) in pathway **1** are all negatively dependent on the temperature, which indicates that, in the first step of the process, OH-addition at the C_1 position is favored at the investigated range of temperatures. In contrast, the TST and all RRKM rate constants for the first bimolecular reaction step ($R \rightarrow IM2b$) in pathway **2** are positively dependent on the temperature. Tables S3a–S3e of the Appendix II also confirm that $k_{IM1 \rightarrow IM2a}$ or $k_{IM1 \rightarrow IM2b}$ are much (at least 10^4 times) smaller than $k_{IM1 \rightarrow R}$, an observation that validates the steady state analysis leading to eq. (4.1).

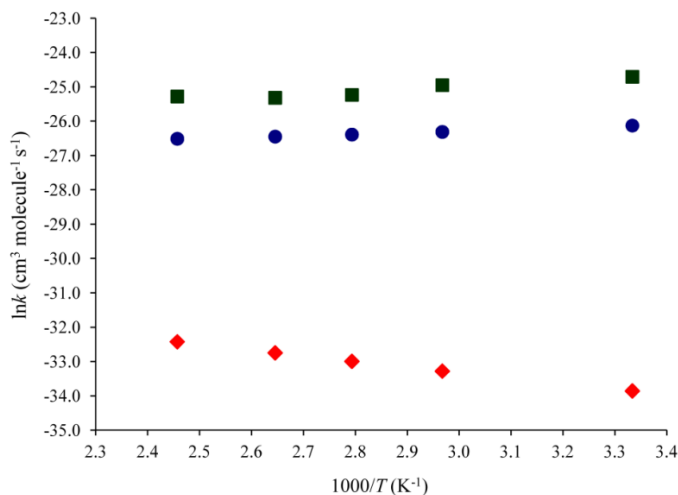


Figure 4.6. Arrhenius plot of the obtained RRKM bimolecular rate constants (for $R \rightarrow IM2x$, with $x=a,b$) versus experiment. Legend: (●) theoretical rate constant for pathway **1**; (◆) theoretical rate constant for pathway **2**; (■) experimental data [9,14,18].

The fact that the first bimolecular reaction step on pathway **1** is characterized by a slightly negative energy barrier whereas on pathway **2** it is characterized by a small positive energy barrier is conceptually not entirely sufficient, however, to explain why the production of 1-naphthol (P1) was experimentally found [26] to be favored by a factor 2:1 with respect to the production of 2-naphthol (P2). To check this fully on safe enough theoretical ground, one must evaluate effective kinetic rate constants that also account for the second unimolecular dissociation reaction step.

Table 4.6. Rate constants (units: unimolecular reactions in s^{-1} ; bimolecular reactions in $\text{cm}^3 \text{molecule}^{-1} \text{s}^{-1}$), effective rate constants, and branching ratios for the reported reaction channels by means of TST theory ($P=1 \text{ bar}$), according to the computed CBS-QB3 energy profiles (see methodology section for details).

T (K)	Rate constant						effective rate constant		branching ratio		k_{exp} [9,14,18]
	R→IM2a	R→IM2b	IM2a→R	IM2b→R	IM2a→P1	IM2b→P2	R→P1	R→P2	$R(1)$	$R(2)$	
300	4.49×10^{-14}	7.91×10^{-15}	3.12×10^{-2}	4.98×10^{-1}	2.76×10^{-6}	2.90×10^{-5}	3.97×10^{-18}	4.61×10^{-19}	89.61	10.39	$(18.6 \pm 1.0) \times 10^{-12}$
337	3.74×10^{-14}	1.41×10^{-14}	1.57×10^0	1.47×10^1	2.65×10^{-4}	2.18×10^{-3}	6.31×10^{-18}	2.09×10^{-18}	75.12	24.88	$(14.6 \pm 5.0) \times 10^{-12}$
358	3.46×10^{-14}	1.87×10^{-14}	8.90×10^0	7.55×10^1	2.37×10^{-3}	1.72×10^{-2}	9.21×10^{-18}	4.26×10^{-18}	68.38	31.62	$(11.0 \pm 4.4) \times 10^{-12}$
378	3.26×10^{-14}	2.40×10^{-14}	3.78×10^1	3.11×10^2	1.51×10^{-2}	9.84×10^{-2}	1.30×10^{-17}	7.59×10^{-18}	63.17	36.83	$(10.1 \pm 4.0) \times 10^{-12}$
407	3.06×10^{-14}	3.33×10^{-14}	2.38×10^2	1.96×10^3	1.56×10^{-1}	9.08×10^{-1}	2.00×10^{-17}	1.54×10^{-17}	56.52	43.48	$(10.5 \pm 4.0) \times 10^{-12}$

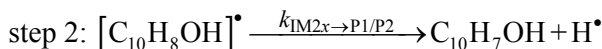
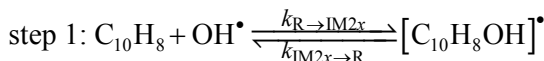
Table 4.7. Rate constants (units: unimolecular reactions in s^{-1} ; bimolecular reactions in $\text{cm}^3 \text{molecule}^{-1} \text{s}^{-1}$), effective rate constants, and branching ratios for the reported reaction channels by means of RRKM theory ($P=1 \text{ bar}$), according to the computed CBS-QB3 energy profiles (see methodology section for details).

T (K)	Rate constant						effective rate constant		branching ratio		k_{exp} [9,14,18]
	R→IM2a	R→IM2b	IM2a→R	IM2b→R	IM2a→P1	IM2b→P2	R→P1	R→P2	$R(1)$	$R(2)$	
300	2.92×10^{-14}	4.65×10^{-15}	2.87×10^{-2}	4.91×10^{-1}	1.47×10^{-6}	1.37×10^{-5}	1.50×10^{-18}	1.30×10^{-19}	92.02	7.98	$(18.6 \pm 1.0) \times 10^{-12}$
337	2.48×10^{-14}	6.76×10^{-15}	1.28×10^0	1.57×10^1	1.59×10^{-4}	1.19×10^{-3}	3.08×10^{-18}	5.12×10^{-19}	85.74	14.26	$(14.6 \pm 5.0) \times 10^{-12}$
358	2.31×10^{-14}	7.93×10^{-15}	7.86×10^0	8.22×10^1	1.48×10^{-3}	1.00×10^{-2}	4.35×10^{-18}	9.65×10^{-19}	81.85	18.15	$(11.0 \pm 4.4) \times 10^{-12}$
378	2.19×10^{-14}	9.02×10^{-15}	3.67×10^1	3.35×10^2	9.92×10^{-3}	6.13×10^{-2}	5.89×10^{-18}	1.65×10^{-18}	78.12	21.88	$(10.1 \pm 4.0) \times 10^{-12}$
407	2.03×10^{-14}	1.04×10^{-14}	2.63×10^2	2.02×10^3	1.13×10^{-1}	6.23×10^{-1}	8.76×10^{-18}	3.21×10^{-18}	73.21	26.79	$(10.5 \pm 4.0) \times 10^{-12}$

Indeed, the supplied TST and RRKM results (Tables 4.6 and 4.7) indicate that, at $P=1$ bar, the post-reactive intermediate IM2b decomposes ~ 10 times faster than the post-reactive intermediate IM2a, which seems also consistent with the view that the formation of 2-naphthol (P2) dominates the formation of 1-naphthol (P1) under ambient pressure, in the absence of molecular oxygen.

According to the RRKM results (Tables S4a–S4j of the Appendix II), this is only at pressures smaller than 0.1 mbar that deviations from the high pressure limit start to become numerically detectable (i.e., larger than ~ 1 %) for these reaction steps (IM2a \rightarrow P1, or IM2b \rightarrow P2). Nevertheless, at such exceedingly low pressures, further careful analyses employing the Master-Equation approach [93] are needed for quantitatively evaluating the outcome of additions of hydroxyl radicals on naphthalene away from chemical equilibrium, and under an inert (He) atmosphere.

To evaluate effective rate constants for the two competitive pathways (1,2) that prevail in the absence of molecular oxygen, and in view of the original hypothesis by Lorenz and Zellner [14], we assume that the kinetics of the whole reaction can be modeled according to a two-step mechanism, involving first a fast and reversible pre-equilibrium between the reactants ($C_{10}H_8$ and OH radicals) and energized adducts (IM2x with $x=a, b$), followed by an irreversible dissociation step (breaking of C–H bond) leading to 1- and 2-naphthol (the products, P1 and P2):



The second step is assumed to be irreversible, because the original experience by Lorenz and Zellner [14] was performed under steady flow conditions in the reaction cell, implying continuous displacements of the reaction towards the formation of 1- and 2-naphthol. Therefore, a steady-state analysis upon the above sequence of reactions leads to the following expressions for the effective rate constants characterizing pathways 1 and 2:

$$k_{\text{eff}}(1) = \frac{k_{R \rightarrow IM2a} k_{IM2a \rightarrow P1}}{k_{IM2a \rightarrow R} + k_{IM2a \rightarrow P1}} \quad (4.4)$$

$$k_{\text{eff}}(2) = \frac{k_{R \rightarrow IM2b} k_{IM2b \rightarrow P2}}{k_{IM2b \rightarrow R} + k_{IM2b \rightarrow P2}} \quad (4.5)$$

In the above equations, $k_{R \rightarrow IM2x}$ is the kinetic rate constant characterizing the forward bimolecular reaction step (in $\text{cm}^3 \text{ molecule}^{-1} \text{ s}^{-1}$), whereas $k_{IM2x \rightarrow P}$ and $k_{IM2x \rightarrow R}$ represent the forward and backward unimolecular reaction rate constants

(in s^{-1}). The supplied RRKM data (Tables S4a–S4j of the Appendix II) indicate that, from 1 bar down to pressures of 0.01 mbar, $k_{\text{IM2a}\rightarrow\text{P1}}$ and $k_{\text{IM2b}\rightarrow\text{P2}}$ are much (at least 10^3 times) smaller than $k_{\text{IM2a}\rightarrow\text{R}}$ and $k_{\text{IM2b}\rightarrow\text{R}}$, respectively, and can thus be neglected from the above denominators. This implies further that, at pressures larger than 0.01 mbar:

$$k_{\text{eff}}(1) = K_c(1) k_{\text{IM2a}\rightarrow\text{P1}} \quad (4.6)$$

$$k_{\text{eff}}(2) = K_c(2) k_{\text{IM2b}\rightarrow\text{P2}} \quad (4.7)$$

where $K_c(1)$ and $K_c(2)$ are the relevant equilibrium constants for the pre-equilibrium between the reactants and the energized adducts:

$$K_c(1) = \frac{k_{\text{R}\rightarrow\text{IM2a}}}{k_{\text{IM2a}\rightarrow\text{R}}} = \frac{[\text{IM2a}]}{[\text{C}_{10}\text{H}_8][\text{OH}^\bullet]} \quad (4.8)$$

$$K_c(2) = \frac{k_{\text{R}\rightarrow\text{IM2b}}}{k_{\text{IM2b}\rightarrow\text{R}}} = \frac{[\text{IM2b}]}{[\text{C}_{10}\text{H}_8][\text{OH}^\bullet]} \quad (4.9)$$

Equations (4.6–4.9) show that the overall kinetics of the hydroxyl radical addition pathways on naphthalene does not depend upon the energy barriers characterizing the first bimolecular rate constants, but upon the Gibb’s free energy differences between the reactants and the energized adducts $[\text{C}_{10}\text{H}_8\text{OH}^\bullet]$ (IM1a, IM1b) as well as upon the energy barriers characterizing the subsequent unimolecular dissociation reaction steps (i.e., cleavages of C–H bonds). We correspondingly report in Tables 4.6 and 4.7, as well as in Tables S4a–S4j of the Appendix II, branching ratios, which were obtained according to:

$$R(1) = \frac{k_{\text{eff}}(1)}{k_{\text{eff}}(1) + k_{\text{eff}}(2)} \quad (4.10)$$

and

$$R(2) = \frac{k_{\text{eff}}(2)}{k_{\text{eff}}(1) + k_{\text{eff}}(2)} \quad (4.11)$$

using eqs. (4.6) and (4.7) for computing $k_{\text{eff}}(1)$ and $k_{\text{eff}}(2)$. These data indicate that, at all considered pressures, and qualitatively in line with the theoretical analysis by Ricca and Bauschlischer [26], as well as with the experimental observation they invoke from a personal communication by M.P. Bernstein, the most abundant product resulting from the oxidation of naphthalene by OH radicals is undoubtedly 1-naphthol (P1). This conclusion will most certainly remain valid at better theoretical levels than CBS-QB3, because we expect this approach to slightly

underestimate, by 1–2 kcal mol⁻¹, the energy barrier (TS2b) characterizing the irreversible dissociation step in the pathway leading to 2-naphthol, and to yield in turn an overestimation by a factor 10–100 of the corresponding rate constant (IM2b→P2), relative to the constant characterizing the other dissociation pathway (IM2a→P1). In view of the supplied RRKM data (Tables S4a–S4j of the Appendix II), it is thus more than certain that, at 300 K, the production of 1-naphthol must dominate the overall reaction mechanism, and this down to extremely low pressures, larger than 10⁻⁸ bar. From these data, and the correspondingly computed regioselectivity indices [RSI=R(1)–R(2), Figure 4.7], we also note overall a decrease of the regioselectivity of the reaction with increasing temperatures and lowering pressures.

The production of 1-naphthol over 2-naphthol with a ratio 2:1 is observed for instance at $P=10^{-3}$ bar and at T around 337 K. Lacking any information on the conditions under which the experiments by M.P. Bernstein were made, we can only strongly advocate further detailed experimental studies of the oxidation mechanisms of naphthalene by hydroxyl radicals, to verify the relevance of our theoretical estimates for branching ratios.

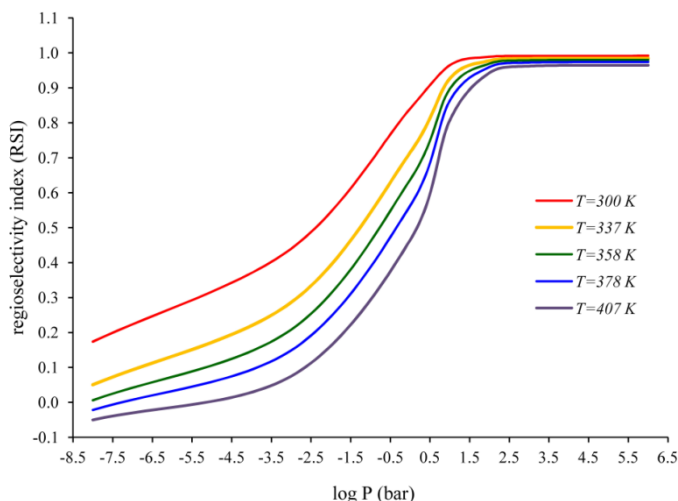


Figure 4.7. Dependence upon the pressure and temperature of the regioselectivity [RSI = $R(1) - R(2)$] of OH radical addition on naphthalene, according to the RRKM estimates of effective rate constants [$k_{\text{eff}}(1), k_{\text{eff}}(2)$] supplied in Tables S4a–S4j (see Appendix II).

Experimental kinetic rate constants ascribed to the first bimolecular reaction steps ($R \rightarrow \text{IM2a}$ and $R \rightarrow \text{IM2b}$) in pathways **1** and **2** can be compared with the corresponding RRKM data displayed in Figure 4.6, for a pressure of 128 mbar.

Our theoretical rate constants for these reaction steps were fitted by means of least-squares regressions to a three-parameter Arrhenius equation ($k=A \cdot T^n \cdot e^{-B/RT}$), to obtain the exponent n , the effective preexponential factor A , and the activation barrier B which characterize pathways **1** and **2** according to the decay rate of the concentration of hydroxyl radicals. This fitting procedure led correspondingly to the following expressions: $k_1(T) = 1.02 \times 10^{-14} T^{-0.369} \exp(340.4/T)$, and $k_2(T) = 2.72 \times 10^{-10} T^{-1.544} \exp(-990.9/T) \text{ cm}^3 \text{ molecule}^{-1} \text{ s}^{-1}$, respectively, at a pressure of 128 mbar and over the temperature range 300–407 K. We emphasize again that, at pressures lower than 10 bar, and in line with the experimental observations by Lorenz and Zellner [14], the rate constants characterizing the first bimolecular reaction steps $R \rightarrow \text{IM2a}$ and $R \rightarrow \text{IM2b}$ decrease and increase, respectively, as the temperature increases (Tables S4a–S4j of the Appendix II).

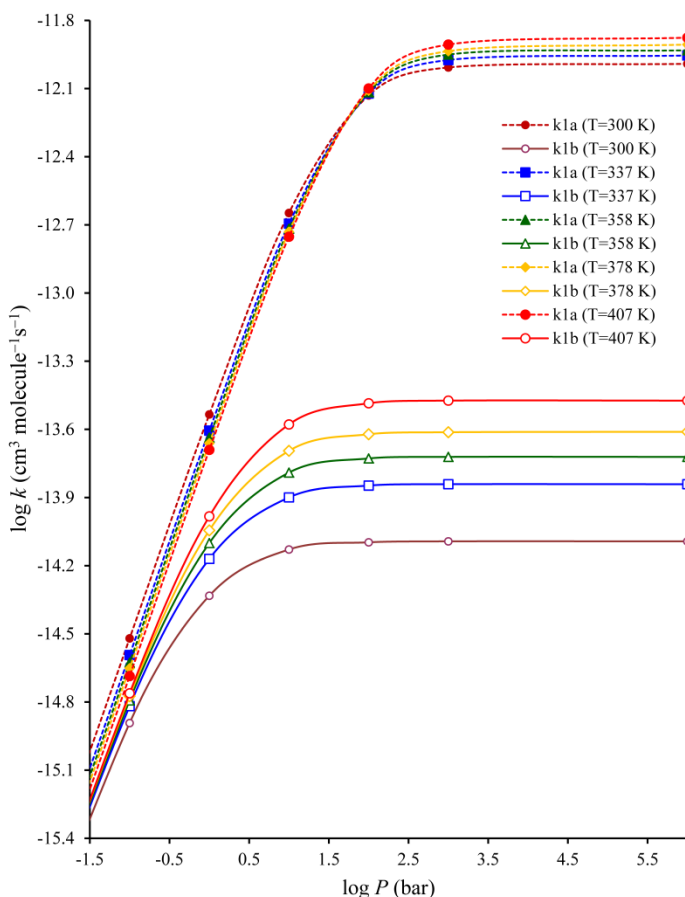


Figure 4.8: Pressure dependence of the bimolecular rate constants for the $R \rightarrow \text{IM2a}$ (k_{1a}) and $R \rightarrow \text{IM2b}$ (k_{1b}) reaction steps [RRKM results, obtained by means of eq. (4.3)].

More specifically, from Figure 4.8 and Table 4.8, it is clear that, at the experimental pressure of 128 mbar [14], the RRKM rate constants obtained from the CBS-QB3 energy profiles for the R→IM2a reaction step along the chemical pathway leading to 1-naphthol underestimate the experimental ones by about two orders of magnitude only. Both the experimental rate constants and theoretical rate constants for this reaction step decrease with increasing temperatures. This qualitatively excellent agreement between theory and experiment makes us believe that the physical chemistry of these complicated processes has been correctly captured: it confirms the relevance of both the proposed reaction mechanism and employed quantum chemical models. Note that the overall rate constants reported in Table 4.8 for the formation of 1-naphthol or 2-naphthol indicate that this reaction is too slow to compete with further reaction channels. Most likely, in the experiment by Lorenz and Zellner [14], removal of the intermediate adducts IM2a and IM2b is most likely to be ascribed to recombination with further OH radicals.

Table 4.8. Rate constants (units: unimolecular reactions in s^{-1} ; bimolecular reactions in $\text{cm}^3 \text{molecule}^{-1} \text{s}^{-1}$), effective rate constants, and branching ratios for the reported reaction channels by means of RRKM theory ($P=128 \text{ mbar}$).

T (K)	Rate constant						effective rate constant		branching ratio		$k_{\text{exp}} \times 10^{12}$ [9,14,18]
	R→IM2a	R→IM2b	IM2a→R	IM2b→R	IM2a→P1	IM2b→P2	R→P1	R→P2	R(1)	R(2)	
300	3.87×10^{-15}	1.49×10^{-15}	2.87×10^{-2}	4.90×10^{-1}	1.47×10^{-6}	1.37×10^{-5}	1.98×10^{-19}	4.17×10^{-20}	82.63	17.37	18.6 ± 1.0
337	3.26×10^{-15}	1.81×10^{-15}	1.28×10^0	1.57×10^1	1.59×10^{-4}	1.19×10^{-3}	4.05×10^{-19}	1.37×10^{-19}	74.69	25.31	14.6 ± 5.0
358	3.02×10^{-15}	1.93×10^{-15}	7.84×10^0	8.16×10^1	1.48×10^{-3}	1.00×10^{-2}	5.70×10^{-19}	2.36×10^{-19}	70.68	29.32	11.0 ± 4.4
378	2.85×10^{-15}	2.03×10^{-15}	3.65×10^1	3.32×10^2	9.91×10^{-3}	6.13×10^{-2}	7.74×10^{-19}	3.75×10^{-19}	67.37	32.63	10.1 ± 4.0
407	2.64×10^{-15}	2.10×10^{-15}	2.61×10^2	1.98×10^3	1.13×10^{-1}	6.23×10^{-1}	1.14×10^{-18}	6.61×10^{-19}	63.36	36.64	10.5 ± 4.0

When Tables 4.6 and 4.7 and Table S4e of the Appendix II are compared, it appears that TST and RRKM data at 1 bar are not all strictly equal, indicating that the high pressure limit has not been reached at this pressure for all considered reaction channels. Very interestingly, upon scrutinizing further the RRKM values in Tables S4a–S4j of the Appendix II, the high (infinite) pressure limit for the IM2x→Px, IM2x→R and IM1→IM2b reaction steps is reached within 1% accuracy when the pressure exceeds 10^{-4} , 10^{-3} and 10^2 bar, respectively, whatever the temperature (see also Figure 4.9 for a logarithmic plot of the bimolecular rate constants for the R→IM2a and R→IM2b reaction steps as a function of the pressure and temperature). These observations can be correlated with energy barriers equal to 28.2 or 29.4 kcal mol⁻¹, 21.4 or 19.4 kcal mol⁻¹, and 3.5 kcal

mol⁻¹, respectively. In line with an effective negative energy barrier (-1 kcal mol⁻¹), this is only at a pressure of 10³ bar that some convergence to the high pressure limit starts to be seen for the IM1→IM2a reaction step. More specifically, Figures 4.8 and 4.9 and the kinetic data supplied in the Appendix II show that pressures larger than 10⁵ bar are required for restoring the validity of the transition state approximation for the first bimolecular reaction steps within ~5% accuracy. Besides the low or even negative energy barriers, such a high pressure value may in addition also be the consequence of the large molecular volume of the reactant and the extent of the depth (~100 kJ mol⁻¹) of the interaction well between naphthalene and hydroxyl radicals.

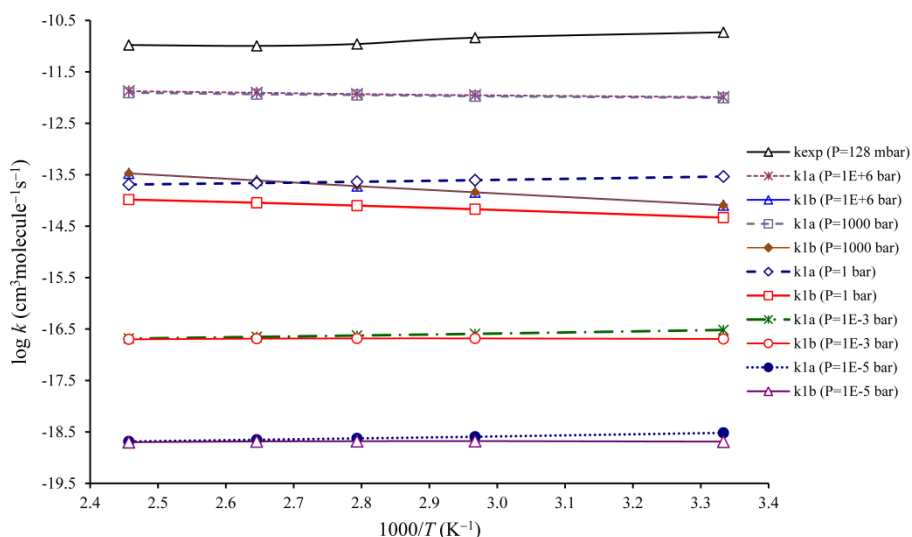


Figure 4.9: Arrhenius plot of the RRKM bimolecular rate constants (k_{1x} , with $x=a,b$) for the $R \rightarrow IM_{2x}$ ($x=a,b$) reaction steps.

4.3.4. Bond Order Analysis

Several bonds are breaking whereas other chemical bonds get formed during the OH addition process. Bond indices were calculated for the $n=9$ bonds which were substantially altered by hydroxyl radical addition; namely, the C₁-C₂, C₂-C₃, C₃-C₄, C₄-C₁₀, C₉-C₁₀, C₁-C₉, C₁-O, C₂-O, and O-H bonds (Figure 4.2); all other bonds remain practically unaltered during the reaction.

The calculated Wiberg bond indices B_i for the reactants (C₁₀H₈ and OH), transition states (TS1a and TS1b) and post-reactive complexes (IM2a and IM2b) enable us (Table 4.9) to examine the progress of the reactions **1** and **2** and position

of the transition states between reactants and products. For both reactions, according to the relative changes in bond order, the most strongly affected chemical bond is C₁–C₂, which during the process becomes a single C–C bond. The chemical reaction pathways **1** and **2** are characterized by a synchronicity value around ~0.87, which reveals a chemical process that is concerted, but not fully synchronic.

Table 4.9. Bond order analysis of structures involved in the chemical reaction pathways **1** and **2** at the B3LYP/6-311G(2d,d,p) level of theory.

Bond												
Pathway		C ₁ -C ₂	C ₂ -C ₃	C ₃ -C ₄	C ₄ -C ₁₀	C ₅ -C ₁₀	C ₁ -C ₉	C ₁ -O	C ₂ -O	H-O	δB_{av}	S_s
(1)	$B_i(R)$	1.554	1.310	1.554	1.272	1.232	1.272	0.000		0.857	0.230	0.868
	$B_i(TS1a)$	1.395	1.344	1.519	1.250	1.242	1.209	0.224		0.837		
	$B_i(IM2a)$	1.030	1.572	1.338	1.195	1.287	0.999	0.891		0.789		
	$\%EV$	30.46	13.14	16.24	28.41	18.46	23.15	25.15		29.31		
(2)	$B_i(R)$	1.554	1.310	1.554	1.272	1.232	1.272		0.000	0.857	0.296	0.874
	$B_i(TS1b)$	1.364	1.216	1.618	1.220	1.221	1.287		0.283	0.833		
	$B_i(IM2b)$	1.038	1.022	1.799	1.126	1.179	1.376		0.881	0.791		
	$\%EV$	36.79	32.45	26.19	35.82	21.87	14.49		32.09	36.73		

Wiberg bond indexes (B_i), % evolution through the reaction coordinate ($\%EV$), average bond index variation (δB_{av}) and Synchronicity parameter (S_s) are shown.

4.3.5. Natural Bond Orbital Analysis

Based on the B3LYP/6-311G(2d,d,p) optimized geometries and electronic structure characteristics of the IM2a and IM2b energized adducts, the NBO analysis of donor–acceptor interactions (Table 4.10) shows that the stabilization energies E_2 (eq. 2.112) associated with the electron delocalization from non-bonding oxygen lone-pair orbitals [n_o] to $\sigma^*(C_1-C_2)$ antibonding orbitals are around 3.3 kcal mol⁻¹. According to the NBO analysis, the $\sigma(C_1-C_2)$ bonding orbital occupancies in these systems are both equal to 0.99, whereas the $\sigma^*(C_1-C_2)$ antibonding orbital occupancies in the energized adducts IM2a and IM2b amount to 0.015 and 0.014, respectively.

In the TS1a and TS1b transition states, there are two non-bonding oxygen lone-pairs and one unpaired electron on the oxygen atom, whereas in the IM2a and IM2b intermediates, there are only two nonbonding oxygen lone-pairs [n_o]. Inspection of the NBO data reported in Table 4.10 for the TS1a and TS1b transition states reveals that a very strong interaction prevails in between one of the

oxygen lone pairs of the hydroxyl radical and the unoccupied $\pi^*(C_1-C_2)$ orbital, resulting for the latter orbital in an occupancy around 0.15. The corresponding stabilization energies range from 8.9 to 14.2 kcal mol⁻¹. These results are in line with the donation of one electron from OH[•] to the $\pi^*(C_1-C_2)$ orbital, during the oxidation process. The NBO analysis demonstrates therefore that anomeric [$n_{O(1)} \rightarrow \sigma^*_{C_1-C_2}$] and hyperconjugative [$n_{O(1)} \rightarrow \pi^*_{C_1-C_2}$] interactions have a significant influence on the computed activation energies and reaction energies. Nevertheless, it appears that the delocalization energy for TS1a is 5.3 kcal mol⁻¹ smaller than that for TS1b (Table 4.10), whereas the [B3LYP/6-311G(2d,d,p)] energy of TS1a is 2.5 kcal mol⁻¹ lower than that of TS1b (Table 4.3). These observations indicate that aromatic effects dominate anomeric and hyperconjugation effects, as one would quite naturally expect.

Table 4.10. NBO occupancies and stabilization energies (in kcal mol⁻¹) characterizing intermediate and transition structures along the chemical reaction pathways **1** and **2** (results obtained at the B3LYP/6-311G(2d,d,p) level of theory).

	B3LYP/6-311G(2d,d,p)			
	IM2a	IM2b	TS1a	TS1b
Occupancies				
$\sigma(C_1-C_2)$	0.9902	0.9906	0.9902	0.9904
$\sigma^*(C_1-C_2)$	0.0149	0.0140	0.0071	0.0071
$\pi(C_1-C_2)$	-	0.8116	0.8499	0.8584
$\pi^*(C_1-C_2)$	-	0.4909	0.1426	0.1532
$n_{O(1)}$	0.9923	0.9925	0.9983	0.9983
$n_{O(2)}$	0.9792	0.9800	0.9922	0.9898
$n_{O(3)}$	-	-	0.9587	0.9411
Stabilization energies (E_2)				
$n_{O(1)} \rightarrow \sigma^*(C_1-C_2)$	3.28	3.27	-	0.03
$n_{O(1)} \rightarrow \pi^*(C_1-C_2)$	-	5.08	0.97	1.48
$n_{O(2)} \rightarrow \pi^*(C_1-C_2)$	-	1.03	-	0.16
$n_{O(3)} \rightarrow \pi^*(C_1-C_2)$	-	-	8.88	14.17

4.4. Conclusions

The oxidation mechanisms of naphthalene initiated by OH radicals in the gas phase have been studied computationally using density functional theory along with various exchange-correlation functionals (B3LYP, ω B97XD, UM05-2x, and UM06-2x) and an extremely large basis set (aug-cc-pVTZ). The supplied reaction energies and activation barriers incorporate zero-point vibrational energy

differences and counterpoise corrections for basis set superposition errors. Comparison has been made with benchmark computational results obtained at the composite CBS-QB3 level of theory. The best agreement with the computed reaction energies and energy barriers is obtained with the UM05-2x exchange-correlation function. Kinetic rate constants were correspondingly estimated in the high pressure limit by means of transition state theory, on the grounds of partition functions calculated using the rigid rotor-harmonic oscillator (RRHO) approximation. Their pressure dependence has been investigated by means of RRKM theory. The main focus of the present study was on the reaction steps involved in the so-called hydroxyl radical addition pathway. Note that the reaction mechanisms involved in the so-called hydrogen abstraction pathway will be subject of a separate study [94], on similar theoretical CBS-QB3 and DFT grounds.

The obtained results indicate that the experimental rate constants supplied by Atkinson [9] correspond to a bimolecular reaction step leading to a molecular energized adduct [$C_{10}H_8OH^*$]. This first reaction step is strongly exergonic at ambient temperature and pressure. In line with experiment, due to the formation of a pre-reactive van der Waals (VdW) molecular complex [$C_{10}H_8\cdots OH$] * , the corresponding transition state lies below the reactant, hence an effective negative activation energy around $-1.5 \text{ kcal mol}^{-1}$ on the reaction pathway leading to 1-naphthol. In contrast, on the reaction pathway leading to 2-naphthol, the first bimolecular reaction step is characterized by a positive activation energy, around $1.0 \text{ kcal mol}^{-1}$.

The formation of the energized adduct is followed by a unimolecular reaction step that is strongly endergonic at ambient temperature and pressure, and which corresponds to the elimination of a hydrogen atom (H^*), yielding 1- or 2-naphthol. Effective rate constants have been calculated according to a steady state analysis upon to a two-step model reaction mechanism, assuming reversibility of the first bimolecular addition reaction step, and irreversibility of the second unimolecular dissociation step. In line with the experimental observations by Lorenz and Zellner [14], the correspondingly obtained branching ratios indicate that the most abundant product resulting from the oxidation of naphthalene by hydroxyl radicals must be 1-naphthol rather than 2-naphthol. These branching ratios also indicate that the regioselectivity of the OH addition pathways onto naphthalene decrease with increasing temperatures and decreasing pressures. In line with slightly positive or even negative activation energies, it was found that the transition state approximation breaks down at ambient pressure (1 bar) for the first bimolecular reaction steps. This is particularly true for the first bimolecular reaction step

involved in the OH[•] addition pathway leading to 1-naphthol, which is characterized by an effective activation energy of $-1.5 \text{ kcal mol}^{-1}$. RRKM calculations show in particular that overwhelmingly high pressures, larger than 10^5 bar , would be required for restoring within $\sim 5\%$ accuracy the validity of this approximation for *all* reaction channels in the OH addition pathway, in particular for the conversion of the pre-reactive VdW complex $[\text{C}_{10}\text{H}_8\cdots\text{OH}]^{\bullet}$ into the molecular energized adduct $\text{C}_{10}\text{H}_8\text{OH}^{\bullet}$.

Analysis of the computed structures, bond orders, and free energy profiles demonstrate that the reaction steps involved in the oxidation of naphthalene by hydroxyl radicals satisfy Leffler–Hammond’s principle: the transition states for the exergonic bimolecular reaction steps are structurally closer to the pre-reactive VdW complexes, whereas the transition states for the subsequent endergonic unimolecular reaction steps are structurally closer to the products, 1- or 2-naphthol. NICS indices and natural bond orbital analysis also show that the computed activation and reaction energies are largely dictated by alterations of aromaticity and, to a lesser extent, by anomeric and hyperconjugative effects pertaining to the delocalization of oxygen lone pairs to neighboring empty $\sigma_{\text{C1-C2}}^*$ and $\pi_{\text{C1-C2}}^*$ orbitals.

4.5. References

- [1] H. Tokiwa, Y. Ohnishi, H.S. Rosenkranz, *CRC Crit. Rev. Toxicol.*, **1986**, 17, 23.
- [2] P.D. Josephy, B. Mannervik, P.O. De Montellano, *Molecular Toxicology*; Oxford University Press: Oxford, 1997.
- [3] A.M. Mastral, M.S. Callen, *Environ. Sci. Technol.*, **2000**, 34, 3051.
- [4] C.E. Boström, P. Gerde, A. Hanberg, B. Jernström, C. Johansson, T. Kyrklund, A. Rannug, M. Törnqvist, K. Victorin, R. Westerholm, *Environ. Health Perspect.*, **2002**, 110, 451.
- [5] S.O. Baek, R.A. Field, M.E. Goldstone, P.W. Kirk, J.N. Lester, R. Perry, *Water, Air, Soil & Pollution.*, **1991**, 60, 279.
- [6] N.J. Bunce, L. Liu, J. Zhu, *Environ. Sci. Technol.*, **1997**, 31, 2252.
- [7] R. Atkinson, J. Arey, *Environ. Health Perspect.*, **1994**, 102, 117.
- [8] X. Qu, Q. Zhang, W. Wang, *Chem. Phys. Lett.*, **2006**, 429, 77.
- [9] R. Atkinson, *J. Phys. Chem. Ref. Data, Monograph*, **1989**, 1, 1.
- [10] R. Atkinson, E.C. Tuazon, J. Arey, *Int. J. Chem. Kinet.*, **1990**, 22, 1071.
- [11] R. Atkinson, *J. Phys. Chem. Ref. Data, Monograph*, **1991**, 20, 459.

- [12] R. Atkinson, E.C. Tuazon, I. Bridier, J. Arey, *Int. J. Chem. Kinet.*, **1994**, *26*, 605.
- [13] J. Sasaki, S.M. Aschmann, E.S.C. Kwok, R. Atkinson, J. Arey, *Environ. Sci. Technol.*, **1997**, *31*, 3173.
- [14] K. Lorenz, R. Zellner, *Ber. Bunsen-Ges. Phys. Chem.*, **1983**, *87*, 629.
- [15] J. Arey, B. Zielinska, R. Atkinson, A.M. Winer, *Atmos. Environ.*, **1967**, *21*, 1437.
- [16] J. Arey, R. Atkinson, B. Zielinska, P.A. McElroy, *Environ. Sci. Technol.*, **1989**, *23*, 321.
- [17] J.L. Durant, A.L. Lafleur, E.F. Plummer, K. Taghizadeh, W.F. Busby, W.G. Thilly, *Environ. Sci. Technol.*, **1998**, *32*, 1894.
- [18] K. Lorenz, R. Zellner, *8th International Symposium on Gas Kinetics*; University of Nottingham, Nottingham, UK, 15–20 July, 1984.
- [19] R. Atkinson, S.M. Aschmann, J.N. Pitts, *Environ. Sci. Technol.*, **1984**, *18*, 110.
- [20] H.W. Biermann, H. Mac Leod, R. Atkinson, A.M. Winer, J.N. Pitts, *Environ. Sci. Technol.*, **1985**, *19*, 244.
- [21] R. Atkinson, S.M. Aschmann, *Int. J. Chem. Kinet.*, **1986**, *18*, 569.
- [22] L.C. Sander, S.A. Wise, In *NIST Chemistry WebBook*; NIST Standard Reference Database 69; National Institute of Standards and Technology: Gaithersburg, MD, (January) 2014, naphthalene (<http://webbook.nist.gov>).
- [23] W.W. Brubaker, R.A. Hites, *J. Phys. Chem. A*, **1998**, *102*, 915.
- [24] V.W. Klöpffer, R. Frank, E.G. Kohl, F. Haag, *Chem. Ztg.*, **1986**, *110*, 57.
- [25] R. Atkinson, *Chem. Rev.*, **1985**, *85*, 69.
- [26] A. Ricca, C.W. Bauschlicher, Jr. *Chem. Phys. Lett.*, **2000**, *328*, 396.
- [27] Z. Zhang, L. Lin, L. Wang, *Phys. Chem. Chem. Phys.*, **2012**, *14*, 2645.
- [28] D.S. Hollman, A.C. Simmonett, H.F. Schaefer, *Phys. Chem. Chem. Phys.*, **2011**, *13*, 2214.
- [29] S.S. Zade, M. Bendikov, *J. Phys. Org. Chem.*, **2012**, *25*, 452.
- [30] C.H. Suresh, S.R. Gadre, *J. Org. Chem.*, **1999**, *64*, 2505.
- [31] R. Casanovas, J. Frau, J. Ortega-castro, A. Salva, J. Donoso, F. Munoz, *Int. J. Quantum. Chem.*, **2010**, *110*, 323.
- [32] J.A. Montgomery, M.J. Frisch, J.W. Ochterski, G.A. Petersson, *J. Chem. Phys.*, **1999**, *110*, 2822.
- [33] J.W. Ochterski, G.A. Petersson, J.A. Montgomery, *J. Chem. Phys.*, **1996**, *104*, 2598.
- [34] M.R. Nyden, G.A. Petersson, *J. Chem. Phys.*, **1981**, *75*, 1843.

- [35] G.A. Petersson, A. Bennett, T.G. Tensfeld, M.A. Al-Laham, W. Shirley, J. Matzaris, *J. Chem. Phys.*, **1988**, *89*, 2193.
- [36] G.A. Petersson, M.A. Al-Laham, *J. Chem. Phys.*, **1991**, *94*, 6081.
- [37] G.A. Petersson, A.K. Yee, A. Bennett, *J. Chem. Phys.*, **1983**, *83*, 5105.
- [38] J.A. Montgomery, J.W. Ochterski, G.A. Petersson, *J. Chem. Phys.*, **1994**, *101*, 5900.
- [39] J.A. Montgomery, M.J. Frisch, J.W. Ochterski, G.A. Petersson, *J. Chem. Phys.*, **2000**, *112*, 6532.
- [40] P. Cysewski, *J. Mol. Struct. (THEOCHEM)*, **2005**, *714*, 29.
- [41] P.v.R. Schleyer, C. Maerker, A. Dransfeld, H. Jiao, N.J.R. van Eikema Hommes, *J. Am. Chem. Soc.*, **1996**, *118*, 6317.
- [42] S. Nigam, C. Majumder, S.K. Kulshreshtha, *J. Chem. Sci.*, **2006**, *118*, 575.
- [43] P.v.R. Schleyer, M. Manoharan, Z.X. Wang, B. Kiran, H.J. Jiao, R. Puchta, N. Hommes, *Org. Lett.*, **2001**, *3*, 2465.
- [44] P.v.R. Schleyer, H. Jiao, B. Goldfuss, P.K. Freeman, *Angew. Chem. Int. Ed. Engl.*, **1995**, *34*, 337.
- [45] A.E. Reed, R.B. Weinstock, F. Weinhold, *J. Chem. Phys.*, **1985**, *83*, 735.
- [46] J.K. Badenhoop, F. Weinhold, *Int. J. Quantum. Chem.*, **1999**, *72*, 269.
- [47] M.J. Frisch, G.W. Trucks, H.B. Schlegel, G.E. Scuseria, M.A. Robb, J.R. Cheeseman, G. Scalmani, V. Barone, B. Mennucci, G.A. Petersson, *et al. Gaussian 09*, Revision B.01; Gaussian: Wallingford, CT, 2009.
- [48] I.I.R. Dennington, T. Keith, J. Millam, K. Eppinnett, W.L. Hovell, R. Gilliland, *GaussView*, Version 3.09; Semichem, Inc.: Shawnee Mission, KS, 2003.
- [49] C. Lee, W. Yang, R.G. Parr, *Phys. Rev B*, **1988**, *37*, 785.
- [50] A.D. Becke, *J. Chem. Phys.*, **1993**, *98*, 5648.
- [51] J.D. Chai, M. Head-Gordon, *Phys. Chem. Chem. Phys.*, **2008**, *10*, 6615.
- [52] Y. Zhao, D.G. Truhlar, *Acc. Chem. Res.*, **2008**, *41*, 157.
- [53] T.H. Dunning, *J. Chem. Phys.*, **1989**, *90*, 1007.
- [54] D.A. McQuarrie, *Statistical Mechanics*; Harper and Row: New York, 1976.
- [55] G.H. Herzberg, *Molecular Spectra and Molecular Structure. II Infrared and Raman Spectra of Polyatomic Molecules*; Van Nostrand Reinhold: New York, 1945.
- [56] S. Canneaux, R. Vandeputte, C. Hammaeher, F. Louis, M. Ribaucour, *J. Phys. Chem. A*, **2012**, *116*, 592.
- [57] F. Fukui, *J. Phys. Chem.*, **1970**, *74*, 4161.
- [58] J.W. McIver, Jr. **1974**, *7*, 72.
- [59] I.V. Tokmakov, M.C. Lin, *J. Phys. Chem. A*, **2002**, *106*, 11309.

- [60] S.F. Boys, F. Bernardi, *Mol. Phys.*, **1970**, *19*, 553.
- [61] M. Huang, Z. Wang, Y. Yang, L. Hao, W. Zhao, X. Gao, L. Fang, W. Zhang, *Int. J. Quantum. Chem.*, **2007**, *107*, 1092.
- [62] K. Walczak, J. Friedrich, M. Dolg, *Chem. Phys.*, **2009**, *365*, 38.
- [63] R. Chang, *Physical Chemistry for the Biosciences*; University Science Books, Sausalito: California, 2005.
- [64] J.W. Moore, R.G. Pearson, *Kinetics and Mechanism-The Study of Homogeneous Chemical Reactions*; 3rd ed., Wiley: New York, 1981.
- [65] H.H. Carstensen, A.M. Dean, O. Deutschmann, *Proc. Combust. Inst.*, **2007**, *31*, 149.
- [66] C. Eckart, *Phys. Rev.*, **1930**, *35*, 1303
- [67] D.H. Varma, P. Raghunath, M.C. Lin, *J. Phys. Chem. A*, **2010**, *114*, 3642.
- [68] S.Y. Wu, P. Raghunath, J.S. Wu, M.C. Lin, *J. Phys. Chem. A*, **2010**, *114*, 633.
- [69] R.G. Gilbert, S.C. Smith, *Theory of Unimolecular and Recombination Reactions*; Blackwell Scientific Publications: Oxford, 1990.
- [70] H.B. Rao, X.Y. Zeng, H. He, Z.R. Li, *J. Phys. Chem. A*, **2011**, *115*, 1602.
- [71] P.J. Robinson, K.A. Holbrook, *Unimolecular Reactions*; Wiley: New York, 1972.
- [72] J.I. Steinfeld, J.S. Francisco, W.L. Hase, *Chemical Kinetics and Dynamics*; Prentice- Hall: Englewood Cliffs, NJ, 1999.
- [73] H. Eyring, S.H. Lin, S.M. Lin, *Basic Chemical Kinetics*; Wiley: New York, **1980**.
- [74] S. Canneaux, F. Bohr, E. Henon, *J. Comput. Chem.*, **2014**, *35*, 82.
- [75] T. Troe, *J. Chem. Phys.*, **1977**, *66*, 4758.
- [76] J.O. Hirschfelder, C.F. Curtiss, R.B. Bird, *Molecular Theory of Gases and Liquids*; Wiley: New York, 1954.
- [77] Y. Iwai, H. Higashi, H. Uchida, Y. Arai, *Fluid. Phase. Equilib.*, **1997**, *127*, 251.
- [78] D.L. Singleton, R.J. Cvetanovic, *J. Am. Chem. Soc.*, **1976**, *98*, 6812.
- [79] J.R. Alvarez-Idaboy, A. Galano, *Theor. Chem. Acc.*, **2010**, *126*, 75.
- [80] X.W. Sheng, L. Mentel, O.V. Gritsenko, E.J. Baerends, *J. Comput. Chem.*, **2011**, *32*, 2896.
- [81] N. Agmon, R.D. Levine, *Chem. Phys. Lett.*, **1977**, *52*, 197.
- [82] J.E. Leffler, *Science*, **1953**, *117*, 340.
- [83] W. Chen, H.B. Schlegel, *J. Chem. Phys.*, **1994**, *101*, 5957.
- [84] J.F. Stanton, *J. Chem. Phys.*, **1994**, *101*, 371.
- [85] L.S. Cederbaum, F. Tarantelli, P. Winkler, *J. Phys. B: At. Mol. Opt. Phys.*, **1990**, *23*, L747.

- [86] L.S. Cederbaum, P. Winkler, *Theor. Chim. Acta.*, **1994**, *88*, 257.
- [87] B. Hajgató, D. Szieberth, P. Geerlings, F. De Proft, M.S. Deleuze, *J. Chem. Phys.*, **2009**, *131*, 224321.
- [88] M. Huzak, B. Hajgató, M.S. Deleuze, *J. Chem. Phys.*, **2011**, *135*, 104704.
- [89] B. Hajgató, M.S. Deleuze, *Chem. Phys. Lett.*, **2012**, *553*, 6.
- [90] M.S. Deleuze, M. Huzak, B. Hajgató, *J. Mol. Mod.*, **2013**, *19*, 2699.
- [91] M.S. Deleuze, L. Claes, E.S. Kryachko, J.P. François, *J. Chem. Phys.*, **2003**, *119*, 3106.
- [92] B. Hajgató, M.S. Deleuze, D.J. Tozer, F. De Proft, *J. Chem. Phys.*, **2008**, *129*, 84308.
- [93] D.R. Glowacki, C.H. Liang, C. Morley, M.J. Pilling, S.H. Robertson, *J. Phys. Chem. A*, **2012**, *116*, 9545.
- [94] A. Shiroudi, M.S. Deleuze, *J. Phys. Chem. A*, **2014**, *118*, 3625.

Chapter 5

Theoretical study of the oxidation mechanisms of naphthalene initiated by hydroxyl radicals: The O₂ addition pathway

5.1. Introduction

Aromatic hydrocarbons, including benzene and polycyclic aromatic hydrocarbons (PAHs), are present in gasoline and diesel fuels [1–4], and are released into the atmosphere principally during incomplete combustion [5,6]. PAHs with two to three rings are mainly in the gas phase under atmospheric conditions [7,8]. These compounds chemically react with tropospheric gases such as ozone, nitrate radicals, and hydroxyl radicals [9,10]. The reactions with these radicals are usually the most important sink reactions of organic compounds in the atmosphere [11,12]. The oxidation of aromatic rings by OH radicals in the gas phase under ambient conditions yields hydroxycyclohexadienyl-type radicals, which can back decompose to the reactants or react further with NO₂ or O₂ to yield highly carcinogenic derivatives [13–22]. Under ambient atmospheric conditions, including severely polluted urban areas, it is known that the reactions of OH-monocyclic aromatic hydrocarbon adducts with O₂ dominate [19].

In two preceding articles [23,24], we have studied the first reaction steps involved in the oxidation pathways of naphthalene, the most volatile and abundant PAH in polluted urban areas, by OH radicals. Whereas the hydrogen abstraction pathway at high temperatures ($T \geq 600$ K) yields 1- and 2-naphthyl radicals, the OH addition pathway which dominates under inert (He) conditions at low temperatures ($T \leq 410$ K) leads to 1- and 2-naphthol. Under atmospheric conditions, however, the

intermediate energized adduct $[\text{C}_{10}\text{H}_8\text{OH}]^{\bullet}$ (R1) involved in the latter reaction is expected to react primarily with triplet molecular oxygen, to form $[\text{C}_{10}\text{H}_8\text{OH}]^{\bullet}\text{-O}_2$ peroxy radicals (R2). O_2 addition onto the R1 energized adduct can occur at five different positions, i.e. onto the C_2 , C_4 , C_5 , C_7 , and C_9 -positions (Figure 5.1). Depending on the relative (*syn* or *anti*) location of the hydroxyl and peroxy substituents with respect to the attacked phenyl ring scaffold, this third reaction step leads on total to 10 different isomers (Figure 5.1), which may be referred, as in a previous study by Zhang *et al.* [25] to as the R1-*i*OO-*anti/syn* ($i = 2, 4, 5, 7, 9$) radicals. Similar reactions of O_2 with $[\text{OH-benzene}]^{\bullet}$ [26–29] and $[\text{OH-toluene}]^{\bullet}$ [30] adducts are known to proceed through a reversible addition of O_2 to the OH-aromatic adduct to form an OH-aromatic- O_2 peroxy radical [22].

Koch *et al.* [22,31–33] have experimentally studied the gas-phase reaction between O_2 and naphthalene-OH radical at 298, 336 and 400 K, by means of flash photolysis/resonance fluorescence (FP/RF). The reported rate constants for the reactions of naphthalene-OH radical with O_2 at 400 K are less than $10^{-17} \text{ cm}^3 \text{ molecule}^{-1} \text{ s}^{-1}$, in accordance with the negative temperature dependence observed in the experiments at 336 and 298 K [31,33] resorting to chemical cycling of radicals [32,34]. Experimental studies of the gas-phase reaction between O_2 and naphthalene-OH radicals are extremely difficult and challenging, and still badly need theoretical modelling for reliable enough insights into the reaction mechanisms.

In a recent theoretical study, Zhang *et al.* [25] investigated the reactions of the energized adduct R1 with molecular oxygen in its triplet electronic ground state, upon considering addition of O_2 in both the *syn* (same side) and *anti* (opposite side) positions with respect to the OH substituent and to the plane defined by the carbon backbone in the adduct (Figure 5.1). According to their results, it was found that the thermodynamically most favorable reaction consists in addition of O_2 onto R1 at the C_2 position (Figure 5.1) and in the *anti* mode, thus with the OH and O_2 substituents lying on opposite sides of the carbon backbone in the peroxy radical. This conclusion is however quite surprising, because one would intuitively expect that addition at the C_2 position in the *syn* mode should be thermodynamically favored by the formation of an intramolecular hydrogen bonding between the terminal oxygen of the peroxy (O_2) group and the hydrogen of the OH group – an observation which led us to undertake a detailed verification of the study by Zhang *et al.* [25].

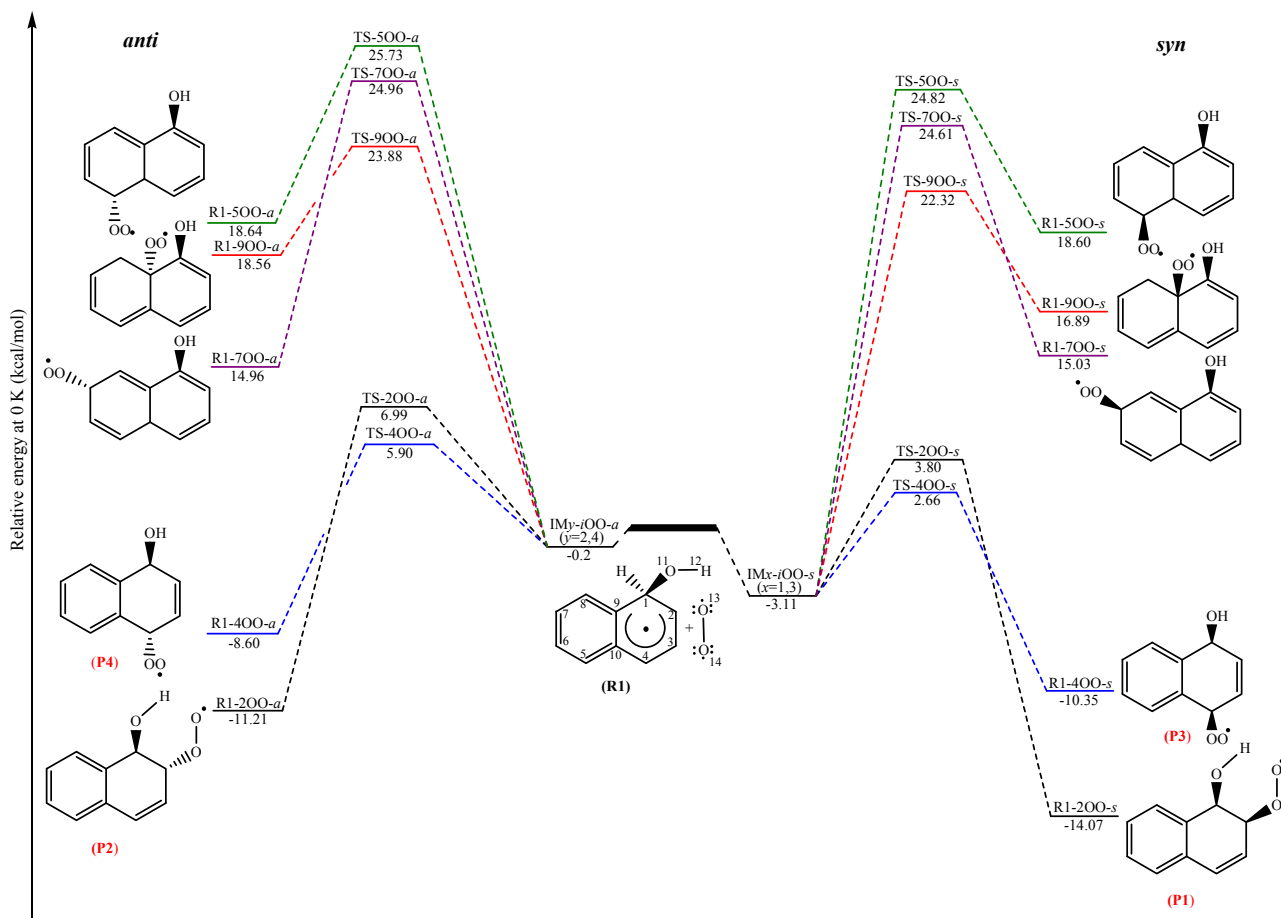


Figure 5.1. Potential energy diagram for the considered reaction pathways at the UM06-2x/aug-cc-pVTZ level of theory.

In addition to the work by Zhang *et al.* [25] we also wish to supply detailed computations of kinetic rate constants for all reaction steps involved in the addition of O₂ onto R1, as well as effective rate constants for the whole process at various temperatures and pressures. In this purpose, use shall be made of transition state theory (TST) [35–44] and statistical RRKM [43–45] theory, in conjunction with the popular B3LYP functional [46,47], but also the ω B97XD functional [48], as well as the UM05-2x [49] and UM06-2x [49,50] functionals which have been specifically designed for accurate studies of chemical reactions, both from a thermodynamic and kinetic viewpoint. For the sake of reliability and accuracy, use shall also be made of Dunning’s augmented correlation consistent polarized valence basis set of triple zeta quality (aug-cc-pVTZ) [51]. This basis set is about twice as large as the 6-311+G(2df,p) basis set that was employed by Zhang *et al.* [25].

In the present work, we also strive to supply further chemical insights into the reaction mechanisms, by analyzing results in terms of natural bond orbital (NBO) occupancies [52,53], and donor-acceptor interaction energies.

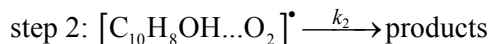
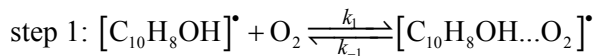
5.2. Computational Details

All calculations that are discussed in the present work have been performed using the Gaussian 09 package of programs [54]. Molecular structures were visualized with GaussView [55]. The molecular structures and harmonic vibrational frequencies of all stationary points of interest were calculated using density functional theory along with a variety of exchange-correlation functionals, namely B3LYP [46,47], ω B97XD [48], UM05-2x [49] and UM06-2x [49,50] functionals, in conjunction with the aug-cc-pVTZ basis set [51].

Frequency calculations were carried out to check the nature of the identified stationary points. The connections between transition states and the corresponding energy minima have been verified according to intrinsic reaction coordinate (IRC) calculations [56] that were carried out at the B3LYP/6-31G(d,p) level using the second-order Gonzalez–Schlegel integration method [57,58]. In line with these frequency calculations, thermodynamic state functions (H , S , G) were obtained from canonical partition functions obtained for an ideal polyatomic gas under a pressure of 1.0 atm using the standard RRHO (rigid rotor harmonic oscillator) approximation and Boltzmann statistics (see refs 59 and 60 or any textbook of molecular statistical mechanics).

In this study, O₂ addition to the [C₁₀H₈OH][•] complex (R1) is analyzed according to the scheme advocated by Singleton and Cvetanovic [61]. With this scheme, it is

assumed that the reaction occurs according to a two-step mechanism, involving first a fast pre-equilibrium between the reactants (R1+O₂) and a prereactive complex [C₁₀H₈OH...O₂]^{*} (IM), followed by the irreversible formation of the naphthalene peroxy radicals [C₁₀H₈OH-O₂]^{*} (R2):



In the above reactions, k_1 is the kinetic rate constant characterizing the forward bimolecular reaction step (in cm³ molecule⁻¹ s⁻¹), whereas k_{-1} and k_2 represent the backward and forward unimolecular reaction rate constants (in s⁻¹). A steady-state analysis of the overall reaction pathway leads to the following expression for the associated rate constant [61]:

$$k_{\text{overall}} = \frac{k_1 k_2}{k_{-1} + k_2} \quad (5.1)$$

Although the energy barrier for k_{-1} has about the same height as that for k_2 , the entropy change for the reverse reaction (IM→R1+O₂) is much larger than for the formation of the products (IM→R2). Thus, k_{-1} is expected to be much larger than k_2 (an assumption that has been checked in details on the basis of RRKM calculations, see data reported in the Appendix III). Based on this assumption, the overall rate constant (k_{overall}) can be calculated as follows:

$$k_{\text{overall}} = K_c k_2 \quad (5.2)$$

with $K_c = k_1/k_{-1}$ the equilibrium constant for the fast pre-equilibrium between the reactants and the prereactive complex (step 1):

$$K_c = \frac{[\text{C}_{10}\text{H}_8\text{OH}\dots\text{O}_2]^{\bullet}}{[\text{C}_{10}\text{H}_8\text{OH}]^{\bullet} [\text{O}_2]} \quad (5.3)$$

Considering basic statistical thermodynamic principles (see in particular eq. 26.3–20 in ref. 62), the equilibrium constant of the fast pre-equilibrium between the reactants and the prereactive complex can be obtained as:

$$K_c = \frac{Q_{\text{IM}}}{Q_{\text{R1}} Q_{\text{O}_2}} \times \frac{V_m(T)}{N_{\text{Av}}} \times \exp \left[-\frac{(E_{\text{IM}} - E_{\text{R1}} - E_{\text{O}_2})}{RT} \right] \quad (5.4)$$

with N_{Av} the Avogadro number, R the ideal gas constant and $V_m(T)=RT/P$ the molar volume of an ideal gas. The kinetic rate constant characterizing the unimolecular dissociation reaction of the prereactive complex is obtained in the high pressure limit by means of transition state theory [35–42]:

$$k_2 = \frac{\sigma k_B T}{h} \times \frac{Q_{\text{TS}}}{Q_{\text{IM}}} \times \exp\left[-\frac{(E_{\text{TS}} - E_{\text{IM}})}{RT}\right] \quad (5.5)$$

In line with the temperatures at which the experiments by Koch *et al.* were conducted [31–34], kinetic rate constants and branching ratios have been obtained at 298, 336 and 400 K and at a pressure of 1 bar (high pressure limit) using transition state theory, and the UM06-2x/aug-cc-pVTZ estimates for activation energies. The rationale behind this choice is that a recent study by Zhao and Truhlar [50] has shown that the UM06-2x exchange-correlation functional is the best one for applications involving main-group thermochemistry, kinetics, non-covalent interactions, and electronic excitation energies to valence and Rydberg states [50].

For the sake of completeness, it is at last worth reminding that the kinetics of bimolecular and unimolecular reactions in atmospheric chemistry can be determined using conventional transition state theory, along with the following equations [63–65]:

$$k_{\text{TST}} = \frac{\sigma k_B T}{h} V_m(T) \frac{Q_{\text{TS}}^\ddagger(T)}{Q_A(T) \cdot Q_B(T)} \exp(-E_a/RT) \quad (5.6)$$

$$k_{\text{TST}} = \frac{\sigma k_B T}{h} \frac{Q_{\text{TS}}^\ddagger(T)}{Q_A(T)} \exp(-E_a/RT) \quad (5.7)$$

In the above equations, σ denotes the reaction symmetry number, Q_A , Q_B , and Q_{TS} represent the total molecular partition functions for the isolated reactants, and transition state associated to the unimolecular dissociation reaction (step 2), respectively. E_a is the classical barrier height (including zero-point vibrational energy contributions), k_B and h are the Boltzmann's and Planck's constants, respectively. Since the computed energy differences account for zero-point vibrational energies, vibrational partition functions were computed using the vibrational ground state as energy reference. Tunneling corrections were assumed to be insignificant, considering the size of the moieties involved in the chemical reactions of interest.

TST gives an estimate of the upper-limit for rate constants as a function of the temperature, and is known to give reliable estimations of rate constants [66,67] in the high pressure limit [68], especially for cases with significant barrier heights (as is the case here) [69]. All supplied rate constants are the results of calculations that were performed using the implementation of this approach in the KiSThELP package [70]. Besides TST, in the present study, statistical RRKM theory [42–44] has been considered to evaluate pressure effects on a microcanonical basis, both in the fall-off regime and towards the high pressure limit, using the implementation of this approach in the KiSThELP program [70]. In these RRKM calculations, a scaling factor of 0.971 was imposed on the frequencies calculated at the UM06-2x/aug-cc-pVTZ level of theory. Collisional stabilization rate constants were computed using Lennard–Jones collision rate theory [11]. The strong collision approximation was used, assuming therefore that every collision deactivates with $\omega = \beta_c \cdot Z_{LJ} \cdot [M]$ being the effective collision frequency, where β_c is the collisional efficiency, Z_{LJ} is the Lennard–Jones (LJ) collision frequency and $[M]$ is the total gas concentration. The retained value for β_c is 0.2. The collision frequencies (Z_{LJ}) were calculated using the LJ parameters: ε/k_B , which depends on the energy depth (ε) of the LJ potential, and σ which represents a dimensional scale of the molecular radius [71]. The retained LJ potential parameters for pure air as diluent gas amount to $\sigma = 3.522 \text{ \AA}$ and $\varepsilon/k_B = 99.2 \text{ K}$ [72,73]. For the naphthalene-OH adduct $[C_{10}H_8OH]^*$, the following parameters have been used: $\sigma = 6.57 \text{ \AA}$ and $\varepsilon/k_B = 612.7 \text{ K}$ [74].

5.3. Results and Discussion

5.3.1. Energetic and Thermodynamic Parameters

Since the $[C_{10}H_8OH]^*$ (R1) radical has several resonant structures, the addition of triplet molecular ($^3\Sigma_g$) oxygen to the $[C_{10}H_8OH]^*$ (R1) radical can occur from *syn* and *anti*-directions at five different positions, namely onto the C₂, C₄, C₅, C₇, and C₉-atoms, yielding 10 isomers referred, as in the study by Zhang *et al.* [25] to as the so-called R1-*i*OO-*anti/syn* (*i* = 2, 4, 5, 7, 9) peroxy radicals, respectively (Figure 5.1). The B3LYP/6-311+G(2df,p) and BB1K/6-311++G(2df,2p) data obtained by Zhang *et al.* [25] are reported in Table 5.1, where they can be compared with our newly supplied DFT data. The reader is referred to Table 5.2 for a presentation at the same theoretical levels of the activation energies to form the peroxy radicals.

In line with chemical intuition, the R1-2OO and R1-4OO *syn/anti* radicals are found to be by far the most stable structures, an observation which is easily explained by the fact that with these isomeric structures, aromaticity is preserved in one of the two benzenoid rings, in contrast with the other ones (R1-*i*OO-*syn/anti*, with $i=5, 7$, and 9) where aromaticity is destroyed in both rings. More specifically, all DFT estimates at room temperature show that O₂ additions onto the C₂ and C₄ positions are exothermic processes ($\Delta H_r < 0$), whereas formation of the R1-*i*OO-*anti/syn* ($i=5, 7, 9$) peroxy radicals requires much higher reaction enthalpies, ranging from 14.3 to 24.3 kcal mol⁻¹ (Table 5.1). The corresponding energy barriers are also much higher (Table 5.2, Figure 5.1). Hence, the formation of these radicals will be negligible under atmospheric conditions. In the sequel, we shall therefore concentrate on the four lowest chemical pathways, corresponding to O₂ addition processes in *syn* and *anti* modes at the C₂ and C₄ positions. In other words, we shall focus on the formation of the R1-*i*OO-*anti/syn* ($i=2, 4$) radicals, yielding the **P1–P4** products (Figure 5.1). For the ease of notations, the corresponding chemical pathways will be correspondingly referred to as reaction pathways **1–4**, in the section on kinetic parameters.

In sharp contrast with the B3LYP and BB1K results by Zhang *et al.* [25], all our DFT calculations demonstrate that, among all isomers, the most stable isomer is the R1-2OO-*syn* one. More specifically, in contrast with the B3LYP and BB1K results by Zhang *et al.* [25] (Table 5.1), the R1-2OO-*syn* isomer is found at all the theoretical levels we considered to be more stable than the R1-2OO-*anti* one. The reactions energies (ΔE_{0K}) characterizing the formation of the R1-2OO-*syn* and R1-4OO-*syn* radicals are all in all lower by about 1.45–2.86 kcal mol⁻¹ and 1.75–1.90 kcal mol⁻¹ than the reactions energies for the formation of the R1-2OO-*anti* and R1-4OO-*anti* peroxy radicals. These stabilization energies are in line with the energies that are usually associated with classical hydrogen bonds, in the range 1.2 to 7.2 kcal mol⁻¹, and find also their origin into an electrostatic interaction between a positively charged hydrogen atom (H₁₂) and a negatively charged oxygen atom (O₁₄) (see further discussion of structural details). We note that this observation is similar to that made in a recent theoretical study of the atmospheric photo-oxidation mechanisms of toluene [75], in which the formation of radical structures resulting from the addition of the peroxy and hydroxyl substituents on the same side was found to be energetically more favorable.

Table 5.1. Reaction energies, reaction enthalpies and Gibb's free reaction energies (in kcal mol⁻¹) for the addition of triplet molecular O₂ on the [C₁₀H₈OH][•] radical.

Species	Method			ω B97XD			UM05-2x			UM06-2x			literature	
	B3LYP			ΔE_{0K}	ΔH°_{298K}	ΔG°_{298K}	ΔE_{0K}	ΔH°_{298K}	ΔG°_{298K}	ΔE_{0K}	ΔH°_{298K}	ΔG°_{298K}	ΔE_{0K}	ΔG°_{298K}
R1 + O ₂	0.00	0.00	0.00	0.00	0.00	0.00	0.00	0.00	0.00	0.00	0.00	0.00	0.00	0.00
R1-200- <i>syn</i>	-6.12	-7.05	4.88	-9.67	-10.58	1.23	-11.70	-12.72	-0.57	-14.07	-15.02	-3.08	-6.55 ^a	4.49 ^a
	(-6.51)	(-7.45)	(4.52)	[-8.86]	[-10.06]	[3.28]							-8.96 ^b	2.03 ^b
IM- <i>i</i> OO- <i>syn</i> (<i>i</i> =2,4)	-0.11	0.20	8.05	-1.04	-0.77	7.35	-1.96	-1.73	6.64	-3.11	-2.82	5.24		
R1-400- <i>syn</i>	-2.35	-3.22	8.58	-6.31	-7.28	4.76	-8.13	-9.10	2.96	-10.35	-11.30	0.67	-2.89 ^a	8.08 ^a
	(-2.84)	(-3.72)	(8.12)	[-5.23]	[-5.78]	[5.56]							-4.59 ^b	6.67 ^b
R1-500- <i>syn</i>	23.86	23.42	33.87	22.27	21.73	32.46	21.32	20.76	31.47	18.60	18.05	28.81	21.89 ^a	31.96 ^a
	(23.43)	(22.97)	(33.48)	[20.04]	[19.34]	[30.50]							23.54 ^b	33.82 ^b
R1-700- <i>syn</i>	20.12	19.67	29.51	19.30	18.71	29.40	17.77	17.14	27.82	15.03	14.45	24.99	21.99 ^a	31.81 ^a
	(19.76)	(19.30)	(29.14)	[17.34]	[16.51]	[28.55]							20.24 ^b	30.35 ^b
R1-900- <i>syn</i>	24.81	24.27	35.48	22.10	21.42	32.97	19.68	18.90	30.83	16.89	16.18	27.83	22.83 ^a	33.96 ^a
	(24.17)	(23.60)	(34.88)	[20.84]	[20.05]	[32.48]							22.90 ^b	34.13 ^b
R1-200- <i>anti</i>	-4.67	-5.42	5.82	-7.63	-8.37	2.81	-8.99	-9.87	1.75	-11.21	-12.05	-0.53	-10.35 ^a	0.53 ^a
	(-4.94)	(-5.69)	(5.56)	[-6.46]	[-7.51]	[4.86]							-9.82 ^b	1.03 ^b
IM- <i>i</i> OO- <i>anti</i> (<i>i</i> =2,4)	1.89	2.47	8.91	1.33	1.81	8.94	0.76	1.14	8.97	-0.20	0.02	8.84		
R1-400- <i>anti</i>	-0.58	-1.24	9.85	-4.56	-5.23	5.87	-6.23	-7.02	4.52	-8.60	-9.38	2.15	-2.27 ^a	8.65 ^a
	(-0.96)	(-1.63)	(9.47)	[-2.67]	[-3.73]	[9.06]							-4.61 ^b	6.29 ^b
R1-500- <i>anti</i>	24.36	23.90	34.36	22.50	21.94	32.71	21.49	20.81	32.01	18.64	17.98	29.09	22.20 ^a	32.22 ^a
	(23.94)	(23.46)	(33.99)	[20.77]	[19.99]	[31.86]							23.11 ^b	33.51 ^b
R1-700- <i>anti</i>	20.06	19.62	29.49	19.15	18.60	29.17	17.53	16.95	27.38	14.96	14.34	25.11	19.67 ^a	28.94 ^a
	(19.73)	(19.28)	(29.01)	[17.51]	[16.64]	[28.94]							20.22 ^b	30.38 ^b
R1-900- <i>anti</i>	-	-	-	23.13	22.58	33.65	21.25	20.60	32.16	18.56	17.93	29.39	-	-
				[21.76]	[21.02]	[33.25]								

a: Ref. [25]; values obtained at the B3LYP/6-311+G(2df,p) level of theory.

b: Ref. [25]; values obtained at the BB1K/6-311++G(2df,2p) level of theory.

- The values in parenthesis were calculated at the B3LYP/6-311+G(2df,p) level of theory (present work).

- The values in square brackets were calculated at the BB1K/6-311++G(2df,2p) level of theory (present work).

Table 5.2. Activation energies, enthalpies and Gibb's free activation energies (in kcal mol⁻¹) for the addition of triplet molecular O₂ on the [C₁₀H₈OH][•] radical.

Species	B3LYP			ω B97XD			UM05-2x			UM06-2x			literature	
	ΔE_{0K}^\ddagger	ΔH_{298K}°	ΔG_{298K}°	ΔE_{0K}^\ddagger	ΔH_{298K}°	ΔG_{298K}°	ΔE_{0K}^\ddagger	ΔH_{298K}°	ΔG_{298K}°	ΔE_{0K}^\ddagger	ΔH_{298K}°	ΔG_{298K}°	ΔE_{0K}^\ddagger	ΔG_{298K}°
R1 + O ₂	0.00	0.00	0.00	0.00	0.00	0.00	0.00	0.00	0.00	0.00	0.00	0.00		
TS-200- <i>syn</i>	1.29 (3.38)	0.47 (2.62)	11.95 (14.01)	4.97	4.25	15.61	5.06	4.18	16.04	3.80	2.99	14.63	5.19 ^a 9.97 ^b	15.46 ^a 19.98 ^b
TS-400- <i>syn</i>	0.02 (2.29)	-0.72 (1.58)	10.49 (12.79)	3.66	2.99	14.09	3.98	3.19	14.71	2.66	1.90	13.44	2.27 ^a 6.79 ^b	12.76 ^a 17.78 ^b
TS-500- <i>syn</i>	21.08 (23.86)	20.45 (23.31)	31.16 (33.88)	25.79	25.26	35.88	26.40	25.83	36.49	24.82	24.32	34.59	21.63 ^a 26.55 ^b	32.03 ^a 36.97 ^b
TS-700- <i>syn</i>	18.97 (21.64)	18.42 (21.17)	28.31 (30.94)	25.57	25.13	35.11	25.74	25.23	35.45	24.61	24.11	34.35	21.63 ^a 27.92 ^b	30.93 ^a 37.43 ^b
TS-900- <i>syn</i>	20.33 (22.93)	19.35 (22.02)	31.55 (34.10)	24.27	23.44	35.28	23.96	23.13	35.06	22.32	21.54	33.30	22.92 ^a 27.32 ^b	34.08 ^a 38.29 ^b
TS-200- <i>anti</i>	3.21 (5.67)	2.62 (5.13)	13.42 (15.88)	7.70	7.16	17.90	8.25	7.59	18.74	6.99	6.39	17.39	3.99 ^a 9.92 ^b	14.15 ^a 20.12 ^b
TS-400- <i>anti</i>	2.86 (5.22)	2.32 (4.75)	12.90 (15.22)	6.99	6.57	16.80	7.31	6.69	17.62	5.90	5.31	16.23	3.63 ^a 7.86 ^b	13.79 ^a 18.5 ^b
TS-500- <i>anti</i>	20.96 (23.81)	20.44 (23.36)	30.48 (33.35)	26.37	25.97	35.82	26.99	26.50	36.84	25.73	25.30	35.33	21.96 ^a 26.89 ^b	32.36 ^a 37.09 ^b
TS-700- <i>anti</i>	19.13 (21.83)	18.56 (21.38)	28.65 (30.99)	25.74	25.37	34.72	26.03	25.51	35.80	24.96	24.44	34.82	21.82 ^a 28.3 ^b	30.98 ^a 37.57 ^b
TS-900- <i>anti</i>	22.37 (25.01)	21.65 (24.35)	33.11 (35.70)	25.69	25.14	36.16	25.61	24.98	36.31	23.88	23.32	34.48	25.0 ^a 28.9 ^b	35.68 ^a 39.7 ^b

a: Ref. [25]; values obtained at the B3LYP/6-311+G(2df,p) level of theory.

b: Ref. [25]; values obtained at the BB1K/6-311++G(2df,2p) level of theory.

- The values in parenthesis were calculated at the B3LYP/6-311+G(2df,p) level of theory (present work).

It is interesting to note that, although the R1-2OO-*syn* peroxy radical represents the most stable form for O₂ addition to the [C₁₀H₈OH][•] adducts, the corresponding activation energy is slightly larger than for the formation of the R1-4OO-*syn* radical. Also because of some extra-stabilization due to the formation of an intramolecular hydrogen bond between the terminal oxygen of the peroxy group (O₁₄) and the hydrogen atom of the hydroxyl group (H₁₂), the barrier heights (ΔE_{0K}^\ddagger) for O₂ addition from the *syn*-direction are lower than those for the *anti*-direction, by about 1.9 to 3.3 kcal mol⁻¹. Similar observations can be made when Gibb's free activation energies are considered: in spite of slightly unfavorable entropy effects, the Gibb's free energies for the *syn* addition modes in C₂ and C₄ positions (11.95–16.04 and 10.49–14.71 kcal mol⁻¹, respectively) are at all the DFT levels we employed systematically lower than the ones for the *anti* modes (13.42–18.74 and 12.90–17.62 kcal mol⁻¹). Therefore, O₂ addition in *syn* positions will be both thermodynamically and kinetically favored over O₂ addition in *anti* positions. Among all possible adducts, the formation of the R1-2OO-*syn* isomer will clearly therefore predominate under thermodynamic control, i.e. at chemical equilibrium. Note that kinetic effects may on the contrary favor the formation of the R1-4OO-*syn* isomer (see further). Both for the *syn* and *anti* modes, O₂ addition in C₂ position is thermodynamically favored over O₂ addition in C₄ position.

We note that the different exchange-correlation functionals that have been employed predict large differences in the relative energies of the identified stationary points, especially with regards to the extent of activation energies. As was to be expected, due to a large self-interaction error, the B3LYP functional systematically yields strong underestimations of the computed activation energies, of the order of 3–4 kcal mol⁻¹, compared with the results obtained with the ω B97XD, UM05-2x and UM06-2x functionals, which most generally do not differ by more than 2 kcal mol⁻¹. Interestingly, we find that the UM06-2x/aug-cc-pVTZ activation energies systematically underestimate the ω B97XD/aug-cc-pVTZ ones by 1 to 2 kcal mol⁻¹, which in turn slightly underestimate the UM05-2x/aug-cc-pVTZ energy barriers, within 0 to 1 kcal mol⁻¹. Therefore, if rather large differences are to be expected with the correspondingly obtained kinetic rate constants, the ultimately obtained branching ratios will exhibit a rather limited dependence upon the employed exchange-correlation functionals.

At last, we note that our B3LYP/aug-cc-pVTZ results for reaction energies and activation energies exhibit considerable differences, up to 3 kcal mol⁻¹, compared with the B3LYP/6-311+G(2df,p) results obtained by Zhang *et al.* in ref. 25. These differences, most obviously, reflect the greater size, flexibility and quality of the aug-cc-pVTZ basis set, which incorporates on total 805 atomic functions,

compared with a total of 496 atomic functions for the 6-311+G(2df,p) basis set. Besides, it is worth reminding that the 6-311G basis set from which the 6-311+G(2df,p) derives is known to exhibit a too compact $2p$ space [76], and to be effectively a basis set of double-zeta quality only in the s -space, due to improperly balanced expansion coefficients [77].

5.3.2. Structural Characteristics of Stationary Points

The optimized geometries of all identified stationary points involved in the chemical pathways for O_2 addition onto the C_2 and C_4 atoms of the $[C_{10}H_8-OH]^{\bullet}$ energized adduct are supplied at all selected DFT levels in Tables 5.3 and 5.4, respectively. The reader is correspondingly referred to Figure 5.2 for detailed atom labelling. Upon examining this Figure, it is clear that, in contrast with the R1-2OO-*syn* and R1-4OO-*syn* peroxy radical species, the structures describing the R1-2OO-*anti* and R1-4OO-*anti* isomers do not allow the formation of an intramolecular hydrogen bond between the hydroxyl (OH) and peroxy (O_2) substituents. Whatever the employed exchange-correlation functional, NBO calculations deliver charges around +0.48 and -0.20 for H_{12} and O_{14} , respectively. These atoms exhibit interdistances in the range 1.97–2.03 Å and 2.27–2.33 Å for the R1-2OO-*syn* and R1-4OO-*syn* radicals, respectively, which are compatible with the idea of a hydrogen bond. On the other hand, these interdistances increase to ~3.87 and ~5.04 Å within the R1-2OO-*anti* and R1-4OO-*anti* structures, and become clearly far too large for any significant stabilizing electrostatic interactions. These structural preferences explain the slightly larger stability, by 1.45–2.86 to 1.75–1.9 kcal mol⁻¹, of the R1-2OO-*syn* and R1-4OO-*syn* structures, relative to the *anti* ones.

Addition of O_2 onto the C_2 atom within the R1 energized adduct results into a lengthening of the C_1-C_2 and C_2-C_3 bonds next to the site of addition, by ~0.03 Å and ~0.13 Å, respectively (Table 5.3). This increase in bond lengths obviously reflects the formation of single C–C bonds around the site of the addition, along with transfer of the π bond electron density to the newly formed C_2-O_{13} bond. Similar structural variations are observed for O_2 addition in C_4 position (Table 5.4), namely an increase of the C_3-C_4 and C_4-C_{10} bond lengths by 0.07–0.09 Å.

In addition, in comparison with the geometries obtained for the $[C_{10}H_8OH]^{\bullet}$ adduct (R1) (Tables 5.3 and 5.4), addition of O_2 to the R1 radical results in a shortening of the C_1-O_{11} bond. For the R1-2OO-*syn* radical, in which the intramolecular hydrogen binding is energetically stronger, the length of the C_1-O_{11} bond is reduced by ~0.03 Å. This reduction in length is a significantly more

important structural variation than that observed with the R1-4OO-*syn* radical, in which the C₁–O₁₁ bond length is reduced by only 0.01 Å, and is therefore consistent with the idea of a stronger intramolecular hydrogen bond. Also in line with the formation of an intramolecular hydrogen bond, the O₁₃–O₁₄ bond length increases from 1.19–1.21 Å to 1.29–1.32 Å, when the molecular structure evolves from the R1 energized adduct to the R1-2OO-*syn* and R1-4OO-*syn* peroxy radicals.

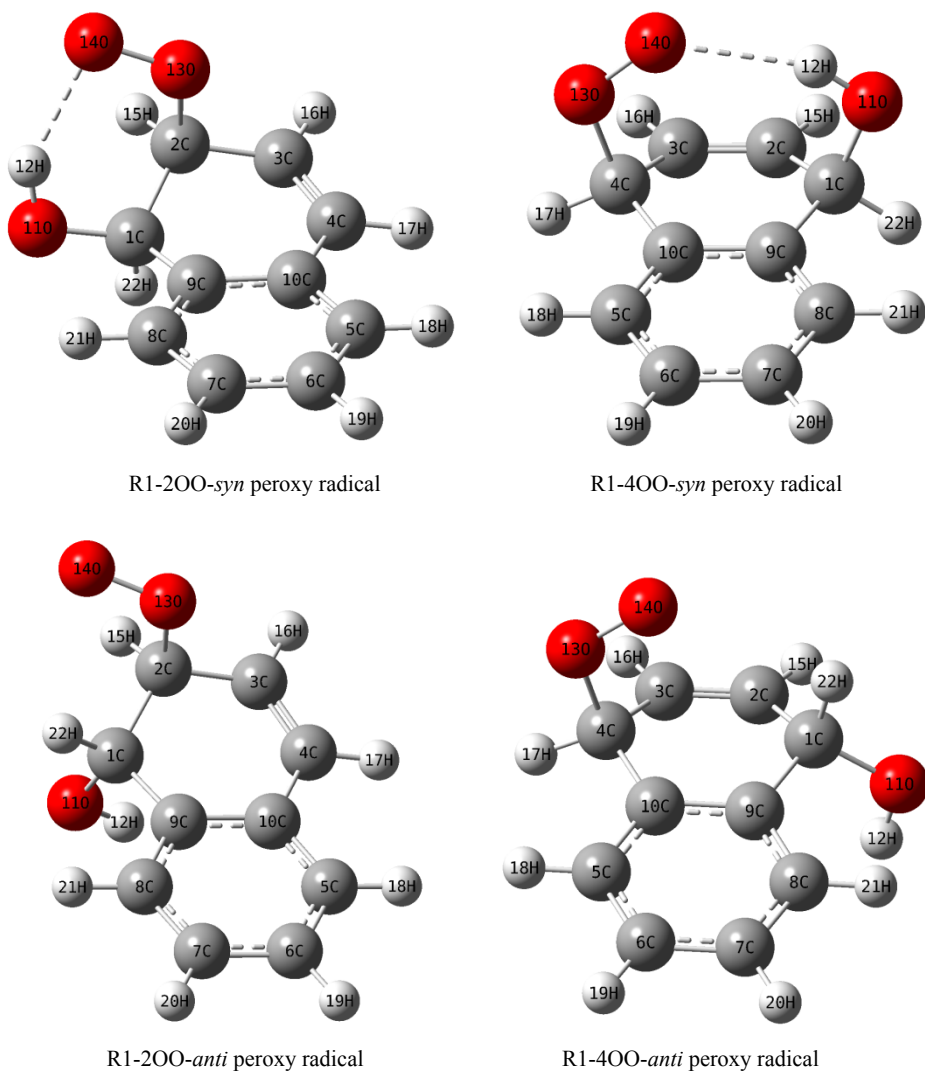


Figure 5.2. Optimized geometries of the R1-2OO and R1-4OO peroxy radicals.

Table 5.3. Structural parameters for all the stationary points that are involved in the reaction $R1+O_2 \rightarrow R1-2OO-syn$ pathway (see Figure 5.2 for detailed atom labeling).

Parameter \ Method	B3LYP				ω B97XD				UM05-2x				UM06-2x			
	R	IM1	TS	P	R	IM1	TS	P	R	IM1	TS	P	R	IM1	TS	P
$r(C_1-C_2)$	1.495	1.495	1.498	1.530	1.494	1.494	1.497	1.526	1.491	1.492	1.494	1.519	1.494	1.495	1.497	1.525
$r(C_2-C_3)$	1.367	1.365	1.396	1.495	1.363	1.361	1.399	1.496	1.363	1.362	1.399	1.495	1.363	1.362	1.399	1.499
$r(C_3-C_4)$	1.401	1.401	1.368	1.338	1.398	1.398	1.361	1.332	1.397	1.397	1.360	1.331	1.400	1.399	1.362	1.333
$r(C_4-C_{10})$	1.429	1.429	1.443	1.459	1.430	1.431	1.448	1.463	1.429	1.430	1.447	1.461	1.431	1.432	1.449	1.464
$r(C_1-C_9)$	1.517	1.516	1.519	1.518	1.514	1.514	1.516	1.514	1.509	1.510	1.511	1.510	1.513	1.514	1.515	1.513
$r(C_9-C_{10})$	1.415	1.414	1.409	1.407	1.407	1.406	1.402	1.400	1.404	1.404	1.400	1.398	1.408	1.407	1.402	1.401
$r(C_1-O_{11})$	1.448	1.442	1.423	1.411	1.431	1.424	1.410	1.400	1.436	1.431	1.416	1.406	1.429	1.424	1.412	1.402
$r(C_2-O_{13})$	-	3.403	2.164	1.495	-	3.198	2.115	1.473	-	3.274	2.090	1.472	-	3.131	2.109	1.467
$r(H_{12}-O_{14})$	-	3.379	3.201	1.971	-	3.440	3.201	1.985	-	3.421	3.180	2.017	-	3.459	3.178	2.033
$r(O_{13}-O_{14})$	1.206	1.213	1.245	1.317	1.196	1.201	1.231	1.301	1.187	1.188	1.223	1.297	1.190	1.192	1.224	1.298
$\theta(C_1-O_{11}-H_{12})$	107.72	107.36	107.56	108.76	107.57	107.24	107.59	108.54	107.58	107.39	107.64	109.10	107.68	107.56	107.68	109.21
$\theta(C_2-O_{13}-O_{14})$	-	94.48	111.92	112.47	-	97.30	112.20	112.55	-	98.44	112.06	111.92	-	100.46	111.86	112.29

- Bond lengths are in angstrom (Å) unit and torsion and dihedral angles are in degrees (°)

Table 5.4. Structural parameters for all the stationary points that are involved in the reaction $R1+O_2 \rightarrow R1-4OO-syn$ pathway (see Figure 5.2 for detailed atom labeling).

Parameter	B3LYP				ω B97XD				UM05-2x				UM06-2x			
	R	IM3	TS	P	R	IM3	TS	P	R	IM3	TS	P	R	IM3	TS	P
$r(C_1-C_2)$	1.495	1.495	1.497	1.503	1.494	1.494	1.496	1.503	1.491	1.492	1.494	1.500	1.494	1.495	1.497	1.504
$r(C_2-C_3)$	1.367	1.365	1.348	1.328	1.363	1.361	1.343	1.323	1.363	1.362	1.342	1.322	1.363	1.362	1.344	1.324
$r(C_3-C_4)$	1.401	1.401	1.421	1.487	1.398	1.398	1.421	1.490	1.397	1.397	1.422	1.489	1.400	1.399	1.423	1.493
$r(C_4-C_{10})$	1.429	1.429	1.439	1.495	1.430	1.431	1.442	1.497	1.429	1.430	1.441	1.494	1.431	1.432	1.442	1.498
$r(C_1-C_9)$	1.517	1.516	1.514	1.513	1.514	1.514	1.511	1.511	1.509	1.510	1.507	1.506	1.513	1.514	1.510	1.510
$r(C_9-C_{10})$	1.415	1.414	1.407	1.396	1.407	1.406	1.399	1.390	1.404	1.404	1.396	1.387	1.408	1.407	1.400	1.390
$r(C_1-O_{11})$	1.448	1.443	1.437	1.437	1.431	1.424	1.421	1.422	1.436	1.431	1.427	1.428	1.429	1.424	1.421	1.422
$r(C_4-O_{13})$	-	2.961	2.148	1.536	-	2.841	2.103	1.490	-	2.966	2.070	1.496	-	2.909	2.094	1.490
$r(H_{12}-O_{14})$	-	2.460	2.290	2.318	-	2.457	2.300	2.268	-	2.416	2.285	2.328	-	2.399	2.281	2.271
$r(O_{13}-O_{14})$	1.206	1.213	1.243	1.305	1.196	1.201	1.229	1.293	1.187	1.188	1.222	1.290	1.190	1.192	1.222	1.290
$\theta(C_1-O_{11}-H_{12})$	107.72	107.36	106.46	106.62	107.57	107.24	106.39	106.43	107.58	107.39	106.36	106.45	107.68	107.56	106.57	106.62
$\theta(C_4-O_{13}-O_{14})$	-	105.04	111.87	113.48	-	103.25	111.14	113.20	-	101.06	110.22	112.22	-	99.08	109.88	112.61

- Bond lengths are in angstrom (Å) unit and torsion and dihedral angles are in degrees (°)

In analogy with the study by Huang *et al.* of hydroxycyclohexadienyl peroxy radicals [78], the transition states for O₂ addition at the C₂ and C₄-positions in the R1 energized adduct involve a six-membered cyclic structure [C₁-O₁₁-H₁₂-O₁₄-O₁₃-C_{*i*} (*i*=2,4)] in which the O₁₄, O₁₃ and C_{*i*} (*i*=2,4) atoms are not co-linear. Indeed, the corresponding bond angles are around 112° (Tables 5.3 and 5.4). Like the corresponding energy minima (Figure 5.2), these transition state structures are also stabilized by an intramolecular hydrogen bond (H₁₂-O₁₄). The hydrogen bond lengths within the TS-2OO-*syn* and TS-4OO-*syn* structures amount to 3.18–3.20 Å and 2.28–2.30 Å, respectively. It can also be noticed that in the transition states involved in the formation of the R1-2OO-*syn* and R1-4OO-*syn* radical species, the forming C₂-O₁₃ and C₄-O₁₃ bond lengths are significantly much longer than in the related products, by 69.09–70.43 % and 70.85–72.27 %, respectively. For the sake of completeness and clarity, it is worth noticing that intermediates IM1 and IM3 on pathways **1** and **3** (O₂ additions in *syn* mode in C₂ or C₄ positions) are structurally almost the same and exhibit practically equal energies, which cannot be distinguished on the scale of Figure 5.1. Similarly, IM2 and IM4 on pathways **2** and **4** (O₂ additions in *anti* mode in C₂ or C₄ positions) have almost the same structures, with almost equal energies.

DFT estimates of n_T values have been derived from an Agmon's analysis [79] of the Gibbs's free energy profile for the *syn*-addition of O₂ to the [C₁₀H₈OH][•] radical are supplied in Table 5.5. In line with these profiles (Figure 5.1), and the structural observations made in the preceding section, the obtained n_T values imply that, at all considered levels of theory, the transition state involved in the formation of the R1-4OO-*syn* radical is more similar to the product than the transition state involved in the formation of the R1-2OO-*syn* radical. The same observation can be made when considering the *anti* mode for O₂ addition onto the [C₁₀H₈OH][•] radical.

Table 5.5. Analysis of the chemical pathways of interest in terms of n_T values.

Pathway	Method			
	B3LYP	ω B97XD	UM05-2x	UM06-2x
R1+O ₂ → R1-2OO- <i>syn</i>	0.6282	0.5205	0.4913	0.4524
R1+O ₂ → R1-4OO- <i>syn</i>	0.8460	0.6016	0.5560	0.5128
R1+O ₂ → R1-2OO- <i>anti</i>	0.6383	0.5426	0.5245	0.4925
R1+O ₂ → R1-4OO- <i>anti</i>	0.8086	0.6058	0.5736	0.5355

5.3.3. Natural Bond Orbital Analysis

In line with the formation of intramolecular hydrogen bonds between the hydroxyl and peroxy substituents, more specifically between H₁₂ and O₁₄, the natural bond orbital analysis of donor-acceptor interactions (Table 5.6) shows that, for both the R1-2OO-*syn* and R1-4OO-*syn* isomers, rather significant stabilization energies (E_2) [eq. 2.112] are associated with electron delocalization from the non-bonding lone-pair orbital in the peroxy substituent [$n(\text{O}_{14})$] to the $\sigma^*_{\text{O}_{11}\text{-H}_{12}}$ antibonding orbital in the hydroxyl substituent. As was noted for the hydroxycyclohexadienyl peroxy radical [76], hyperconjugative interactions lead also to an increase in the population of the $\sigma^*_{\text{O}_{11}\text{-H}_{12}}$ antibonding orbital, which weakens in turn the O₁₁-H₁₂ bond.

More specifically, the natural bond orbital results indicate an hyperconjugative $n_2(\text{O}_{14}) \rightarrow \sigma^*_{\text{O}_{11}\text{-H}_{12}}$ interaction energy in the range 0.79–1.97 kcal mol⁻¹ for the R1-4OO-*syn* isomer. For the R1-2OO-*syn* isomer, delocalization of the oxygen lone pairs, n_1 and n_2 , of the O₁₄ atom onto the H₁₂ atom results in net stabilizations in the energy range 1.43–1.55 kcal mol⁻¹. Hyperconjugative $n_1(\text{O}_{14}) \rightarrow \sigma^*_{\text{O}_{11}\text{-H}_{12}}$ and $n_2(\text{O}_{14}) \rightarrow \sigma^*_{\text{O}_{11}\text{-H}_{12}}$ interactions for the R1-4OO-*syn* radical are lower than 0.38 and 0.53 kcal mol⁻¹, respectively. Besides, decrease of the extent of delocalization of the $n(\text{O}_{14})$ lone pair onto the $\sigma^*_{\text{O}_{11}\text{-H}_{12}}$ antibonding orbital from the R1-2OO-*syn* to the R1-4OO-*syn* structures is concomitant with an increase of the occupation of one of the non-bonding lone-pair orbitals on the O₁₄ atom, more specifically $n_1(\text{O}_{14})$, and a decrease of the population of the other lone pair, $n_2(\text{O}_{14})$.

Table 5.6. NBO occupancies and delocalization energies (E_2) (in kcal mol⁻¹) characterizing at different DFT levels the R1-2OO-*syn* (**1**) and R1-4OO-*syn* (**2**) peroxy radicals (results obtained using the aug-cc-pVTZ basis set).

	B3LYP		ω B97XD		UM05-2x		UM06-2x	
	(1)	(2)	(1)	(2)	(1)	(2)	(1)	(2)
Occupancies								
$\sigma_{\text{O}_{11}\text{-H}_{12}}$	0.994	0.995	0.994	0.994	0.995	0.995	0.994	0.995
$\sigma^*_{\text{O}_{11}\text{-H}_{12}}$	0.011	0.007	0.010	0.006	0.008	0.005	0.008	0.006
$n_1(\text{O}_{14})$	0.993	0.997	0.993	0.997	0.994	0.997	0.994	0.997
$n_2(\text{O}_{14})$	0.981	0.975	0.983	0.979	0.985	0.981	0.985	0.981
Delocalization energies (E_2)								
$n_1(\text{O}_{14}) \rightarrow \sigma^*_{\text{O}_{11}\text{-H}_{12}}$	1.43	< 0.25	1.55	0.38	1.53	< 0.25	1.45	< 0.25
$n_2(\text{O}_{14}) \rightarrow \sigma^*_{\text{O}_{11}\text{-H}_{12}}$	1.74	0.37	1.97	0.53	1.05	0.31	0.79	0.35

The electron density in the $\sigma^*(\text{O}_{11}-\text{H}_{12})$ antibonding orbital in the R1-2OO-*syn* peroxy radical is larger than that found for the R1-4OO-*syn* peroxy radical. Therefore, and also in line with the formation of a stronger intramolecular $\text{H}_{12}-\text{O}_{14}$ hydrogen bond in the R1-2OO-*syn* structure, the $\text{O}_{11}-\text{H}_{12}$ hydroxyl bond in the R1-2OO-*syn* isomer is weaker than the $\text{O}_{11}-\text{H}_{12}$ hydroxyl bond in the R1-4OO-*syn* isomer.

5.3.4. Kinetic Parameters

All kinetic rate constants that are supplied in the sequel were obtained according to our best estimates of energy barriers, i.e. using DFT along with the UM06-2x exchange-correlation functional. Effective rate constants have been computed upon the assumption of a two-step mechanism, involving first a fast and reversible pre-equilibrium between the reactants (R1 and O_2) and a prereactive complex $[\text{C}_{10}\text{H}_8\text{OH}\dots\text{O}_2]^*$ (IM), followed by the irreversible formation of the naphthalene peroxy radicals R1-*i*OO-*syn/anti* ($i=2,4$):



A steady-state analysis upon the above sequence of reactions leads to the following expressions for the effective rate constants characterizing the four retained chemical pathways:

$$k_{\text{eff}}(\mathbf{1}) = \frac{k_{(\text{R1}+\text{O}_2 \rightarrow \text{IM})} k_{(\text{IM} \rightarrow \text{R1-2OO-}i\text{syn})}}{k_{(\text{IM} \rightarrow \text{R1}+\text{O}_2)} + k_{(\text{IM} \rightarrow \text{R1-2OO-}i\text{syn})}} \quad (5.8)$$

$$k_{\text{eff}}(\mathbf{2}) = \frac{k_{(\text{R1}+\text{O}_2 \rightarrow \text{IM})} k_{(\text{IM} \rightarrow \text{R1-2OO-}i\text{anti})}}{k_{(\text{IM} \rightarrow \text{R1}+\text{O}_2)} + k_{(\text{IM} \rightarrow \text{R1-2OO-}i\text{anti})}} \quad (5.9)$$

$$k_{\text{eff}}(\mathbf{3}) = \frac{k_{(\text{R1}+\text{O}_2 \rightarrow \text{IM})} k_{(\text{IM} \rightarrow \text{R1-4OO-}i\text{syn})}}{k_{(\text{IM} \rightarrow \text{R1}+\text{O}_2)} + k_{(\text{IM} \rightarrow \text{R1-4OO-}i\text{syn})}} \quad (5.10)$$

$$k_{\text{eff}}(\mathbf{4}) = \frac{k_{(\text{R1}+\text{O}_2 \rightarrow \text{IM})} k_{(\text{IM} \rightarrow \text{R1-4OO-}i\text{anti})}}{k_{(\text{IM} \rightarrow \text{R1}+\text{O}_2)} + k_{(\text{IM} \rightarrow \text{R1-4OO-}i\text{anti})}} \quad (5.11)$$

with **1** and **2** denoting the formation of the R1-2OO-*syn/anti* radicals, and **3** and **4** denoting the formation of the R1-4OO-*syn/anti* radicals, respectively. In the above equations, $k_{(\text{R1}+\text{O}_2 \rightarrow \text{IM}_i, i=1-4)}$ is the kinetic rate constant characterizing the forward bimolecular reaction step (in $\text{cm}^3 \text{ molecule}^{-1} \text{ s}^{-1}$), whereas $k_{(\text{IM}_i \rightarrow \text{R1-}i\text{OO}(i=2,4)\text{-}i\text{syn/anti})}$ and $k_{(\text{IM}_i \rightarrow \text{R1}+\text{O}_2, i=1-4)}$ represent the forward and backward unimolecular reaction rate constants (in s^{-1}).

Whatever the considered temperature, the effective rate constant for the formation of the R1-4OO-*syn* radical is larger than that obtained for the R1-2OO-*syn* radical, which is in line with a reduction of the activation energy barrier, by ~ 1.1 kcal mol⁻¹ (UM06-2x/aug-cc-pVTZ estimate), on the corresponding chemical reaction pathways. Indeed, the supplied TST and RRKM results (Tables 5.7 and 5.8) obtained along with the UM06-2x/aug-cc-pVTZ approach indicate that rate constants [$k_2(3)$] for the [IM3→R1-4OO-*syn*] unimolecular rearrangement reaction step are larger by factors ranging from 4 to 6, than the rate constants [$k_2(1)$] obtained for the [IM1→R1-2OO-*syn*] unimolecular reaction step. At a pressure of 1 bar, the formation of the R1-4OO-*syn* species will therefore clearly predominate over the formation of the R1-2OO-*syn* species. The same observation holds for pressures ranging from 10⁻¹² to 10⁴ bars (see Tables S1a–S1f in the Appendix III). As is to be expected, because of the involved positive energy barriers, these rate constants increase gradually with increasing temperatures. Rather unsurprisingly, since the equilibrium constants for the first reversible reaction step ($K_c=K_p/RT$) do not depend very much on the site of addition (see data supplied in Tables S2a–S2i in the Appendix III), this results in turn into a larger effective rate constant, by about one order of magnitude, for addition of O₂ in *syn* mode and in C₄ position, compared with the effective rate constants obtained for O₂ addition in *syn* mode and in C₂ position.

Similar observations can be made for the *anti* modes of addition. Here also, in line with lower activation energies (by ~ 1.1 kcal mol⁻¹ as well), rate constants [$k_2(4)$] for the [IM4→R1-4OO-*anti*] unimolecular rearrangement reaction step are larger by factors ranging from 4 to 7, than the rate constants [$k_2(2)$] obtained for the [IM2→R1-2OO-*anti*] unimolecular reaction step. At a pressure of 1.0 bar, the formation of the R1-4OO-*anti* species will therefore also clearly predominate over the formation of the R1-2OO-*anti* species. The same observation holds for pressures ranging from 10⁻¹² to 10⁴ bars (see Tables S1a–S1f in the Appendix III). Again, since the equilibrium constants for the first reversible reaction do not depend very much on the site of addition (see data supplied in Tables S2a–S2i in the Appendix III), this results in turn into a larger effective rate constant, by about one order of magnitude, for addition of O₂ in *anti* mode and in C₄ position, compared with the effective rate constants obtained for O₂ addition in *anti* mode and in C₂ position. Thus, whatever the addition (*syn* or *anti*) mode, O₂ addition in C₄ position is kinetically favored over O₂ addition in C₂ position, in contrast with the expectations drawn from thermodynamics and reaction energies.

Table 5.7. Unimolecular rate constants (in s^{-1}), and effective rate constants (in $cm^3 \text{ molecule}^{-1} s^{-1}$) for the reported reaction channels obtained by means of TST theory ($P=1$ bar), according to the computed UM06-2x/aug-cc-pVTZ energy barrier ($x=1$ or 3, $y=2$ or 4).

T (K)	Rate constant						Effective rate constant ($cm^3 \text{ molecule}^{-1} s^{-1}$)				$k_{\text{exp}} \times 10^{16}$ [31–34]
	<i>anti</i> mode			<i>syn</i> mode			<i>anti</i> mode		<i>syn</i> mode		
	IM x →R1+O $_2$ (k_{-1})	IM2→R1-2OO $k_2(2)$	IM4→R1-4OO $k_2(4)$	IM y →R1+O $_2$ (k_{-1})	IM1→R1-2OO $k_2(1)$	IM3→R1-4OO $k_2(3)$	R1+O $_2$ →R1-2OO [$k_{\text{eff}}(2)$]	R1+O $_2$ →R1-4OO [$k_{\text{eff}}(4)$]	R1+O $_2$ →R1-2OO [$k_{\text{eff}}(1)$]	R1+O $_2$ →R1-4OO [$k_{\text{eff}}(3)$]	
298	1.88×10^{19}	1.16×10^6	9.12×10^6	4.36×10^{16}	1.73×10^5	1.05×10^6	4.82×10^{-21}	3.79×10^{-20}	3.83×10^{-19}	2.32×10^{-18}	8.0 ± 3.0
336	3.92×10^{18}	4.92×10^6	3.10×10^7	1.80×10^{16}	6.95×10^5	3.49×10^6	2.41×10^{-20}	1.52×10^{-19}	1.05×10^{-18}	5.23×10^{-18}	0.8 ± 0.3
400	5.61×10^{17}	2.98×10^7	1.43×10^8	6.11×10^{15}	3.93×10^6	1.56×10^7	1.85×10^{-19}	8.89×10^{-19}	3.65×10^{-18}	1.43×10^{-17}	1.1

Table 5.8. Unimolecular rate constants (in s^{-1}), and effective rate constants (in $cm^3 \text{ molecule}^{-1} s^{-1}$) for the reported reaction channels obtained by means of RRKM theory ($P=1$ bar), according to the computed UM06-2x/aug-cc-pVTZ energy barriers ($x=1$ or 3, $y=2$ or 4).

T (K)	Rate constant						Effective rate constant ($cm^3 \text{ molecule}^{-1} s^{-1}$)				$k_{\text{exp}} \times 10^{16}$ [31–34]
	<i>anti</i> mode			<i>syn</i> mode			<i>anti</i> mode		<i>syn</i> mode		
	IM x →R1+O $_2$ (k_{-1})	IM2→R1-2OO $k_2(2)$	IM4→R1-4OO $k_2(4)$	IM y →R1+O $_2$ (k_{-1})	IM1→R1-2OO $k_2(1)$	IM3→R1-4OO $k_2(3)$	R1+O $_2$ →R1-2OO [$k_{\text{eff}}(2)$]	R1+O $_2$ →R1-4OO [$k_{\text{eff}}(4)$]	R1+O $_2$ →R1-2OO [$k_{\text{eff}}(1)$]	R1+O $_2$ →R1-4OO [$k_{\text{eff}}(3)$]	
298	1.88×10^{19}	1.17×10^6	8.92×10^6	4.36×10^{16}	1.77×10^5	1.07×10^6	4.85×10^{-21}	3.71×10^{-20}	3.92×10^{-19}	2.36×10^{-18}	8.0 ± 3.0
336	3.92×10^{18}	4.85×10^6	2.90×10^7	1.80×10^{16}	7.08×10^5	3.53×10^6	2.68×10^{-20}	1.60×10^{-19}	1.18×10^{-18}	5.90×10^{-18}	0.8 ± 0.3
400	5.61×10^{17}	2.77×10^7	1.17×10^8	6.11×10^{15}	3.96×10^6	1.55×10^7	2.31×10^{-19}	9.79×10^{-19}	4.90×10^{-18}	1.91×10^{-17}	1.1

Since the involved energy barriers are significantly larger, by ~ 3.20 kcal mol $^{-1}$, the formation of the R1-2OO-*anti* and R1-4OO-*anti* species is characterized by significantly lower rate constants at the considered temperatures (298, 336, and 400 K), by one to two orders of magnitude, compared with the formation of the R1-2OO-*syn* and R1-4OO-*syn* isomers (Tables 5.7 and 5.8). With one to two orders of magnitude only of discrepancy, our theoretical effective kinetic rate constants [$k_{\text{eff}}(\mathbf{3})$] for the fastest chemical reaction pathway (O $_2$ addition in *syn* mode and in C $_4$ position) appear to be in excellent agreement with the available experimental data reported at 298, 336 and 400 K by Koch *et al.* [22,31–33] an observation which validates the proposed two-step mechanism.

The reader is referred to Figure 5.3 for an Arrhenius plot of the obtained RRKM estimates at a pressure of 1 bar of the effective rate constants for O $_2$ addition in C $_2$ and C $_4$ positions and in the *syn/anti* addition modes (pathways 1–4), according to the UM06-2x/aug-cc-pVTZ estimates of energy barriers. This Figure clearly confirms that the production of the R1-4OO-*syn* peroxy radical dominates the overall reaction mechanism under atmospheric pressure and at temperatures ranging from 298 to 400 K. The same conclusion holds at much lower pressures, down to 10 $^{-12}$ bar (see Tables S2a–S2i of the Appendix III).

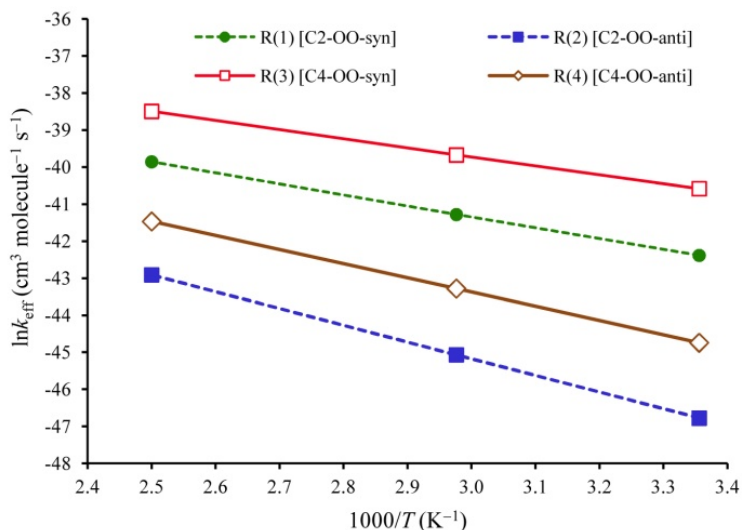


Figure 5.3. Arrhenius plot of the obtained RRKM bimolecular rate constants (for R1+O $_2$ →R1-*i*OO-*syn*, with $i=2,4$) using the UM06-2x/aug-cc-pVTZ approach. Legend: (●) theoretical rate constant obtained for the R1+O $_2$ →R1-2OO-*syn* pathway; (■) theoretical rate constant obtained for the R1+O $_2$ →R1-2OO-*anti* pathway; (□) theoretical rate constant obtained for the R1+O $_2$ →R1-4OO-*syn* pathway; (◇) theoretical rate constant obtained for the R1+O $_2$ →R1-4OO-*anti* pathway.

For the sake of more quantitative insights into the regioselectivity of O₂ addition on the [C₁₀H₈OH][•] radical, we report in Table 5.9 branching ratios at $P = 1$ bar and temperatures of 298, 336, and 400 K, which were obtained for the four retained chemical pathways according to the TST and RRKM estimates for effective rate constants [eqs.(5.8–5.11)]. Under these conditions, TST and RRKM estimates of branching ratios are almost identical.

$$R(i) = \frac{k_{\text{eff}}(i)}{k_{\text{eff}}(1) + k_{\text{eff}}(2) + k_{\text{eff}}(3) + k_{\text{eff}}(4)}; \quad i = 1-4 \quad (5.12)$$

Further RRKM estimates of these branching ratios at the same temperatures and at pressures ranging from 10⁻¹² to 10⁴ bars are supplied in Tables S2a–S2i of the Appendix III.

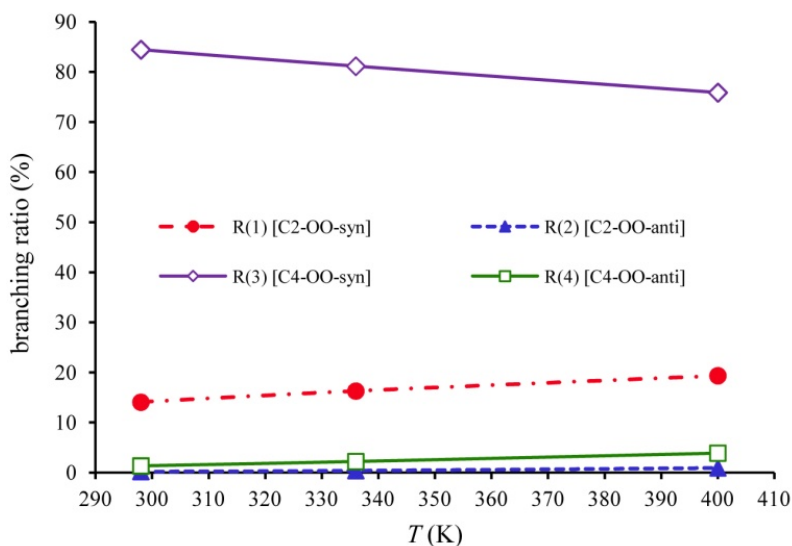


Figure 5.4. Evaluation of branching ratios in function of the temperature for pathways $R1+O_2 \rightarrow R1-iOO-syn$ ($i=2,4$) using the UM06-2x/aug-cc-pVTZ approach. Legend: (●) data obtained for the $R1+O_2 \rightarrow R1-2OO-syn$ pathway; (▲) data obtained for the $R1+O_2 \rightarrow R1-2OO-anti$ pathway; (◇) data obtained for the $R1+O_2 \rightarrow R1-4OO-syn$ pathway; (□) data obtained for the $R1+O_2 \rightarrow R1-4OO-anti$ pathway.

In Figures 5.4 and 5.5, we display the evolution of branching ratios for the *syn*-addition of O₂ in C₂ and C₄ positions as a function of the temperature and pressure, respectively (see also Table 5.8 and Table S3a–S3f of the Appendix III for the corresponding numerical values). These data show that the regioselectivity of

the reactions slightly decreases with increasing temperatures (Figure 5.4) and decreasing pressures (Figure 5.5). In line with the computed energy profile and kinetic rate constants, the formation of the R1-4OO-*syn* isomer (pathway **3**) clearly predominates over the formation of the R1-2OO-*syn* isomer (pathway **1**). In view of the supplied RRKM data (see Tables S2a–S2i of the Appendix III), it is more than certain that, at different temperatures, the production of the R1-4OO-*syn* species dominates the overall reaction mechanism, and this down to extremely low pressures, larger than 10^{-12} bar. Note nevertheless that the computed regioselectivity indices become almost equal to zero at 400 K and pressures lower than 10^{-6} bar. At such pressures and temperatures, the reaction is therefore no longer regioselective, and these both for the *syn* and *anti* modes of addition.

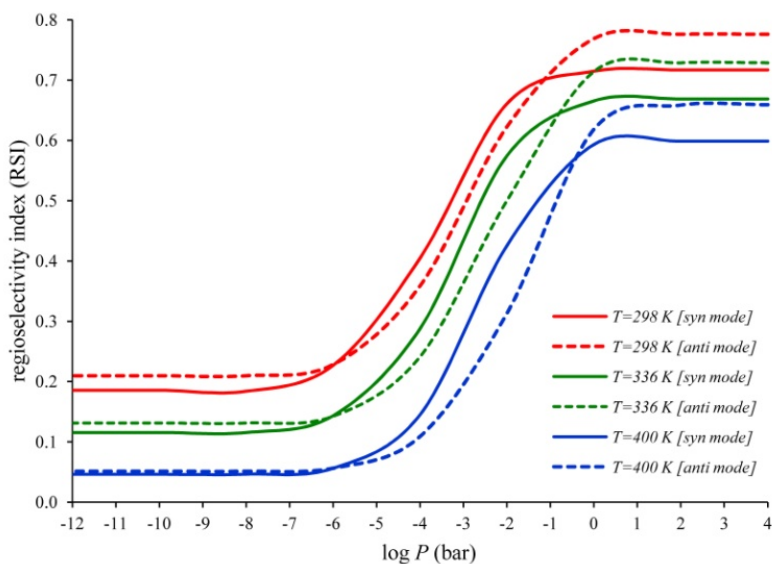


Figure 5.5. Dependence upon the pressure and temperature of the regioselectivities $[RSI=R(3)-R(1)/R(1)+R(3)]$ and $[RSI=R(4)-R(2)/R(2)+R(4)]$ of O_2 addition in *syn* and *anti* modes onto the naphthalene-OH adduct $[C_{10}H_8OH]^*$, according to the RRKM estimates of effective rate constants $[k_{\text{eff}}(\mathbf{1}), k_{\text{eff}}(\mathbf{2}), k_{\text{eff}}(\mathbf{3}), k_{\text{eff}}(\mathbf{4})]$ supplied in Tables S3a–S3f (see Appendix III), based on UM06-2x/aug-cc-pVTZ energy profiles.

Upon inspecting Figure 5.6 and Table 5.9, it is clear that the RRKM effective rate constants obtained from the UM06-2x energy profiles for the $R1+O_2 \rightarrow R1-iOO$ -*syn/anti* ($i=2,4$) reaction pathways increase with increasing temperatures. Upon inspecting the RRKM data displayed in Figure 5.6, it appears quite clearly that, in

line with rather larger energy barriers, ranging from 2.7 to 3.8 kcal mol⁻¹, pressures larger than 10⁻² bar are sufficient for ensuring a saturation within 10 % accuracy of the computed effective kinetic rate constants compared with the high pressure limit. In contrast with our preceding study of the formation of the [C₁₀H₈OH][•] adduct through addition reactions of hydroxyl radicals onto naphthalene [24], the TST approximation may therefore be regarded as valid at standard temperatures and pressures.

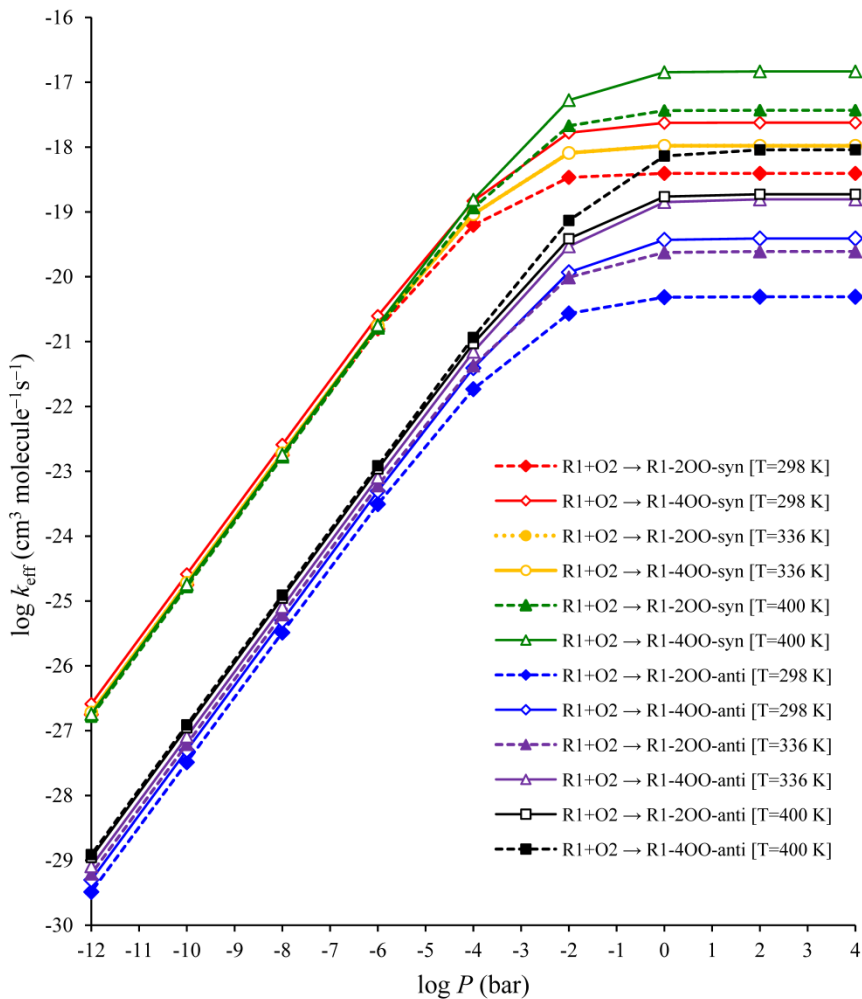


Figure 5.6. Pressure dependence of the bimolecular rate constants for the R1+O₂→R1-*i*OO-*syn/anti* (*i*=2,4) reaction pathways according to the UM06-2x/aug-cc-pVTZ energy profiles [RRKM results, obtained by means of equations (5.8–5.11)].

Table 5.9. Branching ratios for the reported reaction channels obtained by means of TST and RRKM theories ($P=1$ bar), according to the computed UM06-2x/aug-cc-pVTZ energy barriers.

Pathway	Theory		TST			RRKM		
	298 K	336 K	298 K	336 K	400 K	298 K	336 K	400 K
R1+O ₂ →R1-2OO- <i>syn</i>	13.95	16.26	19.19	14.06	16.29	19.36		
R1+O ₂ →R1-2OO- <i>anti</i>	0.18	0.37	0.97	0.17	0.37	0.91		
R1+O ₂ →R1-4OO- <i>syn</i>	84.50	81.01	75.17	84.44	81.14	75.86		
R1+O ₂ →R1-4OO- <i>anti</i>	1.38	2.35	4.67	1.33	2.20	3.87		

As anticipated (see end of section 5.3.1), differences in branching ratios obtained using different theoretical models are all in all quite limited (see Table 5.10): they do not exceed 4% and 10% at 298 K and 400 K, respectively, which confirms further the relevance and numerical robustness of our analysis.

Table 5.10. Branching ratios for the reported reaction channels obtained by means of RRKM theory ($P=1$ bar), at different DFT levels.

Pathway	Theory		B3LYP			ω B97XD			UM05-2x			UM06-2x		
	298 K	336 K	400 K	298 K	336 K	400 K	298 K	336 K	400 K	298 K	336 K	400 K		
													298 K	336 K
R1+O ₂ →R1-2OO- <i>syn</i>	13.17	15.48	18.40	12.32	14.48	17.36	10.65	12.32	14.63	14.06	16.29	19.36		
R1+O ₂ →R1-2OO- <i>anti</i>	1.34	2.35	4.79	0.75	1.22	2.27	0.13	0.30	0.79	0.17	0.37	0.91		
R1+O ₂ →R1-4OO- <i>syn</i>	80.40	74.07	62.39	84.39	80.07	72.71	88.02	85.26	80.31	84.44	81.14	75.86		
R1+O ₂ →R1-4OO- <i>anti</i>	5.09	8.10	14.42	2.54	4.23	7.66	1.20	2.12	4.27	1.33	2.20	3.87		

5.4. Conclusions

The mechanisms for the atmospheric oxidation of naphthalene-OH adduct [C₁₀H₈OH]^{*} (R1) by molecular oxygen in its triplet electronic ground state have been studied computationally using density functional theory along with various exchange-correlation functional (B3LYP, ω B97XD, UM05-2x and UM06-2x) and an extremely large basis set (aug-cc-pVTZ). All our calculations indicate that, from a thermodynamic viewpoint, the most favorable process is O₂ addition at the C₂ position in *syn* mode, followed by O₂ addition at the C₂ position in *anti* mode, O₂ addition at the C₂ position in *anti* mode, and O₂ addition at the C₄ position in *anti* mode, as the second, third and fourth most favorable processes, respectively. In

contrast with recent data by Zhang *et al.* [25], the *syn* modes of addition at the C₂ and C₄ positions appear to be thermodynamically favored over the *anti* one by the formation of an intramolecular hydrogen bond between the hydroxyl and peroxy substituents. Our study confirms that O₂ additions in C₅, C₇ and C₉ positions are highly unlikely processes, due to unfavorable reaction energies and energy barriers.

A combined structural, energetic and natural bond orbital analysis shows that the intramolecular hydrogen bond in the R1-2OO-*syn* radical is stronger than that in the R1-4OO-*syn* radical. Analysis of the computed structures, bond orders and free energy profiles demonstrates that the reaction steps involved in the oxidation of the naphthalene-OH adduct by O₂ satisfy Hammond's principle: the transition state involved in the formation of the R1-4OO-*syn* radical is structurally closer to the product than the transition state involved in the formation of the R1-2OO-*syn* radical.

The calculated energy profiles have been supplemented with calculations of kinetic rate constants and branching ratios under atmospheric pressure and in the fall-off regime, down to pressure of 10⁻¹² bar, using transition state and RRKM theories. The supplied data indicate that, under a kinetic control of the reaction, and in contrast with the situation that prevails at chemical equilibrium (thermodynamic control), the most abundant product resulting from the oxidation of the [C₁₀H₈OH][•] adduct by O₂ must be the R1-4OO-*syn* radical rather than the R1-2OO-*syn* radical. For the *anti* modes as well, O₂ addition in C₄ position is kinetically favored over addition in C₂ position. Upon considering that O₂ addition in *syn* mode in C₄ position must prevail under a kinetic control of the reaction, the rather excellent agreement between our effective kinetic rate constants with the available experimental ones demonstrates the relevance of the proposed two-step reaction mechanism [60]. The computed branching ratios also indicate that the regioselectivity of the reaction decreases with increasing temperatures and decreasing pressures.

5.5. References

- [1] P.T. Williams, M.K. Abbass, G.E. Andrews, K.D. Bartle, *Combust. Flame.*, **1989**, 75, 1.
- [2] S.K. Hoekman, *Environ. Sci. Technol.*, 1992, **26**, 1206.
- [3] B. Zielinska, J. Sagebiel, J.D. McDonald, K. Whitney, D.R. Lawson, *J. Air & Waste Manage. Assoc.*, **2004**, 54, 1138.
- [4] L.C. Marr, T.W. Kirchstetter, R.A. Harley, A.H. Miguel, S.V. Hering, S.K. Hammond, *Environ. Sci. Technol.*, **1999**, 33, 3091.

- [5] M.P. Fraser, G.R. Cass, B.R.T. Simoneit, *Environ. Sci. Technol.*, **1998**, *32*, 2051.
- [6] M. Howsam, K.C. Jones, *Handbook of Environmental Chemistry*; Springer-Verlag: Berlin, **1998**, *3*, 137.
- [7] T.F. Bidleman, *Environ. Sci. Technol.*, **1988**, *22*, 361.
- [8] F. Wania, D. Mackay, *Environ. Sci. Technol.*, **1996**, *30*, 390A.
- [9] D.G. Hendry, R.A. Kenley, *Atmospheric Reaction Products of Organic Compounds*; U.S. Environmental Protection Agency, EPA-560112-79-001, 1979.
- [10] R. Atkinson, K.R. Darnall, A.C. Lloyd, A.M. Winer, J.N. Pitts, *Adv. Photochem.*, **1979**, *11*, 375.
- [11] N.J. Bunce, L. Liu, J. Zhu, *Environ. Sci. Technol.*, **1997**, *31*, 2252.
- [12] R. Atkinson, J. Arey, *Environ. Health Perspect.*, **1994**, *102*, 117.
- [13] R. Atkinson, *J. Phys. Chem. Ref. Data, Monograph*, **1989**, *1*, 1.
- [14] R. Atkinson, E.C. Tuazon, J. Arey, *Int. J. Chem. Kinet.*, **1990**, *22*, 1071.
- [15] R. Atkinson, *J. Phys. Chem. Ref. Data, Monograph*, **1991**, *20*, 459.
- [16] R. Atkinson, E.C. Tuazon, I. Bridier, J. Arey, *Int. J. Chem. Kinet.*, **1994**, *26*, 605.
- [17] J. Sasaki, S.M. Aschmann, E.S.C. Kwok, R. Atkinson, J. Arey, *Environ. Sci. Technol.*, **1997**, *31*, 3173.
- [18] K. Lorenz, R. Zellner, *Ber. Bunsen-Ges. Phys. Chem.*, **1983**, *87*, 629.
- [19] R. Atkinson, J. Arey, *Polycyclic Aromat. Compd.*, **2007**, *27*, 15.
- [20] R. Atkinson, J. Arey, *Chem. Rev.*, **2003**, *103*, 4605.
- [21] C. Bloss, V. Wagner, M.E. Jenkin, R. Volkamer, W.J. Bloss, J.D. Lee, D.E. Heard, K. Wirtz, M. Martin-Reviejo, G. Rea, J.C. Wenger, M.J. Pilling, *Atmos. Chem. Phys.*, **2005**, *5*, 641.
- [22] R. Koch, R. Knispel, M. Elend, M. Siese, C. Zetzsch, *Atmos. Chem. Phys.*, **2007**, *7*, 2057.
- [23] A. Shiroudi, M.S. Deleuze, *J. Phys. Chem. A*, **2014**, *118*, 3625.
- [24] A. Shiroudi, M.S. Deleuze, S. Canneaux, *J. Phys. Chem. A*, **2014**, *118*, 4593.
- [25] Z. Zhang, L. Lin, L. Wang, *Phys. Chem. Chem. Phys.*, **2012**, *14*, 2645.
- [26] B. Bohn, C. Zetzsch, *Phys. Chem. Chem. Phys.*, **1999**, *1*, 5097.
- [27] D. Johnson, S. Raoult, M.T. Rayez, J.C. Rayez, R. Lesclaux, *Phys. Chem. Chem. Phys.*, **2002**, *4*, 4678.
- [28] S.Y. Grebenkin, L.N. Krasnoperov, *J. Phys. Chem. A*, **2004**, *108*, 1953.
- [29] S. Raoult, M.T. Rayez, J.C. Rayez, R. Lesclaux, *Phys. Chem. Chem. Phys.*, **2004**, *6*, 2245.
- [30] B. Bohn, *J. Phys. Chem. A*, **2001**, *105*, 6092.

- [31] R. Koch, C. Zetzsch, *13th International Symposium on Gas Kinetics*; University College Dublin: Ireland, 11–16 September, 1994.
- [32] R. Koch, R. Knispel, M. Siese, C. Zetzsch, *Physico-Chemical Behavior of Atmospheric Pollutants*; European Commission: Brussels/ Luxemburg, 1994.
- [33] C. Zetzsch, R. Koch, B. Bohn, R. Knispel, M. Siese, F. Witte, pp. 247–256 in *Chemical Processes in Atmospheric Oxidation*; edited by G. Le Bras, Springer, Berlin, 1997.
- [34] R. Koch, B. Bohn, C. Zetzsch, *The Oxidizing Capacity of the Troposphere, Physico-Chemical Behavior of Atmospheric Pollutants*; European Commission: Brussels, 1997.
- [35] H. Eyring, *J. Chem. Phys.*, 1935, **3**, 107.
- [36] H.S. Johnston, *Gas Phase Reaction Rate Theory*; Roland Press Co: New York, 1966.
- [37] K.J. Laidler, *Theories of Chemical Reaction Rates*; McGraw-Hill: New York, 1969.
- [38] R.E. Weston, H.A. Schwartz, *Chemical Kinetics*; Prentice-Hall: New York, 1972.
- [39] D. Rapp, *Statistical Mechanics*; Holt, Reinhard, and Winston: New York, 1972.
- [40] E.E. Nikitin, *Theory of Elementary Atomic and Molecular Processes in Gases*; Clarendon Press: Oxford, 1974.
- [41] I.W.M. Smith, *Kinetics and Dynamics of Elementary Gas Reactions*; Butterworths: London, 1980.
- [42] J.I. Steinfeld, J.S. Francisco, W.L. Hase, *Chemical Kinetics and Dynamics*; Prentice-Hall: Englewood Cliffs, NJ, 1989.
- [43] G. Lendvay, *J. Phys. Chem.*, **1989**, *93*, 4422.
- [44] A.E. Reed, L.A. Curtiss, F. Weinhold, *Chem. Rev.*, **1988**, *88*, 899.
- [45] V. Lopez, J. Quijano, S. Luna, P. Ruiz, D. Rios, W. Parra, E. Zapata, J. Gaviria, R. Notario, *Struct. Chem.*, **2013**, *24*, 1811.
- [46] A.D. Becke, *J. Chem. Phys.*, **1993**, *98*, 5648.
- [47] C. Lee, W. Yang, R.G. Parr, *Phys. Rev B*, **1988**, *37*, 785.
- [48] J.D. Chai, M. Head-Gordon, *Phys. Chem. Chem. Phys.*, **2008**, *10*, 6615.
- [49] Y. Zhao, D.G. Truhlar, *Acc. Chem. Res.*, **2008**, *41*, 157.
- [50] Y. Zhao, D.G. Truhlar, *Theor. Chem. Acc.*, **2008**, *120*, 215.
- [51] T.H. Dunning, *J. Chem. Phys.*, **1989**, *90*, 1007.
- [52] A.E. Reed, R.B. Weinstock, *J. Chem. Phys.*, **1985**, *83*, 735.
- [53] J.K. Badenhoop, F. Weinhold, *Int. J. Quantum. Chem.*, **1999**, *72*, 269.

- [54] M.J. Frisch, G.W. Trucks, H.B. Schlegel, G.E. Scuseria, M.A. Robb, J.R. Cheeseman, G. Scalmani, V. Barone, B. Mennucci, G.A. Petersson, *et al.* *Gaussian 09*, Revision B.01; Gaussian, Wallingford, CT, 2009.
- [55] I.I.R. Dennington, T. Keith, J. Millam, K. Eppinnett, W.L. Hovell, R. Gilliland, *GaussView*, Version 3.09; Semichem, Inc., Shawnee Mission, KS, 2003.
- [56] C. Gonzalez, H.B. Schlegel, *J. Chem. Phys.*, **1989**, *90*, 2154.
- [57] J.W. McIver, Jr. *Acc. Chem. Res.*, **1974**, *7*, 72.
- [58] F. Fukui, *J. Phys. Chem.*, **1970**, *74*, 4161.
- [59] D.A. McQuarrie, *Statistical Mechanics*; Harper and Row: New York, 1976.
- [60] G.H. Herzberg, *Molecular Spectra and Molecular Structure. II Infrared and Raman Spectra of Polyatomic Molecules*; Van Nostrand Reinhold: New York, 1945.
- [61] D.L. Singleton, R.J. Cvetanovic, *J. Am. Chem. Soc.*, **1976**, *98*, 6812.
- [62] R.G. Mortimer, *Physical Chemistry*; 3rd ed., Elsevier Academic Press: Burlington, 2008.
- [63] R. Chang, *Physical Chemistry for the Biosciences*; University Science Books, Sausalito: California, 2005.
- [64] J.W. Moore, R.G. Pearson, *Kinetics and Mechanism-The Study of Homogeneous Chemical Reactions*; 3rd ed., Wiley: New York, 1981.
- [65] H.H. Carstensen, A.M. Dean, O. Deutschmann, *Proc. Combust. Inst.*, **2007**, *31*, 149.
- [66] D.H. Varma, P. Raghunath, M.C. Lin, *J. Phys. Chem. A*, **2010**, *114*, 3642.
- [67] S.Y. Wu, P. Raghunath, J.S. Wu, M.C. Lin, *J. Phys. Chem. A*, **2010**, *114*, 633.
- [68] R.G. Gilbert, S.C. Smith, *Theory of Unimolecular and Recombination Reactions*; Blackwell Scientific: Oxford, 1990.
- [69] H.B. Rao, X.Y. Zeng, H. He, Z.R. Li, *J. Phys. Chem. A*, **2011**, *115*, 1602.
- [70] S. Canneaux, F. Bohr, E. Henon, *J. Comput. Chem.*, **2014**, *35*, 82.
- [71] F. Rosas, R.M. Dominguez, M. Tosta, J.R. Mora, E. Marquez, T. Cordova, G. Chuchani, *J. Phys. Org. Chem.*, **2010**, *23*, 743.
- [72] E.A. Mason, L. Monchick, *Humidity and Moisture Measurement and Control in Science and Industry. Survey of the Equation of State and Transport Properties of Moist Gases*; Reinhold Publishing Corp: New York, 1965.
- [73] J.B. Chaddock, *Moist Air Properties from Tabulated Virial Coefficients. Humidity and Moisture Measurement and Control in Science and Industry*; Reinhold Publishing Corp: New York, 1965.
- [74] Y. Iwai, H. Higashi, H. Uchida, Y. Arai, *Fluid Phase Equilib.*, **1997**, *127*, 251.

- [75] I. García-Cruzl, M. Castro, A. Vivier-Bunge, *J. Comput. Chem.*, **2000**, *21*, 716.
- [76] G.E. Scuseria, H.F. Schaefer III, *J. Chem. Phys.*, **1989**, *90*, 3629.
- [77] R.S. Grev, H.F. Schaefer III, *J. Chem. Phys.*, **1989**, *91*, 7305.
- [78] M. Huang, Z. Wang, Y. Yang, L. Hao, W. Zhao, X. Gao, L. Fang, W. Zhang, *Int. J. Quantum. Chem.*, **2007**, *107*, 1092.
- [79] N. Agmon, R.D. Levine, *Chem. Phys. Lett.*, **1977**, *52*, 197.

Chapter 6

Theoretical study of the oxidation mechanisms of naphthalene initiated by hydroxyl radicals: The isomerization processes of naphthalene peroxy radicals

6.1. Introduction

Polycyclic aromatic hydrocarbons (PAHs) are ubiquitous environmental pollutants. Many of these compounds are potentially genotoxic, mutagenic, or carcinogenic [1,2]. Aromatic hydrocarbons constitute a major fraction (~20%) of total volatile organic compounds (VOCs) in urban area [3]. PAHs undergo chemical reactions with scavenger molecules such as O₃, NO, NO₂, O₂, and OH radicals in the gas phase. Naphthalene is the most volatile and abundant PAH due to anthropogenic sources of air pollution, including gasoline engine exhausts and fuel evaporation [4–7], and is reactive at ambient temperature and pressure [8,9]. Reactions of naphthalene in the atmosphere are mainly initiated by OH radical additions yielding [C₁₀H₈OH][•] (R1) radical adducts that subsequently react with O₂ during daylight hours, and with NO₃ radicals during evening and nighttime hours [10,11]. A secondary reaction channel implies hydrogen abstraction, resulting into 1 and 2-naphthyl radicals plus water [12]. Due to very low rate constants, ranging from 10⁻¹⁷ to 1.8×10⁻¹⁶ cm³ molecule⁻¹ s⁻¹ at room temperature [13,14], O₂ addition onto the R1 adducts is experimentally very difficult to study, and requires extensive theoretical calculations for unraveling its mechanism. During their reaction with O₂, the aromatic peroxy radicals are speculated to cyclize to form

bicyclic radicals, which are subject to further O₂ addition reaction steps and subsequent ring fragmentation.

In recent years, many theoretical and experimental studies have highlighted the importance of bicyclic intermediates in the oxidation mechanisms of benzene [15], toluene [16], *p*-xylene [17], and *m*-xylene [18]. The [C₁₀H₈OH][•]-O₂ peroxy radicals can dissociate back to reactants, or isomerize to bicyclic peroxy adducts through unimolecular reaction pathways. They may also react via unimolecular hydrogen transfer reactions that convert them to oxy hydroperoxide radicals. In two previous articles [19,20], we have studied the first reaction steps involved in the oxidation pathways of naphthalene. At low temperatures ($T \leq 410$ K), OH addition reaction pathways dominate under inert (He) conditions, to yield 1- and 2-naphthol, with 1-naphthol being the most abundant product. Under atmospheric conditions, however, the intermediate energized adducts [C₁₀H₈OH][•] that are involved in the latter reaction mechanism are rather expected to dominantly react with triplet molecular oxygen, to form [C₁₀H₈OH][•]-O₂ peroxy radicals (Figure 6.1) which may be referred, as in previous studies by Shiroudi *et al.* [20] as well as Zhang *et al.* [21] to as the R1-*i*OO-*anti/syn* (*i*=2,4) radicals. Similar reactions of O₂ with [OH-benzene][•] [22–25] and [OH-toluene][•] [26] adducts are known to proceed through a reversible addition of O₂ to the OH-aromatic adduct to form an OH-aromatic-O₂ peroxy radical [27]. By analogy with the oxidation reaction mechanisms of benzene [15], toluene [16], *p*-xylene [17], and *m*-xylene [18], the fate of the naphthalene peroxy radical [C₁₀H₈-OH][•]-O₂ adducts must be determined by a competition between isomerization processes to oxy hydroperoxides and to bicyclic peroxy radicals (Figure 6.1) [18].

According to recent theoretical data by our group [20], O₂ addition in *syn* mode onto the [C₁₀H₈OH][•] adduct at the C₄ and C₂ positions (Figure 6.1) are thermodynamically and kinetically the two most favorable processes, due to aromaticity effects, and the formation of an intramolecular hydrogen bond between the terminal oxygen of the peroxy (O₂) group and the hydrogen of the OH group. The corresponding branching ratios at room temperature amount to 85% and 14%, respectively. Consequently, in this work, we only focus on the fate of the products of these two reactions, referred to as the R1-4OO-*syn* and R1-2OO-*syn* species (Figure 6.1), respectively.

The main purpose of the present study is to evaluate reaction and activation energies as well as kinetic rate constants for all unimolecular reaction steps that are displayed in Figure 6.1. These reactions were already studied by Zhang *et al.* [21] using the B3LYP [28,29] and BB1K functionals [30], in conjunction with Pople's type 6-311+G(2df,p) or 6-311++G(2df,2p) basis sets [31–34]. Results obtained by

Zhang *et al.* need to be verified using more reliable exchange-correlation functional and basis sets. Indeed, energy barriers obtained with the B3LYP functional are usually strongly underestimated [35,36], because of self-interaction error [37]. Besides, the 6-311G basis set from which the 6-311+G(2df,p) and 6-311++G(2df,2p) basis sets derive is known to exhibit a too compact $2p$ space [38], and to be effectively a basis set of double-zeta quality only in the s -space, due to improperly balanced expansion coefficients [39]. In our preceding study of the O_2 addition step in the oxidation mechanism of naphthalene initiated by hydroxyl radicals [20], the 6-311+G(2df,p) basis set was found to yield considerable discrepancies, up to 3 kcal mol^{-1} , in the computed reaction and activation energies, compared with results obtained using the (twice as large) Dunning's augmented correlation consistent polarized valence basis set of triple zeta quality (aug-cc-pVTZ) [40]. Also, the energy order that was predicted at the B3LYP/6-311+G(2df,p) level [21] for the lowest and chemically most relevant isomers was found to be incorrect – an observation which led us to undertake the present large-scale verification of the reaction and activation energies obtained by Zhang *et al.* [21] for the formation of bicyclic peroxy radicals with an O–O bridge across a benzenoid ring, and for the formation of oxy hydroperoxide radicals from $[C_{10}H_8OH]^{\bullet}-O_2$ peroxy adducts, through intramolecular hydrogen transfers. For the sake of reliability in the analysis, more specifically for bracketing errors on reaction and activation energies, comparison will be made with results obtained using a variety of exchange-correlation functionals, comprising the popular B3LYP functional, but also the dispersion-corrected ω B97XD functional [41], as well as the UM05-2x [42] and UM06-2x [42,43] functionals, which have been specifically designed for accurate studies of chemical reactions, both from a thermodynamic and kinetic viewpoint.

In addition, kinetic rate constants in the high-pressure limit will be supplied by means of transition state theory (TST) [44–51], and their fall-off behavior at lower pressures will be studied using statistical RRKM theory [52–54], for the purpose of unraveling the detailed experiments by Koch *et al.* [27,55–58] at 298, 336 and 400 K.

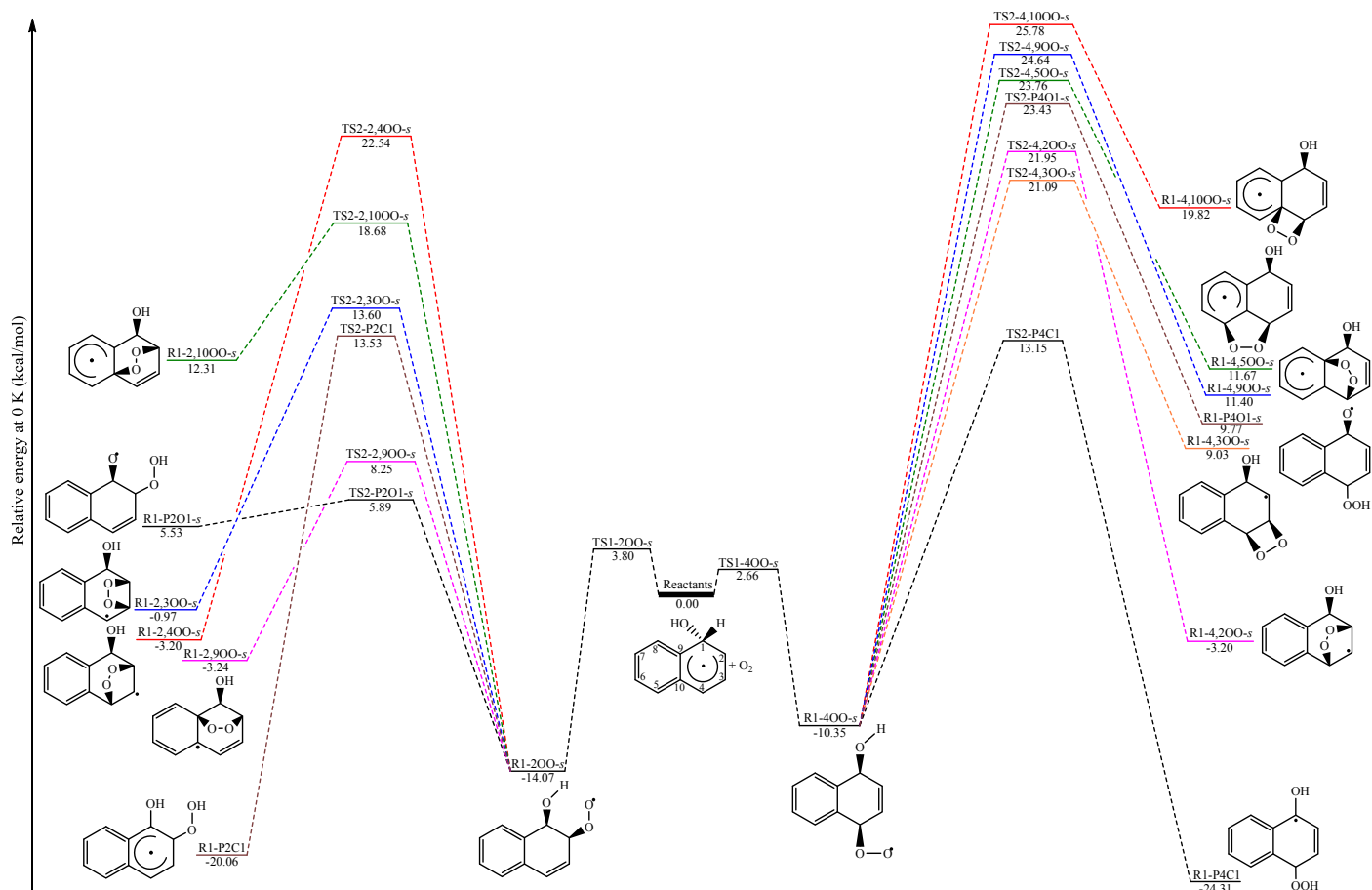


Figure 6.1. Potential energy diagram for considered reaction pathways of the R1-200-*syn* and R1-400-*syn* peroxy radicals at the UM06-2x/aug-cc-pVTZ level of theory.

6.2. Computational Details

All quantum chemical calculations that are discussed in the present contribution were performed using the Gaussian 09 package of programs [59]. The molecular structures and harmonic vibrational frequencies of all stationary points involved in the reaction pathways that are depicted in Figure 6.1 were calculated using DFT along with B3LYP, ω B97XD, UM05-2x and UM06-2x functionals, in conjunction with Dunning's correlation-consistent basis set of triple- ζ quality incorporating *s*, *p*, and *d* diffuse functions (aug-cc-pVTZ basis set) [40].

The intrinsic reaction coordinate (IRC) calculations [60] were carried out in both directions (forward and backward) along the reaction path at the B3LYP/6-31G(d,p) level using the second-order Gonzalez-Schlegel integration method [61,62], in order to verify whether the located transition state structure connects to the relevant energy minima. Frequency calculations were carried out to check the nature of the identified stationary points. In line with these frequency calculations, thermodynamic state functions (*H*, *S*, *G*) were obtained from canonical partition functions (*Q*) obtained for an ideal polyatomic gas under a pressure of 1 atm using the standard RRHO (rigid rotor harmonic oscillator) approximation and Boltzmann statistics (see refs 63 and 64 or any textbook of molecular statistical mechanics).

Rate constants for unimolecular reactions were obtained in the high pressure limit by means of transition state theory, using UM06-2x estimates for the activation energies (*E_a* [including zero-point vibrational energy contributions]), according to [65–67]:

$$k_{\text{TST}} = \kappa(T) \frac{\sigma k_{\text{B}} T}{h} \frac{Q_{\text{TS}}^{\ddagger}(T)}{Q_{\text{A}}(T)} \exp(-E_{\text{a}}/RT) \quad (6.1)$$

Because the moving entity at the transition state involves relatively heavy oxygen atoms, the tunneling factor $\kappa(T)$ has been assumed to be equal to 1 for the ring closure processes implying formation of an –O–O– bridge. On the other hand, in view of a strongly asymmetric energy barrier, an Eckart tunneling correction factor [68] has been considered for evaluating the rate constants characterizing intramolecular hydrogen transfer processes.

Since the computed energy differences account for zero-point vibrational energies, vibrational partition functions were computed using the vibrational ground state as energy reference. TST gives an estimate of the upper-limit for rate constants as a function of the temperature, and is known to give reliable estimations of rate constants [69,70] in the high pressure limit [71], especially for cases with significant barrier heights [72].

Statistical RRKM theory [52–54,73] has been considered to evaluate pressure effects on a microcanonical basis, both in the fall-off regime and towards the high pressure limit, by means of the KiSTheLP program [74].

In line with the temperatures at which the experiments by Koch *et al.* [55–58] were conducted, unimolecular rate constants have been obtained at 298, 336 and 400 K and at a pressure of 1 bar (high pressure limit) using transition state theory, and the UM06-2x/aug-cc-pVTZ estimates for activation energies. The rationale behind this choice is that a recent study by Zhao and Truhlar [43] has shown that the UM06-2x method is the best exchange-correlation functional for applications involving main-group thermochemistry, kinetics, noncovalent interactions, and electronic excitation energies to valence and Rydberg states [43]. In the RRKM calculations, a scaling factor of 0.971 was imposed on the frequencies calculated at the UM06-2x/aug-cc-pVTZ level of theory [75]. Collisional stabilization rate constants were computed using Lennard–Jones (LJ) collision rate theory [76]. The strong collision approximation was used, assuming thereby that every collision deactivates with $\omega = \beta_c \cdot Z_{LJ} \cdot [M]$ being the effective collision frequency, where β_c is the collisional efficiency, Z_{LJ} is the LJ collision frequency and $[M]$ is the total gas concentration. The retained value for β_c is 0.2. The collision frequencies (Z_{LJ}) were calculated using the LJ parameters: ε/k_B , which depends on the energy depth (ε) of the LJ potential, and σ , which represents a dimensional scale of the molecular radius [77]. For pure air (as diluent gas) and the naphthalene peroxy radical $[C_{10}H_8-OH]^{\bullet}-O_2$, the following LJ parameters have been retained: $\sigma = 3.522$ Å, $\varepsilon/k_B = 99.2$ K [78,79] and $\sigma = 6.57$ Å, $\varepsilon/k_B = 612.7$ K [80], respectively.

6.3. Results and Discussion

6.3.1. Energetic and Thermodynamic Parameters

The reader is referred to Tables 6.1 and 6.2 for a detailed thermodynamic characterization of all products and transition states displayed in Figure 6.1. For the ease of notations, the bicyclic epoxy radicals are denoted as R1-*i,j*OO-*syn* (*i*=2,4) species, where *i* and *j* denote the positions of the carbon atoms that are connected by the –OO– bridge. Products resulting from hydrogen transfer reactions from the –C₁H unit and –OH group to the –OO substituent are referred to as R1-PiC1 and R1-PiO1 radicals [21], respectively.

In view of the computed energy barriers and reaction energies, the R1-2OO-*syn* peroxy radical can essentially dissociate back to reactants ($[C_{10}H_8OH]^{\bullet}$ and O_2), isomerize to one of the possible bicyclic peroxy adducts R1-2,3OO-*syn*,

R1-2,4OO-*syn*, R1-2,9OO-*syn* and R1-2,10OO-*syn*, or react via hydrogen atom transfer reactions that convert the peroxy radical to the R1-P2O1-*syn* and R1-P2C1 oxy hydroperoxide radicals. In contrast, besides dissociating back to reactants, the R1-4OO-*syn* peroxy radical will essentially undergo isomerization to the R1-4,2OO-*syn*, R1-4,3OO-*syn*, R1-4,5OO-*syn*, R1-4,9OO-*syn* and R1-4,10OO-*syn* bicyclic peroxy adducts, or conversion into the R1-P4O1-*syn* and R1-P4C1 oxy hydroperoxide radicals through intramolecular hydrogen transfers.

All DFT estimates at room temperature show that, in contrast with the oxidation mechanisms of benzene, toluene, and xylenes [15–18,81], and in line with the observations by Zhang *et al.* [21], all isomerization processes of the R1-*i*OO-*syn* ($i=2,4$) peroxy radicals into the bicyclic R1-*i,j*OO-*syn* species are strongly endothermic ($\Delta H_r > 10 \text{ kcal mol}^{-1}$). Whatever the employed exchange-correlation functional, our DFT calculations demonstrate that, among all products obtained from ring closure processes, the R1-4,2OO-*syn* species is the most stable bicyclic peroxy radical structure (Table 6.1). The R1-2,9OO-*syn* bicyclic peroxy radical represents the most stable form resulting from cyclisation of the R1-2OO-*syn* peroxy radical adduct (Table 6.1). It lies at $4.0 \text{ kcal mol}^{-1}$ above the R1-4,2OO-*syn* species.

The isomerization processes of the R1-2OO-*syn* peroxy radical into the R1-2,9OO-*syn* bicyclic peroxy species are also endothermic, with reactions enthalpies (ΔH_{298K}) ranging from 9.2 to $13.4 \text{ kcal mol}^{-1}$ (Table 6.1), depending on the employed exchange-correlation functional. The corresponding activation barriers (Table 6.2) amount to about 20.8 – $22.7 \text{ kcal mol}^{-1}$.

Conversions of the R1-*i*OO-*syn* ($i=2,4$) peroxy radicals into the R1-P*i*O1 radicals species via intramolecular hydrogen transfers are strongly endothermic processes (Table 6.1), with reaction enthalpies ranging from 16.6 to $21.5 \text{ kcal mol}^{-1}$. Considerable activation energies, up to $34.4 \text{ kcal mol}^{-1}$, are found for these reaction pathways (Table 6.2). In contrast, the conversions of the R1-*i*OO-*syn* ($i=2,4$) peroxy radicals into the R1-P*i*C1 species are exothermic processes, with reaction enthalpies ranging from -13.7 to $-4.0 \text{ kcal mol}^{-1}$ (Table 6.1). Activation energies are in general more limited in this latter case (Table 6.2): their values do not exceed $27.6 \text{ kcal mol}^{-1}$. Among all studied chemical pathways, the lowest activation energies, ranging from 15.7 to $20.5 \text{ kcal mol}^{-1}$, are found for the conversion of the R1-2OO-*syn* species into the R1-P2O1-*syn* one through hydrogen transfer (Table 6.2). This reaction channel will thus, most clearly, be the most competitive one from a kinetic view point. The second most competitive process will be the conversion of the R1-2OO-*syn* species into the R1-2,9-OO-*syn* species

through ring closure, followed by the conversion of the R1-4OO-*syn* species into R1-P4C1 through hydrogen transfer from C₁ to O₁₄ (see Figure 6.2 for atom labelling). In view of the computed energy barriers (Table 6.2), the formation of all other bicyclic peroxy radicals should be negligible under atmospheric conditions, and be probably be less competitive than reactions of the R1-2OO-*syn* and R1-4OO-*syn* peroxy radicals with atmospheric NO.

Note that, whatever the employed exchange-correlation functional, the energy barrier (ΔE_{0K}^\ddagger) for the R1-2OO-*syn*→R1-P2O1-*syn* hydrogen transfer reaction is lower by 0.3–5.1 kcal mol⁻¹ than the barrier for the R1-2OO-*syn*→R1-2,9OO-*syn* cyclisation reaction, due to the allylic and thus weaker nature of the C₁–H bond, compared with the hydroxyl OH bond, but also because of the less strained nature of the involved transition state structures. Indeed, the activation energy does not only depend on the bond strengths, but also on the ring size of the transition state. Specifically, for the R1-2OO-*syn* radical species, migration of the hydroxyl hydrogen involves at the level of the transition state (referred to as TS-P2O1-*syn* in Table 6.2) a 6-membered ring structure which is less strained and therefore more energetically favored than the 5-membered ring transition state structure (referred to as TS-P2C1 in Table 6.2) for migration of the allylic hydrogen. On the contrary, the migration of the hydroxyl H in the R1-4OO-*syn* species involves at the level of the transition state an 6-membered ring which is more strained than the 7-membered ring transition state structure involved in the allylic H migration, hence the much higher energy barriers, ranging from 27.0 to 34.4 kcal mol⁻¹. These observations are in contrast with the barrier heights for the C₆H₆OH-2OO→C₆H₆OH-2,6OO cyclisation processes in benzene oxidation, which are lower than those obtained for hydrogen transfers [15,21]. Further hydrogen migration processes from C₂ to O₁₄ in the R1-2OO-*syn* species and from C₄ to O₁₄ in the R1-4OO-*syn* species (Figure 6.2) were not considered since they involve highly strained 4-membered ring transition states and should therefore require much higher activation energies.

We note that the various exchange-correlation functionals which have been employed predict large differences in the relative energies of the identified stationary points, especially with regards to the extent of activation energies. As was to be expected, because of the large self-interaction error, the B3LYP functional systematically yields strong underestimations of the computed activation energies, up to 6.8 kcal mol⁻¹, compared with the results obtained with the ω B97XD, UM05-2x and UM06-2x functionals, which most generally do not differ by more than 2.0 kcal mol⁻¹.

Table 6.1. Reaction energies, reaction enthalpies and Gibb's free reaction energies (in kcal mol⁻¹) for the isomerization processes of the R1-2OO-*syn* and R1-4OO-*syn* peroxy radicals.

Reaction	Method	B3LYP			ω B97XD			UM05-2x			UM06-2x			literature [21] (ΔE_{0K})	
		ΔE_{0K}	ΔH°_{298K}	ΔG°_{298K}	ΔE_{0K}	ΔH°_{298K}	ΔG°_{298K}	ΔE_{0K}	ΔH°_{298K}	ΔG°_{298K}	ΔE_{0K}	ΔH°_{298K}	ΔG°_{298K}	<i>a</i>	<i>b</i>
Ring-closure processes															
R1-2OO- <i>syn</i> → R1-2,3OO- <i>syn</i>		14.65	14.42	14.69	12.55	12.30	12.57	13.14	12.89	13.26	13.11	12.83	13.29	15.01	9.97
R1-2OO- <i>syn</i> → R1-2,4OO- <i>syn</i>		15.48	15.08	16.15	12.61	12.16	13.35	10.37	9.95	11.03	10.87	10.51	11.53	15.54	8.27
R1-2OO- <i>syn</i> → R1-2,9OO- <i>syn</i>		13.84	13.36	14.87	12.01	11.55	13.01	9.68	9.18	10.66	10.84	10.32	11.88	13.77	7.55
R1-2OO- <i>syn</i> → R1-2,10OO- <i>syn</i>		29.90	29.57	30.69	27.54	27.16	28.40	25.12	24.77	25.82	26.38	25.99	27.17	29.83	23.83
R1-4OO- <i>syn</i> → R1-4,2OO- <i>syn</i>		11.71	11.25	12.44	9.25	8.85	9.82	6.79	6.34	7.51	6.79	6.314	7.52	11.88	6.21
R1-4OO- <i>syn</i> → R1-4,3OO- <i>syn</i>		21.46	21.27	21.56	19.59	19.42	19.62	20.33	20.19	20.24	19.38	19.21	19.38	21.73	18.49
R1-4OO- <i>syn</i> → R1-4,5OO- <i>syn</i>		24.27	23.90	24.86	22.34	22.04	22.75	21.48	21.10	22.04	22.01	21.63	22.62	24.49	20.94
R1-4OO- <i>syn</i> → R1-4,9OO- <i>syn</i>		25.20	24.75	26.12	22.77	22.42	23.46	21.06	20.58	21.93	21.75	21.29	22.62	25.22	20.72
R1-4OO- <i>syn</i> → R1-4,10OO- <i>syn</i>		31.26	31.00	31.80	29.32	29.14	29.65	30.40	30.12	30.91	30.17	29.89	30.74	31.41	29.28
H-transfer processes															
R1-2OO- <i>syn</i> → R1-P2O1- <i>syn</i>		16.65	16.61	16.88	19.78	19.77	20.01	20.71	20.79	20.73	19.60	19.62	19.76		
R1-2OO- <i>syn</i> → R1-P2C1		-7.03	-6.66	-7.51	-4.36	-3.99	-4.88	-5.75	-5.39	-6.26	-5.99	-5.68	-6.37		
R1-4OO- <i>syn</i> → R1-P4O1- <i>syn</i>		20.41	20.58	19.92	21.24	21.47	20.60	20.85	20.98	20.46	20.12	20.23	19.76		
R1-4OO- <i>syn</i> → R1-P4C1		-14.11	-13.72	-14.64	-12.25	-11.77	-12.98	-13.88	-13.43	-14.76	-13.96	-13.53	-14.67	-15.11	-15.11

^a Ref. [21]: values obtained at the B3LYP/6-311+G(2df,p) level.

^b Ref. [21]: values obtained at the BBIK/6-311++G(2df,2p) level.

Table 6.2. Activation energies, enthalpies and Gibb's free activation energies (in kcal mol⁻¹) for the isomerization processes of the R1-2OO-*syn* and R1-4OO-*syn* peroxy radicals.

Reaction	Method	B3LYP			ω B97XD			UM05-2x			UM06-2x			literature [21] (ΔE_{0K})	
		ΔE_{0K}^\ddagger	ΔH_{298K}°	ΔG_{298K}°	ΔE_{0K}^\ddagger	ΔH_{298K}°	ΔG_{298K}°	ΔE_{0K}^\ddagger	ΔH_{298K}°	ΔG_{298K}°	ΔE_{0K}^\ddagger	ΔH_{298K}°	ΔG_{298K}°	<i>a</i>	<i>b</i>
Ring-closure processes															
R1-2OO- <i>syn</i> → TS-2,3OO- <i>syn</i>		24.14	23.79	24.58	26.49	26.13	26.70	26.72	26.41	27.11	27.68	27.34	28.14	24.45	24.07
R1-2OO- <i>syn</i> → TS-2,4OO- <i>syn</i>		34.44	34.04	34.97	36.36	35.92	37.05	34.88	34.47	35.52	36.61	36.16	37.34	33.08	32.79
R1-2OO- <i>syn</i> → TS-2,9OO- <i>syn</i>		20.84	20.24	21.99	22.68	22.06	23.87	20.85	20.26	21.92	22.32	21.71	23.46	20.87	19.05
R1-2OO- <i>syn</i> → TS-2,10OO- <i>syn</i>		32.35	31.87	33.33	33.32	32.83	34.33	31.19	30.70	32.13	32.75	32.24	33.77	32.43	30.33
R1-4OO- <i>syn</i> → TS-4,2OO- <i>syn</i>		29.97	29.39	30.91	32.09	31.58	32.88	31.19	30.59	32.11	32.30	31.73	33.22	30.11	30.71
R1-4OO- <i>syn</i> → TS-4,3OO- <i>syn</i>		28.34	28.09	28.52	30.06	29.87	30.30	30.63	30.33	31.05	31.43	31.16	31.86	28.68	29.66
R1-4OO- <i>syn</i> → TS-4,5OO- <i>syn</i>		32.10	31.60	32.80	33.85	33.41	34.39	33.16	32.67	33.80	34.11	33.61	34.80	32.41	32.93
R1-4OO- <i>syn</i> → TS-4,9OO- <i>syn</i>		32.82	32.18	33.98	35.05	34.49	36.03	33.82	33.20	34.91	34.98	34.38	36.08	32.96	33.41
R1-4OO- <i>syn</i> → TS-4,10OO- <i>syn</i>		33.74	33.38	34.33	34.99	34.74	35.36	35.68	35.32	36.22	36.13	35.80	36.68	34.01	35.25
H-transfer processes															
R1-2OO- <i>syn</i> → TS-P2O1- <i>syn</i>		15.72	15.15	17.18	19.72	19.15	20.44	20.51	19.97	21.15	19.96	19.38	20.67	15.94	19.24
R1-2OO- <i>syn</i> → TS-P2C1		23.12	22.98	23.34	26.51	26.36	26.72	27.57	27.46	27.69	27.61	27.44	27.84	23.57	23.29
R1-4OO- <i>syn</i> → TS-P4O1- <i>syn</i>		26.99	26.44	27.80	32.52	32.07	33.09	34.41	33.95	35.17	33.77	33.29	34.61	27.25	27.27
R1-4OO- <i>syn</i> → TS-P4C1		21.02	20.59	22.01	23.74	23.38	24.56	23.32	22.90	24.23	23.50	23.09	24.43	20.72	21.80

^a Ref. [21]: values obtained at the B3LYP/6-311+G(2df,p) level.

^b Ref. [21]: values obtained at the BBIK/6-311++G(2df,2p) level.

Unlike the observations we made for the preceding O₂ addition step in the oxidation mechanism of naphthalene initiated by hydroxyl radicals [20], our B3LYP/aug-cc-pVTZ results for reaction energies and activation energies are most generally in excellent agreement with the B3LYP/6-311+G(2df,p) results obtained by Zhang *et al.* in ref. 21. In the present study, the largest discrepancies amount to ~1.4 kcal mol⁻¹ for the activation energy characterizing the cyclisation of the R1-2OO-*syn* adduct into the R1-2,4OO-*syn* species, and 1.0 kcal mol⁻¹ for the reaction energy associated to the conversion of the R1-4OO-*syn* adduct into the R1-P4C1 species through intramolecular hydrogen transfer.

A rather obvious reason for this difference in basis set behavior is that O₂ addition processes on naphthalene-OH adducts result into much stronger polarization effects than the presently studied isomerization processes, which an improperly balanced basis set such as 6-311+G(2df,p) fails to quantitatively describe. Indeed, it is worth reminding that the 6-311G basis set from which the 6-311+G(2df,p) used by Zheng *et al.* derives is known to exhibit a too compact 2*p* space [82], and to be effectively a basis set of double-zeta quality only in the *s*-space, due to improperly balanced expansion coefficients [38].

Prior to ending this discussion of reaction energies and energy barriers, it is worth noticing that, at all employed levels of density functional theory, the spin contamination [$\langle S^2 \rangle_{\text{obs}} - 0.75$] never exceeds 0.073 (Tables S1 and S2 of the Appendix IV) and can thus, for all practical purposes, be regarded as relatively marginal.

6.3.2. Structural Characteristics of Stationary Points

The reader is referred to Figure 6.2, Tables 6.3 and 6.4 for a detailed structural characterization of all the stationary points that are involved in the reaction pathways R1-*i*OO-*syn*→P(*i*=2,4) at the UM06-2*x*/aug-cc-pVTZ level. For the R1-2,9OO-*syn* bicyclic peroxy radical, the C₂-O₁₃ and C₉-O₁₄ bond lengths amount to 1.429 Å and 1.461 Å, respectively, whereas for the R1-4,2OO-*syn* bicyclic peroxy radical, the C₄-O₁₃ and C₂-O₁₄ bond lengths are equal to 1.427 Å and 1.433 Å, respectively. The transition states connecting the R1-2,9OO-*syn* and R1-P2O1-*syn* species exhibit much longer C_{*i*}-O₁₄(*i*=2,4) bond lengths, which range from 1.926 Å to 2.022 Å.

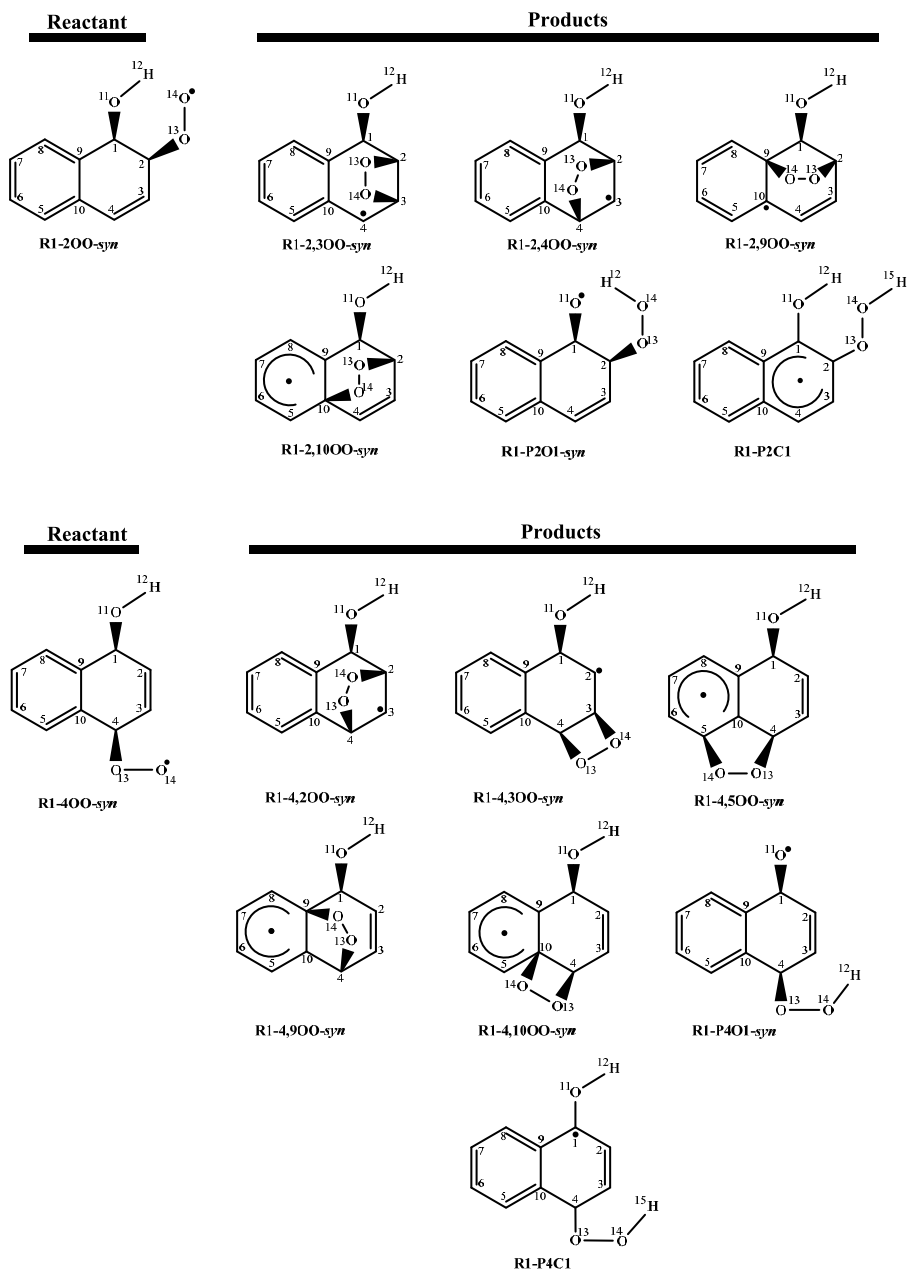


Figure 6.2. Retained atom labeling for characterizing the structures of reactants and products during the isomerization processes.

Table 6.3. Structural parameters for all the stationary points that are involved in the reaction pathway R1-2OO-*syn*→P at the UM06-2x/aug-cc-pVTZ level (see Figure 6.2 for detailed atom labelling).

Bond	Species	R1-2OO- <i>s</i>		R1-2,3OO- <i>s</i>		R1-2,4OO- <i>s</i>		R1-2,9OO- <i>s</i>		R1-2,10OO- <i>s</i>		R1-P2O1- <i>s</i>		R1-P2C1	
		TS	P	TS	P	TS	P	TS	P	TS	P	TS	P	TS	P
$r(\text{C}_1-\text{C}_2)$		1.525	1.514	1.515	1.521	1.537	1.529	1.527	1.539	1.536	1.635	1.604	1.540	1.490	
$r(\text{C}_2-\text{C}_3)$		1.499	1.520	1.522	1.499	1.481	1.502	1.500	1.491	1.498	1.493	1.500	1.496	1.492	
$r(\text{C}_3-\text{C}_4)$		1.333	1.372	1.476	1.376	1.487	1.338	1.345	1.328	1.326	1.331	1.331	1.328	1.334	
$r(\text{C}_4-\text{C}_{10})$		1.464	1.442	1.413	1.467	1.513	1.450	1.434	1.482	1.514	1.463	1.463	1.461	1.450	
$r(\text{C}_9-\text{C}_{10})$		1.401	1.407	1.417	1.400	1.398	1.440	1.506	1.447	1.500	1.399	1.398	1.406	1.427	
$r(\text{C}_1-\text{C}_9)$		1.513	1.516	1.512	1.520	1.522	1.518	1.547	1.507	1.510	1.507	1.508	1.475	1.400	
$r(\text{C}_1-\text{O}_{11})$		1.402	1.410	1.411	1.410	1.409	1.396	1.396	1.405	1.409	1.333	1.335	1.375	1.355	
$r(\text{O}_{11}-\text{H}_{12})$		0.964	0.964	0.965	0.965	0.965	0.966	0.965	0.965	0.965	1.320	-	0.961	0.962	
$r(\text{C}_2-\text{O}_{13})$		1.467	1.426	1.440	1.444	1.443	1.428	1.429	1.444	1.439	1.387	1.400	1.425	1.442	
$r(\text{O}_{13}-\text{O}_{14})$		1.298	1.407	1.451	1.414	1.447	1.396	1.451	1.408	1.444	1.375	1.413	1.377	1.419	
$r(\text{O}_{14}-\text{C}_i) (i=3,4,9,10)$		-	1.908	1.468	2.020	1.447	1.926	1.461	1.818	1.471	-	-	-	-	
$r(\text{H}_{12}-\text{O}_{14})$		-	-	-	-	-	-	-	-	-	1.095	0.974	-	-	
$r(\text{H}_{15}-\text{O}_{14})$		-	-	-	-	-	-	-	-	-	-	-	1.335	0.967	

- Bond lengths are in angstrom (Å).

Table 6.4. Structural parameters for all the stationary points that are involved in the reaction pathway R1-4OO-*syn*→P at the UM06-2x/aug-cc-pVTZ level of theory (see Figure 6.2 for detailed atom labelling).

Bond	Species	R1-4OO- <i>s</i>		R1-4,2OO- <i>s</i>		R1-4,3OO- <i>s</i>		R1-4,5OO- <i>s</i>		R1-4,9OO- <i>s</i>		R1-4,10OO- <i>s</i>		R1-P4O1- <i>s</i>		R1-P4C1	
		TS	P	TS	P	TS	P	TS	P	TS	P	TS	P	TS	P	TS	P
$r(\text{C}_1-\text{C}_2)$		1.504	1.511	1.541	1.505	1.493	1.509	1.514	1.504	1.504	1.504	1.509	1.508	1.504	1.465	1.405	
$r(\text{C}_2-\text{C}_3)$		1.324	1.370	1.481	1.368	1.468	1.324	1.326	1.325	1.327	1.325	1.326	1.325	1.322	1.336	1.354	
$r(\text{C}_3-\text{C}_4)$		1.493	1.506	1.489	1.525	1.533	1.499	1.501	1.503	1.513	1.496	1.494	1.508	1.423	1.504	1.489	
$r(\text{C}_4-\text{C}_{10})$		1.498	1.503	1.516	1.496	1.497	1.503	1.487	1.501	1.488	1.528	1.545	1.503	1.514	1.500	1.510	
$r(\text{C}_9-\text{C}_{10})$		1.390	1.393	1.398	1.395	1.396	1.369	1.349	1.429	1.485	1.428	1.481	1.394	1.390	1.398	1.411	
$r(\text{C}_1-\text{C}_9)$		1.510	1.513	1.512	1.514	1.516	1.515	1.515	1.527	1.559	1.506	1.501	1.520	1.518	1.489	1.432	
$r(\text{C}_1-\text{O}_{11})$		1.422	1.408	1.408	1.422	1.428	1.416	1.415	1.409	1.408	1.424	1.423	1.402	1.370	1.381	1.352	
$r(\text{O}_{11}-\text{H}_{12})$		0.966	0.965	0.965	0.966	0.966	0.963	0.963	0.966	0.965	0.967	0.966	1.344	-	0.961	0.960	
$r(\text{C}_4-\text{O}_{13})$		1.490	1.442	1.427	1.437	1.449	1.436	1.441	1.442	1.435	1.428	1.445	1.460	1.423	1.468	1.441	
$r(\text{O}_{13}-\text{O}_{14})$		1.290	1.382	1.447	1.416	1.452	1.400	1.442	1.397	1.450	1.435	1.452	1.374	1.419	1.362	1.419	
$r(\text{O}_{14}-\text{C}_i) (i=2,3,5,9,10)$		-	2.022	1.433	1.893	1.471	2.285	1.471	1.904	1.452	1.828	1.489	-	-	-	-	
$r(\text{H}_{12}-\text{O}_{14})$		-	-	-	-	-	-	-	-	-	-	-	1.073	0.968	-	-	
$r(\text{H}_{15}-\text{O}_{14})$		-	-	-	-	-	-	-	-	-	-	-	-	-	1.322	0.968	

- Bond lengths are in angstrom (Å).

As expected, the O–O distances are longest in the bicyclic structures. When the R1-*i*OO-*syn* (*i*=2,4) peroxy radicals evolve to bicyclic peroxy radical structures, the length of the O–O bond characteristically increases from 1.290–1.298 Å to 1.413–1.452 Å, while the corresponding C_{*i*}–O₁₃ bond decreases from 1.467–1.490 Å to 1.400–1.449 Å. Upon considering the O₁₃–O₁₄ and C_{*i*}–O₁₃ (*i*=2,4) bond lengths, it appears quite clearly that the transition states connecting the products and reactants on the cyclisation pathways are much closer to the products than to the reactants. This is true also for the intramolecular hydrogen transfer pathways leading to the R1-P2O1-*syn* species. In contrast, the transition state connecting the product and reactant on the hydrogen transfer pathway yielding the R1-P4C1 species is closer to the reactant than to the product. More specifically, the O–O and C₄–O₁₃ bond lengths in this transition state are approximately averaging the corresponding bond length values in the associated reactant and product.

Obviously, the R1-P2O1-*syn* radical will decompose through a breaking of the C₁–C₂ bond, followed by a rapid O–O bond cleavage and further fragmentation processes. Indeed, the C₁–C₂ bond in this species is unusually stretched: it exhibits a length of 1.604 Å.

6.3.3. Kinetic Parameters

All kinetic rate constants that are supplied in the sequel were obtained according to our best estimates of energy barriers, i.e., using DFT along with the UM06-2x exchange-correlation functional. TST and RRKM unimolecular rate constants of the isomerization processes calculated along with the UM06-2x/aug-cc-pVTZ approach are listed in Table 6.5 at a pressure of 1 bar and at temperatures equal to 298, 336 and 400 K, in line with the original experiments by Koch *et al.* [27,55–57]. Further RRKM data computed at lower and higher pressures are provided for the same temperatures in Tables S3s–S3m of the Appendix IV.

The supplied unimolecular TST and RRKM results (Table 6.5) indicate that, at a pressure of 1 bar, the formation of the R1-2,9OO-*syn* species will clearly predominate over the formation of the other bicyclic peroxy species (Figure 6.3). For instance, at 298 K, the estimated rate constants for the cyclization of the R1-2OO-*syn* species into R1-2,9OO-*syn* are of the order of 10⁻⁴ s⁻¹, thus at least 3 orders of magnitude larger than the rate constants that were computed for the other cyclisation processes, which range from ~10⁻¹³ to ~10⁻⁷ s⁻¹ (Table 6.5). Note that, in line with a lower activation energy, the kinetically most competitive process corresponds to the unimolecular formation of the bicyclic radical R1-P2O1-*syn* from the R1-2OO-*syn* peroxy radical through hydrogen transfer: at 298 K, the

corresponding TST and RRKM rate constants amount to 5.12 s^{-1} and 1.79 s^{-1} , respectively. Whatever the considered temperatures, the unimolecular rate constant for the formation of the R1-P2O1-*syn* radical is larger than that obtained for the R1-2,9OO-*syn* radical, which is in line with a reduction of the activation energy barrier, by $2.36 \text{ kcal mol}^{-1}$ on the corresponding chemical reaction pathways. Indeed, the obtained TST and RRKM results (Table 6.5) indicate that rate constants for the R1-2OO-*syn*→R1-P2O1-*syn* unimolecular rearrangement reaction step are larger by four orders of magnitude than the rate constants obtained for the R1-2OO-*syn*→R1-2,9OO-*syn* unimolecular reaction step. At a pressure of 1 bar, the formation of the R1-P2O1-*syn* species will therefore clearly predominate over the formation of the R1-2,9OO-*syn* species, and will be under kinetic control the most competitive reaction pathway for the R1-2OO-*syn* adduct. The same observation holds for pressures ranging from 10^{-12} to 10^4 bars (Tables S3a–S3m in the Appendix IV). As is to be expected, because of the involved positive energy barriers, these rate constants increase gradually with increasing temperatures.

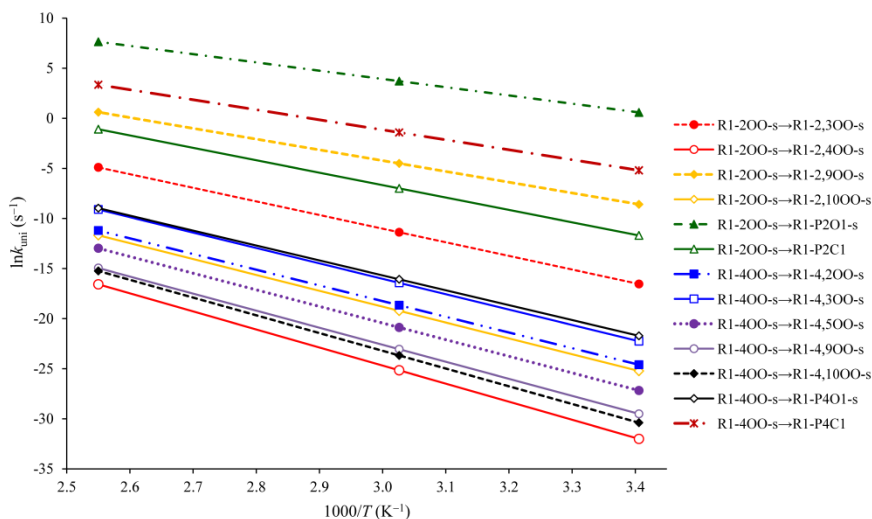


Figure 6.3. Arrhenius plot of the obtained RRKM unimolecular rate constants [for R1-*i*OO-*syn*(*i*=2,4)→P] at the UM06-2x/aug-cc-pVTZ level of theory.

Our TST estimates for the unimolecular kinetic rate constants associated with the ring closure processes are in general in good agreement with the data supplied by Zhang *et al.* at 298 K [21], within one order of magnitude. For these processes, the largest discrepancy is found for the conversion of the R1-2OO-*syn* peroxy radical into the R1-2,9OO-*syn* bicyclic adduct, in the form of a factor ~ 40 between

our estimate and that by Zhang *et al.* Discrepancies increase to two to three orders of magnitude when considering the hydrogen transfer processes, the largest discrepancy being observed for the conversion of the R1-4OO-*syn* peroxy radical into the R1-P4C1 oxy hydroperoxide radical. In this case, the value supplied by Zhang *et al.* [21] underestimates our result by a factor $\sim 3 \times 10^3$. As is well known, uncertainties as small as 2–3 kcal mol⁻¹ on energy barriers (Table 6.2) can obviously incur large errors, of the order of 2 or 3 orders of magnitude, on kinetic rate constants (Table 6.5).

Table 6.5. Unimolecular rate constants (in s⁻¹) for the reported reaction channels obtained by means of TST and RRKM theories ($P=1$ bar), according to the computed UM06-2x/aug-cc-pVTZ energy barrier.

Reaction pathway	Theory			RRKM		
	298 K	336 K	400 K	298 K	336 K	400 K
Ring closure processes						
R1-2OO- <i>syn</i> → R1-2,3OO- <i>syn</i>	1.12×10 ⁻⁷ (6.5×10 ⁻⁶) ^a	1.78×10 ⁻⁵	1.04×10 ⁻²	6.58×10 ⁻⁸	1.15×10 ⁻⁵	7.46×10 ⁻³
R1-2OO- <i>syn</i> → R1-2,4OO- <i>syn</i>	1.63×10 ⁻¹⁴ (1.9×10 ⁻¹²) ^a	1.44×10 ⁻¹¹	7.28×10 ⁻⁸	1.27×10 ⁻¹⁴	1.19×10 ⁻¹¹	6.34×10 ⁻⁸
R1-2OO- <i>syn</i> → R1-2,9OO- <i>syn</i>	2.32×10 ⁻⁴ (9.3×10 ⁻³) ^a	1.31×10 ⁻²	2.10×10 ⁰	1.85×10 ⁻⁴	1.10×10 ⁻²	1.84×10 ⁰
R1-2OO- <i>syn</i> → R1-2,10OO- <i>syn</i>	1.39×10 ⁻¹¹ (6.4×10 ⁻¹¹) ^a	5.40×10 ⁻⁹	9.70×10 ⁻⁶	1.11×10 ⁻¹¹	4.49×10 ⁻⁹	8.50×10 ⁻⁶
R1-4OO- <i>syn</i> → R1-4,2OO- <i>syn</i>	3.78×10 ⁻¹¹ (5.2×10 ⁻¹¹) ^a	1.30×10 ⁻⁸	2.00×10 ⁻⁵	2.07×10 ⁻¹¹	7.88×10 ⁻⁹	1.37×10 ⁻⁵
R1-4OO- <i>syn</i> → R1-4,3OO- <i>syn</i>	3.58×10 ⁻¹⁰ (1.2×10 ⁻⁹) ^a	1.11×10 ⁻⁷	1.51×10 ⁻⁴	2.17×10 ⁻¹⁰	7.37×10 ⁻⁸	1.11×10 ⁻⁴
R1-4OO- <i>syn</i> → R1-4,5OO- <i>syn</i>	2.15×10 ⁻¹² (1.8×10 ⁻¹²) ^a	1.09×10 ⁻⁹	2.75×10 ⁻⁶	1.59×10 ⁻¹²	8.59×10 ⁻¹⁰	2.32×10 ⁻⁶
R1-4OO- <i>syn</i> → R1-4,9OO- <i>syn</i>	2.08×10 ⁻¹³ (4.2×10 ⁻¹³) ^a	1.25×10 ⁻¹⁰	3.87×10 ⁻⁷	1.54×10 ⁻¹³	9.75×10 ⁻¹¹	3.23×10 ⁻⁷
R1-4OO- <i>syn</i> → R1-4,10OO- <i>syn</i>	8.11×10 ⁻¹⁴ (6.0×10 ⁻¹⁴) ^a	6.37×10 ⁻¹¹	2.77×10 ⁻⁷	6.35×10 ⁻¹⁴	5.23×10 ⁻¹¹	2.41×10 ⁻⁷
H-transfer processes						
R1-2OO- <i>syn</i> → R1-P2O1- <i>syn</i>	5.12×10 ⁰ (1.4×10 ⁻²) ^a	9.36×10 ¹	3.74×10 ³	1.79×10 ⁰	4.08×10 ¹	2.07×10 ³
R1-2OO- <i>syn</i> → R1-P2C1	1.36×10 ⁻⁴ (4.0×10 ⁻⁶) ^a	9.12×10 ⁻³	1.90×10 ⁰	8.35×10 ⁻⁶	9.14×10 ⁻⁴	3.36×10 ⁻¹
R1-4OO- <i>syn</i> → R1-P4O1- <i>syn</i>	5.39×10 ⁻⁹ (5.4×10 ⁻⁸) ^a	9.06×10 ⁻⁷	6.07×10 ⁻⁴	3.72×10 ⁻¹⁰	1.05×10 ⁻⁷	1.27×10 ⁻⁴
R1-4OO- <i>syn</i> → R1-P4C1	8.67×10 ⁻² (2.9×10 ⁻⁵) ^a	2.29×10 ⁰	1.50×10 ²	5.53×10 ⁻³	2.43×10 ⁻¹	2.85×10 ¹

^a Ref. [21]. The values in parenthesis were obtained at the BB1K/6-311++G(2df,2p) level of theory.

The reader is referred to Figure 6.3 for an Arrhenius plot of the obtained RRKM estimates at a pressure of 1 bar for the isomerization processes of the R1-2OO-*syn* and R1-4OO-*syn* species, according to the UM06-2x/aug-cc-pVTZ estimates of energy barriers. This Figure clearly confirms that the production of the R1-P2O1-*syn* radical dominates the reaction mechanism under atmospheric pressure and at temperatures ranging from 298 to 400 K. The same conclusion holds at much higher and lower pressures (10^{-12} – 10^4 bar) (Tables S3a–S3m of the Appendix IV).

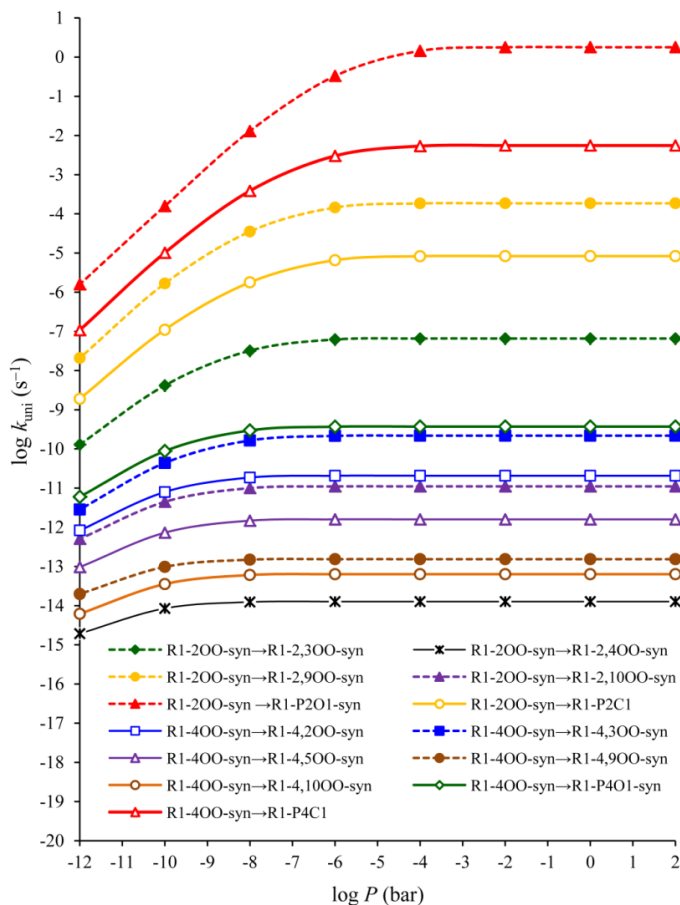


Figure 6.4. Pressure dependence of the unimolecular rate constants for the R1-*i*OO-*syn* ($i=2,4$)→P reaction steps according to the UM06-2x/aug-cc-pVTZ energy profiles.

Since the involved energy barriers are large, the formation of the R1-2,3OO-*syn*, R1-2,4OO-*syn*, R1-2,10OO-*syn*, R1-4,2OO-*syn*, R1-4,3OO-*syn*, R1-4,5OO-*syn*, R1-4,9OO-*syn* and R1-4,10OO-*syn* bicyclic peroxy radicals is characterized

by significantly lower rate constants at the considered temperatures (298, 336, and 400 K), compared with the formation of the R1-2,9OO-*syn* isomer: the rate constants for these processes are smaller by at least three orders of magnitude than the rate constant characterizing the cyclization of the R1-2OO-*syn* species into the R1-2,9OO-*syn* one. For the same reason, at 298 K, the conversion of the R1-*i*OO-*syn* ($i=2,4$) adducts into the R1-P2C1, R1-P4O1-*syn* and R1-P4C1 oxy hydroperoxide radicals through hydrogen transfer is from a kinetic view point at least ~ 100 times less efficient than the conversion of the R1-2OO-*syn* species into the R1-P2O1-*syn* isomer. From the computed rate constants, it appears overall very clearly that the R1-2OO-*syn* peroxy radical is chemically much more reactive than the R1-4OO-*syn* species, and this by at least six orders of magnitude for the ring closure processes, and by two orders of magnitude for the hydrogen transfer processes.

Inspection of Figure 6.4 and Table 6.5 shows that the RRKM unimolecular rate constants obtained for the reported reaction pathways increase with increasing temperatures. Upon inspecting the RRKM data displayed in Figure 6.4, it appears quite clearly that, in line with rather larger energy barriers, ranging from 19.96 to 36.61 kcal mol⁻¹, pressures larger than 10⁻⁶ bar are in general sufficient for ensuring a saturation within 1% accuracy to the high pressure (TST) limit of the RRKM unimolecular rate constants

6.4. Conclusions

The isomerization processes of naphthalene peroxy radicals [C₁₀H₈-OH]^{*}-O₂ into bicyclic peroxy or oxy hydroperoxide radicals via ring closure and intramolecular hydrogen transfers have been studied computationally using density functional theory along with various exchange-correlation functionals (B3LYP, ω B97XD, UM05-2x and UM06-2x) and an extremely large basis set (aug-cc-pVTZ). The calculated energy profiles have been supplemented with calculations of kinetic rate constants under atmospheric pressure and in the fall-off regime, down to pressure of 10⁻¹² bar, using transition state and RRKM theories.

The atmospheric oxidation mechanisms of naphthalene appear to be quite different from that of benzene and its derivatives, and this in many aspects. The cyclisation of the R1-2OO-*syn* peroxy radical into R1-2,9OO-*syn* bicyclic peroxy radical through formation of an O–O bridge is endothermic and reversible, whereas similar ring closure processes occurring during the oxidation of benzene, toluene, and xylenes are exothermic and irreversible [15–18]. All our calculations indicate

that, under a kinetic control of the reactions, the two most favorable processes for the R1-2OO-*syn* peroxy radical are ring closure into the R1-2,9OO-*syn* bicyclic peroxy radical species, and conversion through hydrogen transfer into the R1-P2O1-*syn* oxy hydroperoxide radical. With an unimolecular kinetic rate constant of the order of 5 s^{-1} at $P=1 \text{ bar}$ and $T=298 \text{ K}$, the latter process is, among all studied reaction channels, the most competitive one. Under thermodynamic control of the reactions, the most abundant product derived from the R1-2OO-*syn* intermediate will be the R1-P2C1 species. From a kinetic view point, the R1-2OO-*syn* peroxy radical is chemically much more reactive than the R1-4OO-*syn* species, and this by at least 6 orders of magnitude for the ring closure processes, and by two orders of magnitude for the hydrogen transfer processes. For the R1-4OO-*syn* peroxy radical, all our calculations indicate that, both under kinetic and thermodynamic controls of the reactions, only one process will dominate, which pertains to conversion through hydrogen transfer into the R1-P4C1 oxy hydroperoxide radical.

6.5. References

- [1] P.D. Josephy, B. Mannervik, P.O. de Montellano, *Molecular Toxicology*; Oxford University Press: Oxford, 1997.
- [2] H. Tokiwa, Y. Ohnishi, *CRC Crit. Rev. Toxicol.*, **1986**, *17*, 23.
- [3] I. Suh, D. Zhang, R. Zhang, L.T. Molina, M.J. Molina, *Chem. Phys. Lett.*, **2002**, *364*, 454.
- [4] B. Zielinska, J. Sagebiel, J.D. McDonald, K. Whitney, D.R. Lawson, *J. Air & Waste Manage Assoc.*, **2004**, *54*, 1138.
- [5] L.C. Marr, T.W. Kirchstetter, R.A. Harley, A.H. Miguel, S.V. Hering, S.K. Hammond, *Environ. Sci. Technol.*, **1999**, *33*, 3091.
- [6] M.P. Fraser, G.R. Cass, B.R.T. Simoneit, *Environ. Sci. Technol.*, **1998**, *32*, 2051.
- [7] R. Lu, J. Wu, R.P. Turco, A.M. Winer, R. Atkinson, J. Arey, S.E. Paulson, F.W. Lurmann, A.H. Miguel, A. Eiguren-Fernandez, *Atmos. Environ.*, **2005**, *39*, 489.
- [8] J. Arey, B. Zielinska, R. Atkinson, A.M. Winer, *Atmos. Environ.*, **1967**, *21*, 1437.
- [9] J. Arey, R. Atkinson, B. Zielinska, P.A. McElroy, *Environ. Sci. Technol.*, **1989**, *23*, 321.
- [10] R. Atkinson, J. Arey, *Polycycl. Aromat. Compd.*, **2007**, *27*, 15.
- [11] N. Nishino, R. Atkinson, J. Arey, *Environ. Sci. Technol.*, **2008**, *42*, 9203.
- [12] A. Shiroudi, M.S. Deleuze, *J. Phys. Chem. A*, **2014**, *118*, 3625.

- [13] M. Howsam, K.C. Jones, *The Handbook of Environmental Chemistry*; Springer-Verlag: Berlin, 1998, 3, pp. 137.
- [14] N. Nishino, J. Arey, R. Atkinson, *Environ. Sci. Technol.*, **2012**, *46*, 8198.
- [15] D.R. Glowacki, L. Wang, M.J. Pilling, *J. Phys. Chem. A*, **2009**, *113*, 5385.
- [16] I. Suh, R. Zhang, L.T. Molina, M.J. Molina, *J. Am. Chem. Soc.*, **2003**, *125*, 12655.
- [17] J. Fang, R. Zhang, *J. Phys. Chem. A*, **2006**, *110*, 7728.
- [18] J. Fang, R. Zhang, *J. Phys. Chem. A*, **2008**, *112*, 4314.
- [19] A. Shiroudi, M.S. Deleuze, S. Canneaux, *J. Phys. Chem. A*, **2014**, *118*, 4593.
- [20] A. Shiroudi, M.S. Deleuze, S. Canneaux, *Phys. Chem. Chem. Phys.*, **2015**, *17*, 13719.
- [21] Z. Zhang, L. Lin, L. Wang, *Phys. Chem. Chem. Phys.*, **2012**, *14*, 2645.
- [22] B. Bohn, C. Zetzsch, *Phys. Chem. Chem. Phys.*, **1999**, *1*, 5097.
- [23] D. Johnson, S. Raoult, M.T. Rayez, J.C. Rayez, R. Lesclaux, *Phys. Chem. Chem. Phys.*, **2002**, *4*, 4678.
- [24] S.Y. Grebenkin, L.N. Krasnoperov, *J. Phys. Chem. A*, **2004**, *108*, 1953.
- [25] S. Raoult, M.T. Rayez, J.C. Rayez, R. Lesclaux, *Phys. Chem. Chem. Phys.*, **2004**, *6*, 2245.
- [26] B. Bohn, *J. Phys. Chem. A*, **2001**, *105*, 6092.
- [27] R. Koch, R. Knispel, M. Elend, M. Siese, C. Zetzsch, *Atmos. Chem. Phys.*, **2007**, *7*, 2057.
- [28] A.D. Becke, *J. Chem. Phys.*, **1993**, *98*, 5648.
- [29] C. Lee, W. Yang, R.G. Parr, *Phys. Rev. B*, **1988**, *37*, 785.
- [30] Y. Zhao, B.J. Lynch, D.G. Truhlar, *J. Phys. Chem. A*, **2004**, *108*, 2715.
- [31] W.J. Hehre, L. Radom, P.v.R. Schleyer, J.A. Pople, *Ab initio Molecular Orbital Theory*; Wiley: New York, 1986.
- [32] F. Jensen, *Introduction to Computational Chemistry*; 2nd ed.; Wiley: Chichester, UK, 2007.
- [33] L.A. Curtiss, K. Raghavachari, P.C. Redfern, J.A. Pople, *J. Chem. Phys.* **2000**, *112*, 7374.
- [34] M. Ernzerhof, G.E. Scuseria, *J. Chem. Phys.*, **1999**, *110*, 5029.
- [35] L. Claes, J.-P. François, M.S. Deleuze, *J. Am. Chem. Soc.*, **2002**, *124*, 7563.
- [36] L. Claes, J.-P. François, M.S. Deleuze, *J. Comp. Chem.*, **2003**, *24*, 2023.
- [37] J.P. Perdew, A. Zunger, *Phys. Rev B*, **1981**, *23*, 5048.
- [38] R.S. Grev, H.F. Schaefer III, *J. Chem. Phys.*, **1989**, *91*, 7305.
- [39] A.M. Mastral, M.S. Callen, *Environ. Sci. Technol.*, **2000**, *34*, 3051.
- [40] T.H. Dunning, *J. Chem. Phys.*, **1989**, *90*, 1007.
- [41] J.D. Chai, M. Head-Gordon, *Phys. Chem. Chem. Phys.*, **2008**, *10*, 6615.

- [42] Y. Zhao, D.G. Truhlar, *Acc. Chem. Res.*, **2008**, *41*, 157.
- [43] Y. Zhao, D.G. Truhlar, *Theor. Chem. Acc.*, **2008**, *120*, 215.
- [44] H. Eyring, *J. Chem. Phys.*, **1935**, *3*, 107.
- [45] H.S. Johnston, *Gas Phase Reaction Rate Theory*; Roland Press: New York, 1966.
- [46] K.J. Laidler, *Theories of Chemical Reaction Rates*; McGraw-Hill: New York, 1969.
- [47] R.E. Weston, H.A. Schwartz, *Chemical Kinetics*; Prentice-Hall: New York, 1972.
- [48] D. Rapp, *Statistical Mechanics*; Holt, Rinehart, and Winston: New York, 1972.
- [49] E.E. Nikitin, *Theory of Elementary Atomic and Molecular Processes in Gases*; Clarendon Press: Oxford, 1974.
- [50] I.W.M. Smith, *Kinetics and Dynamics of Elementary Gas Reactions*; Butterworths: London, 1980.
- [51] J.I. Steinfeld, J.S. Francisco, W.L. Hase, *Chemical Kinetics and Dynamics*; Prentice-Hall: Englewood Cliffs, NJ, 1989.
- [52] G. Lendvay, *J. Phys. Chem.*, **1989**, *93*, 4422.
- [53] A.E. Reed, L.A. Curtiss, F. Weinhold, *Chem. Rev.*, **1988**, *88*, 899.
- [54] V. Lopez, J. Quijano, S. Luna, P. Ruiz, D. Rios, W. Parra, E. Zapata, J. Gaviria, R. Notario, *Struct. Chem.*, **2013**, *24*, 1811.
- [55] R. Koch, C. Zetzsch, *13th International Symposium on Gas Kinetics*; University College Dublin, Ireland, 11–16 September, 1994.
- [56] R. Koch, R. Knispel, M. Siese, C. Zetzsch, *Physico-Chemical Behavior of Atmospheric Pollutants*; European Commission, Brussels/Luxemburg, 1994.
- [57] C. Zetzsch, R. Koch, B. Bohn, R. Knispel, M. Siese, F. Witte, *Chemical Processes in Atmospheric Oxidation*; Ed.; G. Le Bras, Springer: Berlin, 1997, pp. 247.
- [58] R. Koch, B. Bohn, C. Zetzsch, *The Oxidizing Capacity of the Troposphere, Physico-Chemical Behavior of Atmospheric Pollutants*; European Commission, Brussels, 1997.
- [59] M.J. Frisch, G.W. Trucks, H.B. Schlegel, G.E. Scuseria, M.A. Robb, J.R. Cheeseman, G. Scalmani, V. Barone, B. Mennucci, G.A. Petersson, *et al.* Gaussian 09, Revision B.01; Gaussian: Wallingford, CT, 2009.
- [60] C. Gonzalez, H.B. Schlegel, *J. Chem. Phys.*, **1989**, *90*, 2154.
- [61] J.W. McIver Jr., *Acc. Chem. Res.*, **1974**, *7*, 72.
- [62] F. Fukui, *F. J. Phys. Chem.*, **1970**, *74*, 4161.
- [63] D.A. McQuarrie, *Statistical Mechanics*; Harper and Row: New York, 1976.

- [64] G.H. Herzberg, *Molecular Spectra and Molecular Structure. II Infrared and Raman Spectra of Polyatomic Molecules*; Van Nostrand Reinhold: New York, 1945.
- [65] R. Chang, *Physical Chemistry for the Biosciences*; University Science Books, Sausalito: California, 2005.
- [66] J.W. Moore, R.G. Pearson, *Kinetics and Mechanism-The Study of Homogeneous Chemical Reactions*; 3rd ed., Wiley: New York, 1981.
- [67] H.H. Carstensen, A.M. Dean, O. Deutschmann, *Proc. Combust. Inst.*, **2007**, *31*, 149.
- [68] W.T. Duncan, R.L. Bell, T.N. Truong, *J. Comp. Chem.*, **1998**, *19*, 1039.
- [69] D.H. Varma, P. Raghunath, M.C. Lin, *J. Phys. Chem. A*, **2010**, *114*, 3642.
- [70] S.Y. Wu, P. Raghunath, J.S. Wu, M.C. Lin, *J. Phys. Chem. A*, **2010**, *114*, 633.
- [71] R.G. Gilbert, S.C. Smith, *Theory of Unimolecular and Recombination Reactions*; Blackwell Scientific: Oxford, 1990.
- [72] H.B. Rao, X.Y. Zeng, H. He, Z.R. Li, *J. Phys. Chem. A*, **2011**, *115*, 1602.
- [73] P.J. Robinson, K.A. Holbrook, *Unimolecular Reactions*; John Wiley & Sons, Inc. (Interscience Division), New York, 1972.
- [74] S. Canneaux, F. Bohr, E. Henon, *J. Comput. Chem.*, **2014**, *35*, 82.
- [75] I.M. Alecu, J. Zheng, Y. Zhao, D.G. Truhlar, *J. Chem. Theory. Comput.*, **2010**, *6*, 2872.
- [76] N.J. Bunce, L. Liu, J. Zhu, *Environ. Sci. Technol.*, **1997**, *31*, 2252.
- [77] F. Rosas, R.M. Dominguez, M. Tosta, J.R. Mora, E. Marquez, T. Cordova, G. Chuchani, *J. Phys. Org. Chem.*, **2010**, *23*, 743.
- [78] E.A. Mason, L. Monchick, *Humidity and Moisture*; Reinhold Publishing Corp.: New York, 1965, *3*, pp. 257.
- [79] J.B. Chaddock, *Humidity and Moisture*; Reinhold Publishing Corp.: New York, 1965, pp. 273.
- [80] Y. Iwai, H. Higashi, H. Uchida, Y. Arai, *Fluid. Phase. Equilib.*, **1997**, *127*, 251.
- [81] Z. Zhang, X. Xu, L. Wang, *J. Phys. Chem. A*, **2013**, *117*, 160.
- [82] G.E. Scuseria, H.F. Schaefer III, *J. Chem. Phys.*, **1989**, *90*, 3629.

Chapter 7

Theoretical study of the oxidation mechanisms of thiophene initiated by hydroxyl radicals

7.1. Introduction

The study of the atmospheric sulfur cycle is becoming important as a result of the increase of the increase in sulfur emissions due to human activities [1]. Increasing emissions of sulfur compounds into the atmosphere due to fossil fuel refining and combustion produce acid rains [2]. If man-made emissions continue to increase, they may reach or exceed natural emissions in the next years [3,4]. Among the reduced sulfur compounds released into the atmosphere from both natural and industrial sources, natural emissions of COS, H₂S and CH₃SCH₃ dominate, but other species such as thiophene, tetrahydrothiophene (THT) and diethylsulfide (DES) must also be considered [5].

Kinetic and mechanistic data for the reactions of sulfur compounds with important oxidant species such as OH, O₃, and NO₃ are required in order to evaluate their atmospheric residence times as well as the ultimate fates of these compounds [6–17]. Since the major gas-phase chemical loss processes that occur in the atmosphere during daytime are reactions involving O₃ and OH radicals, kinetic and mechanistic data for these reactions are especially required for the development of physico-chemical models of atmospheric pollution [14–17]. The most important sink reactions of sulfur compounds in the troposphere are those involving OH radicals [18,19], which play a key role in determining the oxidation power of the atmosphere [20]. Determining the kinetic data for these reactions will contribute to a better understanding of the atmospheric sulfur cycle.

Thiophene may become of increasing importance in both combustion and atmospheric chemistry in years to come due to the development of new energy technologies related to the conversion or combustion of coal, shale oil and petroleum [21,22]. Specially, the kinetics of the oxidation reaction of thiophene by OH radicals must to be quantified in order to allow the lifetime of this compound in the atmosphere to be estimated [23]. The overall rate constants are separated into individual processes involving [24] OH addition onto the C=C double bond and onto the sulfur atom.

The reaction between hydroxyl radicals and thiophene has been studied experimentally by different groups [25–29]. MacLeod *et al.* [27], Lee and Tang [28], as well as Wine and Thompson [25] have studied the gas-phase reactions between hydroxyl radicals and thiophene at low pressures by means of discharge flow electron paramagnetic resonance (EPR). At room temperature, there is a very good agreement between the results obtained by Lee and Tang [28] and MacLeod *et al.*: the overall kinetic rate constants obtained are practically identical [27]. These results differ by a factor of 5 from the results of Atkinson *et al.* [26], obtained relative to the rate constant for the reaction of OH radicals with *n*-hexane at 298 K and a pressure of 1.0 atm. Witte and Zetzsch [29] used a flash photolysis-resonance fluorescence apparatus to investigate the temperature dependence of the reaction between 298 and 471 K at a total pressure of 133 mbar with argon (Ar) as inert gas. They concluded [29] that, at the studied temperatures, the reaction channels related to OH addition onto the C=C double bonds would be expected to have an energy barrier higher than that for OH addition onto the sulfur atom. They also observed a non-exponential decay of OH radicals at temperatures larger than 434 K, while the species produced by OH addition onto the sulfur atom transform back to the reactants at temperatures ranging from 434 to 471 K. Since thiophene is stabilized by resonance, one may assume that the kinetics of the reaction should be similar to the kinetics of the reactions of hydroxyl radicals with benzene and other aromatic hydrocarbons [30,31], where adduct decomposition back to reactants occurs rapidly at temperatures not far above 298 K.

Wine and Thompson [25] have confirmed the value obtained by Atkinson *et al.* [26] using flash photolysis resonance fluorescence. However, the activation energy reported by Wine and Thompson [25] differs very significantly from the activation energy obtained by MacLeod *et al.* [27] at temperatures between 293 and 473 K. The large negative activation energy ($-3.5 \text{ kcal mol}^{-1}$) reported for this reaction by MacLeod *et al.* [27] is very unusual.

Lee and Tang [28] as well as Atkinson *et al.* [26] conjectured that this reaction proceeds via addition; however, there is disagreement between these authors

concerning whether OH adds onto the C=C double bonds or onto the sulfur atom. Indeed, the measured negative activation energies support the contention that both reactions proceed via addition routes. However, it has been unambiguously established whether the addition occurs on the S atom or on the C=C double bonds [1, 24–29]. Since Atkinson *et al.* [26] measured rate constants under tropospheric conditions (i.e. at 1 atm air), the agreement of the results obtained by Wine and Thompson [25] with theirs indicates that there is no dependence of rate constants on O₂ concentration.

An Arrhenius plot of all the kinetic rate constants that were measured or experimentally inferred over the temperature range 255–471 K is depicted in Figure 7.1. As is immediately apparent from this figure, for all reported data series, the rate constant of the reaction between hydroxyl radicals and thiophene exhibits a negative temperature dependence over the studied temperature range, which is equivalent to Arrhenius activation energies of $-(650\pm 142)$ [25], $-(1168\pm 434)$ [32], $-(400\pm 40)$ [29], or $-(3500\pm 400)$ cal mol⁻¹ [27]. Accordingly, a least-square fit of the experimental rate constants yields the following Arrhenius expression [25,26,33]:

$$k = \left(3.20^{+0.73}_{-0.59}\right) \times 10^{-12} e^{(324\pm 65)/T} \text{ cm}^3 \text{ molecule}^{-1} \text{ s}^{-1}$$

The above Arrhenius rate constant decreases with increasing temperature at temperatures ranging from 298 to 473 K [22], confirming presence of negative activation energies. The corresponding values vary from $(9.57\pm 1.15)\times 10^{-12}$ to $(5.3\pm 0.5)\times 10^{-12}$ cm³ molecule⁻¹ s⁻¹.

To explain the disparity in the kinetic data supplied in Figure 7.1, three different pathways (**1–3**) have been suggested for the reaction between thiophene and OH radicals in the gas phase (Figure 7.2). The main purpose of the present study was to investigate these three reaction pathways theoretically, assuming that a two-step mechanism (see the “theory and computational details” section for details). To our knowledge, the theoretical study presented here was the first to investigate the oxidation mechanisms of thiophene that are initiated by hydroxyl radicals. Under experimental conditions, the attack of OH radicals on thiophene is initiated by addition onto the S₁ atom and onto the C=C double bond (C₂ and C₃ atoms) to give the products **P1–P3** (Figure 7.2).

In line with the assumption of a first reversible addition step, the negative activation energies of this reaction at room temperature indicate that a major reaction channel of these adducts is the loss of hydroxyl radicals to regenerate the reactants [25]. Upon investigating the regioselectivity of OH addition reactions on

thiophene under an inert (Ar) atmosphere, it was experimentally observed by Atkinson *et al.* [26] that the reaction pathways **1–2** related to the addition of the OH radical onto the C=C double bonds dominate over OH addition onto the sulfur atom (pathway **3**).

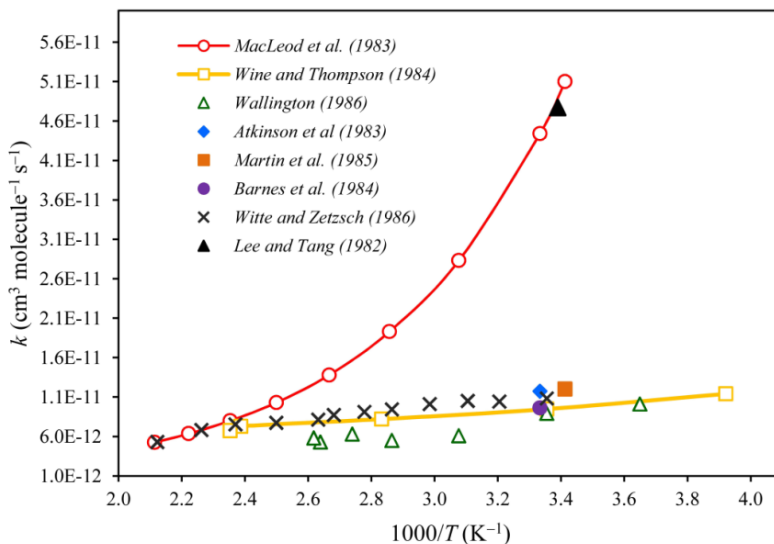


Figure 7.1. Arrhenius plot of the rate constants for the reaction of hydroxyl radicals with thiophene. Legend: (○) MacLeod *et al.* [27]; (□) Win and Thompson [25]; (△) Wallington [32]; (◆) Atkinson *et al.* [26]; (■) Martin *et al.* [2]; (●) Barnes *et al.* [34]; (×) Witte and Zetzsch [29]; (▲) Lee and Tang [28].

To gain more quantitative insights into these reaction mechanisms, we performed a comparison with benchmark theoretical calculations employing the high-level composite CBS-QB3 *ab initio* approach [35–43], in order to determine which exchange-correlation functional gives the most accurate energy barriers and reaction energies. We note that DFT methods alone were found to be insufficient to quantitatively investigating the potential energy surface of the benzene + OH radical interaction along the OH addition and H abstraction reaction pathways, given the inability of many popular DFT functionals to quantitatively describe non-bonded interactions and barrier heights [44]. These observations were also substantiated by recent theoretical studies of the reaction mechanisms and kinetics of oxidation processes of naphthalene by OH radicals [45,46].

With the CBS-QB3 approach, an extrapolation scheme is used to evaluate SCF and correlation energies in the limit of a complete basis set (CBS). The obtained

results will be analyzed in terms of nucleus independent chemical shift (NICS) indices of aromaticity [47–51], natural bond orbital (NBO) occupancies [52,53], and donor-acceptor interaction energies, for the sake of chemical insights.

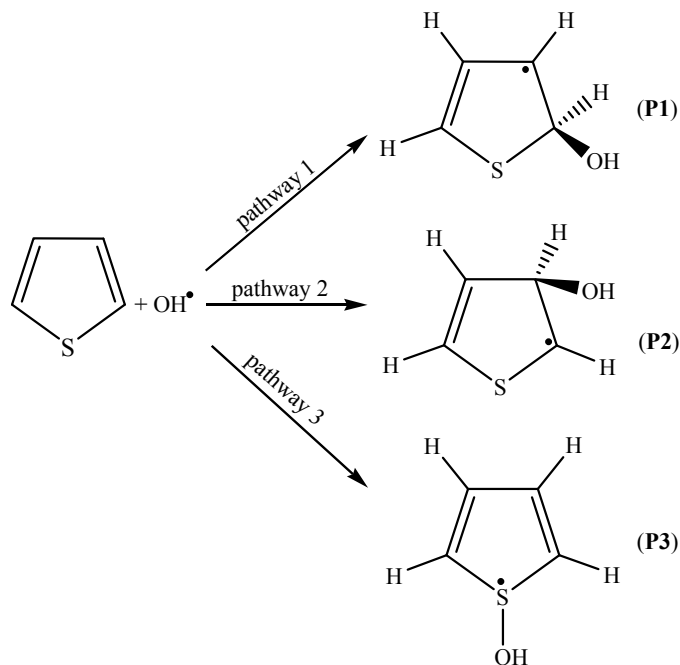


Figure 7.2. Reaction pathways for the oxidation of thiophene by hydroxyl radicals.

7.2. Theory and Computational Details

All calculations that are discussed in the present work have been performed using the Gaussian 09 package of programs [54]. Molecular structures were visualized with GaussView [55]. The molecular structures and harmonic vibrational frequencies of all stationary points of interest were calculated using density functional theory along with a variety of exchange-correlation functionals, namely ωB97XD [56], UM05-2x [57] and UM06-2x [57,58] functionals, in conjunction with the aug-cc-pVTZ basis set [59]. We note that the inclusion of diffuse atomic functions in the basis set is essential for a quantitative enough description of sulfur containing compounds and of non-bonded interactions.

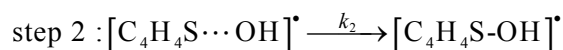
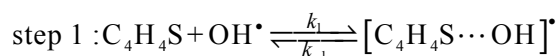
The intrinsic reaction coordinate (IRC) path [60] was traced at the B3LYP/6-31G^{**} level of theory in order to check the proposed mechanism and the connection

of the identified transition structures with the associated minima, using the second-order Gonzalez-Schlegel integration method [60,61].

Energy barriers obtained on DFT grounds were systematically corrected for basis set superposition errors (BSSEs) [62], according to the counterpoise method proposed by Boys and Bernardi [63]. In this *a posteriori* correction method, the energy calculations for the individual monomers are performed using the whole supermolecular basis sets instead of the monomer basis sets. As is well known, in quantum mechanical calculations, BSSEs arise because of the incompleteness of the basis set. No counterpoise corrections are therefore required for CBS-QB3 results, since the CBS-QB3 approach amounts to an extrapolation of CCSD(T) calculations to the asymptotic limit of a complete basis set.

No symmetry constraints were imposed during the geometry optimizations [64,65]. The keyword *nosymm* was used in order to guarantee this matter. In line with these frequency calculations, thermodynamic state functions (H , S , G) were obtained from canonical partition functions obtained for an ideal polyatomic gas under a pressure of 1 atm using the standard RRHO approximation and Boltzmann statistics (see refs 66 and 67 or any textbook of molecular statistical mechanics).

In our study, the oxidation of thiophene by OH radicals has been analyzed according to a two-step mechanism [68,69], involving first a fast pre-equilibrium between the reactants ($C_4H_4S+OH^\bullet$) and a prereactive complex $[C_4H_4S\dots OH]^\bullet$ (IM), and then to the products:



In the above scheme, k_1 and k_{-1} denote the rate constants of the forward and backward reactions associated to the first step, whereas k_2 represent the rate constant corresponding to the second step. A steady-state analysis of the overall reaction pathway leads to the following expression for the associated rate constant [68,70]:

$$k_{\text{overall}} = \frac{k_1 k_2}{k_{-1} + k_2} \quad (7.1)$$

Although the energy barrier for k_{-1} has about the same height as that for k_2 , the entropy change for the reverse reaction (IM \rightarrow R) must be much larger than that for the formation of the products (IM \rightarrow P). Thus, k_{-1} is expected to be much larger than k_2 (an assumption that has been checked in details on the basis of RRKM

calculations, see data reported in the Supplementary Information). Therefore, the overall rate constant (k_{overall}) can be rewritten as:

$$k_{\text{overall}} = K_c k_2 \quad (7.2)$$

with $K_c = k_1/k_{-1}$ the equilibrium constant for fast pre-equilibrium between the reactants and the prereactive complex (step 1):

$$K_c = \frac{[\text{C}_4\text{H}_4\text{S}\cdots\text{OH}]^\bullet}{[\text{C}_4\text{H}_4\text{S}][\text{OH}^\bullet]} \quad (7.3)$$

Applying basic statistical thermodynamic principles (see in particular eq. 26.3–20 in ref. 71), this equilibrium constant can be obtained as follows:

$$K_c = \frac{Q_{\text{IM}}}{Q_{\text{C}_4\text{H}_4\text{S}} \cdot Q_{\text{OH}}} \times \frac{V_m(T)}{N_{\text{Av}}} \times \exp\left(-\frac{(E_{\text{IM}} - E_{\text{C}_4\text{H}_4\text{S}} - E_{\text{OH}})}{RT}\right) \quad (7.4)$$

with N_{Av} the Avogadro number, R the ideal gas constant, and $V_m(T) = RT/P$ the molar volume of an ideal gas. In the high pressure limit (Transition State Theory), the kinetic rate constant characterizing the unimolecular dissociation reaction is given by:

$$k_2 = \kappa(T) \times \frac{\sigma k_{\text{B}} T}{h} \times \frac{Q_{\text{TS}}}{Q_{\text{IM}}} \times \exp\left[-\frac{(E_{\text{TS}} - E_{\text{IM}})}{RT}\right] \quad (7.5)$$

where σ is the reaction pathway degeneracy, and $\kappa(T)$ denotes the Wigner's tunneling factor [72]. In the above equations, $Q_{\text{C}_4\text{H}_4\text{S}}$, Q_{OH} , Q_{IM} , and Q_{TS} represent the total molecular partition functions for the isolated reactants ($\text{C}_4\text{H}_4\text{S}$ and OH^\bullet), prereactive molecular complex (IM), and transition state (TS) associated to the unimolecular dissociation reaction (step 2), respectively. $E_{\text{C}_4\text{H}_4\text{S}}$, E_{OH} , E_{IM} and E_{TS} are the corresponding energies, including B3LYP/6-311G(2d,d,p) estimates for zero-point vibrational contributions. Since the moving entity at the transition state involves a relatively heavy oxygen atom, note that the tunneling factor $\kappa(T)$ was found to be very close to 1 for all studied reactions (see discussion).

All of the values supplied for the unimolecular kinetic rate constants (k_2) come from calculations that were performed using the implementation of canonical variational TST [73–75], and statistical RRKM theory [76–78] in the KiSThelf package [79].

The RRKM approach has been considered to evaluate pressure effects on k_2 and k_{overall} at a canonical level, both in the fall-off regime and towards the high pressure limit. In these RRKM calculations, a scaling factor of 0.99 was imposed on the frequencies calculated at the B3LYP/6-311G(2d,d,p) level of theory. Collisional stabilization rate constants were computed using Lennard–Jones (LJ) collision rate theory [80]. The strong collision approximation was used, assuming therefore that every collision deactivates with $\omega = \beta_c Z_{\text{LJ}}[M]$ being the effective collision frequency, where β_c is the collisional efficiency, Z_{LJ} is the LJ collision frequency and $[M]$ is the total gas concentration. The retained collisional efficient (β_c) was set equal to 0.2. The collision frequencies (Z_{LJ}) were calculated using the LJ parameters: ε/k_{B} , which depends on the energy depth (ε) of the LJ potential and σ , which represents a dimensional scale of the molecular radius [79]. The retained LJ potential parameters for argon as diluent gas amount to $\sigma = 3.465 \text{ \AA}$ and $\varepsilon/k_{\text{B}} = 113.5 \text{ K}$ [81]. For the thiophene-OH adduct $[\text{C}_4\text{H}_4\text{S-OH}]^*$, the following parameters have been used: $\sigma = 3.493 \text{ \AA}$ and $\varepsilon/k_{\text{B}} = 179.2 \text{ K}$ [82].

Canonical variational VTST [83–93] including Wigner’s tunneling corrections has been used, mainly for the sake of validating the RRKM approach at $P = 1 \text{ bar}$. VTST is indeed most commonly regarded as the most reliable approach for estimating kinetic rate coefficients with an accuracy approaching the limits of the assumptions inherent in transition state theory when treating reaction energy profiles involving shallow energy wells and loose transition states [94–99]. In the present work, VTST calculations have been performed in conjunction with a detailed exploration of the IRC path at the UM06-2x/aug-cc-pVTZ level. 10 points on both the forward and reverse IRCs have been retained in these computations, using a step size of 0.1 Bohr.

7.3. Result and Discussion

7.3.1. Structural Analysis

The optimized molecular structures of the intermediate complexes (IM1, IM2, and IM3), transition states (TS1, TS2, and TS3), and products (P1, P2, and P3) in the reactions between thiophene and OH radicals along pathways **1–3** are presented in Tables 7.1 and 7.2, according to the atom labels given in Figure 7.3. The interested reader is referred further to Table S1 in the Appendix V for getting the Cartesian coordinates [B3LYP/6-311G(2d,d,p) results] defining the optimized structures of all identified stationary points. In analogy to the oxidation mechanism of benzene initiated by OH radicals [44], a prereactive molecular complex has been

identified for the reactions of thiophene with OH radicals. According to Alvarez-Idaboy *et al.* [100], such a prereactive complex is a common feature to reactions in between radical species and unsaturated molecules, which finds its origin into long-range coulomb interactions between the reactant molecules [101].

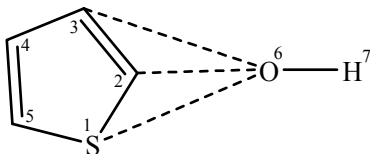


Figure 7.3. Retained atom labeling for characterizing the structures of intermediates and transition states during the oxidation of thiophene by OH radicals (see Tables 7.1 and 7.2).

In line with changes in chemical bond orders, examination of Table 7.2 and comparison of the structures for the intermediates (IM1 and IM2) for chemical pathways **1** and **2** show that addition of an hydroxyl radical at the C₂ (C₃) position results into a significant lengthening of the C₂-C₃ (C₃-C₄) and S₁-C₂ chemical bonds. In addition, OH addition at the S₁ position results into a significant lengthening of the S₁-C₂ and C₅-S₁ chemical bonds. For chemical pathways **1-3**, it appears that the corresponding transition states (TS1, TS2, or TS3) are structurally much closer to the related prereactive intermediates (IM_x with $x=1,2$ or IM3) than the corresponding products (P1, P2, or P3).

According to our data, the IM_x ($x=1,2$) intermediate complexes for pathways **1** and **2** are characterized by C₂-O₆ and C₃-O₆ bond lengths equal to 2.60–2.93 and 2.66–2.88 Å, respectively (Table 7.1). For the IM3 intermediate complex along reaction pathway **3**, the S₁-O₆ bond length amounts to 2.47–3.51 Å (Figure 7.2). At all considered theoretical levels, the C_{*i*}-O₆ ($i=2,3$) forming bond is slightly shorter, by ~0.08 to ~0.15 Å, in the TS2 transition structure on pathway **2** compared with the TS1 transition structure on pathway **1**.

The intermediate (IM_x, $x=1,2$) and transitions states (TS1,TS2) which are involved in the chemical pathways **1** and **2** are characterized by C₂-O₆ and C₃-O₆ “bond” lengths which do not vary by more than ~0.15 and ~0.08 Å from one theoretical level to the other (Table 7.1). On the contrary, with values ranging from 2.47 to 3.51 Å and from 2.06 to 3.31 Å, most significant differences are found for the S₁-O₆ “bond” length in the prereactive intermediates and transition states involved in pathway **3**, respectively, depending on the employed exchange-correlation functional or method (Table 7.2). This prereactive intermediate is a loosely bound complex which is hold mainly by van der Waals (dispersion) forces.

The extreme looseness of this complex and of the associated transition state explains the disparity of the computed bond lengths. Since van der Waals forces are weak, it is very unlikely that improvements of the geometry will strongly affect the activation and reaction energies characterizing this profile. Indeed, the activation energy obtained for pathway **3** from the CBS-QB3 calculations does not differ by more than 0.7 kcal mol⁻¹ from the results of MP2/aug-cc-pVTZ geometry optimizations. In addition, it is worth noting that for this chemical pathway (Table 7.2), the ω B97XD functional is the one which gives the most accurate insights into the structural characteristics of the involved stationary points, in comparison with MP2/aug-cc-pVTZ results. This observation substantiates the very loosely bound, i.e. non-covalent, nature of IM3 and TS3 since this functional has been especially designed for coping with dispersion forces.

The reader is referred to Figure 7.4 for more insights into the electronic structure of the three possible products of hydroxyl radical addition on thiophene, in the form of spin density distributions. These distributions reflect the extent of the delocalization of the free electron through mesomeric effects, but are qualitatively consistent with the chemical structures displayed in Figure 7.2. As was to be expected, for compound P1 (OH group attached to the C₂ atom), the free electron indeed essentially delocalizes on the S₁, C₃, C₄ and C₅ atoms. Similarly, for compound P2 (OH group attached to the C₃ atom), the free electron essentially delocalizes on the S₁, C₂, C₄ and C₅ atoms. At last, and in line with Figure 7.2, the free electron in compound P3 (OH group attached to the S₁ atom) delocalizes symmetrically all over the ring, but exhibits a higher density around the S₁ atom.

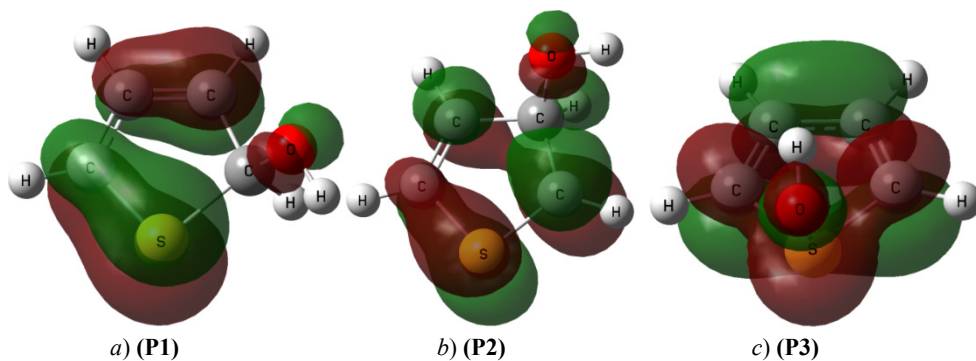


Figure 7.4. Spin density distributions (HOMO) for the three products of the oxidation reaction pathways by hydroxyl radicals [B3LYP/6-311G(2d,d,p) results].

Table 7.1. Structural parameters for all stationary points which are involved in the chemical reaction pathways **1** and **2** (Figure 7.2) for the oxidation of thiophene by hydroxyl radical into related products (P1, P2) ($x=1,2$). (see Figure 7.3 for atom labeling)

Parameter	ω B97XD/aug-cc-pVTZ					UM05-2x/aug-cc-pVTZ					UM06-2x/aug-cc-pVTZ					B3LYP/6-311G(2d,d,p)					MP2/aug-cc-pVTZ				
	IMx	TS1	TS2	P1	P2	IMx	TS1	TS2	P1	P2	IMx	TS1	TS2	P1	P2	IMx	TS1	TS2	P1	P2	IMx	TS1	TS2	P1	P2
$r(S_1-C_2)$	1.715	1.725	1.707	1.862	1.709	1.711	1.725	1.705	1.852	1.708	1.713	1.727	1.705	1.857	1.708	1.728	1.738	1.718	1.892	1.719	1.694	1.708	1.697	1.852	1.716
$r(C_2-C_3)$	1.366	1.383	1.386	1.493	1.489	1.363	1.384	1.384	1.491	1.487	1.362	1.385	1.385	1.493	1.490	1.378	1.390	1.396	1.497	1.500	1.355	1.370	1.362	1.492	1.489
$r(C_3-C_4)$	1.421	1.409	1.438	1.365	1.506	1.422	1.409	1.438	1.366	1.504	1.424	1.410	1.440	1.365	1.507	1.421	1.414	1.445	1.373	1.504	1.427	1.416	1.450	1.355	1.503
$r(C_4-C_5)$	1.359	1.366	1.348	1.391	1.327	1.361	1.367	1.349	1.391	1.326	1.361	1.368	1.349	1.393	1.328	1.369	1.373	1.355	1.397	1.334	1.356	1.343	1.322	1.388	1.312
$r(C_5-S_1)$	1.718	1.715	1.732	1.729	1.758	1.715	1.712	1.730	1.728	1.757	1.716	1.713	1.732	1.727	1.758	1.729	1.727	1.746	1.739	1.770	1.701	1.703	1.718	1.728	1.769
$r(O_6-H_7)$	0.968	0.966	0.965	0.959	0.958	0.970	0.967	0.967	0.960	0.960	0.973	0.969	0.968	0.961	0.961	0.971	0.970	0.969	0.964	0.963	0.972	0.969	0.969	0.965	0.965
$r(C_2-O_6)$	2.599	2.148	2.638	1.405	-	2.765	2.107	2.612	1.413	-	2.922	2.096	2.619	1.407	-	2.436	2.170	2.660	1.410	-	2.900	1.990	-	1.417	-
$r(C_3-O_6)$	2.660	2.666	2.034	-	1.434	2.745	2.635	2.031	-	1.441	2.871	2.640	2.025	-	1.434	2.710	2.706	2.021	-	1.448	2.852	-	1.952	-	1.443
$\angle H_7-O_6-C_2$	85.73	97.08	80.51	109.35	-	75.86	96.83	80.98	109.49	-	69.98	97.65	80.73	109.49	-	91.67	96.13	81.29	108.59	-	74.03	100.89	-	108.26	-
$\angle H_7-O_6-C_3$	81.33	75.84	98.16	-	108.52	68.69	74.75	97.17	-	108.71	63.85	75.18	97.92	-	108.75	81.42	79.20	97.84	-	107.43	68.49	-	100.47	-	107.62

Bond lengths are given in angstroms (Å), and angles are given in degrees (°).

Table 7.2. Structural parameters for all stationary points which are involved in the chemical reaction pathway **3** (Figure 7.2) for the oxidation of thiophene by hydroxyl radical into the related product (P3). (see Figure 7.3 for atom labeling)

Parameter	ω B97XD/aug-cc-pVTZ			UM05-2x/aug-cc-pVTZ			UM06-2x/aug-cc-pVTZ			B3LYP/6-311G(2d,d,p)			MP2/aug-cc-pVTZ		
	IM3	TS3	P3	IM3	TS3	P3	IM3	TS3	P3	IM3	TS3	P3	IM3	TS3	P3
$r(S_1-C_2)$	1.720	1.715	1.719	1.711	1.718	1.712	1.714	1.719	1.713	1.735	1.731	1.730	1.715	1.718	1.725
$r(C_2-C_3)$	1.356	1.359	1.356	1.362	1.356	1.361	1.361	1.358	1.361	1.362	1.364	1.365	1.380	1.376	1.374
$r(C_3-C_4)$	1.427	1.423	1.427	1.422	1.430	1.423	1.425	1.431	1.424	1.433	1.433	1.433	1.421	1.421	1.429
$r(C_4-C_5)$	1.356	1.359	1.356	1.361	1.356	1.362	1.361	1.358	1.361	1.365	1.364	1.362	1.378	1.375	1.374
$r(C_5-S_1)$	1.719	1.716	1.720	1.711	1.718	1.711	1.714	1.719	1.713	1.730	1.731	1.735	1.715	1.718	1.725
$r(O_6-H_7)$	0.968	0.971	0.968	0.973	0.968	0.973	0.975	0.969	0.975	0.972	0.972	0.972	0.981	0.980	0.974
$r(S_1-O_6)$	2.471	2.952	2.471	3.327	2.201	3.311	3.138	2.059	3.156	2.366	2.351	2.366	3.507	3.312	1.788
$\angle H_7-O_6-S_1$	90.02	71.18	90.03	49.04	95.74	49.65	60.90	99.31	60.38	94.93	93.71	94.93	42.75	61.61	105.52

Bond lengths are given in angstroms (Å), and angles are given in degrees (°).

Prior to ending this discussion of geometric structures and parameters, it is worth noticing that, at all considered DFT levels of theory that were used to optimize the geometries of prereactive intermediates, transition states and products, the spin contamination [$\langle S^2 \rangle_{\text{obs}} - 0.75$] never exceeds 0.03 (see Table S2 of the Appendix V) and can thus for all practical purposes be regarded as negligible. For the HF/6-31+G* wavefunction which is required for post-SCF energy calculations at the CCSD(T)/6-31+G* level of theory in the CBS-QB3 procedure, $\langle S^2 \rangle$ may reach values around 1.15 for two of the identified transition states (TS1 and TS2). We remind nevertheless that this at first glance rather strong spin contamination will be at a later stage compensated by CCSD calculations of single-point energies. Note also that, in spite of symmetry breakings of spin-unrestricted wavefunctions and thus huge spin contamination problems [102,103], it has been possible to obtain the ionization energies [104], electron attachment energies [105] and singlet-triplet excitation energies [106] of notoriously difficult compounds, such as *n*-acenes (*n*=1–6), within chemical accuracy (1 kcal mol⁻¹) on extrapolated mono-configurational CCSD(T)/CBS grounds. Therefore, the extent of spin contamination of the starting UHF wavefunction does not necessarily prevent us from using the CBS-QB3 approach for benchmark determinations of the activation and reaction energies of OH radical addition processes on thiophene.

7.3.2. Thermodynamical Analysis

The reader is referred to Tables 7.3 and 7.4 for the total internal energies (comprising BSSE and ZPVE corrections) at 0 K, as well as the enthalpies and Gibb's free energies at 298 K of all identified transition states and intermediates along chemical pathways **1–3** relative to the reactants. In line with experimental Arrhenius activation energies [25–29], all our calculations identify the transition state TS1 on pathway **1** as the lowest transition state, and locate it at 0.1 to ~2.2 kcal mol⁻¹ below the reactants. Our best (CBS-QB3) estimate for the corresponding activation energy amounts to -2.2 kcal mol⁻¹. At the same level, the transition states TS2 and TS3 on pathways **2** and **3** are located at ~1.2 and ~1.6 kcal mol⁻¹ below the reactants, respectively. The activation barrier for pathway **1** was therefore 1.0 and 0.6 kcal mol⁻¹ lower than the barriers to pathways **2** and **3**, respectively (Table 7.4). This difference in the activation energies for the bimolecular reactions R→P1, R→P2 and R→P3 indicates (Figure 7.5) that the formation of product P1 will be kinetically favored over the formation of the products P2 and P3.

Table 7.3. Internal energies, standard enthalpies and Gibb's free energies (in kcal mol⁻¹) of prereactive, and products relative to the reactants along chemical pathways 1–3 at different levels of theory. (*P* = 1 atm)

Species	ωB97XD			UM05-2x			UM06-2x			CBS-QB3		
	Δ <i>E</i> _{0K}	Δ <i>H</i> _{298K} ^o	Δ <i>G</i> _{298K} ^o	Δ <i>E</i> _{0K}	Δ <i>H</i> _{298K} ^o	Δ <i>G</i> _{298K} ^o	Δ <i>E</i> _{0K}	Δ <i>H</i> _{298K} ^o	Δ <i>G</i> _{298K} ^o	Δ <i>E</i> _{0K}	Δ <i>H</i> _{298K} ^o	Δ <i>G</i> _{298K} ^o
Thiophene+OH [*]	0.00	0.00	0.00	0.00	0.00	0.00	0.00	0.00	0.00	0.00	0.00	0.00
IMx (<i>x</i> =1,2)	-2.73	-2.84	4.27	-3.11	-3.29	3.87	-3.82	-3.81	2.71	-2.63	-2.77	4.40
IM3	-2.10	-2.11	4.40	-3.20	-3.31	3.65	-3.71	-3.71	3.07	-1.70	-1.89	5.38
IMx ^a	-2.75	-3.29	4.79	-3.14	-3.63	4.16	-3.33	-3.50	3.83	-2.63	-2.77	4.40
BSSE energy-IMx	0.19			0.23			0.23			0.00		
IM3 ^a	-1.98	-1.97	4.41	-3.10	-3.25	3.94	-3.69	-3.63	2.94	-1.70	-1.89	5.38
BSSE energy-IM3	0.16			0.24			0.23			0.00		
P1	-27.22	-28.17	-18.51	-27.08	-28.03	-18.35	-26.30	-27.25	-17.58	-26.18	-27.12	-17.46
P2	-15.80	-16.57	-7.32	-15.74	-16.47	-7.31	-15.46	-16.24	-6.94	-15.80	-16.56	-7.28
P3	-2.10	-2.11	4.38	-3.20	-3.31	3.65	-3.76	-3.79	3.20	-1.70	-1.89	5.38

^a BSSE-corrected relative energies

Table 7.4. Internal energies, standard enthalpies and Gibb's free energies (in kcal mol⁻¹), and activation entropies (in cal mol⁻¹ K⁻¹) of transition states relative to the reactants along chemical pathways 1–3 at different levels of theory. (*P* = 1 atm)

Species	ωB97XD			UM05-2x			UM06-2x			CBS-QB3			
	Δ <i>E</i> _{0K} [†]	Δ <i>H</i> _{298K} ^{o†}	Δ <i>G</i> _{298K} ^{o†}	Δ <i>E</i> _{0K} [†]	Δ <i>H</i> _{298K} ^{o†}	Δ <i>G</i> _{298K} ^{o†}	Δ <i>E</i> _{0K} [†]	Δ <i>H</i> _{298K} ^{o†}	Δ <i>G</i> _{298K} ^{o†}	Δ <i>E</i> _{0K} [†]	Δ <i>H</i> _{298K} ^{o†}	Δ <i>G</i> _{298K} ^{o†}	Δ <i>S</i> _{298K} ^{o†}
Thiophene + OH [*]	0.00	0.00	0.00	0.00	0.00	0.00	0.00	0.00	0.00	0.00	0.00	0.00	0.00
TS1	-1.93	-2.65	6.22	-0.81	-1.58	7.47	-0.07	-0.82	8.20	-2.18	-2.90	6.00	-29.86
Imaginary frequency TS1 (cm ⁻¹)		241.72 <i>i</i>			410.56 <i>i</i>			422.05 <i>i</i>			188.33 <i>i</i>		
TS2	-0.41	-1.20	7.90	0.68	-0.10	8.99	1.37	0.59	9.70	-1.18	-1.98	7.20	-30.82
Imaginary frequency TS2 (cm ⁻¹)		347.82 <i>i</i>			441.23 <i>i</i>			435.46 <i>i</i>			323.99 <i>i</i>		
TS3	-2.10	-2.58	5.13	-0.82	-1.48	6.93	0.10	-0.63	8.23	-1.57	-2.28	6.51	-29.52
Imaginary frequency TS3 (cm ⁻¹)		69.66 <i>i</i>			158.84 <i>i</i>			96.36 <i>i</i>			27.08 <i>i</i>		
TS1 ^a	-1.43	-2.37	7.01	-0.49	-1.35	7.93	0.16	-0.60	8.41	-2.18	-2.90	6.00	
BSSE energy-TS1	0.22			0.27			0.26			0.00			
TS2 ^a	-0.09	-0.90	8.29	0.64	-0.53	9.28	1.41	0.25	10.08	-1.18	-1.98	7.20	
BSSE energy-TS2	0.26			0.30			0.28			0.00			
TS3 ^a	-1.72	-2.35	5.75	-1.11	-2.12	6.98	0.57	-0.32	8.72	-1.57	-2.28	6.51	
BSSE energy-TS3	0.16			0.25			0.25			0.00			

^a BSSE-corrected relative energies

Reaction energies, enthalpies, entropies and Gibbs free energies of reaction for the oxidation of thiophene by hydroxyl radicals are supplied in Table 7.3. The CBS-QB3 results show that pathways 1–3 are all exothermic processes

($\Delta H \approx -27.1, -16.6, \text{ and } -1.9 \text{ kcal mol}^{-1}$, respectively). Reaction pathways **1** and **2** are exoergic processes ($\Delta G < 0$), whereas pathway **3** was found to be endoergic ($\Delta G > 0$) at ambient temperature and pressure. From the energy profiles supplied in Figure 7.5, it is clear that the formation of product P1 will also be thermodynamically favored, since the reaction is strongly exothermic ($\Delta H = -27.0 \text{ kcal mol}^{-1}$) and exoergic ($\Delta G = -17.5 \text{ kcal mol}^{-1}$). With reaction energies of -15.5 to $-15.8 \text{ kcal mol}^{-1}$, the oxidation of thiophene by a hydroxyl radical via reaction pathway **2** also appears to be a strongly exothermic process, whereas pathway **3** appears to be only slightly exothermic, with a reaction energy of around $-1.7 \text{ kcal mol}^{-1}$ at the CBS-QB3 level.

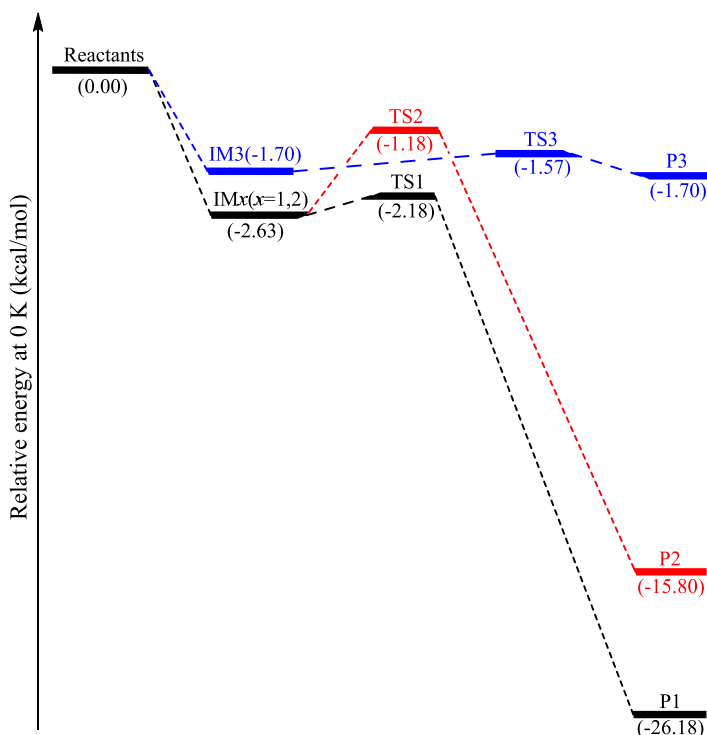


Figure 7.5. CBS-QB3 potential energy profile for the reaction pathways **1–3**.

The CBS-QB3 results show that the energy barriers (IMx→TS1/TS2 or IM3→TS3) encountered along chemical reaction pathways **1–3** amount to ~ 0.5 , ~ 1.5 , and $\sim 0.1 \text{ kcal mol}^{-1}$, respectively. According to our data, the IMx ($x=1,2$) intermediate complex is located ~ 2.6 to $\sim 3.7 \text{ kcal mol}^{-1}$ below the total energy of the reactants, whereas the IM3 intermediate complex is ~ 1.7 to $\sim 3.8 \text{ kcal mol}^{-1}$

below the reactants. In line with the experimental finding of Witte and Zetzsch [29], the computed energy profiles confirm that one of the reaction channels related to OH addition onto the C=C double bond has an energy barrier which is higher than that for OH addition onto the sulfur atom.

The transition states TS1, TS2, and TS3 are characterized by NICS indices of approximately -12.2 , -11.0 and -11.8 kcal mol⁻¹, respectively. Evidently, the more pronounced aromaticity of the TS1 structure explains why it is more stable than the TS2 and TS3 structures. Also, the lower energy of IMx than IM3 reflects the greater aromaticity of the former prereactive molecular complex: indeed, the IMx and IM3 intermediates are characterized by NICS indices of -13.5 and -12.1 , respectively.

We note that, in line with observations made in recent works [45,46,107–110], excluding the BSSE from the UM05-2x and UM06-2x energy barriers improves the agreement with the benchmark and BSSE-free CBS-QB3 results, slightly, presumably because of a fortuitous cancellation of errors (basis set convergence error versus the approximate electron correlation treatment and the neglect of spin-orbit interactions). This observation seems to confirm the superiority of the latter two functionals for chemical kinetics. Nevertheless, some care is needed, because the UM05-2x and UM06-2x functionals do not incorporate corrections for dispersion forces, as is the case with the ω B97XD functional. The computed BSSE corrections are around 0.2–0.3 kcal mol⁻¹, whereas the differences between the ω B97XD and UM06-2x energy barriers range from 1.0 to 2.1 kcal mol⁻¹, so the exchange-correlation functional appears to be far more important than the BSSE corrections, when using a basis set as large as aug-cc-pVTZ. More specifically, BSSE values for IMx and IM3 are in the ranges of 0.19–0.23 and 0.16–0.24 kcal mol⁻¹. Similarly, BSSE values for TS1, TS2, and TS3 range from 0.23 to 0.27, from 0.26 to 0.32, and from 0.16 to 0.25 kcal mol⁻¹, respectively.

The reaction rate constant is determined not only by the activation barrier but also by the activation entropy required to reach the transition state [111]. The activation entropies for the different pathways are given in Table 7.4. Although the vibrational entropy reaches a value of $R/2$ already for a harmonic frequency of about 400 cm⁻¹, the difference from a hindered internal rotor only becomes significant for frequencies below 100 cm⁻¹ and rotational barriers comparable to RT (~ 3 kJ mol⁻¹ at room temperature) [112]. Although TS2 is located ~ 0.3 kcal mol⁻¹ below TS3, this small energy difference is overcompensated for by an entropy difference of 1.3 cal mol⁻¹ K⁻¹ in favor of TS2 at 298 K (Table 7.4), which cause the Gibbs free activation energy for pathway **2** to be ~ 0.7 kcal mol⁻¹ higher

than that for pathway **3**. In the high-pressure limit at 298 K, the rate constant for pathway **3** is therefore expected to be larger by 21% larger than that for pathway **2**.

On the basis our benchmark CBS-QB3 calculations, Agmon's analysis [113] in line with the Hammond's postulate yield n_T values that are equal to 0.20, 0.33, and 0.85 in the R→P1, R→P2, and R→P3 reaction steps, respectively. In line with the computed energy profiles and the structural observations made in the preceding section, this sequence implies that the TS1 and TS2 transition structures are more similar to the reactants, whereas the TS3 transition structure is more similar to the product.

According to R. Atkinson (see in particular his review article in ref. 33b), only the three proposed chemical pathways corresponding to OH addition processes need to be considered when attempting to unravel the available experimental kinetic data. In addition to the three studied chemical pathways, we also considered the possibility of further reaction channels such as ring openings of the most stable thiophene–OH radical adduct (**P1**) into HOHC•–CH=CH–C=S radical species. These channels imply unimolecular reaction steps which are characterized by extremely large activation energies, above 13.4 kcal mol⁻¹, and lead to radical species that lie at about 6.1 and 13.4 kcal mol⁻¹ above **P1**. These ring opening channels are thus unlikely to be very competitive from either a thermodynamic or a kinetic viewpoint.

7.3.3. Natural Bond Orbital Analysis

Inspection of the NBO data and stabilization energies (eq. 2.112) reported in Table 7.5 for the TS1 and TS2 transition states reveals that there is a strong interaction between one of the sulfur lone pairs of thiophene and the unoccupied $\pi^*(C_4-C_5)$ orbital, resulting in occupancies of around 0.14 and 0.1, respectively, for the latter orbital. The corresponding stabilization energies range from ~13.7 to less than ~0.3 kcal mol⁻¹. Evidently, charge-transfer delocalization also contributes to the greater stability of the TS1 structure and, to a lesser extent, of the TS2 structure as compared with the TS3 transition state. More specifically, the natural bond orbital analysis demonstrates that, compared with thiophene, the $n_{S(2)} \rightarrow \pi^*_{C_4-C_5}$ stabilization energies (E_2) strongly influence the activation energies computed for pathway **1** ($E_2 \sim 13.7$ kcal mol⁻¹) and pathway **2** ($E_2 \sim 8.1$ kcal mol⁻¹). According to the NBO analysis, the $\pi(C_4-C_5)$ bonding orbital occupancies in the TS1 and TS2 structures are ~0.87 and ~0.96, whereas the $\pi^*(C_4-C_5)$ antibonding orbital occupancies in these structures are ~0.14 and ~0.10, respectively.

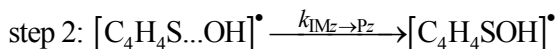
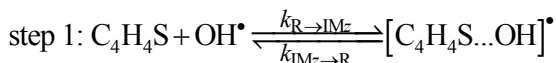
Table 7.5. NBO occupancies and stabilization energies (E_2) (in kcal mol⁻¹) characterizing reactant, intermediates, and transition structures along the chemical reaction pathways **1–3** [results obtained at the B3LYP/6-311G(2d,d,p) level].

	B3LYP/6-311G(2d,d,p)					
	thiophene	IMx	IM3	TS1	TS2	TS3
Occupancies						
$\alpha(C_2-C_3)$	1.9852	0.9925	0.9925	0.9924	0.9928	0.9926
$\sigma^*(C_2-C_3)$	0.3064	0.0079	0.0078	0.0082	0.0083	0.0076
$\sigma(C_3-C_4)$	1.9757	0.9882	0.9879	0.9886	0.9881	0.9879
$\sigma^*(C_3-C_4)$	0.0163	0.0082	0.0083	0.0080	0.0089	0.0082
$\pi(C_4-C_5)$	-	0.9089	0.9424	0.8705	0.9577	-
$\pi^*(C_4-C_5)$	-	0.1415	0.1107	0.1439	0.0988	-
$n_{S(1)}$	1.9851	0.9922	0.9738	0.9920	0.9925	0.9753
$n_{S(2)}$	1.6073	0.8085	-	0.8043	0.7722	-
$n_{O(1)}$	-	0.9975	0.9958	0.9955	0.9928	0.9961
$n_{O(2)}$	-	0.9894	0.9897	0.9848	0.9796	0.9899
Stabilization energies (E_2)						
$n_{S(1)} \rightarrow \sigma^*(C_2-C_3)$	2.15	1.14	1.05	1.09	1.18	0.99
$n_{S(1)} \rightarrow \sigma^*(C_4-C_5)$	< 0.25	1.11	0.94	1.14	1.04	< 0.25
$n_{S(2)} \rightarrow \pi^*(C_4-C_5)$	< 0.25	12.13	0.39	13.74	8.11	< 0.25

In addition, inspection of the NBO data reported in Table 7.5 for the transition states TS1, TS2, and TS3 reveals that there is a weak interaction between one of the sulfur lone pairs of thiophene and the unoccupied $\sigma^*(C_2-C_3)$ orbital, resulting in an occupancy of around 0.01 for the latter orbital. The corresponding stabilization energies range from ~1.0 to ~1.2 kcal mol⁻¹.

7.3.4. Kinetic Analysis

Effective rate constants for reaction pathways **1–3** have been computed upon the assumption of a two-step mechanism, involving first a fast and reversible pre-equilibrium between the reactants (thiophene and OH[•] radical) and a prereactive complex [C₄H₄S...OH][•] (IM_z with z=1–3), followed by an irreversible dissociation step leading to the products:



A steady-state analysis of the above sequence of reactions leads to the following easily tractable expressions for the effective rate constants characterizing the three studied chemical pathways:

$$k_{\text{eff}}(\mathbf{1}) = \frac{k_{\text{R} \rightarrow \text{IM1}} k_{\text{IM1} \rightarrow \text{P1}}}{k_{\text{IM1} \rightarrow \text{R}} + k_{\text{IM1} \rightarrow \text{P1}}} \approx K_{\text{c}(\text{R} \rightleftharpoons \text{IM1})} k_{\text{IM1} \rightarrow \text{P1}} = (RT) K_{\text{p}(\text{R} \rightleftharpoons \text{IM1})} k_{\text{IM1} \rightarrow \text{P1}} \quad (7.6)$$

$$k_{\text{eff}}(\mathbf{2}) = \frac{k_{\text{R} \rightarrow \text{IM2}} k_{\text{IM2} \rightarrow \text{P2}}}{k_{\text{IM2} \rightarrow \text{R}} + k_{\text{IM2} \rightarrow \text{P2}}} \approx K_{\text{c}(\text{R} \rightleftharpoons \text{IM2})} k_{\text{IM2} \rightarrow \text{P2}} = (RT) K_{\text{p}(\text{R} \rightleftharpoons \text{IM2})} k_{\text{IM2} \rightarrow \text{P2}} \quad (7.7)$$

$$k_{\text{eff}}(\mathbf{3}) = \frac{k_{\text{R} \rightarrow \text{IM3}} k_{\text{IM3} \rightarrow \text{P3}}}{k_{\text{IM3} \rightarrow \text{R}} + k_{\text{IM3} \rightarrow \text{P3}}} \approx K_{\text{c}(\text{R} \rightleftharpoons \text{IM3})} k_{\text{IM3} \rightarrow \text{P3}} = (RT) K_{\text{p}(\text{R} \rightleftharpoons \text{IM3})} k_{\text{IM3} \rightarrow \text{P3}} \quad (7.8)$$

In the above equations, $k_{[\text{R} \rightarrow \text{IM}_z, (z=1-3)]}$ is the kinetic rate constant characterizing the forward bimolecular reaction step (in $\text{cm}^3 \text{ molecule}^{-1} \text{ s}^{-1}$), whereas $k_{\text{IM}_z \rightarrow \text{P}}$ and $k_{\text{IM}_z \rightarrow \text{R}}$ represent the forward and backward unimolecular reaction rate constants (in s^{-1}).

To obtain quantitative insights into the regioselectivity of OH addition onto thiophene, branching ratios were obtained for the three chemical pathways of interest, according to VTST and RRKM estimates for effective rate constants [see eqs. (7.6–7.8)] via

$$R(i) = \frac{k_{\text{eff}}(i)}{k_{\text{eff}}(\mathbf{1}) + k_{\text{eff}}(\mathbf{2}) + k_{\text{eff}}(\mathbf{3})} ; \quad i = 1-3 \quad (7.9)$$

The reader is referred to Tables 7.6 and 7.7 for a comparison of the kinetic rate constants and branching ratios obtained at temperatures ranging from 298 to 471 K, and at a pressure of 1 bar using VTST and RRKM theories, in conjunction with the UM06-2x/aug-cc-pVTZ estimates for activation energies. The rationale behind this choice is that the UM06-2x exchange-correlation functional is considered [58] to be the best for applications involving main-group thermochemistry, kinetics, noncovalent interactions, and electronic excitation energies to valence and Rydberg states. In addition, we note that, unlike results obtained at the UM05-2x/aug-cc-pVTZ and ω B97XD/aug-cc-pVTZ levels, the UM06-2x/aug-cc-pVTZ level yields activation and reaction energies of the same order as those found using the benchmark CBS-QB3 approach (Tables 7.3 and 7.4). From this comparison, it appears that kinetic rate constants and branching ratios obtained at a pressure of 1.0 bar using the VTST and RRKM approaches in conjunction with the same energy profiles do not appreciably differ. The largest discrepancy is found for the rate constant characterizing the second unimolecular reaction step in pathway **3** [$k_2(\mathbf{3})$], and this discrepancy does not exceed a factor 3.

Table 7.6. Rate constants (units: unimolecular reactions in s^{-1} ; bimolecular reactions in $cm^3 \text{ molecule}^{-1} s^{-1}$), effective rate constants, and branching ratios for the reported reaction channels by means of VTST theory ($P = 1$ bar), according to the computed UM06-2x energy profiles. ($x=1,2$)

T (K)	Rate constants						Branching ratio (%)		
	IMx→P1 $k_2(1)$	IMx→P2 $k_2(2)$	IM3→P3 $k_2(3)$	R→P1 $k_{\text{eff}}(1)$	R→P2 $k_{\text{eff}}(2)$	R→P3 $k_{\text{eff}}(3)$	R(1)	R(2)	R(3)
298	3.03×10^8	2.13×10^7	3.48×10^8	2.27×10^{-14}	1.60×10^{-15}	1.49×10^{-14}	57.91	4.08	38.01
322	4.81×10^8	4.08×10^7	5.66×10^8	2.78×10^{-14}	2.36×10^{-15}	1.89×10^{-14}	56.67	4.81	38.52
353	7.96×10^8	8.28×10^7	9.60×10^8	3.53×10^{-14}	3.67×10^{-15}	2.48×10^{-14}	55.36	5.76	38.89
380	1.15×10^9	1.39×10^8	1.41×10^9	4.25×10^{-14}	5.14×10^{-15}	3.06×10^{-14}	54.32	6.57	39.11
400	1.47×10^9	1.96×10^8	1.82×10^9	4.85×10^{-14}	6.46×10^{-15}	3.54×10^{-14}	53.67	7.15	39.18
425	1.92×10^9	2.86×10^8	2.41×10^9	5.63×10^{-14}	8.39×10^{-15}	4.19×10^{-14}	52.82	7.87	39.31
442	2.27×10^9	3.61×10^8	2.86×10^9	6.22×10^{-14}	9.89×10^{-15}	4.66×10^{-14}	52.41	8.33	39.26
457	2.60×10^9	4.38×10^8	3.29×10^9	6.74×10^{-14}	1.14×10^{-14}	5.09×10^{-14}	51.97	8.79	39.24
471	2.92×10^9	5.17×10^8	3.73×10^9	7.26×10^{-14}	1.28×10^{-14}	5.53×10^{-14}	51.60	9.10	39.30

Table 7.7. Rate constants (units: unimolecular reactions in s^{-1} ; bimolecular reactions in $cm^3 \text{ molecule}^{-1} s^{-1}$), effective rate constants, and branching ratios for the reported reaction channels by means of RRKM theory ($P = 1$ bar), according to the computed UM06-2x energy profiles. ($x=1,2$)

T (K)	Rate constants						Branching ratio (%)		
	IMx→P1 $k_2(1)$	IMx→P2 $k_2(2)$	IM3→P3 $k_2(3)$	R→P1 $k_{\text{eff}}(1)$	R→P2 $k_{\text{eff}}(2)$	R→P3 $k_{\text{eff}}(3)$	R(1)	R(2)	R(3)
298	1.52×10^8	2.18×10^7	1.16×10^8	1.14×10^{-14}	1.63×10^{-15}	4.96×10^{-15}	63.37	9.06	27.57
322	2.10×10^8	3.90×10^7	1.67×10^8	1.21×10^{-14}	2.25×10^{-15}	5.58×10^{-15}	60.71	11.29	28.00
353	2.88×10^8	7.09×10^7	2.40×10^8	1.28×10^{-14}	3.15×10^{-15}	6.20×10^{-15}	57.79	14.22	27.99
380	3.52×10^8	1.07×10^8	3.03×10^8	1.30×10^{-14}	3.95×10^{-15}	6.57×10^{-15}	55.27	16.79	27.93
400	3.95×10^8	1.37×10^8	3.47×10^8	1.30×10^{-14}	4.52×10^{-15}	6.75×10^{-15}	53.56	18.62	27.81
425	4.41×10^8	1.78×10^8	3.96×10^8	1.29×10^{-14}	5.22×10^{-15}	6.88×10^{-15}	51.60	20.88	27.52
442	4.68×10^8	2.06×10^8	4.25×10^8	1.23×10^{-14}	5.43×10^{-15}	6.66×10^{-15}	50.43	22.26	27.31
457	4.87×10^8	2.31×10^8	4.48×10^8	1.26×10^{-14}	5.99×10^{-15}	6.93×10^{-15}	49.37	23.47	27.16
471	5.03×10^8	2.54×10^8	4.66×10^8	1.25×10^{-14}	6.31×10^{-15}	6.91×10^{-15}	48.60	24.53	26.87

Since VTST calculations cannot be performed for practical reasons in conjunction with a highly accurate but costly quantum chemical approach such as CBS-QB3, it seems logical to consider using the RRKM approach to evaluate kinetic rate constants, since it is then possible to obtain more quantitative estimates for the activation and reaction energies. Besides, pressure effects need to be taken into account to achieve a consistent interpretation of the experimentally available kinetic rate constants. On the other hand, tunneling effects are practically negligible. Indeed, based on the computed CBS-QB3 energy profiles and B3LYP/6-311G(2d,d,p) vibrational frequencies, $\kappa(T)$ values of 1.03, 1.10 and 1.00 were found at 298 K with both TST and VTST calculations for the second unimolecular reaction step of pathways **1–3**, respectively.

Table 7.8 and 7.9 show RRKM estimates for unimolecular (k_2) and effective bimolecular (k_{eff}) rate constants at temperatures ranging from 298 to 471 K and at pressures of 1 bar (Table 7.8) and 133 mbar (Table 7.9). These data were obtained from the computed CBS-QB3 energy profiles and B3LYP/6-311G(2d,d,p) microcanonical ro-vibrational densities of states. Using Table 7.9, theoretical rate constants can also be compared with available experimental data [25–29]. Further RRKM data computed at lower and higher pressures are provided for the same temperatures in Tables S3a–S3i of the Appendix V. The reader is further referred to Tables S3a–S3i in the Appendix V for a detailed evaluation of the temperature dependence of the equilibrium constants (K_p) that characterizing the first reversible reaction step.

An Arrhenius plot of the obtained RRKM values for the effective rate constants of reaction pathways **1–3** is supplied in Figure 7.6. In line with the experimental data of Atkinson *et al.* [26], the RRKM results for the effective rate constants of the reaction pathways **1–3** are negatively dependent on the temperature, regardless of the pressure (see also Tables S3a–S3i of the Appendix V). The RRKM results at the experimental pressure $P=133$ mbar (Table 7.9) indicate that the effective rate constants $k_{\text{eff}}(\mathbf{1})$ for pathway **1** is 1.03–1.36 and 3.91–6.4, time larger, respectively, than the effective rate constants $k_{\text{eff}}(\mathbf{2})$ and $k_{\text{eff}}(\mathbf{3})$ for pathways **2** and **3**. Production of the P1 radical will therefore dominate the overall reaction mechanism under atmospheric pressure and at temperatures ranging from 298 to 471 K in the absence of molecular oxygen. The same observation holds for pressures ranging from 10^{-10} to 10^8 bars (see Tables S4a–S4j in the Appendix V).

Table 7.8. Rate constants (units: unimolecular reactions in s^{-1} ; bimolecular reactions in $cm^3 \text{ molecule}^{-1} s^{-1}$), effective rate constants, and branching ratios for the reported reaction channels by means of RRKM theory ($P = 1 \text{ bar}$), according to the computed CBS-QB3 energy profiles. ($x=1,2$)

T (K)	Rate constants						Branching ratio (%)		
	IM x →P1 $k_2(1)$	IM x →P2 $k_2(2)$	IM3→P3 $k_2(3)$	R→P1 $k_{\text{eff}}(1)$	R→P2 $k_{\text{eff}}(2)$	R→P3 $k_{\text{eff}}(3)$	$R(1)$	$R(2)$	$R(3)$
298	1.05×10^9	7.81×10^8	1.11×10^9	2.29×10^{-15}	1.69×10^{-15}	3.58×10^{-16}	52.79	38.96	8.25
322	1.00×10^9	8.04×10^8	1.04×10^9	1.99×10^{-15}	1.59×10^{-15}	3.25×10^{-16}	50.96	40.72	8.32
353	9.43×10^8	8.11×10^8	9.65×10^8	1.73×10^{-15}	1.49×10^{-15}	2.92×10^{-16}	49.26	42.43	8.31
380	8.94×10^8	8.04×10^8	9.09×10^8	1.56×10^{-15}	1.40×10^{-15}	2.70×10^{-16}	48.30	43.34	8.36
400	8.60×10^8	7.93×10^8	8.72×10^8	1.47×10^{-15}	1.35×10^{-15}	2.57×10^{-16}	47.77	43.87	8.35
425	8.22×10^8	7.75×10^8	8.30×10^8	1.37×10^{-15}	1.30×10^{-15}	2.43×10^{-16}	47.03	44.63	8.34
442	7.97×10^8	7.61×10^8	8.04×10^8	1.32×10^{-15}	1.26×10^{-15}	2.35×10^{-16}	46.89	44.76	8.35
457	7.77×10^8	7.48×10^8	7.83×10^8	1.28×10^{-15}	1.24×10^{-15}	2.29×10^{-16}	46.56	45.11	8.33
471	7.59×10^8	7.35×10^8	7.64×10^8	1.25×10^{-15}	1.21×10^{-15}	2.24×10^{-16}	46.57	45.08	8.35

As could be expected from the negative energy barriers, the RRKM effective rate constants decrease gradually with increasing temperatures. Rather unsurprisingly, since the equilibrium constants for the first reversible reaction step ($K_c = K_p/RT$) do not depend very much on the site of addition (see data supplied in Tables S4a–S4j in the Appendix V), this in turn results in a larger (by about one order of magnitude) effective rate constant for addition of the OH radical onto the C_2 atom as compared with the effective rate constants obtained for OH addition onto the C_3 and S_1 atoms.

Upon considering the obtained branching ratios (Table 7.9), it appears that OH addition onto the C_2 , C_3 and S_1 atoms accounts for 52.45–46.47 %, 39.34–45.08 %, and 8.21–8.46 % of the adduct products overall, respectively (Figure 7.7). The branching ratios for pathways **2** and **3** gradually increase with increasing temperatures. On the contrary, a decrease in the corresponding branching ratio is observed for pathway **1**. Figure 7.7 shows the evolution of the branching ratios for the addition of OH radicals at C_2 , C_3 and S_1 as a function of the temperature (see also Table 7.9 and Tables S4a–S4j of the Appendix V for detailed numerical values at various temperatures ranging from 298 to 471 K, and at pressures ranging from 10^{-10} to 10^8 bar).

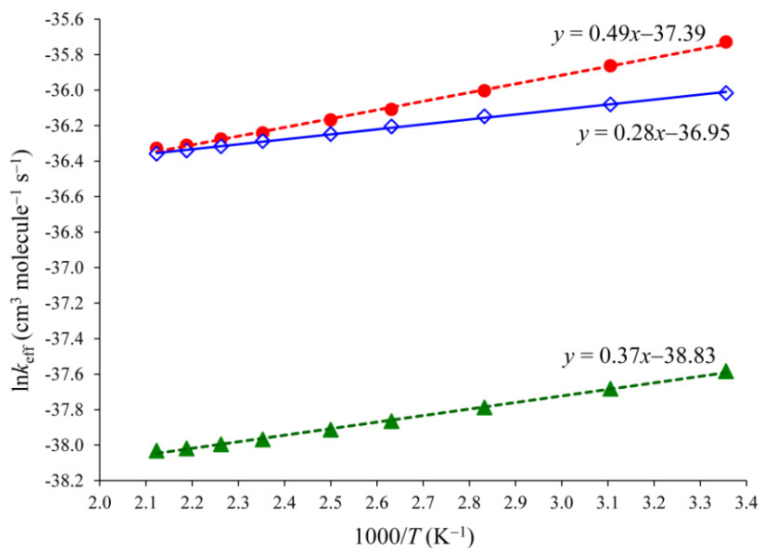


Figure 7.6. Arrhenius plot of the obtained RRKM bimolecular rate constants using the CBS-QB3 approach ($P=133$ mbar). Legend: (●) theoretical rate constant for pathway 1; (◇) theoretical rate constant for pathway 2; (▲) theoretical rate constant for pathway 3.

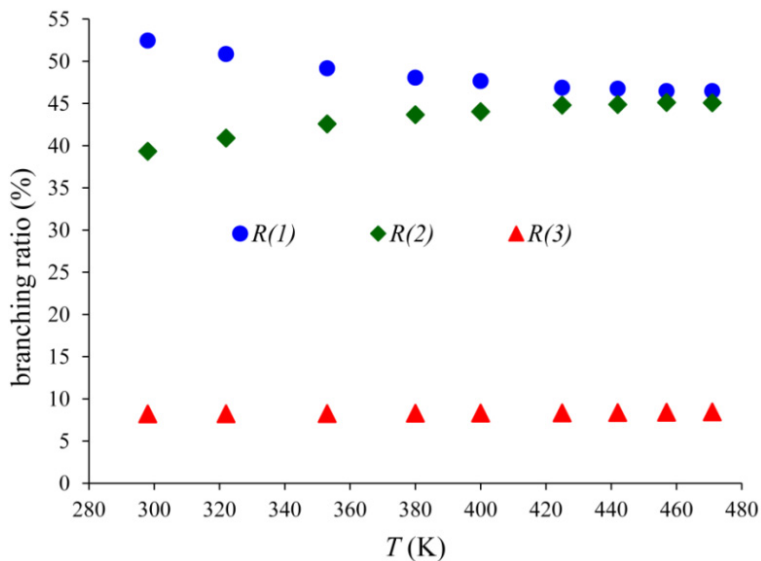


Figure 7.7. Evolution of branching ratios in function of the temperature (CBS-QB3 results).

Table 7.9. Rate constants (units: unimolecular reactions in s^{-1} ; bimolecular reactions in $\text{cm}^3 \text{molecule}^{-1} \text{s}^{-1}$), effective rate constants, and branching ratios for the reported reaction channels by means of RRKM theory ($P=133 \text{ mbar}$), according to the computed CBS-QB3 energy profiles. ($x=1,2$)

T (K)	Rate constants						Branching ratio (%)			$k_{\text{exp}} \times 10^{12}$ ($\text{cm}^3 \text{mol}^{-1} \text{s}^{-1}$)
	IMx→P1 $k_2(\mathbf{1})$	IMx→P2 $k_2(\mathbf{2})$	IM3→P3 $k_2(\mathbf{3})$	R→P1 $k_{\text{eff}}(\mathbf{1})$	R→P2 $k_{\text{eff}}(\mathbf{2})$	R→P3 $k_{\text{eff}}(\mathbf{3})$	R(1)	R(2)	R(3)	
298	1.40×10^8	1.05×10^8	1.47×10^8	3.04×10^{-16}	2.28×10^{-16}	4.76×10^{-17}	52.45	39.34	8.21	$(9.57 \pm 1.15)^a$ $(9.42 \pm 0.34)^b$ $(0.5 \pm 0.04)^c$ $(0.48 \pm 0.06)^d$ $(10.9 \pm 0.7)^e$
322	1.34×10^8	1.08×10^8	1.38×10^8	2.66×10^{-16}	2.14×10^{-16}	4.31×10^{-17}	50.85	40.91	8.24	$(10.5 \pm 0.7)^e$
353	1.26×10^8	1.09×10^8	1.29×10^8	2.31×10^{-16}	2.00×10^{-16}	3.88×10^{-17}	49.17	42.57	8.26	$(8.2 \pm 0.68)^a$
380	1.19×10^8	1.08×10^8	1.21×10^8	2.08×10^{-16}	1.89×10^{-16}	3.59×10^{-17}	48.05	43.66	8.29	$(7.8 \pm 0.3)^e$
400	1.15×10^8	1.06×10^8	1.16×10^8	1.96×10^{-16}	1.81×10^{-16}	3.42×10^{-17}	47.67	44.02	8.32	$(7.7 \pm 0.4)^e$
425	1.09×10^8	1.04×10^8	1.10×10^8	1.82×10^{-16}	1.74×10^{-16}	3.24×10^{-17}	46.86	44.80	8.34	$(7.37 \pm 0.41)^a$
442	1.06×10^8	1.02×10^8	1.07×10^8	1.76×10^{-16}	1.69×10^{-16}	3.15×10^{-17}	46.75	44.89	8.37	$(7.0 \pm 0.2)^e$
457	1.03×10^8	9.99×10^7	1.04×10^8	1.70×10^{-16}	1.65×10^{-16}	3.08×10^{-17}	46.47	45.11	8.42	$(5.6 \pm 0.2)^e$
471	1.01×10^8	9.82×10^7	1.02×10^8	1.67×10^{-16}	1.62×10^{-16}	3.04×10^{-17}	46.47	45.08	8.46	$(5.3 \pm 0.5)^e$

Experimental data: (a) Ref [25]; (b) Ref [26]; (c) Ref [27]; (d) Ref [28]; (e) Ref [29].

In line with the computed energy profiles and kinetic rate constants, the formation of the P1 radical (pathway **1**) clearly predominates over the formation of the P2 and P3 radicals (pathways **2** and **3**) at room temperature. The RRKM data (see Tables S4a–S4j of the Appendix V) indicate that, at temperatures ranging from 298 to 471 K, production of the P1 species will dominate the overall reaction mechanism; this holds true down to extremely low pressures, ($>10^{-10}$ bar). Nevertheless, the regioselectivity of the reaction decreases with increasing temperatures and decreasing pressures.

Effective RRKM theoretical rate constants for the three chemical pathways of interest were fitted by means of least-squares regressions to the three-parameter Arrhenius equation [$k(T) = A \cdot T^n \cdot \exp(-E_a/RT)$] in order to obtain the values of the exponent n , the effective pre-exponential factor A , and the activation barrier E_a that

characterize reaction pathways **1–3**. This fitting procedure led to the following expressions (in $\text{cm}^3 \text{ molecule}^{-1} \text{ s}^{-1}$):

$$\text{Pathway 1: } k_1(T) = 5.17 \times 10^{-20} T^{-1.015} \exp(863.33/T) \quad (7.10)$$

$$\text{Pathway 2: } k_2(T) = 5.75 \times 10^{-16} T^{-0.267} \exp(178.06/T) \quad (7.11)$$

$$\text{Pathway 3: } k_3(T) = 3.85 \times 10^{-20} T^{0.849} \exp(679.52/T) \quad (7.12)$$

at a pressure of 133 mbar and across the temperature range 298–471 K. We emphasize that, at all of the considered temperatures, and in line with the experimental measurements [25–29], the RRKM effective rate constants for pathways **1–3** decrease with the temperature increases (Tables S4a–S4j of the Appendix V). This is obviously the consequence of negative activation energies for the first bimolecular reaction steps.

Upon inspecting Table 7.9, it is quite clear that, at the experimental pressure of 133 mbar [29], the RRKM effective rate constants obtained from the CBS-QB3 energy profiles for the fastest chemical reaction pathway ($\text{R} \rightarrow \text{P1}$, i.e., OH addition at the C_2 position) are about two to three orders of magnitude smaller than the corresponding experimental constants, which corresponds to errors of 3–4.5 kcal mol^{-1} in the computed activation energies at the investigated temperatures (298–471 K). In view of the known levels of error afforded by the CBS-QB3 approach (average and maximum errors of 1.1 and 2.8 kcal mol^{-1} in reaction energies [114]), this semi-quantitative agreement between theory and experimental is quite satisfactory, considering that hindered rotations of the OH group and anharmonic effects in the intermediate and transition states were neglected. Both the experimental and theoretical rate constants for OH addition at the C_2 position decrease with increasing temperature, confirming the idea of a negative activation energy. This fair agreement between theory and experiment makes us believe that the physical chemistry of these complicated processes has been all in all rather correctly captured: it confirms the relevance of both the proposed reaction mechanism and of the employed quantum chemical models. However, some care is needed with our kinetic analysis.

With reaction enthalpies and Gibbs free energies of reaction below -24.4 and $-21.9 \text{ kcal mol}^{-1}$, respectively, the second unimolecular reaction steps in pathways **1** and **2** are highly exothermic and exoergic, and, thus clearly irreversible. The assumption of irreversibility, and therefore eq. (7.8), can be called into question for the second unimolecular reaction step in pathway **3**, which is characterized by

almost zero reaction enthalpy and Gibbs free energy of reaction. Nevertheless, taking into account the reversibility of this reaction step will not yield any qualitatively significant change to the ultimately obtained branching ratios. Indeed, we remind the reader that, according to the RRKM data for branching ratios obtained using the benchmark CBS-QB3 energy profiles, the kinetically less efficient pathway is pathway **3**, with branching ratios of between 8.21% and 8.46% at temperatures of 298–471 K. Taking into account the reversibility of the second unimolecular reaction step in this pathway can only result into a decrease of these branching ratios and strengthen further our conclusion that the most abundant products in the oxidation of thiophene by hydroxyl radicals result from addition processes at the C₁ and C₂ positions.

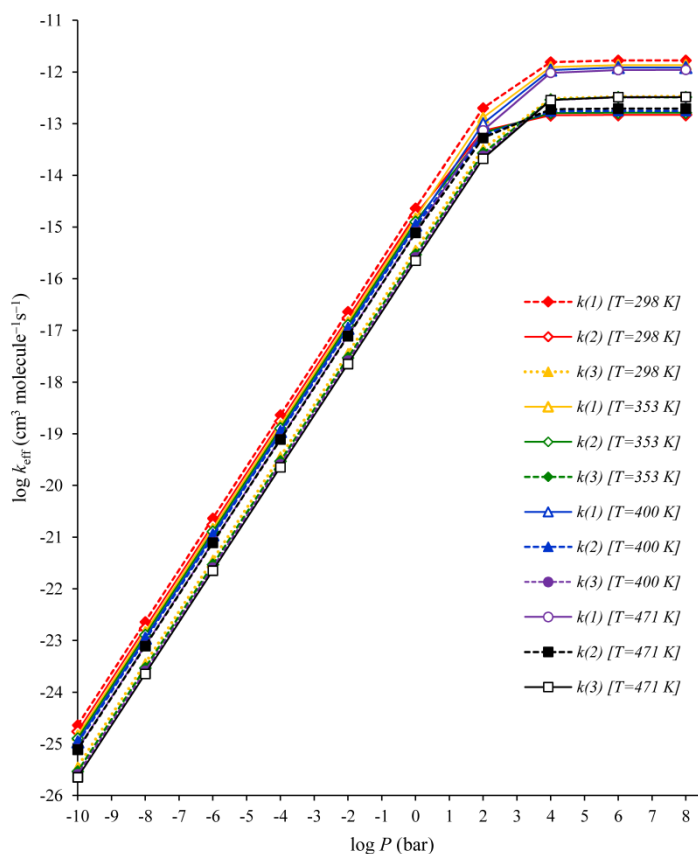


Figure 7.8. Pressure dependence of the RRKM bimolecular rate constants for the reaction pathways 1–3 according to the CBS-QB3 energy profiles [RRKM results, obtained by means of equations (7.6–7.8)].

The pressure dependence of each computed rate constants is depicted at 298, 353, 400 and 471 K in Figure 7.8. It is immediately apparent from this figure that rather high pressures ($>10^4$ bar) are required to ensure saturation at the high pressure limit. This observation is most obviously the consequence of negative activation energies, which makes standard transition state theory invalid at atmospheric pressure (1 bar). Pressure effects must therefore be taken into account on RRKM grounds to gain accurate insights (Table 7.8) into the experimental rate constants by Witte and Zetzsch [29], which were obtained at a pressure of 133 mbar. Compared with the high-pressure limit, in this case the pressure effects result in major (~ 4 orders of magnitude) decreases in the computed rate constants.

7.4. Conclusions

The mechanisms for the oxidation of thiophene initiated by hydroxyl radicals in the gas phase have been studied computationally for the very first time using density functional theory along with various exchange-correlation functionals (ω B97XD, UM05-2x and UM06-2x) and the aug-cc-pVTZ basis set. The reaction energies and activation barriers presented here incorporate zero-point vibrational energy differences and counterpoise corrections for basis set superposition errors. Comparison was made with benchmark computational results obtained at the composite CBS-QB3 level of theory. The best agreement with the computed energy barriers is obtained with the UM06-2x exchange-correlation functional. Kinetic rate constants for unimolecular and bimolecular reaction steps were estimated by means of variational transition state theory (VTST) and statistical Rice-Ramsperger-Kassel-Marcus (RRKM) theory.

This first reaction step for OH addition at the C₂ and C₃ positions (pathways **1** and **2**) is exoergic ($\Delta G < 0$) at ambient temperature and pressure, whereas OH addition onto the sulfur atom (pathway **3**) was found to be an endogenic process ($\Delta G > 0$). In line with experiment, due to the formation of a prereactive van der Waals (VdW) molecular complex $[\text{C}_4\text{H}_4\text{S}\dots\text{OH}]^\ddagger$, the corresponding transition state lies below the reactant, leading to effective negative activation energies of around -2.2 and -1.2 kcal mol⁻¹ for reaction pathways **1** and **2**, respectively. The first bimolecular reaction step involved in pathway **3** is also characterized by a negative activation energy (around -1.6 kcal mol⁻¹).

Effective rate constants were calculated according to a steady state analysis upon a two-step model reaction mechanism, assuming reversibility of the first bimolecular addition reaction step and irreversibility of the second unimolecular dissociation step. In line with the experimental observations of Atkinson *et al.* [26],

the correspondingly branching ratios indicate that the most kinetically efficient process at temperatures ranging from 298 to 471 K is OH addition onto a carbon atom adjacent to the sulfur atom. These ratios also show that the regioselectivity of the reaction decreases with increasing temperatures and decreasing pressures.

In line [88] with the negative activation energies, it was found that the standard transition state approximation breaks down at ambient pressure (1 bar) for the first bimolecular reaction steps. In particular, RRKM calculations showed that exceedingly high pressures, ($>10^4$ bar) are required to restore (to an accuracy of within $\sim 10\%$) the validity of this approximation for all the reaction channels involved in the oxidation of thiophene via the OH addition pathway, especially for the conversion of the prereactive VdW complex $[\text{C}_4\text{H}_4\text{S}\dots\text{OH}]^\bullet$ into the molecular energized adduct $[\text{C}_4\text{H}_4\text{S}-\text{OH}]^\bullet$. NICS indices and natural bond orbital analysis showed that the computed values for the activation energies are influenced mainly by alterations in aromaticity and to a lesser extent by charge-transfer effects pertaining to the delocalization of sulfur lone pairs to neighboring empty π^* orbitals.

A comparison with VTST results led to a validation of RRKM theory for all of the investigated reaction channels. RRKM theory appears to be sufficient to achieve semi-quantitative insights into the experimentally available kinetic rate constants, with discrepancies in the range of two to three orders of magnitude between theory and experiment. More quantitative insights into these rate constants should be amenable by taking into account the reversibility of the second unimolecular reaction step in pathway **3** as well as deviations from canonical energy distributions when evaluating the kinetic rate constants at a microcanonical level. To reach kinetic accuracy (discrepancies of just one order of magnitude between theory and experiment), deviations from the RRHO approximation that was used to evaluate ro-vibrational densities of states (such as hindered rotations of the OH group [115]) should be also taken into account, as well as anharmonic effects at the level of the loosely bound prereactive van der Waals complexes.

7.5. References

- [1] H. MacLeod, J.L. Jourdain, G. Poulet, G. Le Bars, *Atmos. Environ.*, **1984**, *18*, 2621.
- [2] D. Martin, J.L. Jourdain, G. Le Bras, *Int. J. Chem. Kinet.*, **1985**, *17*, 1247.
- [3] D. Möller, *Atmos. Environ.*, **1984**, *18*, 19.
- [4] C.F. Cullis, M.M. Hirschler, *Atmos. Environ.*, **1980**, *14*, 1263.

- [5] G. Mouvier, P. Carlier, *Physico Chemical Behavior of Atmospheric Pollutants*, 3rd European Symposium, Varese, Italy, 10–12 April, 1984.
- [6] R. Atkinson, R.A. Perry, J.N. Pitts Jr., *J. Chem. Phys.*, **1979**, *66*, 1578.
- [7] R. Atkinson, R.A. Perry, J.N. Pitts Jr., *Chem. Phys. Lett.*, **1978**, *54*, 14.
- [8] M.J. Kurylo, *Chem. Phys. Lett.*, **1978**, *58*, 233.
- [9] R.A. Cox, D. Sheppard, *Nature*, **1980**, *284*, 330.
- [10] P.H. Wine, N.M. Kreutter, C.A. Gump, A.R. Ravishankara, *J. Phys. Chem.*, **1981**, *85*, 2660.
- [11] J.H. Lee, I.N. Tang, *J. Chem. Phys.*, **1983**, *78*, 6646.
- [12] H. MacLeod, G. Poulet, G. Le Bras, *J. Chim. Phys.*, **1983**, *80*, 287.
- [13] R. Atkinson, J.N. Pitts Jr., S.M. Aschmann, *J. Phys. Chem.*, **1984**, *88*, 1584.
- [14] B.J. Finlayson-Pitts, J.N. Pitts Jr., *Adv. Environ. Sci. Technol.*, **1977**, *7*, 75.
- [15] R. Atkinson, K.R. Darnall, A.C. Lloyd, A.M. Winer, J.N. Pitts Jr., *Adv. Photochem.*, **1979**, *11*, 375.
- [16] D.G. Hendry, R.A. Kenley, *Atmospheric Reaction Products of Organic Compounds*. EPA-560/12-79-001, June, 1979.
- [17] J.T. Herron, R.E. Huie, J.A. Hodgson, *Chemical Kinetic Data Needs for Modeling the Lower Troposphere*; NBS Spec, Publ. 557, August 1979.
- [18] N.J. Bunce, L. Liu, J. Zhu, *Environ. Sci. Technol.*, **1997**, *31*, 2252.
- [19] R. Atkinson, J. Arey, *Environ. Health. Perspect.*, **1994**, *102*, 117.
- [20] X. Qu, Q. Zhang, W. Wang, *Chem. Phys. Lett.*, **2006**, *429*, 77.
- [21] J.E. Sickles, W.C. Eaton, L.A. Ripperton, R.S. Wright, *Literature Survey of Emissions Associated with Emerging Energy Technologies*; EPA report 600/7-77-104, 1977.
- [22] D. Lucas, N.J. Brown, *Combust. Flame.*, **1983**, *49*, 283.
- [23] J.E. Carpenter, F. Weinhold, *J. Mol. Struct. (THEOCHEM)*, **1988**, *169*, 41.
- [24] R. Atkinson, *Int. J. Chem. Kinet.*, **1987**, *19*, 799.
- [25] P.H. Wine, R.J. Thompson, *Int. J. Chem. Kinet.*, **1984**, *16*, 867.
- [26] R. Atkinson, S.M. Aschmann, W.P.L. Carter, *Int. J. Chem. Kinet.*, **1983**, *15*, 51.
- [27] H. MacLeod, J.L. Jourdain, G. Le Bras, *Chem. Phys. Lett.*, **1983**, *98*, 381.
- [28] J.H. Lee, I.N. Tang, *J. Chem. Phys.*, **1982**, *77*, 4459.
- [29] F. Witte, C. Zetzsch, *9th International Symposium on Gas Kinetics*; University of Bordeaux, Bordeaux, France, 20–25 July, 1986.
- [30] R.A. Perry, R. Atkinson, J.N. Pitts Jr., *J. Phys. Chem.*, **1977**, *81*, 296.
- [31] F.P. Tully, A.R. Ravishankara, R.L. Thompson, J.M. Nicovich, R.C. Shah, N.M. Kreutter, P.H. Wine, *J. Phys. Chem.*, **1981**, *85*, 2262.
- [32] T.J. Wallington, *Int. J. Chem. Kinet.*, **1986**, *18*, 487.

- [33] (a) R. Atkinson, *Chem. Rev.*, **1985**, 85, 69; (b) R. Atkinson, *J. Phys. Chem. Ref. Data*, Monograph **1989**, 1, 1.
- [34] I. Barnes, V. Bastian, K.H. Becker, E.H. Fink, *3rd European Symposium on the Physico-Chemical Behavior of Atmospheric Pollutants*; D. Riedel Publishing Co.: Dordrecht, Holland, 1984.
- [35] R. Casanovas, J. Frau, J. Ortega-castro, A. Salva, J. Donoso, F. Munoz, *Int. J. Quantum. Chem.*, **2010**, 110, 323.
- [36] J.A. Montgomery, M.J. Frisch, J.W. Ochterski, G.A. Petersson, *J. Chem. Phys.*, **1999**, 110, 2822.
- [37] J.W. Ochterski, G.A. Petersson, J.A. Montgomery, *J. Chem. Phys.*, **1996**, 104, 2598.
- [38] M.R. Nyden, G.A. Petersson, *J. Chem. Phys.*, **1981**, 75, 1843.
- [39] G.A. Petersson, A. Bennett, T.G. Tensfeld, M.A. Al-Laham, W. Shirley, J. Matzaris, *J. Chem. Phys.*, **1988**, 89, 2193.
- [40] G.A. Petersson, M.A. Al-Laham, *J. Chem. Phys.*, **1991**, 94, 6081.
- [41] G.A. Petersson, A.K. Yee, A. Bennett, *J. Chem. Phys.*, **1983**, 83, 5105.
- [42] J.A. Montgomery, J.W. Ochterski, G.A. Petersson, *J. Chem. Phys.*, **1994**, 101, 5900.
- [43] J.A. Montgomery, M.J. Frisch, J.W. Ochterski, G.A. Petersson, *J. Chem. Phys.*, **2000**, 112, 6532.
- [44] D.S. Hollman, A.C. Simmonett, H.F. Schaefer, *Phys. Chem. Chem. Phys.*, **2011**, 13, 2214.
- [45] A. Shiroudi, M.S. Deleuze, S. Canneaux, *J. Phys. Chem. A*, **2014**, 118, 4593.
- [46] A. Shiroudi, M.S. Deleuze, *J. Phys. Chem. A*, **2014**, 118, 3625.
- [47] P. Cysewski, *J. Mol. Struct. (THEOCHEM)*, **2005**, 714, 29.
- [48] P.v.R. Schleyer, C. Maerker, A. Dransfeld, H. Jiao, N.J.R. van Eikema Hommes, *J. Am. Chem. Soc.*, **1996**, 118, 6317.
- [49] S. Nigam, C. Majumder, S.K. Kulshreshtha, *J. Chem. Sci.*, **2006**, 118, 575.
- [50] P.v.R. Schleyer, M. Manoharan, Z.X. Wang, B. Kiran, H.J. Jiao, R. Puchta, N. Hommes, *Org. Lett.*, **2001**, 3, 2465.
- [51] P.v.R. Schleyer, H. Jiao, B. Goldfuss, P.K. Freeman, *Angew. Chem. Int. Ed. Engl.*, **1995**, 34, 337.
- [52] A.E. Reed, R.B. Weinstock, F. Weinhold, *J. Chem. Phys.*, **1985**, 83, 735.
- [53] J.K. Badenhop, F. Weinhold, *Int. J. Quantum. Chem.*, **1999**, 72, 269.
- [54] M.J. Frisch, G.W. Trucks, H.B. Schlegel, G.E. Scuseria, M.A. Robb, J.R. Cheeseman, G. Scalmani, V. Barone, B. Mennucci, G.A. Petersson *et al.* Gaussian 09, Revision B.01; Gaussian: Wallingford, CT, 2009.

- [55] I.I.R. Dennington, T. Keith, J. Millam, K. Eppinnett, W.L. Hovell, R. Gilliland, GaussView, Version 3.09; Semichem, Inc.: Shawnee Mission, KS, 2003.
- [56] J.D. Chai, M. Head-Gordon, *Phys. Chem. Chem. Phys.*, **2008**, *10*, 6615.
- [57] Y. Zhao, D.G. Truhlar, *Acc. Chem. Res.*, **2008**, *41*, 157.
- [58] Y. Zhao, D.G. Truhlar, *Theor. Chem. Acc.*, **2008**, *120*, 215.
- [59] T.H. Dunning, *J. Chem. Phys.*, **1989**, *90*, 1007.
- [60] F. Fukui, *J. Phys. Chem.*, **1970**, *74*, 4161.
- [61] J.W. McIver Jr., *Acc. Chem. Res.*, **1974**, *7*, 72.
- [62] I.V. Tokmakov, M.C. Lin, *J. Phys. Chem. A*, **2002**, *106*, 11309.
- [63] S.F. Boys, F. Bernardi, *Mol. Phys.*, **1970**, *19*, 553.
- [64] M. Huang, Z. Wang, Y. Yang, L. HAO, W. Zhao, X. Gao, L. Fang, W. Zhang, *Int. J. Quantum. Chem.*, **2007**, *107*, 1092.
- [65] K. Walczak, J. Friedrich, M. Dolg, *Chem. Phys.*, **2009**, *365*, 38.
- [66] D.A. McQuarrie, *Statistical Mechanics*, Harper and Row: New York, 1976.
- [67] G.H. Herzberg, *Molecular Spectra and Molecular Structure. II Infrared and Raman Spectra of Polyatomic Molecules*; Van Nostrand Reinhold: New York, 1945.
- [68] D.L. Singleton, R.J. Cvetanovic, *J. Am. Chem. Soc.*, **1976**, *98*, 6812.
- [69] J.R. Alvarez-Idaboy, N.M. Diez, A. Vivier-Bunge, *J. Am. Chem. Soc.*, **2000**, *122*, 3715.
- [70] V.H. Uc, J.R. Alvarez-Idaboy, A. Galano, A Vivier-Bunge, *J. Phys. Chem. A*, **2008**, *112*, 7608.
- [71] R.G. Mortimer, *Physical Chemistry*; 3rd ed., Elsevier Academic Press: Burlington, 2008.
- [72] E.P. Wigner, *Z. Phys. Chem.*, **1932**, *B19*, 203.
- [73] E. Vanden-Eijnden, F.A. Tal, *J. Chem. Phys.*, **2005**, *123*, 184103.
- [74] B.C. Garret, D.G. Truhlar, R.S. Grev, A.W. Magnuson, *J. Phys. Chem.*, **1980**, *84*, 1730.
- [75] B.C. Garret, D.G. Truhlar, *J. Am. Chem. Soc.*, **1979**, *101*, 4534.
- [76] J.I. Steinfeld, J.S. Francisco, W.L. Hase, *Chemical Kinetics and Dynamics*; Prentice-Hall: Englewood Cliffs, NJ, 1999.
- [77] P.J. Robinson, K.A. Holbrook, *Unimolecular Reactions*; Wiley: New York, 1972.
- [78] E. Eyring, S.H. Lin, S.M. Lin, *Basic Chemical Kinetics*; Wiley: New York, 1980.
- [79] S. Canneaux, F. Bohr, E. Henon, *J. Comput. Chem.*, **2013**, *35*, 82.
- [80] J. Troe, *J. Chem. Phys.*, **1977**, *66*, 4758.

- [81] F.M. Mourits, H.A. Rummens, *Can. J. Chem.*, **1977**, *55*, 3007.
- [82] J.P. Pellitero, P. Ungerer, A.D. Mackie, *J. Phys. Chem. B*, **2007**, *111*, 4460.
- [83] E. Wigner, *J. Chem. Phys.*, **1937**, *5*, 720.
- [84] J. Horiuti, *Bull. Chem. Soc. Jpn.*, **1938**, *13*, 210.
- [85] J.C. Keck, *J. Chem. Phys.*, **1960**, *32*, 1035.
- [86] J.C. Keck, *Adv. Chem. Phys.*, **1967**, *13*, 85.
- [87] D.G. Truhlar, B.C. Garrett, *Annu. Rev. Phys. Chem.*, **1984**, *35*, 159.
- [88] B.C. Garrett, D.G. Truhlar, *J. Phys. Chem.*, **1979**, *83*, 1052.
- [89] B.C. Garrett, D.G. Truhlar, *J. Chem. Phys.*, **1979**, *70*, 1593.
- [90] D.G. Truhlar, B.C. Garrett, *Acc. Chem. Res.*, **1980**, *13*, 440.
- [91] M.G. Evans, M. Polanyi, *Trans. Faraday. Soc.*, **1938**, *34*, 11.
- [92] D.G. Truhlar, A.D. Isaacson, B.C. Garrett, *Theory of Chemical Reaction Dynamics*; M. Baer, Ed.; CRC Press: Boca Raton, FL, Vol. IV; p 65, 1985.
- [93] T. Baer, W.L. Hase, *Unimolecular Reaction Dynamics*; Oxford University Press, Oxford, 1996.
- [94] B.C. Garrett, D.G. Truhlar, *J. Phys. Chem.*, **1979**, *83*, 1079.
- [95] R.G. Gilbert, S.C. Smith, *Theory of Unimolecular and Recombination Reactions*; Blackwell Scientific: Oxford, 1990.
- [96] S.J. Klippenstein, Y.-C. Yang, V. Ryzhov, R.C. Dunbar, *J. Chem. Phys.*, **1996**, *104*, 4502.
- [97] D.M. Wardlaw, R.A. Marcus, *Adv. Chem. Phys.*, **1988**, *70*, 231.
- [98] W.L. Hase, D.M. Wardlaw, *Bimolecular Collisions*; M.N.R. Ashfold, J.E. Baggott, Eds., Royal Society of Chemistry, London, 1989.
- [99] S.J. Klippenstein, *In The Chemical Dynamics and Kinetics of Small Radicals*; K. Liu, A.F. Wagner, Eds.; World Scientific: Singapore, Vol. 1, 1995.
- [100] J.R. Alvarez-Idaboy, N. Mora-Diez, R.J. Boyd, A. Viver-Bunge, *J. Am. Chem. Soc.*, **2001**, *123*, 2018.
- [101] C.W. Zhou, A.M. Mebel, X.Y. Li, *J. Phys. Chem. A*, **2009**, *113*, 10667.
- [102] M. Huzak, B. Hajgató, M.S. Deleuze, *J. Chem. Phys.*, **2011**, *135*, 104704.
- [103] M.S. Deleuze, M. Huzak, B. Hajgató, *J. Mol. Mod.*, **2013**, *19*, 2699.
- [104] M.S. Deleuze, L. Claes, E.S. Kryachko, J.-P. François, *J. Chem. Phys.*, **2003**, *119*, 3106.
- [105] B. Hajgató, M.S. Deleuze, D.J. Tozer, F. De Proft, *J. Chem. Phys.*, **2008**, *129*, 84308.
- [106] B. Hajgató, D. Szieberth, P. Geerlings, F. De Proft, M.S. Deleuze, *J. Chem. Phys.*, **2009**, *131*, 224321.
- [107] J.R. Alvarez-Idaboy, A. Galano, *Theor. Chem. Acc.*, **2010**, *126*, 75.

- [108] R. Castañeda-Arriaga, J.R. Alvarez-Idaboy, *Int. J. Quantum. Chem.*, **2012**, *112*, 3479.
- [109] M. Cordova-Gomez, C. Iuga, J.R. Alvarez-Idaboy, *Int. J. Quantum. Chem.*, **2012**, *112*, 3508.
- [110] X.W. Sheng, L. Mentel, O.V. Gritsenko, E.J. Baerends, *J. Comput. Chem.*, **2011**, *32*, 2896.
- [111] W. Sun, L. Yang, L. Yu, M. Saeys, *J. Phys. Chem. A*, **2009**, *113*, 7852.
- [112] F. Jensen, *Introduction to Computational Chemistry*; 2nd Ed., John Wiley & Sons: New York, 2007.
- [113] N. Agmon, R.D. Levine, *Chem. Phys. Lett.*, **1977**, *52*, 197.
- [114] D.H. Ess, *Quantum Mechanical Theory of Reactivity and Selectivity in Organic and Organometallic Reactions*; Ph.D. Dissertation, University of California, Los Angeles, 2007.
- [115] S. Canneaux, R. Vandeputte, C. Hammaeher, F. Louis, M. Ribaucour, *J. Phys. Chem. A*, **2012**, *116*, 592.

Chapter 8

Conclusions

In **Chapter 1**, polycyclic aromatic hydrocarbons (PAHs) and their derivatives have been introduced as ubiquitous atmospheric pollutants with toxic, mutagenic, and carcinogenic properties. These compounds are released into the atmosphere as a by-product of combustion processes. PAHs have thus attracted much attention in recent years because of their inherent toxicity. Naphthalene is the most volatile and abundant PAHs in the urban areas. In the atmosphere, the major atmosphere loss process for these semi-volatile PAHs is expected to be by gas-phase reaction with hydroxyl radicals. Reactions of naphthalene in the atmosphere often yield degradation products which may be more carcinogenic than the parent PAH. Thus, it is important to understand the fate of atmospheric naphthalene in oxidation reactions that are initiated by OH^\bullet radicals.

An important first step in oxidation of sulfur compounds after release into the atmosphere from both natural and anthropogenic sources involves also reactions with OH^\bullet radicals which play a key role in determining the oxidation power of the atmosphere. Determining the rate constant for these reactions will contribute to a better understanding of the sulfur cycle in the atmosphere. Moreover, the study of the reaction mechanisms can give some information on the further oxidation steps which lead to SO_2 and sulfates. Thiophene may become of increasing importance both in combustion and in atmospheric chemistry as a result of the development of new energy technologies related to conversion or combustion of coal, shale oil and petroleum. The kinetics of the oxidation reaction of thiophene by OH^\bullet radicals has

therefore to be quantified in order to estimate the lifetime of this compound in the atmosphere.

In **Chapter 2**, a review is given of all employed quantum mechanical theories, such as Hartree-Fock, Møller-Plesset perturbation theory, Coupled Cluster theory and Density Functional Theory (DFT) with emphasis on the employed exchange correlation (B3LYP, ω B97XD, UM05-2x and UM06-2x) functionals. This chapter then proceeds with an introduction to statistical thermodynamic for a review of the approaches which have been employed for computing partition functions and thermodynamic state functions (U , H , S , G). At last, using the formalism of phase space integrals, we derive RRKM theory of unimolecular kinetic rate constants, and its simplifications in the high-pressure limit such as standard transition state theory (TST) and variational transition state theory (VTST).

In **Chapters 3–7**, oxidation mechanisms of naphthalene and thiophene initiated by hydroxyl radicals have been studied theoretically using density functional theory (DFT) along with various exchange-correlation functionals (B3LYP, ω B97XD, UM05-2x and UM06-2x), and an extremely large basis set (aug-cc-pVTZ) at all stages of the present study. For the sake of quantitative insights into these reaction mechanisms, comparison has been made with benchmark computational results obtained at the high-level composite CBS-QB3 *ab initio* approach, in order to determine which exchange-correlation functional gives the most accurate energy barriers and reaction energies. We noted that DFT methods alone were found to be insufficient for quantitatively investigating the potential energy surface associated with the oxidation reaction initiated by hydroxyl radicals, given the inability of many popular DFT functionals to quantitatively describe non-bonded interactions and barrier heights. For the sake of chemical insights, the obtained results were analyzed in terms of nucleus independent chemical shift (NICS) indices of aromaticity, bond orders analysis, natural bond orbital (NBO) occupancies, and donor-acceptor interaction energies. Besides providing energy barriers and reaction energies at the CBS-QB3 theoretical level, a main purpose of the present work was to supply good kinetic equations, kinetic rate constants and branching ratios for the purpose of fully unraveling the original experiments by means of transition state theory (TST) or variational transition state theory (VTST).

For reaction mechanisms that contain a substantial activation energy barrier, transition state theory is suitable. But if no recognizable barrier height exists along the reaction coordinate, both activation energy and activation entropy play an important role in defining the transition state, and canonical VTST should be used in order to supply semi-quantitative results for kinetic rate constants. VTST has

been used in conjunction with the energy profiles which have been computed at the UM06-2x/aug-cc-pVTZ level. The reason for this choice is that the UM06-2x exchange-correlation functional is known to be the best one for applications involving main-group thermochemistry. The UM06-2x/aug-cc-pVTZ level of theory yields the same energy ordering for activation and reaction energies as that found using the benchmark CBS-QB3 approach. Kinetic rate constants and branching ratios obtained using the VTST and statistical Rice-Ramsperger-Kassel-Marcus (RRKM) theoretical approaches in conjunction with the same (UM06-2x/aug-cc-pVTZ) energy profiles do not appreciably differ. It seems therefore justify to claim that RRKM results enable also semi-quantitative insights into kinetic rate constants.

In **Chapter 3**, reaction mechanisms for the initial stages of naphthalene oxidation at high temperatures ($T \geq 600$ K) have been studied theoretically. These stages correspond to the removal of hydrogen atoms by hydroxyl radical and the formation of 1- and 2-naphthyl radicals. The excellent agreement with the available experimental kinetic rate constants demonstrates that a two-step reaction scheme prevails. Analysis of the computed structures, bond orders and free energy profiles demonstrates that the reaction steps involved in the removal of hydrogen atoms by OH radicals satisfy Hammond's principle. Computations of branching ratios also show that these reactions do not exhibit a particularly pronounced site-selectivity.

In **Chapter 4**, the oxidation mechanisms of naphthalene by hydroxyl radicals under inert (He) conditions have been studied theoretically. Comparison with experiment confirms that, on the OH-addition reaction pathway leading to 1-naphthol, the first bimolecular reaction step has an effective negative activation energy around -1.5 kcal mol⁻¹, whereas this step is characterized by an activation energy around 1 kcal mol⁻¹ on the OH-addition reaction pathway leading to 2-naphthol. Effective rate constants have been calculated according to a steady state analysis upon a two-step model reaction mechanism. In line with experiment, the correspondingly obtained branching ratios indicate that, at temperatures lower than 410 K, the most abundant product resulting from the oxidation of naphthalene by hydroxyl radicals must be 1-naphthol rather than 2-naphthol. The regioselectivity of the OH[•] addition onto naphthalene decreases with increasing temperatures and decreasing pressures. Because of slightly positive or even negative activation energies, the RRKM calculations demonstrate that the transition state approximation breaks down at ambient pressure (1 bar) for the first bimolecular reaction steps. Overwhelmingly high pressures, higher than 10^5 bar, would be required for restoring to some extent (within ~ 5 % accuracy) the validity

of this approximation for all the reaction channels that are involved in the OH addition pathway. Analysis of the computed structures, bond orders, and free energy profiles demonstrate that all reaction steps, involved in the oxidation of naphthalene by OH radicals, satisfy Hammond's principle. NICS indices and NBO analysis also show that the computed activation and reaction energies are largely dictated by alterations of aromaticity, and, to a lesser extent, by anomeric and hyperconjugative effects.

In **Chapter 5**, atmospheric oxidation of the naphthalene–OH adduct $[\text{C}_{10}\text{H}_8\text{OH}]^\bullet$ (R1) by molecular oxygen in its triplet electronic ground state has been studied using only density functional theory. From a thermodynamic viewpoint, the most favorable process is O_2 addition at the C_2 position in *syn* mode, followed by O_2 addition at the C_2 position in *anti* mode, O_2 addition at the C_4 position in *syn* mode, and O_2 addition at the C_4 position in *anti* mode, as the second, third and fourth most favorable processes. The *syn* modes of addition at these positions are thermodynamically favored over the *anti* ones by the formation of an intramolecular hydrogen bond between the hydroxyl and peroxy substituents. Analysis of the computed structures, bond orders and free energy profiles demonstrate that the reaction steps, involved in the oxidation of the $[\text{C}_{10}\text{H}_8\text{OH}]^\bullet$ adduct by O_2 , satisfy Hammond's principle. Kinetic rate constants and branching ratios under atmospheric pressure and in the fall-off regime have been supplied, using transition state and RRKM theories. By comparison with experiment, these data confirm the relevance of a two-step reaction mechanism. Whatever the addition mode, O_2 addition in C_4 position is kinetically favored over O_2 addition in C_2 position, in contrast with the expectations drawn from thermodynamics and reaction energies. Under a kinetic control of the reaction, and in line with the computed reaction energy barriers, the most efficient process is O_2 addition at the C_4 position in *syn* mode, followed by O_2 addition at the C_2 position in *syn* mode, O_2 addition at the C_4 position in *anti* mode, and O_2 addition at the C_2 position in *anti* mode as the second, third and fourth most rapid processes. The computed branching ratios also indicate that the regioselectivity of the reaction decreases with increasing temperatures and decreasing pressures.

In **Chapter 6**, the isomerization processes of naphthalene peroxy radicals $[\text{C}_{10}\text{H}_8\text{OH}]^\bullet\text{-O}_2$ into bicyclic peroxy or oxy hydroperoxide radicals via ring closure and intramolecular hydrogen transfers have been studied computationally using only DFT. The cyclization of the R1-2OO-*syn* peroxy radical into the R1-2,9OO-*syn* bicyclic peroxy radical through formation of an O–O bridge is endothermic and reversible. From kinetic viewpoints, the two most favorable

processes for the R1-2OO-*syn* peroxy radical are ring closure into the R1-2,9OO-*syn* bicyclic peroxy radical species, and conversion through hydrogen transfer into the R1-P2O1-*syn* oxy hydroperoxide radical. Among all studied reaction channels, the latter process is the kinetically most competitive one. Also, in view of the computed rate constants, the R1-2OO-*syn* peroxy radical appears to be chemically much more reactive than the R1-4OO-*syn* species. All in all, the atmospheric oxidation mechanisms of naphthalene appear at this reaction stage, to be quite different from that of benzene and its derivatives.

In **Chapter 7**, the oxidation mechanisms of thiophene by hydroxyl radicals under inert conditions (Ar) have been studied using DFT as well as the benchmark CBS-QB3 approach. Kinetic rate constants were estimated by means of VTST and statistical RRKM theory. Effective rate constants were calculated via a steady state analysis based upon a two-step model reaction mechanism. In line with experimental results, the computed branching ratios indicate that the most kinetically efficient process involves OH addition to a carbon atom adjacent to the sulfur atom. Due to the presence of negative activation energies, pressures larger than 10^4 bar are required to reach the high-pressure limit. NICS indices and NBO analysis show that the computed activation energies are dictated by changes in aromaticity and charge-transfer effects due to the delocalization of lone pairs from sulfur to empty π^* orbitals.

List of publications

- [1] A. Shiroudi, M.S. Deleuze, Theoretical study of the oxidation mechanisms of naphthalene initiated by hydroxyl radicals: The H-abstraction pathway, *J. Phys. Chem. A*, **2014**, *118*(20), 3625–3636.
- [2] A. Shiroudi, M.S. Deleuze, S. Canneaux, Theoretical study of the oxidation mechanisms of naphthalene initiated by hydroxyl radicals: The OH-addition pathway, *J. Phys. Chem. A*, **2014**, *118*(26), 4593–4610.
- [3] A. Shiroudi, M.S. Deleuze, S. Canneaux, Theoretical study of the oxidation mechanisms of naphthalene initiated by hydroxyl radicals: The O₂ addition reaction pathways, *Phys. Chem. Chem. Phys.*, 2015, *17*(20), 13719–13732.
- [4] A. Shiroudi, M.S. Deleuze, Reaction mechanisms and kinetics of the isomerization processes of naphthalene peroxy radicals, *Comp. Theor. Chem.*, **2015**, *1074*, 26–35.
- [5] A. Shiroudi, M.S. Deleuze, Theoretical study of the oxidation mechanisms of thiophene initiated by hydroxyl radicals, *J. Mol. Model.*, **2015**, *21*(11), 301/1-301/20.

List of attended conferences, poster presentations and invited lectures

- [1] *Quantum Chemistry in Belgium (QCB11)*, 23rd January 2014, University of Namur, Belgium. Poster presentation, entitled “*Theoretical study of the oxidation mechanisms of naphthalene initiated by hydroxyl radicals*”.
- [2] Invited lecture at the Université de Reims-Champagne-Ardenne, 14th May 2014, Reims, France, entitled “*Theoretical study of the oxidation mechanisms of naphthalene initiated by hydroxyl radicals. The OH addition and H abstraction pathways*”.
- [3] *10th Congress of the World Association of Theoretical and Computational Chemists (WATOC 2014)*, 5–10 October 2014, Santiago, Chile. Poster presentations, entitled “*Quantum chemical and kinetic study of the oxidation mechanisms of naphthalene initiated by hydroxyl radicals. I. The OH addition pathway*” and “*Quantum chemical and kinetic study of the oxidation mechanisms of naphthalene initiated by hydroxyl radicals. II. The H abstraction pathway*”.
- [4] *9th International Conference on Chemical Kinetics (ICCK)*, 28th June–2nd July 2015, Ghent, Belgium. Poster presentations, entitled “*Quantum chemical and kinetic study of the oxidation mechanisms of naphthalene initiated by hydroxyl radicals. I. The OH addition pathway*” and “*Quantum chemical and kinetic study of the oxidation mechanisms of naphthalene initiated by hydroxyl radicals. II. The H abstraction pathway*”.

- [5] *Quantum Chemistry in Belgium (QCB12)*, 16th February 2016, University of Leuven, Belgium, Poster presentations, entitled “*Quantum chemical and kinetic study of the oxidation mechanisms of thiophene initiated by hydroxyl radicals*” and “*Reaction mechanisms and kinetics of the O₂ addition pathways upon the main thiophene-OH adduct: A theoretical study*”.

Appendices

Appendix I

Table S1. Temperature dependence of the equilibrium constants for the first bimolecular reaction step [R \rightleftharpoons IM1] along the chemical pathways **1–2** at different temperatures.

T (K)	K_p (bar $^{-1}$)	K_c (cm 3 molecule $^{-1}$)
636	8.91×10^{-5}	7.83×10^{-24}
665	8.82×10^{-5}	8.10×10^{-24}
727	8.73×10^{-5}	8.76×10^{-24}
873	8.87×10^{-5}	1.07×10^{-23}

Table S2. Expectation value of the $\langle S^2 \rangle$ operator at the reported theoretical levels.

Compound	IM1	TS1a	TS1b	IM2a	IM2b	P1	P2
Method	(0,2)	(0,2)	(0,2)	(0,2)	(0,2)	(0,2)	(0,2)
B3LYP/aug-cc-pVTZ	0.7610	0.7583	0.7581	0.7582	0.7572	0.7587	0.7576
ω B97XD/aug-cc-pVTZ	0.7566	0.7606	0.7602	0.7632	0.7613	0.7641	0.7620
UM05-2x/aug-cc-pVTZ	0.7542	0.7602	0.7599	0.7634	0.7614	0.7641	0.7620
UM06-2x/aug-cc-pVTZ	0.7538	0.7605	0.7601	0.7650	0.7629	0.7654	0.7633
HF/6-31+G* (CBS-QB3)	0.7680	0.8128	0.8095	0.8597	0.8441	0.8630	0.8467

Table S3. Internal energies, enthalpies and Gibb's free energies (in kcal mol $^{-1}$) of intermediate states relative to the reactants along the chemical pathways **1–2** for the oxidation of naphthalene into 1- and 2-naphthyl radicals at a pressure of 1.0 bar and different temperatures [B3LYP/6-311G(2d,d,p) results].

Species	636 K			665 K			727 K			873 K		
	ΔE_{0K}	ΔH_{298K}°	ΔG_{298K}°	ΔE_{0K}	ΔH_{298K}°	ΔG_{298K}°	ΔE_{0K}	ΔH_{298K}°	ΔG_{298K}°	ΔE_{0K}	ΔH_{298K}°	ΔG_{298K}°
Naphthalene + OH*	0.00	0.00	0.00	0.00	0.00	0.00	0.00	0.00	0.00	0.00	0.00	0.00
IM1 [C $_{10}$ H $_8$...OH]*	-3.80	-3.04	9.14	-3.80	-2.96	9.69	-3.80	-2.78	10.86	-3.80	-2.37	13.56
IM2a [C $_{10}$ H $_8$...H $_2$ O]*	-6.54	-4.94	4.12	-6.54	-4.85	4.53	-6.54	-4.65	5.40	-6.54	-4.22	7.38
IM2b [C $_{10}$ H $_8$...H $_2$ O]*	-5.63	-3.84	3.65	-5.63	-3.75	3.99	-5.63	-3.55	4.70	-5.63	-3.10	6.31
P1 (1-naphthyl+H $_2$ O)	-2.24	-1.95	-6.15	-2.24	-1.96	-6.34	-2.24	-2.00	-6.75	-2.24	-2.12	-7.69
P2 (2-naphthyl+H $_2$ O)	-2.30	-1.99	-6.20	-2.30	-1.99	-6.39	-2.30	-2.03	-6.80	-2.30	-2.14	-7.74

Table S4. Internal energies, enthalpies and Gibb's free energies (in kcal mol⁻¹) of transition states relative to the reactants along the chemical pathways **1–2** for the oxidation of naphthalene into 1- and 2-naphtyl radicals at a pressure of 1.0 bar and different temperatures [B3LYP/6-311G(2d,d,p) results].

Species	636 K			665 K			727 K			873 K		
	ΔE_{0K}^\ddagger	ΔH_{298K}°	ΔG_{298K}°	ΔE_{0K}^\ddagger	ΔH_{298K}°	ΔG_{298K}°	ΔE_{0K}^\ddagger	ΔH_{298K}°	ΔG_{298K}°	ΔE_{0K}^\ddagger	ΔH_{298K}°	ΔG_{298K}°
Naphthalene + OH [•]	0.00	0.00	0.00	0.00	0.00	0.00	0.00	0.00	0.00	0.00	0.00	0.00
TS1a	-0.89	-0.95	15.28	-0.89	-0.89	16.02	-0.89	-0.76	17.60	-0.89	-0.44	21.25
TS1b	-0.01	0.09	15.36	-0.01	0.15	16.06	-0.01	0.29	17.54	-0.01	0.62	20.97

Appendix II

Table S1. Eckart tunneling factor for the final unimolecular dissociation reaction step at temperatures ranging from 300 to 407 K.

Temperature	Pathway	Second step	
		IM2a→P1	IM2b→P2
300		2.1069	2.3770
337		1.8531	2.0185
358		1.7556	1.8798
378		1.6630	1.7447
407		1.5000	1.5737

Table S2. Expectation value of the $\langle S^2 \rangle$ operator at the reported theoretical levels.

Quantum model	System	IM1	TS1a	TS1b	IM2a	IM2b	TS2a	TS2b
	(0,2)	(0,2)	(0,2)	(0,2)	(0,2)	(0,2)	(0,2)	(0,2)
B3LYP/aug-cc-pVTZ		0.7610	0.7731	0.7777	0.7798	0.7842	0.7773	0.7773
ω B97XD/aug-cc-pVTZ		0.7566	0.7894	0.7946	0.7976	0.8063	0.7898	0.7908
UM05-2x/aug-cc-pVTZ		0.7542	0.7955	0.7950	0.7962	0.8023	0.7804	0.7816
UM06-2x/aug-cc-pVTZ		0.7538	0.7821	0.7805	0.7805	0.7828	0.7770	0.7763
HF/6-31+G* (CBS-QB3)		0.7680	0.9025	0.9025	1.5527	1.6094	1.0360	1.8713

Table S3: Kinetic rate constants for the first bimolecular reaction step involved in the chemical pathways **1–2** at different pressure and temperatures using RRKM theory.

Table S3a: $T= 300$ K.

Reaction Pressure	IM1→R	IM1→IM2a	IM1→IM2b	R→IM2a	R→IM2b
	(s ⁻¹)	(s ⁻¹)	(s ⁻¹)	(cm ³ mol ⁻¹ s ⁻¹)	(cm ³ mol ⁻¹ s ⁻¹)
10 ⁶	2.94×10 ¹⁵	1.28×10 ¹¹	1.01×10 ⁹	1.02×10 ⁻¹²	8.07×10 ⁻¹⁵
10 ³	2.94×10 ¹⁵	1.23×10 ¹¹	1.01×10 ⁹	9.83×10 ⁻¹³	8.07×10 ⁻¹⁵
10 ²	2.94×10 ¹⁵	9.27×10 ¹⁰	1.00×10 ⁹	7.41×10 ⁻¹³	7.99×10 ⁻¹⁵
10	2.94×10 ¹⁵	2.81×10 ¹⁰	9.30×10 ⁸	2.25×10 ⁻¹³	7.43×10 ⁻¹⁵
1.0	2.94×10 ¹⁵	3.65×10 ⁹	5.82×10 ⁸	2.92×10 ⁻¹⁴	4.65×10 ⁻¹⁵
0.1	2.94×10 ¹⁵	3.78×10 ⁸	1.60×10 ⁸	3.02×10 ⁻¹⁵	1.28×10 ⁻¹⁵
10 ⁻³	2.94×10 ¹⁵	3.80×10 ⁶	2.54×10 ⁶	3.04×10 ⁻¹⁷	2.03×10 ⁻¹⁷
10 ⁻⁴	2.94×10 ¹⁵	3.80×10 ⁵	2.57×10 ⁵	3.04×10 ⁻¹⁸	2.05×10 ⁻¹⁸
10 ⁻⁵	2.94×10 ¹⁵	3.80×10 ⁴	2.57×10 ⁴	3.04×10 ⁻¹⁹	2.05×10 ⁻¹⁹
10 ⁻⁸	2.94×10 ¹⁵	3.80×10 ¹	2.57×10 ¹	3.04×10 ⁻²²	2.05×10 ⁻²²

Table S3b: $T= 337$ K.

Reaction Pressure	IM1→R	IM1→IM2a	IM1→IM2b	R→IM2a	R→IM2b
	(s ⁻¹)	(s ⁻¹)	(s ⁻¹)	(cm ³ mol ⁻¹ s ⁻¹)	(cm ³ mol ⁻¹ s ⁻¹)
10 ⁶	1.68×10 ¹⁵	1.53×10 ¹¹	1.98×10 ⁹	1.11×10 ⁻¹²	1.44×10 ⁻¹⁴
10 ³	1.68×10 ¹⁵	1.46×10 ¹¹	1.98×10 ⁹	1.06×10 ⁻¹²	1.44×10 ⁻¹⁴
10 ²	1.68×10 ¹⁵	1.04×10 ¹¹	1.95×10 ⁹	7.55×10 ⁻¹³	1.42×10 ⁻¹⁴
10	1.68×10 ¹⁵	2.78×10 ¹⁰	1.74×10 ⁹	2.02×10 ⁻¹³	1.26×10 ⁻¹⁴
1.0	1.68×10 ¹⁵	3.42×10 ⁹	9.31×10 ⁸	2.48×10 ⁻¹⁴	6.76×10 ⁻¹⁵
0.1	1.68×10 ¹⁵	3.51×10 ⁸	2.09×10 ⁸	2.55×10 ⁻¹⁵	1.52×10 ⁻¹⁵
10 ⁻³	1.68×10 ¹⁵	3.52×10 ⁶	2.87×10 ⁶	2.55×10 ⁻¹⁷	2.08×10 ⁻¹⁷
10 ⁻⁴	1.68×10 ¹⁵	3.52×10 ⁵	2.90×10 ⁵	2.55×10 ⁻¹⁸	2.10×10 ⁻¹⁸
10 ⁻⁵	1.68×10 ¹⁵	3.52×10 ⁴	2.90×10 ⁴	2.55×10 ⁻¹⁹	2.10×10 ⁻¹⁹
10 ⁻⁸	1.68×10 ¹⁵	3.52×10 ¹	2.90×10 ¹	2.55×10 ⁻²²	2.10×10 ⁻²²

Table S3c: $T= 358$ K.

Reaction Pressure	IM1→R (s ⁻¹)	IM1→IM2a (s ⁻¹)	IM1→IM2b (s ⁻¹)	R→IM2a (cm ³ mol ⁻¹ s ⁻¹)	R→IM2b (cm ³ mol ⁻¹ s ⁻¹)
10 ⁶	1.30×10 ¹⁵	1.67×10 ¹¹	2.71×10 ⁹	1.17×10 ⁻¹²	1.90×10 ⁻¹⁴
10 ³	1.30×10 ¹⁵	1.59×10 ¹¹	2.71×10 ⁹	1.12×10 ⁻¹²	1.90×10 ⁻¹⁴
10 ²	1.30×10 ¹⁵	1.09×10 ¹¹	2.67×10 ⁹	7.65×10 ⁻¹³	1.87×10 ⁻¹⁴
10	1.30×10 ¹⁵	2.74×10 ¹⁰	2.31×10 ⁹	1.92×10 ⁻¹³	1.62×10 ⁻¹⁴
1.0	1.30×10 ¹⁵	3.29×10 ⁹	1.13×10 ⁹	2.31×10 ⁻¹⁴	7.93×10 ⁻¹⁵
0.1	1.30×10 ¹⁵	3.36×10 ⁸	2.30×10 ⁸	2.36×10 ⁻¹⁵	1.61×10 ⁻¹⁵
10 ⁻³	1.30×10 ¹⁵	3.37×10 ⁶	2.96×10 ⁶	2.37×10 ⁻¹⁷	2.08×10 ⁻¹⁷
10 ⁻⁴	1.30×10 ¹⁵	3.37×10 ⁵	2.98×10 ⁵	2.37×10 ⁻¹⁸	2.09×10 ⁻¹⁸
10 ⁻⁵	1.30×10 ¹⁵	3.37×10 ⁴	2.98×10 ⁴	2.37×10 ⁻¹⁹	2.09×10 ⁻¹⁹
10 ⁻⁸	1.30×10 ¹⁵	3.37×10 ¹	2.98×10 ¹	2.37×10 ⁻²²	2.09×10 ⁻²²

Table S3d: $T= 378$ K.

Reaction Pressure	IM1→R (s ⁻¹)	IM1→IM2a (s ⁻¹)	IM1→IM2b (s ⁻¹)	R→IM2a (cm ³ mol ⁻¹ s ⁻¹)	R→IM2b (cm ³ mol ⁻¹ s ⁻¹)
10 ⁶	1.04×10 ¹⁵	1.80×10 ¹¹	3.55×10 ⁹	1.24×10 ⁻¹²	2.45×10 ⁻¹⁴
10 ³	1.04×10 ¹⁵	1.69×10 ¹¹	3.54×10 ⁹	1.16×10 ⁻¹²	2.44×10 ⁻¹⁴
10 ²	1.04×10 ¹⁵	1.13×10 ¹¹	3.47×10 ⁹	7.78×10 ⁻¹³	2.39×10 ⁻¹⁴
10	1.04×10 ¹⁵	2.70×10 ¹⁰	2.93×10 ⁹	1.86×10 ⁻¹³	2.02×10 ⁻¹⁴
1.0	1.04×10 ¹⁵	3.17×10 ⁹	1.31×10 ⁹	2.18×10 ⁻¹⁴	9.02×10 ⁻¹⁵
0.1	1.04×10 ¹⁵	3.23×10 ⁸	2.44×10 ⁸	2.23×10 ⁻¹⁵	1.68×10 ⁻¹⁵
10 ⁻³	1.04×10 ¹⁵	3.24×10 ⁶	2.99×10 ⁶	2.23×10 ⁻¹⁷	2.06×10 ⁻¹⁷
10 ⁻⁴	1.04×10 ¹⁵	3.24×10 ⁵	3.00×10 ⁵	2.23×10 ⁻¹⁸	2.07×10 ⁻¹⁸
10 ⁻⁵	1.04×10 ¹⁵	3.24×10 ⁴	3.00×10 ⁴	2.23×10 ⁻¹⁹	2.07×10 ⁻¹⁹
10 ⁻⁸	1.04×10 ¹⁵	3.24×10 ¹	3.00×10 ¹	2.23×10 ⁻²²	2.07×10 ⁻²²

Table S3e: $T= 407$ K.

Reaction Pressure	IM1→R (s ⁻¹)	IM1→IM2a (s ⁻¹)	IM1→IM2b (s ⁻¹)	R→IM2a (cm ³ mol ⁻¹ s ⁻¹)	R→IM2b (cm ³ mol ⁻¹ s ⁻¹)
10 ⁶	2.47×10 ¹⁴	1.97×10 ¹¹	4.99×10 ⁹	1.33×10 ⁻¹²	3.36×10 ⁻¹⁴
10 ³	2.47×10 ¹⁴	1.84×10 ¹¹	4.98×10 ⁹	1.24×10 ⁻¹²	3.36×10 ⁻¹⁴
10 ²	2.47×10 ¹⁴	1.18×10 ¹¹	4.85×10 ⁹	7.95×10 ⁻¹³	3.27×10 ⁻¹⁴
10	2.47×10 ¹⁴	2.62×10 ¹⁰	3.92×10 ⁹	1.77×10 ⁻¹³	2.64×10 ⁻¹⁴
1.0	2.47×10 ¹⁴	3.02×10 ⁹	1.54×10 ⁹	2.04×10 ⁻¹⁴	1.04×10 ⁻¹⁴
0.1	2.47×10 ¹⁴	3.06×10 ⁸	2.56×10 ⁸	2.06×10 ⁻¹⁵	1.73×10 ⁻¹⁵
10 ⁻³	2.47×10 ¹⁴	3.07×10 ⁶	2.96×10 ⁶	2.07×10 ⁻¹⁷	2.00×10 ⁻¹⁷
10 ⁻⁴	2.47×10 ¹⁴	3.07×10 ⁵	2.97×10 ⁵	2.07×10 ⁻¹⁸	2.00×10 ⁻¹⁸
10 ⁻⁵	2.47×10 ¹⁴	3.07×10 ⁴	2.97×10 ⁴	2.07×10 ⁻¹⁹	2.00×10 ⁻¹⁹
10 ⁻⁸	2.47×10 ¹⁴	3.07×10 ¹	2.97×10 ¹	2.07×10 ⁻²²	2.00×10 ⁻²²

Table S4: Kinetic rate constants for all reaction steps involved in the chemical pathways 1–2 at different pressures and temperatures, using the RRKM theory.

Table S4a:

<i>T</i> (K)	<i>P</i> = 10⁶ bar								Effective rate constants (cm ³ mol ⁻¹ s ⁻¹)		Branching ratio (%)	
	step 1				step 2				<i>k</i> _{eff} (1) R→P1	<i>k</i> _{eff} (2) R→P2	<i>R</i> (1)	<i>R</i> (2)
	<i>k</i> (s ⁻¹)		<i>k</i> (cm ³ mol ⁻¹ s ⁻¹)		<i>k</i> (s ⁻¹)		<i>k</i> (s ⁻¹)					
	IM1→IM2a	IM1→IM2b	R→IM2a	R→IM2b	IM2a→R	IM2b→R	IM2a→P1	IM2b→P2				
300	1.28×10 ¹¹	1.01×10 ⁹	1.02×10 ⁻¹²	8.07×10 ⁻¹⁵	2.87×10 ⁻²	4.91×10 ⁻¹	1.47×10 ⁻⁶	1.37×10 ⁻⁵	5.22×10 ⁻¹⁷	2.25×10 ⁻¹⁹	99.57	0.43
337	1.53×10 ¹¹	1.98×10 ⁹	1.11×10 ⁻¹²	1.44×10 ⁻¹⁴	1.28×10 ⁰	1.57×10 ¹	1.59×10 ⁻⁴	1.19×10 ⁻³	1.38×10 ⁻¹⁶	1.09×10 ⁻¹⁸	99.21	0.79
358	1.67×10 ¹¹	2.71×10 ⁹	1.17×10 ⁻¹²	1.90×10 ⁻¹⁴	7.86×10 ⁰	8.22×10 ¹	1.48×10 ⁻³	1.00×10 ⁻²	2.20×10 ⁻¹⁶	2.31×10 ⁻¹⁸	98.96	1.04
378	1.80×10 ¹¹	3.55×10 ⁹	1.24×10 ⁻¹²	2.45×10 ⁻¹⁴	3.67×10 ¹	3.35×10 ²	9.92×10 ⁻³	6.13×10 ⁻²	3.35×10 ⁻¹⁶	4.48×10 ⁻¹⁸	98.68	1.32
407	1.97×10 ¹¹	4.99×10 ⁹	1.33×10 ⁻¹²	3.36×10 ⁻¹⁴	2.63×10 ²	2.02×10 ³	1.13×10 ⁻¹	6.23×10 ⁻¹	5.71×10 ⁻¹⁶	1.04×10 ⁻¹⁷	98.22	1.78

Table S4b:

<i>T</i> (K)	<i>P</i> = 1000 bar								Effective rate constants (cm ³ mol ⁻¹ s ⁻¹)		Branching ratio (%)	
	step 1				step 2				<i>k</i> _{eff} (1) R→P1	<i>k</i> _{eff} (2) R→P2	<i>R</i> (1)	<i>R</i> (2)
	<i>k</i> (s ⁻¹)		<i>k</i> (cm ³ mol ⁻¹ s ⁻¹)		<i>k</i> (s ⁻¹)		<i>k</i> (s ⁻¹)					
	IM1→IM2a	IM1→IM2b	R→IM2a	R→IM2b	IM2a→R	IM2b→R	IM2a→P1	IM2b→P2				
300	1.23×10 ¹¹	1.01×10 ⁹	9.83×10 ⁻¹³	8.07×10 ⁻¹⁵	2.87×10 ⁻²	4.91×10 ⁻¹	1.47×10 ⁻⁶	1.37×10 ⁻⁵	5.03×10 ⁻¹⁷	2.25×10 ⁻¹⁹	99.55	0.45
337	1.46×10 ¹¹	1.98×10 ⁹	1.06×10 ⁻¹²	1.44×10 ⁻¹⁴	1.28×10 ⁰	1.57×10 ¹	1.59×10 ⁻⁴	1.19×10 ⁻³	1.32×10 ⁻¹⁶	1.09×10 ⁻¹⁸	99.18	0.82
358	1.59×10 ¹¹	2.71×10 ⁹	1.12×10 ⁻¹²	1.90×10 ⁻¹⁴	7.86×10 ⁰	8.22×10 ¹	1.48×10 ⁻³	1.00×10 ⁻²	2.11×10 ⁻¹⁶	2.31×10 ⁻¹⁸	98.92	1.08
378	1.69×10 ¹¹	3.54×10 ⁹	1.16×10 ⁻¹²	2.44×10 ⁻¹⁴	3.67×10 ¹	3.35×10 ²	9.92×10 ⁻³	6.13×10 ⁻²	3.13×10 ⁻¹⁶	4.46×10 ⁻¹⁸	98.60	1.40
407	1.84×10 ¹¹	4.98×10 ⁹	1.24×10 ⁻¹²	3.36×10 ⁻¹⁴	2.63×10 ²	2.02×10 ³	1.13×10 ⁻¹	6.23×10 ⁻¹	5.33×10 ⁻¹⁶	1.04×10 ⁻¹⁷	98.09	1.91

Table S4c:

		P = 100 bar								Effective rate constants (cm ³ mol ⁻¹ s ⁻¹)		Branching ratio (%)	
T (K)	step 1						step 2				R(1)	R(2)	
	k (s ⁻¹)		k (cm ³ mol ⁻¹ s ⁻¹)		k (s ⁻¹)		k (s ⁻¹)		k _{eff} (1)	k _{eff} (2)			
	IM1→IM2a	IM1→IM2b	R→IM2a	R→IM2b	IM2a→R	IM2b→R	IM2a→P1	IM2b→P2	R→P1	R→P2			
300	9.27×10 ¹⁰	1.00×10 ⁹	7.41×10 ⁻¹³	7.99×10 ⁻¹⁵	2.87×10 ⁻²	4.91×10 ⁻¹	1.47×10 ⁻⁶	1.37×10 ⁻⁵	3.80×10 ⁻¹⁷	2.23×10 ⁻¹⁹	99.42	0.58	
337	1.04×10 ¹¹	1.95×10 ⁹	7.55×10 ⁻¹³	1.42×10 ⁻¹⁴	1.28×10 ⁰	1.57×10 ¹	1.59×10 ⁻⁴	1.19×10 ⁻³	9.38×10 ⁻¹⁷	1.08×10 ⁻¹⁸	98.87	1.13	
358	1.09×10 ¹¹	2.67×10 ⁹	7.65×10 ⁻¹³	1.87×10 ⁻¹⁴	7.86×10 ⁰	8.22×10 ¹	1.48×10 ⁻³	1.00×10 ⁻²	1.44×10 ⁻¹⁶	2.27×10 ⁻¹⁸	98.45	1.55	
378	1.13×10 ¹¹	3.47×10 ⁹	7.78×10 ⁻¹³	2.39×10 ⁻¹⁴	3.67×10 ¹	3.35×10 ²	9.92×10 ⁻³	6.13×10 ⁻²	2.10×10 ⁻¹⁶	4.37×10 ⁻¹⁸	97.96	2.04	
407	1.18×10 ¹¹	4.85×10 ⁹	7.95×10 ⁻¹³	3.27×10 ⁻¹⁴	2.63×10 ²	2.02×10 ³	1.13×10 ⁻¹	6.23×10 ⁻¹	3.41×10 ⁻¹⁶	1.01×10 ⁻¹⁷	97.13	2.87	

Table S4d:

		P = 10 bar								Effective rate constants (cm ³ mol ⁻¹ s ⁻¹)		Branching ratio (%)	
T (K)	step 1						step 2				R(1)	R(2)	
	k (s ⁻¹)		k (cm ³ mol ⁻¹ s ⁻¹)		k (s ⁻¹)		k (s ⁻¹)		k _{eff} (1)	k _{eff} (2)			
	IM1→IM2a	IM1→IM2b	R→IM2a	R→IM2b	IM2a→R	IM2b→R	IM2a→P1	IM2b→P2	R→P1	R→P2			
300	2.81×10 ¹⁰	9.30×10 ⁸	2.25×10 ⁻¹³	7.43×10 ⁻¹⁵	2.87×10 ⁻²	4.91×10 ⁻¹	1.47×10 ⁻⁶	1.37×10 ⁻⁵	1.15×10 ⁻¹⁷	2.07×10 ⁻¹⁹	98.23	1.77	
337	2.78×10 ¹⁰	1.74×10 ⁹	2.02×10 ⁻¹³	1.26×10 ⁻¹⁴	1.28×10 ⁰	1.57×10 ¹	1.59×10 ⁻⁴	1.19×10 ⁻³	2.51×10 ⁻¹⁷	9.55×10 ⁻¹⁹	96.33	3.67	
358	2.74×10 ¹⁰	2.31×10 ⁹	1.92×10 ⁻¹³	1.62×10 ⁻¹⁴	7.86×10 ⁰	8.22×10 ¹	1.48×10 ⁻³	1.00×10 ⁻²	3.61×10 ⁻¹⁷	1.97×10 ⁻¹⁸	94.83	5.17	
378	2.70×10 ¹⁰	2.93×10 ⁹	1.86×10 ⁻¹³	2.02×10 ⁻¹⁴	3.67×10 ¹	3.35×10 ²	9.92×10 ⁻³	6.13×10 ⁻²	5.03×10 ⁻¹⁷	3.70×10 ⁻¹⁸	93.15	6.85	
407	2.62×10 ¹⁰	3.92×10 ⁹	1.77×10 ⁻¹³	2.64×10 ⁻¹⁴	2.63×10 ²	2.02×10 ³	1.13×10 ⁻¹	6.23×10 ⁻¹	7.60×10 ⁻¹⁷	8.14×10 ⁻¹⁸	90.33	9.67	

Table S4e:

$P = 1.0$ bar												
T (K)	step 1						step 2		Effective rate constants ($\text{cm}^3 \text{mol}^{-1} \text{s}^{-1}$)		Branching ratio (%)	
	k (s^{-1})		k ($\text{cm}^3 \text{mol}^{-1} \text{s}^{-1}$)		k (s^{-1})		k (s^{-1})		$k_{\text{eff}}(1)$	$k_{\text{eff}}(2)$	$R(1)$	$R(2)$
	IM1→IM2a	IM1→IM2b	R→IM2a	R→IM2b	IM2a→R	IM2b→R	IM2a→P1	IM2b→P2	R→P1	R→P2		
300	3.65×10^9	5.82×10^8	2.92×10^{-14}	4.65×10^{-15}	2.87×10^{-2}	4.91×10^{-1}	1.47×10^{-6}	1.37×10^{-5}	1.50×10^{-18}	1.30×10^{-19}	92.02	7.98
337	3.42×10^9	9.31×10^8	2.48×10^{-14}	6.76×10^{-15}	1.28×10^0	1.57×10^1	1.59×10^{-4}	1.19×10^{-3}	3.08×10^{-18}	5.12×10^{-19}	85.74	14.26
358	3.29×10^9	1.13×10^9	2.31×10^{-14}	7.93×10^{-15}	7.86×10^0	8.22×10^1	1.48×10^{-3}	1.00×10^{-2}	4.35×10^{-18}	9.65×10^{-19}	81.85	18.15
378	3.17×10^9	1.31×10^9	2.19×10^{-14}	9.02×10^{-15}	3.67×10^1	3.35×10^2	9.92×10^{-3}	6.13×10^{-2}	5.89×10^{-18}	1.65×10^{-18}	78.12	21.88
407	3.02×10^9	1.54×10^9	2.03×10^{-14}	1.04×10^{-14}	2.63×10^2	2.02×10^3	1.13×10^{-1}	6.23×10^{-1}	8.76×10^{-18}	3.21×10^{-18}	73.21	26.79

Table S4f:

$P = 0.1$ bar												
T (K)	step 1						step 2		Effective rate constants ($\text{cm}^3 \text{mol}^{-1} \text{s}^{-1}$)		Branching ratio (%)	
	k (s^{-1})		k ($\text{cm}^3 \text{mol}^{-1} \text{s}^{-1}$)		k (s^{-1})		k (s^{-1})		$k_{\text{eff}}(1)$	$k_{\text{eff}}(2)$	$R(1)$	$R(2)$
	IM1→IM2a	IM1→IM2b	R→IM2a	R→IM2b	IM2a→R	IM2b→R	IM2a→P1	IM2b→P2	R→P1	R→P2		
300	3.78×10^8	1.60×10^8	3.02×10^{-15}	1.28×10^{-15}	2.87×10^{-2}	4.90×10^{-1}	1.47×10^{-6}	1.37×10^{-5}	1.55×10^{-19}	3.57×10^{-20}	81.24	18.76
337	3.51×10^8	2.09×10^8	2.55×10^{-15}	1.52×10^{-15}	1.28×10^0	1.57×10^1	1.59×10^{-4}	1.19×10^{-3}	3.17×10^{-19}	1.15×10^{-19}	73.33	26.67
358	3.36×10^8	2.30×10^8	2.36×10^{-15}	1.61×10^{-15}	7.83×10^0	8.15×10^1	1.48×10^{-3}	1.00×10^{-2}	4.44×10^{-19}	1.96×10^{-19}	69.41	30.59
378	3.23×10^8	2.44×10^8	2.23×10^{-15}	1.68×10^{-15}	3.65×10^1	3.30×10^2	9.92×10^{-3}	6.13×10^{-2}	6.03×10^{-19}	3.07×10^{-19}	66.22	33.78
407	3.06×10^8	2.56×10^8	2.06×10^{-15}	1.73×10^{-15}	2.60×10^2	1.97×10^3	1.13×10^{-1}	6.23×10^{-1}	8.85×10^{-19}	5.33×10^{-19}	62.39	37.61

Table S4g:

$P = 10^{-3}$ bar												
<i>T</i> (K)	step 1						step 2		Effective rate constants ($\text{cm}^3 \text{mol}^{-1} \text{s}^{-1}$)		Branching ratio (%)	
	k (s^{-1})		k ($\text{cm}^3 \text{mol}^{-1} \text{s}^{-1}$)		k (s^{-1})		k (s^{-1})		$k_{\text{eff}}(1)$	$k_{\text{eff}}(2)$	<i>R</i> (1)	<i>R</i> (2)
	IM1→IM2a	IM1→IM2b	R→IM2a	R→IM2b	IM2a→R	IM2b→R	IM2a→P1	IM2b→P2	R→P1	R→P2		
300	3.80×10^6	2.54×10^6	3.04×10^{-17}	2.03×10^{-17}	2.72×10^{-2}	4.35×10^{-1}	1.47×10^{-6}	1.37×10^{-5}	1.64×10^{-21}	6.39×10^{-22}	71.99	28.01
337	3.52×10^6	2.87×10^6	2.55×10^{-17}	2.08×10^{-17}	1.13×10^0	1.24×10^1	1.58×10^{-4}	1.18×10^{-3}	3.56×10^{-21}	1.98×10^{-21}	64.30	35.70
358	3.37×10^6	2.96×10^6	2.37×10^{-17}	2.08×10^{-17}	6.55×10^0	5.91×10^1	1.47×10^{-3}	9.91×10^{-3}	5.32×10^{-21}	3.49×10^{-21}	60.39	39.61
378	3.24×10^6	2.99×10^6	2.23×10^{-17}	2.06×10^{-17}	2.84×10^1	2.17×10^2	9.84×10^{-3}	6.03×10^{-2}	7.72×10^{-21}	5.72×10^{-21}	57.44	42.56
407	3.07×10^6	2.96×10^6	2.07×10^{-17}	2.00×10^{-17}	1.79×10^2	1.09×10^3	1.11×10^{-1}	6.02×10^{-1}	1.28×10^{-20}	1.10×10^{-20}	53.75	46.25

Table S4h:

$P = 10^{-4}$ bar												
<i>T</i> (K)	step 1						step 2		Effective rate constants ($\text{cm}^3 \text{mol}^{-1} \text{s}^{-1}$)		Branching ratio (%)	
	k (s^{-1})		k ($\text{cm}^3 \text{mol}^{-1} \text{s}^{-1}$)		k (s^{-1})		k (s^{-1})		$k_{\text{eff}}(1)$	$k_{\text{eff}}(2)$	<i>R</i> (1)	<i>R</i> (2)
	IM1→IM2a	IM1→IM2b	R→IM2a	R→IM2b	IM2a→R	IM2b→R	IM2a→P1	IM2b→P2	R→P1	R→P2		
300	3.80×10^5	2.57×10^5	3.04×10^{-18}	2.05×10^{-18}	2.21×10^{-2}	3.06×10^{-1}	1.46×10^{-6}	1.35×10^{-5}	2.01×10^{-22}	9.04×10^{-23}	68.95	31.05
337	3.52×10^5	2.90×10^5	2.55×10^{-18}	2.10×10^{-18}	8.02×10^{-1}	7.33×10^0	1.56×10^{-4}	1.14×10^{-3}	4.96×10^{-22}	3.27×10^{-22}	60.30	39.70
358	3.37×10^5	2.98×10^5	2.37×10^{-18}	2.09×10^{-18}	4.23×10^0	3.14×10^1	1.43×10^{-3}	9.36×10^{-3}	8.01×10^{-22}	6.23×10^{-22}	56.26	43.74
378	3.24×10^5	3.00×10^5	2.23×10^{-18}	2.07×10^{-18}	1.68×10^1	1.04×10^2	9.39×10^{-3}	5.54×10^{-2}	1.25×10^{-21}	1.10×10^{-21}	53.06	46.94
407	3.07×10^5	2.97×10^5	2.07×10^{-18}	2.00×10^{-18}	9.17×10^1	4.51×10^2	1.02×10^{-1}	5.23×10^{-1}	2.30×10^{-21}	2.32×10^{-21}	49.82	50.18

Table S4i:

$P = 10^{-5}$ bar												
T (K)	step 1						step 2		Effective rate constants ($\text{cm}^3 \text{mol}^{-1} \text{s}^{-1}$)		Branching ratio (%)	
	k (s^{-1})		k ($\text{cm}^3 \text{mol}^{-1} \text{s}^{-1}$)		k (s^{-1})		k (s^{-1})		$k_{\text{eff}}(1)$	$k_{\text{eff}}(2)$	$R(1)$	$R(2)$
	IM1→IM2a	IM1→IM2b	R→IM2a	R→IM2b	IM2a→R	IM2b→R	IM2a→P1	IM2b→P2	R→P1	R→P2		
300	3.80×10^4	2.57×10^4	3.04×10^{-19}	2.05×10^{-19}	1.29×10^{-2}	1.43×10^{-1}	1.40×10^{-6}	1.25×10^{-5}	3.30×10^{-23}	1.79×10^{-23}	64.80	35.20
337	3.52×10^4	2.90×10^4	2.55×10^{-19}	2.10×10^{-19}	3.85×10^{-1}	2.80×10^0	1.42×10^{-4}	9.74×10^{-4}	9.40×10^{-23}	7.30×10^{-23}	56.28	43.72
358	3.37×10^4	2.98×10^4	2.37×10^{-19}	2.09×10^{-19}	1.82×10^0	1.08×10^1	1.25×10^{-3}	7.50×10^{-3}	1.63×10^{-22}	1.45×10^{-22}	52.86	47.14
378	3.24×10^4	3.00×10^4	2.23×10^{-19}	2.07×10^{-19}	6.51×10^0	3.24×10^1	7.77×10^{-3}	4.15×10^{-2}	2.66×10^{-22}	2.65×10^{-22}	50.10	49.90
407	3.07×10^4	2.97×10^4	2.07×10^{-19}	2.00×10^{-19}	3.09×10^1	1.23×10^2	7.72×10^{-2}	3.50×10^{-1}	5.16×10^{-22}	5.67×10^{-22}	47.62	52.38

Table S4j:

$P = 10^{-8}$ bar												
T (K)	step 1						step 2		Effective rate constants ($\text{cm}^3 \text{mol}^{-1} \text{s}^{-1}$)		Branching ratio (%)	
	k (s^{-1})		k ($\text{cm}^3 \text{mol}^{-1} \text{s}^{-1}$)		k (s^{-1})		k (s^{-1})		$k_{\text{eff}}(1)$	$k_{\text{eff}}(2)$	$R(1)$	$R(2)$
	IM1→IM2a	IM1→IM2b	R→IM2a	R→IM2b	IM2a→R	IM2b→R	IM2a→P1	IM2b→P2	R→P1	R→P2		
300	3.80×10^1	2.57×10^1	3.04×10^{-22}	2.05×10^{-22}	2.02×10^{-4}	1.10×10^{-3}	3.29×10^{-7}	1.87×10^{-6}	4.94×10^{-25}	3.48×10^{-25}	58.69	41.31
337	3.52×10^1	2.90×10^1	2.55×10^{-22}	2.10×10^{-22}	3.92×10^{-3}	1.52×10^{-2}	2.01×10^{-5}	8.56×10^{-5}	1.30×10^{-24}	1.18×10^{-24}	52.52	47.48
358	3.37×10^1	2.98×10^1	2.37×10^{-22}	2.09×10^{-22}	1.49×10^{-2}	4.93×10^{-2}	1.32×10^{-4}	4.90×10^{-4}	2.08×10^{-24}	2.06×10^{-24}	50.29	49.71
378	3.24×10^1	3.00×10^1	2.23×10^{-22}	2.07×10^{-22}	4.40×10^{-2}	1.28×10^{-1}	6.25×10^{-4}	2.05×10^{-3}	3.12×10^{-24}	3.26×10^{-24}	48.91	51.09
407	3.07×10^1	2.97×10^1	2.07×10^{-22}	2.00×10^{-22}	1.62×10^{-1}	3.97×10^{-1}	4.19×10^{-3}	1.18×10^{-2}	5.22×10^{-24}	5.77×10^{-24}	47.48	52.52

Appendix III

Table S1: Effective rate constants (in $\text{cm}^3 \text{ molecule}^{-1} \text{ s}^{-1}$) for the reported reaction channels obtained by means of RRKM theory at different pressures and temperatures, according to the computed UM06-2x/aug-cc-pVTZ energy profiles ($x=1,3$ and $y=2,4$).

Table S1a: [$T= 298 \text{ K}$; *syn* isomer]

Reaction \ Pressure	$\text{IMx} \rightarrow \text{R1} + \text{O}_2$ k_{-1} (s^{-1})	$\text{IM1} \rightarrow \text{R1-2OO-}s$ $k_2(\mathbf{1})$ (s^{-1})	$\text{IM3} \rightarrow \text{R1-4OO-}s$ $k_2(\mathbf{3})$ (s^{-1})	$\text{R1} + \text{O}_2 \rightarrow \text{R1-2OO-}s$ $k_{\text{eff}}(\mathbf{1})$ ($\text{cm}^3 \text{ molecule}^{-1} \text{ s}^{-1}$)	$\text{R1} + \text{O}_2 \rightarrow \text{R1-4OO-}s$ $k_{\text{eff}}(\mathbf{3})$ ($\text{cm}^3 \text{ molecule}^{-1} \text{ s}^{-1}$)
1.00×10^4	4.36×10^{16}	1.78×10^5	1.07×10^6	3.93×10^{-19}	2.38×10^{-18}
1.00×10^2	4.36×10^{16}	1.78×10^5	1.07×10^6	3.93×10^{-19}	2.38×10^{-18}
1.00×10^0	4.36×10^{16}	1.77×10^5	1.07×10^6	3.93×10^{-19}	2.36×10^{-18}
1.00×10^{-2}	4.36×10^{16}	1.54×10^5	7.55×10^5	3.41×10^{-19}	1.67×10^{-18}
1.00×10^{-4}	4.36×10^{16}	2.82×10^4	6.65×10^4	6.23×10^{-20}	1.47×10^{-19}
1.00×10^{-6}	4.36×10^{16}	7.09×10^2	1.12×10^3	1.57×10^{-21}	2.49×10^{-21}
1.00×10^{-8}	4.36×10^{16}	8.02×10^0	1.17×10^1	1.78×10^{-23}	2.58×10^{-23}
1.00×10^{-10}	4.36×10^{16}	8.04×10^{-2}	1.17×10^{-1}	1.78×10^{-25}	2.59×10^{-25}
1.00×10^{-12}	4.36×10^{16}	8.04×10^{-4}	1.17×10^{-3}	1.78×10^{-27}	2.59×10^{-27}

Table S1b: [$T= 336 \text{ K}$; *syn* isomer]

Reaction \ Pressure	$\text{IMx} \rightarrow \text{R1} + \text{O}_2$ k_{-1} (s^{-1})	$\text{IM1} \rightarrow \text{R1-2OO-}s$ $k_2(\mathbf{1})$ (s^{-1})	$\text{IM3} \rightarrow \text{R1-4OO-}s$ $k_2(\mathbf{3})$ (s^{-1})	$\text{R1} + \text{O}_2 \rightarrow \text{R1-2OO-}s$ $k_{\text{eff}}(\mathbf{1})$ ($\text{cm}^3 \text{ molecule}^{-1} \text{ s}^{-1}$)	$\text{R1} + \text{O}_2 \rightarrow \text{R1-4OO-}s$ $k_{\text{eff}}(\mathbf{3})$ ($\text{cm}^3 \text{ molecule}^{-1} \text{ s}^{-1}$)
1.00×10^4	1.80×10^{16}	7.11×10^5	3.57×10^6	1.05×10^{-18}	5.29×10^{-18}
1.00×10^2	1.80×10^{16}	7.11×10^5	3.57×10^6	1.05×10^{-18}	5.29×10^{-18}
1.00×10^0	1.80×10^{16}	7.08×10^5	3.53×10^6	1.05×10^{-18}	5.23×10^{-18}
1.00×10^{-2}	1.80×10^{16}	5.49×10^5	2.03×10^6	8.13×10^{-19}	3.01×10^{-18}
1.00×10^{-4}	1.80×10^{16}	6.23×10^4	1.12×10^5	9.23×10^{-20}	1.67×10^{-19}
1.00×10^{-6}	1.80×10^{16}	1.19×10^3	1.59×10^3	1.76×10^{-21}	2.35×10^{-21}
1.00×10^{-8}	1.80×10^{16}	1.29×10^1	1.62×10^1	1.91×10^{-23}	2.41×10^{-23}
1.00×10^{-10}	1.80×10^{16}	1.29×10^{-1}	1.62×10^{-1}	1.91×10^{-25}	2.41×10^{-25}
1.00×10^{-12}	1.80×10^{16}	1.29×10^{-3}	1.62×10^{-3}	1.91×10^{-27}	2.41×10^{-27}

Table S1c: [$T= 400$ K; *syn* isomer]

Pressure	Reaction	IMx→R1+O ₂	IM1→R1-2OO- <i>s</i>	IM3→R1-4OO- <i>s</i>	R1+O ₂ →R1-2OO- <i>s</i>	R1+O ₂ →R1-4OO- <i>s</i>
		k_{-1} (s ⁻¹)	$k_2(\mathbf{1})$ (s ⁻¹)	$k_2(\mathbf{3})$ (s ⁻¹)	$k_{\text{eff}}(\mathbf{1})$ (cm ³ molecule ⁻¹ s ⁻¹)	$k_{\text{eff}}(\mathbf{3})$ (cm ³ molecule ⁻¹ s ⁻¹)
1.00×10 ⁴		6.11×10 ¹⁵	4.00×10 ⁶	1.59×10 ⁷	3.69×10 ⁻¹⁸	1.47×10 ⁻¹⁷
1.00×10 ²		6.11×10 ¹⁵	4.00×10 ⁶	1.59×10 ⁷	3.69×10 ⁻¹⁸	1.47×10 ⁻¹⁷
1.00×10 ⁰		6.11×10 ¹⁵	3.96×10 ⁶	1.55×10 ⁷	3.65×10 ⁻¹⁸	1.43×10 ⁻¹⁷
1.00×10 ⁻²		6.11×10 ¹⁵	2.31×10 ⁶	5.74×10 ⁶	2.13×10 ⁻¹⁸	5.29×10 ⁻¹⁸
1.00×10 ⁻⁴		6.11×10 ¹⁵	1.25×10 ⁵	1.67×10 ⁵	1.15×10 ⁻¹⁹	1.54×10 ⁻¹⁹
1.00×10 ⁻⁶		6.11×10 ¹⁵	1.73×10 ³	1.95×10 ³	1.60×10 ⁻²¹	1.79×10 ⁻²¹
1.00×10 ⁻⁸		6.11×10 ¹⁵	1.79×10 ¹	1.96×10 ¹	1.65×10 ⁻²³	1.81×10 ⁻²³
1.00×10 ⁻¹⁰		6.11×10 ¹⁵	1.79×10 ⁻¹	1.96×10 ⁻¹	1.65×10 ⁻²⁵	1.81×10 ⁻²⁵
1.00×10 ⁻¹²		6.11×10 ¹⁵	1.79×10 ⁻³	1.96×10 ⁻³	1.65×10 ⁻²⁷	1.81×10 ⁻²⁷

Table S1d: [$T= 298$ K; *anti* isomer]

Pressure	Reaction	IMx→R1+O ₂	IM1→R1-2OO- <i>a</i>	IM3→R1-4OO- <i>a</i>	R1+O ₂ →R1-2OO- <i>a</i>	R1+O ₂ →R1-4OO- <i>a</i>
		k_{-1} (s ⁻¹)	$k_2(\mathbf{2})$ (s ⁻¹)	$k_2(\mathbf{4})$ (s ⁻¹)	$k_{\text{eff}}(\mathbf{2})$ (cm ³ molecule ⁻¹ s ⁻¹)	$k_{\text{eff}}(\mathbf{4})$ (cm ³ molecule ⁻¹ s ⁻¹)
1.00×10 ⁴		1.88×10 ¹⁹	1.18×10 ⁶	9.39×10 ⁶	4.92×10 ⁻²¹	3.90×10 ⁻²⁰
1.00×10 ²		1.88×10 ¹⁹	1.18×10 ⁶	9.38×10 ⁶	4.92×10 ⁻²¹	3.90×10 ⁻²⁰
1.00×10 ⁰		1.88×10 ¹⁹	1.17×10 ⁶	8.92×10 ⁶	4.85×10 ⁻²¹	3.71×10 ⁻²⁰
1.00×10 ⁻²		1.88×10 ¹⁹	6.54×10 ⁵	2.82×10 ⁶	2.72×10 ⁻²¹	1.17×10 ⁻²⁰
1.00×10 ⁻⁴		1.88×10 ¹⁹	4.44×10 ⁴	9.44×10 ⁴	1.85×10 ⁻²²	3.92×10 ⁻²²
1.00×10 ⁻⁶		1.88×10 ¹⁹	7.47×10 ²	1.19×10 ³	3.11×10 ⁻²⁴	4.95×10 ⁻²⁴
1.00×10 ⁻⁸		1.88×10 ¹⁹	7.83×10 ⁰	1.20×10 ¹	3.26×10 ⁻²⁶	4.99×10 ⁻²⁶
1.00×10 ⁻¹⁰		1.88×10 ¹⁹	7.84×10 ⁻²	1.20×10 ⁻¹	3.26×10 ⁻²⁸	4.99×10 ⁻²⁸
1.00×10 ⁻¹²		1.88×10 ¹⁹	7.84×10 ⁻⁴	1.20×10 ⁻³	3.26×10 ⁻³⁰	4.99×10 ⁻³⁰

Table S1e: [$T= 336$ K; *anti* isomer]

Pressure	Reaction	IMx→R1+O ₂	IM1→R1-2OO- <i>a</i>	IM3→R1-4OO- <i>a</i>	R1+O ₂ →R1-2OO- <i>a</i>	R1+O ₂ →R1-4OO- <i>a</i>
		k_{-1} (s ⁻¹)	$k_2(\mathbf{2})$ (s ⁻¹)	$k_2(\mathbf{4})$ (s ⁻¹)	$k_{\text{eff}}(\mathbf{2})$ (cm ³ molecule ⁻¹ s ⁻¹)	$k_{\text{eff}}(\mathbf{4})$ (cm ³ molecule ⁻¹ s ⁻¹)
1.00×10 ⁴		3.92×10 ¹⁸	5.00×10 ⁶	3.19×10 ⁷	2.45×10 ⁻²⁰	1.56×10 ⁻¹⁹
1.00×10 ²		3.92×10 ¹⁸	4.99×10 ⁶	3.18×10 ⁷	2.45×10 ⁻²⁰	1.56×10 ⁻¹⁹
1.00×10 ⁰		3.92×10 ¹⁸	4.85×10 ⁶	2.90×10 ⁷	2.37×10 ⁻²⁰	1.42×10 ⁻¹⁹
1.00×10 ⁻²		3.92×10 ¹⁸	2.00×10 ⁶	6.01×10 ⁶	9.79×10 ⁻²¹	2.94×10 ⁻²⁰
1.00×10 ⁻⁴		3.92×10 ¹⁸	8.70×10 ⁴	1.42×10 ⁵	4.26×10 ⁻²²	6.97×10 ⁻²²
1.00×10 ⁻⁶		3.92×10 ¹⁸	1.23×10 ³	1.64×10 ³	6.04×10 ⁻²⁴	8.05×10 ⁻²⁴
1.00×10 ⁻⁸		3.92×10 ¹⁸	1.27×10 ¹	1.65×10 ¹	6.21×10 ⁻²⁶	8.09×10 ⁻²⁶
1.00×10 ⁻¹⁰		3.92×10 ¹⁸	1.27×10 ⁻¹	1.65×10 ⁻¹	6.21×10 ⁻²⁸	8.09×10 ⁻²⁸
1.00×10 ⁻¹²		3.92×10 ¹⁸	1.27×10 ⁻³	1.65×10 ⁻³	6.21×10 ⁻³⁰	8.09×10 ⁻³⁰

Table S1f: [$T=400$ K; *anti* isomer]

Pressure	Reaction	$\text{IM}_x \rightarrow \text{R1} + \text{O}_2$	$\text{IM1} \rightarrow \text{R1-2OO-}a$	$\text{IM3} \rightarrow \text{R1-4OO-}a$	$\text{R1} + \text{O}_2 \rightarrow \text{R1-2OO-}a$	$\text{R1} + \text{O}_2 \rightarrow \text{R1-4OO-}a$
		k_{-1} (s^{-1})	$k_2(\mathbf{2})$ (s^{-1})	$k_2(\mathbf{4})$ (s^{-1})	$k_{\text{eff}}(\mathbf{2})$ ($\text{cm}^3 \text{ molecule}^{-1} \text{ s}^{-1}$)	$k_{\text{eff}}(\mathbf{4})$ ($\text{cm}^3 \text{ molecule}^{-1} \text{ s}^{-1}$)
1.00×10^4		5.61×10^{17}	3.01×10^7	1.46×10^8	1.87×10^{-19}	9.10×10^{-19}
1.00×10^2		5.61×10^{17}	3.01×10^7	1.46×10^8	1.87×10^{-19}	9.08×10^{-19}
1.00×10^0		5.61×10^{17}	2.77×10^7	1.17×10^8	1.72×10^{-19}	7.29×10^{-19}
1.00×10^{-2}		5.61×10^{17}	6.23×10^6	1.19×10^7	3.87×10^{-20}	7.40×10^{-20}
1.00×10^{-4}		5.61×10^{17}	1.50×10^5	1.86×10^5	9.32×10^{-22}	1.16×10^{-21}
1.00×10^{-6}		5.61×10^{17}	1.76×10^3	1.97×10^3	1.09×10^{-23}	1.22×10^{-23}
1.00×10^{-8}		5.61×10^{17}	1.78×10^1	1.97×10^1	1.11×10^{-25}	1.23×10^{-25}
1.00×10^{-10}		5.61×10^{17}	1.78×10^{-1}	1.97×10^{-1}	1.11×10^{-27}	1.23×10^{-27}
1.00×10^{-12}		5.61×10^{17}	1.78×10^{-3}	1.97×10^{-3}	1.11×10^{-29}	1.23×10^{-29}

Table S2: Kinetic rate constants (in s^{-1}), effective rate constants, and branching ratios (in %) for all reaction steps involved in the reported chemical pathways at ambient temperature and different pressures using the RRKM theory, according to the computed UM06-2x/aug-cc-pVTZ energy profiles ($z=1-4$).

Table S2a:

Reaction pathway	$P = 10^4 \text{ bar}$				
	K_p	Rate constant		k_{eff} ($\text{cm}^3 \text{ molecule}^{-1} \text{ s}^{-1}$)	Branching ratio (%)
		k_{-1} $\text{IM}_z \rightarrow \text{R1} + \text{O}_2$	k_2 $\text{IM}_z \rightarrow \text{R2}$		
$T=298 \text{ K}$					
$\text{R1} + \text{O}_2 \rightarrow \text{R1-2OO-}syn$	5.38×10^{-5}	4.36×10^{16}	1.78×10^5	3.93×10^{-19}	13.95
$\text{R1} + \text{O}_2 \rightarrow \text{R1-4OO-}syn$	5.38×10^{-5}	4.36×10^{16}	1.07×10^6	2.38×10^{-18}	84.49
$\text{R1} + \text{O}_2 \rightarrow \text{R1-2OO-}anti$	1.01×10^{-7}	1.88×10^{19}	1.18×10^6	4.92×10^{-21}	0.17
$\text{R1} + \text{O}_2 \rightarrow \text{R1-4OO-}anti$	1.01×10^{-7}	1.88×10^{19}	9.39×10^6	3.90×10^{-20}	1.38
$T=336 \text{ K}$					
$\text{R1} + \text{O}_2 \rightarrow \text{R1-2OO-}syn$	3.60×10^{-5}	4.36×10^{16}	7.11×10^5	1.05×10^{-18}	16.10
$\text{R1} + \text{O}_2 \rightarrow \text{R1-4OO-}syn$	3.60×10^{-5}	4.36×10^{16}	3.57×10^6	5.29×10^{-18}	81.13
$\text{R1} + \text{O}_2 \rightarrow \text{R1-2OO-}anti$	1.19×10^{-7}	1.88×10^{19}	5.00×10^6	2.45×10^{-20}	0.38
$\text{R1} + \text{O}_2 \rightarrow \text{R1-4OO-}anti$	1.19×10^{-7}	1.88×10^{19}	3.19×10^7	1.56×10^{-19}	2.39
$T=400 \text{ K}$					
$\text{R1} + \text{O}_2 \rightarrow \text{R1-2OO-}syn$	2.24×10^{-5}	4.36×10^{16}	4.00×10^6	3.69×10^{-18}	18.94
$\text{R1} + \text{O}_2 \rightarrow \text{R1-4OO-}syn$	2.24×10^{-5}	4.36×10^{16}	1.59×10^7	1.47×10^{-17}	75.43
$\text{R1} + \text{O}_2 \rightarrow \text{R1-2OO-}anti$	1.51×10^{-7}	1.88×10^{19}	3.01×10^7	1.87×10^{-19}	0.96
$\text{R1} + \text{O}_2 \rightarrow \text{R1-4OO-}anti$	1.51×10^{-7}	1.88×10^{19}	1.46×10^8	9.10×10^{-19}	4.67

Table S2b:

Parameter Reaction pathway	$P = 10^2$ bar				
	Rate constant			k_{eff} ($\text{cm}^3 \text{ molecule}^{-1} \text{ s}^{-1}$) R1+O ₂ →R2	Branching ratio (%)
	K_p	k_{-1} IMz→R1+O ₂	k_2 IMz→R2		
T=298 K					
R1+O ₂ →R1-2OO- <i>syn</i>	5.38×10^{-5}	4.36×10^{16}	1.78×10^5	3.93×10^{-19}	13.95
R1+O ₂ →R1-4OO- <i>syn</i>	5.38×10^{-5}	4.36×10^{16}	1.07×10^6	2.38×10^{-18}	84.49
R1+O ₂ →R1-2OO- <i>anti</i>	1.01×10^{-7}	1.88×10^{19}	1.18×10^6	4.92×10^{-21}	0.17
R1+O ₂ →R1-4OO- <i>anti</i>	1.01×10^{-7}	1.88×10^{19}	9.38×10^6	3.90×10^{-20}	1.38
T=336 K					
R1+O ₂ →R1-2OO- <i>syn</i>	3.60×10^{-5}	4.36×10^{16}	7.11×10^5	1.05×10^{-18}	16.10
R1+O ₂ →R1-4OO- <i>syn</i>	3.60×10^{-5}	4.36×10^{16}	3.57×10^6	5.29×10^{-18}	81.13
R1+O ₂ →R1-2OO- <i>anti</i>	1.19×10^{-7}	1.88×10^{19}	4.99×10^6	2.45×10^{-20}	0.38
R1+O ₂ →R1-4OO- <i>anti</i>	1.19×10^{-7}	1.88×10^{19}	3.18×10^7	1.56×10^{-19}	2.39
T=400 K					
R1+O ₂ →R1-2OO- <i>syn</i>	2.24×10^{-5}	4.36×10^{16}	4.00×10^6	3.69×10^{-18}	18.94
R1+O ₂ →R1-4OO- <i>syn</i>	2.24×10^{-5}	4.36×10^{16}	1.59×10^7	1.47×10^{-17}	75.44
R1+O ₂ →R1-2OO- <i>anti</i>	1.51×10^{-7}	1.88×10^{19}	3.01×10^7	1.87×10^{-19}	0.96
R1+O ₂ →R1-4OO- <i>anti</i>	1.51×10^{-7}	1.88×10^{19}	1.46×10^8	9.08×10^{-19}	4.66

Table S2c:

Parameter Reaction pathway	$P = 1.0$ bar				
	Rate constant			k_{eff} ($\text{cm}^3 \text{ molecule}^{-1} \text{ s}^{-1}$) R1+O ₂ →R2	Branching ratio (%)
	K_p	k_{-1} IMz→R1+O ₂	k_2 IMz→R2		
T=298 K					
R1+O ₂ →R1-2OO- <i>syn</i>	5.38×10^{-5}	4.36×10^{16}	1.77×10^5	3.93×10^{-19}	14.06
R1+O ₂ →R1-4OO- <i>syn</i>	5.38×10^{-5}	4.36×10^{16}	1.07×10^6	2.36×10^{-18}	84.44
R1+O ₂ →R1-2OO- <i>anti</i>	1.01×10^{-7}	1.88×10^{19}	1.17×10^6	4.85×10^{-21}	0.17
R1+O ₂ →R1-4OO- <i>anti</i>	1.01×10^{-7}	1.88×10^{19}	8.92×10^6	3.71×10^{-20}	1.33
T=336 K					
R1+O ₂ →R1-2OO- <i>syn</i>	3.60×10^{-5}	4.36×10^{16}	7.08×10^5	1.05×10^{-18}	16.29
R1+O ₂ →R1-4OO- <i>syn</i>	3.60×10^{-5}	4.36×10^{16}	3.53×10^6	5.23×10^{-18}	81.14
R1+O ₂ →R1-2OO- <i>anti</i>	1.19×10^{-7}	1.88×10^{19}	4.85×10^6	2.37×10^{-20}	0.37
R1+O ₂ →R1-4OO- <i>anti</i>	1.19×10^{-7}	1.88×10^{19}	2.90×10^7	1.42×10^{-19}	2.20
T=400 K					
R1+O ₂ →R1-2OO- <i>syn</i>	2.24×10^{-5}	4.36×10^{16}	3.96×10^6	3.65×10^{-18}	19.36
R1+O ₂ →R1-4OO- <i>syn</i>	2.24×10^{-5}	4.36×10^{16}	1.55×10^7	1.43×10^{-17}	75.86
R1+O ₂ →R1-2OO- <i>anti</i>	1.51×10^{-7}	1.88×10^{19}	2.77×10^7	1.72×10^{-19}	0.91
R1+O ₂ →R1-4OO- <i>anti</i>	1.51×10^{-7}	1.88×10^{19}	1.17×10^8	7.29×10^{-19}	3.87

Table S2d:

Parameter Reaction pathway	$P = 10^{-2}$ bar				
	Rate constant			k_{eff} ($\text{cm}^3 \text{ molecule}^{-1} \text{ s}^{-1}$) R1+O ₂ →R2	Branching ratio (%)
	K_p	k_{-1} IMz→R1+O ₂	k_2 IMz→R2		
T=298 K					
R1+O ₂ →R1-2OO- <i>syn</i>	5.38×10^{-5}	4.36×10^{16}	1.54×10^5	3.41×10^{-19}	16.84
R1+O ₂ →R1-4OO- <i>syn</i>	5.38×10^{-5}	4.36×10^{16}	7.55×10^5	1.67×10^{-18}	82.45
R1+O ₂ →R1-2OO- <i>anti</i>	1.01×10^{-7}	1.88×10^{19}	6.54×10^5	2.72×10^{-21}	0.13
R1+O ₂ →R1-4OO- <i>anti</i>	1.01×10^{-7}	1.88×10^{19}	2.82×10^6	1.17×10^{-20}	0.58
T=336 K					
R1+O ₂ →R1-2OO- <i>syn</i>	3.60×10^{-5}	4.36×10^{16}	5.49×10^5	8.13×10^{-19}	21.05
R1+O ₂ →R1-4OO- <i>syn</i>	3.60×10^{-5}	4.36×10^{16}	2.03×10^6	3.01×10^{-18}	77.94
R1+O ₂ →R1-2OO- <i>anti</i>	1.19×10^{-7}	1.88×10^{19}	2.00×10^6	9.79×10^{-21}	0.25
R1+O ₂ →R1-4OO- <i>anti</i>	1.19×10^{-7}	1.88×10^{19}	6.01×10^6	2.94×10^{-20}	0.76
T=400 K					
R1+O ₂ →R1-2OO- <i>syn</i>	2.24×10^{-5}	4.36×10^{16}	2.31×10^6	2.13×10^{-18}	28.28
R1+O ₂ →R1-4OO- <i>syn</i>	2.24×10^{-5}	4.36×10^{16}	5.74×10^6	5.29×10^{-18}	70.23
R1+O ₂ →R1-2OO- <i>anti</i>	1.51×10^{-7}	1.88×10^{19}	6.23×10^6	3.87×10^{-20}	0.51
R1+O ₂ →R1-4OO- <i>anti</i>	1.51×10^{-7}	1.88×10^{19}	1.19×10^7	7.40×10^{-20}	0.98

Table S2e:

Parameter Reaction pathway	$P = 10^{-4}$ bar				
	Rate constant			k_{eff} ($\text{cm}^3 \text{ molecule}^{-1} \text{ s}^{-1}$) R1+O ₂ →R2	Branching ratio (%)
	K_p	k_{-1} IMz→R1+O ₂	k_2 IMz→R2		
T=298 K					
R1+O ₂ →R1-2OO- <i>syn</i>	5.38×10^{-5}	4.36×10^{16}	2.82×10^4	6.23×10^{-20}	29.68
R1+O ₂ →R1-4OO- <i>syn</i>	5.38×10^{-5}	4.36×10^{16}	6.65×10^4	1.47×10^{-19}	70.04
R1+O ₂ →R1-2OO- <i>anti</i>	1.01×10^{-7}	1.88×10^{19}	4.44×10^4	1.85×10^{-22}	0.09
R1+O ₂ →R1-4OO- <i>anti</i>	1.01×10^{-7}	1.88×10^{19}	9.44×10^4	3.92×10^{-22}	0.19
T=336 K					
R1+O ₂ →R1-2OO- <i>syn</i>	3.60×10^{-5}	4.36×10^{16}	6.23×10^4	9.23×10^{-20}	35.44
R1+O ₂ →R1-4OO- <i>syn</i>	3.60×10^{-5}	4.36×10^{16}	1.12×10^5	1.67×10^{-19}	64.13
R1+O ₂ →R1-2OO- <i>anti</i>	1.19×10^{-7}	1.88×10^{19}	8.70×10^4	4.26×10^{-22}	0.16
R1+O ₂ →R1-4OO- <i>anti</i>	1.19×10^{-7}	1.88×10^{19}	1.42×10^5	6.97×10^{-22}	0.27
T=400 K					
R1+O ₂ →R1-2OO- <i>syn</i>	2.24×10^{-5}	4.36×10^{16}	1.25×10^5	1.15×10^{-19}	42.42
R1+O ₂ →R1-4OO- <i>syn</i>	2.24×10^{-5}	4.36×10^{16}	1.67×10^5	1.54×10^{-19}	56.81
R1+O ₂ →R1-2OO- <i>anti</i>	1.51×10^{-7}	1.88×10^{19}	1.50×10^5	9.32×10^{-22}	0.34
R1+O ₂ →R1-4OO- <i>anti</i>	1.51×10^{-7}	1.88×10^{19}	1.86×10^5	1.16×10^{-21}	0.43

Table S2f:

Reaction pathway	Parameter				
	$P = 10^{-6}$ bar				
	K_p	Rate constant		k_{eff} ($\text{cm}^3 \text{ molecule}^{-1} \text{ s}^{-1}$) R1+O ₂ →R2	Branching ratio (%)
k_{-1} IMz→R1+O ₂		k_2 IMz→R2			
T=298 K					
R1+O ₂ →R1-2OO- <i>syn</i>	5.38×10^{-5}	4.36×10^{16}	7.09×10^2	1.57×10^{-21}	38.59
R1+O ₂ →R1-4OO- <i>syn</i>	5.38×10^{-5}	4.36×10^{16}	1.12×10^3	2.49×10^{-21}	61.21
R1+O ₂ →R1-2OO- <i>anti</i>	1.01×10^{-7}	1.88×10^{19}	7.47×10^2	3.11×10^{-24}	0.08
R1+O ₂ →R1-4OO- <i>anti</i>	1.01×10^{-7}	1.88×10^{19}	1.19×10^3	4.95×10^{-24}	0.12
T=336 K					
R1+O ₂ →R1-2OO- <i>syn</i>	3.60×10^{-5}	4.36×10^{16}	1.19×10^3	1.76×10^{-21}	42.68
R1+O ₂ →R1-4OO- <i>syn</i>	3.60×10^{-5}	4.36×10^{16}	1.59×10^3	2.35×10^{-21}	56.98
R1+O ₂ →R1-2OO- <i>anti</i>	1.19×10^{-7}	1.88×10^{19}	1.23×10^3	6.04×10^{-24}	0.15
R1+O ₂ →R1-4OO- <i>anti</i>	1.19×10^{-7}	1.88×10^{19}	1.64×10^3	8.05×10^{-24}	0.20
T=400 K					
R1+O ₂ →R1-2OO- <i>syn</i>	2.24×10^{-5}	4.36×10^{16}	1.73×10^3	1.60×10^{-21}	46.88
R1+O ₂ →R1-4OO- <i>syn</i>	2.24×10^{-5}	4.36×10^{16}	1.95×10^3	1.79×10^{-21}	52.44
R1+O ₂ →R1-2OO- <i>anti</i>	1.51×10^{-7}	1.88×10^{19}	1.76×10^3	1.09×10^{-23}	0.32
R1+O ₂ →R1-4OO- <i>anti</i>	1.51×10^{-7}	1.88×10^{19}	1.97×10^3	1.22×10^{-23}	0.36

Table S2g:

Reaction pathway	Parameter				
	$P = 10^{-8}$ bar				
	K_p	Rate constant		k_{eff} ($\text{cm}^3 \text{ molecule}^{-1} \text{ s}^{-1}$) R1+O ₂ →R2	Branching ratio (%)
k_{-1} IMz→R1+O ₂		k_2 IMz→R2			
T=298 K					
R1+O ₂ →R1-2OO- <i>syn</i>	5.38×10^{-5}	4.36×10^{16}	8.02×10^0	1.78×10^{-23}	40.75
R1+O ₂ →R1-4OO- <i>syn</i>	5.38×10^{-5}	4.36×10^{16}	1.17×10^1	2.58×10^{-23}	59.06
R1+O ₂ →R1-2OO- <i>anti</i>	1.01×10^{-7}	1.88×10^{19}	7.83×10^0	3.26×10^{-26}	0.07
R1+O ₂ →R1-4OO- <i>anti</i>	1.01×10^{-7}	1.88×10^{19}	1.20×10^1	4.99×10^{-26}	0.11
T=336 K					
R1+O ₂ →R1-2OO- <i>syn</i>	3.60×10^{-5}	4.36×10^{16}	1.29×10^1	1.91×10^{-23}	44.07
R1+O ₂ →R1-4OO- <i>syn</i>	3.60×10^{-5}	4.36×10^{16}	1.62×10^1	2.41×10^{-23}	55.60
R1+O ₂ →R1-2OO- <i>anti</i>	1.19×10^{-7}	1.88×10^{19}	1.27×10^1	6.21×10^{-26}	0.14
R1+O ₂ →R1-4OO- <i>anti</i>	1.19×10^{-7}	1.88×10^{19}	1.65×10^1	8.09×10^{-26}	0.19
T=400 K					
R1+O ₂ →R1-2OO- <i>syn</i>	2.24×10^{-5}	4.36×10^{16}	1.79×10^1	1.65×10^{-23}	47.37
R1+O ₂ →R1-4OO- <i>syn</i>	2.24×10^{-5}	4.36×10^{16}	1.96×10^1	1.81×10^{-23}	51.96
R1+O ₂ →R1-2OO- <i>anti</i>	1.51×10^{-7}	1.88×10^{19}	1.78×10^1	1.11×10^{-25}	0.32
R1+O ₂ →R1-4OO- <i>anti</i>	1.51×10^{-7}	1.88×10^{19}	1.97×10^1	1.23×10^{-25}	0.35

Table S2h:

Reaction pathway	$P = 10^{-10}$ bar				
	K_p	Rate constant		k_{eff} ($\text{cm}^3 \text{ molecule}^{-1} \text{ s}^{-1}$) R1+O ₂ →R2	Branching ratio (%)
		k_{-1} IMz→R1+O ₂	k_2 IMz→R2		
T=298 K					
R1+O ₂ →R1-2OO- <i>syn</i>	5.38×10^{-5}	4.36×10^{16}	8.04×10^{-2}	1.78×10^{-25}	40.66
R1+O ₂ →R1-4OO- <i>syn</i>	5.38×10^{-5}	4.36×10^{16}	1.17×10^{-1}	2.59×10^{-25}	59.16
R1+O ₂ →R1-2OO- <i>anti</i>	1.01×10^{-7}	1.88×10^{19}	7.84×10^{-2}	3.26×10^{-28}	0.07
R1+O ₂ →R1-4OO- <i>anti</i>	1.01×10^{-7}	1.88×10^{19}	1.20×10^{-1}	4.99×10^{-28}	0.11
T=336 K					
R1+O ₂ →R1-2OO- <i>syn</i>	3.60×10^{-5}	4.36×10^{16}	1.29×10^{-1}	1.91×10^{-25}	44.07
R1+O ₂ →R1-4OO- <i>syn</i>	3.60×10^{-5}	4.36×10^{16}	1.62×10^{-1}	2.41×10^{-25}	55.60
R1+O ₂ →R1-2OO- <i>anti</i>	1.19×10^{-7}	1.88×10^{19}	1.27×10^{-1}	6.21×10^{-28}	0.14
R1+O ₂ →R1-4OO- <i>anti</i>	1.19×10^{-7}	1.88×10^{19}	1.65×10^{-1}	8.09×10^{-28}	0.19
T=400 K					
R1+O ₂ →R1-2OO- <i>syn</i>	2.24×10^{-5}	4.36×10^{16}	1.79×10^{-1}	1.65×10^{-25}	47.37
R1+O ₂ →R1-4OO- <i>syn</i>	2.24×10^{-5}	4.36×10^{16}	1.96×10^{-1}	1.81×10^{-25}	51.96
R1+O ₂ →R1-2OO- <i>anti</i>	1.51×10^{-7}	1.88×10^{19}	1.78×10^{-1}	1.11×10^{-27}	0.32
R1+O ₂ →R1-4OO- <i>anti</i>	1.51×10^{-7}	1.88×10^{19}	1.97×10^{-1}	1.23×10^{-27}	0.35

Table S2i:

Reaction pathway	$P = 10^{-12}$ bar				
	K_p	Rate constant		k_{eff} ($\text{cm}^3 \text{ molecule}^{-1} \text{ s}^{-1}$) R1+O ₂ →R2	Branching ratio (%)
		k_{-1} IMz→R1+O ₂	k_2 IMz→R2		
T=298 K					
R1+O ₂ →R1-2OO- <i>syn</i>	5.38×10^{-5}	4.36×10^{16}	8.04×10^{-4}	1.78×10^{-27}	40.66
R1+O ₂ →R1-4OO- <i>syn</i>	5.38×10^{-5}	4.36×10^{16}	1.17×10^{-3}	2.59×10^{-27}	59.16
R1+O ₂ →R1-2OO- <i>anti</i>	1.01×10^{-7}	1.88×10^{19}	7.84×10^{-4}	3.26×10^{-30}	0.07
R1+O ₂ →R1-4OO- <i>anti</i>	1.01×10^{-7}	1.88×10^{19}	1.20×10^{-3}	4.99×10^{-30}	0.11
T=336 K					
R1+O ₂ →R1-2OO- <i>syn</i>	3.60×10^{-5}	4.36×10^{16}	1.29×10^{-3}	1.91×10^{-27}	44.07
R1+O ₂ →R1-4OO- <i>syn</i>	3.60×10^{-5}	4.36×10^{16}	1.62×10^{-3}	2.41×10^{-27}	55.60
R1+O ₂ →R1-2OO- <i>anti</i>	1.19×10^{-7}	1.88×10^{19}	1.27×10^{-3}	6.21×10^{-30}	0.14
R1+O ₂ →R1-4OO- <i>anti</i>	1.19×10^{-7}	1.88×10^{19}	1.65×10^{-3}	8.09×10^{-30}	0.19
T=400 K					
R1+O ₂ →R1-2OO- <i>syn</i>	2.24×10^{-5}	4.36×10^{16}	1.79×10^{-3}	1.65×10^{-27}	47.37
R1+O ₂ →R1-4OO- <i>syn</i>	2.24×10^{-5}	4.36×10^{16}	1.96×10^{-3}	1.81×10^{-27}	51.96
R1+O ₂ →R1-2OO- <i>anti</i>	1.51×10^{-7}	1.88×10^{19}	1.78×10^{-3}	1.11×10^{-29}	0.32
R1+O ₂ →R1-4OO- <i>anti</i>	1.51×10^{-7}	1.88×10^{19}	1.97×10^{-3}	1.23×10^{-29}	0.35

Table S3: Dependence upon the pressure and temperature of the regioselectivities [RSI= $R(3)-R(1)/R(1)+R(3)$] and [RSI= $R(4)-R(2)/R(2)+R(4)$] of O₂ addition in *syn* and *anti* modes onto the naphthalene-OH adduct [C₁₀H₈OH][•], according to the RRKM estimates of effective rate constants [$k_{\text{eff}}(1)$, $k_{\text{eff}}(2)$, $k_{\text{eff}}(3)$, $k_{\text{eff}}(4)$].

Table S3a: ($T= 298$ K; *syn* isomer)

P (bar)	$k_{\text{eff}}(1)$	$k_{\text{eff}}(3)$	$k_{\text{eff}}[(1)+(3)]$	$R(1)$	$R(3)$	$\log P$	$[R(3)-R(1)]/[R(3)+R(1)]$
1.00×10^4	3.93×10^{-19}	2.38×10^{-18}	2.77×10^{-18}	13.95	84.49	4	0.7166
1.00×10^2	3.93×10^{-19}	2.38×10^{-18}	2.77×10^{-18}	13.95	84.49	2	0.7166
1.00×10^0	3.93×10^{-19}	2.36×10^{-18}	2.75×10^{-18}	14.06	84.44	0	0.7145
1.00×10^{-2}	3.41×10^{-19}	1.67×10^{-18}	2.01×10^{-18}	16.84	82.45	-2	0.6609
1.00×10^{-4}	6.23×10^{-20}	1.47×10^{-19}	2.09×10^{-19}	29.68	70.04	-4	0.4047
1.00×10^{-6}	1.57×10^{-21}	2.49×10^{-21}	4.06×10^{-21}	38.59	61.21	-6	0.2266
1.00×10^{-8}	1.78×10^{-23}	2.58×10^{-23}	4.36×10^{-23}	40.75	59.06	-8	0.1835
1.00×10^{-10}	1.78×10^{-25}	2.59×10^{-25}	4.37×10^{-25}	40.66	59.16	-10	0.1854
1.00×10^{-12}	1.78×10^{-27}	2.59×10^{-27}	4.37×10^{-27}	40.66	59.16	-12	0.1854

Table S3b: ($T= 336$ K; *syn* isomer)

P (bar)	$k_{\text{eff}}(1)$	$k_{\text{eff}}(3)$	$k_{\text{eff}}[(1)+(3)]$	$R(1)$	$R(3)$	$\log P$	$[R(3)-R(1)]/[R(3)+R(1)]$
1.00×10^4	1.05×10^{-18}	5.29×10^{-18}	6.34×10^{-18}	16.10	81.13	4	0.6688
1.00×10^2	1.05×10^{-18}	5.29×10^{-18}	6.34×10^{-18}	16.10	81.13	2	0.6688
1.00×10^0	1.05×10^{-18}	5.23×10^{-18}	6.28×10^{-18}	16.29	81.14	0	0.6656
1.00×10^{-2}	8.13×10^{-19}	3.01×10^{-18}	3.82×10^{-18}	21.05	77.94	-2	0.5747
1.00×10^{-4}	9.23×10^{-20}	1.67×10^{-19}	2.59×10^{-19}	35.44	64.13	-4	0.2881
1.00×10^{-6}	1.76×10^{-21}	2.35×10^{-21}	4.11×10^{-21}	42.68	56.98	-6	0.1436
1.00×10^{-8}	1.91×10^{-23}	2.41×10^{-23}	4.32×10^{-23}	44.07	55.60	-8	0.1157
1.00×10^{-10}	1.91×10^{-25}	2.41×10^{-25}	4.32×10^{-25}	44.07	55.60	-10	0.1157
1.00×10^{-12}	1.91×10^{-27}	2.41×10^{-27}	4.32×10^{-27}	44.07	55.60	-12	0.1157

Table S3c: ($T= 400$ K; *syn* isomer)

P (bar)	$k_{\text{eff}}(\mathbf{1})$	$k_{\text{eff}}(\mathbf{3})$	$k_{\text{eff}}[(\mathbf{1})+(\mathbf{3})]$	$R(\mathbf{1})$	$R(\mathbf{3})$	$\log P$	$[R(\mathbf{3})-R(\mathbf{1})]/[R(\mathbf{3})+R(\mathbf{1})]$
1.00×10^4	3.69×10^{-18}	1.47×10^{-17}	1.84×10^{-17}	18.94	75.43	4	0.5987
1.00×10^2	3.69×10^{-18}	1.47×10^{-17}	1.84×10^{-17}	18.94	75.44	2	0.5987
1.00×10^0	3.65×10^{-18}	1.43×10^{-17}	1.80×10^{-17}	19.36	75.86	0	0.5933
1.00×10^{-2}	2.13×10^{-18}	5.29×10^{-18}	7.42×10^{-18}	28.28	70.23	-2	0.4259
1.00×10^{-4}	1.15×10^{-19}	1.54×10^{-19}	2.69×10^{-19}	42.42	56.81	-4	0.1450
1.00×10^{-6}	1.60×10^{-21}	1.79×10^{-21}	3.39×10^{-21}	46.88	52.44	-6	0.0560
1.00×10^{-8}	1.65×10^{-23}	1.81×10^{-23}	3.46×10^{-23}	47.37	51.96	-8	0.0462
1.00×10^{-10}	1.65×10^{-25}	1.81×10^{-25}	3.46×10^{-25}	47.37	51.96	-10	0.0462
1.00×10^{-12}	1.65×10^{-27}	1.81×10^{-27}	3.46×10^{-27}	47.37	51.96	-12	0.0462

Table S3d: ($T= 298$ K; *anti* isomer)

P (bar)	$k_{\text{eff}}(\mathbf{2})$	$k_{\text{eff}}(\mathbf{4})$	$k_{\text{eff}}[(\mathbf{2})+(\mathbf{4})]$	$R(\mathbf{2})$	$R(\mathbf{4})$	$\log P$	$[R(\mathbf{4})-R(\mathbf{2})]/[R(\mathbf{4})+R(\mathbf{2})]$
1.00×10^4	4.92×10^{-21}	3.90×10^{-20}	4.39×10^{-20}	0.17	1.38	4	0.7760
1.00×10^2	4.92×10^{-21}	3.90×10^{-20}	4.39×10^{-20}	0.17	1.38	2	0.7760
1.00×10^0	4.85×10^{-21}	3.71×10^{-20}	4.20×10^{-20}	0.17	1.33	0	0.7688
1.00×10^{-2}	2.72×10^{-21}	1.17×10^{-20}	1.44×10^{-20}	0.13	0.58	-2	0.6227
1.00×10^{-4}	1.85×10^{-22}	3.92×10^{-22}	5.77×10^{-22}	0.09	0.19	-4	0.3588
1.00×10^{-6}	3.11×10^{-24}	4.95×10^{-24}	8.06×10^{-24}	0.08	0.12	-6	0.2283
1.00×10^{-8}	3.26×10^{-26}	4.99×10^{-26}	8.25×10^{-26}	0.07	0.11	-8	0.2097
1.00×10^{-10}	3.26×10^{-28}	4.99×10^{-28}	8.25×10^{-28}	0.07	0.11	-10	0.2097
1.00×10^{-12}	3.26×10^{-30}	4.99×10^{-30}	8.25×10^{-30}	0.07	0.11	-12	0.2097

Table S3e: ($T= 336$ K; *anti* isomer)

P (bar)	$k_{\text{eff}}(\mathbf{2})$	$k_{\text{eff}}(\mathbf{4})$	$k_{\text{eff}}[(\mathbf{2})+(\mathbf{4})]$	$R(\mathbf{2})$	$R(\mathbf{4})$	$\log P$	$[R(\mathbf{4})-R(\mathbf{2})]/[R(\mathbf{4})+R(\mathbf{2})]$
1.00×10^4	2.45×10^{-20}	1.56×10^{-19}	1.81×10^{-19}	0.38	2.39	4	0.7285
1.00×10^2	2.45×10^{-20}	1.56×10^{-19}	1.81×10^{-19}	0.38	2.39	2	0.7285
1.00×10^0	2.37×10^{-20}	1.42×10^{-19}	1.66×10^{-19}	0.37	2.20	0	0.7139
1.00×10^{-2}	9.79×10^{-21}	2.94×10^{-20}	3.92×10^{-20}	0.25	0.76	-2	0.5004
1.00×10^{-4}	4.26×10^{-22}	6.97×10^{-22}	1.12×10^{-21}	0.16	0.27	-4	0.2413
1.00×10^{-6}	6.04×10^{-24}	8.05×10^{-24}	1.41×10^{-23}	0.15	0.20	-6	0.1427
1.00×10^{-8}	6.21×10^{-26}	8.09×10^{-26}	1.43×10^{-25}	0.14	0.19	-8	0.1315
1.00×10^{-10}	6.21×10^{-28}	8.09×10^{-28}	1.43×10^{-27}	0.14	0.19	-10	0.1315
1.00×10^{-12}	6.21×10^{-30}	8.09×10^{-30}	1.43×10^{-29}	0.14	0.19	-12	0.1315

Table S3f: ($T= 400$ K; *anti* isomer)

P (bar)	$k_{\text{eff}}(\mathbf{2})$	$k_{\text{eff}}(\mathbf{4})$	$k_{\text{eff}}[(\mathbf{2})+(\mathbf{4})]$	$R(\mathbf{2})$	$R(\mathbf{4})$	$\log P$	$[R(\mathbf{4})-R(\mathbf{2})]/[R(\mathbf{4})+R(\mathbf{2})]$
1.00×10^4	1.87×10^{-19}	9.10×10^{-19}	1.10×10^{-18}	0.96	4.67	4	0.6591
1.00×10^2	1.87×10^{-19}	9.08×10^{-19}	1.10×10^{-18}	0.96	4.66	2	0.6584
1.00×10^0	1.72×10^{-19}	7.29×10^{-19}	9.01×10^{-19}	0.91	3.87	0	0.6182
1.00×10^{-2}	3.87×10^{-20}	7.40×10^{-20}	1.13×10^{-19}	0.51	0.98	-2	0.3132
1.00×10^{-4}	9.32×10^{-22}	1.16×10^{-21}	2.09×10^{-21}	0.34	0.43	-4	0.1090
1.00×10^{-6}	1.09×10^{-23}	1.22×10^{-23}	2.31×10^{-23}	0.32	0.36	-6	0.0563
1.00×10^{-8}	1.11×10^{-25}	1.23×10^{-25}	2.34×10^{-25}	0.32	0.35	-8	0.0513
1.00×10^{-10}	1.11×10^{-27}	1.23×10^{-27}	2.34×10^{-27}	0.32	0.35	-10	0.0513
1.00×10^{-12}	1.11×10^{-29}	1.23×10^{-29}	2.34×10^{-29}	0.32	0.35	-12	0.0513

Appendix IV

Table S1. Expectation values of the $\langle S^2 \rangle$ operator for cyclisation of the R1-2OO-*syn* peroxy radicals at various DFT levels (results obtained using the aug-cc-pVTZ basis set).

Compound \ Method	R1- 2,900- <i>s</i> (0,2)	R1- 2,400- <i>s</i> (0,2)	R1- 2,300- <i>s</i> (0,2)	R1- 2,1000- <i>s</i> (0,2)	R1- P2O1- <i>s</i> (0,2)	R1- P2C1 (0,2)	TS2- 2,900- <i>s</i> (0,2)	TS2- 2,400- <i>s</i> (0,2)	TS2- 2,300- <i>s</i> (0,2)	TS2- 2,1000- <i>s</i> (0,2)	TS2- P2O1- <i>s</i> (0,2)	TS2- P2C1 (0,2)
B3LYP	0.7938	0.7541	0.7764	0.7843	0.7560	0.7772	0.7915	0.7852	0.7791	0.7842	0.7558	0.7633
ω B97XD	0.8227	0.7548	0.7898	0.8018	0.7569	0.7976	0.8185	0.8006	0.7985	0.8042	0.7570	0.7691
UM05-2x	0.8205	0.7545	0.7898	0.8018	0.7569	0.7935	0.8162	0.8124	0.8008	0.8057	0.7593	0.7702
UM06-2x	0.7927	0.7556	0.7759	0.7838	0.7570	0.7775	0.7914	0.7953	0.7840	0.7869	0.7594	0.7670

Table S2. Expectation values of the $\langle S^2 \rangle$ operator for cyclisation of the R1-4OO-*syn* peroxy radicals at various DFT levels (results obtained using the aug-cc-pVTZ basis set).

Compound \ Method	R1- 4,200- <i>s</i> (0,2)	R1- 4,300- <i>s</i> (0,2)	R1- 4,500- <i>s</i> (0,2)	R1- 4,900- <i>s</i> (0,2)	R1- 4,1000- <i>s</i> (0,2)	R1- P4O1- <i>s</i> (0,2)	R1- P4C1 (0,2)	TS2- 4,200- <i>s</i> (0,2)	TS2- 4,300- <i>s</i> (0,2)	TS2- 4,500- <i>s</i> (0,2)	TS2- 4,900- <i>s</i> (0,2)	TS2- 4,1000- <i>s</i> (0,2)	TS2- P4O1- <i>s</i> (0,2)	TS2- P4C1 (0,2)
B3LYP	0.7541	0.7555	0.7857	0.7839	0.7824	0.7546	0.7758	0.7873	0.7745	0.7902	0.7868	0.7869	0.7606	0.7613
ω B97XD	0.7548	0.7561	0.8013	0.7988	0.7981	0.7547	0.7924	0.8030	0.7854	0.8127	0.8093	0.8068	0.7622	0.7656
UM05-2x	0.7545	0.7559	0.8014	0.7997	0.7998	0.7546	0.7903	0.8129	0.7921	0.8130	0.8109	0.8095	0.7646	0.7666
UM06-2x	0.7553	0.7565	0.7832	0.7825	0.7822	0.7547	0.7765	0.7992	0.7811	0.7912	0.7895	0.7885	0.7619	0.7644

Table S3: Unimolecular rate constants for all reaction steps involved in the reported chemical pathways (results obtained by means of RRKM theory at different pressures and temperatures, according to the computed UM06-2x/aug-cc-pVTZ energy profiles).

Table S3a: R1-200-syn→R1-2,300-syn

P (bar)	R1-200-s→P	$\log P$	$\log k_{\text{uni}}$ (R1-200-s→P)
$T = 298 \text{ K}$			
1.00×10^4	6.58×10^{-8}	4	-7.1820
1.00×10^2	6.58×10^{-8}	2	-7.1820
1.00×10^0	6.58×10^{-8}	0	-7.1820
1.00×10^{-2}	6.58×10^{-8}	-2	-7.1820
1.00×10^{-4}	6.57×10^{-8}	-4	-7.1825
1.00×10^{-6}	6.21×10^{-8}	-6	-7.2071
1.00×10^{-8}	3.21×10^{-8}	-8	-7.4930
1.00×10^{-10}	4.17×10^{-9}	-10	-8.3797
1.00×10^{-12}	1.29×10^{-10}	-12	-9.8903
$T = 336 \text{ K}$			
1.00×10^4	1.15×10^{-5}	4	-4.9393
1.00×10^2	1.15×10^{-5}	2	-4.9393
1.00×10^0	1.15×10^{-5}	0	-4.9393
1.00×10^{-2}	1.15×10^{-5}	-2	-4.9393
1.00×10^{-4}	1.14×10^{-5}	-4	-4.9431
1.00×10^{-6}	9.91×10^{-6}	-6	-5.0039
1.00×10^{-8}	3.60×10^{-6}	-8	-5.4437
1.00×10^{-10}	3.20×10^{-7}	-10	-6.4949
1.00×10^{-12}	8.05×10^{-9}	-12	-8.0942
$T = 400 \text{ K}$			
1.00×10^4	7.46×10^{-3}	4	-2.1273
1.00×10^2	7.46×10^{-3}	2	-2.1273
1.00×10^0	7.46×10^{-3}	0	-2.1273
1.00×10^{-2}	7.46×10^{-3}	-2	-2.1273
1.00×10^{-4}	7.29×10^{-3}	-4	-2.1373
1.00×10^{-6}	4.77×10^{-3}	-6	-2.3215
1.00×10^{-8}	9.12×10^{-4}	-8	-3.0400
1.00×10^{-10}	4.72×10^{-5}	-10	-4.3261
1.00×10^{-12}	9.15×10^{-7}	-12	-6.0386

Table S3b: R1-200-syn→R1-2,400-syn

P (bar)	R1-200-s→P	$\log P$	$\log k_{\text{uni}}$ (R1-200-s→P)
$T = 298 \text{ K}$			
1.00×10^4	1.27×10^{-14}	4	-13.8955
1.00×10^2	1.27×10^{-14}	2	-13.8955
1.00×10^0	1.27×10^{-14}	0	-13.8955
1.00×10^{-2}	1.27×10^{-14}	-2	-13.8955
1.00×10^{-4}	1.27×10^{-14}	-4	-13.8955
1.00×10^{-6}	1.27×10^{-14}	-6	-13.8957
1.00×10^{-8}	1.24×10^{-14}	-8	-13.9064
1.00×10^{-10}	8.52×10^{-15}	-10	-14.0696
1.00×10^{-12}	1.94×10^{-15}	-12	-14.7131
$T = 336 \text{ K}$			
1.00×10^4	1.18×10^{-11}	4	-10.9281
1.00×10^2	1.18×10^{-11}	2	-10.9281
1.00×10^0	1.18×10^{-11}	0	-10.9281
1.00×10^{-2}	1.18×10^{-11}	-2	-10.9281
1.00×10^{-4}	1.18×10^{-11}	-4	-10.9281
1.00×10^{-6}	1.18×10^{-11}	-6	-10.9281
1.00×10^{-8}	1.10×10^{-11}	-8	-10.9586
1.00×10^{-10}	5.73×10^{-12}	-10	-11.2418
1.00×10^{-12}	8.87×10^{-13}	-12	-12.0521
$T = 400 \text{ K}$			
1.00×10^4	6.32×10^{-8}	4	-7.1993
1.00×10^2	6.32×10^{-8}	2	-7.1993
1.00×10^0	6.32×10^{-8}	0	-7.1993
1.00×10^{-2}	6.32×10^{-8}	-2	-7.1993
1.00×10^{-4}	6.32×10^{-8}	-4	-7.1993
1.00×10^{-6}	6.24×10^{-8}	-6	-7.2048
1.00×10^{-8}	4.76×10^{-8}	-8	-7.3224
1.00×10^{-10}	1.41×10^{-8}	-10	-7.8508
1.00×10^{-12}	1.23×10^{-9}	-12	-8.9101

Table S3c: R1-200-syn→R1-2,900-syn

P (bar)	R1-200-s→P	$\log P$	$\log k_{\text{uni}}$ (R1-200-s→P)
$T = 298 \text{ K}$			
1.00×10^4	1.85×10^{-4}	4	-3.7328
1.00×10^2	1.85×10^{-4}	2	-3.7328
1.00×10^0	1.85×10^{-4}	0	-3.7328
1.00×10^{-2}	1.85×10^{-4}	-2	-3.7328
1.00×10^{-4}	1.84×10^{-4}	-4	-3.7352
1.00×10^{-6}	1.44×10^{-4}	-6	-3.8416
1.00×10^{-8}	3.52×10^{-5}	-8	-4.4535
1.00×10^{-10}	1.67×10^{-6}	-10	-5.7773
1.00×10^{-12}	2.07×10^{-8}	-12	-7.6840
$T = 336 \text{ K}$			
1.00×10^4	1.10×10^{-2}	4	-1.9586
1.00×10^2	1.10×10^{-2}	2	-1.9586
1.00×10^0	1.10×10^{-2}	0	-1.9586
1.00×10^{-2}	1.10×10^{-2}	-2	-1.9586
1.00×10^{-4}	1.07×10^{-2}	-4	-1.9706
1.00×10^{-6}	6.81×10^{-3}	-6	-2.1669
1.00×10^{-8}	1.09×10^{-3}	-8	-2.9626
1.00×10^{-10}	3.90×10^{-5}	-10	-4.4089
1.00×10^{-12}	4.63×10^{-7}	-12	-6.3344
$T = 400 \text{ K}$			
1.00×10^4	1.84×10^0	4	0.2648
1.00×10^2	1.84×10^0	2	0.2648
1.00×10^0	1.84×10^0	0	0.2648
1.00×10^{-2}	1.84×10^0	-2	0.2648
1.00×10^{-4}	1.67×10^0	-4	0.2227
1.00×10^{-6}	6.40×10^{-1}	-6	-0.1938
1.00×10^{-8}	5.33×10^{-2}	-8	-1.2733
1.00×10^{-10}	1.32×10^{-3}	-10	-2.8794
1.00×10^{-12}	1.48×10^{-5}	-12	-4.8297

Table S3d: R1-200-syn→R1-2,1000-syn

P (bar)	R1-200-s→P	$\log P$	$\log k_{\text{uni}}$ (R1-200-s→P)
$T = 298 \text{ K}$			
1.00×10^4	1.10×10^{-11}	4	-10.9586
1.00×10^2	1.10×10^{-11}	2	-10.9586
1.00×10^0	1.10×10^{-11}	0	-10.9586
1.00×10^{-2}	1.10×10^{-11}	-2	-10.9586
1.00×10^{-4}	1.10×10^{-11}	-4	-10.9586
1.00×10^{-6}	1.10×10^{-11}	-6	-10.9586
1.00×10^{-8}	9.98×10^{-12}	-8	-11.0009
1.00×10^{-10}	4.46×10^{-12}	-10	-11.3507
1.00×10^{-12}	5.06×10^{-13}	-12	-12.2958
$T = 336 \text{ K}$			
1.00×10^4	4.48×10^{-9}	4	-8.3487
1.00×10^2	4.48×10^{-9}	2	-8.3487
1.00×10^0	4.48×10^{-9}	0	-8.3487
1.00×10^{-2}	4.48×10^{-9}	-2	-8.3487
1.00×10^{-4}	4.48×10^{-9}	-4	-8.3487
1.00×10^{-6}	4.44×10^{-9}	-6	-8.3526
1.00×10^{-8}	3.54×10^{-9}	-8	-8.4510
1.00×10^{-10}	1.09×10^{-9}	-10	-8.9626
1.00×10^{-12}	8.70×10^{-11}	-12	-10.0605
$T = 400 \text{ K}$			
1.00×10^4	8.50×10^{-6}	4	-5.0706
1.00×10^2	8.50×10^{-6}	2	-5.0706
1.00×10^0	8.50×10^{-6}	0	-5.0706
1.00×10^{-2}	8.50×10^{-6}	-2	-5.0706
1.00×10^{-4}	8.49×10^{-6}	-4	-5.0711
1.00×10^{-6}	8.04×10^{-6}	-6	-5.0947
1.00×10^{-8}	4.42×10^{-6}	-8	-5.3546
1.00×10^{-10}	7.24×10^{-7}	-10	-6.1403
1.00×10^{-12}	3.52×10^{-8}	-12	-7.4535

Table S3e: R1-2OO-syn→P2O1-syn

P (bar)	R1-2OO-s→P	$\log P$	$\log k_{\text{uni}}$ (R1-2OO-s→P)
$T = 298 \text{ K}$			
1.00×10^4	1.79×10^0	4	0.2529
1.00×10^2	1.79×10^0	2	0.2529
1.00×10^0	1.79×10^0	0	0.2529
1.00×10^{-2}	1.78×10^0	-2	0.2504
1.00×10^{-4}	1.44×10^0	-4	0.1584
1.00×10^{-6}	3.28×10^{-1}	-6	-0.4841
1.00×10^{-8}	1.29×10^{-2}	-8	-1.8894
1.00×10^{-10}	1.57×10^{-4}	-10	-3.8041
1.00×10^{-12}	1.58×10^{-6}	-12	-5.8013
$T = 336 \text{ K}$			
1.00×10^4	4.08×10^1	4	1.6107
1.00×10^2	4.08×10^1	2	1.6107
1.00×10^0	4.08×10^1	0	1.6107
1.00×10^{-2}	4.03×10^1	-2	1.6053
1.00×10^{-4}	2.70×10^1	-4	1.4314
1.00×10^{-6}	3.97×10^0	-6	0.5988
1.00×10^{-8}	1.19×10^{-1}	-8	-0.9245
1.00×10^{-10}	1.37×10^{-3}	-10	-2.8633
1.00×10^{-12}	1.38×10^{-5}	-12	-4.8601
$T = 400 \text{ K}$			
1.00×10^4	2.07×10^3	4	2.07E+03
1.00×10^2	2.07×10^3	2	2.07E+03
1.00×10^0	2.07×10^3	0	2.07E+03
1.00×10^{-2}	1.96×10^3	-2	1.96E+03
1.00×10^{-4}	8.22×10^2	-4	8.22E+02
1.00×10^{-6}	6.08×10^1	-6	6.08E+01
1.00×10^{-8}	1.27×10^0	-8	1.27E+00
1.00×10^{-10}	1.38×10^{-2}	-10	1.38E-02
1.00×10^{-12}	1.39×10^{-4}	-12	1.39E-04

Table S3f: R1-2OO-syn→P2C1

P (bar)	R1-2OO-s→P	$\log P$	$\log k_{\text{uni}}$ (R1-2OO-s→P)
$T = 298 \text{ K}$			
1.00×10^4	8.35×10^{-6}	4	-5.0783
1.00×10^2	8.35×10^{-6}	2	-5.0783
1.00×10^0	8.35×10^{-6}	0	-5.0783
1.00×10^{-2}	8.35×10^{-6}	-2	-5.0783
1.00×10^{-4}	8.29×10^{-6}	-4	-5.0814
1.00×10^{-6}	6.56×10^{-6}	-6	-5.1831
1.00×10^{-8}	1.78×10^{-6}	-8	-5.7496
1.00×10^{-10}	1.10×10^{-7}	-10	-6.9586
1.00×10^{-12}	1.90×10^{-9}	-12	-8.7212
$T = 336 \text{ K}$			
1.00×10^4	9.14×10^{-4}	4	-3.0391
1.00×10^2	9.14×10^{-4}	2	-3.0391
1.00×10^0	9.14×10^{-4}	0	-3.0391
1.00×10^{-2}	9.13×10^{-4}	-2	-3.0395
1.00×10^{-4}	8.90×10^{-4}	-4	-3.0506
1.00×10^{-6}	5.66×10^{-4}	-6	-3.2472
1.00×10^{-8}	1.01×10^{-4}	-8	-3.9957
1.00×10^{-10}	4.56×10^{-6}	-10	-5.3410
1.00×10^{-12}	7.03×10^{-8}	-12	-7.1530
$T = 400 \text{ K}$			
1.00×10^4	3.36×10^{-1}	4	-0.4737
1.00×10^2	3.36×10^{-1}	2	-0.4737
1.00×10^0	3.36×10^{-1}	0	-0.4737
1.00×10^{-2}	3.35×10^{-1}	-2	-0.4750
1.00×10^{-4}	2.98×10^{-1}	-4	-0.5258
1.00×10^{-6}	1.13×10^{-1}	-6	-0.9469
1.00×10^{-8}	1.04×10^{-2}	-8	-1.9830
1.00×10^{-10}	3.10×10^{-4}	-10	-3.5086
1.00×10^{-12}	4.16×10^{-6}	-12	-5.3809

Table S3g: R1-400-syn→R1-4,200-syn

P (bar)	R1-200-s→P	$\log P$	$\log k_{\text{uni}}$ (R1-200-s→P)
$T = 298 \text{ K}$			
1.00×10^4	2.07×10^{-11}	4	-10.6840
1.00×10^2	2.07×10^{-11}	2	-10.6840
1.00×10^0	2.07×10^{-11}	0	-10.6840
1.00×10^{-2}	2.07×10^{-11}	-2	-10.6840
1.00×10^{-4}	2.07×10^{-11}	-4	-10.6840
1.00×10^{-6}	2.07×10^{-11}	-6	-10.6840
1.00×10^{-8}	1.86×10^{-11}	-8	-10.7305
1.00×10^{-10}	7.94×10^{-12}	-10	-11.1002
1.00×10^{-12}	8.32×10^{-13}	-12	-12.0799
$T = 336 \text{ K}$			
1.00×10^4	7.88×10^{-9}	4	-8.1035
1.00×10^2	7.88×10^{-9}	2	-8.1035
1.00×10^0	7.88×10^{-9}	0	-8.1035
1.00×10^{-2}	7.88×10^{-9}	-2	-8.1035
1.00×10^{-4}	7.88×10^{-9}	-4	-8.1035
1.00×10^{-6}	7.80×10^{-9}	-6	-8.1079
1.00×10^{-8}	6.13×10^{-9}	-8	-8.2125
1.00×10^{-10}	1.80×10^{-9}	-10	-8.7447
1.00×10^{-12}	1.33×10^{-10}	-12	-9.8761
$T = 400 \text{ K}$			
1.00×10^4	1.37×10^{-5}	4	-4.8633
1.00×10^2	1.37×10^{-5}	2	-4.8633
1.00×10^0	1.37×10^{-5}	0	-4.8633
1.00×10^{-2}	1.37×10^{-5}	-2	-4.8633
1.00×10^{-4}	1.37×10^{-5}	-4	-4.8633
1.00×10^{-6}	1.29×10^{-5}	-6	-4.8894
1.00×10^{-8}	6.92×10^{-6}	-8	-5.1599
1.00×10^{-10}	1.07×10^{-6}	-10	-5.9706
1.00×10^{-12}	4.89×10^{-8}	-12	-7.3107

Table S3h: R1-400-syn→R1-4,300-syn

P (bar)	R1-200-s→P	$\log P$	$\log k_{\text{uni}}$ (R1-200-s→P)
$T = 298 \text{ K}$			
1.00×10^4	2.17×10^{-10}	4	-9.6635
1.00×10^2	2.17×10^{-10}	2	-9.6635
1.00×10^0	2.17×10^{-10}	0	-9.6635
1.00×10^{-2}	2.17×10^{-10}	-2	-9.6635
1.00×10^{-4}	2.17×10^{-10}	-4	-9.6635
1.00×10^{-6}	2.15×10^{-10}	-6	-9.6676
1.00×10^{-8}	1.64×10^{-10}	-8	-9.7852
1.00×10^{-10}	4.40×10^{-11}	-10	-10.3565
1.00×10^{-12}	2.85×10^{-12}	-12	-11.5452
$T = 336 \text{ K}$			
1.00×10^4	7.37×10^{-8}	4	-7.1325
1.00×10^2	7.37×10^{-8}	2	-7.1325
1.00×10^0	7.37×10^{-8}	0	-7.1325
1.00×10^{-2}	7.37×10^{-8}	-2	-7.1325
1.00×10^{-4}	7.36×10^{-8}	-4	-7.1331
1.00×10^{-6}	7.09×10^{-8}	-6	-7.1494
1.00×10^{-8}	4.28×10^{-8}	-8	-7.3686
1.00×10^{-10}	7.65×10^{-9}	-10	-8.1163
1.00×10^{-12}	3.67×10^{-10}	-12	-9.4353
$T = 400 \text{ K}$			
1.00×10^4	1.11×10^{-4}	4	-3.9547
1.00×10^2	1.11×10^{-4}	2	-3.9547
1.00×10^0	1.11×10^{-4}	0	-3.9547
1.00×10^{-2}	1.11×10^{-4}	-2	-3.9547
1.00×10^{-4}	1.11×10^{-4}	-4	-3.9547
1.00×10^{-6}	9.40×10^{-5}	-6	-4.0269
1.00×10^{-8}	3.33×10^{-5}	-8	-4.4776
1.00×10^{-10}	3.20×10^{-6}	-10	-5.4949
1.00×10^{-12}	1.03×10^{-7}	-12	-6.9872

Table S3i: R1-400-syn→R1-4,500-syn

P (bar)	R1-200-s→P	$\log P$	$\log k_{\text{uni}}$ (R1-200-s→P)
$T = 298 \text{ K}$			
1.00×10^4	1.59×10^{-12}	4	-11.7984
1.00×10^2	1.59×10^{-12}	2	-11.7984
1.00×10^0	1.59×10^{-12}	0	-11.7984
1.00×10^{-2}	1.59×10^{-12}	-2	-11.7984
1.00×10^{-4}	1.59×10^{-12}	-4	-11.7984
1.00×10^{-6}	1.59×10^{-12}	-6	-11.7991
1.00×10^{-8}	1.47×10^{-12}	-8	-11.8322
1.00×10^{-10}	7.29×10^{-13}	-10	-12.1370
1.00×10^{-12}	9.60×10^{-14}	-12	-13.0178
$T = 336 \text{ K}$			
1.00×10^4	8.59×10^{-10}	4	-9.0659
1.00×10^2	8.59×10^{-10}	2	-9.0659
1.00×10^0	8.59×10^{-10}	0	-9.0659
1.00×10^{-2}	8.59×10^{-10}	-2	-9.0659
1.00×10^{-4}	8.59×10^{-10}	-4	-9.0659
1.00×10^{-6}	8.54×10^{-10}	-6	-9.0688
1.00×10^{-8}	7.10×10^{-10}	-8	-9.1486
1.00×10^{-10}	2.47×10^{-10}	-10	-9.6082
1.00×10^{-12}	2.25×10^{-11}	-12	-10.6477
$T = 400 \text{ K}$			
1.00×10^4	2.32×10^{-6}	4	-5.6339
1.00×10^2	2.32×10^{-6}	2	-5.6339
1.00×10^0	2.32×10^{-6}	0	-5.6339
1.00×10^{-2}	2.32×10^{-6}	-2	-5.6339
1.00×10^{-4}	2.32×10^{-6}	-4	-5.6339
1.00×10^{-6}	2.23×10^{-6}	-6	-5.6524
1.00×10^{-8}	1.33×10^{-6}	-8	-5.8775
1.00×10^{-10}	2.46×10^{-7}	-10	-6.6091
1.00×10^{-12}	1.34×10^{-8}	-12	-7.8725

Table S3j: R1-400-syn→R1-4,900-syn

P (bar)	R1-200-s→P	$\log P$	$\log k_{\text{uni}}$ (R1-200-s→P)
$T = 298 \text{ K}$			
1.00×10^4	1.54×10^{-13}	4	-12.8125
1.00×10^2	1.54×10^{-13}	2	-12.8125
1.00×10^0	1.54×10^{-13}	0	-12.8125
1.00×10^{-2}	1.54×10^{-13}	-2	-12.8125
1.00×10^{-4}	1.54×10^{-13}	-4	-12.8125
1.00×10^{-6}	1.53×10^{-13}	-6	-12.8153
1.00×10^{-8}	1.49×10^{-13}	-8	-12.8268
1.00×10^{-10}	9.75×10^{-14}	-10	-13.0110
1.00×10^{-12}	1.98×10^{-14}	-12	-13.7033
$T = 336 \text{ K}$			
1.00×10^4	9.75×10^{-11}	4	-10.0110
1.00×10^2	9.75×10^{-11}	2	-10.0110
1.00×10^0	9.75×10^{-11}	0	-10.0110
1.00×10^{-2}	9.75×10^{-11}	-2	-10.0110
1.00×10^{-4}	9.75×10^{-11}	-4	-10.0110
1.00×10^{-6}	9.73×10^{-11}	-6	-10.0119
1.00×10^{-8}	8.95×10^{-11}	-8	-10.0482
1.00×10^{-10}	4.37×10^{-11}	-10	-10.3595
1.00×10^{-12}	6.03×10^{-12}	-12	-11.2197
$T = 400 \text{ K}$			
1.00×10^4	3.23×10^{-7}	4	-6.4908
1.00×10^2	3.23×10^{-7}	2	-6.4908
1.00×10^0	3.23×10^{-7}	0	-6.4908
1.00×10^{-2}	3.23×10^{-7}	-2	-6.4908
1.00×10^{-4}	3.23×10^{-7}	-4	-6.4908
1.00×10^{-6}	3.18×10^{-7}	-6	-6.4976
1.00×10^{-8}	2.36×10^{-7}	-8	-6.6271
1.00×10^{-10}	6.43×10^{-8}	-10	-7.1918
1.00×10^{-12}	5.03×10^{-9}	-12	-8.2984

Table S3k: R1-400-syn→R1-4,1000-syn

P (bar)	R1-200-s→P	$\log P$	$\log k_{\text{uni}}$ (R1-200-s→P)
$T = 298 \text{ K}$			
1.00×10^4	6.35×10^{-14}	4	-13.1972
1.00×10^2	6.35×10^{-14}	2	-13.1972
1.00×10^0	6.35×10^{-14}	0	-13.1972
1.00×10^{-2}	6.35×10^{-14}	-2	-13.1972
1.00×10^{-4}	6.35×10^{-14}	-4	-13.1972
1.00×10^{-6}	6.34×10^{-14}	-6	-13.1979
1.00×10^{-8}	6.05×10^{-14}	-8	-13.2182
1.00×10^{-10}	3.54×10^{-14}	-10	-13.4510
1.00×10^{-12}	6.20×10^{-15}	-12	-14.2076
$T = 336 \text{ K}$			
1.00×10^4	5.23×10^{-11}	4	-10.2815
1.00×10^2	5.23×10^{-11}	2	-10.2815
1.00×10^0	5.23×10^{-11}	0	-10.2815
1.00×10^{-2}	5.23×10^{-11}	-2	-10.2815
1.00×10^{-4}	5.23×10^{-11}	-4	-10.2815
1.00×10^{-6}	5.21×10^{-11}	-6	-10.2832
1.00×10^{-8}	4.60×10^{-11}	-8	-10.3372
1.00×10^{-10}	1.95×10^{-11}	-10	-10.7100
1.00×10^{-12}	2.33×10^{-12}	-12	-11.6326
$T = 400 \text{ K}$			
1.00×10^4	2.41×10^{-7}	4	-6.6180
1.00×10^2	2.41×10^{-7}	2	-6.6180
1.00×10^0	2.41×10^{-7}	0	-6.6180
1.00×10^{-2}	2.41×10^{-7}	-2	-6.6180
1.00×10^{-4}	2.41×10^{-7}	-4	-6.6180
1.00×10^{-6}	2.34×10^{-7}	-6	-6.6308
1.00×10^{-8}	1.57×10^{-7}	-8	-6.8041
1.00×10^{-10}	3.64×10^{-8}	-10	-7.4389
1.00×10^{-12}	2.53×10^{-9}	-12	-8.5969

Table S3l: R1-400-syn→R1-P401-syn

P (bar)	R1-200-s→P	$\log P$	$\log k_{\text{uni}}$ (R1-200-s→P)
$T = 298 \text{ K}$			
1.00×10^4	3.72×10^{-10}	4	-9.4295
1.00×10^2	3.72×10^{-10}	2	-9.4295
1.00×10^0	3.72×10^{-10}	0	-9.4295
1.00×10^{-2}	3.72×10^{-10}	-2	-9.4295
1.00×10^{-4}	3.72×10^{-10}	-4	-9.4295
1.00×10^{-6}	3.69×10^{-10}	-6	-9.4330
1.00×10^{-8}	2.96×10^{-10}	-8	-9.5287
1.00×10^{-10}	8.80×10^{-11}	-10	-10.0555
1.00×10^{-12}	6.01×10^{-12}	-12	-11.2211
$T = 336 \text{ K}$			
1.00×10^4	1.05×10^{-7}	4	-6.9788
1.00×10^2	1.05×10^{-7}	2	-6.9788
1.00×10^0	1.05×10^{-7}	0	-6.9788
1.00×10^{-2}	1.05×10^{-7}	-2	-6.9788
1.00×10^{-4}	1.05×10^{-7}	-4	-6.9788
1.00×10^{-6}	1.03×10^{-7}	-6	-6.9872
1.00×10^{-8}	6.68×10^{-8}	-8	-7.1752
1.00×10^{-10}	1.33×10^{-8}	-10	-7.8761
1.00×10^{-12}	6.68×10^{-10}	-12	-9.1752
$T = 400 \text{ K}$			
1.00×10^4	1.27×10^{-4}	4	-3.8962
1.00×10^2	1.27×10^{-4}	2	-3.8962
1.00×10^0	1.27×10^{-4}	0	-3.8962
1.00×10^{-2}	1.27×10^{-4}	-2	-3.8962
1.00×10^{-4}	1.27×10^{-4}	-4	-3.8962
1.00×10^{-6}	1.12×10^{-4}	-6	-3.9508
1.00×10^{-8}	4.43×10^{-5}	-8	-4.3536
1.00×10^{-10}	4.68×10^{-6}	-10	-5.3298
1.00×10^{-12}	1.56×10^{-7}	-12	-6.8069

Table S3m: R1-400-syn→R1-P4C1

P (bar)	R1-200-s→P	$\log P$	$\log k_{\text{uni}}$ (R1-200-s→P)
$T = 298 \text{ K}$			
1.00×10^4	5.53×10^{-3}	4	-2.2573
1.00×10^2	5.53×10^{-3}	2	-2.2573
1.00×10^0	5.53×10^{-3}	0	-2.2573
1.00×10^{-2}	5.53×10^{-3}	-2	-2.2573
1.00×10^{-4}	5.34×10^{-3}	-4	-2.2725
1.00×10^{-6}	3.00×10^{-3}	-6	-2.5229
1.00×10^{-8}	3.85×10^{-4}	-8	-3.4145
1.00×10^{-10}	1.01×10^{-5}	-10	-4.9957
1.00×10^{-12}	1.07×10^{-7}	-12	-6.9706
$T = 336 \text{ K}$			
1.00×10^4	2.43×10^{-1}	4	-0.6144
1.00×10^2	2.43×10^{-1}	2	-0.6144
1.00×10^0	2.43×10^{-1}	0	-0.6144
1.00×10^{-2}	2.42×10^{-1}	-2	-0.6162
1.00×10^{-4}	2.21×10^{-1}	-4	-0.6556
1.00×10^{-6}	8.81×10^{-2}	-6	-1.0550
1.00×10^{-8}	7.51×10^{-3}	-8	-2.1244
1.00×10^{-10}	1.63×10^{-4}	-10	-3.7878
1.00×10^{-12}	1.70×10^{-6}	-12	-5.7696
$T = 400 \text{ K}$			
1.00×10^4	2.85×10^1	4	1.4548
1.00×10^2	2.85×10^1	2	1.4548
1.00×10^0	2.85×10^1	0	1.4548
1.00×10^{-2}	2.82×10^1	-2	1.4502
1.00×10^{-4}	2.10×10^1	-4	1.3222
1.00×10^{-6}	4.31×10^0	-6	0.6345
1.00×10^{-8}	2.05×10^{-1}	-8	-0.6882
1.00×10^{-10}	3.46×10^{-3}	-10	-2.4609
1.00×10^{-12}	3.56×10^{-5}	-12	-4.4486

Appendix V

Table S1: Optimized geometries (in cartesian coordinates) of all identified stationary points that are involved in the chemical reaction pathways 1–3 [B3LYP/6-311G(2d,d,p) results].

OH-radical

O	0.00000000	0.00000000	0.10835600
H	0.00000000	0.00000000	-0.86685200

thiophene

C	0.00013000	0.00865700	1.23943300
C	0.00013000	0.00865700	-1.23943300
S	-0.00018700	-1.19374600	0.00000000
C	0.00013000	1.26964900	-0.71290500
C	0.00013000	1.26964900	0.71290500
H	0.00008700	2.16685500	1.31774600
H	0.00008700	2.16685500	-1.31774600
H	-0.00014600	-0.28672800	2.27707700
H	-0.00014600	-0.28672800	-2.27707700

P1

C	-0.91776700	0.12406600	0.39971600
C	1.60350300	-0.10244600	-0.24268500
S	0.34440100	-1.25303500	0.09786500
C	1.18798500	1.22387700	-0.10487400
C	-0.12713300	1.38630400	0.25351200
H	-1.28364800	-0.03074900	1.42241900
H	1.86212100	2.05381300	-0.27978700
H	-0.62932400	2.33649800	0.37501200
O	-1.99135200	0.11775400	-0.51363500
H	-2.59291500	-0.59636300	-0.27567200
H	2.58463400	-0.44747200	-0.53273900

P2

C	-0.00030900	-1.09513400	0.30723700
C	0.88820700	1.19763400	-0.08783200
S	1.52882100	-0.45106100	-0.14390200
C	-0.40746900	1.26077000	0.22290700
C	-1.08514800	-0.06628400	0.43318400
H	1.55592300	2.01876600	-0.30589900
H	-0.13255200	-2.16091000	0.41898200
H	-1.55054600	-0.11568900	1.43248400
H	-0.97185400	2.18220200	0.28154000
O	-2.13655800	-0.18856400	-0.55447100
H	-2.64133300	-0.98080500	-0.34187100

P3

C	-0.39453300	-1.24195800	-0.19311900
C	-0.39433900	1.24191400	-0.19332600
S	0.73997500	-0.00015400	-0.57681900
C	-1.57152500	0.71454800	0.27886800
C	-1.57163900	-0.71432100	0.27900300
O	1.92518700	0.00007700	0.76225600
H	-0.11232500	-2.27292500	-0.32765200
H	-0.11195500	2.27281000	-0.32803200
H	-2.40984800	1.32021100	0.58942300
H	-2.41005700	-1.31979400	0.58966800
H	1.39530200	0.00044400	1.57909600

TS1

C	-0.62632100	-0.11332200	0.74013800
C	1.52192400	0.15215700	-0.48118800
S	0.59042600	-1.17864200	0.10388900
C	0.94218000	1.35906400	-0.17322300
C	-0.26479100	1.21477400	0.54833200
H	-1.37190700	-0.50240300	1.41111900
H	1.36762200	2.31192900	-0.45838000
H	-0.87778900	2.03500600	0.89372700
O	-2.32501400	-0.10302300	-0.61044900
H	-1.83289600	0.18958800	-1.39368800
H	2.43031500	-0.02770400	-1.03575800

TS2

C	-0.02148100	-1.00426400	0.56053200
C	0.92026200	1.15283600	-0.22657200
S	1.43097800	-0.51664900	-0.21685800
C	-0.30740700	1.30880800	0.32595200
C	-0.90288300	0.06165700	0.74612500
H	1.56550700	1.90360000	-0.65635600
H	-0.19008600	-2.03980900	0.80942100
H	-1.73758100	0.00753600	1.42762300
H	-0.81716700	2.25885900	0.40441500
O	-2.27186200	-0.33213400	-0.68775000
H	-1.67237700	-0.32095700	-1.44959100

TS3

C	-0.49140100	-1.24174500	-0.16834100
C	-0.49138900	1.24174200	-0.16835600
S	0.58118400	-0.00001000	-0.71873500
C	-1.60942600	0.71625500	0.40946000
C	-1.60943300	-0.71623900	0.40946900
O	2.41440300	0.00000500	0.75278300
H	-2.40917900	1.31874400	0.81959500
H	-2.40919200	-1.31871500	0.81961100
H	-0.22115000	-2.27747700	-0.30171200
H	-0.22112600	2.27747000	-0.30174000
H	1.85637500	0.00001500	1.54836200

Table S2. Expectation value of the $\langle S^2 \rangle$ operator at the reported theoretical levels.

System	IMx	IM3	TS1	TS2	TS3	P1	P2	P3
Quantum model	(0,2)	(0,2)	(0,2)	(0,2)	(0,2)	(0,2)	(0,2)	(0,2)
ω B97XD/aug-cc-pVTZ	0.7553	0.7574	0.7804	0.7785	0.7537	0.7788	0.7585	0.7574
UM05-2x/aug-cc-pVTZ	0.7538	0.7526	0.7818	0.7776	0.7639	0.7800	0.7579	0.7526
UM06-2x/aug-cc-pVTZ	0.7538	0.7534	0.7756	0.7719	0.7637	0.7715	0.7576	0.7534
HF/6-31+G* (CBS-QB3)	1.0321	0.9535	1.1494	1.1506	0.7662	0.9482	0.8355	0.9535
HF/aug-cc-pVTZ	0.9032	0.9742	1.2029	1.1361	0.7569	0.9509	0.8061	0.9299

Table S3: Kinetic rate constants for the reactions involved in the chemical pathways 1–3 by means of RRKM theory at different pressure and temperatures, according to the computed CBS-QB3 energy profiles. ($x=1,2$)**Table S3a:** $T= 298$ K.

Reaction	IMx→P1	IMx→P2	IM3→P3	R→P1	R→P2	R→P3
Pressure	(s ⁻¹)	(s ⁻¹)	(s ⁻¹)	(cm ³ mol ⁻¹ s ⁻¹)	(cm ³ mol ⁻¹ s ⁻¹)	(cm ³ mol ⁻¹ s ⁻¹)
1.00×10 ⁸	7.69×10 ¹¹	6.81×10 ¹⁰	1.03×10 ⁻¹²	1.67×10 ⁻¹²	1.48×10 ⁻¹³	3.35×10 ⁻¹³
1.00×10 ⁶	7.69×10 ¹¹	6.81×10 ¹⁰	1.03×10 ⁻¹²	1.67×10 ⁻¹²	1.48×10 ⁻¹³	3.34×10 ⁻¹³
1.00×10 ⁴	7.13×10 ¹¹	6.73×10 ¹⁰	9.44×10 ¹¹	1.55×10 ⁻¹²	1.46×10 ⁻¹³	3.06×10 ⁻¹³
1.00×10 ²	9.15×10 ¹⁰	3.35×10 ¹⁰	9.99×10 ¹⁰	1.99×10 ⁻¹³	7.28×10 ⁻¹⁴	3.23×10 ⁻¹⁴
1.00×10 ⁰	1.05×10 ⁹	7.81×10 ⁸	1.11×10 ⁹	2.29×10 ⁻¹⁵	1.69×10 ⁻¹⁵	3.58×10 ⁻¹⁶
1.00×10 ⁻²	1.06×10 ⁷	7.96×10 ⁶	1.11×10 ⁷	2.29×10 ⁻¹⁷	1.73×10 ⁻¹⁷	3.59×10 ⁻¹⁸
1.00×10 ⁻⁴	1.06×10 ⁵	7.96×10 ⁴	1.11×10 ⁵	2.29×10 ⁻¹⁹	1.73×10 ⁻¹⁹	3.59×10 ⁻²⁰
1.00×10 ⁻⁶	1.06×10 ³	7.96×10 ²	1.11×10 ³	2.29×10 ⁻²¹	1.73×10 ⁻²¹	3.59×10 ⁻²²
1.00×10 ⁻⁸	1.06×10 ¹	7.96×10 ⁰	1.11×10 ¹	2.29×10 ⁻²³	1.73×10 ⁻²³	3.59×10 ⁻²⁴
1.00×10 ⁻¹⁰	1.06×10 ⁻¹	7.96×10 ⁻²	1.11×10 ⁻¹	2.29×10 ⁻²⁵	1.73×10 ⁻²⁵	3.59×10 ⁻²⁶

Table S3b: $T= 322$ K.

Reaction	IMx→P1	IMx→P2	IM3→P3	R→P1	R→P2	R→P3
Pressure	(s ⁻¹)	(s ⁻¹)	(s ⁻¹)	(cm ³ mol ⁻¹ s ⁻¹)	(cm ³ mol ⁻¹ s ⁻¹)	(cm ³ mol ⁻¹ s ⁻¹)
1.00×10 ⁸	8.22×10 ¹¹	8.40×10 ¹⁰	1.05×10 ¹²	1.51×10 ⁻¹²	1.54×10 ⁻¹³	3.28×10 ⁻¹³
1.00×10 ⁶	8.21×10 ¹¹	8.40×10 ¹⁰	1.05×10 ¹²	1.51×10 ⁻¹²	1.54×10 ⁻¹³	3.28×10 ⁻¹³
1.00×10 ⁴	7.56×10 ¹¹	8.28×10 ¹⁰	9.54×10 ¹¹	1.39×10 ⁻¹²	1.52×10 ⁻¹³	2.98×10 ⁻¹³
1.00×10 ²	8.86×10 ¹⁰	3.79×10 ¹⁰	9.46×10 ¹⁰	1.63×10 ⁻¹³	6.96×10 ⁻¹⁴	2.95×10 ⁻¹⁴
1.00×10 ⁰	1.00×10 ⁹	8.04×10 ⁸	1.04×10 ⁹	1.99×10 ⁻¹⁵	1.59×10 ⁻¹⁵	3.25×10 ⁻¹⁶
1.00×10 ⁻²	1.01×10 ⁷	8.17×10 ⁶	1.04×10 ⁷	1.84×10 ⁻¹⁷	1.50×10 ⁻¹⁷	3.25×10 ⁻¹⁸
1.00×10 ⁻⁴	1.01×10 ⁵	8.17×10 ⁴	1.04×10 ⁵	1.84×10 ⁻¹⁹	1.50×10 ⁻¹⁹	3.25×10 ⁻²⁰
1.00×10 ⁻⁶	1.01×10 ³	8.17×10 ²	1.04×10 ³	1.84×10 ⁻²¹	1.50×10 ⁻²¹	3.25×10 ⁻²²
1.00×10 ⁻⁸	1.01×10 ¹	8.17×10 ⁰	1.04×10 ¹	1.84×10 ⁻²³	1.50×10 ⁻²³	3.25×10 ⁻²⁴
1.00×10 ⁻¹⁰	1.01×10 ⁻¹	8.17×10 ⁻²	1.04×10 ⁻¹	1.84×10 ⁻²⁵	1.50×10 ⁻²⁵	3.25×10 ⁻²⁶

Table S3c: $T= 353$ K.

Reaction Pressure	IMx→P1 (s ⁻¹)	IMx→P2 (s ⁻¹)	IM3→P3 (s ⁻¹)	R→P1 (cm ³ mol ⁻¹ s ⁻¹)	R→P2 (cm ³ mol ⁻¹ s ⁻¹)	R→P3 (cm ³ mol ⁻¹ s ⁻¹)
1.00×10 ⁸	8.82×10 ¹¹	1.05×10 ¹¹	1.07×10 ¹²	1.36×10 ⁻¹²	1.63×10 ⁻¹³	3.24×10 ⁻¹³
1.00×10 ⁶	8.81×10 ¹¹	1.05×10 ¹¹	1.07×10 ¹²	1.36×10 ⁻¹²	1.63×10 ⁻¹³	3.23×10 ⁻¹³
1.00×10 ⁴	8.03×10 ¹¹	1.04×10 ¹¹	9.62×10 ¹¹	1.24×10 ⁻¹²	1.60×10 ⁻¹³	2.91×10 ⁻¹³
1.00×10 ²	8.45×10 ¹⁰	4.26×10 ¹⁰	8.85×10 ¹⁰	1.31×10 ⁻¹³	6.58×10 ⁻¹⁴	2.68×10 ⁻¹⁴
1.00×10 ⁰	9.43×10 ⁸	8.11×10 ⁸	9.65×10 ⁸	1.73×10 ⁻¹⁵	1.49×10 ⁻¹⁵	2.92×10 ⁻¹⁶
1.00×10 ⁻²	9.44×10 ⁶	8.21×10 ⁶	9.66×10 ⁶	1.46×10 ⁻¹⁷	1.27×10 ⁻¹⁷	2.92×10 ⁻¹⁸
1.00×10 ⁻⁴	9.44×10 ⁴	8.22×10 ⁴	9.66×10 ⁴	1.46×10 ⁻¹⁹	1.27×10 ⁻¹⁹	2.92×10 ⁻²⁰
1.00×10 ⁻⁶	9.44×10 ²	8.22×10 ²	9.66×10 ²	1.46×10 ⁻²¹	1.27×10 ⁻²¹	2.92×10 ⁻²²
1.00×10 ⁻⁸	9.44×10 ⁰	8.22×10 ⁰	9.66×10 ⁰	1.46×10 ⁻²³	1.27×10 ⁻²³	2.92×10 ⁻²⁴
1.00×10 ⁻¹⁰	9.44×10 ⁻²	8.22×10 ⁻²	9.66×10 ⁻²	1.46×10 ⁻²⁵	1.27×10 ⁻²⁵	2.92×10 ⁻²⁶

Table S3d: $T= 380$ K.

Reaction Pressure	IMx→P1 (s ⁻¹)	IMx→P2 (s ⁻¹)	IM3→P3 (s ⁻¹)	R→P1 (cm ³ mol ⁻¹ s ⁻¹)	R→P2 (cm ³ mol ⁻¹ s ⁻¹)	R→P3 (cm ³ mol ⁻¹ s ⁻¹)
1.00×10 ⁸	9.27×10 ¹¹	1.24×10 ¹¹	1.08×10 ¹²	1.27×10 ⁻¹²	1.70×10 ⁻¹³	3.22×10 ⁻¹³
1.00×10 ⁶	9.26×10 ¹¹	1.24×10 ¹¹	1.08×10 ¹²	1.27×10 ⁻¹²	1.70×10 ⁻¹³	3.21×10 ⁻¹³
1.00×10 ⁴	8.37×10 ¹¹	1.22×10 ¹¹	9.67×10 ¹¹	1.15×10 ⁻¹²	1.67×10 ⁻¹³	2.87×10 ⁻¹³
1.00×10 ²	8.11×10 ¹⁰	4.56×10 ¹⁰	8.39×10 ¹⁰	1.11×10 ⁻¹³	6.25×10 ⁻¹⁴	2.49×10 ⁻¹⁴
1.00×10 ⁰	8.94×10 ⁸	8.04×10 ⁸	9.09×10 ⁸	1.56×10 ⁻¹⁵	1.40×10 ⁻¹⁵	2.70×10 ⁻¹⁶
1.00×10 ⁻²	8.95×10 ⁶	8.12×10 ⁶	9.10×10 ⁶	1.23×10 ⁻¹⁷	1.11×10 ⁻¹⁷	2.70×10 ⁻¹⁸
1.00×10 ⁻⁴	8.95×10 ⁴	8.12×10 ⁴	9.10×10 ⁴	1.23×10 ⁻¹⁹	1.11×10 ⁻¹⁹	2.70×10 ⁻²⁰
1.00×10 ⁻⁶	8.95×10 ²	8.12×10 ²	9.10×10 ²	1.23×10 ⁻²¹	1.11×10 ⁻²¹	2.70×10 ⁻²²
1.00×10 ⁻⁸	8.95×10 ⁰	8.12×10 ⁰	9.10×10 ⁰	1.23×10 ⁻²³	1.11×10 ⁻²³	2.70×10 ⁻²⁴
1.00×10 ⁻¹⁰	8.95×10 ⁻²	8.12×10 ⁻²	9.10×10 ⁻²	1.23×10 ⁻²⁵	1.11×10 ⁻²⁵	2.70×10 ⁻²⁶

Table S3e: $T= 400$ K.

Reaction Pressure	IMx→P1 (s ⁻¹)	IMx→P2 (s ⁻¹)	IM3→P3 (s ⁻¹)	R→P1 (cm ³ mol ⁻¹ s ⁻¹)	R→P2 (cm ³ mol ⁻¹ s ⁻¹)	R→P3 (cm ³ mol ⁻¹ s ⁻¹)
1.00×10 ⁸	9.58×10 ¹¹	1.38×10 ¹¹	1.09×10 ¹²	1.22×10 ⁻¹²	1.76×10 ⁻¹³	3.22×10 ⁻¹³
1.00×10 ⁶	9.57×10 ¹¹	1.38×10 ¹¹	1.09×10 ¹²	1.22×10 ⁻¹²	1.76×10 ⁻¹³	3.21×10 ⁻¹³
1.00×10 ⁴	8.58×10 ¹¹	1.35×10 ¹¹	9.70×10 ¹¹	1.09×10 ⁻¹²	1.72×10 ⁻¹³	2.86×10 ⁻¹³
1.00×10 ²	7.86×10 ¹⁰	4.73×10 ¹⁰	8.08×10 ¹⁰	9.99×10 ⁻¹⁴	6.02×10 ⁻¹⁴	2.38×10 ⁻¹⁴
1.00×10 ⁰	8.60×10 ⁸	7.93×10 ⁸	8.72×10 ⁸	1.47×10 ⁻¹⁵	1.35×10 ⁻¹⁵	2.57×10 ⁻¹⁶
1.00×10 ⁻²	8.61×10 ⁶	8.00×10 ⁶	8.73×10 ⁶	1.10×10 ⁻¹⁷	1.02×10 ⁻¹⁷	2.57×10 ⁻¹⁸
1.00×10 ⁻⁴	8.61×10 ⁴	8.00×10 ⁴	8.73×10 ⁴	1.10×10 ⁻¹⁹	1.02×10 ⁻¹⁹	2.57×10 ⁻²⁰
1.00×10 ⁻⁶	8.61×10 ²	8.00×10 ²	8.73×10 ²	1.10×10 ⁻²¹	1.02×10 ⁻²¹	2.57×10 ⁻²²
1.00×10 ⁻⁸	8.61×10 ⁰	8.00×10 ⁰	8.73×10 ⁰	1.10×10 ⁻²³	1.02×10 ⁻²³	2.57×10 ⁻²⁴
1.00×10 ⁻¹⁰	8.61×10 ⁻²	8.00×10 ⁻²	8.73×10 ⁻²	1.10×10 ⁻²⁵	1.02×10 ⁻²⁵	2.57×10 ⁻²⁶

Table S3f: $T= 425$ K.

Reaction Pressure	IMx→P1 (s ⁻¹)	IMx→P2 (s ⁻¹)	IM3→P3 (s ⁻¹)	R→P1 (cm ³ mol ⁻¹ s ⁻¹)	R→P2 (cm ³ mol ⁻¹ s ⁻¹)	R→P3 (cm ³ mol ⁻¹ s ⁻¹)
1.00×10 ⁸	9.93×10 ¹¹	1.56×10 ¹¹	1.10×10 ¹²	1.16×10 ⁻¹²	1.83×10 ⁻¹³	3.23×10 ⁻¹³
1.00×10 ⁶	9.91×10 ¹¹	1.56×10 ¹¹	1.10×10 ¹²	1.16×10 ⁻¹²	1.83×10 ⁻¹³	3.22×10 ⁻¹³
1.00×10 ⁴	8.82×10 ¹¹	1.52×10 ¹¹	9.72×10 ¹¹	1.03×10 ⁻¹²	1.78×10 ⁻¹³	2.85×10 ⁻¹³
1.00×10 ²	7.56×10 ¹⁰	4.89×10 ¹⁰	7.72×10 ¹⁰	8.87×10 ⁻¹⁴	5.73×10 ⁻¹⁴	2.26×10 ⁻¹⁴
1.00×10 ⁰	8.22×10 ⁸	7.75×10 ⁸	8.30×10 ⁸	1.37×10 ⁻¹⁵	1.30×10 ⁻¹⁵	2.43×10 ⁻¹⁶
1.00×10 ⁻²	8.22×10 ⁶	7.81×10 ⁶	8.31×10 ⁶	9.65×10 ⁻¹⁸	9.15×10 ⁻¹⁸	2.43×10 ⁻¹⁸
1.00×10 ⁻⁴	8.22×10 ⁴	7.81×10 ⁴	8.31×10 ⁴	9.65×10 ⁻²⁰	9.16×10 ⁻²⁰	2.43×10 ⁻²⁰
1.00×10 ⁻⁶	8.22×10 ²	7.81×10 ²	8.31×10 ²	9.65×10 ⁻²²	9.16×10 ⁻²²	2.43×10 ⁻²²
1.00×10 ⁻⁸	8.22×10 ⁰	7.81×10 ⁰	8.31×10 ⁰	9.65×10 ⁻²⁴	9.16×10 ⁻²⁴	2.43×10 ⁻²⁴
1.00×10 ⁻¹⁰	8.22×10 ⁻²	7.81×10 ⁻²	8.31×10 ⁻²	9.65×10 ⁻²⁶	9.16×10 ⁻²⁶	2.43×10 ⁻²⁶

Table S3g: $T= 442$ K.

Reaction Pressure	IMx→P1 (s ⁻¹)	IMx→P2 (s ⁻¹)	IM3→P3 (s ⁻¹)	R→P1 (cm ³ mol ⁻¹ s ⁻¹)	R→P2 (cm ³ mol ⁻¹ s ⁻¹)	R→P3 (cm ³ mol ⁻¹ s ⁻¹)
1.00×10 ⁸	1.01×10 ¹²	1.68×10 ¹¹	1.11×10 ¹²	1.14×10 ⁻¹²	1.88×10 ⁻¹³	3.24×10 ⁻¹³
1.00×10 ⁶	1.01×10 ¹²	1.67×10 ¹¹	1.11×10 ¹²	1.13×10 ⁻¹²	1.87×10 ⁻¹³	3.23×10 ⁻¹³
1.00×10 ⁴	8.97×10 ¹¹	1.63×10 ¹¹	9.72×10 ¹¹	1.00×10 ⁻¹²	1.83×10 ⁻¹³	2.85×10 ⁻¹³
1.00×10 ²	7.37×10 ¹⁰	4.96×10 ¹⁰	7.50×10 ¹⁰	8.25×10 ⁻¹⁴	5.56×10 ⁻¹⁴	2.19×10 ⁻¹⁴
1.00×10 ⁰	7.97×10 ⁸	7.61×10 ⁸	8.04×10 ⁸	1.32×10 ⁻¹⁵	1.26×10 ⁻¹⁵	2.35×10 ⁻¹⁶
1.00×10 ⁻²	7.98×10 ⁶	7.66×10 ⁶	8.05×10 ⁶	8.93×10 ⁻¹⁸	8.57×10 ⁻¹⁸	2.35×10 ⁻¹⁸
1.00×10 ⁻⁴	7.98×10 ⁴	7.66×10 ⁴	8.05×10 ⁴	8.93×10 ⁻²⁰	8.57×10 ⁻²⁰	2.35×10 ⁻²⁰
1.00×10 ⁻⁶	7.98×10 ²	7.66×10 ²	8.05×10 ²	8.93×10 ⁻²²	8.57×10 ⁻²²	2.35×10 ⁻²²
1.00×10 ⁻⁸	7.98×10 ⁰	7.66×10 ⁰	8.05×10 ⁰	8.93×10 ⁻²⁴	8.57×10 ⁻²⁴	2.35×10 ⁻²⁴
1.00×10 ⁻¹⁰	7.98×10 ⁻²	7.66×10 ⁻²	8.05×10 ⁻²	8.93×10 ⁻²⁶	8.57×10 ⁻²⁶	2.35×10 ⁻²⁶

Table S3h: $T= 457$ K.

Reaction Pressure	IMx→P1 (s ⁻¹)	IMx→P2 (s ⁻¹)	IM3→P3 (s ⁻¹)	R→P1 (cm ³ mol ⁻¹ s ⁻¹)	R→P2 (cm ³ mol ⁻¹ s ⁻¹)	R→P3 (cm ³ mol ⁻¹ s ⁻¹)
1.00×10 ⁸	1.03×10 ¹²	1.78×10 ¹¹	1.11×10 ¹²	1.11×10 ⁻¹²	1.92×10 ⁻¹³	3.25×10 ⁻¹³
1.00×10 ⁶	1.03×10 ¹²	1.78×10 ¹¹	1.11×10 ¹²	1.11×10 ⁻¹²	1.92×10 ⁻¹³	3.25×10 ⁻¹³
1.00×10 ⁴	9.08×10 ¹¹	1.73×10 ¹¹	9.73×10 ¹¹	9.79×10 ⁻¹³	1.86×10 ⁻¹³	2.85×10 ⁻¹³
1.00×10 ²	7.21×10 ¹⁰	5.01×10 ¹⁰	7.32×10 ¹⁰	7.77×10 ⁻¹⁴	5.41×10 ⁻¹⁴	2.14×10 ⁻¹⁴
1.00×10 ⁰	7.77×10 ⁸	7.48×10 ⁸	7.83×10 ⁸	1.28×10 ⁻¹⁵	1.24×10 ⁻¹⁵	2.29×10 ⁻¹⁶
1.00×10 ⁻²	7.78×10 ⁶	7.52×10 ⁶	7.83×10 ⁶	8.38×10 ⁻¹⁸	8.11×10 ⁻¹⁸	2.29×10 ⁻¹⁸
1.00×10 ⁻⁴	7.78×10 ⁴	7.52×10 ⁴	7.83×10 ⁴	8.38×10 ⁻²⁰	8.11×10 ⁻²⁰	2.29×10 ⁻²⁰
1.00×10 ⁻⁶	7.78×10 ²	7.52×10 ²	7.83×10 ²	8.38×10 ⁻²²	8.11×10 ⁻²²	2.29×10 ⁻²²
1.00×10 ⁻⁸	7.78×10 ⁰	7.52×10 ⁰	7.83×10 ⁰	8.38×10 ⁻²⁴	8.11×10 ⁻²⁴	2.29×10 ⁻²⁴
1.00×10 ⁻¹⁰	7.78×10 ⁻²	7.52×10 ⁻²	7.83×10 ⁻²	8.38×10 ⁻²⁶	8.11×10 ⁻²⁶	2.29×10 ⁻²⁶

Table S3i: $T=471$ K.

Reaction Pressure	IMx→P1 (s ⁻¹)	IMx→P2 (s ⁻¹)	IM3→P3 (s ⁻¹)	R→P1 (cm ³ mol ⁻¹ s ⁻¹)	R→P2 (cm ³ mol ⁻¹ s ⁻¹)	R→P3 (cm ³ mol ⁻¹ s ⁻¹)
1.00×10 ⁸	1.05×10 ¹²	1.87×10 ¹¹	1.12×10 ¹²	1.10×10 ⁻¹²	1.96×10 ⁻¹³	3.27×10 ⁻¹³
1.00×10 ⁶	1.05×10 ¹²	1.87×10 ¹¹	1.11×10 ¹²	1.09×10 ⁻¹²	1.96×10 ⁻¹³	3.26×10 ⁻¹³
1.00×10 ⁴	9.18×10 ¹¹	1.82×10 ¹¹	9.73×10 ¹¹	9.60×10 ⁻¹³	1.90×10 ⁻¹³	2.85×10 ⁻¹³
1.00×10 ²	7.06×10 ¹⁰	5.05×10 ¹⁰	7.15×10 ¹⁰	7.38×10 ⁻¹⁴	5.27×10 ⁻¹⁴	2.10×10 ⁻¹⁴
1.00×10 ⁰	7.59×10 ⁸	7.35×10 ⁸	7.64×10 ⁸	1.25×10 ⁻¹⁵	1.21×10 ⁻¹⁵	2.24×10 ⁻¹⁶
1.00×10 ⁻²	7.59×10 ⁶	7.39×10 ⁶	7.65×10 ⁶	7.94×10 ⁻¹⁸	7.73×10 ⁻¹⁸	2.24×10 ⁻¹⁸
1.00×10 ⁻⁴	7.59×10 ⁴	7.39×10 ⁴	7.65×10 ⁴	7.94×10 ⁻²⁰	7.73×10 ⁻²⁰	2.24×10 ⁻²⁰
1.00×10 ⁻⁶	7.59×10 ²	7.39×10 ²	7.65×10 ²	7.94×10 ⁻²²	7.73×10 ⁻²²	2.24×10 ⁻²²
1.00×10 ⁻⁸	7.59×10 ⁰	7.39×10 ⁰	7.65×10 ⁰	7.94×10 ⁻²⁴	7.73×10 ⁻²⁴	2.24×10 ⁻²⁴
1.00×10 ⁻¹⁰	7.59×10 ⁻²	7.39×10 ⁻²	7.65×10 ⁻²	7.94×10 ⁻²⁶	7.73×10 ⁻²⁶	2.24×10 ⁻²⁶

Table S4: Thermodynamic equilibrium constants, K_p (in bar⁻¹), unimolecular kinetic rate constants (k_2 s⁻¹), effective bimolecular rate constants (cm³ molecule⁻¹ s⁻¹) and branching ratios (in %) for the chemical pathways **1–3** ($x=1,2$) at different pressures and temperatures, using RRKM theory, and according to the computed CBS-QB3 energy profiles.**Table S4a:**

		$P = 10^{-10}$ bar									
T (K)	Equilibrium constants (bar ⁻¹)		Unimolecular rate constants (s ⁻¹)			Effective rate constants (cm ³ molecule ⁻¹ s ⁻¹)			Branching ratios (%)		
	$K_p(x)$	$K_p(3)$	$k_2(1)$	$k_2(2)$	$k_2(3)$	$k_{\text{eff}}(1)$	$k_{\text{eff}}(2)$	$k_{\text{eff}}(3)$	$R(1)$	$R(2)$	$R(3)$
	R⇌IMx	R⇌IM3	IMx→P1	IMx→P2	IM3→P3	R→P1	R→P2	R→P3			
298	5.27×10 ⁻⁵	7.87×10 ⁻⁶	1.06×10 ⁻¹	7.96×10 ⁻²	1.11×10 ⁻¹	2.29×10 ⁻²⁵	1.73×10 ⁻²⁵	3.59×10 ⁻²⁶	52.30	39.51	8.20
322	4.46×10 ⁻⁵	7.59×10 ⁻⁶	1.01×10 ⁻¹	8.17×10 ⁻²	1.04×10 ⁻¹	1.84×10 ⁻²⁵	1.50×10 ⁻²⁵	3.25×10 ⁻²⁶	50.20	40.93	8.87
353	3.76×10 ⁻⁵	7.35×10 ⁻⁶	9.44×10 ⁻²	8.22×10 ⁻²	9.66×10 ⁻²	1.46×10 ⁻²⁵	1.27×10 ⁻²⁵	2.92×10 ⁻²⁶	48.31	42.03	9.66
380	3.33×10 ⁻⁵	7.22×10 ⁻⁶	8.95×10 ⁻²	8.12×10 ⁻²	9.10×10 ⁻²	1.23×10 ⁻²⁵	1.11×10 ⁻²⁵	2.70×10 ⁻²⁶	47.13	42.53	10.34
400	3.09×10 ⁻⁵	7.16×10 ⁻⁶	8.61×10 ⁻²	8.00×10 ⁻²	8.73×10 ⁻²	1.10×10 ⁻²⁵	1.02×10 ⁻²⁵	2.57×10 ⁻²⁶	46.28	42.91	10.81
425	2.85×10 ⁻⁵	7.12×10 ⁻⁶	8.22×10 ⁻²	7.81×10 ⁻²	8.31×10 ⁻²	9.65×10 ⁻²⁶	9.16×10 ⁻²⁶	2.43×10 ⁻²⁶	45.43	43.13	11.44
442	2.72×10 ⁻⁵	7.11×10 ⁻⁶	7.98×10 ⁻²	7.66×10 ⁻²	8.05×10 ⁻²	8.93×10 ⁻²⁶	8.57×10 ⁻²⁶	2.35×10 ⁻²⁶	44.99	43.17	11.84
457	2.62×10 ⁻⁵	7.11×10 ⁻⁶	7.78×10 ⁻²	7.52×10 ⁻²	7.83×10 ⁻²	8.38×10 ⁻²⁶	8.11×10 ⁻²⁶	2.29×10 ⁻²⁶	44.62	43.18	12.19
471	2.54×10 ⁻⁵	7.12×10 ⁻⁶	7.59×10 ⁻²	7.39×10 ⁻²	7.65×10 ⁻²	7.94×10 ⁻²⁶	7.73×10 ⁻²⁶	2.24×10 ⁻²⁶	44.33	43.16	12.51

Table S4b:

$P = 10^{-8}$ bar											
T (K)	Equilibrium constants (bar^{-1})		Unimolecular rate constants (s^{-1})			Effective rate constants ($\text{cm}^3 \text{molecule}^{-1} \text{s}^{-1}$)			Branching ratios (%)		
	$K_P(x)$	$K_P(3)$	$k_2(1)$	$k_2(2)$	$k_2(3)$	$k_{\text{eff}}(1)$	$k_{\text{eff}}(2)$	$k_{\text{eff}}(3)$	$R(1)$	$R(2)$	$R(3)$
	$R \rightleftharpoons \text{IM}x$	$R \rightleftharpoons \text{IM}3$	$\text{IM}x \rightarrow \text{P}1$	$\text{IM}x \rightarrow \text{P}2$	$\text{IM}3 \rightarrow \text{P}3$	$R \rightarrow \text{P}1$	$R \rightarrow \text{P}2$	$R \rightarrow \text{P}3$			
298	5.27×10^{-5}	7.87×10^{-6}	1.06×10^1	7.96×10^0	1.11×10^1	2.29×10^{-23}	1.73×10^{-23}	3.59×10^{-24}	52.30	39.51	8.20
322	4.46×10^{-5}	7.59×10^{-6}	1.01×10^1	8.17×10^0	1.04×10^1	1.84×10^{-23}	1.50×10^{-23}	3.25×10^{-24}	50.20	40.93	8.87
353	3.76×10^{-5}	7.35×10^{-6}	9.44×10^0	8.22×10^0	9.66×10^0	1.46×10^{-23}	1.27×10^{-23}	2.92×10^{-24}	48.31	42.03	9.66
380	3.33×10^{-5}	7.22×10^{-6}	8.95×10^0	8.12×10^0	9.10×10^0	1.23×10^{-23}	1.11×10^{-23}	2.70×10^{-24}	47.13	42.53	10.34
400	3.09×10^{-5}	7.16×10^{-6}	8.61×10^0	8.00×10^0	8.73×10^0	1.10×10^{-23}	1.02×10^{-23}	2.57×10^{-24}	46.28	42.91	10.81
425	2.85×10^{-5}	7.12×10^{-6}	8.22×10^0	7.81×10^0	8.31×10^0	9.65×10^{-24}	9.16×10^{-24}	2.43×10^{-24}	45.43	43.13	11.44
442	2.72×10^{-5}	7.11×10^{-6}	7.98×10^0	7.66×10^0	8.05×10^0	8.93×10^{-24}	8.57×10^{-24}	2.35×10^{-24}	44.99	43.17	11.84
457	2.62×10^{-5}	7.11×10^{-6}	7.78×10^0	7.52×10^0	7.83×10^0	8.38×10^{-24}	8.11×10^{-24}	2.29×10^{-24}	44.62	43.18	12.19
471	2.54×10^{-5}	7.12×10^{-6}	7.59×10^0	7.39×10^0	7.65×10^0	7.94×10^{-24}	7.73×10^{-24}	2.24×10^{-24}	44.33	43.16	12.51

Table S4c:

$P = 10^{-6}$ bar											
T (K)	Equilibrium constants (bar^{-1})		Unimolecular rate constants (s^{-1})			Effective rate constants ($\text{cm}^3 \text{molecule}^{-1} \text{s}^{-1}$)			Branching ratios (%)		
	$K_P(x)$	$K_P(3)$	$k_2(1)$	$k_2(2)$	$k_2(3)$	$k_{\text{eff}}(1)$	$k_{\text{eff}}(2)$	$k_{\text{eff}}(3)$	$R(1)$	$R(2)$	$R(3)$
	$R \rightleftharpoons \text{IM}x$	$R \rightleftharpoons \text{IM}3$	$\text{IM}x \rightarrow \text{P}1$	$\text{IM}x \rightarrow \text{P}2$	$\text{IM}3 \rightarrow \text{P}3$	$R \rightarrow \text{P}1$	$R \rightarrow \text{P}2$	$R \rightarrow \text{P}3$			
298	5.27×10^{-5}	7.87×10^{-6}	1.06×10^3	7.96×10^2	1.11×10^3	2.29×10^{-21}	1.73×10^{-21}	3.59×10^{-22}	52.30	39.51	8.20
322	4.46×10^{-5}	7.59×10^{-6}	1.01×10^3	8.17×10^2	1.04×10^3	1.84×10^{-21}	1.50×10^{-21}	3.25×10^{-22}	50.20	40.93	8.87
353	3.76×10^{-5}	7.35×10^{-6}	9.44×10^2	8.22×10^2	9.66×10^2	1.46×10^{-21}	1.27×10^{-21}	2.92×10^{-22}	48.31	42.03	9.66
380	3.33×10^{-5}	7.22×10^{-6}	8.95×10^2	8.12×10^2	9.10×10^2	1.23×10^{-21}	1.11×10^{-21}	2.70×10^{-22}	47.13	42.53	10.34
400	3.09×10^{-5}	7.16×10^{-6}	8.61×10^2	8.00×10^2	8.73×10^2	1.10×10^{-21}	1.02×10^{-21}	2.57×10^{-22}	46.28	42.91	10.81
425	2.85×10^{-5}	7.12×10^{-6}	8.22×10^2	7.81×10^2	8.31×10^2	9.65×10^{-22}	9.16×10^{-22}	2.43×10^{-22}	45.43	43.13	11.44
442	2.72×10^{-5}	7.11×10^{-6}	7.98×10^2	7.66×10^2	8.05×10^2	8.93×10^{-22}	8.57×10^{-22}	2.35×10^{-22}	44.99	43.17	11.84
457	2.62×10^{-5}	7.11×10^{-6}	7.78×10^2	7.52×10^2	7.83×10^2	8.38×10^{-22}	8.11×10^{-22}	2.29×10^{-22}	44.62	43.18	12.19
471	2.54×10^{-5}	7.12×10^{-6}	7.59×10^2	7.39×10^2	7.65×10^2	7.94×10^{-22}	7.73×10^{-22}	2.24×10^{-22}	44.33	43.16	12.51

Table S4d:

$P = 10^{-4}$ bar											
T (K)	Equilibrium constants (bar ⁻¹)		Unimolecular rate constants (s ⁻¹)			Effective rate constants (cm ³ molecule ⁻¹ s ⁻¹)			Branching ratios (%)		
	$K_P(x)$	$K_P(3)$	$k_2(1)$	$k_2(2)$	$k_2(3)$	$k_{\text{eff}}(1)$	$k_{\text{eff}}(2)$	$k_{\text{eff}}(3)$	$R(1)$	$R(2)$	$R(3)$
	R \rightleftharpoons IMx	R \rightleftharpoons IM3	IMx \rightarrow P1	IMx \rightarrow P2	IM3 \rightarrow P3	R \rightarrow P1	R \rightarrow P2	R \rightarrow P3			
298	5.27 \times 10 ⁻⁵	7.87 \times 10 ⁻⁶	1.06 \times 10 ⁵	7.96 \times 10 ⁴	1.11 \times 10 ⁵	2.29 \times 10 ⁻¹⁹	1.73 \times 10 ⁻¹⁹	3.59 \times 10 ⁻²⁰	52.30	39.51	8.20
322	4.46 \times 10 ⁻⁵	7.59 \times 10 ⁻⁶	1.01 \times 10 ⁵	8.17 \times 10 ⁴	1.04 \times 10 ⁵	1.84 \times 10 ⁻¹⁹	1.50 \times 10 ⁻¹⁹	3.25 \times 10 ⁻²⁰	50.20	40.93	8.87
353	3.76 \times 10 ⁻⁵	7.35 \times 10 ⁻⁶	9.44 \times 10 ⁴	8.22 \times 10 ⁴	9.66 \times 10 ⁴	1.46 \times 10 ⁻¹⁹	1.27 \times 10 ⁻¹⁹	2.92 \times 10 ⁻²⁰	48.31	42.03	9.66
380	3.33 \times 10 ⁻⁵	7.22 \times 10 ⁻⁶	8.95 \times 10 ⁴	8.12 \times 10 ⁴	9.10 \times 10 ⁴	1.23 \times 10 ⁻¹⁹	1.11 \times 10 ⁻¹⁹	2.70 \times 10 ⁻²⁰	47.13	42.53	10.34
400	3.09 \times 10 ⁻⁵	7.16 \times 10 ⁻⁶	8.61 \times 10 ⁴	8.00 \times 10 ⁴	8.73 \times 10 ⁴	1.10 \times 10 ⁻¹⁹	1.02 \times 10 ⁻¹⁹	2.57 \times 10 ⁻²⁰	46.28	42.91	10.81
425	2.85 \times 10 ⁻⁵	7.12 \times 10 ⁻⁶	8.22 \times 10 ⁴	7.81 \times 10 ⁴	8.31 \times 10 ⁴	9.65 \times 10 ⁻²⁰	9.16 \times 10 ⁻²⁰	2.43 \times 10 ⁻²⁰	45.43	43.13	11.44
442	2.72 \times 10 ⁻⁵	7.11 \times 10 ⁻⁶	7.98 \times 10 ⁴	7.66 \times 10 ⁴	8.05 \times 10 ⁴	8.93 \times 10 ⁻²⁰	8.57 \times 10 ⁻²⁰	2.35 \times 10 ⁻²⁰	44.99	43.17	11.84
457	2.62 \times 10 ⁻⁵	7.11 \times 10 ⁻⁶	7.78 \times 10 ⁴	7.52 \times 10 ⁴	7.83 \times 10 ⁴	8.38 \times 10 ⁻²⁰	8.11 \times 10 ⁻²⁰	2.29 \times 10 ⁻²⁰	44.62	43.18	12.19
471	2.54 \times 10 ⁻⁵	7.12 \times 10 ⁻⁶	7.59 \times 10 ⁴	7.39 \times 10 ⁴	7.65 \times 10 ⁴	7.94 \times 10 ⁻²⁰	7.73 \times 10 ⁻²⁰	2.24 \times 10 ⁻²⁰	44.33	43.16	12.51

Table S4e:

$P = 10^{-2}$ bar											
T (K)	Equilibrium constants (bar ⁻¹)		Unimolecular rate constants (s ⁻¹)			Effective rate constants (cm ³ molecule ⁻¹ s ⁻¹)			Branching ratios (%)		
	$K_P(x)$	$K_P(3)$	$k_2(1)$	$k_2(2)$	$k_2(3)$	$k_{\text{eff}}(1)$	$k_{\text{eff}}(2)$	$k_{\text{eff}}(3)$	$R(1)$	$R(2)$	$R(3)$
	R \rightleftharpoons IMx	R \rightleftharpoons IM3	IMx \rightarrow P1	IMx \rightarrow P2	IM3 \rightarrow P3	R \rightarrow P1	R \rightarrow P2	R \rightarrow P3			
298	5.27 \times 10 ⁻⁵	7.87 \times 10 ⁻⁶	1.06 \times 10 ⁶	7.96 \times 10 ⁶	1.11 \times 10 ⁷	2.29 \times 10 ⁻¹⁷	1.73 \times 10 ⁻¹⁷	3.59 \times 10 ⁻¹⁸	52.30	39.51	8.20
322	4.46 \times 10 ⁻⁵	7.59 \times 10 ⁻⁶	1.01 \times 10 ⁷	8.17 \times 10 ⁶	1.04 \times 10 ⁷	1.84 \times 10 ⁻¹⁷	1.50 \times 10 ⁻¹⁷	3.25 \times 10 ⁻¹⁸	50.20	40.93	8.87
353	3.76 \times 10 ⁻⁵	7.35 \times 10 ⁻⁶	9.44 \times 10 ⁶	8.21 \times 10 ⁶	9.66 \times 10 ⁶	1.46 \times 10 ⁻¹⁷	1.27 \times 10 ⁻¹⁷	2.92 \times 10 ⁻¹⁸	48.31	42.03	9.66
380	3.33 \times 10 ⁻⁵	7.22 \times 10 ⁻⁶	8.95 \times 10 ⁶	8.12 \times 10 ⁶	9.10 \times 10 ⁶	1.23 \times 10 ⁻¹⁷	1.11 \times 10 ⁻¹⁷	2.70 \times 10 ⁻¹⁸	47.13	42.53	10.34
400	3.09 \times 10 ⁻⁵	7.16 \times 10 ⁻⁶	8.61 \times 10 ⁶	8.00 \times 10 ⁶	8.73 \times 10 ⁶	1.10 \times 10 ⁻¹⁷	1.02 \times 10 ⁻¹⁷	2.57 \times 10 ⁻¹⁸	46.28	42.91	10.81
425	2.85 \times 10 ⁻⁵	7.12 \times 10 ⁻⁶	8.22 \times 10 ⁶	7.81 \times 10 ⁶	8.31 \times 10 ⁶	9.65 \times 10 ⁻¹⁸	9.15 \times 10 ⁻¹⁸	2.43 \times 10 ⁻¹⁸	45.45	43.10	11.45
442	2.72 \times 10 ⁻⁵	7.11 \times 10 ⁻⁶	7.98 \times 10 ⁶	7.66 \times 10 ⁶	8.05 \times 10 ⁶	8.93 \times 10 ⁻¹⁸	8.57 \times 10 ⁻¹⁸	2.35 \times 10 ⁻¹⁸	44.99	43.17	11.84
457	2.62 \times 10 ⁻⁵	7.11 \times 10 ⁻⁶	7.78 \times 10 ⁶	7.52 \times 10 ⁶	7.83 \times 10 ⁶	8.38 \times 10 ⁻¹⁸	8.11 \times 10 ⁻¹⁸	2.29 \times 10 ⁻¹⁸	44.62	43.18	12.19
471	2.54 \times 10 ⁻⁵	7.12 \times 10 ⁻⁶	7.59 \times 10 ⁶	7.39 \times 10 ⁶	7.65 \times 10 ⁶	7.94 \times 10 ⁻¹⁸	7.73 \times 10 ⁻¹⁸	2.24 \times 10 ⁻¹⁸	44.33	43.16	12.51

Table S4f:

$P = 1.0$ bar											
T (K)	Equilibrium constants (bar^{-1})		Unimolecular rate constants (s^{-1})			Effective rate constants ($\text{cm}^3 \text{molecule}^{-1} \text{s}^{-1}$)			Branching ratios (%)		
	$K_p(x)$	$K_p(3)$	$k_2(1)$	$k_2(2)$	$k_2(3)$	$k_{\text{eff}}(1)$	$k_{\text{eff}}(2)$	$k_{\text{eff}}(3)$	$R(1)$	$R(2)$	$R(3)$
	$\text{R} \rightleftharpoons \text{IMx}$	$\text{R} \rightleftharpoons \text{IM3}$	$\text{IMx} \rightarrow \text{P1}$	$\text{IMx} \rightarrow \text{P2}$	$\text{IM3} \rightarrow \text{P3}$	$\text{R} \rightarrow \text{P1}$	$\text{R} \rightarrow \text{P2}$	$\text{R} \rightarrow \text{P3}$			
298	5.27×10^{-5}	7.87×10^{-6}	1.05×10^9	7.81×10^8	1.11×10^9	2.29×10^{-15}	1.69×10^{-15}	3.58×10^{-16}	52.79	38.96	8.25
322	4.46×10^{-5}	7.59×10^{-6}	1.00×10^9	8.04×10^8	1.04×10^9	1.99×10^{-15}	1.59×10^{-15}	3.25×10^{-16}	50.96	40.72	8.32
353	3.76×10^{-5}	7.35×10^{-6}	9.43×10^8	8.11×10^8	9.65×10^8	1.73×10^{-15}	1.49×10^{-15}	2.92×10^{-16}	49.26	42.43	8.31
380	3.33×10^{-5}	7.22×10^{-6}	8.94×10^8	8.04×10^8	9.09×10^8	1.56×10^{-15}	1.40×10^{-15}	2.70×10^{-16}	48.30	43.34	8.36
400	3.09×10^{-5}	7.16×10^{-6}	8.60×10^8	7.93×10^8	8.72×10^8	1.47×10^{-15}	1.35×10^{-15}	2.57×10^{-16}	47.77	43.87	8.35
425	2.85×10^{-5}	7.12×10^{-6}	8.22×10^8	7.75×10^8	8.30×10^8	1.37×10^{-15}	1.30×10^{-15}	2.43×10^{-16}	47.03	44.63	8.34
442	2.72×10^{-5}	7.11×10^{-6}	7.97×10^8	7.61×10^8	8.04×10^8	1.32×10^{-15}	1.26×10^{-15}	2.35×10^{-16}	46.89	44.76	8.35
457	2.62×10^{-5}	7.11×10^{-6}	7.77×10^8	7.48×10^8	7.83×10^8	1.28×10^{-15}	1.24×10^{-15}	2.29×10^{-16}	46.56	45.11	8.33
471	2.54×10^{-5}	7.12×10^{-6}	7.59×10^8	7.35×10^8	7.64×10^8	1.25×10^{-15}	1.21×10^{-15}	2.24×10^{-16}	46.57	45.08	8.35

Table S4g:

$P = 10^2$ bar											
T (K)	Equilibrium constants (bar^{-1})		Unimolecular rate constants (s^{-1})			Effective rate constants ($\text{cm}^3 \text{molecule}^{-1} \text{s}^{-1}$)			Branching ratios (%)		
	$K_p(x)$	$K_p(3)$	$k_2(1)$	$k_2(2)$	$k_2(3)$	$k_{\text{eff}}(1)$	$k_{\text{eff}}(2)$	$k_{\text{eff}}(3)$	$R(1)$	$R(2)$	$R(3)$
	$\text{R} \rightleftharpoons \text{IMx}$	$\text{R} \rightleftharpoons \text{IM3}$	$\text{IMx} \rightarrow \text{P1}$	$\text{IMx} \rightarrow \text{P2}$	$\text{IM3} \rightarrow \text{P3}$	$\text{R} \rightarrow \text{P1}$	$\text{R} \rightarrow \text{P2}$	$\text{R} \rightarrow \text{P3}$			
298	5.27×10^{-5}	7.87×10^{-6}	9.15×10^{10}	3.35×10^{10}	9.99×10^{10}	1.99×10^{-13}	7.28×10^{-14}	3.23×10^{-14}	65.44	23.94	10.62
322	4.46×10^{-5}	7.59×10^{-6}	8.86×10^{10}	3.79×10^{10}	9.46×10^{10}	1.63×10^{-13}	6.96×10^{-14}	2.95×10^{-14}	62.19	26.55	11.26
353	3.76×10^{-5}	7.35×10^{-6}	8.45×10^{10}	4.26×10^{10}	8.85×10^{10}	1.31×10^{-13}	6.58×10^{-14}	2.68×10^{-14}	58.59	29.43	11.99
380	3.33×10^{-5}	7.22×10^{-6}	8.11×10^{10}	4.56×10^{10}	8.39×10^{10}	1.11×10^{-13}	6.25×10^{-14}	2.49×10^{-14}	55.95	31.50	12.55
400	3.09×10^{-5}	7.16×10^{-6}	7.86×10^{10}	4.73×10^{10}	8.08×10^{10}	9.99×10^{-14}	6.02×10^{-14}	2.38×10^{-14}	54.32	32.74	12.94
425	2.85×10^{-5}	7.12×10^{-6}	7.56×10^{10}	4.89×10^{10}	7.72×10^{10}	8.87×10^{-14}	5.73×10^{-14}	2.26×10^{-14}	52.61	33.99	13.40
442	2.72×10^{-5}	7.11×10^{-6}	7.37×10^{10}	4.96×10^{10}	7.50×10^{10}	8.25×10^{-14}	5.56×10^{-14}	2.19×10^{-14}	51.56	34.75	13.69
457	2.62×10^{-5}	7.11×10^{-6}	7.21×10^{10}	5.01×10^{10}	7.32×10^{10}	7.77×10^{-14}	5.41×10^{-14}	2.14×10^{-14}	50.72	35.31	13.97
471	2.54×10^{-5}	7.12×10^{-6}	7.06×10^{10}	5.05×10^{10}	7.15×10^{10}	7.38×10^{-14}	5.27×10^{-14}	2.10×10^{-14}	50.03	35.73	14.24

Table S4h:

$P = 10^4$ bar											
T (K)	Equilibrium constants (bar^{-1})		Unimolecular rate constants (s^{-1})			Effective rate constants ($\text{cm}^3 \text{molecule}^{-1} \text{s}^{-1}$)			Branching ratios (%)		
	$K_p(x)$	$K_p(3)$	$k_2(1)$	$k_2(2)$	$k_2(3)$	$k_{\text{eff}}(1)$	$k_{\text{eff}}(2)$	$k_{\text{eff}}(3)$	$R(1)$	$R(2)$	$R(3)$
	$\text{R} \rightleftharpoons \text{IMx}$	$\text{R} \rightleftharpoons \text{IM3}$	$\text{IMx} \rightarrow \text{P1}$	$\text{IMx} \rightarrow \text{P2}$	$\text{IM3} \rightarrow \text{P3}$	$\text{R} \rightarrow \text{P1}$	$\text{R} \rightarrow \text{P2}$	$\text{R} \rightarrow \text{P3}$			
298	5.27×10^{-5}	7.87×10^{-6}	7.13×10^{11}	6.73×10^{10}	9.44×10^{11}	1.55×10^{-12}	1.46×10^{-13}	3.06×10^{-13}	77.42	7.29	15.28
322	4.46×10^{-5}	7.59×10^{-6}	7.56×10^{11}	8.28×10^{10}	9.54×10^{11}	1.39×10^{-12}	1.52×10^{-13}	2.98×10^{-13}	75.54	8.26	16.20
353	3.76×10^{-5}	7.35×10^{-6}	8.03×10^{11}	1.04×10^{11}	9.62×10^{11}	1.24×10^{-12}	1.60×10^{-13}	2.91×10^{-13}	73.33	9.46	17.21
380	3.33×10^{-5}	7.22×10^{-6}	8.37×10^{11}	1.22×10^{11}	9.67×10^{11}	1.15×10^{-12}	1.67×10^{-13}	2.87×10^{-13}	71.70	10.41	17.89
400	3.09×10^{-5}	7.16×10^{-6}	8.58×10^{11}	1.35×10^{11}	9.70×10^{11}	1.09×10^{-12}	1.72×10^{-13}	2.86×10^{-13}	70.41	11.11	18.48
425	2.85×10^{-5}	7.12×10^{-6}	8.82×10^{11}	1.52×10^{11}	9.72×10^{11}	1.03×10^{-12}	1.78×10^{-13}	2.85×10^{-13}	68.99	11.92	19.09
442	2.72×10^{-5}	7.11×10^{-6}	8.97×10^{11}	1.63×10^{11}	9.72×10^{11}	1.00×10^{-12}	1.83×10^{-13}	2.85×10^{-13}	68.12	12.47	19.41
457	2.62×10^{-5}	7.11×10^{-6}	9.08×10^{11}	1.73×10^{11}	9.73×10^{11}	9.79×10^{-13}	1.86×10^{-13}	2.85×10^{-13}	67.52	12.83	19.66
471	2.54×10^{-5}	7.12×10^{-6}	9.18×10^{11}	1.82×10^{11}	9.73×10^{11}	9.60×10^{-13}	1.90×10^{-13}	2.85×10^{-13}	66.90	13.24	19.86

Table S4i:

$P = 10^6$ bar											
T (K)	Equilibrium constants (bar^{-1})		Unimolecular rate constants (s^{-1})			Effective rate constants ($\text{cm}^3 \text{molecule}^{-1} \text{s}^{-1}$)			Branching ratios (%)		
	$K_p(x)$	$K_p(3)$	$k_2(1)$	$k_2(2)$	$k_2(3)$	$k_{\text{eff}}(1)$	$k_{\text{eff}}(2)$	$k_{\text{eff}}(3)$	$R(1)$	$R(2)$	$R(3)$
	$\text{R} \rightleftharpoons \text{IMx}$	$\text{R} \rightleftharpoons \text{IM3}$	$\text{IMx} \rightarrow \text{P1}$	$\text{IMx} \rightarrow \text{P2}$	$\text{IM3} \rightarrow \text{P3}$	$\text{R} \rightarrow \text{P1}$	$\text{R} \rightarrow \text{P2}$	$\text{R} \rightarrow \text{P3}$			
298	5.27×10^{-5}	7.87×10^{-6}	7.69×10^{11}	6.81×10^{10}	1.03×10^{12}	1.67×10^{-12}	1.48×10^{-13}	3.34×10^{-13}	77.60	6.88	15.52
322	4.46×10^{-5}	7.59×10^{-6}	8.21×10^{11}	8.40×10^{10}	1.05×10^{12}	1.51×10^{-12}	1.54×10^{-13}	3.28×10^{-13}	75.80	7.73	16.47
353	3.76×10^{-5}	7.35×10^{-6}	8.81×10^{11}	1.05×10^{11}	1.07×10^{12}	1.36×10^{-12}	1.63×10^{-13}	3.23×10^{-13}	73.67	8.83	17.50
380	3.33×10^{-5}	7.22×10^{-6}	9.26×10^{11}	1.24×10^{11}	1.08×10^{12}	1.27×10^{-12}	1.70×10^{-13}	3.21×10^{-13}	72.12	9.65	18.23
400	3.09×10^{-5}	7.16×10^{-6}	9.57×10^{11}	1.38×10^{11}	1.09×10^{12}	1.22×10^{-12}	1.76×10^{-13}	3.21×10^{-13}	71.05	10.25	18.70
425	2.85×10^{-5}	7.12×10^{-6}	9.91×10^{11}	1.56×10^{11}	1.10×10^{12}	1.16×10^{-12}	1.83×10^{-13}	3.22×10^{-13}	69.67	10.99	19.34
442	2.72×10^{-5}	7.11×10^{-6}	1.01×10^{12}	1.67×10^{11}	1.11×10^{12}	1.13×10^{-12}	1.87×10^{-13}	3.23×10^{-13}	68.90	11.40	19.70
457	2.62×10^{-5}	7.11×10^{-6}	1.03×10^{12}	1.78×10^{11}	1.11×10^{12}	1.11×10^{-12}	1.92×10^{-13}	3.25×10^{-13}	68.22	11.80	19.98
471	2.54×10^{-5}	7.12×10^{-6}	1.05×10^{12}	1.87×10^{11}	1.11×10^{12}	1.09×10^{-12}	1.96×10^{-13}	3.26×10^{-13}	67.62	12.16	20.22

Table S4h:

$P = 10^8 \text{ bar}$											
T (K)	Equilibrium constants (bar^{-1})		Unimolecular rate constants (s^{-1})			Effective rate constants ($\text{cm}^3 \text{ molecule}^{-1} \text{ s}^{-1}$)			Branching ratios (%)		
	$K_p(x)$ $\text{R} \rightleftharpoons \text{IMx}$	$K_p(3)$ $\text{R} \rightleftharpoons \text{IM3}$	$k_2(1)$ $\text{IMx} \rightarrow \text{P1}$	$k_2(2)$ $\text{IMx} \rightarrow \text{P2}$	$k_2(3)$ $\text{IM3} \rightarrow \text{P3}$	$k_{\text{eff}}(1)$ $\text{R} \rightarrow \text{P1}$	$k_{\text{eff}}(2)$ $\text{R} \rightarrow \text{P2}$	$k_{\text{eff}}(3)$ $\text{R} \rightarrow \text{P3}$	$R(1)$	$R(2)$	$R(3)$
298	5.27×10^{-5}	7.87×10^{-6}	7.69×10^{11}	6.81×10^{10}	1.03×10^{12}	1.67×10^{-12}	1.48×10^{-13}	3.35×10^{-13}	77.57	6.87	15.56
322	4.46×10^{-5}	7.59×10^{-6}	8.22×10^{11}	8.40×10^{10}	1.05×10^{12}	1.51×10^{-12}	1.54×10^{-13}	3.28×10^{-13}	75.80	7.73	16.47
353	3.76×10^{-5}	7.35×10^{-6}	8.82×10^{11}	1.05×10^{11}	1.07×10^{12}	1.36×10^{-12}	1.63×10^{-13}	3.24×10^{-13}	73.63	8.83	17.54
380	3.33×10^{-5}	7.22×10^{-6}	9.27×10^{11}	1.24×10^{11}	1.08×10^{12}	1.27×10^{-12}	1.70×10^{-13}	3.22×10^{-13}	72.08	9.65	18.27
400	3.09×10^{-5}	7.16×10^{-6}	9.58×10^{11}	1.38×10^{11}	1.09×10^{12}	1.22×10^{-12}	1.76×10^{-13}	3.22×10^{-13}	71.01	10.24	18.74
425	2.85×10^{-5}	7.12×10^{-6}	9.93×10^{11}	1.56×10^{11}	1.10×10^{12}	1.16×10^{-12}	1.83×10^{-13}	3.23×10^{-13}	69.63	10.98	19.39
442	2.72×10^{-5}	7.11×10^{-6}	1.01×10^{12}	1.68×10^{11}	1.11×10^{12}	1.14×10^{-12}	1.88×10^{-13}	3.24×10^{-13}	69.01	11.38	19.61
457	2.62×10^{-5}	7.11×10^{-6}	1.03×10^{12}	1.78×10^{11}	1.11×10^{12}	1.11×10^{-12}	1.92×10^{-13}	3.25×10^{-13}	68.22	11.80	19.98
471	2.54×10^{-5}	7.12×10^{-6}	1.05×10^{12}	1.87×10^{11}	1.12×10^{12}	1.10×10^{-12}	1.96×10^{-13}	3.27×10^{-13}	67.78	12.08	20.15

Samenvatting

In **Hoofdstuk 1** werden polycyclische aromatische koolwaterstoffen (PAHs) en hun derivaten geïntroduceerd als alomtegenwoordige atmosferische pollutanten met toxische, mutagene en kankerverwekkende eigenschappen. Deze verbindingen worden in de atmosfeer gebracht als een bijproduct van verbrandingsprocessen. PAHs trokken dus in recente jaren veel aandacht omwille van hun inherente toxiciteit. Naftaleen is de vluchtigste en meest voorkomende PAH in de stedelijke gebieden. In de troposfeer wordt verwacht dat het meest atmosferische verliesproces voor deze semi-vluchtige PAHs een gasfase reactie is met hydroxyl radicalen. Atmosferische reacties van naftaleen leveren dikwijls meer carcinogene degradatieproducten op dan het originele PAH. Het is bijgevolg belangrijk om de vernietiging van atmosferisch naftaleen te begrijpen door oxidatiereacties met OH* radicalen.

Een belangrijke eerste stap in de oxidatie van zwavelverbindingen na vrijlating in de atmosfeer van zowel natuurlijke als antropogene bronnen heeft ook te maken met reacties van OH* radicalen met de zwavelverbindingen welke een sleutelrol spelen bij de oxiderende kracht van de atmosfeer. Bepaling van de snelheidsconstante van deze reacties zal bijdragen tot een beter inzicht in de atmosferische zwavelcyclus. De studie van de reactiemechanismen kan bovendien bijkomende informatie opleveren voor de verdere oxidatiestappen die leiden tot SO₂ en sulfaten. Thiofeen kan belangrijker worden zowel bij verbrandingsprocessen als in de atmosferische chemie als gevolg van de ontwikkeling van nieuwe energietechnologieën in verband met de conversie en verbranding van kolen, schaalolie en petroleum. Meer specifiek moet de kinetiek

ven de oxidatiereactie van thiofeen met OH^\bullet radicalen gekwantificeerd worden om de levensduur van deze verbinding in de atmosfeer te schatten.

In **Hoofdstuk 2** wordt een overzicht van alle gebruikte kwantummechanische theorieën gegeven, zoals Hartree-Fock theorie, Møller-Plesset storingstheorie, “Coupled Cluster” theorie evenals dichtheidsfunctionaal theorie (DFT), met hoofdfocus op de gebruikte uitwisselings-correlatie functionalen (B3LYP, ω B97XD, UM05-2x en UM06-2x). Dit hoofdstuk vervolgt met een inleiding tot statistische thermodynamica en een overzicht van de gebruikte methoden voor de berekening van partitiefuncties en thermodynamische functies (U , H , S , G). Tot slot, gebruik makend van het formalisme van faseruimte integralen, wordt de RRKM theorie voor unimoleculaire kinetische snelheidsconstanten weergegeven, samen met simplicaties in de limiet voor hoge drukken zoals transitietoestandstheorie (TST) evenals variationele transitietoestandstheorie (VTST).

In **Hoofdstukken 3–7** werden de oxidatiemechanismen van naftaleen en thiofeen, geïnitieerd door hydroxyl radicalen, theoretisch bestudeerd met dichtheidsfunctionaal theorie (DFT) gebruik makend van verschillende uitwisselings-correlatie functionalen (B3LYP, ω B97XD, UM05-2x en UM06-2x) en een zeer grote basisset (aug-cc-pVTZ) tijdens alle stadia van de studie. Met het oog op kwantitatieve inzichten in deze reactiemechanismen werden vergelijkingen gemaakt met benchmark computationele resultaten verkregen op hoog niveau met de samengestelde CBS-QB3 *ab initio* benadering ten einde uit te maken welke uitwisselings-correlatie functionaal de meest accurate energiebarrières en reactie-energieën oplevert. Er werd genoteerd dat DFT methodes alleen onvoldoende zijn voor kwantitatief onderzoek van het potentiaaloppervlak geassocieerd met de oxidatiereactie, geïnitieerd door hydroxyl radicalen, gegeven het onvermogen van vele populaire DFT functionalen om niet-gebonden interacties en barrièrehoogten kwantitatief te beschrijven. Met het oog op chemische inzichten werden de verkregen resultaten geanalyseerd in termen van nucleus independent chemical shift (NICS) aromaticiteitsindices, bindingsorden, natural bond orbital (NBO) bezettingen en donor-acceptor interactie-energieën. Naast het bekomen van energiebarrières en reactie-energieën op CBS-QB3 niveau was het hoofddoel van de voorliggende studie het leveren van goede kinetische vergelijkingen, kinetische snelheidsconstanten en branching ratios om de originele experimenten volledig te ontrafelen via transitietoestandstheorie (TST) of variationele transitietoestandstheorie (VTST).

Voor reactiemechanismen met een substantiële activeringsenergie barrière is transitietoestandstheorie niet geschikt. Indien echter geen waarneembare

barrièrehoogte bestaat langs de reactiecoördinaat spelen zowel de activeringsenergie als activeringsentropie een belangrijke rol bij het definiëren van de transitietoestand en kanonische VTST moet gebruikt worden om semikwantitatieve resultaten te bekomen voor de kinetische snelheidsconstanten. VTST werd gebruikt samen met de energieprofielen berekend op het UM06-2x/aug-cc-pVTZ niveau. De reden voor deze keuze is dat de UM06-2x uitwisselings-correlatie functionaal gekend is als zijnde de beste voor thermochemische toepassingen voor elementen uit de hoofdgroepen. Het UM06-2x/aug-cc-pVTZ niveau levert dezelfde energie ordening op voor activerings- en reactie-energieën als deze gevonden voor de benchmark CBS-QB3 benadering. Kinetische snelheidsconstanten en branching ratios verkregen via de VTST en statistische Rice–Ramsperger–Kassel–Markus (RRKM) benaderingen, samen met dezelfde (UM06-2x/aug-cc-pVTZ) energieprofielen, verschillen niet veel van elkaar. Het blijkt bijgevolg gewettigd te stellen dat RRKM resultaten eveneens semikwantitatieve inzichten opleveren in de kinetische snelheidsconstanten.

In **Hoofdstuk 3** werden reactiemechanismen voor de aanvangsstadia van de naftaleen oxidatie bij hoge temperaturen ($T \geq 600$ K) theoretisch bestudeerd. Deze stadia corresponderen met de verwijdering van waterstofatomen door hydroxyl radicalen en de vorming van 1- en 2-naftyl radicalen. De uitstekende overeenkomst met de beschikbare experimentele kinetische snelheidsconstanten tonen aan dat een tweestaps reactieschema prevaleert. Analyse van de berekende structuren, bindingsorden en vrije energieprofielen toont aan dat de reactiestappen, betrokken bij de verwijdering van waterstofatomen door OH radicalen, voldoen aan het Hammond principe. Berekeningen van de branching ratios tonen eveneens aan dat deze reacties geen uitgesproken site-selectivity vertonen.

In **Hoofdstuk 4** werden de oxidatiemechanismen van naftaleen door hydroxyl radicalen onder inerte (He) condities theoretisch bestudeerd. Vergelijking met het experiment bevestigt dat bij de OH-additie het reactiepad leidend tot 1-naftol, de eerste bimoleculaire reactiestap een effectieve negatieve activeringsenergie heeft rond $-1.5 \text{ kcal mol}^{-1}$ terwijl deze stap gekarakteriseerd wordt door een activeringsenergie rond 1 kcal mol^{-1} voor het OH-additie reactiepad leidend tot 2-naftol. Effectieve snelheidsconstanten werden berekend volgens een steady state analyse op een tweestaps model reactiemechanisme. In overeenstemming met het experiment, wijzen de corresponderende verkregen “branching ratios” er op, dat bij temperaturen beneden 410 K, het meest voorkomend product bij de oxidatie van naftaleen door hydroxyl radicalen, 1-naftol moet zijn eerder dan 2-naftol. De regio selectiviteit van de OH[•] additive op naftaleen daalt met

toenemende temperatuur en dalende drukken. Wegens de licht positieve of zelfs negatieve activeringsenergieën, tonen de RRKM berekeningen aan dat de transitietoestandsbenadering het laat afweten bij atmosferische druk (1 bar) voor de eerste bimoleculaire reactiestappen. Zeer hoge drukken, hoger dan 10^5 bar, blijken nodig te zijn om in zekere mate (binnen ~ 5 % nauwkeurigheid) de geldigheid van de benadering te herstellen voor al de reactiekanalen die betrokken zijn bij het OH additie reactiepad. Analyse van de berekende structuren, bindingsorden en vrije energieprofielen tonen aan dat al de reactiestappen welke betrokken zijn bij de oxidatie van naftaleen door OH radicalen, voldoen aan het principe van Hammond. NICS indices en NBO analyse tonen nook aan dat de berekende activerings- en reactie-energieën grotendeels gedictieerd worden door alternaties van de aromaticiteit en, in mindere mate, door anomere hyperconjugatie-effecten.

In **Hoofdstuk 5** werd de atmosferische oxidatie van het naftaleen-OH adduct $[\text{C}_{10}\text{H}_8\text{OH}]^*$ (R1) door moleculaire zuurstof in de triplet grondtoestand bestudeerd door enkel dichtheidsfunctionaal theorie aan te wenden. Vanuit thermodynamisch oogpunt is het gunstigste proces O_2 additie aan de C_2 positie in *syn* mode gevolgd door O_2 additie aan de C_2 positie in *anti* mode, O_2 additie aan de C_4 positie in *syn* mode en O_2 additie aan de C_4 positie in *anti* mode als tweede, derde en vierde meest gunstige proces. De *syn* additie modes aan deze posities zijn thermodynamisch begunstigd over de *anti* modes door de vorming van intramoleculaire waterstofbindingen tussen de hydroxyl en peroxy substituenten. Analyse van de berekende structuren, bindingsorden en vrije energieprofielen tonen aan dat de reactiestappen, betrokken in de oxidatie van het $[\text{C}_{10}\text{H}_8\text{OH}]^*$ adduct door O_2 voldoen aan het principe van Hammond. Kinetische snelheidsconstanten en branching ratios onder atmosferische druk en in het fall-off regime werden bekomen via transitietoestand en RRKM theorieën. Door vergelijking met het experiment bevestigen deze data de relevantie van een tweestaps reactiemechanisme. Welke ook de additie mode, de O_2 additie in C_4 positie is kinetisch bevoordeligd over O_2 additie in C_2 positie in tegenstelling met de verwachtingen vanuit de thermodynamica en reactie-energieën. Onder een kinetische controle van de reactie en in lijn met de berekende reactie energiebarrières, is het meest efficiënte proces de O_2 additie aan de C_4 positie in *syn* mode, gevolgd door O_2 additie aan de C_2 positie in *anti* mode, O_2 additie aan de C_4 positie in *anti* mode, en O_2 additie aan de C_2 positie in *anti* mode, als het tweede, derde en vierde snelste proces. De berekende branching ratios wijzen er ook op dat de regio selectiviteit van de reactie daalt met stijgende temperatuur en dalende drukken.

In **Hoofdstuk 6** werd het isomerisatieproces van naftaleen peroxide radicalen $[\text{C}_{10}\text{H}_8\text{OH}]^{\bullet}-\text{O}_2$ in peroxi of oxi hydroperoxide radicalen via ringsluiting en intramoleculaire waterstof transfers computationeel bestudeerd met alleen DFT. De cyclisatie van het R1-2OO-*syn* peroxy radicaal in het R1-2,9OO-*syn* bicyclische peroxy radicaal door vorming van een O–O brug is endotherm en reversibel. Vanuit kinetisch standpunt zijn de twee meest begunstigde processen voor het R1-2OO-*syn* peroxy radicaal ringsluiting tot het R1-2,9OO-*syn* bicyclische radicaal en conversie door waterstoftransfer tot het R1-P2O1-*syn* oxy hydroperoxide radicaal. Onder al de bestudeerde reactiekanalen is het laatste proces kinetisch het meest competitieve. Vanuit de berekende snelheidsconstanten blijkt dat het R1-2OO-*syn* peroxy radicaal chemisch veel meer reactief is dan de R1-4OO-*syn* species. Alles samen genomen blijken de atmosferische oxidatiemechanismen van naftaleen sterk verschillend te zijn van deze van benzeen en derivaten er van.

In **Hoofdstuk 7** werden de oxidatiemechanismen van thiofeen door hydroxyl radicalen onder inerte omstandigheden (Ar) bestudeerd met DFT en met de benchmark CBS-QB3 benadering. Kinetische snelheidsconstanten werden berekend met VTST en met de statistische RRKM theorie. Effectieve snelheidsconstanten werden berekend via een steady state analyse gebaseerd op een tweestaps model reactiemechanisme. In overeenstemming met de experimentele resultaten wijzen de berekende branching ratios er op dat het kinetisch meest efficiënte proces betrekking heeft op OH additie aan een koolstofatoom naast een zwavelatoom. Wegens de aanwezigheid van negatieve activeringsenergieën zijn drukken hoger dan 10^4 bar vereist om de hoge druk limiet te bereiken. NICS indices en NBO analyse tonen aan dat de berekende activeringsenergieën gedecteerd worden door veranderingen in aromaticiteit en ladingsoverdracht effecten te wijten aan vrije elektronenparen van zwavel naar ledige π^* orbitalen.